1

Kinetic stability of Chapman–Enskog plasmas

Archie F.A. Bott [1,2,3,†], **S.C. Cowley** [4] **and A.A. Schekochihin** [1,5]

[1]Department of Physics, University of Oxford, Parks Road, Oxford OX1 3PU, UK

[2]Trinity College, Broad St, Oxford OX1 3BH, UK

[3]Department of Astrophysical Sciences, Princeton University, Peyton Hall, Princeton, NJ 08544, USA

[4]Princeton Plasma Physics Laboratory, 100 Stellarator Road, Princeton, NJ 08540, USA

[5]Merton College, Merton St, Oxford OX1 4JD, UK

In this paper, we investigate the kinetic stability of classical, collisional plasma – that is, plasma in which the mean-free-path λ of constituent particles is short compared with the length scale L over which fields and bulk motions in the plasma vary macroscopically, and the collision time is short compared with the evolution time. Fluid equations are typically used to describe such plasmas, since their distribution functions are close to being Maxwellian. The small deviations from the Maxwellian distribution are calculated via the Chapman–Enskog (CE) expansion in $\lambda/L \ll 1$, and determine macroscopic momentum and heat fluxes in the plasma. Such a calculation is only valid if the underlying CE distribution function is stable at collisionless length scales and/or time scales. We find that at sufficiently high plasma β, the CE distribution function can be subject to numerous microinstabilities across a wide range of scales. For a particular form of the CE distribution function arising in strongly magnetised plasma (*viz.* plasma in which the Larmor periods of particles are much smaller than collision times), we provide a detailed analytic characterisation of all significant microinstabilities, including peak growth rates and their associated wavenumbers. Of specific note is the discovery of several new microinstabilities, including one at sub-electron-Larmor scales (the 'whisper instability') whose growth rate in certain parameter regimes is large compared with other instabilities. Our approach enables us to construct the kinetic stability maps of classical, two-species collisional plasma in terms of λ, the electron inertial scale d_e and the plasma β. This work is of general consequence in emphasising the fact that high-β collisional plasmas can be kinetically unstable; for strongly magnetised CE plasmas, the condition for instability is $\beta \gtrsim L/\lambda$. In this situation, the determination of transport coefficients via the standard CE approach is not valid.

Keywords: astrophysical plasmas, fusion plasma, plasma instabilities

---

† Email address for correspondence: archie.bott@physics.ox.ac.uk

1. Introduction

Answering the question of when a plasma can be described adequately by fluid equations is fundamental for a comprehensive understanding of plasma dynamics. It is well known that some physical effects in plasmas – for example, Landau damping – specifically require a fully kinetic description in terms of distribution functions of the plasma's constituent particles (Landau 1946). However, for many other plasma processes, a detailed description of the underlying particle distribution provides little additional understanding of the essential physics governing that process. Characterising such processes with fluid equations, which describe the evolution of macroscopic physical quantities such as density, fluid velocity and temperature, often simplifies the description and therefore aids understanding. Fluid equations are also easier to solve numerically than kinetic equations: the latter reside in six-dimensional phase space (and time), with three additional dimensions – the velocity space – when compared with the former. The underlying difficulty associated with determining when a plasma is a fluid is finding a closed set of equations in the macroscopic plasma variables. The derivation of fluid equations from the Maxwell–Vlasov–Landau equations governing the evolution of the plasma's distribution functions is carried out by taking moments (that is, integrating the governing equations and their outer products with velocity $\boldsymbol{v}$ over velocity space). However, the resulting equations are not closed: the evolution equation of the zeroth-order moment (density) requires knowledge of the evolution of the first-order moment, the evolution equation for the first-order moment needs the second-order moment and so on. For plasma-fluid equations to be able to describe the evolution of a plasma without reference to that plasma's underlying distribution functions, a closure hypothesis or an approximation relating higher-order moments to lower ones is required.

For a collisional plasma – i.e. one in which the mean free paths λ_s and collision times τ_s of the ions and electrons ($s = i, e$) are much smaller than the typical length scale L and time scale τ_L on which macroscopic properties of the plasma change – there is a procedure for achieving such a closure: the Chapman–Enskog (CE) expansion (Chapman & Cowling 1970; Enskog 1917; Cercignani 1988). It is assumed that, in a collisional plasma, the small perturbations of the distribution functions away from a Maxwellian equilibrium have typical size $\epsilon \sim \lambda_s/L \sim \tau_s/\tau_L \ll 1$ (assuming sonic motions, and $\lambda_i \sim \lambda_e$). Since the perturbation is small, its form can be determined explicitly by performing an asymptotic expansion of the Maxwell–Vlasov–Landau equations. Once the underlying distribution is known, the relevant moments can be calculated – in particular, the momentum and heat fluxes are the second- and third-order moments of the $O(\epsilon)$ non-Maxwellian component of the distribution function. The CE expansion applied to a two-species magnetised plasma was worked out by Braginskii (1965). Subsequent studies have refined and extended various aspects of his calculation (Epperlein 1984; Mikhailovskii & Tsypin 1984; Epperlein & Haines 1986; Helander, Krasheninnikov & Catto 1994; Simakov & Catto 2004). In this paper, we will refer to the distribution functions associated with the CE expansion as CE distribution functions, and plasmas with particle distribution functions given by CE distribution functions as CE plasmas.

However, the theory constructed as outlined above is incomplete. For the CE expansion to provide an adequate fluid closure, the resulting distribution functions must be stable to all kinetic instabilities with length scales shorter than the longest mean free path, and time scales shorter than the macroscopic plasma time scale τ_L. Such instabilities (if present) are known as microinstabilities. We emphasise that these microinstabilities should be distinguished conceptually from instabilities describable by the closed set of plasma-fluid equations: for example, Rayleigh–Taylor (Rayleigh 1883; Taylor 1950;

Takabe *et al.* 1985; Kull 1991), magnetorotational (Balbus & Hawley 1991; Hawley & Balbus 1991), magnetoviscous (Quataert, Dorland & Hammett 2002; Balbus 2004; Islam & Balbus 2005) or magnetothermal/heat-flux-driven buoyancy instabilities (Balbus 2000, 2001; Quataert 2008; Kunz 2011). Kinetic microinstabilities should also be distinguished from the small-scale instabilities that arise in solving higher-order ($O(\epsilon^2)$) fluid equations obtained from the CE asymptotic expansion (for neutral fluids, these are called the Burnett equations – see García-Colín, Velasco & Uribe 2008). Such instabilities are not physical because they arise at scales where the equations themselves do not apply (Bobylev 1982). Fluid instabilities do not call into question the validity of the fluid equations themselves; in contrast, if microinstabilities occur, the plasma-fluid equations obtained through the closure hypothesis are physically invalid, irrespective of their own stability.

Microinstabilities have been studied in depth for a wide range of classical plasmas by many authors; see, for e.g. Davidson (1983), Gary (1993) and Hasegawa (2012) for three different general perspectives on microinstability theory. Although it can be shown that a Maxwellian distribution is always immune to such instabilities (Bernstein 1958; Krall & Trivelpiece 1973), anisotropic distribution functions are often not (Kahn 1962; Furth 1963; Kalman, Montes & Quemada 1968). A notable example is the Weibel instability, which occurs in counter-streaming unmagnetised plasmas (Fried 1959; Weibel 1959). The linear theory of such instabilities is generally well known (for modern reviews, see Lazar, Schlickeiser & Poedts 2009; Ibscher, Lazar & Schlickeiser 2012). Microinstabilities in magnetised plasma have also been comprehensively studied. The ion firehose and mirror instabilities are known to occur in plasmas with sufficient ion-pressure anisotropy and large enough plasma β (Chandrasekhar, Kaufman & Watson 1958; Parker 1958; Vedenov & Sagdeev 1958; Hasegawa 1969; Hall 1981; Hellinger 2007), while electron-pressure anisotropy can also result in microinstabilities of various types (Kennel & Petschek 1966; Hollweg & Völk 1970; Gary & Madland 1985).

A number of authors have noted that microinstabilities, if present, will have a significant effect on the macroscopic transport properties of plasmas (Kahn 1964; Schekochihin *et al.* 2005, 2008; Melville, Schekochihin & Kunz 2016; Riquelme, Quataert & Verscharen 2016; Komarov *et al.* 2016, 2018; Roberg-Clark *et al.* 2018*a*; Drake *et al.* 2021). Typically (although not always), once the small-scale magnetic and electric fields associated with microinstabilities have grown, they will start to scatter particles, which in turn will alter the plasma's distribution functions. This has micro- and macroscopic consequences for plasma behaviour. From the microscopic perspective, it changes the course of the evolution of the microinstabilities themselves – by e.g. reducing the anisotropy of the underlying particle distribution functions (Hellinger *et al.* 2014; Riquelme, Quataert & Verscharen 2018). From the macroscopic perspective, the changes to the distribution functions will alter both heat and momentum fluxes in the plasma (which, as previously mentioned, are determined by non-Maxwellian terms in the distribution function). In this picture, a plasma subject to microinstabilities in some sense generates its own effective anomalous collisionality (Schekochihin *et al.* 2008; Kunz, Schekochihin & Stone 2014; Mogavero & Schekochihin 2014; Squire *et al.* 2017; Kunz *et al.* 2020). The typical values of the altered fluxes attained must depend on the saturated state of microinstabilities (Schekochihin *et al.* 2010). Exploring the mechanisms leading to saturation of both unmagnetised, Weibel-type instabilities (e.g. Davidson *et al.* 1972; Lemons, Winske & Gary 1979; Califano *et al.* 1998; Califano, Cecchi & Chiuderi 2002; Kato 2005; Pokhotelov & Amariutei 2011; Ruyer *et al.* 2015) and magnetised instabilities (e.g. Kuznetsov, Passot & Sulem 2007; Pokhotelov *et al.* 2008; Rosin *et al.* 2011; Rincon, Schekochihin & Cowley 2015; Riquelme, Quataert & Verscharen 2015) continues to be an active research area. Simulation results (Hellinger *et al.* 2009; Guo, Sironi & Narayan 2014; Kunz *et al.* 2014; Melville *et al.* 2016; Riquelme

et al. 2016; Guo, Sironi & Narayan 2018; Bott *et al.* 2021*a*) support the claim that the saturation amplitude of such microinstabilities is typically such that the plasma maintains itself close to marginality of the relevant instability.

Do these kinetic instabilities afflict the CE distribution function? Naively, it might be assumed not, since it is 'almost' Maxwellian. However, it turns out that, provided the plasma β is sufficiently high, small distortions from a Maxwellian can be sufficient to lead to instability. Instabilities of a CE distribution function in an unmagnetised plasma were first explored by Kahn (1964), who considered a collisional electron plasma (mean free path λ_e) with macroscopic variations in density, temperature and velocity (scale $\sim L$). He showed that the CE distribution function in such a plasma would have two non-Maxwellian terms of order λ_e/L – an antisymmetric term associated with heat flux, and another term associated with velocity shear – and that the latter term would result in the so-called transverse instability. Kahn (1964) also claimed that this instability would lead to a significant change in the plasma viscosity, and other transport coefficients. Albright (1970*a*,*b*) further developed the theory of the transverse instability, including a quasi-linear theory resulting in isotropisation of the underlying electron distribution function.

The stability of the CE distribution function was later considered by Ramani & Laval (1978). They found that in an initially unmagnetised two-species plasma supporting a fluid-scale electron-temperature gradient (scale L_T, no flow shear), the second-order terms (in λ/L_T) in the electron distribution function could result in the formation of unstable waves, with typical real frequencies $\varpi \propto \lambda_e/L_T$, and growth rates $\gamma_{\mathrm{RL}} \propto (\lambda_e/L_T)^2$. Similarly to Kahn (1964), they argued that the presence of such instabilities would suppress the macroscopic heat flux in the plasma (which in a collisional plasma is carried predominantly by electrons). This particular instability has also been proposed as an explanation for the origin of the cosmic magnetic field (Okabe & Hattori 2003). Subsequent authors have explored further the idea that non-Maxwellian components of the electron distribution function required to support a macroscopic heat flux can lead to kinetic instability. Levinson & Eichler (1992) considered the effect of introducing a uniform, macroscopic magnetic field into the same problem, and found that a faster instability feeding off first-order heat-flux terms in the CE distribution function – the whistler instability – arose at the electron-Larmor scale, with $\gamma_{\mathrm{whistler},T} \propto \lambda_e/L_T$. A quasi-linear theory of this instability was subsequently constructed by Pistinner & Eichler (1998). Both Levinson & Eichler (1992) and Pistinner & Eichler (1998) proposed that the instability at saturation would result in a suppressed heat flux (see also Gary & Li 2000). More recently, the whistler instability has been studied in simulations of high-β plasma – with two groups independently finding both the onset of instability at electron scales, and evidence of a suppression of heat flux (Roberg-Clark *et al.* 2016, 2018*a*; Komarov *et al.* 2018; Roberg-Clark *et al.* 2018*b*). Drake *et al.* (2021) constructed a theoretical model for whistler-regulated heat transport based on a set of reasonable assumptions that were motivated by these prior simulations.

The possibility of microinstabilities associated with the ion CE distribution function was also considered by Schekochihin *et al.* (2005), who found that weakly collisional, magnetised plasma undergoing subsonic, turbulent shearing motions can be linearly unstable to firehose and mirror instabilities at sufficiently high β_i (where β_i is the ion plasma beta). This is because the shearing motions give rise to an ion-pressure anisotropy $\Delta_i \sim \lambda_i^2/L_V^2$, where L_V is the length scale associated with the shearing motions. For $|\Delta_i| \gtrsim \beta_i^{-1}$, the mirror- and firehose-instability thresholds can be crossed (the mirror instability is trigged by sufficiently positive pressure anisotropy, the firehose instability

by negative pressure anisotropy). Beyond its threshold, the maximum firehose-instability growth rate γ_{fire} was found to satisfy $\gamma_{\text{fire}} \propto |\Delta_i + 2/\beta_i|^{1/2}$, whilst for the mirror instability, the maximum growth rate was $\gamma_{\text{mirr}} \propto \Delta_i - 1/\beta_i$. Such destabilisation of shearing motions was confirmed numerically by Kunz *et al.* (2014), followed by many others (e.g. Riquelme *et al.* 2015, 2016, 2018; Melville *et al.* 2016).

In this paper, we examine the criteria for the CE distribution function to be stable to microinstabilities at collisionless scales – i.e. at $k\lambda_s \gg 1$ (where k is the microinstability wavenumber), and $\gamma\tau_L \gg 1$. In a two-species plasma with a fixed mass ratio $\mu_e \equiv m_e/m_i$, $T_e = T_i$ and an ion charge Z_i that is not very large, these criteria turn out to be relationships between three dimensionless parameters: λ/L, d_e/L and β, where $\lambda \equiv \lambda_e = Z_i^2\lambda_i$ is the mean free path for both ions and electrons in a hydrogen plasma, and d_e is the electron inertial scale. The first criterion (which we refer to as the β-stabilisation condition) is that the ratio λ/L be much smaller than the reciprocal of the plasma β, *viz.* $\lambda\beta/L \ll 1$. This condition arises because the microinstabilities discussed in this paper are stabilised (usually by Lorentz forces) at sufficiently low β. The second criterion (the collisional-stabilisation condition) is that the characteristic wavenumber k_{peak} of the fastest-growing microinstability in the absence of collisional effects be comparable to (or smaller than) the reciprocal of the mean free path: $k_{\text{peak}}\lambda \lesssim 1$. Unlike the β-stabilisation condition, we do not justify this condition rigorously, because our calculations are only valid for wavenumbers k such that $k\lambda \gg 1$; thus, we cannot say anything definitive about the $k\lambda \lesssim 1$ regime. We do, however, show that another, more restrictive stabilisation condition that one might naively expect to exist on account of collisions – that microinstabilities cannot occur if their growth rate γ is smaller than the collision frequency (*viz.* $\gamma\tau_s \lesssim 1$) – does not, in fact, apply to the most significant microinstabilities in CE plasma. There are good physical reasons to believe that the CE distribution function is stable against collisionless microinstabilities if the collisional-stabilisation condition $k_{\text{peak}}\lambda \lesssim 1$ is satisfied: not least that the typical growth time of the fastest microinstability in CE plasma (calculated neglecting collisional damping of microinstabilities) becomes comparable to the macroscopic evolution time scale τ_L. We thus assume the validity of the collisional-stabilisation condition throughout this paper. How k_{peak} relates to the other physical parameters is in general somewhat complicated; however, typically, the collisional-stabilisation condition can be written as a lower bound on the ratio d_e/L. For example, in the limit of very high β, it is $d_e/L > (m_e/m_i)^{-1/6}(\lambda/L)^{2/3}$ (see § 4.2).

If both the β-stabilisation and collisional-stabilisation conditions are violated, we demonstrate that CE plasma will be subject to at least one microinstability, and quite possibly multiple microinstabilities across a wide range of scales. Some of these microinstabilities are thresholdless – that is, without including collisional effects, they will occur for CE distributions departing from a Maxwellian distribution by an asymptotically small amount. Note that all significant microinstabilities associated with the CE distribution function are 'low frequency': their growth rate γ satisfies $\gamma \ll kv_{\text{th}s}$, where k is the typical wavenumber of the instability, and $v_{\text{th}s}$ the thermal velocity of the particles of species s. This property enables a small anisotropy of the distribution function to create forces capable of driving microinstabilities (see § 2.5).

In this paper, we characterise all significant microinstabilities that arise at different values of λ/L, β and d_e/L for a particular form of the CE distribution function appropriate for a strongly magnetised plasma – that is, a plasma where the Larmor radii of ions and electrons are much smaller than the corresponding mean free paths of these particles. We treat this particular case because of its importance to astrophysical systems, which almost always possess macroscopic magnetic fields of sufficient strength to magnetise their constituent particles (Schekochihin & Cowley 2006). Our characterisation

of microinstabilities focuses on providing the maximum microinstability growth rates, as well as the wavenumbers at which this growth occurs. We find that there exist two general classes of microinstabilities: those driven by the non-Maxwellian component of the CE distribution associated with temperature gradients, and those driven by the non-Maxwellian component associated with bulk velocity gradients ('shear'). We refer to these two non-Maxwellian terms (which exist for both the ion and electron CE distribution functions) as the CE temperature-gradient terms and the CE shear terms, respectively. Microinstabilities driven by the CE temperature-gradient terms are called the CE temperature-gradient-driven (CET) microinstabilities, while those driven by the CE shear terms are the CE shear-driven (CES) microinstabilities.

As expected, within this general microinstability classification scheme, we recover a number of previously identified microinstabilities, including the (electron-shear-driven) transverse instability (which we discuss in §§ 4.3.3 and 4.4.9), the whistler instability (§ 4.3.2), the electron mirror instability (§ 4.3.4), the electron firehose instability (§§ 4.4.6 and 4.4.7), the ordinary-mode instability (§ 4.4.11), the (electron-temperature-gradient-driven) whistler heat-flux instability (§§ 3.3.1 and 3.3.2) and the (ion-shear-driven) mirror (§ 4.3.1) and firehose (§§ 4.4.1, 4.4.2, 4.4.3, 4.4.4 and 4.4.5) instabilities. We also find four microinstabilities that, to our knowledge, have not been previously discovered: two ion-temperature-gradient-driven ones at ion Larmor scales – the slow-hydromagnetic-wave instability (§ 3.3.3) and the long-wavelength kinetic-Alfvén wave instability (§ 3.3.4) – and two electron-shear-driven ones – the electron-scale-transition (EST) instability (§ 4.4.8) and the whisper instability (§ 4.4.10) – at electron-Larmor and sub-electron-Larmor scales, respectively. Of these microinstabilities, the whisper instability seems to be of particular significance: it has an extremely large growth rate in certain parameter regimes, and is associated with a new high-β wave in a Maxwellian plasma, which also appears to have previously escaped attention. For convenience, a complete index of microinstabilities discussed in this paper is given in table 1, while the peak growth rates of these microinstabilities and the scales at which they occur (for a hydrogen CE plasma) are given in table 2. There do exist microinstabilities in CE plasma that are not represented in tables 1 and 2; however, we claim that the instabilities discussed in this paper are the most significant, on account of their large growth rates and/or low β-stabilisation thresholds compared with the unrepresented ones.

Having systematically identified all significant microinstabilities, we can construct 'stability maps' of strongly magnetised CE plasma using 'phase diagrams' over a two-dimensional (λ/L, d_e/L) parameter space at a fixed β. An example of such a map (for a hydrogen plasma with equal ion and electron temperatures) is shown in figure 1. The entire region of the (λ/L, d_e/L) space depicted in figure 1 could naively be characterised as pertaining to classical, collisional plasma, and thus describable by fluid equations, with transport coefficients given by standard CE theory. However, there is a significant region of the parameter space (which is demarcated by boundaries corresponding to the β-stabilisation and collisional-stabilisation conditions) that is unstable to microinstabilities. In fact, in strongly magnetised plasma, the collisional-stabilisation condition is never satisfied, because there exist microinstabilities whose characteristic length scales are the ion- and electron-Larmor radii, respectively; this being the case, only the β-stabilisation condition guarantees kinetic stability.

The effect of microinstabilities being present in CE plasma would be to change the non-Maxwellian components of the distribution function, and therefore to alter the CE-prescribed resistivity, thermal conductivity and/or viscosity. Identifying the dominant microinstability or microinstabilities in such plasmas (as is done in figure 1 for a hydrogen

Microinstability name	Section(s)	Other names occurring in literature	Driving CE term
Mirror instability	4.3.1	—	Ion-velocity shear
Firehose instability	4.4.1, 4.4.2, 4.4.3, 4.4.4, 4.4.5	Garden-hose instability	Ion-velocity shear
Slow-hydromagnetic-wave instability*	3.3.3	—	Ion-temperature gradient
Long-wavelength kinetic-Alfvén wave (KAW) instability*	3.3.4	—	Ion-temperature gradient
CES whistler instability	4.3.2	Electron-cyclotron (whistler) instability	Electron-velocity shear
Electron mirror instability	4.3.4	KAW, field-swelling instability	Electron-/ion-velocity shear
Electron firehose instability	4.4.6, 4.4.7	KAW instability	Electron-/ion-velocity shear
Electron-scale-transition (EST) instability*	4.4.8	—	Electron-velocity shear
Whisper instability*	4.4.10	—	Electron-velocity shear
Transverse instability	4.3.3, 4.4.9	Small-anisotropy Weibel instability	Electron-velocity shear
Ordinary-mode instability	4.4.11	—	Electron-velocity shear
CET whistler instability	3.3.1, 3.3.2	Whistler heat flux instability	Electron-temp. gradient

TABLE 1. Index of microinstabilities. The microinstabilities listed here are those discussed in the main text, with the relevant sections indicated. We also indicate whether these microinstabilities are driven by macroscopic electron-/ion-temperature gradients associated with the CE distribution function, or by macroscopic electron/ion velocity gradients (shears): see § 2.2.1 for a discussion of this classification. Newly identified microinstabilities are indicated with an asterisk.

plasma) is then necessary for calculating the true transport coefficients, which are likely determined by the effective collisionality associated with the saturated state of the dominant microinstability rather than by Coulomb collisions. Although such calculations are not undertaken in this paper, it seems possible that the modified transport coefficients could be determined self-consistently in terms of macroscopic plasma properties such as temperature gradients or velocity shears. We note that the calculation presented here assumes that the CE distribution function is determined without the microinstabilities and thus is only correct when the plasma is stable. Therefore, strictly speaking, the only conclusion one can make when the CE plasma is unstable is that the naive CE values of transport coefficients should not be taken as correct.

We emphasise that kinetic instability of CE plasmas is a phenomenon of practical importance as well as academic interest. We illustrate this in tables 3 and 4, where the possibility of microinstabilities is considered for a selection of physical systems composed of classical, collisional plasma. We find that, while there exist some systems where CE plasmas are immune to microinstabilities – for example, the photosphere

Microinstability name	Wavenumber scale	Growth rate $(\times \Omega_e)$	β-threshold
Mirror instability	$k_\parallel \rho_i \lesssim k_\perp \rho_i \sim 1$	$\mu_e \epsilon$	$\epsilon\beta \sim 1$
Parallel firehose instability	$k_\parallel \rho_i \sim k_\perp \rho_i \sim \epsilon^{1/2}, k_\perp \ll \epsilon^{1/4} k_\parallel$	$\mu_e \epsilon$	$\epsilon\beta \sim 1$
Oblique firehose instability	$k_\parallel \rho_i \sim \epsilon^{1/4}, k_\perp \sim k_\parallel$	$\mu_e \epsilon^{3/4}$	$\epsilon\beta \sim 1$
Critical-line firehose instability ($\epsilon \gtrsim 10^{-6}$)	$k_\parallel \rho_i \approx \sqrt{3/2}\, k_\perp \rho_i < 1$	$\mu_e \epsilon^{1/2}$	$\epsilon\beta \sim 1$
Critical-line firehose instability ($\epsilon \ll 10^{-6}$)	$k_\parallel \rho_i \approx \sqrt{3/2}\, k_\perp \rho_i \sim \epsilon^{1/12}$	$\mu_e \epsilon^{7/12}$	$\epsilon\beta \sim 1$
Slow-hydro.-wave instability	$k_\perp \rho_i \lesssim k_\parallel \rho_i \sim 1$	$\mu_e^{5/4} \epsilon$	$\epsilon\beta \sim \mu_e^{-1/4}$
Long-wavelength KAW instability	$k_\parallel \rho_i < k_\perp \rho_i \sim 1$	$\mu_e^{5/4} \epsilon k_\parallel/k_\perp$	$\epsilon\beta \sim \mu_e^{-1/4}$
CES whistler instability	$k_\perp \rho_e \lesssim k_\parallel \rho_e \sim 1$	$\mu_e^{1/2} \epsilon$	$\epsilon\beta \sim \mu_e^{-1/2}$
Electron mirror instability	$k_\parallel \rho_e \lesssim k_\perp \rho_e \sim 1$	$\mu_e^{1/2} \epsilon$	$\epsilon\beta \sim \mu_e^{-1/2}$
Parallel electron firehose instability	$k_\perp \rho_e \lesssim k_\parallel \rho_e \sim 1$	$\mu_e \epsilon$	$\epsilon\beta \sim \mu_e^{-1/2}$
Oblique electron firehose instability	$k_\parallel \rho_e \lesssim k_\perp \rho_e \sim 1$	$\mu_e^{1/2} \epsilon$	$\epsilon\beta \sim \mu_e^{-1/2}$
EST instability ($\epsilon\beta^{5/7} \lesssim \mu_e^{-1/2}$)	$k_\parallel \rho_e < 1 \lesssim k_\perp \rho_e \sim \epsilon^{1/2}\beta^{1/2}\mu_e^{1/4}$	$\mu_e^{5/4} \epsilon^{5/2} \beta^{3/2}$	$\epsilon\beta \sim \mu_e^{-1/2}$
EST instability ($\epsilon\beta^{5/7} \gtrsim \mu_e^{-1/2}$)	$k_\parallel \rho_e < 1 \ll k_\perp \rho_e \sim \epsilon^{1/5}\mu_e^{1/10}$	$\mu_e^{1/5} \epsilon^{2/5}$	$\epsilon\beta \sim \mu_e^{-1/2}$
Whisper instability	$k_\parallel \rho_e < 1 \ll k_\perp \rho_e \sim \epsilon^{1/2}\beta^{1/2}\mu_e^{1/4}$	$\mu_e^{3/8} \epsilon^{3/4} \beta^{1/4}$	$\epsilon\beta \sim \beta^{2/7}\mu_e^{-1/2}$
Parallel transverse instability	$k_\perp \rho_e \lesssim k_\parallel \rho_e \sim \epsilon^{1/2}\beta^{1/2}\mu_e^{1/4}$	$\mu_e^{3/4} \epsilon^{3/2} \beta^{1/2}$	$\epsilon\beta \sim \mu_e^{-1/2}$
Oblique transverse instability	$1 \lesssim k_\parallel \rho_e \lesssim k_\perp \rho_e \sim \epsilon^{1/2}\beta^{1/2}\mu_e^{1/4}$	$\mu_e^{3/4} \epsilon^{3/2} \beta^{1/2}$	$\epsilon\beta \sim \mu_e^{-1/2}$
Ordinary-mode instability	$k_\parallel = 0, k_\perp \rho_e \sim \epsilon^{1/2}\beta^{1/2}\mu_e^{1/4}$	$\mu_e^{3/4} \epsilon^{3/2} \beta^{1/2}$	$\epsilon\beta \sim \beta^{2/3}\mu_e^{-1/2}$
CET whistler instability	$k_\perp \rho_e \lesssim k_\parallel \rho_e \sim \epsilon^{1/5}\beta^{1/5}\mu_e^{1/20}$	$\mu_e^{1/4} \epsilon$	$\epsilon\beta \sim \mu_e^{-1/4}$

TABLE 2. Properties of microinstabilities. Typical wavenumbers and maximum growth rates of microinstabilities in strongly magnetised hydrogen CE plasma, and their β-stabilisation thresholds. Here, $\mu_e = m_e/m_i$. We assume scalings (2.55) to relate the magnitude of CE temperature-gradient-driven and CE shear-driven microinstabilities. These scalings lead to the non-Maxwellian component of the ion distribution function having magnitude $\sim\epsilon = Ma\,\lambda/L_V$, where $\lambda = \lambda_e = \lambda_i$, L_V is the length scale of the CE plasma's bulk fluid motions in the direction parallel to the guide magnetic field (see (2.13d)) and Ma is the Mach number of those bulk motions. The quoted wavenumbers and growth rates apply when the β-stabilisation threshold is exceeded by an order-unity or much larger factor.
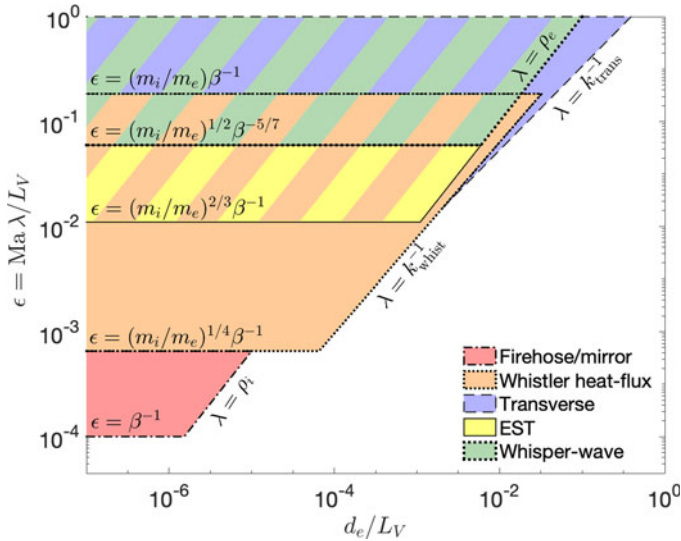
FIGURE 1. Stability map for the CE distribution function. Idealised illustration of the stability of strongly magnetised, classical, collisional hydrogen plasma to microinstabilities for different (non-dimensionalised) values of the mean free path $\lambda = \lambda_e = \lambda_i$ and the electron inertial scale d_e. Here, the length scale L_V to which λ and d_e are normalised is the length scale of the CE plasma's bulk fluid motions in the direction parallel to the guide magnetic field (see (2.13d)); we assume scalings (2.55) to relate the magnitude of CE temperature-gradient-driven and CE shear-driven microinstabilities, so the CE expansion parameter is $\epsilon = Ma\,\lambda/L_V$ (see the caption of table 2 for definitions). The white region of the $(d_e/L_V, Ma\,\lambda/L_V)$ stability map is stable; the coloured regions are not. In the unstable regions, the fastest-growing microinstability is indicated by colour according to the figure's legend; in the regions where multiple microinstabilities could be operating simultaneously, multiple colours have been employed. The plasma beta β here was taken to be $\beta = 10^4$, and the Mach number $Ma = 1$.

and chromosphere – there are many other astrophysical plasma systems that are likely susceptible to them. Similar considerations apply to a range of laser plasmas, including plasmas generated in inertial-confinement-fusion and laboratory-astrophysics experiments. Indeed, a recent experiment carried out on the National Ignition Facility (NIF) – part of a wider programme of work exploring magnetic-field amplification in turbulent laser plasmas (Tzeferacos *et al.* 2018; Bott *et al.* 2021*c*,*b*, 2022) – found evidence for the existence of large-amplitude local temperature fluctuations over a range of scales, a finding that was inconsistent with Spitzer thermal conduction (Meinecke *et al.* 2022). This claim was corroborated by magnetohydrodynamic (MHD) simulations (with the code FLASH) of the experiment that modelled thermal conduction either using the Spitzer model, or no explicit thermal conduction model: the latter simulations were found to be much closer to the actual experimental data. Because the plasma created in the NIF experiment is also anticipated by our theory to be susceptible to CE microinstabilities, observations of a discrepancy with CE-derived transport coefficients are tantalising. We note that the idea of microinstabilities emerging in both collisional astrophysical plasmas and laser plasmas is not a new one: see, e.g. Schekochihin *et al.* (2005) or Hellinger & Trávníček (2015) in the former context; in the latter, Epperlein & Bell (1987) or Bell *et al.* (2020). However, to our knowledge there does not exist a systematic treatment of the general kinetic stability of CE plasmas. This is the gap that this paper attempts to fill.

Environment	T_e (eV)	T_i (eV)	n_e (cm^{-3})	B (G)	L (cm)
Warm intergalactic medium (WIGM)	10^2	10^2	10^{-5}	10^{-8}	3×10^{24}
Intracluster medium (ICM)	10^4	10^4	10^{-2}	10^{-5}	3×10^{23}
IGM post reionisation	1	1	10^{-6}	10^{-19}	3×10^{24}
Solar photosphere	1	1	10^{17}	500	10^7
Solar chromosphere	1	1	10^{12}	10	10^7
Burning ICF hot spot (NIF)	10^4	10^4	2×10^{25}	8×10^7	5×10^{-3}
Laser-ablated plasma (long pulse)	10^3	5×10^2	4×10^{21}	10^6	10^{-2}
NIF 'TDYNO' laser plasma	10^3	10^3	5×10^{20}	10^6	10^{-2}

TABLE 3. Plasma parameters for some physical systems composed of classical, collisional plasma. The values of temperature and density of the WIGM given here are from Nicastro, Mathur & Elvis (2008), while those of the ICM come from Fabian (1994). The estimates of the typical magnetic-field strengths and scale lengths for both the WIGM and the ICM are from Ryu *et al.* (2008). For simplicity, we have assumed equal ion and electron temperatures; however, we acknowledge that there is some uncertainty as to the validity of this assumption (see, e.g. Yoshida, Furlanetto & Hernquist 2005). Barkana & Loeb (2001) is the source of estimates for the IGM post reionisation. Estimates for typical solar parameters are from Wiegelmann, Thalmann & Solanki (2014) and Stix (2012). The values of the temperature, electron density and scale length for ICF hot spots are from Abu-Shawareb (2022), who reported the first DT experiments carried out on the NIF to exceed the Lawson criterion for ignition; the estimates of the magnetic-field strength come from numerical simulations of a burning ICF hot spot with a similar fusion energy yield (Sadler *et al.* 2022). The parameters for the laser-ablated carbon-hydrogen plasma are from an experiment on the OMEGA laser facility, with a 1 ns, 500 J pulse with a 0.351 μm wavelength (Li *et al.* 2007); we assume that the measured fields are found in front of the critical-density surface when estimating the density. The 'TDYNO' laser plasma is a turbulent carbon-hydrogen plasma that was produced as part of a recent laboratory astrophysics experiment on the NIF which found evidence of suppressed heat conduction (Meinecke *et al.* 2022). Naturally, the systems described here often support a range of density, temperatures and magnetic fields, so the values provided should be understood as representative, but negotiable.

This paper has the following structure. In § 2, we discuss kinetic and fluid descriptions of classical plasma. We then describe the CE expansion in collisional plasma: we work out the CE distribution function arising in a two-species strongly magnetised plasma, evaluate the friction forces, heat and momentum fluxes necessary to construct a closed set of plasma-fluid equations and systematically estimate the size of the non-Maxwellian components of this distribution. Next, we discuss qualitatively the existence and nature of microinstabilities potentially arising in CE plasma, before presenting the methodology that we later use to perform the full linear, kinetic stability calculation. We provide an overview of this methodology in § 2.4, and then a much more detailed exposition of it in § 2.5: in particular, we describe in the latter how a simple form of the dispersion relation for the fastest microinstabilities can be obtained by considering the low-frequency limit $\gamma \ll k v_{\text{ths}}$ of the hot-plasma dispersion relation, and how this simplified dispersion relation can be solved analytically. Readers who are uninterested in the technical details of this calculation are encouraged to pass over § 2.5; knowledge of its contents is not a pre-requisite for subsequent sections. In §§ 3 and 4, we construct stability maps (analogous to figure 1) showing the parameter ranges in which the CE distribution function is stable, to CET and CES microinstabilities, respectively. The parameters are β and λ/L, and we

Environment	λ_e/L	λ_i/L	d_e/L	β	$\beta\lambda_e/L$	ρ_e/λ_e	ρ_i/λ_i	$k_{\text{peak}}\lambda_e$
WIGM	2×10^{-3}	2×10^{-3}	2×10^{-17}	10^4	20	10^{-12}	10^{-11}	10^{12}
ICM	10^{-2}	10^{-2}	10^{-17}	10^2	1	10^{-14}	10^{-13}	10^{14}
Reion. IGM	10^{-7}	10^{-7}	10^{-16}	10^{22}	10^{15}	0.5	20	10^5
Photosphere	6×10^{-12}	6×10^{-12}	2×10^{-10}	30	10^{-10}	110	4×10^3	10^{-4}
Chromosphere	2×10^{-7}	2×10^{-7}	5×10^{-8}	1	10^{-7}	0.2	6	0.2
ICF hot spot	5×10^{-3}	3×10^{-2}	2×10^{-5}	3×10^3	15	0.2	20	6
Laser-abl. pl.	7×10^{-3}	3×10^{-4}	8×10^{-4}	200	1	0.4	800	2.5
NIF TDYNO	6×10^{-2}	2×10^{-2}	2×10^{-3}	45	2.5	0.1	200	10

TABLE 4. Derived plasma parameters for systems composed of classical, collisional plasma. All parameters are calculated using Huba (1994), except for $k_{\text{peak}}\lambda_e$. This is calculated by considering all possible instabilities, and then finding the magnitude of $k_{\text{peak}}\lambda_e$ for the fastest-growing instability satisfying $k_{\text{peak}}\lambda_e \gtrsim 1$. Depending on the values of other parameters, the fastest-growing instability varies between systems; in the WIGM, ICM, ICF, laser-ablation and TDYNO plasmas, the whistler heat-flux instability is the fastest-growing one, while in the reionised IGM, the transverse instability is. Formulae for λ_e and λ_i are also given by (2.14a,b).

construct separate stability maps for CET and CES microinstabilities in order to take into account the fact that L is in general not the same in the situations where these two types of microinstabilities occur. In § 3, we also discuss the significant CET microinstabilities that can occur (or not) at different values λ/L and β, and provide simple analytic characterisations of them; in § 4, we do the same for significant CES microinstabilities. Finally, in § 5, we discuss the general implications of these instabilities for classical, collisional plasmas, and consider future research directions. Throughout this paper, most lengthy calculations are exiled to appendices; a glossary of mathematical notation is given in Appendix A.

2. Problem set-up

2.1. *Kinetic vs fluid description of classical plasma*

The evolution of classical plasma is most generally described by kinetic theory, via the solution of Maxwell–Vlasov–Landau equations for the distribution functions of constituent particles. More specifically, in a kinetic description of a (non-relativistic) plasma, the distribution function $f_s(\mathbf{r}, \mathbf{v}, t)$ of the particle of species s satisfies

$$\frac{\partial f_s}{\partial t} + \mathbf{v} \cdot \nabla f_s + \frac{Z_s e}{m_s}\left(\mathbf{E} + \frac{\mathbf{v} \times \mathbf{B}}{c}\right) \cdot \frac{\partial f_s}{\partial \mathbf{v}} = \sum_{s'} \mathfrak{C}(f_s, f_{s'}), \quad (2.1)$$

where t is time, $\mathbf{r}$ spatial position, $\mathbf{v}$ the velocity, e the elementary charge, $Z_s e$ the charge and m_s the mass of species s, $\mathbf{E}$ the electric field, $\mathbf{B}$ the magnetic field, c the speed of light and $\mathfrak{C}(f_s, f_{s'})$ the collision operator for interactions between species s and s'. Here, we do not yet give a specific form for $\mathfrak{C}(f_s, f_{s'})$; in general, an appropriate choice is the full Landau collision operator (Helander & Sigmar 2005), but to aid tractability of some calculations that we carry out subsequently (see § 2.4.2), we will in some instances adopt simpler models such as the Krook operator (Bhatnagar, Gross & Krook 1954).

Equation (2.1) is coupled to Maxwell's equations:

$$\nabla \cdot \boldsymbol{E} = 4\pi \sum_s Z_s e \int \mathrm{d}^3 \boldsymbol{v} f_s, \tag{2.2a}$$

$$\nabla \cdot \boldsymbol{B} = 0, \tag{2.2b}$$

$$\nabla \times \boldsymbol{E} = -\frac{1}{c} \frac{\partial \boldsymbol{B}}{\partial t}, \tag{2.2c}$$

$$\nabla \times \boldsymbol{B} = \frac{1}{c} \frac{\partial \boldsymbol{E}}{\partial t} + \frac{4\pi}{c} \sum_s Z_s e \int \mathrm{d}^3 \boldsymbol{v}\, \boldsymbol{v} f_s. \tag{2.2d}$$

Together, (2.1) and (2.2) form a closed set of governing equations.

The density n_s, bulk fluid velocity V_s and temperature T_s of species s can be formally defined in terms of moments of the distribution function:

$$n_s \equiv \int \mathrm{d}^3 \boldsymbol{v} f_s, \tag{2.3a}$$

$$V_s \equiv \frac{1}{n_s} \int \mathrm{d}^3 \boldsymbol{v}\, \boldsymbol{v} f_s, \tag{2.3b}$$

$$T_s \equiv \frac{1}{n_s} \int \mathrm{d}^3 \boldsymbol{v}\, \frac{1}{3} m_s |\boldsymbol{v} - V_s|^2 f_s. \tag{2.3c}$$

Governing 'fluid' equations are then derived by integrating (2.1) or outer products of (2.1) and the velocity variable $\boldsymbol{v}$ with respect to $\boldsymbol{v}$:

$$\left.\frac{\mathrm{D} n_s}{\mathrm{D} t}\right|_s + n_s \nabla \cdot V_s = 0, \tag{2.4a}$$

$$m_s n_s \left.\frac{\mathrm{D} V_s}{\mathrm{D} t}\right|_s = -\nabla p_s - \nabla \cdot \boldsymbol{\pi}_s + Z_s e n_s \left(\boldsymbol{E} + \frac{V_s \times \boldsymbol{B}}{c}\right) + \boldsymbol{R}_s, \tag{2.4b}$$

$$\frac{3}{2} n_s \left.\frac{\mathrm{D} T_s}{\mathrm{D} t}\right|_s + p_s \nabla \cdot V_s = -\nabla \cdot \boldsymbol{q}_s - \boldsymbol{\pi}_s : \nabla V_s + \mathcal{Q}_s, \tag{2.4c}$$

where

$$\left.\frac{\mathrm{D}}{\mathrm{D} t}\right|_s \equiv \frac{\partial}{\partial t} + V_s \cdot \nabla \tag{2.5}$$

is the convective derivative with respect to the fluid motions of species s, p_s the pressure, $\boldsymbol{\pi}_s$ the viscosity tensor and $\boldsymbol{q}_s$ the heat flux of species s, $\boldsymbol{R}_s$ the friction force on this species due to collisional interactions with other species, and $\mathcal{Q}_s$ the heating rate due to inter-species collisions. The latter quantities are formally defined in terms of the distribution function as follows:

$$p_s \equiv \int \mathrm{d}^3 \boldsymbol{v}\, \frac{1}{3} m_s |\boldsymbol{v} - V_s|^2 f_s = n_s T_s, \tag{2.6a}$$

$$\boldsymbol{\pi}_s \equiv -p_s \boldsymbol{I} + \int \mathrm{d}^3 \boldsymbol{v}\, m_s (\boldsymbol{v} - V_s)(\boldsymbol{v} - V_s) f_s, \tag{2.6b}$$

$$\boldsymbol{q}_s \equiv \int \mathrm{d}^3 \boldsymbol{v}\, \frac{1}{2} m_s |\boldsymbol{v} - V_s|^2 (\boldsymbol{v} - V_s) f_s, \tag{2.6c}$$

$$\boldsymbol{R}_s \equiv \sum_{s'} \int \mathrm{d}^3\boldsymbol{v} \, m_s \boldsymbol{v} \, \mathfrak{C}(f_s, f_{s'}), \tag{2.6d}$$

$$\mathcal{Q}_s \equiv -\boldsymbol{R}_s \cdot \boldsymbol{V}_s + \sum_{s'} \int \mathrm{d}^3\boldsymbol{v} \, \frac{1}{2} m_s |\boldsymbol{v}|^2 \, \mathfrak{C}(f_s, f_{s'}). \tag{2.6e}$$

The distribution function only appears in Maxwell's equations via its zeroth and first moments; namely, Gauss' law (2.2a) and the Maxwell–Ampère law (2.2d) can be written as

$$\boldsymbol{\nabla} \cdot \boldsymbol{E} = 4\pi \sum_s Z_s e n_s, \tag{2.7a}$$

$$\boldsymbol{\nabla} \times \boldsymbol{B} = \frac{1}{c} \frac{\partial \boldsymbol{E}}{\partial t} + \frac{4\pi}{c} \sum_s Z_s e n_s \boldsymbol{V}_s. \tag{2.7b}$$

Unlike the kinetic description, the fluid equations (2.4) combined with Maxwell's equations (2.2b), (2.2d), (2.7a) and (2.7b) are not a closed system: knowledge of the distribution function, not just of n_s, $\boldsymbol{V}_s$ or T_s, is required to calculate momentum and heat fluxes, as well as the friction force or heating.

As discussed in the Introduction, solving fluid equations as opposed to kinetic equations is advantageous in many cases of interest. Since the dimensionality of the kinetic system is greater (a six-dimensional phase space vs three-dimensional position space), solving the kinetic system introduces both significant numerical and conceptual complexity. However, the system of fluid equations (2.4) is only usable if some type of closure can be introduced to calculate $\boldsymbol{\pi}_s$, $\boldsymbol{q}_s$, $\boldsymbol{R}_s$ and $\mathcal{Q}_s$ in terms of n_s, $\boldsymbol{V}_s$ and T_s. For classical plasmas, such a closure is generally not possible, except in the case of strongly collisional plasmas.

2.2. *The Chapman–Enskog expansion*

2.2.1. *The CE distribution functions*

For a classical, collisional plasma – i.e. a plasma where the mean free path λ_s of particles of species s satisfies $\lambda_s/L \ll 1$ for all s, L being the length scale over which the macroscopic properties of the plasma vary – a formal procedure exists for deriving a closed system of fluid equations from a kinetic description of the plasma. This procedure is the CE expansion, which gives distribution functions that are close to, but not exactly, Maxwellian. We call them CE distribution functions. The non-Maxwellian components of the CE distribution functions of particle species s are proportional to λ_s/L, and must be present in order to support gradients of n_s, $\boldsymbol{V}_s$ and T_s on $O(L)$ length scales, because (2.6b–e) are all zero for a Maxwellian plasma.

We consider a collisional electron–ion plasma (in which, by definition, $\mu_e \equiv m_e/m_i \ll 1$) with the property that all constituent particle species are strongly magnetised by the macroscopically varying magnetic field $\boldsymbol{B}$: that is, the Larmor radius $\rho_s \equiv m_s v_{\mathrm{th}s} c/|Z_s|e|\boldsymbol{B}|$ satisfies $\rho_s \ll \lambda_s$ both for the ions and for the electrons (here, $v_{\mathrm{th}s} \equiv \sqrt{2T_s/m_s}$ is the thermal speed of species s). Equivalently, a strongly magnetised plasma is one in which the Larmor frequency $\Omega_s \equiv e|Z_s|/m_s c$ satisfies $\Omega_s \tau_s \gg 1$, where τ_s is the collision time of species s. In such a plasma, the macroscopic variation of the fluid moments is locally anisotropic with respect to $\boldsymbol{B}$; L is the typical length scale of variation in the direction locally parallel to $\boldsymbol{B}$. It can then be shown that, to first order of the CE expansion in $\lambda_s/L \ll 1$, and to zeroth order in $\rho_s/\lambda_s \ll 1$, the CE distribution functions of the electrons

and ions are

$$f_e(\tilde{v}_{e\parallel}, \tilde{v}_{e\perp}) = \frac{n_e}{v_{\mathrm{the}}^3 \pi^{3/2}} \exp\left(-\tilde{v}_e^2\right)$$

$$\times \left\{1 + \left[\eta_e^T A_e^T(\tilde{v}_e) + \eta_e^R A_e^R(\tilde{v}_e) + \eta_e^u A_e^u(\tilde{v}_e)\right] \tilde{v}_{e\parallel} + \epsilon_e C_e(\tilde{v}_e) \left(\tilde{v}_{e\parallel}^2 - \frac{\tilde{v}_{e\perp}^2}{2}\right)\right\}, \tag{2.8a}$$

$$f_i(\tilde{v}_{i\parallel}, \tilde{v}_{i\perp}) = \frac{n_i}{v_{\mathrm{thi}}^3 \pi^{3/2}} \exp\left(-\tilde{v}_i^2\right)$$

$$\times \left\{1 + \eta_i A_i(\tilde{v}_i)\tilde{v}_{i\parallel} + \epsilon_i C_i(\tilde{v}_i) \left(\tilde{v}_{i\parallel}^2 - \frac{\tilde{v}_{i\perp}^2}{2}\right)\right\}. \tag{2.8b}$$

Let us define the various symbols employed in (2.8), before discussing the origin of these expressions and their significance for formulating fluid equations (see § 2.2.2).

The particle velocity $\boldsymbol{v}$ (with the corresponding speed $v = |\boldsymbol{v}|$) is split into components parallel and perpendicular to the macroscopic magnetic field $\boldsymbol{B} = B\hat{z}$ as $\boldsymbol{v} = v_\parallel \hat{z} + \boldsymbol{v}_\perp$, and the perpendicular plane is in turn characterised by two vectors $\hat{x}$ and $\hat{y}$ chosen so that $\{\hat{x}, \hat{y}, \hat{z}\}$ is an orthonormal basis. The perpendicular velocity is related to these basis vectors by the gyrophase angle ϕ:

$$\boldsymbol{v}_\perp = v_\perp \left(\cos\phi\,\hat{x} - \sin\phi\,\hat{y}\right). \tag{2.9}$$

The non-dimensionalised peculiar velocity $\tilde{v}_s$ in the rest frame of the ion fluid is defined by $\tilde{v}_s \equiv (\boldsymbol{v} - \boldsymbol{V}_i)/v_{\mathrm{th}s}$, $\tilde{v}_s \equiv |\tilde{v}_s|$, $\tilde{v}_{s\parallel} \equiv \hat{z} \cdot \tilde{v}_s$ and $\tilde{v}_{s\perp} \equiv |\tilde{v}_s - \tilde{v}_{s\parallel}\hat{z}|$. The number densities satisfy the quasi-neutrality condition

$$Z_i n_i = n_e, \tag{2.10}$$

where we have utilised $Z_e = -1$. We emphasise that n_s, $\{\hat{x}, \hat{y}, \hat{z}\}$ and $v_{\mathrm{th}s}$ all vary over length scales L in the plasma, but not on shorter scales (at least not in the direction locally parallel to $\boldsymbol{B}$). The functions $A_e^T(\tilde{v}_e)$, $A_e^R(\tilde{v}_e)$, $A_e^u(\tilde{v}_e)$, $C_e(\tilde{v}_e)$, $A_i(\tilde{v}_i)$ and $C_i(\tilde{v}_i)$ are isotropic functions whose precise forms depend only on the collision operator assumed in the original kinetic equation. Their magnitude is $O(1)$ when $\tilde{v}_e \sim 1$ or $\tilde{v}_i \sim 1$, for electrons and ions, respectively. Finally, the parameters η_e^T, η_e^R, η_e^u, η_i, ϵ_e and ϵ_i are defined as follows:

$$\eta_e^T = \lambda_e \nabla_\parallel \log T_e = \mathrm{sgn}(\nabla_\parallel \log T_e) \frac{\lambda_e}{L_T}, \tag{2.11a}$$

$$\eta_e^R = \lambda_e \frac{R_{e\parallel}}{p_e}, \tag{2.11b}$$

$$\eta_e^u = \lambda_e \frac{m_e u_{ei\parallel}}{T_e \tau_e}, \tag{2.11c}$$

$$\eta_i = \lambda_i \nabla_\parallel \log T_i = \mathrm{sgn}(\nabla_\parallel \log T_i) \frac{\lambda_i}{L_{T_i}}, \tag{2.11d}$$

$$\epsilon_e = \frac{\lambda_e}{v_{\mathrm{the}}} \left(\hat{z}\hat{z} - \frac{1}{3}\boldsymbol{I}\right) : \boldsymbol{W}_e = \mathrm{sgn}\left[\left(\hat{z}\hat{z} - \frac{1}{3}\boldsymbol{I}\right) : \boldsymbol{W}_e\right] \frac{V_e}{v_{\mathrm{the}}} \frac{\lambda_e}{L_{V_e}}, \tag{2.11e}$$

$$\epsilon_i = \frac{\lambda_i}{v_{\mathrm{thi}}} \left(\hat{z}\hat{z} - \frac{1}{3}\boldsymbol{I}\right) : \boldsymbol{W}_i = \mathrm{sgn}\left[\left(\hat{z}\hat{z} - \frac{1}{3}\boldsymbol{I}\right) : \boldsymbol{W}_i\right] \frac{V_i}{v_{\mathrm{thi}}} \frac{\lambda_i}{L_V}, \tag{2.11f}$$

where λ_e is the electron mean free path, λ_i the ion mean free path, τ_e the electron collision time, $R_{e\parallel} \equiv \hat{z} \cdot \boldsymbol{R}_e$ the parallel electron-friction force, $\boldsymbol{u}_{ei} \equiv \boldsymbol{V}_e - \boldsymbol{V}_i$ the relative electron–ion velocity, $u_{ei\parallel} \equiv \hat{z} \cdot \boldsymbol{u}_{ei}$,

$$\boldsymbol{W}_s = \nabla \boldsymbol{V}_s + (\nabla \boldsymbol{V}_s)^{\mathrm{T}} - \tfrac{2}{3} (\nabla \cdot \boldsymbol{V}_s) \boldsymbol{I} \tag{2.12}$$

the traceless rate-of-strain tensor of species s, V_e (V_i) the bulk electron-(ion-)fluid speed and

$$L_T \equiv \left| \nabla_\parallel \log T_e \right|^{-1}, \tag{2.13a}$$

$$L_{T_i} \equiv \left| \nabla_\parallel \log T_i \right|^{-1}, \tag{2.13b}$$

$$L_{V_e} \equiv V_e \left| \left(\hat{z}\hat{z} - \tfrac{1}{3}\boldsymbol{I} \right) : \boldsymbol{W}_e \right|^{-1}, \tag{2.13c}$$

$$L_V \equiv V_i \left| \left(\hat{z}\hat{z} - \tfrac{1}{3}\boldsymbol{I} \right) : \boldsymbol{W}_i \right|^{-1}, \tag{2.13d}$$

are, respectively, the electron and ion temperature and the electron- and ion-flow length scales parallel to the background magnetic field. The mean free paths are formally defined for a two-species plasma by

$$\lambda_e \equiv v_{\mathrm{th}e}\tau_e, \tag{2.14a}$$

$$\lambda_i \equiv v_{\mathrm{th}i}\tau_i, \tag{2.14b}$$

and the collision times τ_e and τ_i are given in terms of macroscopic plasma parameters by

$$\tau_e \equiv \frac{3m_e^{1/2}T_e^{3/2}}{4\sqrt{2\pi}Z_i^2 e^4 n_i \log \Lambda_{\mathrm{CL}}}, \tag{2.15a}$$

$$\tau_i \equiv \frac{3m_i^{1/2}T_i^{3/2}}{4\sqrt{2\pi}Z_i^4 e^4 n_i \log \Lambda_{\mathrm{CL}}}, \tag{2.15b}$$

where $\log \Lambda_{\mathrm{CL}}$ is the Coulomb logarithm (Braginskii 1965).[1] In a collisional plasma, η_e^T, η_e^R, η_e^u, η_i, ϵ_e and ϵ_i are assumed small. We note that all these parameters can be either positive or negative, depending on the orientation of temperature and velocity gradients.

It is clear from their definitions that each of the non-Maxwellian terms associated with the parameters η_e^T, η_e^R, η_e^u, η_i, ϵ_e and ϵ_i is linked to a different macroscopic physical quantity. Thus, η_e^T and η_i are proportional to the electron- and ion-temperature gradients, respectively; we will therefore refer to the associated non-Maxwellian terms as the CE electron-temperature-gradient term and the CE ion-temperature-gradient term. We refer to the non-Maxwellian term proportional to η_e^R as the CE electron-friction term, to the non-Maxwellian term proportional to η_e^u as the CE electron–ion-drift term, and the non-Maxwellian terms proportional to ϵ_e and ϵ_i as the CE electron-shear term and the CE ion-shear term. The friction and electron–ion-drift terms appear in the electron CE distribution function but not the ion CE distribution function because of our choice to define all velocities in the ion-fluid rest frame. We note that, while macroscopic variation of both the electron and ion densities is *a priori* allowed in our plasma, the derivation of the CE distribution functions reveals that such variation does not directly give rise to a non-Maxwellian perturbation to the CE distribution function (see Appendix B.1).

---

[1]Braginskii defined his ion collision time as equal to (2.15*b*) multiplied by a factor of $\sqrt{2}$; for the sake of species equality, we remove this factor.

The derivation of the CE distribution functions (2.8) for a two-species strongly magnetised plasma undergoing sonic motions (that is, $V_i \sim v_{thi}$) from the kinetic equation (2.1) was first completed by Braginskii (1965) for arbitrary values of ρ_s/λ_s. We do not reproduce the full derivation in the main text, but, for the reader's convenience, we provide a derivation of (2.8) in Appendix B.1. The gist of the full derivation is to assume that the distribution function is close to a Maxwellian, with parameters that only evolve on a slow time scale $t' \sim tL/\lambda_e \sim tL/\lambda_i \gg t$. The kinetic equation (2.1) is then expanded and solved order by order in $\lambda_e/L \sim \lambda_i/L \ll 1$, allowing for the calculation of the (small) non-Maxwellian components of the distribution function. The small parameters η_e^T, η_e^R, η_e^u, η_i, ϵ_e and ϵ_i, as well as the isotropic functions $A_e^T(\tilde{v}_e)$, $A_e^R(\tilde{v}_e)$, $A_e^u(\tilde{v}_e)$, $C_e(\tilde{v}_e)$, $A_i(\tilde{v}_i)$ and $C_i(\tilde{v}_i)$ emerge during this calculation. In Appendix B.2, we provide a simple illustration of how the isotropic functions are determined by the specific choice of collision operator; in Appendices B.2.1 and B.2.2, we calculate them explicitly for Krook and Lorentz collision operators, respectively. For the full Landau collision operator, the equivalent calculation is more complicated, but can be performed (for example) by expanding the isotropic functions in Sonine polynomials (see Helander & Sigmar 2005).

2.2.2. *Closure of fluid equations (2.4)*

Once the CE distribution function has been calculated, the desired fluid closure can be obtained by evaluating the heat fluxes, the friction forces, and the momentum fluxes (2.6) associated with the non-Maxwellian components of the CE distribution functions. These calculations were carried out in full for arbitrary values of ρ_s/λ_s by Braginskii (1965).

We do not reproduce the full fluid closure relations here; instead, we illustrate how the non-Maxwellian terms in the CE distribution functions (2.8) give rise to the friction force and heat fluxes parallel to the macroscopic magnetic field, as well as to the viscosity tensor. In a strongly magnetised two-species plasma (where $\rho_s \ll \lambda_s$), parallel friction forces and heat fluxes are typically much larger than their perpendicular or diamagnetic counterparts.

(i) <u>Heat fluxes</u>. Recalling (2.6c), the parallel heat flux $q_{s\parallel} \equiv \hat{\boldsymbol{z}} \cdot \boldsymbol{q}_s$ associated with species s is given by

$$q_{s\parallel} = \frac{1}{2} \int \mathrm{d}^3 \boldsymbol{v}'_s \, m_s \left| \boldsymbol{v}'_s \right|^2 v'_{s\parallel} f_s, \tag{2.16}$$

where $\boldsymbol{v}'_s \equiv \boldsymbol{v} - \boldsymbol{V}_s$. Noting that the electron distribution function (2.8a) is specified in the rest frame of the ions, not electrons, it is necessary first to calculate the electron distribution function in the electron rest frame before calculating the parallel electron heat flux. An expression for this quantity is given by (B18) in Appendix B.1 as part of our derivation of (2.8a):

$$f_e(v'_{e\parallel}, v'_{e\perp}) = \frac{n_e}{v_{the}^3 \pi^{3/2}} \exp\left(-\frac{|\boldsymbol{v}'_e|^2}{v_{the}^2}\right)$$

$$\times \left\{ 1 + \left[\eta_e^T A_e^T\left(\frac{|\boldsymbol{v}'_e|}{v_{the}}\right) + \eta_e^R A_e^R\left(\frac{|\boldsymbol{v}'_e|}{v_{the}}\right) + \eta_e^u \left(A_e^u\left(\frac{|\boldsymbol{v}'_e|}{v_{the}}\right) - 1 \right) \right] \frac{v'_{e\parallel}}{v_{the}} \right.$$

$$\left. + \epsilon_e C_e\left(\frac{|\boldsymbol{v}'_e|}{v_{the}}\right) \left(\frac{v'^2_{e\parallel}}{v_{the}^2} - \frac{v'^2_{e\perp}}{2v_{the}^2} \right) \right\}. \tag{2.17}$$

Now substituting (2.17) into (2.16) (with $s = e$), we find that the parallel electron heat flux is

$$q_{e\parallel} = -n_e T_e v_{the} \left[\mathcal{A}_e^T \eta_e^T + \mathcal{A}_e^R \eta_e^R + \left(\mathcal{A}_e^u - \tfrac{1}{2} \right) \eta_e^u \right], \tag{2.18}$$

where

$$\mathcal{A}_e^{T,R,u} = -\frac{4}{3\sqrt{\pi}} \int_0^\infty \mathrm{d}\tilde{v}_e \, \tilde{v}_e^6 A_e^{T,R,u}(\tilde{v}_e) \exp\left(-\tilde{v}_e^2\right). \tag{2.19}$$

The minus signs in the definitions of $\mathcal{A}_e^{T,R,u}$ have been introduced so that $\mathcal{A}_e^{T,R,u} \geqslant 0$ for a typical collision operator (determining that these constants are indeed positive for any given collision operator is non-trivial, but it is a simple exercise to show this for a Krook collision operator, using the expressions for $A_e^T(\tilde{v}_e)$, $A_e^R(\tilde{v}_e)$ and $A_e^u(\tilde{v}_e)$ given in Appendix B.2.1). Expression (2.18) for the electron heat flux can be rewritten as

$$q_{e\parallel} = -\kappa_e^\parallel \nabla_\parallel T_e - \left[\mathcal{A}_e^u - \frac{1}{2} - \frac{\mathcal{A}_e^R}{\tilde{\mathcal{A}}_e^R}\left(\tilde{\mathcal{A}}_e^u - \frac{1}{2}\right) \right] n_e T_e u_{ei\parallel}, \tag{2.20}$$

where the parallel electron heat conductivity is defined by

$$\kappa_e^\parallel = 2\left(\mathcal{A}_e^T - \frac{\mathcal{A}_e^R}{\tilde{\mathcal{A}}_e^R}\tilde{\mathcal{A}}_e^T\right)\frac{n_e T_e \tau_e}{m_e}, \tag{2.21}$$

and

$$\tilde{\mathcal{A}}_e^{T,R,u} = -\frac{4}{3\sqrt{\pi}} \int_0^\infty \mathrm{d}\tilde{v}_e \, \tilde{v}_e^4 A_e^{T,R,u}(\tilde{v}_e) \exp\left(-\tilde{v}_e^2\right). \tag{2.22}$$

Numerical evaluation of the coefficients $\mathcal{A}_e^{T,R,u}$ and $\tilde{\mathcal{A}}_e^{T,R,u}$ for the Landau collision operator gives (Braginskii 1965)

$$q_{e\parallel} \simeq -3.16\frac{n_e T_e \tau_e}{m_e}\nabla_\parallel T_e + 0.71 n_e T_e u_{ei\parallel}. \tag{2.23}$$

The ion heat flux can be calculated directly from (2.16) ($s = i$) using (2.8b):

$$q_{i\parallel} = -n_i T_i v_{\mathrm{thi}}\mathcal{A}_i \eta_i, \tag{2.24}$$

where

$$\mathcal{A}_i = -\frac{4}{3\sqrt{\pi}} \int_0^\infty \mathrm{d}\tilde{v}_i \, \tilde{v}_i^6 A_i(\tilde{v}_i) \exp\left(-\tilde{v}_i^2\right). \tag{2.25}$$

This becomes

$$q_{i\parallel} = -\kappa_i^\parallel \nabla_\parallel T_i, \tag{2.26}$$

where the parallel ion heat conductivity is

$$\kappa_i^\parallel = -2\mathcal{A}_i\frac{n_i T_i \tau_i}{m_i} \simeq -3.9\frac{n_i T_i \tau_i}{m_i}. \tag{2.27}$$

The last equality is for the Landau collision operator (Braginskii 1965). Note that the absence of a term proportional to the electron–ion-drift in the ion heat flux (2.24) is physically due to the smallness of the ion–electron collision operator (Helander & Sigmar 2005).

(ii) <u>Friction force.</u> We evaluate the friction force by considering the electron–ion-drift associated with electron CE distribution function. Namely, noting that

$$u_{ei\parallel} = \frac{v_{\text{the}}^4}{n_e} \int d^3 \tilde{\boldsymbol{v}}_e \, \tilde{v}_{e\parallel} f_e, \tag{2.28}$$

it follows from (2.8a) that

$$u_{ei\parallel} = v_{\text{the}} \left(\tilde{\mathcal{A}}_e^T \eta_e^T + \tilde{\mathcal{A}}_e^R \eta_e^R + \tilde{\mathcal{A}}_e^u \eta_e^u \right). \tag{2.29}$$

This expression can in turn be used to relate the parallel electron-friction force $R_{e\parallel}$, defined in (2.6d), to electron flows and temperature gradients

$$R_{e\parallel} = -\left(\frac{2\tilde{\mathcal{A}}_e^u + 1}{2\tilde{\mathcal{A}}_e^R} \right) \frac{n_e m_e u_{ei\parallel}}{\tau_e} - \frac{\tilde{\mathcal{A}}_e^T}{\tilde{\mathcal{A}}_e^R} n_e \nabla_\parallel T_e. \tag{2.30}$$

Evaluating the coefficients $\tilde{\mathcal{A}}_e^T$, $\tilde{\mathcal{A}}_e^R$ and $\tilde{\mathcal{A}}_e^u$ for the full Landau collision operator, one finds (Braginskii 1965)

$$R_{e\parallel} \simeq -0.51 \frac{n_e m_e u_{ei\parallel}}{\tau_e} - 0.71 n_e \nabla_\parallel T_e. \tag{2.31}$$

(iii) <u>Viscosity tensor.</u> For gyrotropic distributions such as the CE distribution functions (2.8), the viscosity tensor $\boldsymbol{\pi}_s$ of species s defined by (2.6b) – which is the momentum flux excluding the convective terms and isotropic pressure – is given by

$$\boldsymbol{\pi}_s = \left(p_{s\parallel} - p_{s\perp} \right) \left(\hat{\boldsymbol{z}}\hat{\boldsymbol{z}} - \tfrac{1}{3}\boldsymbol{I} \right), \tag{2.32}$$

where the parallel pressure $p_{s\parallel}$ and the perpendicular pressure $p_{s\perp}$ are defined by

$$p_{s\parallel} \equiv \int d^3 \boldsymbol{v}_s' \, m_s |v_{s\parallel}'|^2 f_s = n_s T_s \left(1 - \frac{2}{3}\epsilon_s \mathcal{C}_s \right), \tag{2.33a}$$

$$p_{s\perp} \equiv \frac{1}{2} \int d^3 \boldsymbol{v}_s' \, m_s |\boldsymbol{v}_{s\perp}'|^2 f_s = n_s T_s \left(1 + \frac{1}{3}\epsilon_s \mathcal{C}_s \right), \tag{2.33b}$$

with the last expressions having been obtained on substitution of the CE distribution function (2.8), and

$$\mathcal{C}_s = -\frac{8}{5\sqrt{\pi}} \int_0^\infty d\tilde{v}_s \, \tilde{v}_s^6 C_s(\tilde{v}_s) \exp\left(-\tilde{v}_s^2 \right). \tag{2.34}$$

The sign of the constant $\mathcal{C}_s$ is again chosen so that $\mathcal{C}_s > 0$ for typical collision operators; for the Landau collision operator, $\mathcal{C}_e \simeq 1.1$ and $\mathcal{C}_i \simeq 1.44$ (Braginskii 1965). We note for reference that the parameter ϵ_s (see (2.11e–f)) has a simple

relationship to the pressure anisotropy of species s: utilising (2.33), one finds

$$\Delta_s \equiv \frac{p_{s\perp} - p_{s\parallel}}{p_s} = \mathcal{C}_s \epsilon_s. \tag{2.35}$$

Using (2.33), the viscosity tensor (2.32) can be written

$$\boldsymbol{\pi}_s = -\frac{\mu_{vs}}{2} \left(\hat{z}\hat{z} - \frac{1}{3}\boldsymbol{I} \right) \left(\hat{z}\hat{z} - \frac{1}{3}\boldsymbol{I} \right) : \boldsymbol{W}_s, \tag{2.36}$$

where the dynamic viscosity of species s is

$$\mu_{vs} \equiv 2\mathcal{C}_s n_s T_s \tau_s. \tag{2.37}$$

(iv) Thermal energy transfer between species. It can be shown that for the CE distribution functions (2.8), the rate of thermal energy transfer from electrons to ions $\mathcal{Q}_e$ is simply

$$\mathcal{Q}_e = -\boldsymbol{R}_e \cdot \boldsymbol{u}_{ei}, \tag{2.38}$$

while the rate of thermal energy transfer from ions to electrons vanishes: $\mathcal{Q}_i \approx 0$. This is because the ion–electron collision rate is assumed small (by a factor of the mass ratio) compared with the ion–ion collision rate when deriving (2.8*b*), and is thus neglected. Braginskii (1965) shows that, in fact, there is a non-zero (but small) rate of transfer

$$\mathcal{Q}_i = -\mathcal{Q}_e - \boldsymbol{R}_e \cdot \boldsymbol{u}_{ei} = \frac{3n_e m_e}{m_i \tau_e} (T_e - T_i). \tag{2.39}$$

The time scale on which the ion and electron temperatures equilibrate is the ion–electron temperature equilibration time

$$\tau_{ie}^{\text{eq}} \equiv \tfrac{1}{2} \mu_e^{-1/2} \tau_i. \tag{2.40}$$

In summary, the non-Maxwellian components of the CE distribution function are essential for a collisional plasma to be able to support fluxes of heat and momentum. More specifically, (2.20) demonstrates that the electron heat fluxes in a CE plasma are proportional to both temperature gradients and electron–ion drifts, and are carried by the electron-temperature-gradient, friction and electron–ion-drift terms of the CE distribution function. In contrast, the ion heat fluxes (2.26) are proportional only to ion temperature gradients (and carried by the CE ion-temperature-gradient term). Momentum fluxes (2.36) for electrons and ions are carried by the CE electron- and ion-shear terms, respectively, and are proportional to components of the rate-of-strain tensor.

2.2.3. *Relative size of non-Maxwellian terms in the CE distribution function*

In the case of magnetised, two-species plasma satisfying $T_i \sim T_e$, (2.11) can be used to estimate the size of the small parameters η_e^T, η_e^R, η_e^u, η_i, ϵ_e and ϵ_i. Although these parameters are *a priori* proportional to λ_s/L for both ions and electrons, their precise magnitudes are, in fact, subtly different. Namely, the terms associated with η_e^T, η_e^R, η_e^u and η_i are gradients of the electron and ion temperatures and electron–ion relative parallel drift velocities, whereas terms associated with ϵ_e and ϵ_i involve gradients of the bulk flows (cf. (2.11)) – and these gradients do not necessarily occur on the same length scale.

Recalling that the (electron) temperature and the (ion) flow length scales parallel to the macroscopic magnetic field are defined by (cf. (2.13))

$$L_T = \left| \mathbf{\nabla}_\parallel \log T_e \right|^{-1}, \tag{2.41a}$$

$$L_V = \frac{1}{V_i} \left| \left(\hat{z}\hat{z} - \frac{1}{3}\mathbf{I} \right) : \mathbf{W}_i \right|^{-1}, \tag{2.41b}$$

where $\mathbf{W}_i$ is the ion rate-of-strain tensor (2.12), and assuming that $L_{T_i} = |\mathbf{\nabla}_\parallel \log T_i|^{-1} \sim L_T$ (an assumption we will check *a posteriori*), it follows from (2.11) that

$$\eta_e^T \sim \frac{\lambda_e}{L_T}, \tag{2.42a}$$

$$\eta_e^R \sim \lambda_e \frac{R_{e\parallel}}{p_e} \sim \frac{\lambda_e}{L_T} \sim \eta_e^T, \tag{2.42b}$$

$$\eta_e^u \sim \frac{u_{ei\parallel}}{v_{\mathrm{the}}} \sim \frac{\lambda_e}{L_T} \sim \eta_e^T, \tag{2.42c}$$

$$\eta_i \sim \frac{\lambda_i}{L_T} \sim \frac{1}{Z_i^2} \eta_e^T, \tag{2.42d}$$

$$\epsilon_e \sim \frac{V_i}{v_{\mathrm{the}}} \frac{\lambda_e}{L_V} \sim Ma\, \mu_e^{1/2} \frac{L_T}{L_V} \eta_e^T, \tag{2.42e}$$

$$\epsilon_i \sim \frac{V_i}{v_{\mathrm{thi}}} \frac{\lambda_i}{L_V} \sim Ma\, \frac{L_T}{Z_i^2 L_V} \eta_e^T, \tag{2.42f}$$

where $Ma \equiv V_i/v_{\mathrm{thi}}$ is the Mach number. Note that, to arrive at (2.42b), we assumed that $R_{e\parallel} \sim p_e/L_T$ and $u_{ei\parallel} \sim v_{\mathrm{the}}\lambda_e/L_T$, justified by (2.30) and (2.29), respectively. The relative magnitudes of η_e^T, η_e^R, η_e^u, η_i, ϵ_e and ϵ_i therefore depend on the Mach number of the plasma, as well as on the length scales L_T and L_V.

In the work of Braginskii (1965), who *a priori* presumes all 'fluid' quantities in the plasma to vary on just a single scale $L \sim L_T \sim L_V$, with sonic ordering $Ma \lesssim 1$, determining the relative size of these parameters for a hydrogen plasma ($Z_i = 1$) is simple:

$$\epsilon_e \sim \mu_e^{1/2} \epsilon_i \ll \epsilon_i \sim \eta_i \sim \eta_e^T \sim \eta_e^R \sim \eta_e^u. \tag{2.43}$$

However, in most interesting applications, this single-scale ordering is incorrect. In a plasma with $\lambda_s/L \ll 1$ under Braginskii's ordering, motions on many scales naturally arise. The fluid Reynolds number in such a plasma is given by

$$Re \equiv \frac{V_0 L_0}{\nu}, \tag{2.44}$$

where V_0 is the typical fluid velocity at the scale L_0 of driving motions and $\nu \equiv \mu_{vi}/m_i n_i \sim v_{\mathrm{thi}}\lambda_i$ is the kinematic viscosity (see (2.37)). Typically, this number is large:

$$Re \sim \frac{V_0}{v_{\mathrm{thi}}} \frac{L_0}{\lambda_i} \gtrsim \frac{1}{\epsilon_i} \gg 1, \tag{2.45}$$

where we have assumed $Ma_0 \equiv V_0/v_{\mathrm{thi}} \lesssim 1$, in line with Braginskii's sonic ordering. Therefore, such a plasma will naturally become turbulent and exhibit motions across a

range of scales. As a consequence, velocity and temperature fluctuations on the smallest (fluid) scales must be considered, since the associated shears and temperature gradients are the largest. To estimate η_e^T, η_e^R, η_e^u, η_i, ϵ_e and ϵ_i accurately, we must determine the magnitude of these gradients.

First, let ℓ_ν be the smallest scale on which the velocity varies due to turbulent motions (the Kolmogorov scale), with velocity fluctuations on scales $\ell \ll \ell_\nu$ being suppressed by viscous diffusion. Then it follows that $Re_{\ell_\nu} \sim 1$, where $Re_\ell \equiv V(\ell)\ell/\nu$ is the scale-dependent Reynolds number and $V(\ell)$ is the typical fluid velocity on scale ℓ. For Kolmogorov turbulence,

$$\frac{V(\ell)}{V_0} \sim \left(\frac{\ell}{L_0}\right)^{1/3} \sim \left(\frac{Re_\ell}{Re}\right)^{1/4}, \tag{2.46}$$

and $\ell/L_0 \sim (Re_\ell/Re)^{3/4}$, which gives $V(\ell)/\ell \sim (V_0/L_0)(Re_\ell/Re)^{-1/2}$, and thus, from (2.45),

$$\frac{V(\ell_\nu)}{\ell_\nu} \sim \frac{V_0}{L_0}\left(\frac{Re_{\ell_\nu}}{Re}\right)^{-1/2} \sim Ma_0^{1/2}\left(\frac{\lambda_i}{L_0}\right)^{-1/2}\frac{V_0}{L_0}. \tag{2.47}$$

We therefore conclude that

$$L_V \sim \ell_\nu \frac{V_0}{V(\ell_\nu)} \sim L_0 Ma_0^{-1/2}\left(\frac{\lambda_i}{L_0}\right)^{1/2}. \tag{2.48}$$

Next, the smallest scale on which the electron temperature varies, ℓ_χ, is the scale below which temperature fluctuations are suppressed by thermal diffusion; it satisfies $Pe_{\ell_\chi} \sim 1$, where $Pe_\ell \equiv V(\ell)\ell/\chi$ is the scale-dependent Péclet number and $\chi \equiv 2\kappa_e^\parallel/3n_e \sim v_{\mathrm{the}}\lambda_e$ is the (parallel) thermal diffusivity (see (2.21)). Because temperature is passively advected by the flow, the temperature fluctuation $T(\ell)$ at any scale $\ell > \ell_\chi$ obeys the same scaling as the bulk velocity:

$$\frac{T(\ell)}{T(L_0)} \sim \frac{V(\ell)}{V_0} \sim \left(\frac{Pe_\ell}{Pe}\right)^{1/4}. \tag{2.49}$$

In addition, the magnitude of temperature fluctuations at the driving scale is related to the mean temperature by the Mach number of the driving-scale motions, $T(L_0) \sim T_0 Ma_0$, which then gives

$$\frac{T(\ell)}{T_0} \sim Ma_0\left(\frac{Pe_\ell}{Pe}\right)^{1/4}, \tag{2.50}$$

where $Pe \equiv Pe_{L_0}$. It follows from an analogous argument to that just given for the velocity fluctuations that

$$\frac{T(\ell_\chi)}{\ell_\chi} \sim \frac{T_0}{L_0}Ma_0 Pe^{1/2}. \tag{2.51}$$

Under Braginskii's ordering, the Prandtl number of CE plasma is

$$Pr \equiv \frac{\nu}{\chi} = \frac{Pe}{Re} \sim \frac{v_{\mathrm{thi}}\lambda_i}{v_{\mathrm{the}}\lambda_e} \sim \mu_e^{1/2} \ll 1, \tag{2.52}$$

and, therefore,

$$L_T \sim \ell_\chi \frac{T_0}{T(\ell_\chi)} \sim L_0 \mu_e^{-1/4} Ma_0^{-3/2}\left(\frac{\lambda_i}{L_0}\right)^{1/2}. \tag{2.53}$$

Thus, $L_V \sim Ma_0 \mu_e^{1/4} L_T \ll L_T$ under the assumed ordering.

Finally, we consider whether our *a priori* assumption that $L_{T_i} \sim L_T$ is, in fact, justified. A sufficient condition for ion-temperature gradients to be the same as electron-temperature gradients is for the evolution time τ_L of all macroscopic motions to be much longer than the ion–electron equilibration-time τ_{ie}^{eq} defined by (2.40). Since $\tau_L \gtrsim \ell_\nu/V(\ell_\nu)$, it follows that

$$\frac{\tau_L}{\tau_{ie}^{\text{eq}}} \sim \left(\frac{m_i}{m_e}\right)^{1/2} Ma_0^{3/2}\left(\frac{\lambda_i}{L_0}\right)^{1/2} \sim \epsilon_i \left(\frac{m_i}{m_e}\right)^{1/2}. \tag{2.54}$$

Thus, if $\epsilon_i \gg \mu_e^{1/2}$, we conclude that collisional equilibration of ion and electron temperatures might be too inefficient to regulate small-scale ion-temperature fluctuations, in which case it would follow that $L_{T_i} < L_T$. However, it has been previously demonstrated via numerical solution of the Vlasov–Fokker–Planck equation that the CE expansion procedure breaks down due to non-local transport effects if λ_e/L is only moderately small (Bell, Evans & Nicholas 1981); thus, the only regime in which there is not ion–electron equilibration over all scales is one where the CE expansion is not valid anyway. In short, we conclude that assuming $L_{T_i} \sim L_T$ is reasonable.

Bringing these considerations together with (2.42), we find that

$$\eta_e^T \sim \mu_e^{1/4} Ma_0 \frac{\lambda_i}{L_V} \sim Ma_0^{3/2}\mu_e^{1/4}\left(\frac{\lambda_i}{L_0}\right)^{1/2} \sim \eta_e^R \sim \eta_e^u \sim \eta_i, \tag{2.55a}$$

$$\epsilon_e \sim \mu_e^{1/2} Ma_0 \frac{\lambda_i}{L_V} \sim \mu_e^{1/2}Ma_0^{3/2}\left(\frac{\lambda_i}{L_0}\right)^{1/2}, \tag{2.55b}$$

$$\epsilon_i \sim Ma_0 \frac{\lambda_i}{L_V} \sim Ma_0^{3/2}\left(\frac{\lambda_i}{L_0}\right)^{1/2}. \tag{2.55c}$$

Thus, we conclude that the largest distortions of the ion CE distribution are due to flow gradients, while temperature gradients cause the greatest distortions of the electron CE distribution function.

In deriving the estimates (2.55) of the small parameters η_e^T, η_e^R, η_e^u, η_i, ϵ_e and ϵ_i, we assumed that the motions of the plasma (including those at the Kolmogorov scale) satisfied Kolmogorov's statistical theory of turbulence. There are several reasonable grounds on which this assumption could be questioned. First of these is intermittency: it is a long-standing result that the distribution of turbulent velocities at a given scale in hydrodynamic turbulence becomes increasingly non-Gaussian as that scale decreases (see, e.g. Davidson 2015). This has the consequence that (2.55) may overestimate the size of the non-Maxwellian terms in the CE distribution function for the majority of the plasma's volume, but underestimate it significantly in localised regions. Another objection is the now generally accepted finding that turbulent fluids with sufficiently strong magnetic fields do not behave like hydrodynamic fluids: instead, turbulent motions tend to become anisotropic with respect to the background magnetic field if the latter's energy becomes greater than the former (Goldreich & Sridhar 1995; Schekochihin *et al.* 2009). When applied to turbulent motions at the Kolmogorov scale where motions are assumed to behave as we have proposed, this condition becomes

$$\frac{m_i n_i V(\ell_\nu)^2/2}{B^2/8\pi} \sim \frac{m_i n_i V_0^2/2}{B^2/8\pi}\frac{V(\ell_\nu)^2}{V_0^2} \sim Ma_0^{3/2}\left(\frac{\lambda_i}{L_0}\right)^{1/2}\beta_i \sim \epsilon_i\beta_i, \tag{2.56}$$

where

$$\beta_s \equiv \frac{8\pi n_s T_s}{B^2} \tag{2.57}$$

is the plasma beta of species s. So, whenever $\beta_i \ll \epsilon_i^{-1}$, the assumption that the turbulence is unmagnetised is unlikely to be a good one, whereas if β_i is sufficiently large ($\beta_i \gtrsim \epsilon_i^{-1}$), it is more reasonable. As we have already outlined in the introduction (cf. figure 1), the case in which β_i is large will tend to be our focus in this paper; so we conclude that the scalings (2.55) will generally be the pertinent ones.

2.3. *Kinetic stability of classical, collisional plasma*

2.3.1. *Overview*

We have seen that the CE expansion provides a procedure for the calculation of the distribution functions arising in a classical, collisional plasma in terms of gradients of temperature, electron–ion drifts and bulk fluid velocities; these calculations in turn allow for the closure of the system (2.4) of fluid equations. However, these same gradients are sources of free energy in the plasma, so they can lead to instabilities. Some of these instabilities will be 'fluid', i.e. they are captured within the CE description and are features of the fluid dynamics of plasmas; others are kinetic ('microinstabilities'), and their existence implies that the CE expansion is, in fact, illegitimate. Our primary purpose in this paper is to determine when such microinstabilities do not occur in a strongly magnetised two-species plasma. If, however, they do occur, we wish to determine their growth rates. We begin by making a few general qualitative comments concerning the existence and nature of these microinstabilities, before presenting the technical details of their derivation.

2.3.2. *Existence of microinstabilities in classical, collisional plasma*

It might naively be assumed that a classical, collisional plasma is kinetically stable, on two grounds. The first of these is that the distribution function of such a plasma is 'almost' Maxwellian, and thus stable. While it is certainly the case that a plasma whose constituent particles have Maxwellian distribution functions is kinetically stable (Bernstein 1958; Krall & Trivelpiece 1973), it is also known that a plasma with anisotropic particle distribution functions is typically not (Furth 1963; Kalman *et al.* 1968; Davidson 1983; Gary 1993). The (small) non-Maxwellian component of the CE distribution function is anisotropic (as, e.g. was explicitly demonstrated by the calculation of pressure anisotropy in § 2.2.2), and thus we cannot *a priori* rule out microinstabilities associated with this anisotropy.

The second naive reason for dismissing the possibility of microinstabilities in classical, collisional plasma is the potentially stabilising effect of collisional damping on microinstability growth rates. If collisional processes are sufficiently dominant to be responsible for the mediation of macroscopic momentum and heat fluxes in the plasma, it might be naively inferred that they would also suppress microinstabilities. This is, in fact, far from guaranteed, for the following reason. The characteristic scales of the microinstabilities are not fluid scales, but are rather intrinsic plasma length scales related to quantities such as the Larmor radius ρ_s or the inertial scale d_s of species s, or the Debye length λ_D – quantities given in terms of macroscopic physical properties of plasma by

$$\rho_s = \frac{m_s v_{\text{th}s} c}{|Z_s| e |\boldsymbol{B}|}, \tag{2.58a}$$

$$d_s \equiv \left(\frac{4\pi Z_s^2 e^2 n_s}{m_s c^2} \right)^{-1/2} = \rho_s \beta_s^{-1/2}, \tag{2.58b}$$

$$\lambda_{\mathrm{D}} \equiv \left(\sum_s \frac{4\pi Z_s^2 e^2 n_s}{T_s} \right)^{-1/2} = \left(\sum_s \frac{2c}{d_s^2 v_{\mathrm{th}s}} \right)^{-1/2}. \tag{2.58c}$$

The crucial observation is then that the dynamics on characteristic microinstability scales may be collisionless. For a classical, collisional hydrogen plasma (where $\lambda \equiv \lambda_e \sim \lambda_i$ for $T_e \sim T_i$), the mean free path is much larger than the Debye length: $\lambda/\lambda_{\mathrm{D}} \sim n_e \lambda_{\mathrm{D}}^3 \gg 1$; so there exists a range of wavenumbers k on which microinstabilities are both possible ($k\lambda_{\mathrm{D}} \lesssim 1$) and collisionless ($k\lambda \gg 1$). For a strongly magnetised collisional plasma, $\lambda_s \gg \rho_s$ for all species by definition; thus, any microinstability with a characteristic scale comparable to the Larmor radius of any constituent particle will be effectively collisionless. We note that such a range of collisionless wavenumbers only exists in classical (*viz.* weakly coupled) plasmas; in strongly coupled plasmas, for which $\lambda \lesssim \lambda_{\mathrm{D}}$, all hypothetically possible microinstability wavenumber scales are collisional. Thus the phenomenon of microinstabilities in collisional plasmas is solely a concern for the classical regime.

2.3.3. *A simple example: the firehose instability in CE plasmas*

Perhaps the simplest example of a microinstability that can occur in CE plasma is the firehose instability. This example was previously discussed by Schekochihin *et al.* (2005), but we nonetheless outline it here to illustrate the central concept of our paper.

Consider bulk fluid motions of the plasma on length scales L_V that are much smaller than the mean free path λ_i, but much larger than the ion-Larmor radius ρ_i; the characteristic frequencies associated with these motions are assumed to be much smaller that the ion Larmor frequency Ω_i, but much larger than the inverse of the ion collision time τ_i^{-1}. Under these assumptions, the following four statements can be shown to be true (Schekochihin *et al.* 2005):

(i) The bulk velocities of the electron and ion species are approximately equal: $V_e \approx V_i$.

(ii) The electric field in a frame co-moving with the ion fluid vanishes; transforming to the stationary frame of the system, this gives

$$E = -\frac{V_i \times B}{c}. \tag{2.59}$$

(iii) The contribution of the displacement current to the Maxwell–Ampère law (2.2*d*) is negligible, and so

$$e n_e (V_i - V_e) \approx \frac{c}{4\pi} \nabla \times B. \tag{2.60}$$

(iv) The electron and ion viscosity tensors both take the form (2.32), and the electron-pressure anisotropy, defined by (2.35), is small compared with the ion pressure anisotropy: $\Delta_e \ll \Delta_i$.

It then follows directly from (2.4*b*), summed over both ion and electron species, that

$$m_i n_i \left. \frac{\mathrm{D}V_i}{\mathrm{D}t} \right|_i = -\nabla \left(\frac{B^2}{8\pi} + p_{e\perp} + p_{i\perp} \right) - \nabla \cdot \left[\hat{z}\hat{z} \left(p_{i\perp} - p_{i\parallel} \right) \right] + \frac{B \cdot \nabla B}{4\pi}. \tag{2.61}$$

We remind the reader that $\hat{z} = \boldsymbol{B}/B$, and emphasise that we have neglected the electron inertial term on the grounds that it is small compared with the ion inertial term:

$$m_e n_e \left.\frac{\mathrm{D}\boldsymbol{V}_e}{\mathrm{D}t}\right|_e \ll m_i n_i \left.\frac{\mathrm{D}\boldsymbol{V}_i}{\mathrm{D}t}\right|_i. \tag{2.62}$$

The evolution of the magnetic field is described by the induction equation

$$\left.\frac{\mathrm{D}\boldsymbol{B}}{\mathrm{D}t}\right|_i = \boldsymbol{B} \cdot \nabla \boldsymbol{V}_i - B\nabla \cdot \boldsymbol{V}_i, \tag{2.63}$$

which is derived by substituting (2.59) into Faraday's law (2.2c).

Now consider small-amplitude perturbations with respect to a particular macroscale state of the plasma

$$\delta \boldsymbol{V}_i = \widehat{\delta \boldsymbol{V}}_{i\perp} \exp\{\mathrm{i}\left(\boldsymbol{k}\cdot\boldsymbol{r}-\omega t\right)\}, \tag{2.64a}$$

$$\delta \boldsymbol{B} = \widehat{\delta \boldsymbol{B}}_{\perp} \exp\{\mathrm{i}\left(\boldsymbol{k}\cdot\boldsymbol{r}-\omega t\right)\}, \tag{2.64b}$$

whose characteristic frequency ω is much greater than that of the plasma's bulk fluid motions (but is still much smaller than Ω_i), whose wavevector $\boldsymbol{k} = k_\parallel \hat{z}$ is parallel to $\boldsymbol{B}$, and assume also that the velocity and magnetic-field perturbations are perpendicular to $\boldsymbol{B}$. It is then easy to show that (2.61) and (2.63) become

$$-\mathrm{i}m_i n_i \omega \widehat{\delta \boldsymbol{V}}_{i\perp} = \mathrm{i}\left(\frac{B^2}{4\pi}+p_{i\perp}-p_{i\parallel}\right)k_\parallel \frac{\widehat{\delta \boldsymbol{B}}_\perp}{B}, \tag{2.65a}$$

$$-\mathrm{i}\omega\widehat{\delta \boldsymbol{B}}_\perp = \mathrm{i}Bk_\parallel \widehat{\delta \boldsymbol{V}}_{i\perp}, \tag{2.65b}$$

where $p_{i\perp}$ and $p_{i\parallel}$ are the perpendicular and parallel ion pressures associated with the macroscale state (which, on account of its comparatively slow evolution compared with the perturbation, can be regarded a quasi-equilibrium). Physically, the macroscale flow gives rise to different values of $p_{i\perp}$ and $p_{i\parallel}$, and thereby an ion-pressure anisotropy Δ_i, because it changes the strength B of the macroscale magnetic field; thanks to the effective conservation of the first and second adiabatic moments of the ions on the evolution time scale of the macroscale flow (Chew *et al.* 1956), an increase (decrease) in B results in an increase (decrease) in $p_{i\perp}$, and a decrease (increase) in $p_{i\parallel}$. The dispersion relation for the perturbation is then

$$\omega^2 = k_\parallel^2 v_{\mathrm{th}i}^2 \left(\frac{1}{\beta_i}+\frac{\Delta_i}{2}\right), \tag{2.66}$$

where β_i, defined by (2.57), is the ion plasma beta. For a sufficiently negative ion-pressure anisotropy, *viz.* $\Delta_i < -2/\beta_i$, the perturbation is unstable. This instability is known as the (parallel) firehose instability.

The underlying physics of the parallel firehose instability has been discussed extensively elsewhere (see Rosin *et al.* (2011), and references therein; also see § 4.4.1). Here, we simply note that the firehose instability arises in a magnetised plasma with sufficiently negative pressure anisotropy as compared with the inverse of the ion plasma beta; because the ion CE distribution function has a small, non-zero pressure anisotropy, this statement applies

to CE plasma at large β_i. We also observe that the product of the growth rate (2.66) of the firehose instability with the ion–ion collision time satisfies

$$\omega \tau_i \sim k_\parallel \lambda_i \left| \frac{1}{\beta_i} + \Delta_i \right|^{1/2} \sim \frac{1}{\beta_i} \frac{\lambda_i}{\rho_i}, \tag{2.67}$$

where we have assumed that $\Delta_i \lesssim -2\beta_i^{-1}$, and employed the (non-trivial) result that the peak growth of the parallel firehose instability occurs at wavenumbers satisfying $k_\parallel \rho_i \sim \beta_i^{-1/2}$ (see §§ 4.4.1 and 4.4.2). Thus, if $\beta_i \ll \lambda_i/\rho_i$ – a condition easily satisfied in weakly collisional astrophysical environments such as the ICM (see table 4) – it follows that $\omega \tau_i \gg 1$, and so collisional damping is unable to inhibit the parallel firehose in a CE plasma.[2] This failure is directly attributable to its characteristic wavelength being at collisionless scales: the parallel wavenumber satisfies $k_\parallel \lambda_i \sim \beta_i^{-1/2} \lambda_i/\rho_i \gg 1$.

This simple example clearly illustrates that microinstabilities are indeed possible in a classical, collisional plasma, for precisely the reasons given in § 2.3.2.

2.3.4. *Which microinstabilities are relevant*

Although the naive arguments described in § 2.3.2 do not imply kinetic stability of CE plasma, these same arguments do lead to significant restrictions on the type of microinstabilities that can arise. Namely, for some plasma modes, the small anisotropy of CE distribution functions is an insufficient free-energy source for overcoming the competing collisionless damping mechanisms that ensure stability for pure Maxwellian distribution functions – e.g. Landau damping or cyclotron damping. For other plasma modes, the characteristic length scales are so large that collisional damping does suppress growth. In magnetised plasmas, there also exist cyclotron harmonic oscillations that, despite minimal damping, can only become unstable for sufficiently large anisotropy of the particle distribution function: e.g. the electrostatic Harris instability (Harris 1959; Hall, Heckrotte & Kammash 1964). Since the anisotropy threshold for such microinstabilities is typically $\Delta_s \gtrsim 1$ (Shima & Hall 1965), they cannot operate in a CE plasma.

We claim that there are only two classes of microinstabilities that can be triggered in a CE plasma. The first are quasi-cold-plasma modes: these are modes whose frequency is so large that resonant wave–particle interactions (Landau or cyclotron resonances) only occur with electrons whose speed greatly exceeds the electron thermal speed $v_{\mathrm{th}e}$. Collisionless damping of such modes is typically very weak, and thus small anisotropies of particle distribution functions can be sufficient to drive an instability. Well-known examples of a small non-Maxwellian part of the distribution function giving rise to microinstabilities include the bump-on-tail instability associated with a fast beam of electrons (see § 3.3.3 of Davidson 1983), or the whistler instability for small temperature anisotropies (see § 3.3.5 of Davidson 1983). The existence of such instabilities for the CE distribution can be demonstrated explicitly: e.g. the peak growth rate of the bump-on-tail instability associated with the CE distribution function ('the CE bump-on-tail instability') is calculated in Appendix D.3. However, the growth rates γ of such instabilities are exponentially small in $\lambda_e/L \ll 1$. This claim, which is explicitly proven for the CE bump-on-tail instability in Appendix D.3, applies to all electrostatic instabilities (see Appendix D.4), and it can be argued that it also applies to all quasi-cold-plasma modes (see Appendix E). When combined with the constraint that the resonant wave–particle interactions required for such instabilities cannot occur if $\gamma \tau_r \lesssim 1$, where τ_r is the collision time of the resonant particles,

---

[2]In fact, the naive condition $\gamma \tau_i \lesssim 1$ is not sufficient to ensure collisional stabilisation of the firehose instability; the true stabilisation condition is instead $k_\parallel \lambda_i \lesssim 1$ (see § 2.5.7 for a discussion of this claim).

the exponential smallness of the growth rate suggests that such microinstabilities will not be significant provided λ_e/L really is small. As discussed in § 2.2.3, plasmas in which λ_e/L is only moderately small are not well modelled as CE plasmas anyway, and thus, for the rest of this paper, we will not study quasi-cold-plasma-mode instabilities.

The second class of allowed microinstabilities comprises modes that are electromagnetic and low frequency in the sense that the complex frequency ω of the microinstability satisfies, for at least one particle species s,

$$\frac{\omega}{k v_{\text{th}s}} \sim \left(\frac{\lambda_s}{L}\right)^\iota \ll 1, \tag{2.68}$$

where ι is some order-unity number. Low-frequency electromagnetic modes are in general only subject to weak Landau and cyclotron damping (of order $\omega/k v_{\text{th}s} \ll 1$ or less), and thus can become unstable for small distribution-function anisotropies. By contrast, electromagnetic modes satisfying $\omega \sim k v_{\text{th}s}$ would typically generate strong inductive electric fields, which would in turn be subject to significant Landau or cyclotron damping, overwhelming any unstable tendency. The firehose instability introduced in § 2.3.3 is one example of this type of microinstability: it satisfies (2.68) with $\iota = 1/2$, provided its β-stabilisation threshold is surpassed.

In this paper, we will focus on microinstabilities in this second class. Whilst small compared with the streaming rate $k v_{\text{th}s}$ of species s, the growth rates satisfying (2.68) can still be significantly larger than the rate at which the plasma evolves on macroscopic scales, and thus invalidate the CE expansion. We do not in this paper present a rigorous proof that there are no microinstabilities of the CE distribution function which do not fall into either of the two classes considered above. However, there do exist more precise arguments supporting the latter claim than those based on physical intuition just presented; these are discussed further in §§ 2.4.2 and 2.5.8.

The microinstabilities satisfying (2.68) fall into two sub-classes. The first sub-class consists of microinstabilities driven by the CE temperature-gradient, CE electron-friction and CE electron–ion-drift terms in the CE distribution functions (2.8); we refer to these collectively as CE temperature-gradient-driven microinstabilities, or CET microinstabilities, on account of the parameters η_e^R and η_e^u scaling with temperature gradients (see § 2.2.2). The second sub-class is microinstabilities driven by the CE shear terms, or CE shear-driven microinstabilities (CES microinstabilities). This sub-classification is necessary for two reasons. First, the velocity-space anisotropy associated with the CE shear terms is different from other non-Maxwellian terms, and thus different types of microinstabilities can emerge for the two sub-classes. Secondly, as was discussed in § 2.2.3 for the case of CE plasma, the typical size of small parameters η_e^T, η_e^R, η_e^u and η_i is different from that of ϵ_e and ϵ_i. In our initial overview of our calculations (§ 2.4) and in the more detailed discussion of our method (§ 2.5), we will consider all microinstabilities driven by the non-Maxwellian terms of the CE distribution together; however, when it comes to presenting detailed results, we will consider CET and CES microinstabilities separately (§§ 3 and 4, respectively).

2.4. *Linear stability calculation: overview*

2.4.1. *General dispersion relation*

Our linear kinetic stability calculation proceeds as follows: we consider an electromagnetic perturbation with wavevector $\boldsymbol{k}$ and (complex) frequency ω of

the form

$$\delta \boldsymbol{E} = \widehat{\delta \boldsymbol{E}} \exp\left\{\mathrm{i}\left(\boldsymbol{k} \cdot \boldsymbol{r} - \omega t\right)\right\}, \tag{2.69a}$$

$$\delta \boldsymbol{B} = \widehat{\delta \boldsymbol{B}} \exp\left\{\mathrm{i}\left(\boldsymbol{k} \cdot \boldsymbol{r} - \omega t\right)\right\}, \tag{2.69b}$$

in a plasma with the equilibrium electron and ion distribution functions given by (2.8a) and (2.8b), respectively. We assume that all macroscopic parameters in the CE distribution function are effectively constant on the time scales and length scales associated with microinstabilities: this is equivalent to assuming that $k\lambda_e, k\lambda_i \gg 1$ (where $k \equiv |\boldsymbol{k}|$ is the wavenumber of the perturbation), and $|\omega| \tau_L \gg 1$. To minimise confusion between quantities evolving on short, collisionless time scales, and those on long, fluid time scales, we relabel the equilibrium number density of species s as n_{s0}, and the macroscopic magnetic field as $\boldsymbol{B}_0$ in subsequent calculations. For notational convenience, we define

$$\eta_e \equiv \eta_e^T, \tag{2.70}$$

and

$$A_e(\tilde{v}_e) \equiv A_e^T(\tilde{v}_e) + \frac{\eta_e^R}{\eta_e^T} A_e^R(\tilde{v}_e) + \frac{\eta_e^u}{\eta_e^T} A_e^u(\tilde{v}_e), \tag{2.71}$$

which in turn allows for the equilibrium distribution function of species s to be written as

$$f_{s0}(\tilde{v}_{s\parallel}, \tilde{v}_{s\perp}) = \frac{n_{s0}}{v_{\mathrm{th}s}^3 \pi^{3/2}} \exp\left(-\tilde{v}_s^2\right)\left[1 + \eta_s A_s(\tilde{v}_s)\tilde{v}_{s\parallel} + \epsilon_s C_s(\tilde{v}_s)\left(\tilde{v}_{s\parallel}^2 - \frac{\tilde{v}_{s\perp}^2}{2}\right)\right]. \tag{2.72}$$

Finally, without loss of generality, we can set $\boldsymbol{V}_i = 0$ by choosing to perform the kinetic calculation in the frame of the ions; thus, $\tilde{\boldsymbol{v}}_s = \boldsymbol{v}/v_{\mathrm{th}s}$.

It is well known (Stix 1962; Parra 2017) that the electric field of all linear electromagnetic perturbations in a collisionless, magnetised plasma with equilibrium distribution function f_{s0} must satisfy

$$\left[\frac{c^2 k^2}{\omega^2}\left(\hat{\boldsymbol{k}}\hat{\boldsymbol{k}} - \boldsymbol{I}\right) + \boldsymbol{\mathfrak{E}}\right] \cdot \widehat{\delta \boldsymbol{E}} = 0, \tag{2.73}$$

where $\hat{\boldsymbol{k}} \equiv \boldsymbol{k}/k$ is the direction of the perturbation,

$$\boldsymbol{\mathfrak{E}} \equiv \boldsymbol{I} + \frac{4\pi\mathrm{i}}{\omega}\boldsymbol{\sigma}, \tag{2.74}$$

the plasma dielectric tensor and $\boldsymbol{\sigma}$ the plasma conductivity tensor. The hot-plasma dispersion relation is then given by

$$\det\left[\frac{c^2 k^2}{\omega^2}\left(\hat{\boldsymbol{k}}\hat{\boldsymbol{k}} - \boldsymbol{I}\right) + \boldsymbol{\mathfrak{E}}\right] = 0. \tag{2.75}$$

The conductivity tensor in a hot, magnetised plasma is best displayed in an orthogonal coordinate system with basis vectors $\{\hat{\boldsymbol{x}}, \hat{\boldsymbol{y}}, \hat{\boldsymbol{z}}\}$ defined in terms of $\boldsymbol{B}_0$ and $\boldsymbol{k}$:

$$\hat{\boldsymbol{z}} \equiv \frac{\boldsymbol{B}_0}{B_0}, \quad \hat{\boldsymbol{x}} \equiv \frac{\boldsymbol{k}_\perp}{k_\perp} \equiv \frac{\boldsymbol{k} - k_\parallel \hat{\boldsymbol{z}}}{k_\perp}, \quad \hat{\boldsymbol{y}} \equiv \hat{\boldsymbol{z}} \times \hat{\boldsymbol{x}}, \tag{2.76a–c}$$

where $B_0 \equiv |\boldsymbol{B}_0|$, $k_\parallel \equiv \boldsymbol{k} \cdot \hat{\boldsymbol{z}}$, and $k_\perp \equiv |\boldsymbol{k}_\perp|$. In this notation, $\boldsymbol{k} = k_\parallel \hat{\boldsymbol{z}} + k_\perp \hat{\boldsymbol{x}}$. The conductivity tensor is then given by

$$\boldsymbol{\sigma} = \sum_s \boldsymbol{\sigma}_s = -\frac{\mathrm{i}}{4\pi\omega} \sum_s \omega_{\mathrm{ps}}^2 \left[\frac{2}{\sqrt{\pi}} \frac{k_\parallel}{|k_\parallel|} \int_{-\infty}^{\infty} \mathrm{d}\tilde{w}_{s\parallel} \, \tilde{w}_{s\parallel} \int_0^{\infty} \mathrm{d}\tilde{v}_{s\perp} \, \Lambda_s(\tilde{w}_{s\parallel}, \tilde{v}_{s\perp}) \hat{\boldsymbol{z}}\hat{\boldsymbol{z}} \right.$$
$$\left. + \tilde{\omega}_{s\parallel} \frac{2}{\sqrt{\pi}} \int_{C_L} \mathrm{d}\tilde{w}_{s\parallel} \int_0^{\infty} \mathrm{d}\tilde{v}_{s\perp} \, \tilde{v}_{s\perp}^2 \, \Xi_s(\tilde{w}_{s\parallel}, \tilde{v}_{s\perp}) \sum_{n=-\infty}^{\infty} \frac{\boldsymbol{R}_{sn}}{\zeta_{sn} - \tilde{w}_{s\parallel}} \right], \quad (2.77)$$

where

$$\omega_{\mathrm{ps}} \equiv \sqrt{\frac{4\pi Z_s^2 e^2 n_{s0}}{m_s}}, \qquad (2.78)$$

$$\tilde{w}_{s\parallel} \equiv \frac{k_\parallel \tilde{v}_{s\parallel}}{|k_\parallel|}, \qquad (2.79)$$

$$\tilde{\rho}_s \equiv \frac{m_s c v_{\mathrm{ths}}}{Z_s e B_0} = \frac{|Z_s|}{Z_s} \rho_s, \qquad (2.80)$$

$$\tilde{\omega}_{s\parallel} \equiv \frac{\omega}{|k_\parallel| v_{\mathrm{ths}}}, \qquad (2.81)$$

$$\zeta_{sn} \equiv \tilde{\omega}_{s\parallel} - \frac{n}{|k_\parallel| \tilde{\rho}_s}, \qquad (2.82)$$

$$\tilde{f}_{s0}(\tilde{v}_{s\parallel}, \tilde{v}_{s\perp}) \equiv \frac{\pi^{3/2} v_{\mathrm{ths}}^3}{n_{s0}} f_{s0} \left(\frac{k_\parallel}{|k_\parallel|} v_{\mathrm{ths}} \tilde{w}_{s\parallel}, v_{\mathrm{ths}} \tilde{v}_{s\perp} \right), \qquad (2.83)$$

$$\Lambda_s(\tilde{w}_{s\parallel}, \tilde{v}_{s\perp}) \equiv \tilde{v}_{s\perp} \frac{\partial \tilde{f}_{s0}}{\partial \tilde{w}_{s\parallel}} - \tilde{w}_{s\parallel} \frac{\partial \tilde{f}_{s0}}{\partial \tilde{v}_{s\perp}}, \qquad (2.84)$$

$$\Xi_s(\tilde{w}_{s\parallel}, \tilde{v}_{s\perp}) \equiv \frac{\partial \tilde{f}_{s0}}{\partial \tilde{v}_{s\perp}} + \frac{\Lambda_s(\tilde{w}_{s\parallel}, \tilde{v}_{s\perp})}{\tilde{\omega}_{s\parallel}}, \qquad (2.85)$$

$$(\boldsymbol{R}_{sn})_{xx} \equiv \frac{n^2 J_n(k_\perp \tilde{\rho}_s \tilde{v}_{s\perp})^2}{k_\perp^2 \tilde{\rho}_s^2 \tilde{v}_{s\perp}^2}, \qquad (2.86a)$$

$$(\boldsymbol{R}_{sn})_{xy} \equiv \frac{\mathrm{i}n J_n(k_\perp \tilde{\rho}_s \tilde{v}_{s\perp}) J_n'(k_\perp \tilde{\rho}_s \tilde{v}_{s\perp})}{k_\perp \tilde{\rho}_s \tilde{v}_{s\perp}}, \qquad (2.86b)$$

$$(\boldsymbol{R}_{sn})_{xz} \equiv \frac{n J_n(k_\perp \tilde{\rho}_s \tilde{v}_{s\perp})^2}{k_\perp \tilde{\rho}_s \tilde{v}_{s\perp}} \frac{k_\parallel \tilde{w}_{s\parallel}}{|k_\parallel| \tilde{v}_{s\perp}}, \qquad (2.86c)$$

$$(\boldsymbol{R}_{sn})_{yx} \equiv -(\boldsymbol{R}_{sn})_{xy}, \qquad (2.86d)$$

$$(\boldsymbol{R}_{sn})_{yy} \equiv J_n'(k_\perp \tilde{\rho}_s \tilde{v}_{s\perp})^2, \qquad (2.86e)$$

$$(\boldsymbol{R}_{sn})_{yz} \equiv -\mathrm{i}n J_n(k_\perp \tilde{\rho}_s \tilde{v}_{s\perp}) J_n'(k_\perp \tilde{\rho}_s \tilde{v}_{s\perp}) \frac{k_\parallel \tilde{w}_{s\parallel}}{|k_\parallel| \tilde{v}_{s\perp}}, \qquad (2.86f)$$

$$(\boldsymbol{R}_{sn})_{zx} \equiv (\boldsymbol{R}_{sn})_{xz}, \qquad (2.86g)$$

$$(\boldsymbol{R}_{sn})_{zy} \equiv -(\boldsymbol{R}_{sn})_{yz}, \tag{2.86h}$$

$$(\boldsymbol{R}_{sn})_{zz} \equiv \frac{\tilde{w}_{s\parallel}^2}{\tilde{v}_{s\perp}^2} J_n(k_\perp \tilde{\rho}_s \tilde{v}_{s\perp})^2. \tag{2.86i}$$

Here, $(\boldsymbol{R}_{sn})_{xy} = \hat{\boldsymbol{x}} \cdot \boldsymbol{R}_{sn} \cdot \hat{\boldsymbol{y}}$, and similarly for other components of $\boldsymbol{R}_{sn}$. The integration in (2.77) is carried out over the Landau contour C_L; this is simply the real axis for growing perturbations, but has a more complicated form for non-growing ones (Landau 1946; Schekochihin 2024). For the reader's convenience, a summary of the derivation of the hot-plasma dispersion relation is given in Appendix C.

We note that the dielectric and conductivity tensors have the following symmetries:

$$\mathfrak{E}_{yx} = -\mathfrak{E}_{xy}, \quad \mathfrak{E}_{zx} = \mathfrak{E}_{xz}, \quad \mathfrak{E}_{zy} = -\mathfrak{E}_{yz}, \tag{2.87a–c}$$

$$\sigma_{yx} = -\sigma_{xy}, \quad \sigma_{zx} = \sigma_{xz}, \quad \sigma_{zy} = -\sigma_{yz}, \tag{2.88a–c}$$

where, for tensors with no species subscript, we use the notation $\mathfrak{E}_{xy} \equiv \hat{\boldsymbol{x}} \cdot \mathfrak{E} \cdot \hat{\boldsymbol{y}}$. We also observe that if $f_{s0}(v_\parallel, v_\perp)$ is an even function with respect to $v_\parallel$, then, for $k_\parallel > 0$,

$$\sigma_{xx}(-k_\parallel) = \sigma_{xx}(k_\parallel), \tag{2.89a}$$

$$\sigma_{xy}(-k_\parallel) = \sigma_{xy}(k_\parallel), \tag{2.89b}$$

$$\sigma_{xz}(-k_\parallel) = -\sigma_{xz}(k_\parallel), \tag{2.89c}$$

$$\sigma_{yy}(-k_\parallel) = \sigma_{yy}(k_\parallel), \tag{2.89d}$$

$$\sigma_{yz}(-k_\parallel) = -\sigma_{yz}(k_\parallel), \tag{2.89e}$$

$$\sigma_{zz}(-k_\parallel) = \sigma_{zz}(k_\parallel), \tag{2.89f}$$

with the remaining components of the conductivity tensor given by (2.87a–c). If $f_{s0}(v_\parallel, v_\perp)$ is an odd function with respect to $v_\parallel$, then

$$\sigma_{xx}(-k_\parallel) = -\sigma_{xx}(k_\parallel), \tag{2.90a}$$

$$\sigma_{xy}(-k_\parallel) = -\sigma_{xy}(k_\parallel), \tag{2.90b}$$

$$\sigma_{xz}(-k_\parallel) = \sigma_{xz}(k_\parallel), \tag{2.90c}$$

$$\sigma_{yy}(-k_\parallel) = -\sigma_{yy}(k_\parallel), \tag{2.90d}$$

$$\sigma_{yz}(-k_\parallel) = \sigma_{yz}(k_\parallel), \tag{2.90e}$$

$$\sigma_{zz}(-k_\parallel) = -\sigma_{zz}(k_\parallel). \tag{2.90f}$$

These symmetries can be used to determine completely the behaviour of perturbations with $k_\parallel < 0$ directly from perturbations with $k_\parallel > 0$, without any additional calculations. Thus, unless stated otherwise, from this point on, we assume $k_\parallel > 0$, and thus $\tilde{w}_{s\parallel} = \tilde{v}_{s\parallel}$ (see (2.79)).

2.4.2. *Simplifications of dispersion relation: overview of our approach*

The full hot-plasma dispersion relation (2.75) is a transcendental equation, and thus, for general distribution functions, the growth rates of perturbations can only be determined numerically; this hinders the systematic investigation of stability over wide-ranging parameter regimes. However, adopting a few simplifications both to the form of the CE distribution functions (2.72) and to the type of microinstabilities being considered (see § 2.3.4) turns out to be advantageous when attempting a systematic study. It enables us

to obtain simple analytical results for microinstability growth rates and characteristic wavenumbers, as well as greatly reducing the numerical cost of evaluating these quantities. The former allows us to make straightforward comparisons between microinstabilities, while the latter facilitates the calculation of stability plots over a wide range of parameters without requiring intensive computational resources.

First, we choose a Krook collision operator, with constant collision time τ_s for each species s (Bhatnagar *et al.* 1954), when evaluating the isotropic functions $A_e^T(\tilde{v}_e)$, $A_e^R(\tilde{v}_e)$, $A_e^u(\tilde{v}_e)$, $A_i(\tilde{v}_i)$, $C_e(\tilde{v}_e)$ and $C_i(\tilde{v}_i)$ in (2.72). As was explained in § 2.2.1, these functions are determined by the collision operator. While the full Landau collision operator might seem to be the most appropriate choice, the conductivity tensor $\boldsymbol{\sigma}$ defined by (2.77) cannot be written in terms of standard mathematical functions if this choice is made. Instead, the relevant integrals must be done numerically. If a simplified collision operator is assumed, $\boldsymbol{\sigma}$ can be evaluated analytically with only a moderate amount of algebra. In Appendix B.2.1, we show that for the Krook collision operator

$$A_e^T(\tilde{v}_e) = -\left(\tilde{v}_e^2 - \tfrac{5}{2}\right), \tag{2.91a}$$

$$A_e^R(\tilde{v}_e) = -1, \tag{2.91b}$$

$$A_e^u(\tilde{v}_e) = 0, \tag{2.91c}$$

$$A_i(\tilde{v}_e) = -\left(\tilde{v}_i^2 - \tfrac{5}{2}\right), \tag{2.91d}$$

$$C_e(\tilde{v}_e) = -1, \tag{2.91e}$$

$$C_i(\tilde{v}_i) = -1, \tag{2.91f}$$

where it is assumed that $\tilde{v}_e$, $\tilde{v}_i \ll \eta_e^{-1/3}$, $\epsilon_i^{-1/2}$ in order that the CE distribution functions retain positive signs (the vanishing of the CE electron–ion-drift term is discussed in Appendix B.2.1). Adopting the Krook collision operator has the additional advantage of allowing a simple prescription for collisional damping of microinstabilities to be introduced self-consistently into our stability calculation (see § 2.5.7 for further discussion of this).

Secondly, as discussed in § 2.3.4, the most important microinstabilities associated with the CE distribution function are low frequency, i.e. they satisfy (2.68). Therefore, instead of solving the full hot-plasma dispersion relation, we can obtain a less complicated algebraic dispersion relation. We also always consider electromagnetic rather than electrostatic perturbations. This is because it can be shown for a CE plasma that purely electrostatic microinstabilities are limited to the quasi-cold-plasma modes (see Appendix D). Describing how the simplified dispersion relation for low-frequency, electromagnetic perturbations is obtained from the full hot-plasma dispersion relation requires a rather lengthy exposition, and necessitates the introduction of a substantial amount of additional mathematical notation. In addition to this, certain shortcomings of this approach warrant an extended discussion. Readers who are interested these details will find them in the next section (§ 2.5). Readers who are instead keen to see the results of the stability calculations as soon as possible are encouraged to jump to §§ 3 and 4.

2.5. *Linear stability calculation: detailed methodology*

2.5.1. *Low-frequency condition in a magnetised plasma*

Before applying to the hot-plasma dispersion relation (2.75) the simplifications discussed in § 2.4.2, we refine the low-frequency condition (2.68) based on the specific form (2.77) of the conductivity tensor for a magnetised plasma. It is clear that the equilibrium distribution function only affects the conductivity tensor via the functions

$\Lambda_s(\tilde{v}_{s\parallel}, \tilde{v}_{s\perp})$ and $\varXi_s(\tilde{v}_{s\parallel}, \tilde{v}_{s\perp})$ (see (2.84) and (2.85)). For a distribution function of the form (2.72), it can be shown that

$$\Lambda_s(\tilde{v}_{s\parallel}, \tilde{v}_{s\perp}) = -\tilde{v}_{s\perp} \exp\left(-\tilde{v}_s^2\right) \left[\eta_s A_s(\tilde{v}_s) - 3\epsilon_s C_s(\tilde{v}_s)\tilde{v}_{s\parallel}\right], \tag{2.92}$$

and

$$\begin{aligned}
\varXi_s(\tilde{v}_{s\parallel}, \tilde{v}_{s\perp}) = -\tilde{v}_{s\perp} \exp\left(-\tilde{v}_s^2\right) &\left[2 + 2\tilde{v}_{s\parallel}\eta_s A_s(\tilde{v}_s) - \frac{\tilde{v}_{s\parallel}}{\tilde{v}_s}\eta_s A_s'(\tilde{v}_s) \right. \\
&+ 2\epsilon_s C_s(\tilde{v}_s)\left(\tilde{v}_{s\parallel}^2 - \frac{\tilde{v}_{s\perp}^2}{2} + \frac{1}{2}\right) - \frac{1}{\tilde{v}_s}\left(\tilde{v}_{s\parallel}^2 - \frac{\tilde{v}_{s\perp}^2}{2}\right)\epsilon_s C_s'(\tilde{v}_s) \\
&\left. + \frac{\eta_s}{\tilde{\omega}_{s\parallel}}A_s(\tilde{v}_s) - 3\frac{\epsilon_s}{\tilde{\omega}_{s\parallel}}C_s(\tilde{v}_s)\tilde{v}_{s\parallel} \right], \tag{2.93}
\end{aligned}$$

where the first term in the square brackets in (2.93) originates from the Maxwellian part of the distribution function. A comparison of the size of the second, third, fourth and fifth terms with the first indicates that for $\tilde{v}_s \sim 1$ – for which $\varXi_s$ attains its largest characteristic values – the non-Maxwellian terms of the CE distribution function only provide a small, $O(\eta_e, \epsilon_e)$ contribution, and thus the conductivity is only altered slightly. However, considering the sixth and seventh terms in the square brackets in (2.93) (which are only present thanks to the anisotropy of the CE distribution function), it is clear that the non-Maxwellian contribution to the conductivity tensor can be significant for $\tilde{v}_s \sim 1$ provided the frequency (2.81) satisfies one of

$$\tilde{\omega}_{s\parallel} \sim \eta_s \ll 1 \quad \text{or} \quad \tilde{\omega}_{s\parallel} \sim \epsilon_s \ll 1. \tag{2.94}$$

Thus, the relevant low-frequency condition in a magnetised plasma involves the parallel particle streaming rate $k_\parallel v_{\text{th}s}$.

There do exist certain caveats to the claim that it is necessary for microinstabilities of CE plasma to satisfy (2.94); we defer detailed statement and discussion of these caveats – as well as of other potential shortcomings of our approach – to §§ 2.5.6, 2.5.7 and 2.5.8.

2.5.2. *Simplification I: non-relativistic electromagnetic fluctuations*

The requirement that the mode be electromagnetic, combined with the fact we are interested in non-relativistic fluctuations ($\omega \ll kc$) enables our first simplification. We see from (2.75) that for any perturbation of interest, the dielectric tensor must satisfy $\|\mathfrak{E}\| \gtrsim k^2c^2/\omega^2 \gg 1$ (where $\|\cdot\|$ is the Euclidean tensor norm); therefore, it simplifies to

$$\mathfrak{E} \approx \frac{4\pi i}{\omega}\sigma. \tag{2.95}$$

This amounts to ignoring the displacement current in the Ampère–Maxwell law, leaving Ampère's original equation. For convenience of exposition, we denote the contribution of each species s to (2.95) by

$$\mathfrak{E}_s \equiv \frac{4\pi i}{\omega}\sigma_s. \tag{2.96}$$

2.5.3. *Simplification II: expansion of dielectric tensor in $\omega \ll k_\parallel v_{\mathrm{th}s}$*

The next simplification involves an expansion of the matrices $\mathfrak{E}_s$ in the small parameters $\tilde{\omega}_{s\parallel} \sim \eta_s \sim \epsilon_s \ll 1$. The general principle of the expansion is as follows. We first divide the matrix $\mathfrak{E}_s$ (see (2.74), (2.77) and (2.96)) into the Maxwellian contribution $\boldsymbol{M}_s$ and the non-Maxwellian one $\boldsymbol{P}_s$:

$$\mathfrak{E}_s = \frac{\omega_{\mathrm{p}s}^2}{\omega^2} \left(\boldsymbol{M}_s + \boldsymbol{P}_s \right), \tag{2.97}$$

where the $\omega_{\mathrm{p}s}^2/\omega^2$ factor is introduced for later convenience. Next, we note that, for a Maxwellian distribution, $\Lambda_s(\tilde{v}_{s\parallel}, \tilde{v}_{s\perp}) = 0$ (see (2.84)), whereas $\Lambda_s \sim \epsilon_s, \eta_s$ for the non-Maxwellian component of the CE distribution function. Thus, from (2.77) considered under the ordering $k\rho_s \sim 1$, $\boldsymbol{M}_s = O(\tilde{\omega}_{s\parallel})$ as $\tilde{\omega}_{s\parallel} \to 0$, while $\boldsymbol{P}_s = O(\eta_s, \epsilon_s)$. The expansion of $\boldsymbol{M}_s$ and $\boldsymbol{P}_s$ in $\tilde{\omega}_{s\parallel}$ is, therefore,

$$\boldsymbol{M}_s\big(\tilde{\omega}_{s\parallel}, \boldsymbol{k}\big) \equiv \tilde{\omega}_{s\parallel} \boldsymbol{M}_s^{(0)}(\boldsymbol{k}) + \tilde{\omega}_{s\parallel}^2 \boldsymbol{M}_s^{(1)}(\boldsymbol{k}) + \ldots, \tag{2.98a}$$

$$\boldsymbol{P}_s\big(\tilde{\omega}_{s\parallel}, \boldsymbol{k}\big) \equiv \boldsymbol{P}_s^{(0)}(\boldsymbol{k}) + \tilde{\omega}_{s\parallel} \boldsymbol{P}_s^{(1)}(\boldsymbol{k}) + \ldots, \tag{2.98b}$$

where the matrices $\boldsymbol{M}_s^{(0)}$ and $\boldsymbol{M}_s^{(1)}$ are $O(1)$ functions of $\boldsymbol{k}$ only, and $\boldsymbol{P}_s^{(0)}$ and $\boldsymbol{P}_s^{(1)}$ are $O(\eta_s, \epsilon_s)$. We then expand $\mathfrak{E}_s$ as follows:

$$\mathfrak{E}_s = \tilde{\omega}_{s\parallel} \mathfrak{E}_s^{(0)} + \tilde{\omega}_{s\parallel}^2 \mathfrak{E}_s^{(1)} + \ldots, \tag{2.99}$$

where

$$\mathfrak{E}_s^{(0)} \equiv \frac{\omega_{\mathrm{p}s}^2}{\omega^2} \left[\boldsymbol{M}_s^{(0)}(\boldsymbol{k}) + \frac{1}{\tilde{\omega}_{s\parallel}} \boldsymbol{P}_s^{(0)}(\boldsymbol{k}) \right], \tag{2.100a}$$

$$\mathfrak{E}_s^{(1)} \equiv \frac{\omega_{\mathrm{p}s}^2}{\omega^2} \left[\boldsymbol{M}_s^{(1)}(\boldsymbol{k}) + \frac{1}{\tilde{\omega}_{s\parallel}} \boldsymbol{P}_s^{(1)}(\boldsymbol{k}) \right]. \tag{2.100b}$$

2.5.4. *Additional symmetries of low-frequency dielectric tensor $\mathfrak{E}_s^{(0)}$*

The tensor $\mathfrak{E}_s^{(0)}$ defined by (2.100a) has some rather convenient additional symmetries, which lead to significant simplification of the dispersion relation. In Appendix F we show that in combination with the general symmetries (2.87a–c), which apply to $\mathfrak{E}_s^{(0)}$ in addition to $\mathfrak{E}$, for any distribution function of particle species s with a small anisotropy:

$$(\mathfrak{E}_s^{(0)})_{xz} = -\frac{k_\perp}{k_\parallel} (\mathfrak{E}_s^{(0)})_{xx}, \tag{2.101a}$$

$$(\mathfrak{E}_s^{(0)})_{yz} = \frac{k_\perp}{k_\parallel} (\mathfrak{E}_s^{(0)})_{xy}, \tag{2.101b}$$

$$(\mathfrak{E}_s^{(0)})_{zz} = \frac{k_\perp^2}{k_\parallel^2} (\mathfrak{E}_s^{(0)})_{xx}. \tag{2.101c}$$

These symmetries have the consequence that

$$\hat{\boldsymbol{k}} \cdot \mathfrak{E}_s^{(0)} = \mathfrak{E}_s^{(0)} \cdot \hat{\boldsymbol{k}} = 0. \tag{2.102}$$

As a result of this identity, it is convenient to calculate the components of $\mathfrak{E}_s^{(0)}$ (and $\mathfrak{E}_s$) in the coordinate basis $\{\boldsymbol{e}_1, \boldsymbol{e}_2, \boldsymbol{e}_3\}$ defined by

$$\boldsymbol{e}_1 \equiv \hat{\boldsymbol{y}} \times \hat{\boldsymbol{k}}, \quad \boldsymbol{e}_2 \equiv \hat{\boldsymbol{y}}, \quad \boldsymbol{e}_3 \equiv \hat{\boldsymbol{k}}. \tag{2.103a–c}$$

Carrying out this calculation (see Appendix F), we find

$$(\mathfrak{E}_s^{(0)})_{11} = \frac{k^2}{k_\parallel^2} (\mathfrak{E}_s^{(0)})_{xx}, \qquad (2.104a)$$

$$(\mathfrak{E}_s^{(0)})_{12} = -(\mathfrak{E}_s^{(0)})_{21} = \frac{k}{k_\parallel} (\mathfrak{E}_s^{(0)})_{xy}, \qquad (2.104b)$$

$$(\mathfrak{E}_s^{(0)})_{22} = (\mathfrak{E}_s^{(0)})_{yy}, \qquad (2.104c)$$

$$(\mathfrak{E}_s^{(0)})_{13} = (\mathfrak{E}_s^{(0)})_{31} = (\mathfrak{E}_s^{(0)})_{23} = (\mathfrak{E}_s^{(0)})_{32} = (\mathfrak{E}_s^{(0)})_{33} = 0, \qquad (2.104d)$$

where $(\mathfrak{E}_s^{(0)})_{ij}$ is the (i, j)th component of $\mathfrak{E}_s^{(0)}$ in the basis $\{\boldsymbol{e}_1, \boldsymbol{e}_2, \boldsymbol{e}_3\}$. We conclude that, if $k\rho_s \sim 1$ and $\tilde{\omega}_{s\parallel} \ll 1$, the components of $\mathfrak{E}_s$ satisfy

$$(\mathfrak{E}_s)_{13} \sim (\mathfrak{E}_s)_{23} \sim (\mathfrak{E}_s)_{33} \sim \tilde{\omega}_{s\parallel}(\mathfrak{E}_s)_{11} \sim \tilde{\omega}_{s\parallel}(\mathfrak{E}_s)_{12} \sim \tilde{\omega}_{s\parallel}(\mathfrak{E}_s)_{22}. \qquad (2.105)$$

These components can be written in terms of the components of $\mathfrak{E}_s$ in the $\{\hat{\boldsymbol{x}}, \hat{\boldsymbol{y}}, \hat{\boldsymbol{z}}\}$ coordinate frame (see (2.76a–c)) via a coordinate transformation; the resulting expressions are rather bulky, so we do not reproduce them here – they are detailed in Appendix G.

2.5.5. *Consequences for dispersion relation*

On account of the additional symmetries described in the previous section, a simplified dispersion relation for low-frequency modes can be derived in place of the full hot-plasma dispersion relation (2.75). However, depending on the frequency and characteristic wavelengths of modes, this derivation has a subtlety because of the large discrepancy between ion and electron masses. In, e.g. a two-species plasma with $\mu_e = m_e/m_i \ll 1$ (and ion charge Z_i), we have

$$\frac{\tilde{\omega}_{e\parallel}}{\tilde{\omega}_{i\parallel}} = \sqrt{\mu_e \tau}, \qquad (2.106)$$

where $\tau = T_i/T_e$. If $\tau \sim 1$ (as would be expected in a collisional plasma on macroscopic evolution time scales τ_L greater than the ion–electron temperature-equilibration time τ_{ie}^{eq} – cf. (2.54)), then $\tilde{\omega}_{i\parallel} \sim \mu_e^{-1/2}\tilde{\omega}_{e\parallel} \gg \tilde{\omega}_{e\parallel}$. Thus, in general, $\tilde{\omega}_{i\parallel} \not\sim \tilde{\omega}_{e\parallel}$, and any dispersion relation will, in principle, depend on an additional (small) dimensionless parameter μ_e. This introduces various complications to the simplified dispersion relation's derivation, most significant of which being that, since $\rho_e = Z_i \mu_e^{1/2} \tau^{-1/2} \rho_i \ll \rho_i$ (for $Z_i \gtrsim 1$), to assume the ordering $k\rho_s \sim 1$ for both ions and electrons is inconsistent (see §2.5.6).

To avoid the description of our approach being obscured by these complications, we consider a special case at first: we adopt the ordering $k\rho_e \sim 1$ in a two-species plasma and assume that $\tilde{\omega}_{i\parallel} \sim \mu_e^{-1/2}\tilde{\omega}_{e\parallel} \ll 1$. In this case, $\tilde{\omega}_{i\parallel}\|\mathfrak{E}_i^{(0)}\| \sim \mu_e^{1/2}Z_i\tau^{-1/2}\tilde{\omega}_{e\parallel}\|\mathfrak{E}_e^{(0)}\| \ll \tilde{\omega}_{e\parallel}\|\mathfrak{E}_e^{(0)}\|$, and so the dielectric tensor $\mathfrak{E}$ is given by

$$\mathfrak{E} = \tilde{\omega}_{e\parallel}\mathfrak{E}^{(0)} + \tilde{\omega}_{e\parallel}^2 \mathfrak{E}^{(1)} + \dots, \qquad (2.107)$$

where

$$\mathfrak{E}^{(0)} \equiv \mathfrak{E}_e^{(0)} + \frac{\tilde{\omega}_{i\parallel}}{\tilde{\omega}_{e\parallel}}\mathfrak{E}_i^{(0)} \approx \mathfrak{E}_e^{(0)}, \qquad (2.108a)$$

$$\mathfrak{E}^{(1)} \equiv \mathfrak{E}_e^{(1)} + \frac{\tilde{\omega}_{i\parallel}^2}{\tilde{\omega}_{e\parallel}^2}\mathfrak{E}_i^{(1)}. \qquad (2.108b)$$

Thus, to leading order in the $\tilde{\omega}_{e\parallel} \ll 1$ expansion, only the electron species contributes to the dielectric tensor for electron-Larmor-scale modes. We revisit the derivation of simplified dispersion relations for CE microinstabilities more generally in § 2.5.6.

To derive the simplified dispersion relation for electron-Larmor-scale modes, we start by considering the component of (2.73) for the electric field that is parallel to the wavevector $\hat{\boldsymbol{k}}$,

$$\hat{\boldsymbol{k}} \cdot \boldsymbol{\mathfrak{E}} \cdot \widehat{\delta \boldsymbol{E}} = 0, \tag{2.109}$$

and then substitute the expanded form (2.107) of the dielectric tensor (with $s = e$). The orthogonality of $\boldsymbol{\mathfrak{E}}_e^{(0)}$ to $\hat{\boldsymbol{k}}$ – *viz.* (2.102) – implies that (2.109) becomes

$$\hat{\boldsymbol{k}} \cdot \boldsymbol{\mathfrak{E}}^{(1)} \cdot \widehat{\delta \boldsymbol{E}} = \mathfrak{E}_{33}^{(1)} \hat{\boldsymbol{k}} \cdot \widehat{\delta \boldsymbol{E}} + \hat{\boldsymbol{k}} \cdot \boldsymbol{\mathfrak{E}}^{(1)} \cdot \widehat{\delta \boldsymbol{E}}_T = O(\tilde{\omega}_{e\parallel} |\widehat{\delta \boldsymbol{E}}|), \tag{2.110}$$

where the transverse electric field is defined by $\widehat{\delta \boldsymbol{E}}_T \equiv \widehat{\delta \boldsymbol{E}} \cdot (\boldsymbol{I} - \hat{\boldsymbol{k}}\hat{\boldsymbol{k}})$. In Appendix D.2, we show that for $\tilde{\omega}_{e\parallel}, \tilde{\omega}_{i\parallel} \ll 1$,

$$\mathfrak{E}_{33}^{(1)} \approx \frac{\omega_{pe}^2}{\omega^2} \frac{2k_\parallel^2}{k^2} (1 + Z_i \tau^{-1}) \left[1 + O(\eta_e, \epsilon_e)\right]. \tag{2.111}$$

Since this is strictly positive, we can rewrite (2.110) to give the electrostatic field in terms of the transverse electric field:

$$\hat{\boldsymbol{k}} \cdot \widehat{\delta \boldsymbol{E}} = - \left(\mathfrak{E}_{33}^{(1)}\right)^{-1} \left(\hat{\boldsymbol{k}} \cdot \boldsymbol{\mathfrak{E}}^{(1)} \cdot \widehat{\delta \boldsymbol{E}}_T\right). \tag{2.112}$$

We conclude that $|\hat{\boldsymbol{k}} \cdot \widehat{\delta \boldsymbol{E}}| \sim |\widehat{\delta \boldsymbol{E}}_T|$ for all low-frequency perturbations with $k_\parallel \sim k$; a corollary of this result is that there can be no low-frequency purely electrostatic perturbations (see Appendix D.4.1 for an alternative demonstration of this).

We can now derive the dispersion relation from the other two components of (2.73),

$$\left[\frac{c^2 k^2}{\omega^2} \left(\hat{\boldsymbol{k}}\hat{\boldsymbol{k}} - \boldsymbol{I}\right) + \left(\hat{\boldsymbol{k}}\hat{\boldsymbol{k}} - \boldsymbol{I}\right) \cdot \boldsymbol{\mathfrak{E}}\right] \cdot \widehat{\delta \boldsymbol{E}} = 0, \tag{2.113}$$

by (again) substituting the expanded dielectric tensor (2.107) into (2.113):

$$\left[\tilde{\omega}_{e\parallel} \boldsymbol{\mathfrak{E}}^{(0)} + \frac{c^2 k^2}{\omega^2} \left(\hat{\boldsymbol{k}}\hat{\boldsymbol{k}} - \boldsymbol{I}\right)\right] \cdot \widehat{\delta \boldsymbol{E}}_T = - \left(\hat{\boldsymbol{k}}\hat{\boldsymbol{k}} - \boldsymbol{I}\right) \cdot \left(\boldsymbol{\mathfrak{E}} - \tilde{\omega}_{e\parallel} \boldsymbol{\mathfrak{E}}^{(0)}\right) \cdot \widehat{\delta \boldsymbol{E}}, \tag{2.114}$$

where we have used the identity

$$\boldsymbol{\mathfrak{E}}^{(0)} = \left(\hat{\boldsymbol{k}}\hat{\boldsymbol{k}} - \boldsymbol{I}\right) \cdot \boldsymbol{\mathfrak{E}}^{(0)} \cdot \left(\hat{\boldsymbol{k}}\hat{\boldsymbol{k}} - \boldsymbol{I}\right), \tag{2.115}$$

and ordered $k^2 c^2 / \omega^2 \sim \tilde{\omega}_{e\parallel} \|\boldsymbol{\mathfrak{E}}^{(0)}\|$. The ratio of the right-hand side of (2.114) to the left-hand side is $O(\tilde{\omega}_{e\parallel})$; we thus conclude that, to leading order in the $\tilde{\omega}_{e\parallel} \ll 1$

expansion,

$$\left[\tilde{\omega}_{e\parallel} \mathfrak{E}_e^{(0)} + \frac{c^2 k^2}{\omega^2} \left(\hat{k}\hat{k} - I \right) \right] \cdot \widehat{\delta E}_T = 0, \tag{2.116}$$

and the dispersion relation is approximately

$$\left[\tilde{\omega}_{e\parallel} (\mathfrak{E}_e^{(0)})_{11} - \frac{k^2 c^2}{\omega^2} \right] \left[\tilde{\omega}_{e\parallel} (\mathfrak{E}_e^{(0)})_{22} - \frac{k^2 c^2}{\omega^2} \right] + \left[\tilde{\omega}_{e\parallel} (\mathfrak{E}_e^{(0)})_{12} \right]^2 = 0. \tag{2.117}$$

Finally, writing the dielectric tensor in terms of $\boldsymbol{M}_e$ and $\boldsymbol{P}_e$ as defined by (2.97), we find

$$\left[\tilde{\omega}_{e\parallel} (\boldsymbol{M}_e^{(0)})_{11} + (\boldsymbol{P}_e^{(0)})_{11} - k^2 d_e^2 \right] \left[\tilde{\omega}_{e\parallel} (\boldsymbol{M}_e^{(0)})_{22} + (\boldsymbol{P}_e^{(0)})_{22} - k^2 d_e^2 \right]$$
$$+ \left[\tilde{\omega}_{e\parallel} (\boldsymbol{M}_e^{(0)})_{12} + (\boldsymbol{P}_e^{(0)})_{12} \right]^2 = 0, \tag{2.118}$$

where $d_e = c/\omega_{\mathrm{pe}}$ is the electron inertial scale (see (2.58*b*)). This can be re-written as a quadratic equation in ω – and thus, expressions for the complex frequency of any low-frequency perturbation can be found for any given positive wavenumber. We note that the electron inertial scale is related to the electron-Larmor radius by $d_e = \rho_e \beta_e^{-1/2}$; therefore, our expansion scheme is only consistent with the low-frequency assumption (2.94) under our assumed ordering, $\tilde{\omega}_{e\parallel} \sim \beta_e^{-1}$, when $\beta_e \gg 1$.

We note that one only needs to know $\mathfrak{E}_e^{(0)}$ in order to obtain the dispersion relation of low-frequency perturbations and the transverse component of the electric field, whereas to determine the electrostatic component of the electric field (and other quantities, such as the density perturbation – see Appendix H), one must go to higher order in the $\tilde{\omega}_{e\parallel} \ll 1$ expansion. Since we are primarily interested in microinstability growth rates and wavenumber scales, we will not explicitly calculate the electrostatic fields associated with perturbations using (2.112), and thus can avoid the rather laborious calculation of $\mathfrak{E}^{(1)}$ for CE distribution functions. We do, however, in Appendix G.1.3 derive an explicit expression for $\mathfrak{E}^{(1)}$ for a plasma with Maxwellian distribution functions for all particle species; this in turn allows us to relate the electrostatic electric field to the transverse field for such a plasma (see Appendix I).

For the sake of completeness, we also observe that if the non-Maxwellian part of the CE distribution function is even with respect to $v_\parallel$, the transformation rules (2.89) combined with (2.104) imply that a perturbation with a negative parallel wavenumber $k_\parallel$ will obey exactly the same dispersion relation as a perturbation for a positive parallel wavenumber, *viz.* for $k_\parallel > 0$,

$$\boldsymbol{P}_e^{(0)}\left(-k_\parallel, k_\perp\right) = \boldsymbol{P}_e^{(0)}\left(k_\parallel, k_\perp\right). \tag{2.119}$$

If instead the non-Maxwellian part is odd, then, for $k_\parallel > 0$,

$$\boldsymbol{P}_e^{(0)}\left(-k_\parallel, k_\perp\right) = -\boldsymbol{P}_e^{(0)}\left(k_\parallel, k_\perp\right). \tag{2.120}$$

The dispersion relation for perturbations with $k_\parallel < 0$ can, therefore, be recovered by considering perturbations with $k_\parallel > 0$, but under the substitution $\boldsymbol{P}_e^{(0)} \to -\boldsymbol{P}_e^{(0)}$. Thus, we can characterise all unstable perturbations under the assumption that $k_\parallel > 0$.

In all subsequent calculations, we require the Maxwellian part $\boldsymbol{M}_e^{(0)}$ of the dielectric tensor. The elements of the matrix $\boldsymbol{M}_s^{(0)}$ of species s are as follows:

$$(\boldsymbol{M}_s^{(0)})_{11} = \mathrm{i}\frac{k^2}{k_\parallel^2}F\left(k_\parallel\tilde{\rho}_s, k_\perp\tilde{\rho}_s\right), \tag{2.121a}$$

$$(\boldsymbol{M}_s^{(0)})_{12} = -\mathrm{i}\frac{k}{k_\parallel}G\left(k_\parallel\tilde{\rho}_s, k_\perp\tilde{\rho}_s\right), \tag{2.121b}$$

$$(\boldsymbol{M}_s^{(0)})_{21} = \mathrm{i}\frac{k}{k_\parallel}G\left(k_\parallel\tilde{\rho}_s, k_\perp\tilde{\rho}_s\right), \tag{2.121c}$$

$$(\boldsymbol{M}_s^{(0)})_{22} = \mathrm{i}H\left(k_\parallel\tilde{\rho}_s, k_\perp\tilde{\rho}_s\right), \tag{2.121d}$$

where the functions $F(x, y)$, $G(x, y)$ and $H(x, y)$ are

$$F(x, y) \equiv \frac{4\sqrt{\pi}}{y^2}\exp\left(-\frac{y^2}{2}\right)\sum_{m=1}^{\infty}m^2 I_m\left(\frac{y^2}{2}\right)\exp\left(-\frac{m^2}{x^2}\right), \tag{2.122a}$$

$$G(x, y) \equiv \exp\left(-\frac{y^2}{2}\right)\sum_{m=-\infty}^{\infty}m\,\mathrm{Re}\,Z\left(\frac{m}{x}\right)\left[I_m'\left(\frac{y^2}{2}\right) - I_m\left(\frac{y^2}{2}\right)\right], \tag{2.122b}$$

$$H(x, y) \equiv F(x, y) + \sqrt{\pi}y^2\exp\left(-\frac{y^2}{2}\right)\sum_{m=-\infty}^{\infty}\left[I_m\left(\frac{y^2}{2}\right) - I_m'\left(\frac{y^2}{2}\right)\right]\exp\left(-\frac{m^2}{x^2}\right), \tag{2.122c}$$

where $I_m(\alpha)$ is the mth modified Bessel function, and

$$Z(z) = \frac{1}{\sqrt{\pi}}\int_{C_L}\frac{\mathrm{d}u\exp\left(-u^2\right)}{u - z}, \tag{2.123}$$

is the plasma dispersion function (Fried & Conte 1961). The derivation of these results from the full dielectric tensor (which is calculated in Appendix G.1.1) for a plasma whose constituent particles all have Maxwellian distributions is presented in Appendices G.1.2 (expansion in the $\{\hat{x}, \hat{y}, \hat{z}\}$ basis) and G.1.3 (expansion in the $\{e_1, e_2, e_3\}$ basis).

2.5.6. *Effect of multiple species on dispersion-relation derivations*

We now relax the assumptions adopted in §2.5.5 that the low-frequency modes of interest are on electron-Larmor scales, and discuss how we derive simplified dispersion relations for (low-frequency) CE microinstabilities more generally.

First, it is unnecessarily restrictive to assume that, for all CE microinstabilities, $\tilde{\omega}_{s\parallel} \ll 1$ for all particle species. There are some instabilities for which $\tilde{\omega}_{e\parallel} \sim \eta_e \sim \epsilon_e \ll 1$ while $\tilde{\omega}_{i\parallel} \gtrsim 1$. Recalling the orderings $\tilde{\omega}_{e\parallel} \sim \beta_e^{-1}$ and $k\rho_e \sim 1$ that were adopted for the electron-Larmor-scale instabilities described in §2.5.5, it follows that $\tilde{\omega}_{i\parallel} \gtrsim 1$ whenever $\beta_e \lesssim \tau^{-1/2}\mu_e^{-1/2}$; in other words, electron-Larmor-scale CE microinstabilities in plasmas with β_e that is not too large will satisfy $\tilde{\omega}_{i\parallel} \gtrsim 1$. Therefore, we cannot naively apply our low-frequency approximation to both $\mathfrak{E}_e$ and $\mathfrak{E}_i$ in all cases of interest. We will remain cognisant of this in the calculations that follow – a concrete example of $\tilde{\omega}_{i\parallel} \gtrsim 1$ will be considered in §3.3.1.

Secondly, because of the large separation between electron- and ion-Larmor scales, it is necessary to consider whether the approximation $\boldsymbol{M}_s(\tilde{\omega}_{s\parallel}, \boldsymbol{k}) \approx \tilde{\omega}_{s\parallel}\boldsymbol{M}_s^{(0)}(\boldsymbol{k})$ remains

valid for parallel or perpendicular wavenumbers much larger or smaller than the inverse Larmor radii of each species. We show in Appendix G.1.6 that the leading-order term in the $\tilde{\omega}_{s\parallel} \ll 1$ expansion remains larger than higher-order terms for all $k_{\parallel}\rho_s \gtrsim 1$ (as, indeed, was implicitly assumed in §2.5.5). However, for $k_{\parallel}\rho_s$ sufficiently small, the same statement does not hold for all components of $\boldsymbol{M}_s$. More specifically, it is shown in the same appendix that the dominant contribution to $\boldsymbol{M}_s(\boldsymbol{k})$ when $k_{\parallel}\rho_s \ll 1$ instead comes from the quadratic term $\tilde{\omega}_{s\parallel}^2 \boldsymbol{M}_s^{(1)}(\boldsymbol{k})$ (rather than any higher-order term). Thus, in general, our simplified dispersion relation for low-frequency modes in a two-species plasma has the form of a quartic in ω, rather than a quadratic, if $k_{\parallel}\rho_s \ll 1$ for at least the electron species. Physically, the reason why a quadratic dispersion relation is no longer a reasonable approximation is the existence of more than two low-frequency modes in a two-species Maxwellian plasma in certain wavenumber regimes. For example, for quasi-parallel modes with characteristic parallel wavenumbers satisfying $k_{\parallel}\rho_i \ll 1$, there are four low-frequency modes (see §4.4.1). Nevertheless, in other situations, the components of $\boldsymbol{M}_s(\boldsymbol{k})$ for which the $\boldsymbol{M}_s(\tilde{\omega}_{s\parallel}, \boldsymbol{k}) \approx \tilde{\omega}_{s\parallel}\boldsymbol{M}_s^{(0)}(\boldsymbol{k})$ approximation breaks down are not important, on account of their small size compared with terms in the dispersion relation associated with other Maxwellian components. In this case, the original quadratic dispersion relation is sufficient. An explicit wavenumber regime in which this is realised is $k_{\parallel}\rho_e \sim k_{\perp}\rho_e \ll 1$ but $k\rho_i \gg 1$ – see §§4.3.4 and 4.4.7.

Taking these multiple-species effects into account, the reasons behind the decision made in §2.3.4 to consider the CES microinstabilities separately from the CET microinstabilities come into plain focus. First, the characteristic sizes of the CE electron-temperature-gradient and ion-temperature-gradient terms are comparable ($\eta_i \sim \eta_e$), while the CE ion-shear term is much larger than the CE electron-shear term: $\epsilon_i \sim \mu_e^{-1/2}\epsilon_e$. This has the consequence that the natural orderings of $\tilde{\omega}_{e\parallel}$ and $\tilde{\omega}_{i\parallel}$ with respect to other parameters are different for CES and CET microinstabilities. Secondly, the fact that the velocity-space anisotropy associated with the CE temperature-gradient terms differs from the CE shear terms – which excite microinstabilities with different characteristic wavevectors – means that the form of the dispersion relations of CET and CES microinstabilities are distinct. More specifically, the dispersion relation for CET microinstabilities at both electron and ion scales can always be simplified to a quadratic equation in ω; in contrast, for CES microinstabilities, the dispersion relation cannot in general be reduced to anything simpler than a quartic.

2.5.7. *Modelling collisional effects on CE microinstabilities*

As proposed thus far, our method for characterising microinstabilities in a CE plasma does not include explicitly the effect of collisions on the microinstabilities themselves. In principle, this can be worked out by introducing a collision operator into the linearised Maxwell–Vlasov–Landau equation from which the hot-plasma dispersion relation (2.75) is derived. Indeed, if a Krook collision operator is assumed (as was done in §2.4.2 when determining the precise form of the CE distribution functions of ions and electrons), the resulting modification of the hot-plasma dispersion relation is quite simple: the conductivity tensor (2.77) remains the same, but with the substitution

$$\tilde{\omega}_{s\parallel} \rightarrow \hat{\omega}_{s\parallel} \equiv \tilde{\omega}_{s\parallel} + \frac{\mathrm{i}}{k_{\parallel}\lambda_s}, \tag{2.124}$$

in the resonant denominators (see Appendix C). As for how this affects the simplifications to the dispersion relation outlined in §2.5.3, the expansion parameter in the dielectric

tensor's expansion (2.99) is altered, becoming $\hat{\omega}_{s\parallel} \ll 1$ (as opposed to $\tilde{\omega}_{s\parallel} \ll 1$); in other words, $\|\mathfrak{E}_s^{(1)}\|/\|\mathfrak{E}_s^{(0)}\| \sim \hat{\omega}_{s\parallel}$.

The latter result leads to an seemingly counterintuitive conclusion: collisions typically fail to stabilise low-frequency instabilities in CE plasma if $\omega\tau_s \lesssim 1$ (where τ_s is the collision time of species s) but $k_\parallel v_{\mathrm{th}i}\tau_s = k_\parallel\lambda_s \gg 1$. This is because the simplified dispersion relation (2.118) only involves leading-order terms in the expanded dielectric tensor. These terms are independent of $\hat{\omega}_{s\parallel}$, and thus the growth rate of any microinstability that is adequately described by (2.118) does not depend on the size of $\omega\tau_s$. For these microinstabilities, the effect of collisions only becomes relevant if

$$k_\parallel\lambda_s \lesssim 1. \tag{2.125}$$

This is inconsistent with the assumptions $k\lambda_e \gg 1$, $k\lambda_i \gg 1$ made when setting up our calculation in § 2.4.1. Thus, the only regime where collisions can reasonably be included in our calculation is one where they are typically not important. An exception to this rule arises when two-species plasma effects mean that the first-order terms in the $\hat{\omega}_{s\parallel} \ll 1$ expansion are needed for a correct characterisation of the growth rate of certain microinstabilities (see § 2.5.6); for these instabilities, we include the effect of collisions using (2.124).

Although our calculation is not formally valid when (2.125) holds, so we cannot show explicitly that growth ceases, this condition nonetheless represents a sensible criterion for suppression of microinstabilities by collisional damping. Physically, it signifies that collisions are strong enough to scatter a particle before it has streamed across a typical wavelength of fluctuation excited by a microinstability. This collisional scattering prevents particles from being resonant, which in turn would suppress the growth of many different microinstabilities. However, we acknowledge that there exist microinstabilities that do not involve resonant-particle populations (e.g., the firehose instability – see §§ 2.3.3 and 4.4.1), and thus it cannot be rigorously concluded from our work that all microinstabilities are suppressed when (2.125) applies.

Yet even without an actual proof of collisional stabilisation, there is another reason implying that (2.125) is a reasonable threshold for microinstabilities: the characteristic growth time of microinstabilities at wavenumbers satisfying (2.125) is comparable to the evolution time τ_L of macroscopic motions in the plasma. To illustrate this idea, we consider the ordering (2.94) relating the complex frequency of microinstabilities to the small parameter ϵ_s for CES (CE shear-driven) microinstabilities, and use it to estimate

$$\omega\tau_L \sim \epsilon_s k_\parallel v_{\mathrm{th}s}\tau_L \lesssim \epsilon_s \frac{L_V}{\lambda_s}\frac{v_{\mathrm{th}s}}{V}, \tag{2.126}$$

where $V \sim L_V/\tau_L$ is the characteristic ion bulk-flow velocity. Considering orderings (2.55), it follows that $\epsilon_e \sim \mu_e^{1/2}\epsilon_i$, and so

$$\epsilon_i\frac{v_{\mathrm{th}i}}{V} \sim \epsilon_e\frac{v_{\mathrm{th}e}}{V} \sim \frac{\lambda_e}{L_V} \sim \frac{\lambda_i}{L_V}. \tag{2.127}$$

Then (2.126) becomes

$$\omega\tau_L \lesssim 1, \tag{2.128}$$

implying (as claimed) that the CES microinstability growth rate is smaller than the fluid turnover rate τ_L^{-1}. Spelled out clearly, this means that the underlying quasiequilibrium state changes before going unstable. Similar arguments can be applied to CET (CE temperature-gradient-driven) microinstabilities.

Thus, (2.125) represents a lower bound on the characteristic wavenumbers at which microinstabilities can operate. We shall therefore assume throughout the rest of this paper that microinstabilities are suppressed (or rendered irrelevant) if they satisfy (2.125).

2.5.8. *Caveats: microinstabilities in CE plasma where $\omega/k_\parallel v_{\mathrm{th}s} \not\sim \eta_s, \epsilon_s$*

As mentioned in § 2.4.2, there are a number of important caveats to the claim that the ordering (2.94) must be satisfied by microinstabilities in a CE plasma.

The first of these is that our comparison of non-Maxwellian with the Maxwellian terms in expression (2.93) for $\varXi_s$ is in essence a pointwise comparison at characteristic values of $\tilde{v}_s$ for which $\varXi_s$ attains its largest typical magnitude. However, $\varXi_s$ affects the components of the conductivity tensor via the velocity integral of its product with a complicated function of frequency and wavenumber (see (2.77)). Thus, it does not necessarily follow that the ratio of the integrated responses of the Maxwellian and non-Maxwellian contributions to the conductivity tensor is the same as the pointwise ratio of the respective contributions to $\varXi_s$. In some circumstances, this can result in the Maxwellian part being smaller than anticipated, leading to faster microinstabilities. An example of this phenomenon was given in § 2.5.6: for $k_\parallel \rho_s \ll 1$, the characteristic magnitude of the Maxwellian contribution to some components of the dielectric tensor is $O(\tilde{\omega}_{s\parallel}^2)$, as compared with the naive estimate $O(\tilde{\omega}_{s\parallel})$. This leads to certain CES microinstabilities (for example, the CE ion-shear-driven firehose instability – § 4.4.1) satisfying a modified low-frequency condition

$$\tilde{\omega}_{s\parallel} \sim \epsilon_s^{1/2} \ll 1. \tag{2.129}$$

A similar phenomenon affects the limit $k_\parallel \to 0$ for fixed $k_\perp$, in which case it can be shown that the Maxwellian contribution to σ_{zz} is $O(k_\parallel/k_\perp)$; this leads to a CES microinstability (the CE electron-shear-driven ordinary-mode instability – see § 4.4.11) satisfying a modified ordering

$$\frac{\omega}{k_\perp v_{\mathrm{th}s}} \sim \epsilon_s \ll 1. \tag{2.130}$$

The second caveat is that for some plasma modes, the particles predominantly responsible for collisionless damping or growth are suprathermal, i.e. $\tilde{v}_s \gg 1$. Then the previous comparison of terms in (2.93) is not applicable. Modes of this sort are the quasi-cold plasma modes discussed in § 2.3.4 and Appendix D. They can be unstable, but always with a growth rate that is exponentially small in η_s and ϵ_s.

In spite of these two caveats, we proceed by considering the full hot-plasma dispersion relation (2.75) in the low-frequency limit $\omega \ll k_\parallel v_{\mathrm{th}s}$. This approach enables the treatment of all microinstabilities satisfying condition

$$\tilde{\omega}_{s\parallel} \sim \eta_s^{\iota_\eta}, \quad \epsilon_s^{\iota_\epsilon} \ll 1, \tag{2.131a,b}$$

where ι_η and ι_ϵ are fractional powers not much smaller than unity. Similarly to the discussion in § 2.3.4, we claim that the microinstabilities satisfying the low-frequency condition (2.131a,b) are likely to be the most rapid of all possible microinstabilities in CE plasma. A formal justification of this claim relies on the argument – presented in Appendix E – that for all plasma modes satisfying $\omega \gtrsim k_\parallel v_{\mathrm{th}s}$ and $|\mathrm{Re}\,\omega| \gg |\mathrm{Im}\,\omega|$, the growth rate is exponentially small in η_s and ϵ_s. By definition, this class of modes includes the quasi-cold modes. In a plasma where $\epsilon_s, \eta_s \ll 1$, the growth rates of such microinstabilities will be exponentially small, and thus of little significance. The only situation that we are aware of in which the low-frequency condition (2.131a,b) is not appropriate is the aforementioned CES ordinary-mode instability; a separate treatment of it involving the full hot-plasma dispersion relation is provided in Appendix K.3.13.

3. CET (Chapman–Enskog, temperature-gradient-driven) microinstabilities

3.1. *Form of CE distribution function*

We consider first the non-Maxwellian terms of the CE distribution function arising from temperature gradients and electron–ion drifts. Neglecting bulk-flow gradients (*viz.* setting $\epsilon_s = 0$ for both species – see (2.11*e,f*)), the CE distribution functions (2.72) for the electrons and ions become

$$f_{e0}(\tilde{v}_{e\parallel}, \tilde{v}_{e\perp}) = \frac{n_{e0}}{v_{\text{th}e}^3 \pi^{3/2}} \exp\left(-\tilde{v}_e^2\right) \left\{ 1 - \tilde{v}_{\parallel e} \left[\eta_e^T \left(\tilde{v}_e^2 - \frac{5}{2} \right) + \eta_e^R \right] \right\}, \quad (3.1a)$$

$$f_{i0}(\tilde{v}_{i\parallel}, \tilde{v}_{i\perp}) = \frac{n_{i0}}{v_{\text{th}i}^3 \pi^{3/2}} \exp\left(-\tilde{v}_i^2\right) \left\{ 1 - \eta_i \tilde{v}_{\parallel i} \left(\tilde{v}_i^2 - \frac{5}{2} \right) \right\}, \quad (3.1b)$$

where we have written out explicitly the electron-temperature-gradient (η_e^T, η_i – see (2.11*a,d*)) and electron-friction (η_e^R – see (2.11*b*)) terms under the assumption that the Maxwell–Vlasov–Landau system from which these CE distribution functions were derived is governed by a Krook collision operator. We remind the reader that the electron–ion-drift term (η_e^u – see (2.11*c*)) disappears for this choice of collision operator. We also observe that the non-Maxwellian part of the distribution functions (3.1) have odd parity; thus, any unstable mode with $k_\parallel > 0$ has a corresponding unstable mode with $k_\parallel < 0$ and the signs of η_e^T, η_e^R, and η_i reversed (see §2.5.5, last paragraph). For the rest of this section, we therefore take $k_\parallel > 0$ without loss of generality; the behaviour of modes with $k_\parallel < 0$ can be inferred via this symmetry relation.

The precise methodology that we employ to calculate the growth rates of CET microinstabilities is described in Appendix J; here, we focus on the results of those calculations. In §3.2, we will present the overview of the CET stability landscape, while the microinstabilities referred to there will be treated analytically in §3.3.

3.2. *Stability*

We determine the stability (or otherwise) of the CE distribution functions of the form (3.1*a*) and (3.2*b*) for different values of η_e^T, η_e^R and η_i, the electron inertial scale d_e, the electron-temperature scale length $L_T = |\nabla_\parallel \log T_e|^{-1}$ and for fixed electron and ion plasma betas (β_e and β_i, respectively). Stability calculations are carried out for particular combinations of values of η_e^T, η_e^R, η_i, d_e, L_T, β_e and β_i by solving for the maximum microinstability growth rate across all wavevectors (see Appendix J for explanation of how this is done), and determining whether this growth rate is positive for the microinstabilities whose wavelength is smaller than the Coulomb mean free paths (a condition necessary for our calculation to be valid).

The results of one such stability calculation – for a temperature-equilibrated hydrogen plasma ($\eta_e^T = \eta_i$, $\beta_i = \beta_e$) – are presented in figure 2. In spite of the five-dimensional ($\eta_e^T, \eta_e^R, d_e/L_T, \beta_e$) parameter space that seemingly needs to be explored, we can, in fact, convey the most salient information concerning the stability of the CE distribution functions (3.1) using plots over a two-dimensional ($d_e/L_T, \lambda_e/L_T$) parameter space at a fixed β_e (where we remind the reader that $\lambda_e/L_T = |\eta_e^T|$ – see (2.11*a*)). This reduction in phase-space dimensionality is possible for two reasons. First, dimensional analysis implies that the salient stability thresholds of CET microinstabilities cannot depend on d_e and L_T separately, but only on the ratio d_e/L_T. Secondly, it transpires that the CE electron-friction term of the form given in (3.1*a*) does not drive any microinstabilities, bur merely modifies the real frequency of perturbations with respect to their Maxwellian frequencies (this
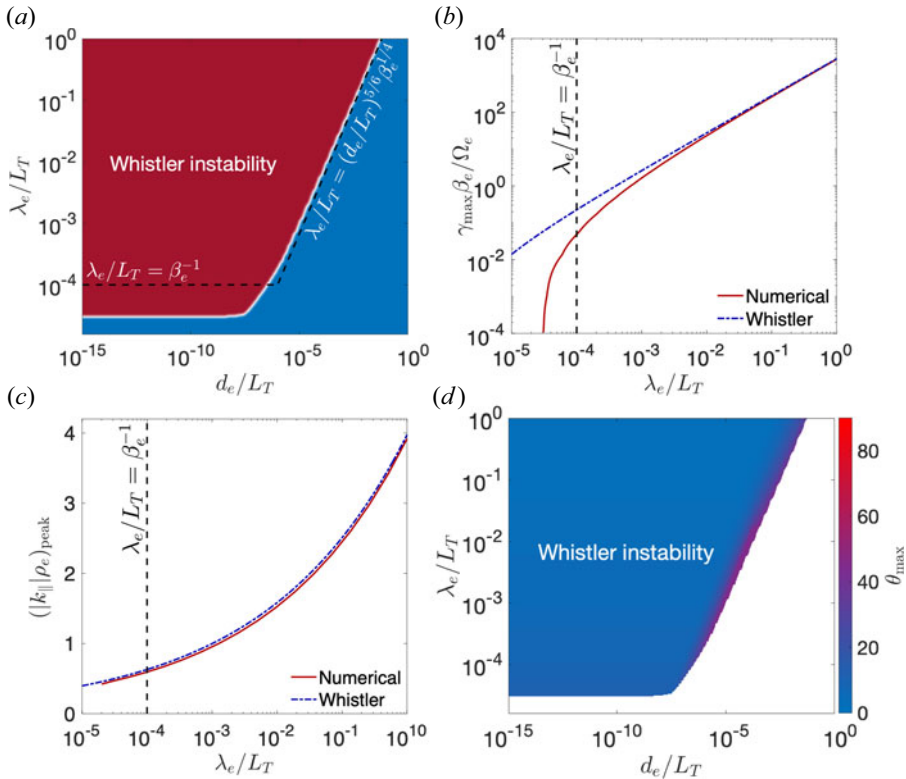
FIGURE 2. The CE-distribution-function stability map for CET microinstabilities. Exploration of the stability of the CE distribution functions (3.1a) and (3.1b) for different values of small parameters η_e^T, η_e^R and η_i, and the ratio of the electron inertial scale d_e to the temperature scale length L_T, in a temperature-equilibrated hydrogen plasma. In this plot, we chose $\eta_e^R = 0$ and $\eta_e^T = \eta_i$, and then show $\lambda_e/L_T = |\eta_e^T|$ with equal logarithmic spacing in the range $[10^{-5}, 10^0]$; d_e/L_T is chosen with equal logarithmic spacing in the range $[10^{-15}, 10^0]$. The total size of the grid is 400^2. For reasons of efficiency, we calculate growth rates on a 40^2 grid in wavenumber space with logarithmic spacing for both parallel and perpendicular wavenumbers. In this plot, $\beta_e = \beta_i = 10^4$. (a) Stable (blue) and unstable (red) regions of $(d_e/L_T, \lambda_e/L_T)$ phase space. The theoretically anticipated collisional cutoff (right – see (3.4)) and β-stabilisation threshold (bottom) of the CET whistler instability are shown as black dashed lines. (b) Maximum normalised microinstability growth rate (red) vs λ_e/L_T for a fixed electron inertial scale $d_e/L_T = 10^{-15}$, along with analytically predicted maximum growth rate for the CET whistler instability in the limit $\lambda_e \beta_e/L_T \gg 1$ (blue, see (3.10)). (c) Parallel wavenumber of fastest-growing microinstability (red) vs λ_e/L_T for a fixed electron inertial scale $d_e/L_T = 10^{-15}$, along with the same quantity analytically predicted for the CET whistler instability in the limit $\lambda_e \beta_e/L_T \gg 1$ (blue, see (3.11)). (d) Wavevector angle $\theta \equiv \tan^{-1}(k_\perp/k_\parallel)$ of the fastest-growing instability over $(d_e/L_T, \lambda_e/L_T)$ parameter space.

is proven in Appendix J.1). Thus, we can set $\eta_e^R = 0$ without qualitatively altering the stability properties of the CE distribution functions (3.1).

Figure 2(a) shows the regions of instability and stability of the CE distribution function (3.1) over the $(d_e/L_T, \lambda_e/L_T)$ parameter space. The unstable region is bracketed by two thresholds. For d_e/L_T below a critical value $(d_e/L_T)_{c0}$, stability is independent of d_e/L_T, and only depends on the relative magnitude of λ_e/L_T and β_e: CET microinstabilities

are quenched if $\lambda_e \beta_e / L_T \ll 1$. For $d_e / L_T \gtrsim (d_e / L_T)_{c0}$, and $\lambda_e \beta_e / L_T \gtrsim 1$, stability is attained at fixed λ_e / L_T for $d_e / L_T > (d_e / L_T)_c$, where $(d_e / L_T)_c$ increases monotonically with λ_e / L_T. If $\lambda_e \beta_e / L_T \gtrsim 1$ and $d_e / L_T \lesssim (d_e / L_T)_c$, then the CE distribution function (3.1) is unstable.

The fastest-growing CET microinstability is the whistler (heat-flux) instability: whistler waves driven unstable by the small anisotropy of the CE electron-temperature-gradient term (see § 3.3.1). That this instability with wavevector parallel to the magnetic field is indeed the dominant microinstability is most easily ascertained by comparing simple analytic expressions for its peak growth rate and wavevector with the equivalent quantities recorded when performing the general stability calculation (see figure 2b–d). The maximum microinstability growth rate matches the analytic result (3.10) for the CET whistler instability in the limit $\lambda_e \beta_e / L_T \gg 1$, while the parallel wavenumber $(|k_\parallel| \rho_e)_{\text{peak}}$ of the fastest-growing mode is extremely well described by (3.11). In addition, figure 2(d) demonstrates that the parallel instability is indeed the fastest. The CET whistler instability has been considered previously by a number of authors (see references in § 3.3.1); we note that these prior studies of this instability suggest that, nonlinearly, oblique CET whistler modes may be the more important ones, even though linearly the parallel modes are the fastest growing (see § 3.3.2).

The two thresholds demarcating the unstable region can then be associated with stabilisation conditions of the CET whistler instability, each with a simple physical interpretation. The first condition is the β-stabilisation condition of the whistler instability. It is shown in § 3.3.1 that when $\lambda_e \beta_e / L_T \ll 1$, cyclotron damping on whistler modes is sufficiently strong that only quasi-parallel modes with parallel wavenumbers $k_\parallel \rho_e \lesssim (\lambda_e \beta_e / L_T)^{1/3} \ll 1$ can be destabilised by the anisotropy of the CE distribution function, and that the peak growth rate $\gamma_{\text{whistler},T}$ of these unstable modes is exponentially small in $\lambda_e \beta_e / L_T$ compared with the electron Larmor frequency (see (3.8)): $\gamma_{\text{whistler},T} / \Omega_e \sim \lambda_e \exp\left[-(\lambda_e \beta_e / 2 L_T)^{-2/3}\right] / L_T$. This means that if $\lambda_e \beta_e / L_T$ is reduced below unity, the growth rate of the CET whistler instability decreases dramatically, and thus the instability is unable to operate effectively on time scales shorter than those over which the CE plasma is evolving macroscopically.

The second condition is collisional stabilisation of the CET whistler instability. Naively, it might be expected that two conditions must be satisfied in order for the microinstability to operate: that its growth rate must satisfy $\gamma_{\text{whistler},T} \tau_e \gg 1$, and its characteristic wavenumber $k \lambda_e \gg 1$ (see (2.125)). Noting that for the CET whistler instability (cf. (3.10)),

$$\frac{\gamma_{\text{whistler},T} \tau_e}{k \lambda_e} = \frac{\gamma_{\text{whistler},T}}{k v_{\text{th}e}} \sim \frac{\lambda_e}{L_T} \left(\frac{\lambda_e \beta_e}{L_T} \right)^{-1/5} \ll 1, \tag{3.2}$$

it follows that the former condition is more restrictive. Written as a condition on d_e / L_T in terms of λ_e / L_T (and using $\gamma_{\text{whistler},T} \sim \lambda_e \Omega_e / L_T$ – see (3.10)), $\gamma_{\text{whistler},T} \tau_e \gg 1$ becomes

$$\frac{d_e}{L_T} \ll \beta_e^{-5/2} \left(\frac{\lambda_e \beta_e}{L_T} \right)^2, \tag{3.3}$$

while the condition $k \lambda_e \gg 1$ on the instability wavenumber $k_\parallel \rho_e \sim (\lambda_e \beta_e / L_T)^{1/5}$ (see (3.11)) leads to

$$\frac{d_e}{L_T} \ll \left(\frac{d_e}{L_T} \right)_c \equiv \beta_e^{-3/2} \left(\frac{\lambda_e \beta_e}{L_T} \right)^{6/5}. \tag{3.4}$$

It is the latter that agrees well with the true result, as shown in figure 2(a), implying that $(d_e / L_T)_{c0} = \beta_e^{-3/2}$. The (arguably surprising) result that the CET whistler instability can

operate even if $\gamma_{\mathrm{whistler},T}\tau_e \lesssim 1$ is, in fact, a generic feature of low-frequency (*viz.* $\omega \ll k v_{\mathrm{th}e}$) plasma instabilities (see § 2.5.7). The physical instability mechanism underlying such modes can be sustained provided the time taken for thermal particles (in this case, electrons) to cross the mode's wavelength is much shorter than the collision time, irrespective of the mode's own frequency – in other words, $\tau_e k v_{\mathrm{th}e} = k\lambda_e \gg 1$. We point out that the collisional-stabilisation condition of the CET whistler instability can never be satisfied in a strongly magnetised plasma if $\lambda_e \beta_e / L_T \gtrsim 1$: this is because its wavenumber k satisfies $k^{-1} \lesssim \rho_e \ll \lambda_e$.

Whilst it is the fastest-growing one (assuming $\eta_e^T \sim \eta_i$), the CET whistler instability is not the only CET microinstability of interest. There are two other instabilities driven by the CET ion-temperature-gradient term, neither of which has previously been identified, to our knowledge: the slow (hydromagnetic) wave instability (see § 3.3.3), and the long-wavelength KAW instability (see § 3.3.4). The former, whose characteristic wavenumber scale satisfies $k\rho_i \sim 1$, has a larger characteristic growth rate $\gamma_{\mathrm{SW}} \sim \lambda_i \Omega_i / L_{T_i}$ (where $L_{T_i} = |\nabla_\parallel \log T_i|^{-1}$ is the scale length of the ion-temperature-gradient). Similarly to the CET whistler instability, the CET slow-wave instability has β-stabilisation and collisional-stabilisation conditions $\lambda_i \beta_i / L_{T_i} \ll 1$ and $\lambda_i \lesssim \rho_i$, respectively. Thus, unless $\lambda_i \beta_i / L_{T_i} > \lambda_e \beta_e / L_{T_e}$ (a condition equivalent to $\tau^3 L_{T_e}/L_{T_i} > Z_i^3$, where $\tau = T_i/T_e$), the CET slow-wave instability only operates when the CET whistler-wave instability does, but on larger, ion rather than electron, scales. Nevertheless, the CET slow-wave instability is worth noting because, on account of being an ion instability, it should continue to operate even if the electron-scale CET whistler instability modifies the underlying electron distribution function. The slow-wave instability will then be responsible for modifying the ion distribution function. We are not aware of any work on the CET slow-wave instability and, thus, on its effect on ion heat conduction.

Readers who are interested in knowing more about the properties and growth rates of CET microinstabilities are encouraged to continue § 3.3; those who are focused on the wider question of the kinetic stability of the CE distribution function should jump ahead to § 4.

3.3. *CET microinstability classification*

3.3.1. *Parallel whistler (heat-flux) instability*

The CET whistler instability, which has been studied previously by a number of authors (Levinson & Eichler 1992; Pistinner & Eichler 1998; Gary & Li 2000; Roberg-Clark *et al.* 2016; Komarov *et al.* 2018; Roberg-Clark *et al.* 2018*a*,*b*; Kuzichev *et al.* 2019; Shaaban *et al.* 2019; Drake *et al.* 2021), is driven by parallel electron heat fluxes. These heat fluxes introduce the asymmetry to the CE electron distribution function (i.e. the electron-temperature-gradient term), which, if it is sufficiently large, can overcome electron-cyclotron damping of (electromagnetic) whistler waves and render them unstable. The instability is mediated by gyroresonant wave–particle interactions that allow whistlers to drain free energy from electrons with parallel velocities $v_\parallel = \pm\Omega_e/k_\parallel$. For a positive, parallel electron heat flux, which is driven by an anti-parallel temperature gradient ($\nabla_\parallel T_e < 0$, so $\eta_e^T < 0$), it is only whistlers with a positive parallel wavenumber that are unstable. Whistler waves with both parallel and oblique wavevectors with respect to the magnetic field can be destabilised, although the parallel modes are the fastest-growing ones.

The CET whistler instability is most simply characterised analytically for parallel wavenumbers (i.e. $k = k_\parallel$). Then, it can be shown (see Appendix J.3.1, and also Levinson & Eichler 1992; Roberg-Clark *et al.* 2016) that the real frequency ϖ and growth rate γ at
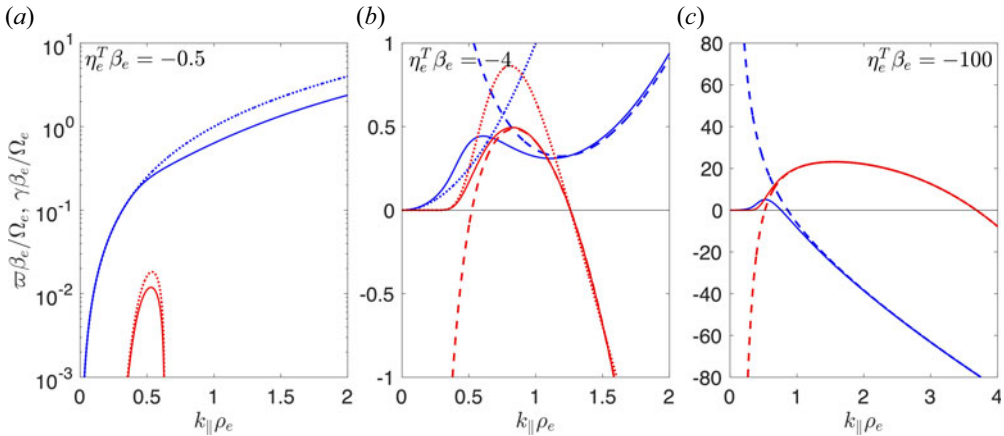
FIGURE 3. Parallel CET whistler instability. Dispersion curves of unstable whistler modes, whose instability is driven by the electron-temperature-gradient term in the CE distribution function (3.1a), for wavevectors that are co-parallel with the background magnetic field (*viz.* $\boldsymbol{k} = k_\parallel \hat{\boldsymbol{z}}$). The frequency (solid blue) and growth rates (solid red) of the modes are calculated using (3.5a) and (3.5b), respectively. The resulting frequencies and growth rates, when normalised as $\gamma \beta_e / \Omega_e$, are functions of the dimensionless quantity $\eta_e^T \beta_e$; we show the dispersion curves for three different values of $\eta_e^T \beta_e$. The approximations (3.6a) and (3.6b) for the frequency (dotted blue) and growth rate (dotted red) in the limit $k_\parallel \rho_e \ll 1$ are also plotted, as are the approximations (3.9a) and (3.9b) for the frequency (dashed blue) and growth rate (dashed red) in the limit $k_\parallel \rho_e \gg 1$.

arbitrary $k_\parallel > 0$ are given by

$$\frac{\varpi}{\Omega_e} = \eta_e^T \left(\frac{k_\parallel \rho_e}{4} - \frac{1}{2k_\parallel \rho_e} \right) - \frac{\left(\eta_e^T / 2 + k_\parallel^3 \rho_e^3 / \beta_e \right) \operatorname{Re} Z \left(1/k_\parallel \rho_e \right)}{\left[\operatorname{Re} Z \left(1/k_\parallel \rho_e \right) \right]^2 + \pi \exp \left(-2/k_\parallel^2 \rho_e^2 \right)}, \tag{3.5a}$$

$$\frac{\gamma}{\Omega_e} = - \frac{\sqrt{\pi} \left(\eta_e^T / 2 + k_\parallel^3 \rho_e^3 / \beta_e \right)}{\left[\operatorname{Re} Z \left(1/k_\parallel \rho_e \right) \right]^2 \exp \left(1/k_\parallel^2 \rho_e^2 \right) + \pi \exp \left(-1/k_\parallel^2 \rho_e^2 \right)}. \tag{3.5b}$$

For $\eta_e^T > 0$, $\gamma < 0$, but if $\eta_e^T < 0$, then γ is non-negative for $k_\parallel \rho_e \leqslant (\eta_e^T \beta_e / 2)^{1/3}$. The dispersion curves $\varpi = \varpi(k_\parallel)$ and $\gamma = \gamma(k_\parallel)$ of unstable whistler waves with parallel wavevectors for three different values of $|\eta_e^T| \beta_e$ are plotted in figure 3 using the above formulae. For $|\eta_e^T| \beta_e \gtrsim 1$, the range of unstable parallel wavenumbers, $\Delta k_\parallel$, is comparable to the characteristic wavenumber of the instability: $\Delta k_\parallel \sim k_\parallel \sim \rho_e^{-1}$.

The expressions (3.5a) and (3.5b) can be simplified in two subsidiary limits, which in turn allows for the derivation of analytic expressions for the maximum growth rate of the instability and the (parallel) wavenumber at which that growth rate is realised.

First, adopting the ordering $k_\parallel \rho_e \sim (|\eta_e^T| \beta_e)^{1/3} \ll 1$ under which the destabilising η_e^T terms and the stabilising electron finite-Larmor-radius (FLR) terms are the same order, we

find

$$\varpi \approx \frac{k_\parallel^2 \rho_e^2}{\beta_e} \Omega_e, \tag{3.6a}$$

$$\gamma \approx -\frac{\sqrt{\pi}}{k_\parallel^2 \rho_e^2} \left(\frac{\eta_e^T}{2} + \frac{k_\parallel^3 \rho_e^3}{\beta_e} \right) \exp\left(-\frac{1}{k_\parallel^2 \rho_e^2} \right) \Omega_e. \tag{3.6b}$$

The frequency corresponds to that of a whistler wave in the $k_\parallel \rho_e \ll 1$ limit (Boldyrev *et al.* 2013). The fastest growth, which occurs at the wavenumber

$$k_\parallel \rho_e \approx \left(\frac{|\eta_e^T| \beta_e}{2} \right)^{1/3} - \frac{|\eta_e^T| \beta_e}{4}, \tag{3.7}$$

is exponentially slow in $|\eta_e^T| \beta_e \ll 1$:

$$\gamma_{\max} \approx \frac{3\sqrt{\pi}}{4} |\eta_e^T| \exp\left[-\frac{2^{2/3}}{\left(|\eta_e^T| \beta_e \right)^{2/3}} - 1 \right] \Omega_e. \tag{3.8}$$

Next, considering the opposite limit $k_\parallel \rho_e \gg 1$, we obtain

$$\varpi \approx \left[\eta_e^T \beta_e \left(\frac{1}{4} k_\parallel \rho_e - \frac{\pi - 2}{2\pi k_\parallel \rho_e} \right) + \frac{2}{\pi} k_\parallel^2 \rho_e^2 \right] \frac{\Omega_e}{\beta_e}, \tag{3.9a}$$

$$\gamma \approx -\frac{1}{\sqrt{\pi}} \left[\eta_e^T \beta_e \left(\frac{1}{2} - \frac{4 - \pi}{2\pi k_\parallel^2 \rho_e^2} \right) + k_\parallel^3 \rho_e^3 \right] \frac{\Omega_e}{\beta_e}. \tag{3.9b}$$

We then find that the maximum growth rate of the parallel mode is given by

$$\gamma_{\max} \approx \frac{|\eta_e^T|}{\sqrt{\pi}} \left\{ 1 - \left[\frac{1}{\sqrt{\pi}} \left(\frac{4}{\pi} - 1 \right) \right]^{3/5} \left[\left(\frac{3}{2} \right)^{2/5} - \left(\frac{2}{3} \right)^{3/5} \right] \left(|\eta_e^T| \beta_e \right)^{-2/5} \right\} \Omega_e$$

$$\approx 0.56 |\eta_e^T| \left[1 - 0.13 \left(|\eta_e^T| \beta_e \right)^{-2/5} \right] \Omega_e, \tag{3.10}$$

at the parallel wavenumber

$$k_\parallel \rho_e = \left[\frac{2}{3\sqrt{\pi}} \left(\frac{4}{\pi} - 1 \right) \right]^{1/5} \left(|\eta_e^T| \beta_e \right)^{1/5} \approx 0.63 \left(|\eta_e^T| \beta_e \right)^{1/5}. \tag{3.11}$$

In addition, we see that the real frequency of modes with $k_\parallel \rho_e \lesssim (|\eta_e^T| \beta_e/2)^{1/3}$ is larger than the growth rate of the mode: $\varpi \sim k_\parallel \rho_e \gamma \gg \gamma$. Thus, these modes oscillate more rapidly than they grow.

The approximate expressions for (3.6) and (3.9) are valid in the limits $|\eta_e^T| \beta_e \ll 1$ and $|\eta_e^T| \beta_e \gg 1$, respectively, and are plotted in figure 3 alongside the exact results (3.5). Of particular note is the accuracy of the approximate expression (3.9b) for the growth rate when $k_\parallel \rho_e \gtrsim 0.6$; this suggests that (3.10) is a reasonable estimate of the peak growth rate for $|\eta_e^T| \beta_e \gtrsim 1$.

3.3.2. *Oblique whistler (heat-flux) instability*

Analytical expressions for the frequency and growth rate of unstable modes with an oblique wavevector at an angle to the magnetic field are more complicated than the analogous expressions for parallel modes. In Appendix J.3, we show that there are two low-frequency oblique modes, whose complex frequencies ω are given by

$$\omega = \frac{\Omega_e}{\beta_e} k_\parallel \rho_e \frac{-B_T \pm \sqrt{B_T^2 + 4A_T C_T}}{2A_T}, \tag{3.12}$$

where the coefficients $A_T = A_T(k_\parallel \rho_e, k_\perp \rho_e, \eta_e^T \beta_e)$, $B_T = B_T(k_\parallel \rho_e, k_\perp \rho_e, \eta_e^T \beta_e)$ and $C_T = C_T(k_\parallel \rho_e, k_\perp \rho_e, \eta_e^T \beta_e)$ are composed of the sums and products of the special functions defined in (2.122), and also other special functions defined in Appendix G.3. For a given wavenumber, we can use (3.12) to calculate the growth rates of any unstable oblique modes – and, in particular, demonstrate that positive growth rates are present for certain values of η_e^T. When they do exist, (3.12) suggests that they will have the typical size $\gamma \sim \Omega_e/\beta_e \sim \eta_e^T \Omega_e$ when $k\rho_e \sim 1$ and $\eta_e^T \beta_e \sim 1$.

For $\eta_e^T > 0$, we find that both modes (3.12) are damped; for $\eta_e^T < 0$, one mode is damped for all wavenumbers, but the other is not. Figure 4 shows the maximum (positive) growth rate γ (normalised to Ω_e/β_e) of this mode at a fixed value of η_e^T, for a range of β_e. The growth rate is calculated by evaluating the imaginary part of (3.12) at a given wavenumber. For $-\eta_e^T < 1/\beta_e$, the mode of interest is damped for most wavenumbers, except for a small region of wavenumbers quasi-parallel to the magnetic field: in this region, there is a very small growth rate $\gamma \ll \Omega_e/\beta_e$ (figure 4a). This finding is consistent with the exponentially small growth rates found for the parallel whistler modes (see (3.8)). When $-\eta_e^T \sim 1/\beta_e$, there is a marked change in behaviour: a larger region of unstable modes appears, with $\gamma \sim \Omega_e/\beta_e$, at wavenumbers $k\rho_e \sim 1$ (figure 4b,c). The growth rate is the largest for parallel modes – but there also exist oblique modes with $k_\perp \lesssim k_\parallel$ whose growth rate is close to the peak growth rate. For example, for $\eta_e^T \beta_e = -4$, we find that the growth rate of the fastest-growing mode with a wavevector angle $\theta = 10°$ is only $\sim 2\%$ smaller than the fastest-growing parallel mode; for a wavevector angle $\theta = 20°$, the reduction is by $\sim 6\%$; and for $\theta = 30°$, the reduction is by $\sim 20\%$. Finally, if $-\eta_e^T \gg 1/\beta_e$, there exists a extended region of unstable modes, with $1 \lesssim k\rho_e \lesssim |\eta_e^T \beta_e|^{1/3}$, and $\gamma \sim |\eta_e^T \Omega_e|$ (figure 4d). Again, the peak growth rate is at $k_\perp = 0$, but oblique modes also have a significant growth rate (for unstable modes with $\theta = 30°$, the reduction in the largest growth rate compared with the fastest-growing parallel mode is only by $\sim 4\%$). Most of the unstable modes have a non-zero real frequency: for $-\eta_e^T \sim 1/\beta_e$, $\omega \sim \gamma$ (figure 4e), while for $-\eta_e^T \gg 1/\beta_e$, $\omega \gg \gamma$ for $k\rho_e \gg 1$ (figure 4f). Note, however, that in the latter case there exists a band of wavenumbers at which there is no real frequency.

In summary, we have (re-)established that the fastest-growing modes of the CET whistler instability are parallel to the magnetic field; however, we have shown semi-analytically (a novel result of this work) that the growth of oblique perturbations can be almost as large. This result is of some significance, because it has been argued that oblique whistler modes are necessary for the instability to scatter heat-carrying electrons efficiently (see, e.g. Komarov *et al.* 2018). It was proposed previously that such modes could arise from modifications to the CET electron-temperature-gradient terms induced by the unstable parallel whistler modes rendering the oblique modes the fastest-growing ones; our calculations suggest that it would only a require a small change to the CET whistler growth rates for this to be realised.

As a further aside, we observe that in a plasma with sufficiently high plasma β_e, these oblique modes are in fact closer in nature to KAWs than to whistler waves.
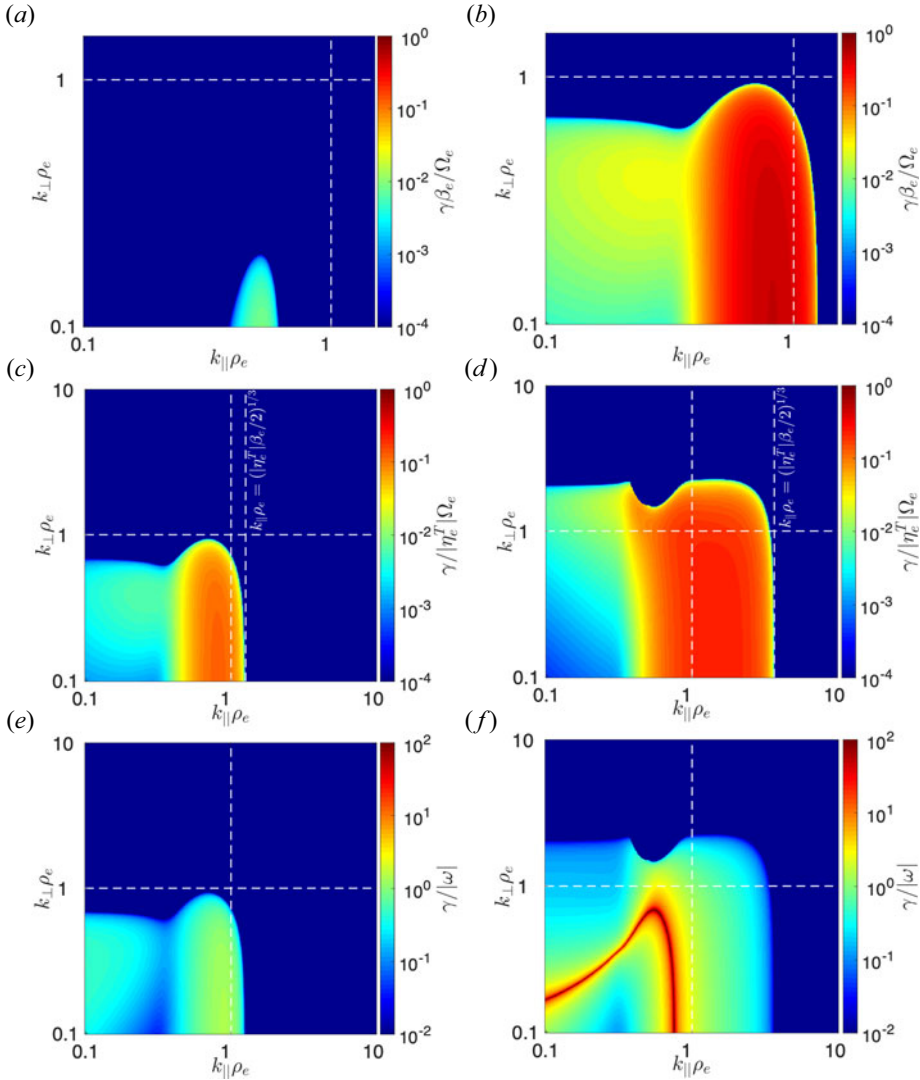
FIGURE 4. Oblique CET whistler instabilities. Maximum positive growth rates of unstable whistler modes whose instability is driven by the electron-temperature-gradient term in CE distribution function (3.1a), at arbitrary wavevectors with respect to the background magnetic field. The growth rates of the modes are calculated by taking the imaginary part of (3.12), where coefficients A_T, B_T and C_T are known functions of the wavevector. The growth rates are calculated on a 400^2 grid, with equal logarithmic spacing in both perpendicular and parallel directions between the minimum and maximum wavenumbers. The resulting growth rates, when normalised as $\gamma \beta_e / \Omega_e$, are functions of the dimensionless quantity $\eta_e^T \beta_e$; (a) $\eta_e^T \beta_e = -0.5$, (b) $\eta_e^T \beta_e = -4$. (c) Same as (b) but with normalisation $\gamma / |\eta_e^T| \Omega_e$. (d) Same as (c), but with $\eta_e^T \beta_e = -100$. (e) Ratio of growth rate to absolute value of real frequency for unstable modes for $\eta_e^T \beta_e = -4$. (f) Same as (e), but with $\eta_e^T \beta_e = -100$.

Whistler waves are characterised as having effectively immobile ions ($\omega \gg k_\perp v_{\text{th}i}$), while KAWs have warm ions ($\omega \ll k_\perp v_{\text{th}i}$); as a consequence, whistler waves have a negligible density perturbation ($\delta n_e \ll Z_i e n_e \varphi / T_i$, where φ is the electrostatic potential associated with the wave), while KAWs do not: $\delta n_e \approx Z_i e n_e \varphi / T_i$ (Boldyrev *et al.* 2013). In a

$\beta_e \sim 1$ plasma for $k_\perp \gtrsim k_\parallel$, the real frequency of whistler modes satisfies $\omega/k_\perp v_{\text{thi}} \sim k_\parallel \rho_i/\beta_e \sim k_\parallel \rho_i$; thus, we conclude from our above considerations that the two waves must operate in different regions of wavenumber space, *viz.* $k_\parallel \rho_i \ll 1$, $k_\perp \rho_i > 1$ for KAWs, and $k_\parallel \rho_i \gg 1$ for whistlers. However, for $\beta_e \gtrsim \mu_e^{-1/2}$ (where $\mu_e = m_e/m_i$) and $k_\perp \sim k_\parallel \gg \rho_i^{-1}$, the frequency of whistler waves is too low for $\omega \gg k_\perp v_{\text{thi}}$ to be satisfied whilst also maintaining $k_\parallel \rho_e \ll 1$. Instead, the ions participate in the wave mechanism, and $\delta n_e \approx -Z_i e n_e \varphi/T_i$ (see Appendix H.2).

For further discussion of the physics of the whistler instability (as well as its nonlinear evolution), see Komarov *et al.* (2018) and the other references given at the beginning of § 3.3.1.

3.3.3. *Slow-(hydromagnetic)-wave instability*

Although parallel ion heat fluxes in a classical, collisional plasma are typically much weaker than electron heat fluxes, they can still act as a free-energy source for instabilities, by introducing anisotropy to the ion distribution function (3.1*b*) (i.e. the CE ion-temperature-gradient term). Furthermore, anisotropy in the ion distribution function can enable the instability of plasma modes that are not destabilised by the CE electron-temperature-gradient term. This exact situation is realised in the CET slow-hydromagnetic-wave instability, in which a sufficiently large CET ion-temperature-gradient term counteracts the effect of ion-cyclotron damping on slow hydromagnetic waves. The slow hydromagnetic wave (or slow wave) (Rogister 1971; Foote & Kulsrud 1979) is the left-hand-polarised quasi-parallel electromagnetic mode in high-β plasma; it exists for parallel wavenumbers $k_\parallel$ that satisfy $\beta_i^{-1/2} \ll k_\parallel \rho_i \lesssim 1$, and has a characteristic frequency $\omega \approx 2\Omega_i/\beta_i$. To the authors' knowledge, no instability of the slow wave due to the ion heat flux has previously been reported. The instability's mechanism is analogous to the CET whistler instability: the slow waves drain energy from ions with parallel velocities $v_\parallel = \pm\Omega_i/k_\parallel$ via gyroresonant wave–particle interactions. For an anti-parallel ion-temperature gradient (i.e. $\nabla_\parallel T_i < 0$, so $\eta_i < 0$), slow waves propagating down the temperature gradient are destabilised, while those propagating up the temperature gradient are not.

As before, the slow-wave instability is most easily characterised in the subsidiary limit $k_\perp \rho_i \to 0$ ($k = k_\parallel$). Under the ordering $k_\parallel \rho_i \sim 1$, the real frequency ϖ and growth rate γ are given by (see Appendix J.4.1)

$$\frac{\varpi}{\Omega_i} = \eta_i \left(\frac{k_\parallel \rho_i}{4} - \frac{1}{2k_\parallel \rho_i} \right) - \frac{k_\parallel^2 \rho_i^2 \left[\text{Re}\, Z(1/k_\parallel \rho_i) + k_\parallel \rho_i \right] (\eta_i/4 + k_\parallel \rho_i/\beta_i)}{\left[\text{Re}\, Z(1/k_\parallel \rho_i) + k_\parallel \rho_i \right]^2 + \pi \exp\left(-2/k_\parallel^2 \rho_i^2 \right)}, \quad (3.13a)$$

$$\frac{\gamma}{\Omega_i} = -\frac{\sqrt{\pi} k_\parallel^2 \rho_i^2 \left(\eta_i/4 + k_\parallel \rho_i/\beta_i \right)}{\left[\text{Re}\, Z(1/k_\parallel \rho_i) + k_\parallel \rho_i \right]^2 \exp\left(1/k_\parallel^2 \rho_i^2 \right) + \pi \exp\left(-1/k_\parallel^2 \rho_i^2 \right)}. \quad (3.13b)$$

The CET electron-temperature-gradient term does not appear because its contributions to the frequency and growth rate are much smaller than the equivalent contributions of the CET ion-temperature-gradient term at $k_\parallel \rho_i \sim 1$. Plots of $\varpi = \varpi(k_\parallel)$ and $\gamma = \gamma(k_\parallel)$ for different values of $\eta_i \beta_i < 0$ are shown in figure 5.

As with the CET whistler instability, we can derive simple expressions for the peak growth rate (and the wavenumber associated with that growth rate) in subsidiary limits.
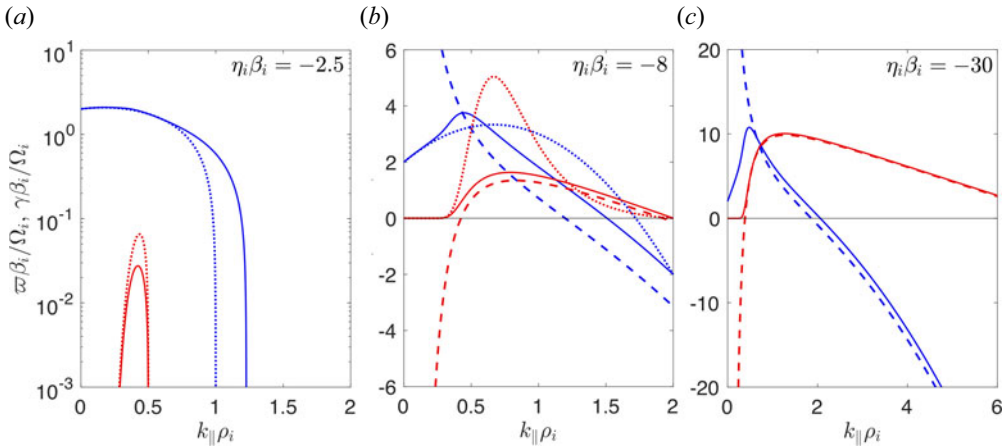
FIGURE 5. Parallel CET slow-hydromagnetic-wave instability. Dispersion curves of slow hydromagnetic waves whose instability is driven by the ion-temperature-gradient term in the CE distribution function (3.1b), for wavevectors co-parallel with the background magnetic field (viz. $k = k_\parallel \hat{z}$). The frequency (solid blue) and growth rates (solid red) of the modes are calculated using (3.13a) and (3.13b), respectively. The resulting frequencies and growth rates, when normalised as $\gamma \beta_i/\Omega_i$, are functions of the dimensionless quantity $\eta_i \beta_i$; we show the dispersion curves for three different values of $\eta_i \beta_i$. The approximations (3.14) and (3.15) for the frequency (dotted blue) and growth rate (dotted red) in the limit $k_\parallel \rho_i \ll 1$ are also plotted, as are the approximations (3.18a) and (3.18b) for the frequency (dashed blue) and growth rate (dashed red) in the limit $k_\parallel \rho_i \gg 1$.

First, ordering $k_\parallel \rho_i \sim |\eta_i|\beta_i/4 \ll 1$ so that the destabilising η_i terms and the stabilising ion FLR terms are the same order, we find that the real frequency (3.13a) becomes

$$\varpi \approx \frac{2\Omega_i}{\beta_i}\left(1 - \frac{1}{4}k_\parallel \rho_i \eta_i \beta_i - \frac{3}{2}k_\parallel^2 \rho_i^2\right), \tag{3.14}$$

which is precisely that of the slow hydromagnetic wave, with first-order FLR corrections included (Foote & Kulsrud 1979). For $\eta_i < 0$ and $k_\parallel \rho_i < |\eta_i|\beta_i/4$, the growth rate (3.13b) is positive:

$$\gamma \approx -\frac{4\sqrt{\pi}}{k_\parallel^4 \rho_i^4}\left(\frac{\eta_i}{4} + \frac{k_\parallel \rho_i}{\beta_i}\right)\exp\left(-\frac{1}{k_\parallel^2 \rho_i^2}\right)\Omega_i. \tag{3.15}$$

The maximum growth rate (which is exponentially small in $\eta_i \beta_i/4 \ll 1$) is

$$\gamma_{\max} \approx \frac{8\sqrt{\pi}}{|\eta_i|\beta_i^2}\exp\left(-\frac{16}{|\eta_i|^2\beta_i^2} - 1\right)\Omega_i, \tag{3.16}$$

achieved at the parallel wavenumber

$$k_\parallel \rho_i \approx \frac{|\eta_i|\beta_i}{4} - \frac{|\eta_i|^3\beta_i^3}{128}. \tag{3.17}$$

In the opposite limit, $k_\parallel \rho_i \sim (|\eta_i|\beta_i/4)^{1/3} \gg 1$, we obtain

$$\varpi \approx -\left(\eta_i \beta_i \frac{1 - \pi/4}{k_\parallel \rho_i} - k_\parallel^2 \rho_i^2 \right) \frac{\Omega_i}{\beta_i}, \tag{3.18a}$$

$$\gamma \approx -\sqrt{\pi} \left[\frac{\eta_i}{4} \beta_i \left(1 - \frac{\pi - 3}{k_\parallel^2 \rho_i^2} \right) + k_\parallel \rho_i \right] \frac{\Omega_i}{\beta_i}. \tag{3.18b}$$

The maximum positive growth rate is

$$\gamma_{\max} \approx \frac{\sqrt{\pi}}{4} \left\{ 1 - 3 \left[4 \left(\pi - 3 \right) \right]^{1/3} \left(|\eta_i|\beta_i \right)^{-2/3} \right\} |\eta_i|\Omega_i \approx 0.44 \left[1 - 2.48 \left(|\eta_i|\beta_i \right)^{-2/3} \right] |\eta_i|\Omega_i, \tag{3.19}$$

realised for $\eta_i < 0$ at the parallel wavenumber

$$k_\parallel \rho_i \approx \left(\frac{\pi - 3}{2} \right)^{1/3} (|\eta_i|\beta_i)^{1/3} \approx 0.41 \, (|\eta_i|\beta_i)^{1/3} . \tag{3.20}$$

We note that, in contrast to the CET whistler instability, the real frequency of the fastest-growing unstable mode is smaller than its growth rate: $\omega_{\mathrm{peak}}/\gamma_{\max} \approx 0.36(|\eta_i|\beta_i)^{-1/3}$.

The approximate expressions (3.14), (3.15), (3.18a) and (3.18b) for the frequency and growth rate in the limits $k_\parallel \rho_i \ll 1$ and $k_\parallel \rho_i \gg 1$, are plotted in figure 5, along with the exact results (3.13).

As with the CET whistler instability, a general expression for the complex frequency of oblique ion CET instabilities can be derived in the form (see Appendix J.4)

$$\omega = \frac{\Omega_i}{\beta_i} k_\parallel |\rho_i| \frac{-\tilde{B}_T \pm \sqrt{\tilde{B}_T^2 + 4\tilde{A}_T \tilde{C}_T}}{2\tilde{A}_T}, \tag{3.21}$$

where $\tilde{A}_T = \tilde{A}_T(k_\parallel \rho_i, k_\perp \rho_i, \eta_i \beta_i)$, $\tilde{B}_T = \tilde{B}_T(k_\parallel \rho_i, k_\perp \rho_i, \eta_i \beta_i)$ and $\tilde{C}_T = \tilde{C}_T(k_\parallel \rho_i, k_\perp \rho_i, \eta_i \beta_i)$ are again sums and products of various special mathematical functions defined in (2.122). Investigating such modes by evaluating (3.21) numerically for a range of wavenumbers (see figure 6), we find that, for $\eta_i < 0$, there is one mode that is always damped and one that can be unstable. For $-\eta_i \lesssim 4/\beta_i$, the unstable modes are restricted to quasi-parallel modes (see figure 6a); for $-\eta_i \gtrsim 4/\beta_i$, there is a much broader spectrum of unstable modes (including oblique ones). The positive growth rates of the unstable mode are shown in figure 6(b) for $\eta_i \beta_i = -8$. The typical growth rate γ satisfies $\gamma \sim \Omega_i/\beta_i \sim \eta_i \Omega_i$, as anticipated from (3.21). We also observe in figure 6(b) the existence of an unstable mode at quasi-perpendicular wavenumbers, which is discussed in § 3.3.4.

In summary, an ion-temperature gradient can destabilise ion-Larmor-scale, slow hydromagnetic waves via a similar mechanism to an electron-temperature gradient destabilising electron-Larmor-scale whistler waves. If $\beta_i \gg L_{T_i}/\lambda_i$, the characteristic growth rate of these modes is $\gamma \sim \lambda_i \Omega_i/L_{T_i}$. Unstable modes whose wavevector is parallel to $\mathbf{B}_0$ grow most rapidly, although the growth rate of (moderately) oblique modes is only somewhat smaller. While the CET whistler instability is faster growing than the CET slow-wave instability, both modes grow much more quickly than characteristic hydrodynamic time scales in a strongly magnetised plasma. In any conceivable saturation mechanism, the electron mode will adjust the electron heat flux, and the ion mode the
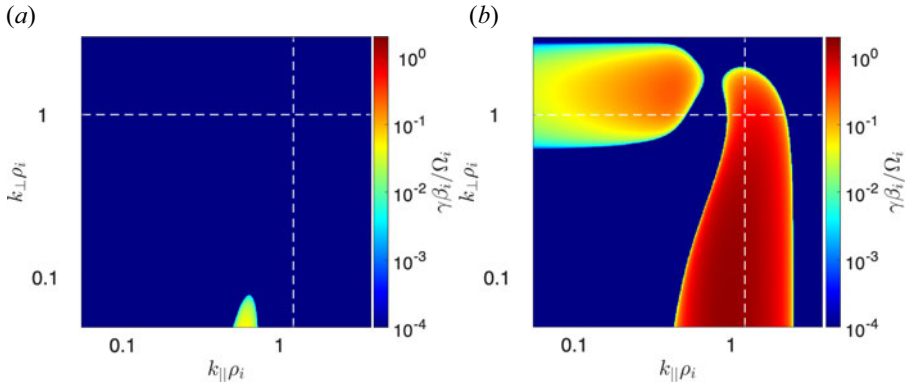
FIGURE 6. Oblique CET ion-Larmor-scale instabilities. Maximum positive growth rates of unstable ion-Larmor-scale modes whose instability is driven by the CE ion-temperature-gradient term in the CE distribution function (3.1b), at arbitrary wavevectors with respect to the background magnetic field. The growth rates of all modes are calculated by taking the imaginary part of (3.21), with coefficients $\tilde{A}_T$, $\tilde{B}_T$ and $\tilde{C}_T$ being known functions of the wavevector (see Appendix J.4). The growth rates are calculated on a 400^2 grid, with logarithmic spacing in both perpendicular and parallel directions between the minimum and maximum wavenumber magnitudes. The resulting growth rates, when normalised as $\gamma\beta_i/\Omega_i$, are functions of $\eta_i\beta_i$; (*a*) $\eta_i\beta_i = -2.5$, (*b*) $\eta_i\beta_i = -8$. The unstable $k_\parallel\rho_i \ll k_\perp\rho_i \sim 1$ modes appearing in (*b*) are dealt with in § 3.3.4.

ion heat flux. Thus, it seems likely that understanding the evolution (and ultimately, the saturation) of both instabilities would be necessary to model correctly the heat transport in a classical, collisional plasma that falls foul of the β-stabilisation condition.

3.3.4. *Long-wavelength kinetic-Alfvén-wave instability*

The instability observed in figure 6(*b*) at wavevectors satisfying $k_\parallel\rho_i \ll k_\perp\rho_i \sim 1$ is different in nature to the slow-hydromagnetic-wave instability: it is an ion-temperature-gradient-driven instability of long-wavelength KAWs. Like the CET slow-wave instability, it operates on account of resonant wave–particle interactions that allow free energy to be drained from the anisotropy of the ion distribution function, which itself arises from the ion-temperature gradient. However, the gyroresonances $v_\parallel \approx \pm\Omega_i/k_\parallel$ operate inefficiently for modes with $k_\parallel\rho_i \ll 1$ in a CE plasma, because there are comparatively few particles with $v_\parallel \gg v_{\mathrm{th}i}$; the dominant resonance is instead the Landau resonance $v_\parallel = \omega/k_\parallel$. More specifically, KAWs with $k_\perp\rho_i \gtrsim 1$, which are usually subject to strong Landau and Barnes damping (that is, the damping rate of the waves is comparable to their real frequency), can be destabilised if the (ion) plasma beta is sufficiently large: $\beta_i \gtrsim L_{T_i}/\lambda_i$. In figure 6(*b*), the peak growth rate of the CET KAW instability is smaller than that of the CET slow-hydromagnetic-wave instability by an order of magnitude; as will be shown below, this is, in fact, a generic feature of the instability.

Similarly to quasi-parallel unstable modes, quasi-perpendicular ones such as unstable KAWs can be characterised analytically, allowing for a simple identification of unstable modes and their peak growth rates. It can be shown (see Appendix J.4.2) that, in the limit $k_\parallel\rho_i \ll 1$, $k_\perp\rho_i \sim 1$, the complex frequency of the low-frequency ($\omega \ll k_\parallel v_{\mathrm{th}i}$) modes in a

plasma whose ion distribution function is (3.1*b*) is

$$\frac{\omega}{k_\parallel v_{\mathrm{th}i}} = \frac{\eta_i \mathcal{G}_i}{2\,(1-\mathcal{F}_i)} + \frac{k_\perp \rho_i}{\beta_i\,(1-\mathcal{F}_i)^2}\left[-\frac{\mathrm{i}\sqrt{\pi}}{2}k_\perp \rho_i \left(\mathcal{F}_i + \sqrt{\frac{\mu_e Z_i^2}{\tau}}\right)\right.$$

$$\left.\pm \sqrt{1 - \frac{\pi}{4}\frac{k_\perp^2 \rho_i^2}{\beta_i}\left(\mathcal{F}_i + \sqrt{\frac{\mu_e Z_i^2}{\tau}}\right)^2 - \frac{\mathrm{i}\sqrt{\pi}\eta_i \beta_i}{4}\frac{2\mathcal{G}_i - \mathcal{F}_i\,(1-\mathcal{F}_i)}{1-\mathcal{F}_i}}\right], \quad (3.22)$$

where $\mathcal{F}_i \equiv \mathcal{F}(k_\perp \rho_i)$, $\mathcal{G}_i \equiv \mathcal{G}(k_\perp \rho_i)$ and

$$\mathcal{F}(\alpha) \equiv \exp\left(-\frac{\alpha^2}{2}\right)\left[I_0\left(\frac{\alpha^2}{2}\right) - I_1\left(\frac{\alpha^2}{2}\right)\right], \quad (3.23)$$

$$\mathcal{G}(\alpha) \equiv 2\alpha^2 \mathcal{F}(\alpha) - \exp\left(-\frac{\alpha^2}{2}\right)I_1\left(\frac{\alpha^2}{2}\right). \quad (3.24)$$

In a Maxwellian plasma (i.e. when $\eta_i = 0$), (3.22) becomes

$$\frac{\omega}{k_\parallel v_{\mathrm{th}i}} = \frac{1}{(1-\mathcal{F}_i)^2}\left[-\frac{\mathrm{i}\sqrt{\pi}}{2}\frac{k_\perp^2 \rho_i^2}{\beta_i}\left(\mathcal{F}_i + \sqrt{\frac{\mu_e Z_i^2}{\tau}}\right)\right.$$

$$\left.\pm \sqrt{\frac{k_\perp^2 \rho_i^2}{\beta_i^2} - \frac{\pi}{4}\frac{k_\perp^4 \rho_i^4}{\beta_i^2}\left(\mathcal{F}_i + \sqrt{\frac{\mu_e Z_i^2}{\tau}}\right)^2}\right]. \quad (3.25)$$

In the subsidiary limit $k_\perp \rho_i \gg 1$, we recover $\omega \approx \pm k_\parallel v_{\mathrm{th}i} k_\perp \rho_i / \beta_i$, which is the well-known dispersion relation of a KAW (Schekochihin *et al.* 2009; Boldyrev *et al.* 2013; Kunz *et al.* 2018).

For $\eta_i \neq 0$, we find that, for modes with a positive propagation direction with respect to the background magnetic field (*viz.* $k_\parallel > 0$), there is an instability provided

$$\eta_i \lesssim -3.14\left(1 + 6.5\sqrt{\frac{\mu_e Z_i^2}{\tau}}\right)\beta_i^{-1}, \quad (3.26)$$

with the perpendicular wavenumber $k_\perp \rho_i$ of the fastest-growing unstable mode at fixed $k_\parallel$ just beyond this threshold being approximately given by

$$k_\perp \rho_i \approx 1.77\left(1 - 3.4\sqrt{\frac{\mu_e Z_i^2}{\tau}}\right). \quad (3.27)$$

Figure 7 shows the real frequency and growth rate of such modes at three different (negative) values of $\eta_i \beta_i$. As η_i is decreased beyond the threshold, modes over an increasingly large range of perpendicular wavenumbers are destabilised at both super- and sub-ion-Larmor scales. Indeed, in the limit $|\eta_i| \beta_i \gg 1$, the peak growth rate $\gamma_{\max}$ (for a fixed $k_\parallel$) occurs at a perpendicular wavenumber $k_\perp \rho_i < 1$, which decreases as $|\eta_i| \beta_i$
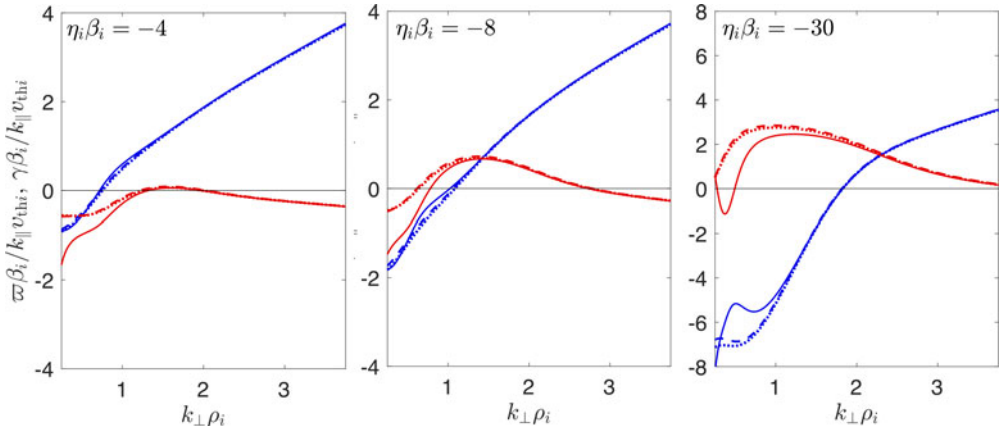
FIGURE 7. Quasi-perpendicular CET KAW instability. Dispersion curves of unstable KAWs whose instability is driven by the ion-temperature-gradient term in the CE distribution function (3.1b), for wavevectors that are almost perpendicular to the background magnetic field (*viz.* $k_\perp \gg k_\parallel$). The frequency (blue) and growth rates (red) of unstable modes are calculated at (small) fixed values of $k_\parallel \rho_i$ from the real and imaginary parts of (3.21); the solid curves are calculated for $k_\parallel \rho_i = 0.35$, while the dashed curves are for $k_\parallel \rho_i = 0.05$. The resulting frequencies and growth rates, when normalised as $\gamma \beta_i / k_\parallel v_{\mathrm{th}i}$, are functions of the dimensionless quantity $\eta_i \beta_i$; we show the dispersion curves for three different values of $\eta_i \beta_i$. The frequency (dotted blue) and growth rate (dotted red) in the limit $k_\parallel \rho_i \ll 1$, which are calculated by taking the real and imaginary parts of (3.22), are also plotted.

increases. Such modes are, in fact, no longer well described physically as KAWs; their analogues in a Maxwellian plasma are Barnes-damped, non-propagating slow modes.

Although it is possible to characterise analytically the peak growth rate of the unstable modes (and the perpendicular wavenumber at which such growth is attained) in the limit $k_\parallel \rho_i \ll 1$ by analysing (3.22), such estimates do not capture accurately the behaviour of the fastest-growing modes across all wavevectors, because these fastest-growing modes occur at finite values of $k_\parallel \rho_i$; at such values, the dependence of the frequency and growth rate on $k_\perp \rho_i$ departs somewhat from (3.22) (see figure 7). Instead, we find numerically that, for $\eta_i \beta_i \lesssim -6$,

$$\gamma_{\mathrm{max}} \approx 0.025 |\eta_i| \Omega_i \quad \text{at} \ (k_\parallel \rho_i)_{\mathrm{peak}} \approx 0.35, \tag{3.28}$$

independent of the specific value of either η_i or β_i. For values of $k_\parallel \rho_i$ that are larger than $(k_\parallel \rho_i)_{\mathrm{peak}}$, the instability is quenched. It is clear that, in comparison with the slow-hydromagnetic-wave instability, the growth rate of the fastest-growing perpendicular modes is small (see (3.18)). This difference can be attributed to the fact that, for unstable modes in the limit $|\eta_i| \beta_i \gg 1$, $\gamma_{\mathrm{max}} \sim |\eta_i| k_\parallel \rho_i \Omega_i$ and the value of $k_\parallel \rho_i$ at which maximum growth is achieved is still rather small compared with unity. We conclude that the instability of slow hydromagnetic waves that are driven by an ion-temperature gradient is likely to be more significant than the analogous instability of quasi-perpendicular/KAW modes.

4. CES (Chapman–Enskog, shear-driven) microinstabilities

4.1. *Form of CE distribution function*

Next, we consider the non-Maxwellian terms of the CE distribution arising from bulk-flow gradients. If we set $\eta_s = 0$ for both ions and electrons (*viz.* neglecting both temperature

gradients and electron–ion drifts), the CE distribution functions (2.8) for both species become

$$f_{s0}(v_\parallel, v_\perp) = \frac{n_{s0}}{v_{\text{ths}}^3 \pi^{3/2}} \exp\left(-\tilde{v}_s^2\right) \left[1 - \epsilon_s \left(\frac{v_\parallel^2}{v_{\text{ths}}^2} - \frac{v_\perp^2}{2v_{\text{ths}}^2}\right)\right], \quad (4.1)$$

where we have again chosen the isotropic functions $C_s(\tilde{v}_s)$ to be the ones that arise from the Krook collision operator (see § 2.4.2). We note that for this choice of collision operator, the constant $\mathcal{C}_s$ defined by (2.34) is $\mathcal{C}_s \approx 3/2$, and so the relationship (2.35) between the CE distribution functions' pressure anisotropy Δ_s and the shear parameter ϵ_s becomes

$$\Delta_s = \tfrac{3}{2}\epsilon_s. \quad (4.2)$$

We also observe that the CE shear terms have even parity with respect to the parallel velocity $v_\parallel$, and thus for any unstable mode with positive parallel wavenumber $k_\parallel > 0$, there is a corresponding unstable mode with $k_\parallel < 0$. This conclusion has the consequence that the sign of ϵ_s (which is the same as the sign of $(\hat{z}\hat{z} - I/3) : W_s$, where W_s is the rate-of-strain tensor of species s – see (2.12)) has a significant effect on possible types of CES microinstabilities. Thus, we must consider the cases $\epsilon_s > 0$ (positive pressure anisotropy, $\Delta_s > 0$) and $\epsilon_s < 0$ (negative pressure anisotropy, $\Delta_s < 0$) separately. For easier comparison with previous work by other authors, we will sometimes substitute $\epsilon_s = 2\Delta_s/3$, and work in terms of Δ_s.

As with the discussion of CET microinstabilities in § 3, in the main text, we only present the main findings of our calculations: namely, the overview of the CES stability landscape (§ 4.2), and the analytical characterisation of CES microinstabilities with $\epsilon_s > 0$ (§ 4.3) and $\epsilon_s < 0$ (§ 4.4). The methodology underlying the calculations of growth rates of CES microinstabilities is presented in Appendix K. Similarly to § 3, for the rest of this section, we assume without loss of generality that $k_\parallel > 0$ in all formulae.

4.2. *Stability*

The stability of CE distribution functions of the form (4.1) is determined as a function of the parameters ϵ_i, ϵ_e, d_e, β_e, β_i and the velocity scale length $L_V = |(\hat{z}\hat{z} - \tfrac{1}{3}I) : W_i/V_i|^{-1}$ by assessing whether the maximum microinstability growth rate across all wavelengths smaller than λ_e and λ_i is negative or positive (see Appendix K for the methodology underpinning this calculation). As with the temperature-gradient-driven instabilities, we report the results of stability calculations that pertain to a temperature-equilibrated hydrogen plasma; that is, the particular case in which $\beta_i = \beta_e$ and $\epsilon_e = \mu_e^{1/2}\epsilon_i$ [where we recall that the characteristic magnitude of the CE electron velocity-shear term in such a plasma is smaller than the analogous CE ion-velocity-shear term by a factor of $\mu_e^{1/2} = (m_e/m_i)^{1/2}$]. Because ϵ_i can take both positive and negative values (see § 4.1), we do one stability calculation for each case; the results of these two calculations are shown in figures 8 and 9, respectively. The key characteristics of the stability of the CE distribution function (4.1) for ions and electrons can be shown using plots over a two-dimensional $(d_e/L_V, Ma\,\lambda_e/L_V)$ parameter space at fixed β_e and Ma – we remind the reader that $Ma\,\lambda_e/L_V = |\epsilon_i|$, and that the Mach number Ma is assumed to satisfy $Ma \lesssim 1$ – as opposed to the five-dimensional $(\epsilon_i, d_e, L_V, \beta_e, Ma)$ parameter space that might naively be anticipated. This is because dimensional analysis again implies that d_e and L_V must appear in the stability boundary in the combination d_e/L_V, and the two relevant stability thresholds are only functions of the product of Ma and d_e/L_V rather than their independent values.
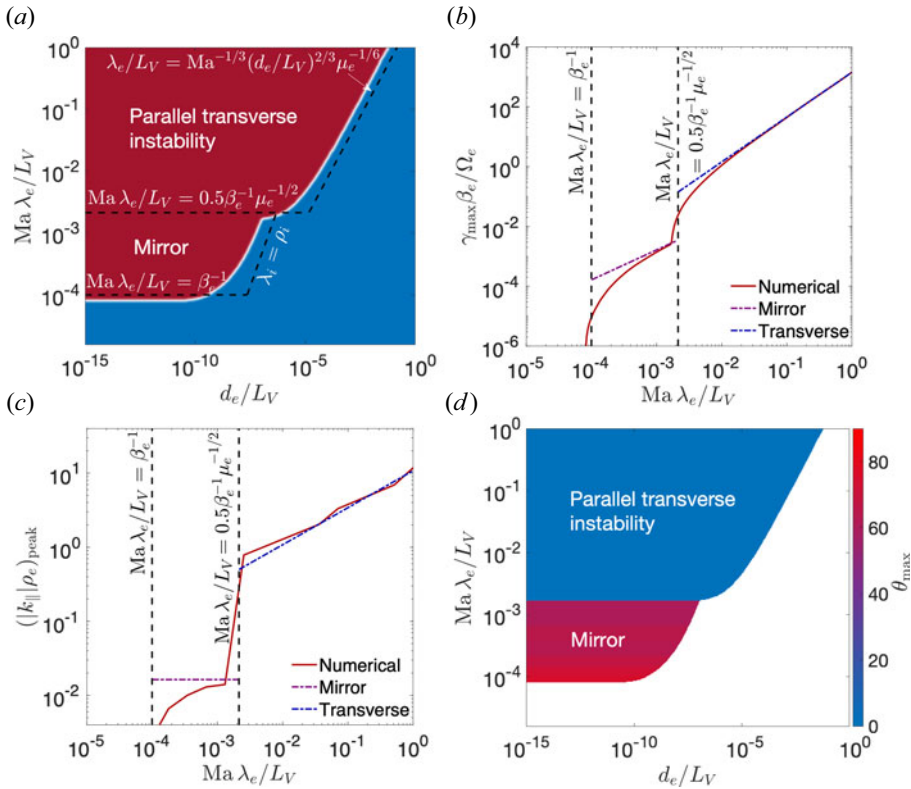
FIGURE 8. The CE-distribution-function stability map for CES microinstabilities driven by positive pressure anisotropy. Exploration of the stability of the ion and electron CE distribution functions (4.1) for different positive values of small parameters ϵ_e and ϵ_i (*viz.* electron- or ion-pressure anisotropies), and the ratio of the electron inertial scale d_e to the velocity scale length L_V, in a temperature-equilibrated hydrogen plasma. In this plot, we chose $\epsilon_e = \mu_e^{1/2}\epsilon_i$, and then show $Ma\,\lambda_e/L_V = |\epsilon_i|$ with equal logarithmic spacing in the range $[10^{-5}, 10^0]$; d_e/L_V is chosen with equal logarithmic spacing in the range $[10^{-15}, 10^0]$. The total size of the grid is 400^2. For reasons of efficiency, we calculate growth rates on a 40^2 grid in wavenumber space with logarithmic spacing for both parallel and perpendicular wavenumbers. In this plot, $\beta_e = \beta_i = 10^4$, and $Ma = 1$. (*a*) Stable (blue) and unstable (red) regions of $(d_e/L_V, Ma\,\lambda_e/L_V)$ phase space. The theoretically anticipated collisional cutoffs (right – see (4.5)) and β-stabilisation thresholds (horizontal dashed lines) for the CES mirror and parallel transverse instabilities, respectively, are also shown. (*b*) Maximum normalised microinstability growth rate (red) vs $Ma\,\lambda_e/L_V$ for a fixed electron inertial scale $d_e/L_V = 10^{-15}$, along with the maximum growth rate for the mirror instability (purple) in the limit $Ma\,\lambda_e\beta_e/L_V \gg 1$ (see (4.13)), and for the parallel transverse instability in the limit $Ma\,\lambda_e\beta_e/L_V \gg \mu_e^{-1/2}$ (see (4.31), with $\theta = 0°$). (*c*) Parallel wavenumber of the fastest-growing microinstability (red) vs $Ma\,\lambda_e/L_V$ for a fixed electron inertial scale $d_e/L_V = 10^{-15}$, along with the same quantity analytically predicted for the mirror instability (purple) in the limit $Ma\,\lambda_e\beta_e/L_V \gg 1$ (see (4.14a,b)), and for the parallel transverse instability (blue) in the limit $Ma\,\lambda_e\beta_e/L_V \gg \mu_e^{-1/2}$ (see (4.33a,b), with $\theta = 0°$). (*d*) Wavevector angle $\theta \equiv \tan^{-1}(k_\parallel/k_\perp)$ of the fastest-growing instability over the $(d_e/L_V, Ma\,\lambda_e\beta_e/L_V)$ parameter space.
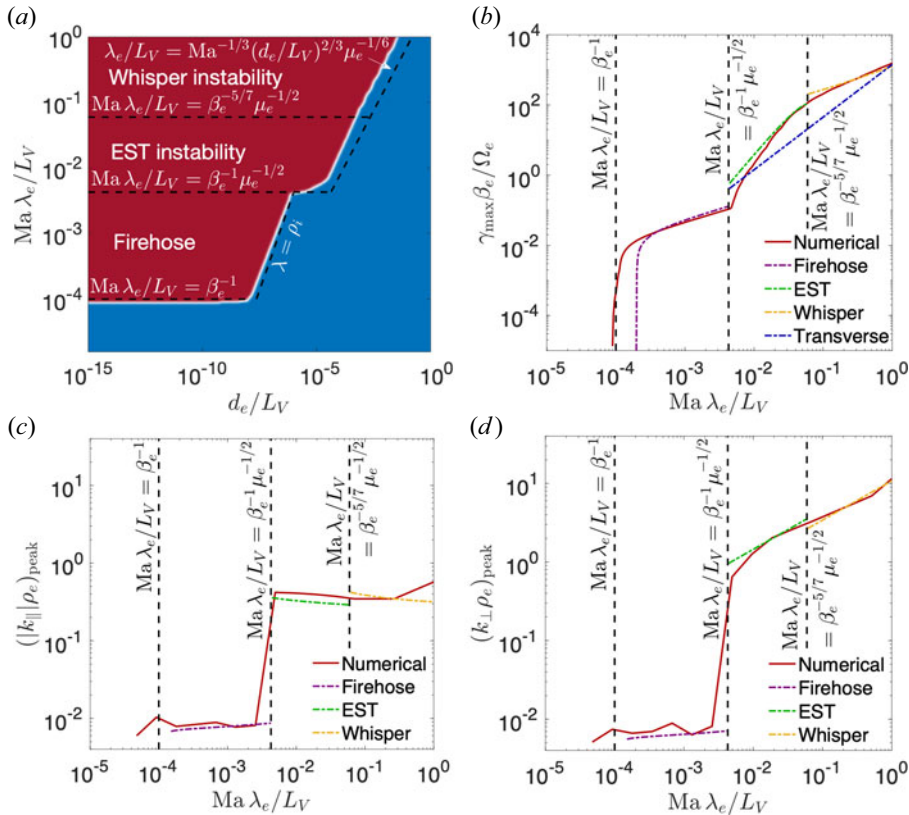
FIGURE 9. The CE-distribution-function stability map for CES microinstabilities driven by negative pressure anisotropy. Same as figure 8, but for negative values of the small parameters ϵ_e and ϵ_i. (*a*) Stable (blue) and unstable (red) regions of $(d_e/L_V, Ma\,\lambda_e/L_V)$ phase space. The theoretically anticipated collisional cutoffs (right – see (4.5)) for the CES firehose and oblique transverse instabilities, respectively, and the β-stabilisation thresholds (horizontal dashed lines) for the CES firehose, CES EST and whisper instabilities are also shown. (*b*) Maximum normalised microinstability growth rate (red) vs $Ma\,\lambda_e/L_V$ for a fixed electron inertial scale $d_e/L_V = 10^{-15}$, along with analytically predicted maximum growth rate for the firehose instability (purple) (see (4.66)), for the EST instability (green) in the limit $\mu_e^{-1/2}\beta_e^{-5/7} \gg Ma\,\lambda_e/L_V \gg \mu_e^{-1/2}\beta_e^{-1}$ (see (4.98)) for the whisper instability (yellow) in the limit $\mu_e^{-1/2}\beta_e^{-1/3} \gg Ma\,\lambda_e/L_V \gg \mu_e^{-1/2}\beta_e^{-5/7}$ (see (4.110)), and for the oblique transverse instability (blue) in the limit $Ma\,\lambda_e/L_V \gg \mu_e^{-1/2}\beta_e^{-1}$ (see (4.101)). (*c*) Same as (*b*), but for the parallel wavenumber of the fastest-growing microinstability. The analytical predictions of this quantity for the firehose instability (purple) (see (4.67)), for the EST instability (green) (see (4.99*b*)) and for the whisper instability (yellow) (see (4.111*b*)), respectively, are also shown. (*d*) Same as (*b*), but for the perpendicular wavenumber of the fastest-growing microinstability. The analytical predictions of this quantity for the firehose instability (purple) (see (4.67)), for the EST instability (green) (see (4.99*a*)) and for the whisper instability (yellow) (see (4.111*a*)), are also shown.

The regions of stability presented in figure 8(*a*) for $\epsilon_i > 0$ (*viz.* for shear flows that drive positive pressure anisotropy) and in figure 9(*a*) for $\epsilon_i < 0$ (*viz.* for shear flows driving negative pressure anisotropy), respectively, are broadly similar to the region of stability

for CET microinstabilities described in § 3.2 (and shown in figure 2a), but with one crucial difference. Once again, for d_e/L_V less than a critical value $(d_e/L_V)_{c0}$, stability is independent of d_e/L_V, and there are no instabilities for $Ma\,\lambda_e\beta_e/L_V \ll 1$; for $d_e/L_V \gtrsim (d_e/L_V)_{c0}$ and $Ma\,\lambda_e\beta_e/L_V > 1$, stability is guaranteed if (and only if) $d_e/L_V > (d_e/L_V)_c$ at fixed $Ma\,\lambda_e/L_V$, where $(d_e/L_V)_c$ is a monotonically increasing function of $Ma\,\lambda_e/L_V$. As before, these two bounding thresholds correspond to the β-stabilisation conditions and collisional-stabilisation conditions, respectively, of CES microinstabilities. However, the dependence of $(d_e/L_V)_c$ on $Ma\,\lambda_e/L_V$ is more complicated than the analogous relationship between $(d_e/L_T)_c$ and $Ma\,\lambda_e/L_T$ that was presented in figure 2(a). Namely, if $Ma\,\lambda_e/L_T \gtrsim \beta_e^{-1}\mu_e^{-1/2}$, then $(d_e/L_V)_c$ suddenly shifts towards a larger value, with the subsequent (power-law) relationship between $(d_e/L_V)_c$ and $Ma\,\lambda_e/L_V$ being distinct from the analogous relationship when $Ma\,\lambda_e/L_T \lesssim \beta_e^{-1}\mu_e^{-1/2}$. This behaviour is the result of a feature of the unstable region that is present for CES but not CET microinstabilities: different instabilities being dominant in different regions of the $(d_e/L_V, Ma\,\lambda_e/L_V)$ parameter space. As we will see, this arises because CES microinstabilities on ion scales have less stringent β-stabilisation thresholds than those on electron scales. Although their regions of stability are qualitatively similar, the types of microinstabilities that arise when $\epsilon_i > 0$ or $\epsilon_i < 0$ are quite different, so we now discuss each case in turn.

4.2.1. *Positive pressure anisotropy*

For $\epsilon_i > 0$ and $0.5\mu_e^{-1/2}\beta_e^{-1} \gtrsim Ma\,\lambda_e/L_V \gg \beta_e^{-1}$, the fastest-growing CES microinstability is the mirror instability: that is, a non-propagating, compressible slow mode on ion scales that is destabilised by positive ion pressure anisotropy. For $Ma\,\lambda_e\beta_e/L_V \gtrsim 0.5\mu_e^{-1/2}$, a faster-growing CES microinstability emerges on electron-Larmor scales, driven by positive electron-pressure anisotropy: the whistler (electron-cyclotron) instability. For fixed β_i, the CES mirror instability can operate at smaller values of $Ma\,\lambda_e/L_V$ than the CES whistler instability, because the mirror-instability threshold $\Delta_i\beta_i = 3\,Ma\,\lambda_e\beta_i/2L_V \geq 1$ (see § 4.3.1) is a less stringent condition on $Ma\,\lambda_e/L_V$ for fixed β_e than the threshold $\Delta_e\beta_e = 3\mu_e^{1/2}\,Ma\,\lambda_e\beta_i/2L_V \gtrsim 0.5$ of the CES whistler instability (see § 4.3.2). On the other hand, once $Ma\,\lambda_e\beta_e/L_V \gtrsim 0.5\mu_e^{-1/2}$, the maximum growth rate of the CES mirror instability $\gamma_{\text{mirr}} \sim \Delta_i\Omega_i$ is much smaller than that of the CES whistler instability: $\gamma_{\text{whistler},S} \sim \Delta_e\Omega_e \sim \mu_e^{-1/2}\Delta_i\Omega_i \gg \Delta_i\Omega_i$. For $Ma\,\lambda_e\beta_e/L_V \gg \mu_e^{-1/2}$, in addition to unstable whistler modes, modes on sub-electron-Larmor scales are also destabilised: this is the parallel transverse instability, a microinstability that is essentially unmagnetised ($k\rho_i \gg 1$) in character. When it can operate, the CES parallel transverse instability has a much larger growth rate than the unstable electron-Larmor-scale whistler waves, $\gamma_{\text{trans}} \sim \Delta_e(\Delta_e\beta)^{1/2}\Omega_e \gg \gamma_{\text{whist}} \sim \Delta_e\Omega_e$, so if $Ma\,\lambda_e\beta_e/L_V \gg \mu_e^{-1/2}$, the transverse instability dominates.

Numerical evidence for the dominance of the CES mirror instability when $\mu_e^{-1/2} \gg Ma\,\lambda_e/L_V \gg 1$, and then the CES parallel transverse instability when $Ma\,\lambda_e/L_V \gg \mu_e^{-1/2}$, can be produced by isolating the maximum growth rate, the parallel wavenumber and the wavevector angle associated with peak growth for the unstable regions of the $(d_e/L_V, Ma\,\lambda_e/L_V)$ parameter space. Figure 8(b) shows that, for fixed d_e/L_V and a range of $Ma\,\lambda_e/L_V$, the peak microinstability growth rate is a reasonable match for that of the mirror instability (*viz.* (4.13)) for $0.5\mu_e^{-1/2}\beta_e^{-1} \gtrsim Ma\,\lambda_e/L_V \gg \beta_e^{-1}$, and a good match for the parallel transverse instability (*viz.* (4.31)) for $Ma\,\lambda_e/L_V \gtrsim \mu_e^{-1/2}\beta_e^{-1}$. Figure 8(c) demonstrates that, for $\mu_e^{-1/2}\beta_e^{-1} \gtrsim Ma\,\lambda_e/L_V \gg \beta_e^{-1}$, the (non-dimensionalised) parallel wavenumber $(k_\parallel\rho_e)_{\text{peak}}$ of peak growth satisfies $(k_\parallel\rho_e)_{\text{peak}} \sim \mu_e^{-1/2}$, in agreement with the expected parallel wavenumber of the fastest-growing mirror modes (see (4.14a,b)). At $Ma\,\lambda_e/L_V \sim \mu_e^{-1/2}\beta_e^{-1}$, there is a dramatic shift in $(k_\parallel\rho_e)_{\text{peak}}$ to a value $(k_\parallel\rho_e)_{\text{peak}} \gtrsim 1$ that

agrees with the expected parallel wavenumber of the parallel transverse instability (see (4.33a,b)). As for the peak-growth wavevector angle (figure 8d), for $\beta_e^{-1} \lesssim Ma\,\lambda_e/L_V \lesssim \mu_e^{-1/2}\beta_e^{-1}$, the dominant instability is oblique (as would be expected for the mirror instability), while for $Ma\,\lambda_e/L_V \gtrsim 0.5\mu_e^{-1/2}\beta_e^{-1}$, it is parallel (implying that the CES whistler/parallel transverse instability dominates). We conclude that the mirror instability is indeed dominant when $0.5\mu_e^{-1/2}\beta_e^{-1} \gtrsim Ma\,\lambda_e/L_V \gg \beta_e^{-1}$, and the parallel transverse instability when $Ma\,\lambda_e/L_V \gg \mu_e^{-1/2}\beta_e^{-1}$.

4.2.2. *Negative pressure anisotropy*

Now considering the case when $\epsilon_i < 0$, i.e. the case of negative pressure anisotropy, the only CES microinstability that operates when $\mu_e^{-1/2}\beta_e^{-1} \gtrsim Ma\,\lambda_e/L_V \gg \beta_e^{-1}$ is the firehose instability: the destabilisation of Alfvén waves by ion-pressure anisotropies $\Delta_i \lesssim -1/\beta_i$.[3] If $Ma\,\lambda_e/L_V \gtrsim \mu_e^{-1/2}\beta_e^{-1}$, several electron-scale CES microinstabilities arise, all of which tend to have larger growth rates than the firehose instability. The first of these to develop (at $Ma\,\lambda_e/L_V \sim \mu_e^{-1/2}\beta_e^{-1}$) is the oblique electron firehose instability: the destabilisation of oblique kinetic-Alfvén waves by negative electron-pressure anisotropy. For $\mu_e^{-1/2}\beta_e^{-1} \lesssim Ma\,\lambda_e/L_V \lesssim \mu_e^{-1/2}\beta_e^{-5/7}$, the EST instability begins to operate; this is a non-propagating quasi-perpendicular mode on electron-Larmor scales ($k_\perp \rho_e \sim 1 \gg k_\parallel \rho_e$), which, while damped in a Maxwellian plasma, is unstable for sufficiently negative electron pressure anisotropies, and grows more rapidly than the oblique electron firehose instability. For $\mu_e^{-1/2}\beta_e^{-5/7} \lesssim Ma\,\lambda_e/L_V \lesssim \mu_e^{-1/2}\beta_e^{-1/3}$, the EST instability is surpassed by the whisper instability: the instability of a newly discovered propagating wave in a Maxwellian plasma (a whisper wave) whose perpendicular wavelength is on sub-electron-Larmor scales ($k_\perp \rho_e \gg 1$), but whose parallel wavelength is above the electron-Larmor scale ($k_\parallel \rho_e < 1$). Finally, when $Ma\,\lambda_e/L_V \gtrsim \mu_e^{-1/2}\beta_e^{-1/3}$, the oblique transverse instability comes to predominate; unlike either the oblique electron firehose, the EST or whisper instabilities, it is unmagnetised in nature (like its parallel relative). Of these four instabilities, the oblique electron firehose and transverse instabilities have been identified previously (see references in §§ 4.4.7 and 4.4.9, respectively), but not the EST or whisper instabilities.

We support these claims (in an analogous manner to the $\epsilon_i > 0$ case) by calculating the growth rate of the dominant microinstabilities for given points in the (d_e/L_V, $Ma\,\lambda_e/L_V$) parameter space. Figure 9(b) shows the maximum growth rate for a fixed value of d_e/L_V. For $\mu_e^{-1/2}\beta_e^{-1} \gtrsim Ma\,\lambda_e/L_V \gg \beta_e^{-1}$, the peak growth rate follows the analytical prediction for the ion firehose instability, $\gamma_{\text{fire}} \sim |\Delta_i|^{1/2}\Omega_i/\sqrt{\log 1/|\Delta_i|}$, when $\Delta_i \ll -2/\beta_i$ (see (4.66)). For $Ma\,\lambda_e/L_V \gtrsim \mu_e^{-1/2}\beta_e^{-1}$, the peak growth rate becomes much greater than γ_{fire}; for $\beta_e^{-5/7} \gtrsim \mu_e^{1/2}Ma\,\lambda_e/L_V \gg \beta_e^{-1}$, it instead matches that of the EST instability, $\gamma_{\text{EST}} \sim |\Delta_e|(|\Delta_e|\beta_e)^{3/2}\Omega_e/\sqrt{\log|\Delta_e|\beta_e}$ (see (4.98)), where we remind the reader that $|\Delta_e| = 3\mu_e^{1/2}Ma\,\lambda_e/2L_V$. For $\mu_e^{1/2}Ma\,\lambda_e/L_V \gg \beta_e^{-5/7}$, the observed growth rate agrees with an analytical prediction for the whisper instability, $\gamma_{\text{whisp}} \sim |\Delta_e|^{1/2}(|\Delta_e|\beta_e)^{1/4}\Omega_e/\sqrt{\log|\Delta_e|\beta_e}$ (see (4.110)). Finally, because of the value of β_e chosen for this numerical example, the condition $Ma\,\lambda_e/L_V \gtrsim \mu_e^{-1/2}\beta_e^{-1/3}$ under which the oblique transverse instability dominates is never met for $Ma\,\lambda_e/L_V \ll 1$, and thus the numerically measured growth rate of the dominant CES microinstability is larger than the transverse instability's peak growth rate $\gamma_{\text{trans}} \sim |\Delta_e|(|\Delta_e|\beta_e)^{1/2}\Omega_e$ (see (4.101)) for the entire range of $Ma\,\lambda_e/L_V$ that we show in figure 9(b), (blue line).

---

[3]In the limit of wavelengths much larger than the ion-Larmor radius, the firehose-instability threshold is well known to be $\Delta_i = (\Delta_i)_c < -2/\beta_i$. However, for plasmas whose ion species have either a CE distribution function or a bi-Maxwellian distribution, the instability threshold for oblique ion-Larmor-scale firehose modes is somewhat less stringent: see § 4.4.1.

A further confirmation that the most important microinstabilities are those that we have explicitly identified is obtained by calculating the parallel and perpendicular wavenumbers associated with the dominant microinstability. Figures 9(*c*) and 9(*d*) show that, for $\beta_e^{-1} \ll Ma\,\lambda_e/L_V \ll \mu_e^{-1/2}\beta_e^{-1}$, $(k_\parallel\rho_e)_{\mathrm{peak}} \sim (k_\perp\rho_e)_{\mathrm{peak}} \sim \mu_e^{1/2}$. These values of $(k_\parallel\rho_e)_{\mathrm{peak}}$ are consistent with the properties of the fastest-growing unstable firehose modes (see §§ 4.4.1 and 4.4.4), whose parallel wavenumber (approximately) satisfies $(k_\parallel\rho_i)_{\mathrm{peak}} \sim 1/\sqrt{\log 1/|\Delta_i|}$ when $\Delta_i \ll -2/\beta_i$ (see (4.67)), and whose wavevector angle is $\theta_{\mathrm{peak}} \approx 39^\circ$. At $Ma\,\lambda_e/L_V \sim \mu_e^{-1/2}\beta_e^{-1}$, the magnitudes of the parallel and perpendicular wavenumbers changes abruptly, to $(k_\parallel\rho_e)_{\mathrm{peak}} \sim (k_\perp\rho_e)_{\mathrm{peak}} \sim 1$; this is in line with expectations from the onset of the oblique electron firehose instability when $|\Delta_e|\beta_e \sim 1$. For $Ma\,\lambda_e/L_V \gg \beta_e^{-1}$ ($|\Delta_e|\beta_e \gg 1$), the parallel scale of the fastest-growing mode remains above electron-Larmor scales $[(k_\parallel\rho_e)_{\mathrm{peak}} < 1]$, while $(k_\perp\rho_e)_{\mathrm{peak}}$ increases monotonically above unity. Both findings match theoretical expectations concerning the evolution of the parallel and perpendicular wavenumbers of the EST and whisper instabilities as functions of increasing $|\Delta_e|\beta_e$, and analytic formulae for these quantities are in reasonable agreement with the numerical results (see §§ 4.4.8 and 4.4.10).

4.2.3. *Collisional stabilisation*

For both $\epsilon_i > 0$ and $\epsilon_i < 0$, the shift in $(d_e/L_V)_c$ at $Ma\,\lambda_e/L_V \sim \mu_e^{-1/2}\beta_e^{-1}$ observed in figures 8(*a*) and 9(*a*) can be explained in terms of the ion-scale and electron-scale microinstabilities having distinct collisional-stabilisation conditions of the form (2.125) (*viz.* $k\lambda_e \sim k\lambda_i \lesssim 1$), with the condition on the ion-scale instabilities being more restrictive. The wavenumbers k_{mirr} and k_{fire} at which maximal growth of the ion mirror and firehose instabilities occurs satisfy $k_{\mathrm{mirr}}\rho_i \sim 1$ and $k_{\mathrm{fire}}\rho_i \lesssim 1$, respectively, for $Ma\,\lambda_e\beta_e/L_V \gg 1$, leading to the collisional-stabilisation condition

$$\frac{\lambda_e}{L_V} \lesssim \frac{\rho_i}{L_V} \sim \mu_e^{-1/2}\beta_e^{1/2}\frac{d_e}{L_V}. \tag{4.3}$$

For the electron-scale microinstabilities, the parallel and the oblique transverse instabilities have the largest (common) wavenumber of all such instabilities that operate when $\epsilon_i > 0$ and $\epsilon_i < 0$, respectively, and so provide the most demanding collisional-stabilisation conditions. For both transverse instabilities, the wavenumber at which peak growth occurs satisfies $k_{\mathrm{trans}}\rho_e \sim (\mu_e^{1/2}Ma\,\lambda_e\beta_e/L_V)^{1/2}$ (see (4.32)), which in turn can be rearranged to give the collisional-stabilisation condition

$$\frac{\lambda_e}{L_V} \lesssim Ma^{-1/3}\mu_e^{-1/6}\left(\frac{d_e}{L_V}\right)^{2/3}. \tag{4.4}$$

Bringing these results together, we find

$$\left(\frac{d_e}{L_V}\right)_c = \begin{cases} \mu_e^{1/2}\beta_e^{-1/2}\lambda_e/L_V, & \beta_e^{-1} \ll Ma\,\lambda_e/L_V < \mu_e^{-1/2}\beta_e^{-1}, \\ \mu_e^{1/4}Ma^{1/2}\,(\lambda_e/L_V)^{3/2}, & Ma\,\lambda_e/L_V \gtrsim \mu_e^{-1/2}\beta_e^{-1}, \end{cases} \tag{4.5}$$

with $(d_e/L_V)_{c0} = \mu_e^{1/2}\beta_e^{-3/2}$. This matches asymptotically the numerical results shown in figures 8(*a*) and 9(*a*). These findings confirm that, once again, the relevant collisional-stabilisation condition for the microinstabilities with wavenumber k is $k\lambda_e = k\lambda_i \lesssim 1$ (*viz.* (2.125)), as opposed to the more restrictive conditions $\gamma\tau_i \lesssim 1$ and $\gamma\tau_e \lesssim 1$ on the CES ion-scale and electron-scale instabilities, respectively. Similarly to the collisional-stabilisation condition on the CET whistler instability (see § 3.2), we note that

the collisional-stabilisation condition on any of these microinstabilities can never actually be satisfied in a strongly magnetised plasma, because $k\lambda_i \gtrsim \lambda_i/\rho_i \gg 1$ for the ion-scale instabilities, and $k\lambda_e \gtrsim \lambda_e/\rho_e \gg 1$ for the electron-scale instabilities.

4.2.4. *Outline of the rest of this section*

Further discussion about the properties and growth rates of CES microinstabilities with $\epsilon_s > 0$ (*viz.* those driven by positive pressure anisotropy) can be found in § 4.3, with the mirror, whistler and transverse instabilities discussed in §§ 4.3.1, 4.3.2 and 4.3.3, respectively. In addition to these, there is another instability (the electron mirror instability) that can be driven by positive pressure anisotropy of CE distribution functions that we note in passing: it consists in KAWs driven unstable by the CE electron-shear term, and to some extent by the ion-shear term (§ 4.3.4). The electron mirror instability does not appear to be the fastest-growing CES microinstability anywhere in the $(d_e/L_V, Ma\,\lambda_e/L_V)$ parameter space; since the instability is subdominant to two other electron-scale instabilities (the whistler and transverse instabilities), this would seem to imply that the instability is comparatively less important.

CES microinstabilities with $\epsilon_s < 0$ (*viz.* those driven by negative pressure anisotropy) are explored in § 4.4. The firehose instability is overviewed in § 4.4.1, with then four subclasses of the instability (parallel, oblique, critical line and sub-ion-Larmor scale) considered in §§ 4.4.2, 4.4.3, 4.4.4 and 4.4.5. The oblique electron firehose instability is discussed in § 4.4.7, the EST instability in § 4.4.8, the oblique transverse instability in § 4.4.9 and the whisper instability in § 4.4.10. We identify two additional CES microinstabilities which are never the fastest-growing microinstability in any unstable region: the parallel electron firehose instability (§ 4.4.6), which (in spite of its name) has a different underlying physical mechanism than the oblique electron firehose, and the ordinary-mode instability (§ 4.4.11), which only operates at very high β_e ($\beta_e \gtrsim |\Delta_e|^{-3}$), and is only characteristically distinct from the oblique transverse instability in a regime in which it is slower growing.

Readers who do not wish to dwell on specific CES microinstabilities should proceed directly to § 5.

4.3. *CES microinstability classification: positive pressure anisotropy ($\epsilon_i > 0$)*

4.3.1. *Mirror instability*

The CES mirror instability consists in the destabilisation of compressive slow modes by a sufficiently large positive ion-pressure anisotropy associated with the ion-shear term of the ion CE distribution function. In a high-β plasma with Maxwellian ion and electron distribution functions, the slow mode – which is one of the two plasma modes which exist at oblique wavevector angles $\theta \gtrsim \beta_i^{-1/4}$ (the other being the shear-Alfvén wave), and consists of a perturbation to the magnetic field's strength – is non-propagating, being subject to strong Barnes' (equivalently, transit-time) damping (Barnes 1966). This damping is the result of Landau-resonant interactions between the slow mode and co-moving ions with $v_\parallel = \omega/k_\parallel$; since, for a distribution function that decreases monotonically with $v_\parallel > 0$, there are more ions with $v_\parallel < \omega/k_\parallel$ than with $v_\parallel > \omega/k_\parallel$, there is a net transfer of free energy from the slow modes to the ions (as a particle acceleration process, this is sometimes called betatron acceleration). However, in a plasma with $\Delta_i > 0$, there is an increase in the relative number of ions with large pitch angles in the troughs of the slow mode's magnetic-field strength perturbation, giving rise to excess perpendicular pressure. When $\Delta_i > 1/\beta_i$, this excess pressure overbalances the magnetic pressure, leading to the mirror instability. In CE plasma with $0 < \Delta_i\beta_i - 1 \ll 1$, only quasi-perpendicular long-wavelength mirror modes ($k_\parallel\rho_i \ll k_\perp\rho_i \ll 1$) are destabilised;

for larger values of Δ_i, a broad range of slow modes (including ion-Larmor-scale ones) become unstable. Chronologically, the earliest discussions of the mirror instability in pressure-anisotropic plasmas are due to Parker (1958) and Hasegawa (1969). Southwood & Kivelson (1993) provide a detailed and lucid discussion of the linear physics of the mirror instability (see also Kunz *et al.* 2015); various analytical (Pokhotelov *et al.* 2008; Rincon *et al.* 2015) and numerical (Hellinger *et al.* 2009; Kunz *et al.* 2014; Riquelme *et al.* 2015; Melville *et al.* 2016) studies investigating its nonlinear evolution have also been carried out.

The CES mirror instability can be characterised analytically – and simple expressions derived for the maximum growth rate and the wavevector at which that growth is attained – in the limit of marginal instability. First, we define the threshold parameter $\Gamma_i \equiv \beta_i \Delta - 1$, where $\Delta \equiv \Delta_i + \Delta_e = (1 + \mu_e^{1/2})\Delta_i$, and assume that $\Gamma_i \ll 1$. It can then be shown (see Appendix K.3.2) that under the orderings

$$k_\parallel \rho_i \sim k_\perp^2 \rho_i^2 \sim \Gamma_i \ll 1, \quad \frac{\gamma}{\Omega_i} \sim \frac{\Gamma_i^2}{\beta_i} \ll 1, \qquad (4.6a,b)$$

the mirror modes have a growth rate given by

$$\frac{\gamma}{\Omega_i} = \frac{k_\parallel \rho_i}{\sqrt{\pi}\beta_i} \left(\Gamma_i - \frac{3}{2}\frac{k_\parallel^2}{k_\perp^2} - \frac{3}{4}k_\perp^2 \rho_i^2 \right). \qquad (4.7)$$

This is the same result as the growth rate of the mirror instability in a bi-Maxwellian plasma, with (the anticipated) threshold $\Gamma_i > 0$ (Hellinger 2007). The peak growth rate γ_{max} is then given by

$$\gamma_{\text{max}} = \frac{\Gamma_i^2}{6\sqrt{2\pi}\beta_i}\Omega_i, \qquad (4.8)$$

achieved at the wavenumber

$$(k_\parallel \rho_i)_{\text{peak}} = \frac{\Gamma_i}{3\sqrt{2}}, \quad (k_\perp \rho_i)_{\text{peak}} = \frac{\Gamma_i^{1/2}}{\sqrt{3}}. \qquad (4.9a,b)$$

This recovers the results of Hellinger (2007).

Figure 10 illustrates the accuracy of the above predictions for γ (and therefore γ_{max}), $(k_\parallel \rho_i)_{\text{peak}}$ and $(k_\perp \rho_i)_{\text{peak}}$ by comparing them with the equivalent values obtained numerically using the general method outlined in Appendix K for a particular value of $\Gamma_i \ll 1$. The wavenumber dependence of the numerically determined growth rate (see figure 10a) corroborates that, close to marginality, the unstable mirror modes are quasi-perpendicular; more quantitatively, the values of $k_\parallel \rho_i$ and $k_\perp \rho_i$ at which peak growth is obtained numerically match (4.9a,b). Furthermore, the growth rate (4.7) agrees well with the numerical result when plotted as a function of $k_\parallel \rho_i$ with fixed $k_\perp \rho_i$, and also as a function of $k_\perp \rho_i$ with fixed $k_\parallel \rho_i$ (figure 10b).

In contrast, for finite $\Gamma_i \gtrsim 1$, simple expressions for γ_{max}, $(k_\parallel \rho_i)_{\text{peak}}$ and $(k_\perp \rho_i)_{\text{peak}}$ are challenging to derive analytically. Our numerical calculations indicate that, when $\Gamma_i \sim 1$, a broad range of (purely growing) oblique modes becomes unstable, with maximum growth rate $\gamma_{\text{max}} \sim \Omega_i/\beta_i \sim \Delta\Omega_i$ attained when $k_\parallel \rho_i \lesssim k_\perp \rho_i \sim 1$ (figure 11a). Therefore, asymptotic expansions that treat $k_\perp \rho_i$ and $k_\parallel \rho_i$ as small or large cannot be used to derive simplified expressions for the growth rate of the fastest-growing mirror modes. While the expressions (4.9a,b) for the wavenumber of peak growth derived in the case of
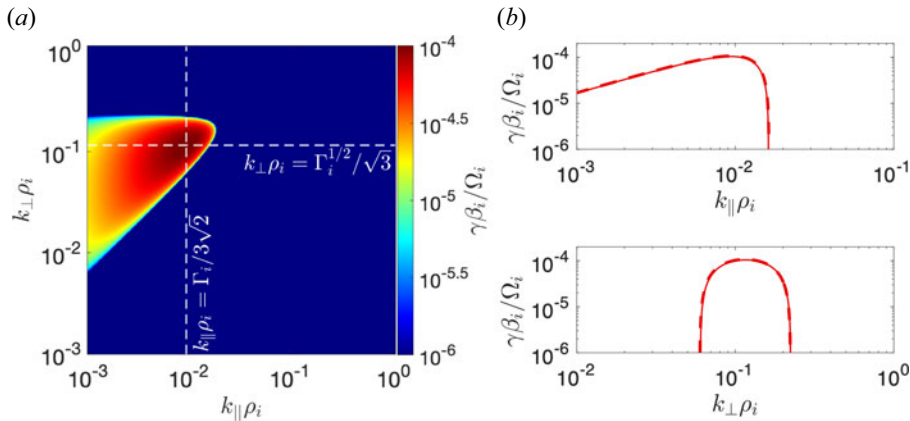
FIGURE 10. Mirror instability at $\Gamma_i = \Delta\beta_i - 1 \ll 1$. (*a*) Growth rates of unstable mirror modes resulting from the CE ion-shear term in the CE distribution function (4.1) for $\Gamma_i = 0.04 \ll 1$ ($\Delta\beta_i = 1.04$). The growth rates of all modes are calculated using the approach outlined in Appendix K.3. The growth rates are calculated on a 400^2 grid, with logarithmic spacing in both perpendicular and parallel directions between the minimum and maximum wavenumber magnitudes. The resulting growth rates, when normalised as $\gamma\beta_i/\Omega_i$, are functions of the dimensionless quantity $\Delta\beta_i$. The dashed white lines indicate the analytical prediction (4.9*a,b*) for the wavenumber at which peak growth is achieved. (*b*) The mirror mode's growth rate (solid line) as a function of $k_\parallel\rho_i$ with $k_\perp\rho_i = \Gamma_i^{1/2}/\sqrt{3}$ (top), and as a function of $k_\perp\rho_i$ with $k_\parallel\rho_i = \Gamma_i/3\sqrt{2}$ (bottom). The dashed lines show the analytical prediction (4.7) for these quantities.

near-marginality remain qualitatively correct, they are no longer quantitatively accurate; the same conclusion applies to the expression (4.7) for the growth rate when $k_\parallel\rho_i \sim k_\perp\rho_i \sim 1$ (figure 11*b*). That being said, an expression similar to (4.7) can be derived (see Appendix K.3.2) for long-wavelength unstable mirror modes that satisfy the ordering

$$k_\parallel\rho_i \sim k_\perp\rho_i \ll 1, \quad \frac{\gamma}{\Omega_i} \sim \frac{k_\parallel\rho_i}{\beta_i} \sim \Delta k_\parallel\rho_i \ll 1. \qquad (4.10a,b)$$

This expression is

$$\frac{\gamma}{\Omega_i} = \frac{k_\parallel\rho_i}{\sqrt{\pi}\beta_i}\left(\Gamma_i - \frac{\Gamma_i + 3}{2}\frac{k_\parallel^2}{k_\perp^2}\right). \qquad (4.11)$$

It implies that all such modes with

$$k_\perp > \left(\frac{3 + \Gamma_i}{2\Gamma_i}\right)^{1/2} k_\parallel, \qquad (4.12)$$

will be unstable, a prediction that is consistent with the unstable region observed in figure 11(*a*).

When $\Gamma_i \gg 1$, but $\Gamma_i < (m_i/m_e)^{1/2}$, the region of $(k_\parallel, k_\perp)$ space in which mirror modes are unstable is qualitatively similar to the $\Gamma_i \sim 1$ case, albeit more extended (figure 12*a*). We find that in this limit, the maximum growth rate $\gamma_{\max}$ becomes directly proportional to
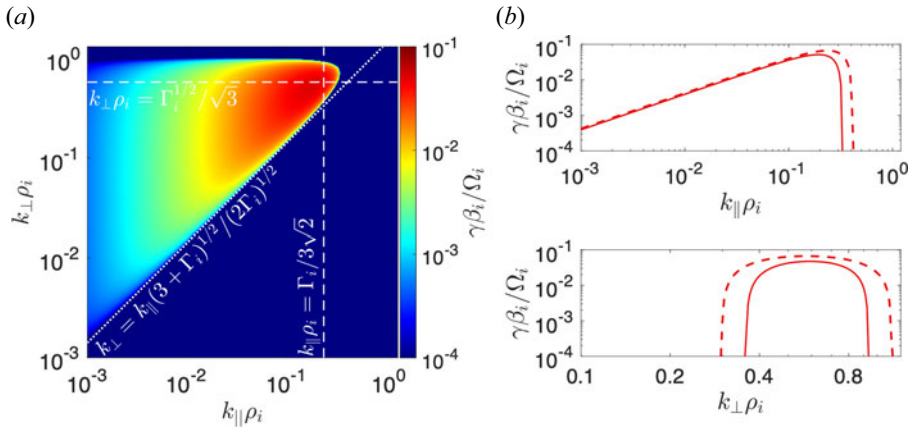
FIGURE 11. Mirror instability at $\Gamma_i = \Delta\beta_i - 1 \sim 1$. (*a*) Growth rates of unstable mirror modes resulting from the CE ion-shear term in the CE distribution function (4.1) for $\Gamma_i = 1$ ($\Delta\beta_i = 2$). The growth rates of all modes are calculated in the same way as in figure 10. The dashed white lines indicate the analytic prediction (4.9*a*,*b*) for the parallel/perpendicular wavenumber at which peak growth is achieved, while the dotted line indicates the analytical prediction (4.12) for the perpendicular wavenumber above which long-wavelength ($k_\parallel\rho_i \lesssim k_\perp\rho_i \ll 1$) mirror modes become unstable. (*b*) The mirror mode's growth rate (solid line) as a function of $k_\parallel\rho_i$ with $k_\perp\rho_i = \Gamma_i^{1/2}/\sqrt{3}$ (top), and as a function of $k_\perp\rho_i$ with $k_\parallel\rho_i = \Gamma_i/3\sqrt{2}$ (bottom). The dashed lines show the analytical prediction (4.7) for this quantity.

Δ (see figure 12*b*), in contrast to the marginal case (4.7):

$$\gamma_{\text{max}} \approx 0.2\Delta\Omega_i. \tag{4.13}$$

This growth is attained at parallel and perpendicular wavenumbers

$$(k_\perp\rho_i)_{\text{peak}} \approx 1.2, \quad (k_\parallel\rho_i)_{\text{peak}} \approx 0.7, \tag{4.14a,b}$$

which depend only weakly on $\Delta\beta_i$.

Some understanding of these results can be derived by considering the dispersion relation of mirror modes on sub-ion-Larmor scales. Adopting the ordering

$$k_\parallel\rho_i \sim k_\perp\rho_i \sim (\Delta_i\beta_i)^{1/2} \gg 1, \quad \frac{\gamma}{\Omega_i} \sim \Delta_i, \tag{4.15a,b}$$

while assuming that $\Delta_i\beta_i \ll \mu_e^{-1/2}$, one finds (see Appendix K.3.2) that

$$\frac{\gamma}{\Omega_i} \approx \frac{k_\parallel}{k}\sqrt{\left(\frac{k^2\rho_i^2}{\beta_i} - \Delta_i\frac{k_\parallel^2 - k_\perp^2}{k^2}\right)\left(\Delta_i\frac{k_\parallel^2}{k^2} - \frac{k^2\rho_i^2}{\beta_i}\right)}. \tag{4.16}$$

This can be re-written in terms of the wavevector angle $\theta = \tan^{-1}(k_\perp/k_\parallel)$ as

$$\frac{\gamma}{\Omega_i} \approx \cos\theta\sqrt{\left[\frac{k^2\rho_i^2}{\beta_i} - \Delta_i\left(\cos^2\theta - \sin^2\theta\right)\right]\left(\Delta_i\cos^2\theta - \frac{k^2\rho_i^2}{\beta_i}\right)}. \tag{4.17}$$

Analysing this expression leads to three conclusions. First, for $\theta > 45°$, there is an instability at all wavenumbers satisfying $k\rho_i < (\Delta_i\beta_i)^{1/2}\cos\theta$, explaining the expansion
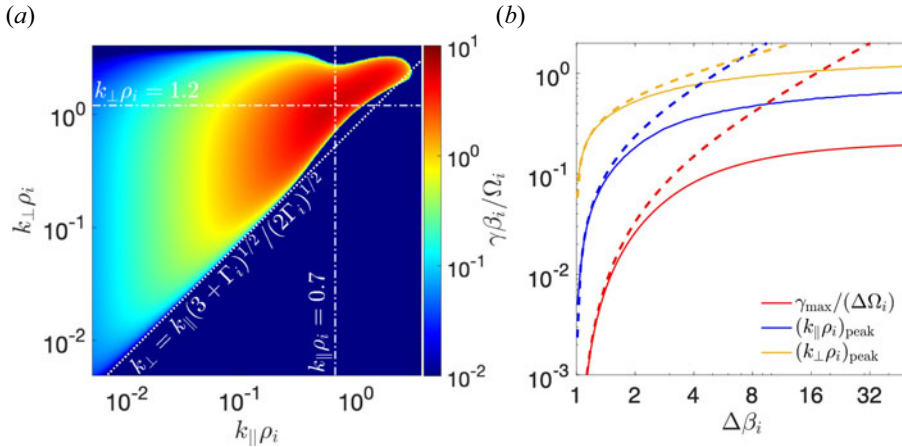
FIGURE 12. Mirror instability at $\Gamma_i = \Delta\beta_i \gg 1$. (*a*) Growth rates of unstable mirror modes resulting from the CE ion-shear term in the CE distribution function (4.1) for $\Gamma_i = 29 \gg 1$ ($\Delta\beta_i = 30$). The growth rates of all modes are calculated in the same way as in figure 10. The dot-dashed white lines indicate the parallel/perpendicular wavenumbers (4.14*a,b*) at which peak growth is achieved, while the dotted line indicates the analytical prediction (4.12) for the perpendicular wavenumber above which long-wavelength ($k_\parallel \rho_i \lesssim k_\perp \rho_i \ll 1$) mirror modes become unstable. (*b*) Normalised maximum positive growth rate $\gamma_{\max}/\Delta\Omega_i$ (solid red line) of the unstable mirror mode as a function of $\Delta\beta_i$ along with the parallel (solid blue line) and perpendicular (solid yellow line) wavenumbers, $(k_\parallel \rho_i)_{\text{peak}}$ and $(k_\perp \rho_i)_{\text{peak}}$ respectively, at which that growth is attained. The analytical prediction (4.7) of $\gamma_{\max}$ for marginally unstable modes, as well as the analogous predictions (4.9*a,b*) for $(k_\parallel \rho_i)_{\text{peak}}$ and $(k_\perp \rho_i)_{\text{peak}}$, are shown as dashed lines.

of the unstable region of $(k_\parallel, k_\perp)$-space with increasing $\Delta_i \beta_i$. For $\theta \leqslant 45°$, growth only occurs over a more limited range of wavenumbers $\sqrt{\cos^2\theta - \sin^2\theta} < k\rho_i/(\Delta_i\beta_i)^{1/2} < \cos\theta$. Secondly, growth in this limit is maximised when $k\rho_i \ll (\Delta_i\beta_i)^{1/2}$, with the maximal growth rate

$$\gamma_{\max} = \frac{1}{3\sqrt{3}}\Delta_i\Omega_i \approx 0.19\Delta_i\Omega_i, \tag{4.18}$$

attained at $\cos\theta = 1/\sqrt{3}$ ($\theta \approx 55°$). This expression for $\gamma_{\max}$ is (surprisingly) close to the numerically measured peak growth rate (4.13). For $k\rho_i \sim (\Delta_i\beta_i)^{1/2}$, the maximum growth rate is smaller than (4.18) by an order-unity factor. Finally, when $k\rho_i \gg (\Delta_i\beta_i)^{1/2}$, *viz.* in a wavenumber regime where there are no unstable mirror modes, (4.16) becomes imaginary, implying that the modes have a real frequency given by

$$\omega \approx \pm k_\parallel k_\perp \rho_e \frac{\Omega_e}{\beta_i}. \tag{4.19}$$

This is the dispersion relation of KAWs in a high-β plasma.[4] In short, at $\Delta_i\beta_i \gg 1$, KAWs are also destabilised by positive ion-pressure anisotropy in addition to longer-wavelength

---

[4]We note that (4.19) is also the same dispersion relation as that of oblique whistler waves (see, e.g. Galtier & Meyrand 2015). However, as was discussed in §3.3.1, in a high-β plasma ($\beta_e \gg \mu_e^{-1/2}$), the small frequency ($\omega \ll k_\parallel v_{\text{thi}}$) of perturbations prohibits all but parallel perturbations from not interacting significantly with the ions, and thus we believe that the modes are more accurately identified as KAWs.

mirror modes. We note that KAWs can also be destabilised by positive electron anisotropy, but the characteristic wavelength of such modes is preferentially comparable to electron-Larmor scales (see § 4.3.4).

4.3.2. *Whistler instability*

The CES whistler instability arises when the free energy associated with positive electron-pressure anisotropy Δ_e of the electron CE distribution function destabilises whistler waves, overwhelming both the electron-cyclotron damping (which is the dominant stabilisation mechanism for whistler waves with $k_\parallel \rho_e \sim 1$) and the Landau damping due to the ion species (the dominant stabilisation mechanism for waves with $k_\parallel \rho_e \ll 1$). In the special case of static ions, electron-cyclotron damping can be overcome by a positive electron-pressure anisotropy of any magnitude for whistler waves with sufficiently long wavelengths. Retaining mobile ions, the instability operates only if Δ_e exceeds a threshold of order $(\Delta_e)_c \sim \beta_e^{-1}$. When $\Delta_e > (\Delta_e)_c$, gyroresonant interactions between electrons with $v_\parallel = \pm \Omega_e / k_\parallel$ and whistler waves allow for free energy to pass from the former to the latter, and so an increasingly broad spectrum of unstable parallel and oblique modes emerges on electron-Larmor scales. The analogue of this instability in a bi-Maxwellian plasma was found by Kennel & Petschek (1966), and it has since been studied numerically in moderately high-β plasma ($\beta_e \sim 1$–10) by several authors (e.g. Gary & Wang 1996; Guo *et al.* 2014; Riquelme *et al.* 2016).

Similarly to the CET whistler instability, the simplest characterisation of the CES whistler instability is for unstable parallel whistler modes (*viz.* $k \approx k_\parallel$). Assuming that these modes satisfy the orderings

$$\tilde{\omega}_{e\parallel} = \frac{\omega}{k_\parallel v_{\text{th}e}} \sim \Delta_e \sim \frac{1}{\beta_e}, \quad k_\parallel \rho_e \sim 1, \tag{4.20a,b}$$

it can be shown (see Appendix K.3.3) that their real frequency ϖ and growth rate γ satisfy

$$\frac{\varpi \beta_e}{\Omega_e} = \pm \Delta_e \beta_e \pm \frac{k_\parallel \rho_e \left[\Delta_e \beta_e \left(1 + \mu_e^{1/2} \right) - k_\parallel^2 \rho_e^2 \right] \operatorname{Re} Z \left(1 / k_\parallel \rho_e \right)}{\left[\operatorname{Re} Z \left(1 / k_\parallel \rho_e \right) \right]^2 + \pi \exp \left(-2 / k_\parallel^2 \rho_e^2 \right)}, \tag{4.21a}$$

$$\frac{\gamma \beta_e}{\Omega_e} = \frac{k_\parallel \rho_e \left[\exp \left(-1 / k_\parallel^2 \rho_e^2 \right) + \mu_e^{1/2} \right] \left(\Delta_e \beta_e - k_\parallel^2 \rho_e^2 \right) + \mu_e^{1/2} \Delta_e \beta_e \operatorname{Re} Z \left(1 / k_\parallel \rho_e \right)}{\left[\operatorname{Re} Z \left(1 / k_\parallel \rho_e \right) \right]^2 / \sqrt{\pi} + \sqrt{\pi} \exp \left(-2 / k_\parallel^2 \rho_e^2 \right)}, \tag{4.21b}$$

where the terms proportional to $\mu_e^{1/2}$ are associated with the ion species.[5] In the limit $\mu_e \to 0$, formally there is always instability provided $\Delta_e \beta_e > 0$; however, for a hydrogen plasma ($\mu_e \approx 1/1836$), it can be shown numerically that the numerator of (4.21b) only becomes positive (over a narrow interval of parallel wavenumbers around $k_\parallel \rho_e \approx 0.60$) for $\Delta_e \beta_e > 0.56$. The dispersion curves $\varpi(k_\parallel)$ and $\gamma(k_\parallel)$ of the unstable whistler waves in a hydrogen plasma for three different values of $\Delta_e \beta_e$ that are above the necessary value for instability are shown in figure 13. When $\Delta_e \beta_e \gtrsim 1$, the growth rate is positive for a range $\Delta k_\parallel \sim \rho_e^{-1}$ around $k_\parallel \rho_e \sim 1$, attaining a characteristic magnitude $\gamma \sim \varpi \sim \Omega_e / \beta_e$.

---

[5]Formally, these terms are $O(\mu_e^{1/2})$ under our assumed ordering, and so should be dropped. However, because of the exponential dependence of the other damping/growth terms on $k_\parallel \rho_e$, these terms play an important role for moderate values of $k_\parallel \rho_e$, *viz.* $\mu_e^{1/2} \exp \left(1 / k_\parallel^2 \rho_e^2 \right) \geqslant 1$ for $k_\parallel \rho_e \lesssim \sqrt{2} / \sqrt{\log m_i / m_e} \approx 0.5$, so we retain them.
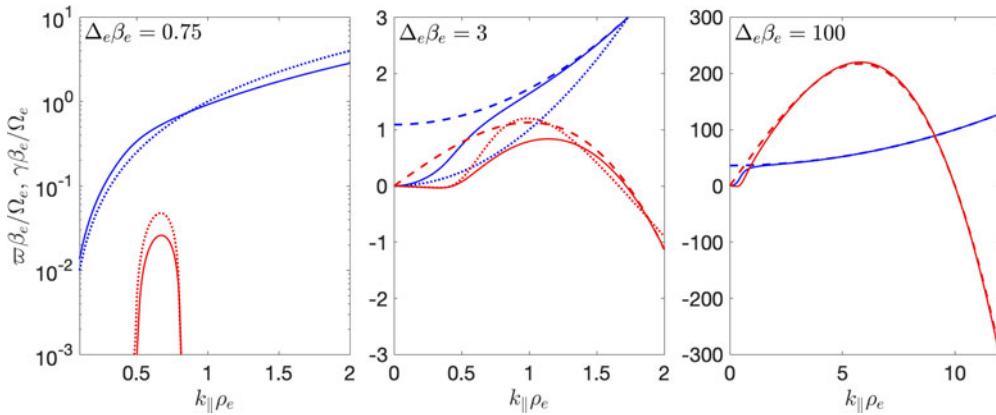
FIGURE 13. Parallel CES whistler instability. Dispersion curves of unstable whistler modes whose instability is driven by the electron-shear term in CE distribution function (4.1), for wavevectors that are co-parallel with the background magnetic field (*viz.* $\boldsymbol{k} = k_\parallel \hat{\boldsymbol{z}}$). The frequency (solid blue) and growth rate (solid red) of the modes are calculated using (4.21*a*) and (4.21*b*), respectively. The resulting frequencies and growth rates, when normalised as $\gamma\beta_e/\Omega_e$, are functions of the dimensionless quantity $\Delta_e\beta_e$; we show the dispersion curves for three different values of $\Delta_e\beta_e$. The approximations (4.22*a*) and (4.22*b*) for the frequency (dotted blue) and growth rate (dotted red) in the limit $k_\parallel\rho_e \ll 1$ are also plotted, as are the approximations (4.24*a*) and (4.24*b*) for the frequency (dashed blue) and growth rate (dashed red) in the limit $k_\parallel\rho_e \gg 1$.

As before, we characterise the growth rate for various values of $\Delta_e\beta_e$ by taking subsidiary limits. First, for $\Delta_e\beta_e \ll 1$, a necessary (though not always sufficient) condition for positive growth is $k_\parallel\rho_e < (\Delta_e\beta_e)^{1/2} \ll 1$. We therefore expand (4.21) in $k_\parallel\rho_e \sim (\Delta_e\beta_e)^{1/2} \ll 1$, finding that

$$\varpi \approx \frac{k_\parallel^2\rho_e^2}{\beta_e}\Omega_e, \tag{4.22a}$$

$$\gamma \approx \frac{\sqrt{\pi}}{k_\parallel\rho_e}\left\{\exp\left(-\frac{1}{k_\parallel^2\rho_e^2}\right)\left(\Delta_e - \frac{k_\parallel^2\rho_e^2}{\beta_e}\right) - \mu_e^{1/2}\frac{k_\parallel^2\rho_e^2}{\beta_e}\right\}\Omega_e. \tag{4.22b}$$

Similarly to what we showed in § 3.3.1 for the CET whistler instability, we have once again found unstable whistler waves. For comparison's sake, the approximate expressions (4.22) are plotted in figure 13 in addition to their exact analogues (4.21); it is clear that there is reasonable agreement for a moderately small value of $\Delta_e\beta_e$, but that the approximations become less accurate for $k_\parallel\rho_e \gtrsim 0.5$ and $\Delta_e\beta_e > 1$.

In the limit $\mu_e \to 0$, the expression (4.22*b*) for the growth rate is very similar to that of the whistler (electron-cyclotron) instability in a plasma with a bi-Maxwellian distribution and positive electron-pressure anisotropy (Davidson 1983). In this case, whistler modes with $k_\parallel\rho_e < (\Delta_e\beta_e)^{1/2}$ are always unstable, although the growth rate of such modes is exponentially small in $\Delta_e\beta_e \ll 1$ as compared with the frequency (4.22*a*), and so $\gamma \ll \varpi \sim \Omega_e/\beta_e$. By contrast, with small but finite $\mu_e = m_e/m_i$, it can be shown analytically

that, for (4.22*b*) to be positive, $\Delta_e > (\Delta_e)_c$, where

$$
(\Delta_e)_c = \frac{1}{\beta_e W_{\mathrm{Lam}} \left[\mu_e^{-1/2} \exp\left(-1\right) \right]}
$$

$$
\approx \frac{1}{\beta_e} \frac{1}{\log\left(\mu_e^{-1/2}\right) - 1 - \log\left[\log\left(\mu_e^{-1/2}\right) - 1\right]}. \tag{4.23}
$$

Here, $W_{\mathrm{Lam}}(x)$ denotes the Lambert W function (Corless *et al.* 1996). Unstable modes first develop around $(k_\parallel \rho_e)_c = (\Delta_e)_c^{1/2}/[(\Delta_e)_c + 1/\beta_e]^{1/2}$. In a hydrogen plasma, this gives $(\Delta_e)_c \approx 0.49/\beta_e$ and $(k_\parallel \rho_e)_c \approx 0.57$, which are similar to the instability threshold and wavenumber, respectively, determined numerically if γ is computed for arbitrary values of $k_\parallel \rho_e$; the small discrepancy is due to the finite value of $k_\parallel \rho_e$ at which instability first emerges. Formally, $(\Delta_e)_c \to 0$ as $\mu_e \to 0$, but the limit converges only logarithmically in μ_e, suggesting that in an actual plasma, the CES whistler instability will generically have a threshold at a finite value of $\Delta_e \beta_e$.

Let us now turn to the opposite subsidiary limit $\Delta_e \beta_e \gg 1$. We find from (4.21*b*) that maximal growth occurs at $k_\parallel \rho_e \sim (\Delta_e \beta)^{1/2} \gg 1$

$$
\varpi \approx \frac{1}{\pi} \left[\Delta_e \left(\pi - 2\right) + \frac{k_\parallel^2 \rho_e^2}{\beta_e} \right] \Omega_e, \tag{4.24a}
$$

$$
\gamma \approx \frac{k_\parallel \rho_e}{\sqrt{\pi}} \left(\Delta_e - \frac{k_\parallel^2 \rho_e^2}{\beta_e} \right) \Omega_e. \tag{4.24b}
$$

Alongside $k_\parallel \rho_e \ll 1$ approximations, these approximations are plotted in figure 13, and agree well with the numerical results for $\Delta_e \beta_e \gtrsim 3$ and $k_\parallel \rho_e \gtrsim 2$. The maximum growth rate

$$
\gamma_{\mathrm{max}} = \frac{2}{3\sqrt{3\pi}} \Delta_e (\Delta_e \beta_e)^{1/2} \Omega_e \approx 0.22 \Delta_e (\Delta_e \beta_e)^{1/2} \Omega_e, \tag{4.25}
$$

is attained at the parallel wavenumber

$$
(k_\parallel \rho_e)_{\mathrm{peak}} = \left(\frac{\Delta_e \beta_e}{3} \right)^{1/2}. \tag{4.26}
$$

A notable feature of the CES whistler instability in this subsidiary limit is that the fastest-growing modes are on sub-electron-Larmor scales; thus, such modes are arguably better conceptualised not as whistler modes, but as unstable, unmagnetised plasma modes (see § 4.3.3).

Similarly to the CET whistler instability, analytical expressions for the frequency and growth rate of unstable modes that have an oblique wavevector angle are much less simple that the analogous expressions for parallel whistler modes. It can be shown (see Appendix K.2) that the complex frequency of such modes is given by

$$
\omega = \frac{\Omega_e}{\beta_e} k_\parallel \rho_e \frac{-\mathrm{i} B_S \pm \sqrt{-B_S^2 + 4 A_S C_S}}{2 A_S}, \tag{4.27}
$$

where the functions $A_S = A_S(k_\parallel \rho_e, k_\perp \rho_e, \Delta_e \beta_e)$, $B_S = B_S(k_\parallel \rho_e, k_\perp \rho_e, \Delta_e \beta_e)$ and $C_S = C_S(k_\parallel \rho_e, k_\perp \rho_e, \Delta_e \beta_e)$ are composed of the sums and products of special mathematical
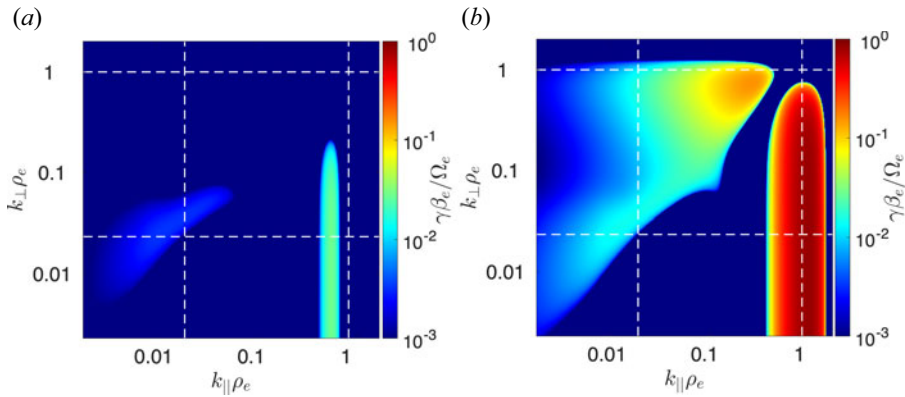
(*a*)   (*b*)

FIGURE 14. Oblique unstable modes at $\Delta_e \beta_e \sim 1$: (*a*) $\Delta_e \beta_e = 0.75$; (*b*) $\Delta_e \beta_e = 3$. Maximum positive growth rates of linear perturbations resulting from CE ion- and electron-shear terms in the CE distribution function (4.1) for $\Delta_e \beta_e \sim 1$. Here, a temperature-equilibrated hydrogen plasma is considered, *viz.* $\Delta_e = \mu_e^{1/2} \Delta_i$, and $\beta_i = \beta_e$. The growth rates of all modes are calculated using the approach outlined in Appendix K.3. The growth rates are calculated on a 400^2 grid, with logarithmic spacing between wavenumbers in both perpendicular and parallel directions. The resulting growth rates, when normalised as $\gamma \beta_e / \Omega_e$, are functions of $\Delta_e \beta_e$, or, equivalently, $\epsilon_e \beta_e$. The vertical dashed lines indicate $k_\parallel \rho_i = 1$ and $k_\parallel \rho_e = 1$, respectively, while the horizontal ones indicate $k_\perp \rho_i = 1$ and $k_\perp \rho_e = 1$.

functions. When $\Delta_e \beta_e \sim 1$, (4.27) implies that if there is an instability, its growth rate will be of order $\gamma \sim \Omega_e / \beta_e$ at $k_\parallel \rho_e, k_\perp \rho_e \sim 1$.

To confirm this expectation, in figure 14 we plot the maximum growth rate (obtained numerically) of oblique modes across the $(k_\parallel, k_\perp)$-plane for two of the values of $\Delta_e \beta_e$ used in figure 13. For $\Delta_e \beta_e$ not far beyond the threshold of the CES whistler instability (figure 14*a*), the unstable modes are quasi-parallel and have growth rates $\gamma \ll \Omega_e / \beta_e$ (cf. figure 13*a*). For $\Delta_e \beta_e \gtrsim 1$, a broader spectrum of wavenumbers becomes unstable (figure 14*b*). The parallel mode remains the fastest growing in this case; however, oblique modes with $k_\perp \lesssim k_\parallel / 2$ also have growth rates of comparable magnitude: e.g. the fastest-growing mode with wavevector angle $\theta = 10°$ has $\gamma_{\max} / \gamma_{\max}(k_\perp = 0) \approx 0.93$, and for a wavevector angle $\theta = 10°$, $\gamma_{\max} / \gamma_{\max}(k_\perp = 0) \approx 0.76$. For more oblique angles, the growth rate is reduced significantly: e.g. for $\theta = 30°$, $\gamma_{\max} / \gamma_{\max}(k_\perp = 0) \approx 0.22$. Thus, we conclude that a spectrum of oblique modes in addition to parallel ones is indeed destabilised, with $\gamma \sim \Omega_e / \beta_e \lesssim \gamma(k_\perp = 0)$.

We note that, in addition to oblique CES whistler modes, whose characteristic wavenumber domain is $k_\perp \rho_e \lesssim k_\parallel \rho_i \sim 1$, we observe two other unstable modes in figure 14(*a*) with different characteristic values of $k_\parallel$ and $k_\perp$. The first of these, which exists on ion scales, is the CES mirror instability, which we already discussed in § 4.3.1. The second is the CES electron mirror instability – we shall consider this instability in § 4.3.4.

4.3.3. *Parallel transverse instability*

As was shown in § 4.2, in the limit $\Delta_e \beta_e \gg 1$, the fastest-growing CES microinstability is essentially unmagnetised, and is a variant of the so-called transverse instability (Kahn 1962, 1964; Albright 1970*b*). This instability is also sometimes referred to as the resonant (electron) Weibel instability, or the Weibel instability at small anisotropy (Fried 1959; Weibel 1959). Both the linear theory of this instability and its physical mechanism have been explored extensively for bi-Maxwellian plasmas (see, e.g. Lazar *et al.* 2009; Ibscher

et al. 2012), and various studies (both analytical and numerical) of its nonlinear evolution have also been performed (Albright 1970*a*; Davidson *et al.* 1972; Lemons *et al.* 1979; Califano *et al.* 1998, 2002; Kato 2005; Pokhotelov & Amariutei 2011; Ruyer *et al.* 2015). For the small anisotropy case that is relevant to CE plasma, the mechanism of the instability is somewhat subtle, involving both non-resonant and Landau-resonant wave–particle interactions. In a Maxwellian plasma, transverse modes are non-propagating and Landau-damped by electrons with velocities $v \approx \omega/k_\parallel$. However, this damping can be reversed by the free energy associated with positive electron-pressure anisotropy at wavenumbers that satisfy $kd_e \lesssim \Delta_e^{1/2}$; the electron Landau damping increases more rapidly with k than the instability's drive, which in turn sets the wavenumber at which peak growth occurs. The requirement for the corresponding scale to be well below the electron-Larmor scale – and thus for the plasma to be quasi-unmagnetised with respect to the transverse modes – sets the restriction $\Delta_e \beta_e \gg 1$ on the instability's operation. In general, transverse modes whose wavevectors are co-parallel to the velocity-space direction along which the temperature is smallest are the fastest growing; in the case of a CE electron distribution function of the form (4.1) with $\Delta_e > 0$, these modes' wavevectors are parallel to the magnetic field. However, a broad spectrum of oblique transverse modes is also destabilised when $\Delta_e > 0$.

To characterise the transverse instability's growth analytically, we first assume $\Delta_e \beta_e \gg 1$, and then take directly the unmagnetised limit of the full CES dispersion relation (see Appendix K.3.4) under the orderings

$$k_\perp \rho_e \sim k_\parallel \rho_e \sim (\Delta_e \beta_e)^{1/2} \gg 1, \quad \tilde{\omega}_{e\parallel} = \frac{\omega}{k_\parallel v_{\mathrm{th}e}} \sim \Delta_e. \quad (4.28a,b)$$

We obtain two non-propagating modes (real frequency $\varpi = 0$) that have growth rates

$$\gamma_1 = \frac{k v_{\mathrm{th}e}}{\sqrt{\pi}} \left(\Delta_e \frac{k_\parallel^2 - k_\perp^2}{k^2} - \frac{k^2 \rho_e^2}{\beta_e} \right), \quad (4.29a)$$

$$\gamma_2 = \frac{k v_{\mathrm{th}e}}{\sqrt{\pi}} \left(\Delta_e \frac{k_\parallel^2}{k^2} - \frac{k^2 \rho_e^2}{\beta_e} \right). \quad (4.29b)$$

For $\Delta_e > 0$, the growth rate of the second mode is always positive and larger than that of the first mode; the first mode only has a positive growth rate provided $k_\perp < k_\parallel$. Now taking the subsidiary limit $k_\parallel \rho_e \gg k_\perp \rho_e \gg 1$, we find that both roots have the same growth rate

$$\gamma \approx \frac{k_\parallel v_{\mathrm{th}e}}{\sqrt{\pi}} \left(\Delta_e - \frac{k_\parallel^2 \rho_e^2}{\beta_e} \right), \quad (4.30)$$

which is identical to (4.24*b*). We note by comparison with (4.24*a*) that the unmagnetised limit fails to recover the non-zero real frequencies of the $k_\parallel \rho_e \gg 1$ whistler modes; this is because the ratio of these modes' real frequency ϖ to their growth rate γ is $\varpi/\gamma \sim 1/k_\parallel \rho_e \ll 1$.

The maximum growth rate $\gamma_{\max}$ of the second mode (4.29*b*) for an oblique wavevector with angle θ is

$$\gamma_{\max} = \frac{2}{3\sqrt{3\pi}} \cos^3 \theta \, \Delta_e (\Delta_e \beta_e)^{1/2} \Omega_e, \quad (4.31)$$
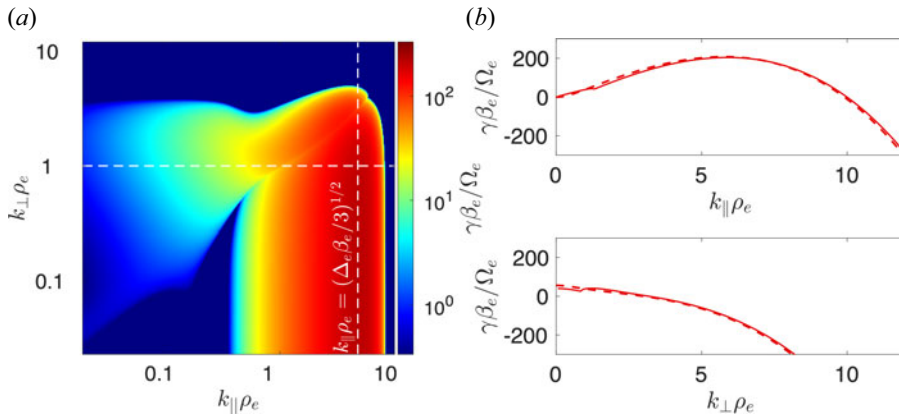
FIGURE 15. Oblique unstable modes at $\Delta_e \beta_e \gg 1$. (*a*) Maximum positive growth rates of linear perturbations resulting from CE ion- and electron-shear terms in the CE distribution function (4.1) for $\Delta_e \beta_e = 100$. Here, a temperature-equilibrated hydrogen plasma is considered, *viz.* $\Delta_e = \mu_e^{1/2} \Delta_i$ and $\beta_i = \beta_e$. The growth rates of all modes are calculated in the same way as figure 14. The vertical dashed line indicates the value of $k_\parallel \rho_e$ at which maximum growth of the parallel transverse instability is attained (see (4.33a,b)), while the horizontal one indicates $k_\perp \rho_e = 1$. (*b*) The transverse mode's growth rate (solid line) as a function of $k_\parallel \rho_e$ with $k_\perp \rho_e = 1$ (top), and as a function of $k_\perp \rho_e$ with $k_\parallel \rho_e = (\Delta_e \beta_e / 3)^{1/2}$ (bottom). The dashed lines show the analytical prediction (4.29b) for this quantity.

attained at the (total) wavenumber

$$(k\rho_e)_{\text{peak}} = \cos\theta \left(\frac{\Delta_e \beta_e}{3} \right)^{1/2}. \tag{4.32}$$

The parallel and perpendicular wavenumbers of this maximum growth are then

$$(k_\parallel \rho_e)_{\text{peak}} = \cos^2\theta \left(\frac{\Delta_e \beta_e}{3} \right)^{1/2}, \quad (k_\perp \rho_e)_{\text{peak}} = \cos\theta \sin\theta \left(\frac{\Delta_e \beta_e}{3} \right)^{1/2}. \tag{4.33a,b}$$

In the special case of parallel modes ($\theta = 0°$), this recovers the peak growth rate (4.25) of the CES whistler instability at $k_\parallel$ in the limit $\Delta_e \beta_e \gg 1$.

In figure 15, we demonstrate that the fastest-growing unstable modes in the limit $\Delta_e \beta_e \gg 1$ are indeed transverse ones. This figure shows the numerically determined growth rate as a function of $k_\parallel$ and $k_\perp$), for a particular large value of $\Delta_e \beta_e$. A broad range of sub-electron-Larmor-scale modes are unstable (figure 15*a*), with the parallel wavenumber of the fastest-growing ones closely agreeing with the analytical prediction (4.33a,b). The analytical expression (4.29b) for the transverse instability's growth rate also agrees well with the numerical result as a function of both $k_\parallel$ and $k_\perp$ (figure 15*b*).

4.3.4. *Electron mirror instability*

The oblique microinstability evident in figure 14(*b*) at sub-ion-Larmor scales is the CES electron mirror instability: the destabilisation of KAWs by excess perpendicular electron pressure (*viz.* $\Delta_e > 0$) associated with the CE electron-shear term. The instability (which has also been referred to as the field-swelling instability – see Basu & Coppi 1984) is perhaps confusingly named, given that its physical mechanism is rather different to that of the (ion-scale) mirror instability: non-resonant interactions between the anisotropic
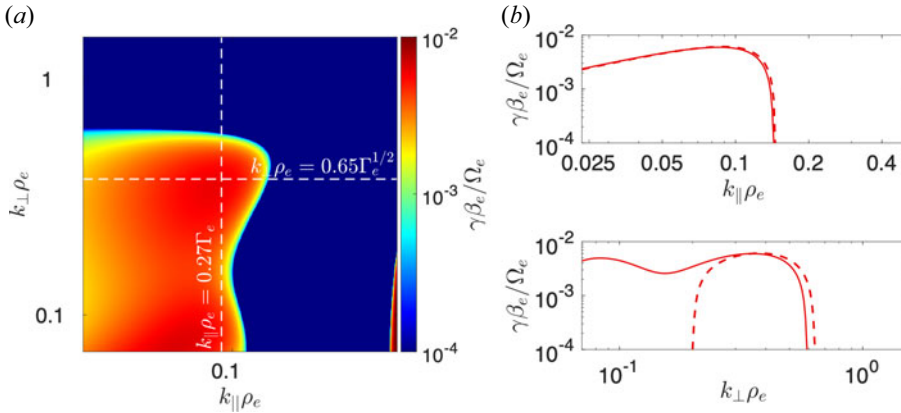
FIGURE 16. Electron mirror instability at $\Gamma_e = \Delta_e\beta_e - 1 \ll 1$. (*a*) Growth rates of unstable electron mirror modes associated with the CE distribution function (4.1) for $\Gamma_e = 1/3$ ($\Delta_e\beta_e = 4/3$). The growth rates of all modes are calculated in the same way as figure 14. The dashed white lines indicate the analytical prediction (4.37) for the parallel/perpendicular wavenumber at which peak growth is achieved. (*b*) Plot of the electron mirror mode's growth rate (solid line) as a function of $k_\parallel\rho_e$ with $k_\perp\rho_e = 0.65\Gamma_e^{1/2}$ (top), and as a function of $k_\perp\rho_e$ with $k_\parallel\rho_e = 0.27\Gamma_e$ (bottom). The dashed lines show the analytical prediction (4.35) for this quantity.

distribution of electrons and the KAWs causes the restoring force underpinning the latter's characteristic oscillation to be negated if $\Delta_e > 1/\beta_e$. The electron mirror instability has been extensively explored in $\beta_e \sim 1$ plasma (see Hellinger & Štverák (2018), and references therein); in plasmas with $\beta_e \gg 1$, it has been analytically characterised and its physical mechanism elucidated in the quasi-perpendicular ($k_\parallel \ll k_\perp$) limit of gyrokinetics (Kunz *et al.* 2018). Here, we find that once its marginality condition ($\Delta_e = 1/\beta_e$) is surpassed sufficiently, oblique modes with $k_\parallel \lesssim k_\perp$ are also destabilised.

As with the mirror instability, a simple analytic characterisation of the CES electron mirror instability can be performed in the case of marginal instability. We define the marginality parameter $\Gamma_e \equiv \Delta_e\beta_e - 1$, and adopt the ordering

$$k_\perp^2\rho_e^2 \sim k_\parallel\rho_e \sim \tilde{\omega}_{e\parallel}\beta_e \sim \Gamma_e \ll 1, \tag{4.34}$$

with the additional assumption that $\Gamma_e \gg \mu_e^{1/2}$ in order that the effect of ion-pressure anisotropy can be neglected. Then, it can be shown (see Appendix K.3.5) that the growth rate is

$$\frac{\gamma}{\Omega_e} = \frac{k_\parallel\rho_e}{\beta_e}\left[-\frac{3\sqrt{\pi}}{4}k_\perp^2\rho_e^2 + \sqrt{\frac{3}{2}\Gamma_e k_\perp^2\rho_e^2 - \frac{9}{4}k_\parallel^2\rho_e^2 + \frac{9}{16}(\pi-2)k_\perp^4\rho_e^4}\right]. \tag{4.35}$$

It follows that the maximum growth rate is

$$\gamma_{\max} = \frac{\left[\pi - 8 + \sqrt{\pi(16+\pi)}\right]^{3/2}}{48(\pi-2)}\left[\sqrt{\frac{\pi + 4 + \sqrt{\pi(16+\pi)}}{\pi - 8 + \sqrt{\pi(16+\pi)}}} - \sqrt{\frac{\pi}{\pi-2}}\right]\frac{\Gamma_e^2}{\beta_e}\Omega_e$$

$$\approx 0.055\frac{\Gamma_e^2}{\beta_e}\Omega_e, \tag{4.36}$$

attained at

$$(k_\parallel \rho_e)_{\text{peak}} = \sqrt{\frac{\pi - 8 + \sqrt{\pi\,(16+\pi)}}{36\,(\pi-2)}}\,\Gamma_e \approx 0.27\Gamma_e, \qquad (4.37a)$$

$$(k_\perp \rho_e)_{\text{peak}} = \sqrt{\frac{\pi - 8 + \sqrt{\pi\,(16+\pi)}}{6\,(\pi-2)}}\,\Gamma_e^{1/2} \approx 0.65\Gamma_e^{1/2}. \qquad (4.37b)$$

Figure 16 demonstrates that these predictions are accurate by comparing them with numerical results for a particular (small) value of Γ_e. More specifically, figure 16(*a*) shows that the location in the $(k_\parallel, k_\perp)$ plane at which the maximum growth of the electron mirror instability is attained closely matches the analytical prediction (4.37), while figure 16(*b*) confirms that the wavenumber dependence of the growth rate agrees with (4.35) for $k_\perp \rho_e \gtrsim \mu_e^{1/4}$. We note that, in addition to the electron mirror, another instability operating at smaller characteristic values of $k_\perp \rho_e$ is evident in figure 16. These are the $k_\perp \rho_i \gtrsim 1$ mirror modes driven unstable by the CE ion-shear term that were discussed in § 4.3.1; for $1 \ll k\rho_i \ll \mu_e^{-1/4}$, the ion-pressure anisotropy associated with the CE ion-shear terms remains a greater free-energy source for KAW instabilities than the CE electron-shear term, even when $\Delta_e > 1/\beta_e$.

For $\Gamma_e \gtrsim 1$, our near-marginal theory anticipates that peak growth occurs at electron-Larmor scales ($k_\parallel \rho_e \lesssim k_\perp \rho_e \sim 1$), with $\gamma_{\max} \sim \Omega_e/\beta_e$. These expectations are indeed realised numerically, as shown in figure 17 (see also figure 14). The expression (4.35) for the growth rate as a function of wavenumber that was derived in the case of $\Gamma_e \ll 1$ remains qualitatively – but not quantitatively – accurate (see figure 17*b*). Figure 18 shows that a similar conclusion holds for the expression (4.36) for the peak growth rate, and also for the expressions (4.37*a*) and (4.37*b*) of the parallel and perpendicular wavenumbers at which that growth occurs.

To confirm our prior claim in § 4.2 that the CES parallel whistler instability is faster growing than the electron mirror instability, we show the former's numerically computed growth rate on figure 18(*a*); as it approaches the asymptotic value (4.25) that is valid in the limit $\Delta_e \beta_e \gg 1$, we observe that the electron mirror's growth rate is a factor of ~ 3 smaller (cf. figure 15*a*). The parallel wavenumber at which peak growth of the whistler instability occurs is also larger than the analogous quantity for the electron mirror by an order-unity factor.

While we cannot derive a simple analytic expression for the growth rate of the dominant electron mirror modes when $\Gamma_e \gtrsim 1$, we can calculate this quantity for long-wavelength (*viz.* $k\rho_e \ll 1$) modes. For this calculation, we assume that $k\rho_e \sim \mu_e^{1/4} \ll 1$, $k_\perp \sim k_\parallel$ and the ordering

$$\tilde{\omega}_{e\parallel} = \frac{\omega}{k_\parallel v_{\text{th}e}} \sim \frac{k\rho_e}{\beta_e} \sim |\Delta_e| k\rho_e. \qquad (4.38)$$
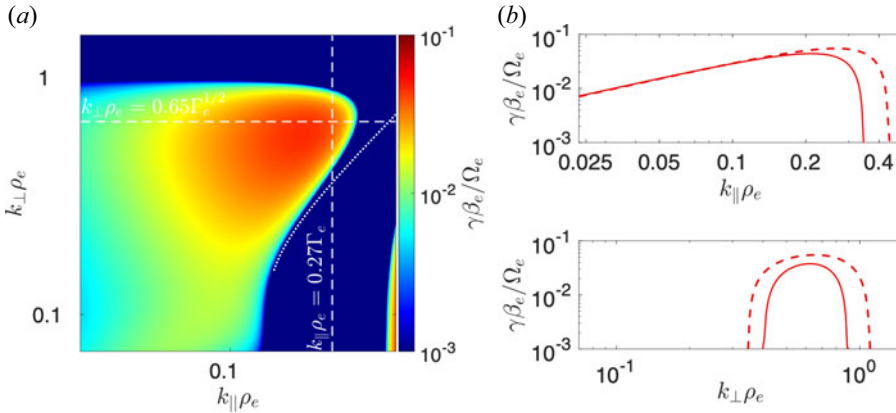
FIGURE 17. Electron mirror instability at $\Gamma_e = \Delta_e \beta_e - 1 \sim 1$. (a) Growth rates of unstable electron mirror modes associated with the CE distribution function (4.1) for $\Gamma_e = 1$ ($\Delta_e \beta_e = 2$). The growth rates of all modes are calculated in the same way as figure 14. The dashed white lines indicate the analytical prediction (4.37) for the parallel/perpendicular wavenumber at which peak growth is achieved, while the dotted line indicates the analytical prediction (4.43) for the total wavenumber below which oblique long-wavelength ($k_\parallel \rho_e < k_\perp \rho_e \ll 1$) electron mirror modes become unstable. (b) The electron mirror mode's growth rate (solid line) as a function of $k_\parallel \rho_e$ with $k_\perp \rho_e = 0.65 \Gamma_e^{1/2}$ (top), and as a function of $k_\perp \rho_e$ with $k_\parallel \rho_e = 0.27 \Gamma_e$ (bottom). The dashed lines show the analytical prediction (4.35) for this quantity.

Under these assumptions, we obtain (see Appendix K.3.5) two modes whose complex frequencies ω are given by

$$
\omega \approx \pm k_\parallel \rho_e \Omega_e \left\{ \left[\frac{1}{\beta_e} + \Delta_e \left(\frac{1}{2} - \mu_e^{1/2} \frac{k_\parallel^2 \rho_e^2 - k_\perp^2 \rho_e^2}{k^4 \rho_e^4} \right) \right] \right.
$$
$$
\left. \times \left[\frac{k^2 \rho_e^2}{\beta_e} - \Delta_e \left(k_\perp^2 \rho_e^2 + \mu_e^{1/2} \frac{k_\parallel^2}{k^2} - \frac{1}{2} k_\parallel^2 \rho_e^2 \right) \right] \right\}^{1/2}. \tag{4.39}
$$

The terms proportional to $\mu_e^{1/2} \Delta_e$ are associated with the CE ion-shear term, which plays a non-negligible role for $k \rho_e \lesssim \mu_e^{1/4}$. In the subsidiary limit $k \rho_e \ll \mu_e^{1/4}$, (4.39) becomes the dispersion relation (4.18) obtained in § 4.3.1 for unstable mirror modes in the limit $\Delta_i \beta_i \gg 1$. In the opposite subsidiary limit $k \rho_e \gg \mu_e^{1/4}$ (but $k \rho_e \ll 1$), (4.39) simplifies to

$$
\omega \approx \pm k_\parallel \rho_e \Omega_e \sqrt{\left(\frac{1}{\beta_e} + \frac{\Delta_e}{2} \right) \left[\frac{k^2 \rho_e^2}{\beta_e} - \Delta_e \left(k_\perp^2 \rho_e^2 - \frac{1}{2} k_\parallel^2 \rho_e^2 \right) \right]}. \tag{4.40}
$$

For $k_\parallel \ll k_\perp$, this recovers the high-β limit of the dispersion relation for unstable KAWs previously derived in the gyrokinetic calculations of Kunz et al. (2018); our calculations show that this dispersion relation also applies to oblique ($k_\parallel \lesssim k_\perp$) electron mirror modes. For $\Delta_e > 0$, we (as expected) have an unstable root if and only if

$$
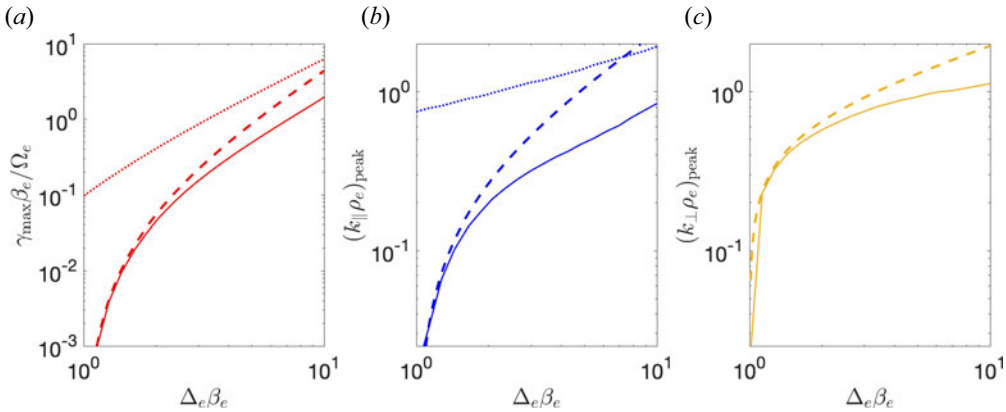\Delta_e > \frac{1}{\beta_e}, \tag{4.41}
$$

FIGURE 18. The maximum growth of the electron mirror instability. The maximum normalised growth rate $\gamma_e \beta_e / \Omega_e$ ((a), solid red line) of unstable electron mirror modes as a function of $\Delta_e \beta_e$, as well as parallel ((b), solid blue line) and perpendicular ((c), solid yellow line) wavenumbers, $(k_\parallel \rho_e)_{\text{peak}}$ and $(k_\perp \rho_e)_{\text{peak}}$, respectively, at which that growth is attained. The analytical prediction (4.36) of $\gamma_{\max}$ for marginally unstable electron mirror modes, as well as the analogous predictions (4.37) for $(k_\parallel \rho_e)_{\text{peak}}$ and $(k_\perp \rho_e)_{\text{peak}}$, are shown as dashed lines. The dotted lines are the maximum growth rate and (parallel) wavenumber of peak growth for the CET parallel whistler instability (see § 4.3.2) as functions of $\Delta_e \beta_e$.

with the unstable mode's growth rate being

$$\gamma \approx k_\parallel \rho_e \Omega_e \sqrt{\left(\frac{1}{\beta_e} + \frac{\Delta_e}{2}\right)\left[\Delta_e\left(k_\perp^2 \rho_e^2 - \frac{1}{2}k_\parallel^2 \rho_e^2\right) - \frac{k^2 \rho_e^2}{\beta_e}\right]}. \qquad (4.42)$$

We can now provide an analytical demonstration that a broad spectrum of electron mirror modes is unstable if $\Gamma_e \gtrsim 1$. It follows directly from (4.39) that instability arises for all modes with $k_\perp > k_\parallel$ if the following constraint on the total wavenumber k is satisfied:

$$k\rho_i < \sqrt{\frac{2\mu_e^{1/2}(\Gamma_e + 1)\cos^2\theta}{(\Gamma_e + 3)\cos^2\theta - 2\Gamma_e \sin^2\theta}}, \qquad (4.43)$$

where $\theta = \tan^{-1}(k_\perp / k_\parallel)$ is, as normal, the wavevector angle. The validity of this bound is illustrated in figure 17(a). (4.43) is particularly simple to interpret in the subsidiary limit $k\rho_e \gg \mu_e^{1/4}$, yielding a lower bound on θ alone:

$$\theta > \tan^{-1}\sqrt{\frac{\Gamma_e + 3}{2\Gamma_e}}. \qquad (4.44)$$

For $\Gamma_e \ll 1$ (but $\Gamma_e > 0$), this implies that the only unstable electron mirror modes are quasi-perpendicular, as anticipated from our calculations pertaining to the marginal state of the instability. On the other hand, for $\Gamma_e \gtrsim 1$, modes with a wide range of wavevector angles will be destabilised.

4.4. *CES microinstability classification: negative pressure anisotropy* ($\epsilon_i < 0$)

4.4.1. *Firehose instability*

The best-known instability to be triggered by either negative ion or electron-pressure anisotropy associated with the CE ion- and electron-shear terms, respectively, is the

CES firehose instability. The linear theory of the firehose (or garden-hose) instability in high-β plasma, the first studies of which were completed over half a century ago (Rosenbluth 1956; Chandrasekhar *et al.* 1958; Parker 1958; Vedenov & Sagdeev 1958), has previously been explored in the contexts of plasmas with bi-Maxwellian distributions (e.g. Kennel & Sagdeev 1967; Davidson & Völk 1968; Yoon, Wu & de Assis 1993; Hellinger & Matsumoto 2000), CE distributions (e.g. Schekochihin *et al.* 2005) and even characterisations that are independent of the ion distribution function (e.g. Schekochihin *et al.* 2010; Kunz *et al.* 2015). Its physical mechanism is well established: negative pressure anisotropies reduce the elasticity of magnetic-field lines that gives rise to Alfvén waves, and can completely reverse it when Δ_i is negative enough. The long-wavelength 'fluid' firehose instability (whose mechanism is independent of the particular ion distribution function) is non-resonant in nature; however, resonant damping mechanisms such as Barnes damping or cyclotron damping play an important role in regulating the growth of modes on scales comparable to the ion-Larmor scale, and thereby set the scale of peak firehose growth. Beyond linear theory, nonlinear analytical studies of the parallel firehose instability in high-β plasma have been completed (e.g. Rosin *et al.* 2011), as well as numerical ones (e.g. Kunz *et al.* 2014; Melville *et al.* 2016; Riquelme *et al.* 2018).

While there is much in common between firehose modes across all wavevector angles, there are certain differences that, on account of their significance for determining the fastest-growing firehose mode, are important to highlight. Based on these differences, firehose modes can be categorised into three different types: quasi-parallel, oblique and critical-line firehose modes. Quasi-parallel firehose modes, which are destabilised left-handed and/or right-handed high-β Alfvén waves (Kennel & Sagdeev 1967; Davidson & Völk 1968), exist inside a narrow cone of wavevector angles $\theta \lesssim \beta_i^{-1/4}$ (Achterberg 2013). The peak wavenumber of their growth ($k_\parallel \rho_i \sim |\Delta_i + 2/\beta_i|^{1/2}$) is determined by gyroviscosity, an FLR effect (Schekochihin *et al.* 2010). For $\theta \gtrsim \beta_i^{-1/4}$, the characteristic low-frequency (*viz.* $\omega \ll \Omega_i$) waves that exist above ion-Larmor-scales in high-β plasma are shear-Alfvén waves and (compressible) slow modes; the former remains susceptible to firehose instability, but, on account of its FLR coupling to the slow mode, its instability proceeds quite differently at sufficiently small wavenumbers ($k\rho_i \gtrsim |\Delta_i + 2/\beta_i|^{1/2}$), with peak growth occurring at smaller scales ($k_\parallel \rho_i \sim |\Delta_i + 2/\beta_i|^{1/4} \ll 1$). Finally, along a 'critical line' in the ($k_\parallel, k_\perp$) plane ($k_\perp \approx \sqrt{2/3}k_\parallel$, $\theta \approx 39°$), the FLR coupling between the slow mode and shear-Alfvén wave becomes anomalously weak due to two opposing FLR effects cancelling each other out. This results in much weaker collisionless damping on critical-line firehose modes, and so they can exist on scales that are close to (though, as we prove here for the first time, not strictly at) the ion-Larmor scale. Thus critical-line firehose modes are generically the fastest-growing ones in high-β plasma (Schekochihin *et al.* 2005).

We support this claim with figure 19, which shows the maximum growth rate of the firehose-unstable modes as a function of both $k_\parallel$ and $k_\perp$ for two different (unstable) values of $\Delta_i\beta_i$ (and with the same value of β_i as was used to calculate the stability maps presented in § 4.2). Both examples confirm that, although a broad spectrum of unstable parallel and oblique firehose modes emerge when $\Delta_i\beta_i + 2 \lesssim -1$, it is the critical-line firehose modes that are the fastest growing.

The value of Δ_i required to trigger the CES firehose instability is, as with the case of the firehose instability in a plasma with a bi-Maxwellian ion distribution, dependent on the scale of the unstable firehose modes. For long-wavelength firehose modes (i.e. those with $k\rho_i \ll 1$), the threshold is $\Delta_i < (\Delta_i)_c = -2/\beta_i$; it can be shown that this
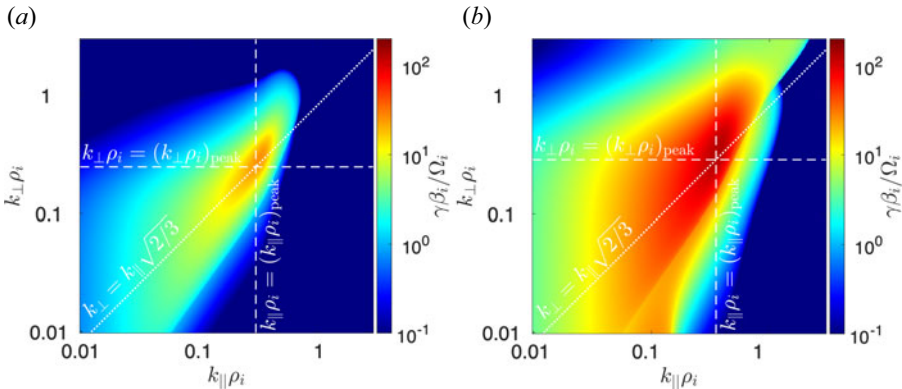
FIGURE 19. The CES firehose instability when $\Delta_i \beta_i + 2 \lesssim -1$. Maximum positive growth rates of linear perturbations resulting from the CE ion-shear term in the CE distribution function (4.1) with Δ_i negative enough to surpass the long-wavelength firehose-instability threshold $\Delta_i = -2/\beta_i$ by at least an order-unity factor. The growth rates of all modes are calculated using the approach outlined in Appendix K.3. The growth rates are calculated on a 400^2 grid, with logarithmic spacing in both perpendicular and parallel directions between wavenumbers. The resulting growth rates, when normalised as $\gamma \beta_i / \Omega_i$, are functions of two dimensionless parameters only: Δ_i and β_i. The dashed white lines indicate the analytical predictions (4.67) for the parallel/perpendicular wavenumber at which peak growth is achieved, while the dotted line indicates the critical line $k_\perp = k_\parallel \sqrt{2/3}$ along which the firehose growth rate is predicted to be maximal; (*a*) $\Delta_i \beta_i = -3$, (*b*) $\Delta_i \beta_i = -30$. In both cases, $\beta_i = 10^4$.

result is independent of the particular form of the ion distribution function (Schekochihin *et al.* 2010). However, our numerical solutions for the wavenumber-dependent growth rate of firehose modes in CE plasma when $\Delta_i > -2/\beta_i$ (see figure 20*a*) suggest that oblique ion-Larmor-scale firehose modes can be destabilised at less negative pressure anisotropies. This is consistent with the findings of previous studies of the oblique firehose in $\beta \sim 1$ plasma (Hellinger & Matsumoto 2000; Hellinger & Trávníček 2008; Astfalk & Jenko 2016), although this finding has not until now been comprehensively studied in plasma with $\beta \gg 1$. We can, in fact, calculate the threshold semi-analytically for the CES firehose instability as a function of wavenumber (see Appendix K.2.2); the results, which are shown in figure 20(*b*) show that oblique firehose modes with $k_\parallel \rho_i \approx 0.45$, $k_\perp \rho_i \approx 0.3$ become unstable when $\Delta_i \approx -1.35/\beta_i$. The reduced threshold of ion-Larmor-scale firehose modes, which can be shown to depend only on fourth- and higher-order moments of the ion distribution function, is considered in greater depth in Bott *et al.* (2023, in prep.).

The growth of the three different sub-categories of unstable CES firehose modes (quasi-parallel, oblique and critical-line firehoses) can be described analytically. However, the relative orderings of $\tilde{\omega}_{i\parallel}$, $k_\parallel \rho_i$, $k_\perp \rho_i$, β_i and $|\Delta_i|$ for these sub-categories are different, so it is necessary to treat them separately.

4.4.2. *Quasi-parallel firehose instability*

The relevant orderings of parameters for quasi-parallel firehose modes is

$$\tilde{\omega}_{i\parallel} = \frac{\omega}{k_\parallel v_{\text{th}i}} \sim \beta_i^{-1/2} \sim |\Delta_i|^{1/2} \sim k_\parallel \rho_i, \tag{4.45}$$

with the additional small wavenumber-angle condition

$$k_\perp \rho_i \ll \beta_i^{-1/4} k_\parallel \rho_i \sim \beta_i^{-3/4}. \tag{4.46}$$
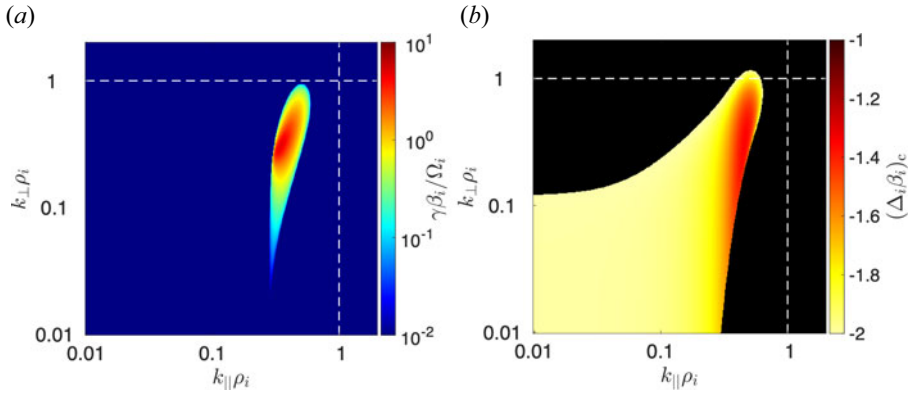
FIGURE 20. Onset of the CES firehose instability. (*a*) Maximum positive growth rates of linear perturbations resulting from the CE ion-shear term in the CE distribution function (4.1) with $\beta_i = 10^4$ and $\Delta_i = -1.7/\beta_i$ (a value at which the long-wavelength firehose instability is absent, because $\Delta_i > -2/\beta_i$). The growth rates of all modes are calculated in the same way as figure 19. (*b*) Threshold value $(\Delta_i \beta_i)_c$ of $\Delta_i \beta_i$ at which modes with parallel and perpendicular wavenumber $k_\parallel$ and $k_\perp$, respectively, become firehose unstable. Regions of $(k_\parallel, k_\perp)$ that are shaded black are stable.

Under the ordering (4.45), we find (see Appendix K.3.6) that there are four modes with complex frequencies given by

$$\frac{\omega}{\Omega_i} = \pm k_\parallel \rho_i \left(\frac{1}{4} k_\parallel \rho_i \pm \sqrt{\frac{1}{16} k_\parallel^2 \rho_i^2 + \frac{1}{\beta_i} + \frac{\Delta_i}{2}} \right), \qquad (4.47)$$

where the $\pm$ signs can be chosen independently. This is the standard parallel firehose dispersion relation (Kennel & Sagdeev 1967; Davidson & Völk 1968; Schekochihin *et al.* 2010). To (re-)identify the modes that are destabilised by the negative ion-pressure anisotropy, we set $\Delta_i = 0$: the resulting dispersion relation agrees with Foote & Kulsrud (1979), recovering the dispersion relation of Alfvén waves in the limit $k_\parallel \rho_i \ll \beta_i^{-1/2}$ (see their (19)) and the dispersion relation of the slow and fast hydromagnetic waves in the limit $k_\parallel \rho_i \gg \beta_i^{-1/2}$ (see their (20)). The growth rate of the unstable parallel firehose modes that follows from (4.47) is shown in figure 21 for several different values of Δ_i and β_i; the results closely match the analogous result determined numerically.[6]

For non-zero Δ_i and fixed $k_\parallel \rho_i$, (4.47) implies that we have instability provided

$$|\Delta_i| > \frac{2}{\beta_i} + \frac{1}{8} k_\parallel^2 \rho_i^2. \qquad (4.48)$$

---

[6]An inquisitive reader might wonder why the numerical solution suggests that, in addition to the long-wavelength parallel firehose modes, parallel ion-Larmor-scale modes are also unstable in some cases (see figure 21*b*), albeit with a much smaller growth rate. This instability is the CES resonant parallel firehose instability, so named because of its mediation via gyroresonant interactions between ions and ion-Larmor-scale modes (Yoon *et al.* 1993). In a $\beta_i \sim 1$ plasma, this instability can have a growth rate comparable to (or even larger than) the longer-wavelength non-resonant firehose modes; however, because of the exponential dependence of the resonant parallel firehose instability's growth rate on $|\Delta_i|^{-1} \sim \beta_i$, the instability is generically much weaker than the non-resonant firehose in plasma with $\beta_i \gg 1$ (see Bott *et al.*, in prep.). In the language of §2.3.4, resonant parallel firehose modes are quasi-cold in CE plasma. We therefore do not consider this instability further in this paper.
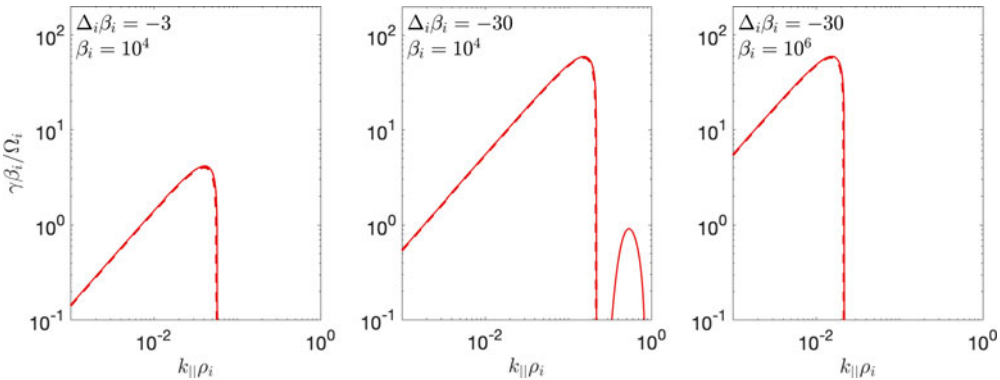
FIGURE 21. Parallel CES firehose instability. Growth rates of Alfvén waves whose instability is driven by the CE ion-shear term in the CE distribution function (4.1), for wavevectors co-parallel with the background magnetic field (*viz.* $\boldsymbol{k} = k_{\parallel}\hat{\boldsymbol{z}}$). The growth rates (solid lines) of all modes are calculated in the same way as figure 19. We show the growth rates for a selection of different values of $\Delta_i\beta_i$ and β_i. The approximation (4.47) for the growth rate (dashed red) in the limit $k_{\parallel}\rho_i \ll 1$ is also plotted.

The fastest-growing mode

$$\frac{\gamma_{\max}}{\Omega_i} = \left| \frac{2}{\beta_i} + \Delta_i \right|, \tag{4.49}$$

occurs at the characteristic wavenumber

$$(k_{\parallel}\rho_i)_{\text{peak}} = 2 \left| \frac{2}{\beta_i} + \Delta_i \right|^{1/2}. \tag{4.50}$$

For $k_{\parallel}\rho_i > 2\sqrt{2}|2\beta_i^{-1} + \Delta_i|^{1/2}$, the unstable mode is stabilised. This agrees with previous analytical characterisations of the firehose instability (Rosin *et al.* 2011).

4.4.3. *Oblique firehose instability*

In this case, we order

$$\tilde{\omega}_{i\parallel} \sim \frac{1}{\beta_i^{1/2}} \sim |\Delta_i|^{1/2} \sim k_{\parallel}^2\rho_i^2 \sim k_{\perp}^2\rho_i^2. \tag{4.51}$$

Aside from the finite propagation angle of oblique modes, the key difference between the oblique and quasiparallel cases is the larger magnitude of the typical wavenumber $k\rho_i \sim \beta_i^{-1/4}$. The unstable oblique firehose modes have the complex frequency (see Appendix K.3.7)

$$\frac{\omega}{\Omega_i} = -k_{\parallel}\rho_i \left[\frac{\mathrm{i}}{8\sqrt{\pi}k_{\perp}^2\rho_i^2} \left(k_{\parallel}^2\rho_i^2 - \frac{3}{2}k_{\perp}^2\rho_i^2 \right)^2 \right.$$
$$\left. \pm \sqrt{\frac{1}{\beta_i} + \frac{\Delta_i}{2} - \frac{1}{64\pi k_{\perp}^4\rho_i^4} \left(k_{\parallel}^2\rho_i^2 - \frac{3}{2}k_{\perp}^2\rho_i^2 \right)^4} \right]. \tag{4.52}$$

Setting $|\Delta_i| = 0$, and considering the subsidiary limit $k\rho_i \ll \beta_i^{-1/4}$, we recover the dispersion relation of the shear-Alfvén mode (Foote & Kulsrud 1979).
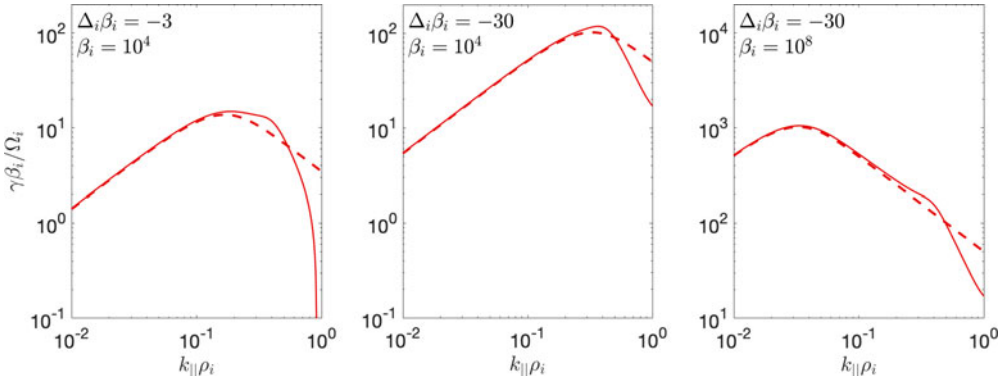
FIGURE 22. Oblique CES firehose instability. Growth rates of the shear-Alfvén mode whose instability is driven by the CE ion-shear term in the CE distribution function (4.1), for wavevectors at an angle $\theta = 60°$ with the background magnetic field (*viz.* $k_\perp = \sqrt{3}k_\parallel$). The growth rates (solid lines) of all modes are calculated in the same way as figure 19. We show the growth rates for a selection of different values of $\Delta_i \beta_i$ and β_i. The approximation (4.52) for the growth rate (dashed red) in the limit $k_\parallel \rho_i \ll 1$ is also plotted.

Similarly to the quasi-parallel firehose instability, the instability condition is still

$$\Delta_i < -\frac{2}{\beta_i}. \tag{4.53}$$

If this condition is met, the maximum growth rate of the instability is

$$\frac{\gamma_{\max}}{\Omega_i} \approx \left(\frac{8\pi}{27}\right)^{1/4} \left|\frac{2}{\beta_i} + \Delta_i\right|^{3/4} \tan\theta \left[1 - \frac{3}{2}\tan^2\theta\right]^{-1}, \tag{4.54}$$

and is attained at (parallel) wavenumber

$$(k_\parallel \rho_i)_{\text{peak}} \approx \left(\frac{32\pi}{3}\right)^{1/4} \left|\frac{2}{\beta_i} + \Delta_i\right|^{1/4} \tan\theta \left[1 - \frac{3}{2}\tan^2\theta\right]^{-1}, \tag{4.55}$$

where $\theta = \tan^{-1}(k_\perp/k_\parallel)$ is (again) the wavevector angle with respect to the magnetic field. In contrast to the quasi-parallel case, if the condition (4.53) is met, the instability persists for all wavenumbers satisfying $k\rho_i \lesssim 1$, albeit with a decreasing growth rate beyond the parallel wavenumber given by (4.55). We notice that along the critical line $k_\perp = k_\parallel \sqrt{2/3}$ ($\theta \approx 39°$), the maximum growth rate (4.54) of the oblique firehose diverges. This divergence is mathematically the result of failing to take into account higher-order terms in the $k\rho_i \ll 1$ expansion, but, as was discussed earlier in this section, it is indicative of a physical effect (*viz.* much faster growth of firehose modes with $k_\perp = k_\parallel \sqrt{2/3}$).

The degree to which the growth rate of unstable modes determined from (4.52) follows a numerical solution for a particular choice of θ is demonstrated in figure 22. The agreement is reasonable, although an increasingly large discrepancy develops as $k\rho_i$ approaches unity due to FLR effects.

4.4.4. *Critical-line firehose instability*

In this third and final case, we set $k_\perp = k_\parallel \sqrt{2/3}$. The FLR coupling between the shear-Alfvén mode and the Barnes'-damped slow-mode then vanishes to leading order

in $k\rho_i \ll 1$, and next-order FLR terms must be considered. Depending on the value of β_i, we find two sub-cases.

First, for $\beta_i \sim \Delta_i^{-1} \gg 10^6$ – a numerical bound that we will justify *a posteriori* following our calculations – the FLR term responsible for setting the wavenumber of the fastest-growing mode is the second-order correction to the FLR coupling between the shear-Alfvén and slow modes. The appropriate ordering to adopt then depends on the relative magnitude of Δ_i and β_i^{-1}. For $\Delta_i\beta_i + 2 \lesssim -1$, we use the ordering

$$\tilde{\omega}_{i\parallel} \sim \frac{1}{\beta_i^{1/2}} \sim |\Delta_i|^{1/2} \sim k_\parallel^6 \rho_i^6. \tag{4.56}$$

In this case, we find (see Appendix K.3.8) that the frequency of the two shear-Alfvén modes is given by

$$\frac{\omega}{\Omega_i} = -k_\parallel \rho_i \left[\frac{6889 i k_\parallel^6 \rho_i^6}{27\,648\sqrt{\pi}} \pm \sqrt{\left(\frac{1}{\beta_i} + \frac{\Delta_i}{2}\right) - \frac{6889^2}{27\,648^2\pi} k_\parallel^{12} \rho_i^{12}} \right]. \tag{4.57}$$

The wavelength at which the growth rate is maximised scales with an extraordinarily low power of $|2\beta_i^{-1} + \Delta_i|$:

$$(k_\parallel \rho_i)_{\text{peak}} \approx \frac{2^{19/12} 3^{1/2} \pi^{1/12}}{83^{1/3} 35^{1/12}} \left| \frac{2}{\beta_i} + \Delta_i \right|^{1/12} \approx 0.97 \left| \frac{2}{\beta_i} + \Delta_i \right|^{1/12}, \tag{4.58}$$

with associated maximum growth rate

$$\frac{\gamma_{\text{max}}}{\Omega_i} \approx \frac{2^{13/12} 3^{1/2} \pi^{1/12}}{83^{1/3} 35^{1/12}} \left| \frac{2}{\beta_i} + \Delta_i \right|^{7/12} \approx 0.58 \left| \frac{2}{\beta_i} + \Delta_i \right|^{7/12}. \tag{4.59}$$

As discussed in § 4.4.1, the instability threshold for critical-line firehose modes is not (4.53), but is a less stringent value. We can demonstrate this analytically by showing that, for $\Delta_i \simeq -2/\beta_i$, critical-line firehose modes are still unstable. Adopting the ordering

$$\tilde{\omega}_{i\parallel} \sim \frac{1}{\beta_i^{3/5}} \sim k_\parallel^6 \rho_i^6, \tag{4.60}$$

it follows (see Appendix K.3.8) that the growth rate of the critical-line firehose modes is

$$\frac{\gamma}{\Omega_i} = -k_\parallel \rho_i \left[\frac{6889 k_\parallel^6 \rho_i^6}{27\,648\sqrt{\pi}} \pm \sqrt{\frac{5}{4\beta_i} k_\parallel^2 \rho_i^2 + \frac{6889^2}{27\,648^2\pi} k_\parallel^{12} \rho_i^{12}} \right]. \tag{4.61}$$

The maximum growth rate of such modes is then given by

$$\frac{\gamma_{\text{max}}}{\Omega_i} \approx \frac{2^3 5^{7/10} 3^{3/2} \pi^{1/5}}{83^{4/5} 7^{7/10}} \beta_i^{-7/10} \approx 1.2 \beta_i^{-7/10}, \tag{4.62}$$

obtained at parallel wavenumber

$$(k_\parallel \rho_i)_{\text{peak}} \approx \frac{25^{1/10} 3^{1/2} \pi^{1/10}}{83^{2/5} 7^{1/10}} \beta_i^{-1/10} \approx 0.64 \beta_i^{-1/10}. \tag{4.63}$$

When $\beta_i \sim \Delta_i^{-1} \ll 10^6$ the fastest-growing critical-line firehose modes have a sufficiently large wavenumber that the effect of FLR coupling between shear-Alfvén

and slow modes is sub-dominant to the effect of cyclotron damping. Assuming that $\Delta_i \beta_i + 2 \lesssim -1$ and adopting the ordering

$$\tilde{\omega}_{i\parallel} \sim \frac{1}{\beta_i^{1/2}} \sim |\Delta_i|^{1/2}, \quad k_\parallel \rho_i \sim \frac{1}{\sqrt{\log 1/\left|\beta_i^{-1} + \Delta_i/2\right|}}, \tag{4.64a,b}$$

we show in Appendix K.3.8 that the frequency of the shear-Alfvén modes becomes

$$\frac{\omega}{\Omega_i} = -\frac{i\sqrt{\pi}}{2k_\parallel \rho_i} \exp\left(-\frac{1}{k_\parallel^2 \rho_i^2}\right) \pm k_\parallel \rho_i \sqrt{\left(\frac{1}{\beta_i} + \frac{\Delta_i}{2}\right) - \frac{\pi}{4k_\parallel^4 \rho_i^4} \exp\left(-\frac{1}{k_\parallel^2 \rho_i^2}\right)}. \tag{4.65}$$

In this case, the maximum growth rate

$$\frac{\gamma_{\text{max}}}{\Omega_i} \approx (k_\parallel \rho_i)_{\text{peak}} \left|\frac{1}{\beta_i} + \frac{\Delta_i}{2}\right|^{1/2}, \tag{4.66}$$

is attained at

$$(k_\parallel \rho_i)_{\text{peak}} \approx \frac{\sqrt{2}}{\sqrt{\log 1/\left|\beta_i^{-1} + \Delta_i/2\right|}} \left[1 - \frac{4 \log\left(\log 1/\sqrt{\left|\beta_i^{-1} + \Delta_i/2\right|}\right)}{\log 1/\left|\beta_i^{-1} + \Delta_i/2\right|}\right]. \tag{4.67}$$

Figure 19 corroborates that the analytical approximation (4.67) provides a reasonable estimate of the parallel wavenumber at which peak growth occurs.

Similarly to the $\beta_i \gg 10^6$ regime, when $\beta_i \ll 10^6$, critical-line firehose modes still grow when $\Delta_i \approx -2/\beta_i$. Their growth rate as a function of wavenumber is given by

$$\frac{\gamma}{\Omega_i} = -\frac{\sqrt{\pi}}{2k_\parallel \rho_i} \exp\left(-\frac{1}{k_\parallel^2 \rho_i^2}\right) \pm k_\parallel \rho_i \sqrt{\frac{5}{4\beta_i} k_\parallel^2 \rho_i^2 + \frac{\pi}{4k_\parallel^4 \rho_i^4} \exp\left(-\frac{1}{k_\parallel^2 \rho_i^2}\right)}. \tag{4.68}$$

The maximum of (4.68),

$$\frac{\gamma_{\text{max}}}{\Omega_i} \approx \frac{\sqrt{5}}{2} (k_\parallel \rho_i)_{\text{peak}}^2 \beta_i^{-1/2}, \tag{4.69}$$

is achieved at

$$(k_\parallel \rho_i)_{\text{peak}} \approx \frac{\sqrt{2}}{\sqrt{\log(\pi\beta_i/20)}} \left\{1 - \frac{3 \log\left[\log(\pi\beta_i/20)/2\right]}{\log(\pi\beta_i/20)}\right\}. \tag{4.70}$$

By comparing the expressions (4.57) and (4.65) for the complex frequency of shear-Alfvén modes – specifically, the ratio of the final terms – the dependence on β_i (equivalently, Δ_i) of the relative importance of FLR slow-mode coupling and cyclotron damping can be determined. This ratio is $\sim 0.16 k_\parallel^8 \rho_i^8 \exp(-1/k_\parallel^2 \rho_i^2)$, with equality being achieved when $k_\parallel \rho_i \approx 0.3$. Using (4.58) to estimating the value of $|2\beta_i^{-1} + \Delta_i|$ at which this value of $k_\parallel \rho_i$ is achieved, we find that $|2\beta_i^{-1} + \Delta_i| \approx 8 \times 10^{-7}$. Assuming $|\Delta_i \beta_i^{-1} + 2| \sim 1$, we conclude that, for $\beta_i \lesssim 10^6$, cyclotron damping will determine the wavenumber cutoff, with this transition value of β_i proportional to the value of $|\Delta_i|\beta_i$. This estimate can
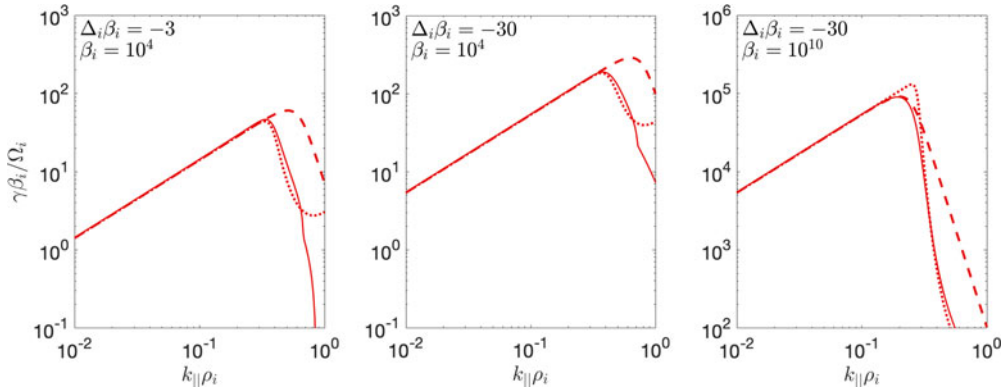
FIGURE 23. Critical-line CES firehose instability. Growth rates of shear-Alfvén modes whose instability is driven by the CE ion-shear term in the CE distribution function (4.1), for wavevectors at an angle $\theta \approx 39°$ with the background magnetic field (*viz.* $k_\perp = \sqrt{2/3} k_\parallel$). The growth rates (solid lines) of all modes are calculated in the same way as figure 19. We show the growth rates for a selection of different values of $\Delta_i \beta_i$ and β_i. The approximations (4.57) and (4.65) for the growth rate (dashed and dotted red, respectively) in the limit $k_\parallel \rho_i \ll 1$ are also plotted.

be validated numerically by comparing (4.57) and (4.65) with the numerically determined growth rate (see figure 23). We indeed find that, for $\beta_i \sim \Delta_i^{-1} \ll 10^6$, the effect of cyclotron damping sets the wavenumber of peak growth, while FLR slow-mode coupling does so for $\beta_i \sim \Delta_i^{-1} \gg 10^6$. In both cases, the superior of the two analytic approximations closely matches the numerical growth rate.

These results suggest that, for very large β_i, the wavenumber of the maximum growth of the firehose instability satisfies $k\rho_i \ll 1$, rather than $k\rho_i \sim 1$. This result might seem to contradict previous authors who claim to have found numerical evidence that the fastest growth rates of the firehose instability occur at $k\rho_i \sim 1$ (Yoon *et al.* 1993; Schekochihin *et al.* 2005; Kunz *et al.* 2014); however, given the logarithmic dependence of the characteristic wavenumber (4.67), we conclude that it would take simulations at very high β_i to be able to distinguish between $k\rho_i \sim 1$ and $k\rho_i \sim \beta_i^{-1/12} \ll 1$. In addition, the results presented in figure 20(*b*) indicate that firehose modes with $k\rho_i \sim 1$ have a less stringent instability threshold on Δ_i than (4.53), providing an opportunity for such modes to grow significantly before longer-wavelength modes can do so. In short, it seems reasonable to assume for all practical purposes that the dominant firehose modes occur at $k\rho_i \sim 1$, provided β_i is not extremely large.

4.4.5. *Sub-ion-Larmor-scale firehose instability*

Figure 19(*b*) also suggests that, once $|\Delta_i|\beta_i \gg 1$, firehose modes on sub-ion-Larmor scales develop – albeit with a smaller growth rate than the critical-line ones. Similarly to sub-ion-Larmor-scale mirror modes (see the end of § 4.3.1), we can characterise these modes analytically by adopting the ordering

$$k_\parallel \rho_i \sim k_\perp \rho_i \sim (|\Delta_i|\beta_i)^{1/2} \gg 1, \quad \frac{\gamma}{\Omega_i} \sim \Delta_i. \quad (4.71a,b)$$

If we also assume that $|\Delta_i|\beta_i \ll \mu_e^{-1/2}$, it is shown in Appendix K.3.2 that the growth rate of these modes is given by

$$
\begin{aligned}
\frac{\gamma}{\Omega_i} &\approx \frac{k_\parallel}{k} \sqrt{\left(-\Delta_i \frac{k_\perp^2 - k_\parallel^2}{k^2} - \frac{k^2 \rho_i^2}{\beta_i}\right)\left(\frac{k^2 \rho_i^2}{\beta_i} - \Delta_i \frac{k_\parallel^2}{k^2}\right)} \\
&= \cos\theta \sqrt{\left[-\Delta_i\left(\sin^2\theta - \cos^2\theta\right) - \frac{k^2 \rho_i^2}{\beta_i}\right]\left(\frac{k^2 \rho_i^2}{\beta_i} - \Delta_i \cos^2\theta\right)}.
\end{aligned} \tag{4.72}
$$

If $\Delta_i < 0$, we have an instability for all modes with $\theta > 45°$ whose total wavenumber satisfies

$$
k\rho_i < \sqrt{|\Delta_i|\beta_i \left(\sin^2\theta - \cos^2\theta\right)}. \tag{4.73}
$$

Analogously to the sub-ion-Larmor-scale mirror modes (cf. (4.18)), the growth is maximised when $k\rho_i \ll (|\Delta_i|\beta_i)^{1/2}$ and $\theta \approx 55°$, with

$$
\gamma_{\max} = \frac{1}{3\sqrt{3}}|\Delta_i|\Omega_i \approx 0.19|\Delta_i|\Omega_i. \tag{4.74}
$$

In contrast to the case of the mirror instability, this growth rate is asymptotically small in $\Delta_i \ll 1$ compared with the peak growth rate of the critical-line firehose modes (cf. (4.59) and (4.67)), and thus the instability of sub-ion-Larmor-scale firehose modes is always subdominant. For completeness, we note that, once $|\Delta_i|\beta_i \sim \mu_e^{-1/2}$, the electron-pressure anisotropy associated with the CE electron-shear term begins to play a comparable role to the ion-pressure anisotropy for modes with $k\rho_i \sim (|\Delta_i|\beta_i)^{1/2}$. In this case, the expression for the growth rate becomes

$$
\begin{aligned}
\frac{\gamma}{\Omega_i} &\approx \frac{k_\parallel}{k} \left\{\left[-\Delta_i \frac{k_\perp^2 - k_\parallel^2}{k^2} - k^2 \rho_i^2\left(\frac{1}{\beta_i} + \frac{\mu_e^{1/2}\Delta_i}{2}\right)\right]\right. \\
&\quad \left. \times \left[\frac{k^2 \rho_i^2}{\beta_i} - \Delta_i\left(\mu_e^{1/2}k_\perp^2\rho_i^2 - \frac{1}{2}\mu_e^{1/2}k_\parallel^2\rho_i^2 + \frac{k_\parallel^2}{k^2}\right)\right]\right\}^{1/2}.
\end{aligned} \tag{4.75}
$$

The bound (4.73) on the total wavenumber required for the instability of modes with $k_\perp > k_\parallel$ is then

$$
k\rho_i < \sqrt{\frac{|\Delta_i|\beta_i \left(\sin^2\theta - \cos^2\theta\right)}{1 + \mu_e^{1/2}\Delta_i\beta_i/2}}. \tag{4.76}
$$

Because the denominator tends to zero as $\Delta_i \to -2\mu_e^{-1/2}\beta_i^{-1}$, the bound becomes increasingly weak, and so the region of $(k_\parallel, k_\perp)$-space in which there is instability extends significantly towards electron-Larmor scales. This extension precedes the onset of the oblique electron firehose instability (see § 4.4.7).

4.4.6. *Parallel electron firehose instability*

The CES parallel electron firehose instability arises when the negative electron-pressure anisotropy ($\Delta_e < 0$) associated with the CE electron-shear term becomes a sufficiently large free-energy source to overcome the relatively weak collisionless damping mechanisms that act on long-wavelength ($k_\parallel\rho_e \ll 1$) quasiparallel whistler waves by

changing their handedness from right to left handed. More specifically, whistler waves with quasi-parallel wavevectors do not have a component of electric field parallel to $\boldsymbol{B}_0$, and so are not subject to electron-Landau damping. Electron-cyclotron damping does occur, but is very inefficient for $k_\parallel \rho_e \ll 1$. The resonant interaction primarily responsible for damping is that between the whistler waves and Maxwellian ions in the CE plasma streaming along field lines with $v_\parallel \ll v_{\mathrm{th}i}$. When the handedness of the whistler waves changes, this interaction instead leads to the waves' growth. Because the resonant interaction driving the instability involves the plasma's ions, the CES parallel electron firehose instability has a rather small growth rate compared with other CES electron-scale microinstabilities, with growth disappearing entirely in the special case of cold ions. The parallel wavenumber of peak growth, which is a small but finite fraction of the electron-Larmor scale, *viz.* $(k_\parallel \rho_e)_{\mathrm{peak}} \approx 0.4$ for $\Delta_e \lesssim -2/\beta_e$, is set by electron-cyclotron damping, which prevents shorter-wavelength modes from becoming unstable. The CES parallel electron firehose instability was first identified by Hollweg & Völk (1970) and has been studied subsequently using theory and simulations in plasma with $\beta_e \sim 1$–20 by a number of authors (e.g. Paesold & Benz 1999; Li & Habbal 2000; Messmer 2002; Gary & Nishimura 2003; Camporeale & Burgess 2008, 2010; Riquelme *et al.* 2018).

To characterise the parallel electron firehose instability analytically, we can simply use the expressions (4.21*a*) and (4.21*b*) given in § 4.3.2 for the real frequency ϖ and growth rate γ, respectively, of the parallel whistler waves that satisfy the ordering

$$\tilde{\omega}_{e\parallel} = \frac{\omega}{k_\parallel v_{\mathrm{th}e}} \sim \Delta_e \sim \frac{1}{\beta_e}, \tag{4.77}$$

and have $k_\parallel \rho_e \sim 1$, but this time with $\Delta_e \beta_e < 0$. Plots of the dispersion curves $\varpi(k_\parallel)$ and $\gamma(k_\parallel)$ of CES parallel electron firehose modes are then shown in figure 24 for a selection of different (negative) values of $\Delta_e \beta_e$. In a hydrogen plasma, we find an instability for $\Delta_e < (\Delta_e)_c \approx -1.7/\beta_e$. For $\Delta_e \lesssim -2/\beta_e$, modes with $k_\parallel \rho_e \lesssim 0.4$ become unstable. Figure 24 also shows that parallel electron firehose modes generically have a real frequency that is much greater than their growth rate ($\varpi \sim \Omega_e/\beta_e \gg \gamma$); however, this frequency changes sign at a wavenumber which, when $\Delta_e \lesssim -2/\beta_e$, is comparable to the wavenumber $(k_\parallel \rho_e)_{\mathrm{peak}}$ at which peak growth occurs.

These results can be elucidated by considering the expressions (4.21) in the subsidiary limit

$$k_\parallel \rho_i \sim \frac{1}{\sqrt{\log\left(2\mu_e^{-1/2}|1 + 2/\Delta_e\beta_e|\right)}} \ll 1. \tag{4.78}$$

Then (4.21) simplifies to

$$\varpi = \pm\left[\left(1 + \frac{\Delta_e\beta_e}{2}\right) k_\parallel^2 \rho_e^2 - \mu_e^{1/2}\Delta_e\beta_e\right]\frac{\Omega_e}{\beta_e}, \tag{4.79a}$$

$$\gamma = \frac{\sqrt{\pi}}{k_\parallel \rho_e}\left[\Delta_e \exp\left(-\frac{1}{k_\parallel^2 \rho_e^2}\right) - \left(\frac{\Delta_e}{2} + \frac{1}{\beta_e}\right)\mu_e^{1/2}k_\parallel^2 \rho_e^2\right]\Omega_e. \tag{4.79b}$$

These approximations are plotted alongside (4.21) in figure 24; the agreement is qualitative rather than quantitative for $\Delta_e \sim -2/\beta_e$, but becomes increasingly good as Δ_e is decreased further.

Using these simplified expressions, we can derive approximate analytical expressions for the instability's threshold $(\Delta_e)_c$, as well as its peak growth rate and the wavenumber at
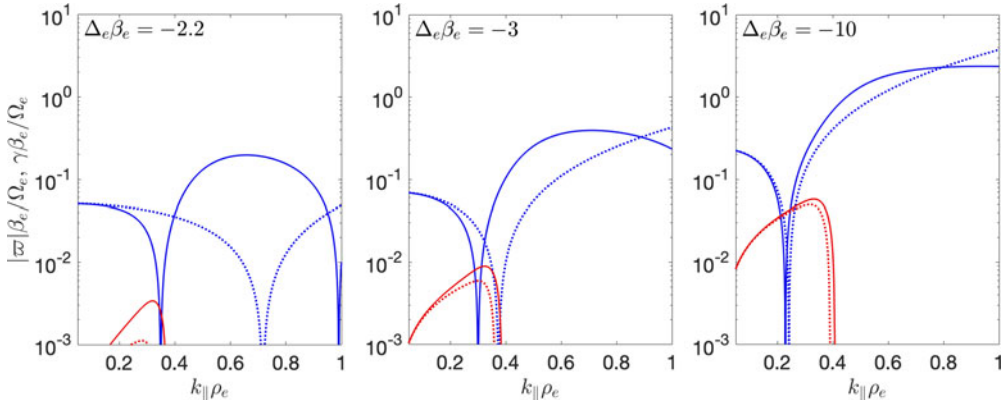
FIGURE 24. Parallel CES electron firehose instability. Dispersion curves of unstable whistler modes, whose instability is driven by the negative electron-pressure anisotropy associated with the electron-shear term in CE distribution function (4.1), for wavevectors that are co-parallel with the background magnetic field (*viz.* $\boldsymbol{k} = k_\parallel \hat{\boldsymbol{z}}$). The frequency (solid blue) and growth rates (solid red) of the modes are calculated using (4.21*a*) and (4.21*b*), respectively. The resulting frequencies and growth rates, when normalised as $\gamma \beta_e / \Omega_e$, are functions of the dimensionless quantity $\Delta_e \beta_e$; we show the dispersion curves for three different values of $\Delta_e \beta_e$. The $k_\parallel \rho_e \ll 1$ approximations (4.79*a*) for the frequency (dotted-blue) and (4.79*b*) growth rate (dotted-red) are also plotted.

which that growth occurs. First considering the sign of (4.79), it is easy to show that there exists a range of wavenumbers $k_\parallel$ at which $\gamma > 0$ if and only if $\Delta_e < -2/\beta_e$, so $(\Delta_e)_{\rm c} \approx -2/\beta_e$. This is somewhat more stringent than the numerically observed threshold, a discrepancy attributable to FLR effects, not taken into account by the approximation (4.79*b*). When $\Delta_e < -2/\beta_e$, it can be proven that the growth rate (4.79*b*) is maximised at

$$(k_\parallel \rho_e)_{\rm peak} \approx \frac{1}{\sqrt{\log\left(\mu_e^{-1/2}|1/2 + 1/\Delta_e\beta_e|\right)}} \left\{ 1 - \frac{\log\left[\sqrt{2}\log\left(\mu_e^{-1/2}|1/2 + 1/\Delta_e\beta_e|\right)\right]}{\log\left(\mu_e^{-1/2}|1/2 + 1/\Delta_e\beta_e|\right)} \right\},$$
(4.80)

attaining the value

$$\gamma_{\rm max} = \sqrt{\pi}\mu_e^{1/2}(k_\parallel \rho_e)_{\rm peak} \left| \frac{\Delta_e}{2} + \frac{1}{\beta_e} \right| \Omega_e.$$
(4.81)

Comparing (4.81) with the characteristic magnitude of ϖ evaluated using (4.79*a*) at $k_\parallel \rho_e = (k_\parallel \rho_e)_{\rm peak}$ (and assuming that $(k_\parallel \rho_e)_{\rm peak} \gtrsim \mu_e^{1/4}$), we conclude that $\gamma \lesssim \mu_e^{1/4}\varpi$, thereby explaining our previous observation that the growth rate of parallel electron firehose modes is generically much smaller than the real frequency of those modes. We can also show that the one exception to this occurs when $(k_\parallel \rho_e)_{\rm peak} \approx \mu_e^{1/4}[2\Delta_e\beta_e/(1 + 2\Delta_e\beta_e)]^{1/2}$, an approximate expression for the wavenumber below which ϖ changes sign. As we will see, the characteristic growth rate of the CES parallel electron firehose is typically much smaller than its oblique relative in high-β plasma (see § 4.4.7), a conclusion that also applies in $\beta_e \sim 1$ plasmas with bi-Maxwellian distributions (see Li & Habbal 2000).

4.4.7. *Oblique electron firehose instability*

In spite of its similar name, the CES oblique electron firehose instability is quite distinct from its parallel cousin: it is a non-propagating mode than arises from the destabilisation of oblique KAWs by a sufficiently negative electron-pressure anisotropy. The linear theory of the analogous instability in $\beta_e \sim 1$ plasma with bi-Maxwellian electrons was first presented by Li & Habbal (2000), with a number of simulation studies of this instability having been conducted subsequently (Gary & Nishimura 2003; Camporeale & Burgess 2008, 2010; Riquelme *et al.* 2018). The high-β variant of the (linear) instability for general anisotropic electron distribution functions was studied in the $k_\parallel \ll k_\perp$ limit of gyrokinetics by Kunz *et al.* (2018). In contrast to the findings of Gary & Nishimura (2003), who showed that the oblique electron firehose instability in a bi-Maxwellian plasma at $\beta_e \sim 1$ involves gyroresonant wave–particle interactions between electrons and the unstable modes, instability of CES oblique electron firehose modes at $\beta_e \gg 1$ is essentially non-resonant, with sufficient large negative electron-pressure anisotropies negating the restoring force that underpins the oscillation of high-β KAWs.

Similarly to the parallel electron firehose instability, the CES oblique electron firehose instability is triggered when $\Delta_e \lesssim -2/\beta_e$. The precise value of the threshold depends on the wavevector of the mode being destabilised. Analogously to the parallel electron firehose, long-wavelength oblique electron firehose modes are unstable when $\Delta_e < (\Delta_e)_c = -2/\beta_e$. However, figure 25(*a*) shows that there is positive growth of $k\rho_e \sim 1$ oblique electron firehose modes for less negative values of Δ_e, illustrating that the threshold is less stringent for such modes. This phenomenon is reminiscent of the ion firehose instability (see figure 20): ion-Larmor-scale oblique firehose modes also have a less stringent threshold than longer-wavelength modes. In addition to the $k\rho_e \sim 1$ modes, a region of unstable KAWs with characteristic wavenumbers $\mu_e^{1/2} \ll k\rho_e \ll \mu_e^{1/4}$, $k_\perp \sim k_\parallel$, is evident in figure 25(*a*). These modes, which were discussed at the end of § 4.4.1, are destabilised by negative ion-pressure anisotropy; the extent of this region closely matches the analytic prediction (4.76). Using a similar semi-analytic approach to that employed for the case of the ion firehose instability (see Appendix K.2.2), we can determine the approximate threshold for the oblique electron firehose instability as a function of $k_\parallel \rho_e$ and $k_\perp \rho_e$. The results are shown in figure 25(*b*); modes with $k_\parallel \rho_e \sim 0.5$, $k_\perp \rho_e \sim 0.4$ have the least stringent threshold ($\Delta_e \approx -1.4/\beta_e$).

Well into the unstable regime, i.e. when $\Delta_e \beta_e + 2 \lesssim -1$, electron firehose modes across a broad range of wavevectors are destabilised (see figure 26*a*). The fastest-growing electron firehose modes are oblique and occur at electron-Larmor scales ($k_\perp \rho_e \sim 1 > k_\parallel \rho_e$), with characteristic growth rate $\gamma \sim |\Delta_e| \Omega_e \sim \Omega_e/\beta_e$. This growth rate is much larger than the peak growth rate of the parallel electron firehose instability (4.81).

Similarly to the electron mirror instability, a simple analytic expression for the growth rate of the fastest-growing electron firehose modes when $\Delta_e \beta_e + 2 \lesssim -1$ is challenging to establish. We can, however, characterise the growth of two particular classes of electron firehose modes analytically.

The first of these are long-wavelength (*viz.* $k\rho_e \ll 1$) electron firehose modes. For these, we adopt the same ordering (4.38) as was considered when characterising long-wavelength electron mirror modes:

$$k_\parallel \rho_e \sim k_\perp \rho_e \sim \mu_e^{1/4} \ll 1, \quad \tilde{\omega}_{e\parallel} = \frac{\omega}{k_\parallel v_{\mathrm{th}e}} \sim \frac{k\rho_e}{\beta_e} \sim |\Delta_e| k\rho_e. \qquad (4.82a,b)$$
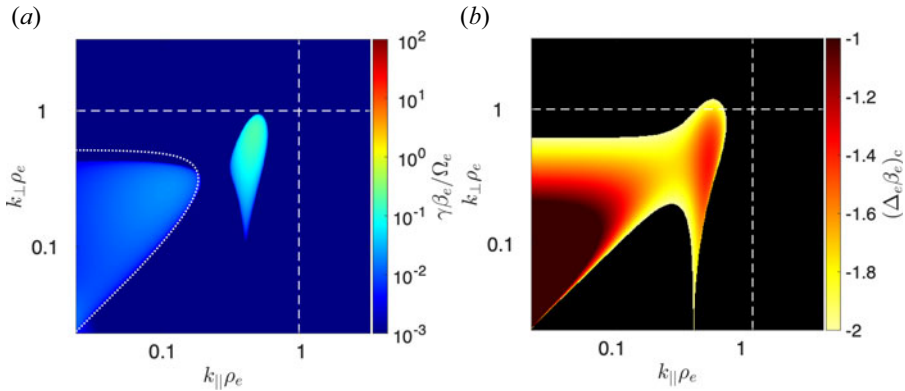
FIGURE 25. Onset of the CES oblique electron firehose instability. (*a*) Maximum positive growth rates of linear perturbations resulting from both the CE ion- and electron-shear term in the CE distribution function (4.1) with $\beta_i = 10^4$ and $\Delta_e = -1.7/\beta_e$ (which is above the long-wavelength oblique electron-firehose instability-threshold $\Delta_e = -2/\beta_e$). The growth rates of all modes are calculated in the same way as figure 19. The resulting growth rates are normalised as $\gamma\beta_e/\Omega_e$ are functions of the dimensionless parameter $\Delta_e\beta_e$. The dotted line denotes the instability boundary (4.76) on KAWs driven unstable by ion-pressure anisotropy of the CE ion-shear term. (*b*) Threshold value of $\Delta_e\beta_e$ at which modes with parallel and perpendicular wavenumber $k_\parallel$ and $k_\perp$, respectively, become unstable. Regions of $(k_\parallel, k_\perp)$ that are shaded black are stable.
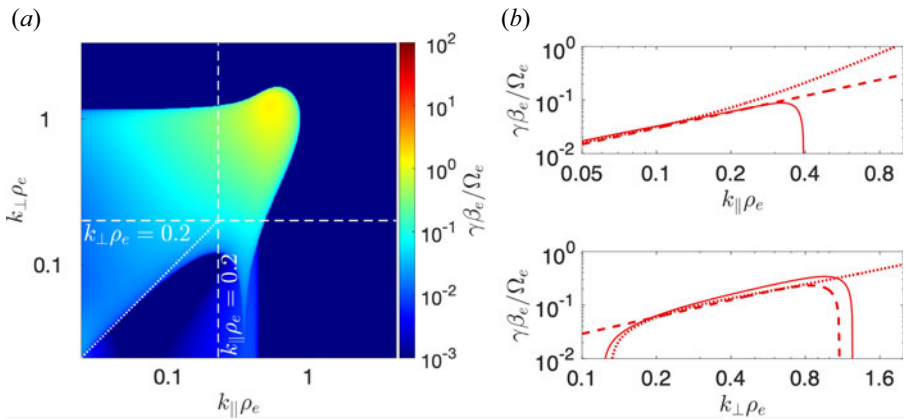
FIGURE 26. Oblique electron firehose instability at $\Delta_e\beta_e + 2 \lesssim -1$. (*a*) Maximum positive growth rates of linear perturbations resulting from CE ion- and electron-shear terms in the CE distribution function (4.1) for $\Delta_e\beta_e = -3$. Here, a temperature-equilibrated hydrogen plasma is considered, *viz.* $\Delta_e = \mu_e^{1/2}\Delta_i$, and $\beta_i = \beta_e$. The growth rates of all modes are calculated in the same way as figure 25. (*b*) Plots of the oblique electron firehose mode growth rate (solid line) as a function of $k_\parallel\rho_e$ with $k_\perp\rho_e = 0.2$ (top), and as a function of $k_\perp\rho_e$ with $k_\parallel\rho_e = 0.2$ (bottom). The dotted and dashed lines show the analytical predictions (4.83) and (4.86), respectively.

We then obtain a closed-form expression (cf. (4.39), and also (4.75)) for the complex frequencies of the electron firehose modes:

$$\omega \approx \pm k_\parallel \rho_e \Omega_e \left\{ \left[\frac{1}{\beta_e} + \Delta_e \left(\frac{1}{2} - \mu_e^{1/2} \frac{k_\parallel^2 \rho_e^2 - k_\perp^2 \rho_e^2}{k^4 \rho_e^4} \right) \right] \right.$$
$$\left. \times \left[\frac{k^2 \rho_e^2}{\beta_e} - \Delta_e \left(k_\perp^2 \rho_e^2 + \mu_e^{1/2} \frac{k_\parallel^2}{k^2} - \frac{1}{2} k_\parallel^2 \rho_e^2 \right) \right] \right\}^{1/2}. \tag{4.83}$$

If $\Delta_e < -2/\beta_e$, the right-hand side of (4.83) is purely imaginary for $k_\perp > k_\parallel$, and so we have positive growth for all long-wavelength electron firehose modes with $\theta > 45°$.[7] This approximation should be compared with the numerically determined growth rate in figure 26(b). If it is further assumed that $\mu_e^{1/4} \ll k\rho_e \ll 1$, $k_\perp \sim k_\parallel$, it is shown in §4.3.4 that (4.83) simplifies to an analogue of (4.40), *viz.*

$$\omega \approx \pm k_\parallel \rho_e \Omega_e \sqrt{\left(\frac{1}{\beta_e} + \frac{\Delta_e}{2} \right) \left(k^2 \rho_e^2 \frac{1}{\beta_e} + \frac{\Delta_e}{2} \left[k_\parallel^2 \rho_e^2 - 2k_\perp^2 \rho_e^2 \right] \right)}. \tag{4.84}$$

This result is again in agreement with the gyrokinetic calculations of Kunz *et al.* (2018). Extrapolating (4.84) to $k_\parallel \rho_e \sim k_\perp \rho_e \sim 1$, we recover that $\gamma \sim \Omega_e/\beta_e$ when $|\Delta_e \beta_e + 2| \gtrsim 1$.

A second sub-category of electron firehose modes that can be described analytically are quasi-perpendicular ones. For any fixed $k_\parallel \rho_e \ll 1$, the most rapidly growing modes are strongly anisotropic: they occur when the perpendicular wavelength is comparable to the electron Larmor radius, $k_\perp \rho_e \sim 1$. These modes can therefore be elucidated analytically by considering their dispersion relation under the ordering

$$\tilde{\omega}_{e\parallel} \sim |\Delta_e| \sim \frac{1}{\beta_e}, \tag{4.85}$$

in the wavenumber domain $\mu_e^{1/2} \ll k_\parallel \rho_e \ll k_\perp \rho_e \sim 1$. We solve the dispersion relation (see Appendix K.3.10) to find

$$\frac{\omega}{\Omega_e} = \frac{k_\parallel \rho_e}{\mathcal{F}(k_\perp \rho_e)} \left\{ -\mathrm{i} \frac{\sqrt{\pi}}{2} \left[\frac{k_\perp^2 \rho_e^2}{\beta_e} + \Delta_e \mathcal{H}(k_\perp \rho_e) \right] \pm \sqrt{\mathfrak{D}\,(k_\perp \rho_e, \beta_e, \Delta_e)} \right\}, \tag{4.86}$$

where the discriminant is

$$\mathfrak{D}\,(k_\perp \rho_e, \beta_e, \Delta_e) \equiv \left[\frac{k_\perp^2 \rho_e^2}{\beta_e} + \Delta_e \mathcal{H}(k_\perp \rho_e) \right]$$
$$\times \left\{ \frac{1}{\beta_e} \left(1 - \frac{\pi}{4} k_\perp^2 \rho_e^2 \right) - \Delta_e \left[\frac{\pi}{4} \mathcal{H}(k_\perp \rho_e) + \mathcal{F}(k_\perp \rho_e) \right] \right\}, \tag{4.87}$$

and the two auxiliary functions are (cf. (3.24))

$$\mathcal{F}(\alpha) = \exp\left(-\frac{\alpha^2}{2} \right) \left[I_0 \left(\frac{\alpha^2}{2} \right) - I_1 \left(\frac{\alpha^2}{2} \right) \right], \tag{4.88}$$

$$\mathcal{H}(\alpha) \equiv 1 - \exp\left(-\frac{\alpha^2}{2} \right) I_0 \left(\frac{\alpha^2}{2} \right). \tag{4.89}$$

---

[7]In fact, this condition is stronger than necessary to guarantee instability – but the exact condition is somewhat complicated, so we omit discussion of it.

As a sanity check, we observe that in the subsidiary limit $k_\perp \rho_e \ll 1$, (4.86) becomes

$$\omega \approx \pm k_\perp k_\parallel \rho_e^2 \Omega_e \sqrt{\left(\frac{1}{\beta_e} + \frac{\Delta_e}{2}\right)\left(\frac{1}{\beta_e} - \Delta_e\right)}, \tag{4.90}$$

returning us to the dispersion relation (4.84) of unstable kinetic Alfvén waves taken in the limit $k_\parallel \ll k_\perp$.

In the case when $\Delta_e < -2\beta_e^{-1}$, one of the modes described by (4.86) can be destabilised by sufficiently negative pressure anisotropy, and become purely growing. The wavenumbers susceptible to this instability are those satisfying

$$k_\perp^2 \rho_e^2 \left[1 - \exp\left(-\frac{k_\perp^2 \rho_e^2}{2}\right) I_0\left(\frac{k_\perp^2 \rho_e^2}{2}\right)\right]^{-1} < |\Delta_e|\beta_e. \tag{4.91}$$

Provided $\Delta_e < -2\beta_e^{-1}$ and $|\Delta_e|\beta_e \sim 1$, this gives a range of unstable perpendicular wavenumbers $k_\perp \rho_e \lesssim 1$. That these wavenumbers are indeed unstable follows immediately from the observation that if (4.91) holds, then the discriminant (4.87) satisfies

$$\mathfrak{D}(k_\perp \rho_e, \beta_e, \Delta_e) = -\pi \left[\Delta_e \mathcal{H}(k_\perp \rho_e) - \frac{k_\perp^2 \rho_e^2}{\beta_e}\right]\left[\Delta_e \mathcal{H}(k_\perp \rho_e) - \frac{k_\perp^2 \rho_e^2}{\beta_e} + \frac{1}{\beta_e} + |\Delta_e|\mathcal{F}(k_\perp \rho_e)\right]$$
$$< \pi \left[\Delta_e \mathcal{H}(k_\perp \rho_e) - \frac{k_\perp^2 \rho_e^2}{\beta_e}\right]^2, \tag{4.92}$$

from which it follows that the imaginary part of (4.86) for the '+' root is positive. When $|\Delta_e \beta_e + 2| \sim 1$, the characteristic growth rate of the instability is

$$\gamma_{\max} \sim k_\parallel \rho_e |\Delta_e|\Omega_e, \tag{4.93}$$

which is consistent with the numerical findings shown in figure 26(*a*). Indeed, (4.86) agrees reasonably with the numerically determined growth rate for small values of $k_\parallel \rho_i$ (see figure 26*b*).

One particularly interesting subsidiary limit of (4.90) is $|\Delta_e|\beta_e \gg 1$, in which it can be shown that, under the ordering $k_\perp \rho_e \sim (|\Delta_e|\beta_e)^{1/2} \gg 1$, the growth rate is

$$\gamma \approx \pi k_\parallel k_\perp^3 \rho_e^4 \left(|\Delta_e| - \frac{k_\perp^2 \rho_e^2}{\beta_e}\right) \Omega_e. \tag{4.94}$$

This implies that the perpendicular wavelength of peak growth transitions smoothly to values below the electron-Larmor radius as $|\Delta_e|\beta_e$ is increased beyond order-unity values. As we shall discuss in the next section, these unstable sub-electron-Larmor-scale modes are best regarded as a distinct instability from the electron firehose, and so we introduce it properly in a new section.

4.4.8. *Electron-scale-transition instability*

When $|\Delta_e|\beta_e$ is increased significantly past unity, the fastest-growing microinstability changes character from that of a destabilised KAW, and instead becomes a destabilised non-propagating mode. The authors of this paper are not aware of this instability having been identified previously; we call it the EST instability, on account of it providing a smooth transition between unstable KAWs with $k_\perp \rho_e \ll 1$, and microinstabilities on sub-electron scales ($k_\perp \rho_e \gtrsim 1$). Unstable EST modes are quasi-perpendicular ($k_\parallel \rho_e < 1 \lesssim$
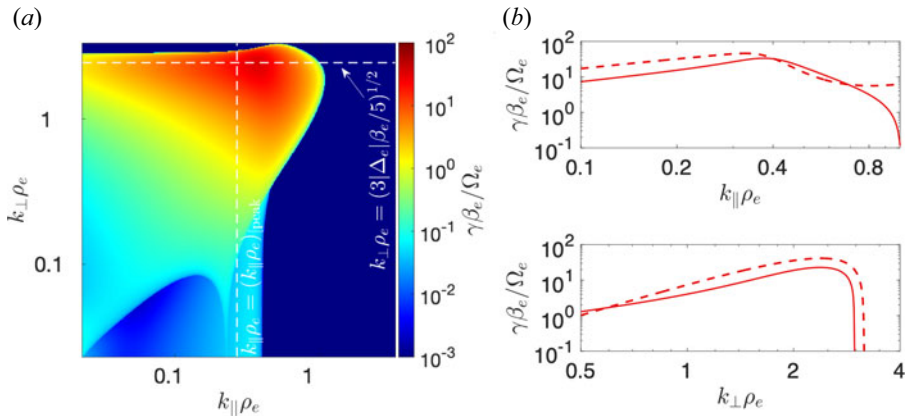
FIGURE 27. The CES EST instability. (*a*) Maximum positive growth rates of linear perturbations resulting from CE ion- and electron-shear terms in the CE distribution function (4.1) for $\Delta_e \beta_e = -10$ and $\beta_e = 10^4$. Here, a temperature-equilibrated hydrogen plasma is considered *viz.* $\Delta_e = \mu_e^{1/2} \Delta_i$, and $\beta_i = \beta_e$. The growth rates of all modes are calculated in the same way as figure 25. (*b*) Plot of the EST mode growth rate (solid line) as a function of $k_{\parallel} \rho_e$ with $k_{\perp} \rho_e = (3|\Delta_e|\beta_e/5)^{1/2}$ (top), and as a function of $k_{\perp} \rho_e$ with $k_{\parallel} \rho_e = (k_{\parallel} \rho_e)_{\text{peak}}$ (bottom), where $(k_{\parallel} \rho_e)_{\text{peak}}$ is given by (4.99*b*). The dotted and dashed lines show the analytical prediction (4.97).

$k_{\perp} \rho_e \lesssim \beta_e^{1/7}$), with the parallel wavenumber of the fastest-growing modes determined by a balance between the instability's drive and the electron-cyclotron damping that arises at sufficiently large $k_{\parallel} \rho_e$. In contrast to the oblique electron firehose instability, Landau-resonant electrons with $v_{\parallel} \approx \omega/k_{\parallel}$ also play a role in the EST instability's physical mechanism.

To demonstrate that the EST modes are not unstable KAWs, we consider the expression (4.86) in a Maxwellian plasma (*viz.* $\Delta_e = 0$). It is easy to show that in this case, $\mathfrak{D}(k_{\perp} \rho_e, \beta_e, \Delta_e) \leqslant 0$ if and only if

$$k_{\perp} \rho_e \geqslant \frac{2}{\sqrt{\pi}}. \tag{4.95}$$

Thus, for sufficiently large values of $k_{\perp} \rho_e$, KAWs cease to be able to propagate, and we obtain two purely damped non-propagating modes. Thus, any microinstabilities for $\Delta_e < 0$ associated with these modes can no longer be considered to be unstable KAWs. Substituting (4.95) into the threshold condition (4.91), we estimate that EST modes first become unstable when $\Delta_e < (\Delta_e)_c \approx -3/\beta_e$.

As Δ_e is decreased below $(\Delta_e)_c$, the EST modes quickly acquire a faster growth rate than all the other CES microinstabilities that can operate for such values of Δ_e. We illustrate this numerically in figure 27(*a*) by showing the maximum growth rate of all CES microinstabilities as a function of $(k_{\parallel}, k_{\perp})$ for a particular value of $\Delta_e < 0$. The EST modes with $k_{\parallel} \rho_e, k_{\perp} \rho_e > 1$ are the fastest growing, with $\gamma \gg \Omega_e/\beta_e$.

In the limit $|\Delta_e|\beta_e \gg 1$ (but $|\Delta_e|\beta_e \ll \beta_e^{2/7}$), the maximum growth rate of the EST instability can be estimated analytically. Adopting the orderings

$$k_{\parallel} \rho_e \sim \frac{1}{\sqrt{\log |\Delta_e|\beta_e}}, \quad k_{\perp} \rho_e \sim (|\Delta_e|\beta_e)^{1/2}, \quad \frac{\omega}{k_{\parallel} v_{\text{the}}} \sim |\Delta_e|^{5/2} \beta_e^{3/2}, \tag{4.96a–c}$$

it can be shown (see Appendix K.3.11) that the EST mode has the growth rate

$$\frac{\gamma}{\Omega_e} = \pi k_\parallel k_\perp^3 \rho_e^4 \left(|\Delta_e| - \frac{k_\perp^2 \rho_e^2}{\beta_e} \right) \left\{ 1 + \frac{\pi k_\perp^2 \rho_e^2}{k_\parallel^2 \rho_e^2} \left[4 \exp\left(-\frac{1}{k_\parallel^2 \rho_e^2} \right) + \sqrt{\pi} \mu_e^{1/2} k_\parallel^3 \rho_e^3 \right] \right\}^{-1},$$

(4.97)

where the term proportional to $\mu_e^{1/2}$ is associated with Landau damping on the ion species. Taking the subsidiary limit $k_\parallel \rho_e \ll 1/\sqrt{\log |\Delta_e| \beta_e}$, we recover (4.94). The EST mode's growth rate is, therefore, anticipated to be positive provided $k_\perp \rho_e < (|\Delta_e| \beta_e)^{1/2}$. It can then be shown that (4.97) has the approximate maximum value

$$\gamma_{\max} \approx \frac{6\sqrt{3}\pi}{25\sqrt{5}} (k_\parallel \rho_e)_{\text{peak}} \left[1 - \frac{3\pi^{3/2}}{5} \mu_e^{1/2} (k_\parallel \rho_e)_{\text{peak}} |\Delta_e| \beta_e \right] |\Delta_e| (|\Delta_e| \beta_e)^{3/2} \Omega_e, \quad (4.98)$$

at the wavenumbers

$$(k_\perp \rho_e)_{\text{peak}} = \left(\frac{3|\Delta_e| \beta_e}{5} \right)^{1/2}, \quad (4.99a)$$

$$(k_\parallel \rho_e)_{\text{peak}} = \frac{1}{\sqrt{\log (24\pi |\Delta_e| \beta_e/5)}} \left[1 - \frac{\log\log (24\pi |\Delta_e| \beta_e/5)}{\log 24\pi |\Delta_e| \beta/5} \right]. \quad (4.99b)$$

The growth rate (4.97) is plotted in figure 27(*b*) along with the numerically determined growth rate; reasonable agreement is found.

We note that, for perpendicular wavenumbers $k_\perp \rho_e \gtrsim \beta_e^{1/7}$, the characteristic quasi-perpendicular plasma modes in a Maxwellian plasma are not EST modes, but are instead whisper waves (see § 4.4.10). Therefore, when $|\Delta_e| \beta_e \gtrsim \beta_e^{2/7}$ (see (4.106)), the expressions (4.98) and (4.99a) for the EST mode's maximum growth rate and the perpendicular wavenumber at which that growth is attained are no longer valid. Instead, when $|\Delta_e| \beta_e \gtrsim \beta_e^{2/7}$, the fastest-growing EST modes (which coexist with faster-growing unstable whisper waves) are those close to the scale $k_\perp \rho_e \sim \Delta_e^{-1/5}$; extrapolating from (4.97), we find that $\gamma_{\max} \sim |\Delta_e|^{2/5} \Omega_e / \sqrt{\log |\Delta_e| \beta_e}$.

4.4.9. *Oblique transverse instability*

The transverse instability (whose physical mechanism was discussed in § 4.3.3) can be excited for sufficiently large negative electron pressure anisotropies as well as positive ones; however, when $\Delta_e < 0$, the fastest-growing modes are highly oblique with respect to the background magnetic field as opposed to parallel to it. In contrast to the $\Delta_e > 0$ case, the oblique transverse instability does not become the fastest-growing CES microinstability for all $\Delta_e \ll -\beta_e^{-1}$, only becoming so once its maximum growth rate exceeds the electron-Larmor frequency (which occurs when $\Delta_e \lesssim -\beta_e^{-1/3}$). While $\Delta_e > -\beta_e^{-1/3}$, the fastest-growing oblique transverse modes, which have $k_\perp \rho_e \sim (|\Delta_e| \beta_e)^{1/2}$, are confined to the parallel wavenumbers satisfying $k_\parallel \rho_e \gtrsim 1$. Their growth is outcompeted by the EST and whisper instabilities (see §§ 4.4.8 and 4.4.10, respectively), which have $k_\parallel \rho_e < 1$; this is illustrated numerically in figure 28(*a*) for a particular large, negative value of $\Delta_e \beta_e$.

As for their analytical characterisation, transverse modes have identical growth rates to those obtained in the $\Delta_e > 0$ case, given by (4.29a,b). For $\Delta_e < 0$, only the first mode can have positive growth, and such growth is only realised if $k_\perp > k_\parallel$. Now taking the
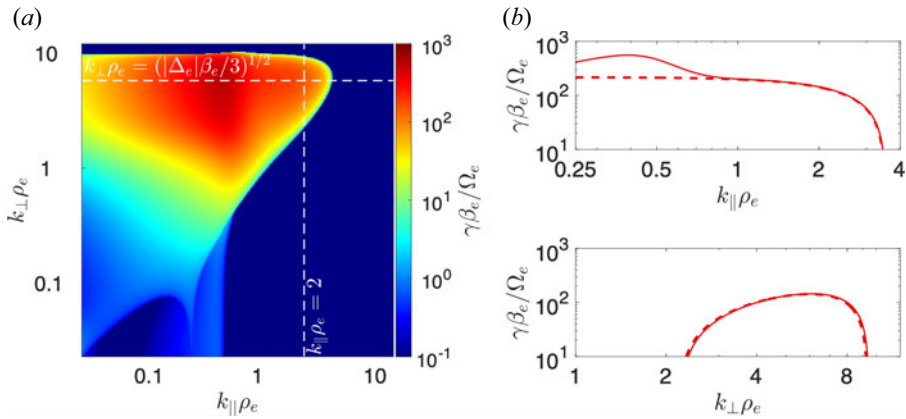
FIGURE 28. The CES oblique transverse instability. (*a*) Maximum positive growth rates of linear perturbations resulting from CE ion- and electron-shear terms in the CE distribution function (4.1) for $\Delta_e \beta = -100$ and $\beta_e = 10^4$. Here, a temperature-equilibrated hydrogen plasma is considered *viz.* $\Delta_e = \mu_e^{1/2} \Delta_i$, and $\beta_i = \beta_e$. The growth rates of all modes are calculated in the same way as figure 25. (*b*) Plot of the oblique transverse mode's growth rate (solid line) as a function of $k_\parallel \rho_e$ with $k_\perp \rho_e = (|\Delta_e| \beta_e / 3)^{1/2}$ (top), and as a function of $k_\perp \rho_e$ with $k_\parallel \rho_e = 2$ (bottom). The dotted and dashed lines show the analytical prediction (4.97).

quasi-perpendicular unmagnetised limit $k_\perp \rho_e \gg k_\parallel \rho_e \gg 1$, we find that this mode has the growth rate

$$\gamma \approx \frac{k_\perp v_{\text{the}}}{\sqrt{\pi}} \left(-\Delta_e - \frac{k_\perp^2 \rho_e^2}{\beta_e} \right). \tag{4.100}$$

This expression is mathematically identical to the parallel transverse instability (4.30) (§ 4.3.3), except with substitution $k_\parallel \rightarrow k_\perp$; the maximum growth rate of the oblique transverse instability is, therefore,

$$\gamma_{\text{max}} = \frac{2}{3\sqrt{3\pi}} (|\Delta_e| \beta_e)^{1/2} |\Delta_e| \Omega_e, \tag{4.101}$$

at the (perpendicular) wavenumber

$$(k_\perp \rho_e)_{\text{peak}} = \left(\frac{\Delta_e \beta_e}{3} \right)^{1/2}. \tag{4.102}$$

(4.100) is compared with the numerically determined growth rate in figure 28(*b*); we find that the approximation is excellent provided $k_\parallel \rho_e \gtrsim 1$.

We note that, based on our analysis, the oblique transverse mode is anticipated always to have a smaller growth rate than the EST instability (4.98) when $1 \ll |\Delta_e| \beta_e \lesssim \beta_e^{2/7}$:

$$\frac{\gamma_{\text{EST}}}{\gamma_{\text{trans}}} \sim \frac{|\Delta_e| \beta_e}{\sqrt{\log |\Delta_e| \beta_e}} \gg 1. \tag{4.103}$$

4.4.10. *Whisper instability*

When $\Delta_e \lesssim -\beta_e^{-5/7}$ (but $\Delta_e \gg -\beta_e^{-1/3}$), the dominant CES microinstability is the CES whisper instability. The instability is so named, because it consists in the destabilisation of the whisper wave, a plasma wave whose existence has not previously been identified:

it is therefore of some interest.[8] The likely reason for its previous neglect relates to the somewhat esoteric regime in which such a wave exists – a magnetised plasma with $\beta_e \gg 1$ that might naively be expected to support essentially unmagnetised perturbations at $k\rho_e \gg 1$. The energetically dominant magnetic component of the wave is perpendicular to both $\boldsymbol{k}$ and $\boldsymbol{B}_0$ (*viz.* δB_y), and the wave itself has no electron-number-density perturbation unless β_e is extremely large. Its operation (and also the operation of its instability in a CE plasma) involves both resonant and non-resonant interactions between electrons and the wave. More specifically, it is the non-resonant interaction of electrons at the edge of their Larmor orbits with the parallel electric field associated with the whisper wave that gives rise to the phase-shifted current perturbation necessary for wave propagation, while the primary damping mechanisms (Landau and Barnes' damping, respectively) of whisper waves are mediated by resonant wave–particle interactions. The physical mechanism of this wave and its instability (which is most clearly explored within the quasi-perpendicular limit of gyrokinetics) will be discussed further in a future paper.

We characterise the whisper instability's growth analytically in the limits $\mu_e^{1/2} \ll k_\parallel \rho_e \ll 1$, $k_\perp \rho_e \gg 1$ and $\Delta_e \beta_e \gg 1$ under the orderings

$$\tilde{\omega}_{e\parallel} = \frac{\omega}{k_\parallel v_{\mathrm{th}e}} \sim \frac{1}{\beta_e^{2/7}} \sim \frac{1}{k_\perp^2 \rho_e^2} \sim \frac{1}{\Delta_e \beta_e}, \quad k_\parallel \rho_e \sim \frac{1}{\sqrt{\log |\Delta_e|\beta_e}} \ll 1. \quad (4.104a,b)$$

It can be shown (see Appendix K.3.12) that such modes have complex frequencies

$$\frac{\omega}{\Omega_e} = -\mathrm{i}\left[\frac{\sqrt{\pi}}{2k_\parallel \rho_e} \exp\left(-\frac{1}{k_\parallel^2 \rho_e^2} \right) + \frac{k_\parallel \rho_e}{8\sqrt{\pi} k_\perp^2 \rho_e^2} \right]$$
$$\pm k_\parallel \rho_e \sqrt{ \frac{\sqrt{\pi}}{4} k_\perp \rho_e \left(\frac{k_\perp^2 \rho_e^2}{\beta_e} + \Delta_e \right) - \left[\frac{\sqrt{\pi}}{2k_\parallel^2 \rho_e^2} \exp\left(-\frac{1}{k_\parallel^2 \rho_e^2} \right) + \frac{1}{8\sqrt{\pi} k_\perp^2 \rho_e^2} \right]^2 }.$$
$$(4.105)$$

It is a simple matter to ascertain that the right-hand side of (4.105) is either purely real or purely imaginary, and thus modes are approximately either non-propagating with growth rate γ or purely oscillating with frequency ϖ. The dispersion curves $\varpi(k_\perp)$ and $\gamma(k_\perp)$ are plotted in figure 29. To interpret (4.105), we take subsidiary limits.

We first consider $1 \ll k_\perp \rho_e \sim (|\Delta_e|\beta_e)^{1/2} \ll \beta_e^{1/7}$. In this case, the second term in the square root is much larger than the first, so the expression for the '+' root simplifies to the dispersion relation (4.97) of the EST instability. However, when the perpendicular wavenumber (4.99a) of the EST instability's peak growth derived from (4.97) exceeds $(k_\perp \rho_e)_{\mathrm{peak}} \gtrsim 3^{1/7}2^{-5/7}\pi^{-3/14}\beta_e^{1/7} \approx 0.56\beta_e^{1/7}$, this simplification is no longer justifiable. Therefore, when so when

$$|\Delta_e|\beta_e \gtrsim \frac{5}{2^{10/7}3^{5/7}\pi^{3/7}} \beta_e^{2/7} \approx 0.52\beta_e^{2/7}, \quad (4.106)$$

(4.97) is no longer, in fact, a valid description of the EST mode's growth rate.

---

[8]We have named whisper waves as such because they always have a higher frequency than their whistler-wave counterparts, and, on account of their small characteristic scale, are likely to have lower amplitudes than whistlers. The analogy of a whistle to a whisper seemed apt to us.
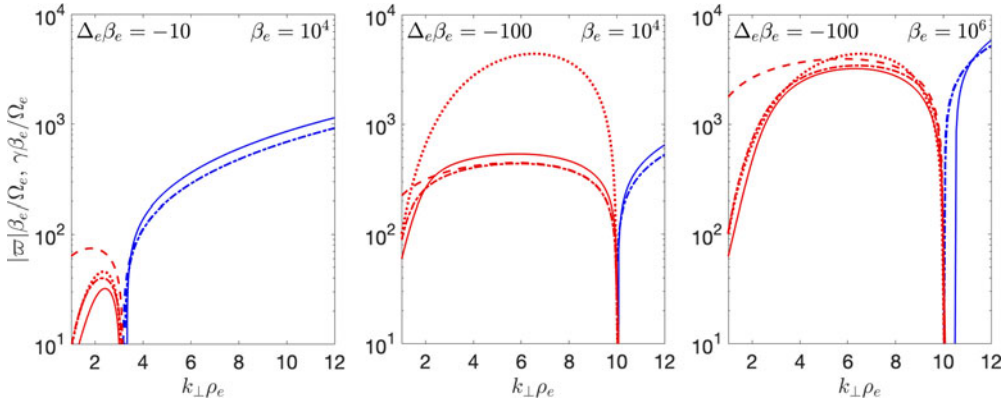
FIGURE 29. The CES EST vs whisper instability. Growth rates of EST and whisper modes whose instability is driven by the CE electron-shear term in the CE distribution function (4.1), for quasi-perpendicular ($k_\parallel \ll k_\perp$) wavevectors with respect to the background magnetic field. The growth rates (solid lines) of all modes are calculated in the same way as figure 25 for a selection of different values of $\Delta_e \beta_e$ and β_e, and $k_\parallel \rho_e = 0.35$. The approximations (4.97), (4.105), and (4.109) for the real frequency (dotted, dot-dashed and dashed blue, respectively) and growth rate (dotted, dot-dashed and dashed red, respectively) in the limit $k_\parallel \rho_e \ll 1$, $k_\perp \rho_e \gg 1$, are also plotted.

Now considering the subsidiary limit $k_\perp \rho_e \sim (|\Delta_e| \beta_e)^{1/2} \gg \beta_e^{1/7}$ and $k_\parallel \rho_e \ll 1/\sqrt{\log |\Delta_e| \beta_e}$ of (4.105), we find two propagating modes:

$$\frac{\omega}{\Omega_e} \approx \pm \frac{\pi^{1/4}}{2} k_\parallel \rho_e \sqrt{k_\perp \rho_e \left(\frac{k_\perp^2 \rho_e^2}{\beta_e} + \Delta_e \right)}. \qquad (4.107)$$

If we set $\Delta_e = 0$ in order to identify the underlying Maxwellian mode, this reduces to

$$\frac{\omega}{\Omega_e} \approx \pm \frac{\pi^{1/4}}{2} k_\parallel \rho_e \frac{(k_\perp \rho_e)^{3/2}}{\beta_e^{1/2}}. \qquad (4.108)$$

This dispersion relation, which does not coincide with any previously identified plasma wave, is that of the whisper wave.

The presence of this wave in the case of $\Delta_e < 0$ results in a purely unstable mode provided $\beta_e^{-1/7} \ll k_\perp \rho_e < (|\Delta_e| \beta_e)^{1/2}$ and retaining finite $k_\parallel \rho_e$. In this subsidiary limit, the growth rate of the instability is

$$\frac{\gamma}{\Omega_e} = -\frac{\sqrt{\pi}}{2 k_\parallel \rho_e} \exp \left(-\frac{1}{k_\parallel^2 \rho_e^2} \right)$$

$$\pm k_\parallel \rho_e \sqrt{ \frac{\sqrt{\pi}}{4} k_\perp \rho_e \left(|\Delta_e| - \frac{k_\perp^2 \rho_e^2}{\beta_e} \right) + \frac{\pi}{2 k_\parallel^4 \rho_e^4} \exp \left(-\frac{2}{k_\parallel^2 \rho_e^2} \right) }. \qquad (4.109)$$

This has the maximum value

$$\gamma_{\max} \approx \frac{\pi^{1/4}}{\sqrt{2}} (k_\parallel \rho_e)_{\text{peak}} (|\Delta_e| \beta_e)^{1/4} |\Delta_e|^{1/2} \Omega_e, \qquad (4.110)$$

at the wavenumbers

$$(k_\perp \rho_e)_{\text{peak}} = \left(\frac{|\Delta_e| \beta_e}{3} \right)^{1/2}, \tag{4.111a}$$

$$(k_\parallel \rho_e)_{\text{peak}} = \frac{2}{\sqrt{3 \log |\Delta_e| \beta_e}} \left[1 - \frac{4 \log 3 \, (\log |\Delta_e| \beta_e / 4)}{3 \log |\Delta_e| \beta_e} \right]. \tag{4.111b}$$

Thus, the maximum growth rate of whisper instability has different scalings with $|\Delta_e|$ and β_e than either the EST instability (4.98) or the oblique transverse instability (4.101). When $|\Delta_e| \beta_e \gtrsim \beta_e^{2/7}$, (4.105) implies that the growth rate γ continues to increase beyond the maximum value of $k_\perp \rho_e$ at which the EST modes can exist, and thus the whisper instability, if it is operating, is always dominant over the EST instability. Whether it is also dominant over the oblique transverse instability depends on the choice of β_e and Δ_e. We can quantify this explicitly, by considering the ratio of the oblique transverse instability's growth rate (4.101) to that of the whisper instability

$$\frac{\gamma_{\text{trans}}}{\gamma_{\text{whisper}}} \sim \sqrt{\log (|\Delta_e| \beta_e)} \, (|\Delta_e| \beta_e)^{1/4} |\Delta_e|^{1/2}. \tag{4.112}$$

We see that for $|\Delta_e|^3 \beta_e \ll 1$, $\gamma_{\text{trans}} \ll \gamma_{\text{whisper}}$. Thus for $|\Delta_e|^{-7/5} \ll \beta_e \ll |\Delta_e|^{-3}$, the whisper instability dominates. This condition certainly holds for the particular value of Δ_e considered in figure 28; to support our claim, in figure 30(*a*) we plot the analytical approximation (4.109) along with the numerically determined growth rate for the fixed values of $k_\perp \rho_e$ and $k_\parallel \rho_e$, respectively, at which the whisper instability is predicted to achieve its maximum growth. The growth rate of the whisper instability, which is correctly captured by our analytic approximation, does indeed exceed that of the transverse instability by an appreciable factor.

For $\beta_e \gtrsim |\Delta_e|^{-3}$, (4.110) implies that, in fact, $\gamma/k_\parallel v_{\text{th}e} \sim 1$. This violates the condition of validity of the method that we have generally used to evaluate CES microinstability growth rates numerically (see § 2.5.8, and also Appendix K). The divergence of the true growth rates (calculated by solving the full hot-plasma dispersion relation numerically) from those arising from the solution of the low-frequency ($\omega \ll k_\parallel v_{\text{th}e}$) dispersion relation (K23) for increasing β_e is illustrated in figure 30(*b*). For $\gamma \gtrsim \Omega_e$, we find that the distinction between $k_\parallel \rho_e < 1$ modes and $k_\parallel \rho_e > 1$ modes vanishes; furthermore, the fastest-growing modes (including the modes with $k_\parallel = 0$) come to resemble the transverse instability when $\beta_e \gg |\Delta_e|^{-3}$; this feature, which indicates the emergence of yet another distinct CES instability, is discussed in the next section.

4.4.11. *Ordinary-mode instability*

The final instability we consider in this paper is the CES ordinary-mode (electromagnetic) instability: the destabilisation of the ordinary mode at sub-electron-Larmor scales by negative electron-pressure anisotropy. The bi-Maxwellian equivalent of the instability was first identified by Davidson & Wu (1970); for a more recent linear study of the instability, see Ibscher *et al.* (2012). For the characteristically small electron-pressure anisotropies that are associated with the CE electron-shear term, this instability can only arise at very large values of β_e. For purely perpendicular modes ($k_\parallel = 0$) in a magnetised plasma, resonant wave–particle interactions cannot arise, and so the ordinary-mode's instability mechanism is non-resonant.

The CES ordinary-mode instability is most simply characterised by considering modes that are exactly perpendicular to the guide magnetic field (*viz.* $k_\parallel = 0$). In this case, it can
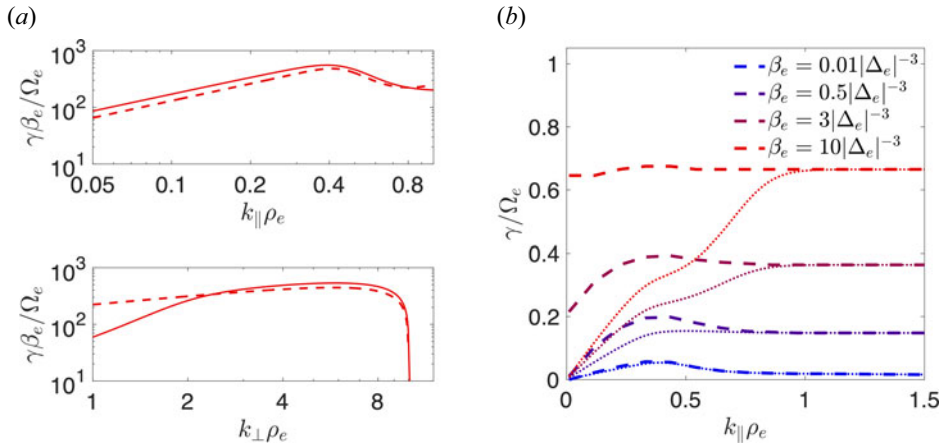
(*a*) (*b*)

FIGURE 30. The CES whisper instability. (*a*) Plot of the whisper instability's growth rate as a function of $k_\parallel \rho_e$ with $k_\perp \rho_e = (|\Delta_e|\beta_e/3)^{1/2}$ (top), and as a function of $k_\perp \rho_e$ with $k_\parallel \rho_e = (k_\parallel \rho_e)_{\text{peak}}$ (bottom), where $(k_\parallel \rho_e)_{\text{peak}}$ is given by (4.111*b*), for $\Delta_e \beta = -100$ and $\beta_e = 10^4$ (cf. figure (28)). The numerically determined value of this quantity is calculated in the same way as figure 25. The dotted and dashed lines show the analytical prediction (4.109). (*b*) Divergence of growth rates (dotted lines) arising from using the approach outlined in Appendix K (which involves solving a simplified 'low-frequency' dispersion relation) as compared with the full hot-plasma dispersion relation (dashed lines) when $\beta_e \sim |\Delta_e|^{-3}$. Here, $\Delta_e = -0.01$, $k_\perp \rho_e = (|\Delta_e|\beta_e/3)^{1/2}$ and β_e is varied. For reference, $\beta_e = 0.01|\Delta_e|^{-3} = 10^4$ corresponds to the same values of β_e and Δ_e as considered in figure 28.

be shown (see Appendix K.3.13) that, if the ordinary mode is destabilised, its growth rate is given by the equation

$$\sum_{n=1}^{\infty} \frac{2\gamma^2}{\gamma^2 + n^2 \Omega_e^2} \exp\left(-\frac{k_\perp^2 \rho_e^2}{2}\right) I_n\left(\frac{k_\perp^2 \rho_e^2}{2}\right) = -\Delta_e - k_\perp^2 d_e^2 - \exp\left(-\frac{k_\perp^2 \rho_e^2}{2}\right) I_0\left(\frac{k_\perp^2 \rho_e^2}{2}\right).$$
(4.113)

This dispersion relation is very similar to that derived by Davidson & Wu (1970) for the ordinary-mode instability in the case of a bi-Maxwellian distribution. If the electron-pressure anisotropy is insufficient to destabilise the ordinary mode, the mode is undamped, and its real frequency satisfies

$$\sum_{n=1}^{\infty} \frac{2\varpi^2}{n^2 \Omega_e^2 - \varpi^2} \exp\left(-\frac{k_\perp^2 \rho_e^2}{2}\right) I_n\left(\frac{k_\perp^2 \rho_e^2}{2}\right) = \Delta_e + k_\perp^2 d_e^2 + \exp\left(-\frac{k_\perp^2 \rho_e^2}{2}\right) I_0\left(\frac{k_\perp^2 \rho_e^2}{2}\right).$$
(4.114)

The dispersion curves $\varpi(k_\perp)$ and $\gamma(k_\perp)$ for a selection of different values of β_e and at fixed Δ_e are shown in figure 31.

We can use the ordinary-mode dispersion relation (4.113) to derive the threshold for this instability at exactly perpendicular wavevectors. We note that the left-hand side of (4.113) is strictly positive; thus for solutions to exist, it is required that there exist a range of perpendicular wavenumbers over which the right-hand side of (4.113) is also positive. For $k_\perp \rho_e \lesssim 1$, the right-hand side is always negative because $|\Delta_e| \ll 1$. We therefore consider
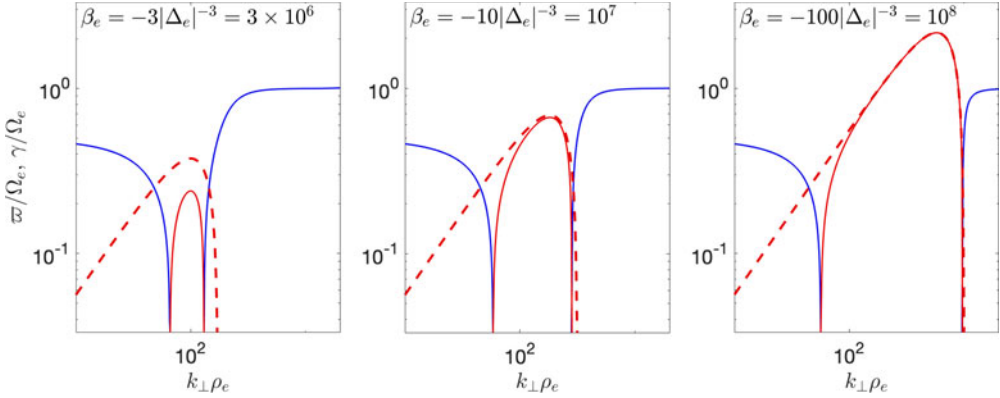
FIGURE 31. The CES ordinary-mode instability. Growth rates of ordinary modes whose instability is driven by the CE electron-shear term in the CE distribution function (4.1), for perpendicular ($k_{\parallel} = 0$) wavevectors with respect to the background magnetic field. The growth rates (solid lines) of the modes are calculated using (4.113) and (4.114). We show the growth rates for a selection of different values of β_e and for $\Delta_e = 0.01$. The approximation (4.121) of the growth rate in the limit $k_{\perp}\rho_e \gg \gamma/\Omega_e \gg 1$ is also plotted (dashed red).

the limit $k_{\perp}\rho_e \gg 1$ (assuming $\gamma \sim \Omega_e$), for which

$$\frac{1}{\sqrt{\pi}k_{\perp}\rho_e} \sum_{n=1}^{\infty} \frac{2\gamma^2}{\gamma^2 + n^2\Omega_e^2} \approx |\Delta_e| - \frac{k_{\perp}^2\rho_e^2}{\beta_e} - \frac{1}{\sqrt{\pi}k_{\perp}\rho_e}. \tag{4.115}$$

The right-hand side of (4.115) is maximal when

$$k_{\perp}\rho_e = \left(\frac{\beta_e}{2\sqrt{\pi}}\right)^{1/3}, \tag{4.116}$$

and, when maximal, also greater than zero if and only if

$$|\Delta_e|^3\beta_e > \frac{27}{4\pi}. \tag{4.117}$$

Therefore the threshold (4.117) is a necessary condition for a purely perpendicular instability to exist. It is also a sufficient condition, because the left-hand side of (4.115) becomes arbitrarily small for small γ. Comparing the threshold (4.117) with figure 30(*b*), we conclude that the emergence of an instability with a purely perpendicular wavenumber at around $\beta_e \sim |\Delta_e|^{-3}$ is consistent with numerical expectations. In the limit $\beta_e \gg \Delta_e^{-3}$, all modes whose perpendicular wavenumbers satisfy

$$\sqrt{\pi}|\Delta_e|^{-1} < k_{\perp}\rho_e < (|\Delta_e|\beta_e)^{1/2} \tag{4.118}$$

are unstable.

One can also show analytically that for $\gamma \gg \Omega_e$, these unstable ordinary modes grow at the same rate as unstable oblique transverse modes (§ 4.4.9). Motivated by the fact that $\gamma \ll k_{\perp}v_{\text{th}e}$ for the oblique transverse instability, or, equivalently, $\gamma/\Omega_e \ll k_{\perp}\rho_e$, we first consider (4.113) in the limit $k_{\perp}\rho_e \gg \gamma/\Omega_e \sim 1$; we will subsequently take the subsidiary

limit $\gamma/\Omega_e \gg 1$. The relevant dispersion relation is (4.115), which can be rewritten as

$$\frac{1}{\sqrt{\pi}k_\perp\rho_e}\left[\frac{\gamma\pi}{\Omega_e}\coth\left(\frac{\gamma\pi}{\Omega_e}\right) - 1\right] \approx -\Delta_e - \frac{k_\perp^2\rho_e^2}{\beta_e} - \frac{1}{\sqrt{\pi}k_\perp\rho_e}, \qquad (4.119)$$

using the summation identity

$$\sum_{n=1}^{\infty}\frac{2\gamma^2}{\gamma^2 + n^2\Omega_e^2} = \frac{\gamma\pi}{\Omega_e}\coth\left(\frac{\gamma\pi}{\Omega_e}\right) - 1. \qquad (4.120)$$

Now assuming $\gamma \gg \Omega_e$ and using $\coth x \approx 1$ for any number $x \gg 1$, we deduce

$$\frac{\gamma}{\Omega_e} = -\frac{k_\perp\rho_e}{\sqrt{\pi}}\left(\Delta_e + \frac{k_\perp^2\rho_e^2}{\beta_e}\right), \qquad (4.121)$$

which is equivalent to (4.100). Since $|\Delta_e| \ll 1$, our result is consistent with our initial assumption $\gamma/\Omega_e \ll k_\perp\rho_e$. We note that, at wavenumbers that do not satisfy (4.118), ordinary modes and oblique transverse modes behave quite differently: such ordinary modes have real frequencies and are neither growing nor damped, whereas transverse modes remain non-propagating.

In summary, we conclude that, when $\beta_e \gg |\Delta_e|^{-3}$, the CES ordinary-mode instability is the dominant CES microinstability, but that in this limit, the fastest growing unstable modes are essentially identical to the unstable unmagnetised oblique transverse modes already described in § 4.4.9.

5. Discussion and conclusions

In this paper, we have shown that the CE description of classical, collisional plasma is valid for a wide range of plasma conditions. Microinstabilities are stabilised in such plasmas by two effects: collisional damping of instabilities, or β-dependent thresholds arising from a non-zero macroscopic magnetic field. In particular, we have demonstrated that predictions for transport based on the CE theory should not fail on account of kinetic instabilities in a collisional plasma whose constituent ions and electrons are strongly magnetised and that has $\beta \lesssim 1$. By identifying the stable region for the leading-order corrections in the CE expansion, we have *de facto* identified the stable region for corrections to arbitrary order: if one of the above effects is enough to maintain stability, any perturbations arising from smaller corrections will be unable to overcome the same effect. However, we have also demonstrated that for plasmas with $\beta \gg 1$ there exists a significant region of the $(d_e/L, \lambda/L)$ parameter space in which fast, small-scale instabilities are both possible and, in fact, generic. Indeed, in the strongly magnetised plasmas (that is, $\rho_s \ll \lambda_s$ for both electrons and ions) on which we have focused our investigation, it transpires that collisional damping is never able to prevent the most important kinetic instabilities, and thus strongly magnetised, high-β plasmas cannot be modelled by standard CE theory if $\lambda/L \gtrsim 1/\beta$. This finding has significant implications for our understanding of various plasma environments, including those found in astrophysical contexts and also those created in laser-plasma experiments on high-energy laser facilities.

When kinetic instabilities do arise in a CE plasma, we claim that we have characterised the most significant of them systematically. Using an analytical approach based on asymptotic methods, we have been able to derive simple expressions for the thresholds and growth rates of these kinetic instabilities in terms of basic parameters such as β, λ/L and the mass ratio $\mu_e = m_e/m_i$. Three of the instabilities – the CET whistler instability

(§ 3.3.1), the CET slow-wave instability (§ 3.3.3), and the CET long-wavelength KAW instability (§ 3.3.4) – are driven by heat fluxes in a CE plasma, while the remaining ten – the CES mirror instability (§ 4.3.1), the CES whistler instability (§ 4.3.2), the CES transverse instability (§§ 4.3.3 and 4.4.9), the CES electron mirror instability (§ 4.3.4), the CES firehose instability (§§ 4.4.2, 4.4.3, 4.4.4, and 4.4.5), the CES parallel and oblique electron firehose instabilities (§§ 4.4.6 and 4.4.7, respectively), the CES EST instability (§ 4.4.8), the CES whisper instability (§ 4.4.10) and the CES ordinary-mode instability (§ 4.4.11) – are driven by ion- and/or electron-velocity shears. While many of these instabilities, or versions thereof, had been considered previously, four of them (the CET slow-wave, CET long-wavelength KAW, CES EST and CES whisper instabilities) are new; the whisper instability in particular seems to be of some interest both conceptually and practically, because it is associated with a newly discovered plasma wave (the whisper wave), and the instability is much faster than its competitors over quite a wide range of values of λ/L and β. The consequences of the existence of the whisper (and EST) instabilities for astrophysical and laser plasmas, in particular for magnetic-field generation, will be addressed in future work.

An important question to address is that of the dominant microinstability overall: in a given plasma (with fixed d_e/L, λ/L and β), amongst the many instabilities that we have found, which is the dominant one? As we explained in § 2.2.3, the answer to this question depends on assumptions about the relative magnitude of temperature- and velocity-gradient scale lengths L_T and L_V. Here, we assume $Ma\,\lambda/L_V$ to be large enough to trigger all of the aforementioned instabilities, and also adopt the scalings (2.55) in § 2.2.3 for a CE plasma whose largest-scale fluid motions are sonic ($Ma \lesssim 1$). As we discussed in the final paragraph of § 2.2.3, our first assumption (which necessitates that $\beta_i \gg \epsilon_i^{-1}$) in fact supports our second one. We then find that the three most competitive ones are on electron scales: the CET whistler, CES whisper and transverse instabilities. These have growth rates (see (3.10), (4.31) and (4.110), respectively)

$$\gamma_{\text{whistler},T} \sim \eta_e \Omega_e \sim \mu_e^{1/4} Ma \frac{\lambda_i}{L_V} \Omega_e, \tag{5.1a}$$

$$\gamma_{\text{whisper}} \sim \frac{|\epsilon_e|^{3/4} \beta_e^{1/4}}{\left[\log |\epsilon_e \beta_e|\right]^{1/2}} \Omega_e \sim \left(\frac{\lambda_i}{L_V}\right)^{3/4} \frac{\mu_e^{3/8} Ma^{3/4} \beta_e^{1/4}}{\left[\log\left(\mu_e^{1/2} \beta_e Ma\,\lambda_i/L_V\right)\right]^{1/2}} \Omega_e, \tag{5.1b}$$

$$\gamma_{\text{trans}} \sim \epsilon_e^{3/2} \beta_e^{1/2} \Omega_e \sim \mu_e^{3/4} \left(\frac{\lambda_i}{L_V}\right)^{3/2} \beta_e^{1/2} \Omega_e. \tag{5.1c}$$

Although the threshold for the CET whistler instability is less restrictive than for the whisper instability, at the whisper instability threshold $|\epsilon_e|\beta_e \sim \beta_e^{2/7} \sim |\epsilon_e|^{-2/5}$ it follows that

$$\frac{\gamma_{\text{whistler},T}}{\gamma_{\text{whisper}}} \sim \frac{\eta_e \left[\log \epsilon_e \beta_e\right]^{1/2}}{\epsilon_e^{2/5}} \sim \mu_e^{1/20} \left(\frac{\lambda_i}{L_V}\right)^{3/5} \left[\log\left(\mu_e^{1/2} \beta_e Ma\,\lambda_i/L_V\right)\right]^{1/2} \ll 1. \tag{5.2}$$

Thus, the fact that CE plasmas typically support fluid motions on smaller scales than temperature gradients (see § 2.2.3) implies that CES microinstabilities are more potent at sufficiently high plasma β_e. Yet, for $\beta_e \lesssim \mu_e^{-1/2} Ma^{-1} L_V/\lambda_i$, the CET whistler instability is the most rapidly growing microinstability. Finally, for $\beta_e \lesssim \mu_e^{-1/4} Ma^{-1} L_V/\lambda_i$, none of these electron-scale instabilities is triggered at all, with only the ion-scale firehose and mirror instabilities operating. In short, the dominant microinstability is a

complicated function of the parameter regime. For reference, in table 2 of § 1 we show the (approximate) growth rates for all of the instabilities considered in this paper if the scalings (2.55) are adopted, and figure 1 shows a schematic stability map for the same case.[9]

We believe that our study – which is the first systematic investigation of the kinetic stability of a classical, collisional, magnetised plasma – provides a significant step forward towards a comprehensive understanding of this state of matter. It is perhaps inevitable, however, given the conceptual extent of the problem, that there remain a number of questions concerning the stability of the CE distribution function that we have not addressed here. In terms of linear theory, a numerical study using a better collision operator to find the exact stability boundaries could be usefully carried out – although we do not anticipate that this would lead to an alteration of the basic scalings of those boundaries derived in this paper. Another issue not addressed by this work is that of linear coupling between CET and CES microinstabilities; it is not immediately obvious to what extent microinstabilities with similar growth rates might aid each other's growth. The analysis could also be extended to two-species plasmas not in thermal equilibrium, as well as high-Z_i plasmas (with important applications in laser-plasma physics). Numerical simulations using collisional particle-in-cell or Vlasov codes could be employed to confirm the validity of the predictions made in this paper. Another possible research direction that could prove to be fruitful concerns the application of thermodynamic arguments to CE microinstabilities, such as those propounded by Fowler (1968) and more recently by Helander (2017). Such arguments have previously been used to derive bounds on growth rates, and also the amplitude that unstable electrostatic fluctuations can attain in magnetised plasmas. While the use of analogous arguments to characterise CE microinstabilities would require a generalisation of those arguments to include electromagnetic fluctuations, this may not be too challenging for microinstabilities such as the whisper instability that can be described by reduced models (e.g. gyrokinetics).

Perhaps the most interesting future development of this work would be the determination of transport coefficients for plasmas falling into the unstable regimes. This requires quasi-linear or nonlinear treatment. Nonetheless, the results presented here can be seen as both a guide and a warning to those wishing to address this fundamental question. They are a guide in the sense that a correct characterisation of transport coefficients requires knowledge of the fastest-growing linear modes, which our study provides. But they are also as a warning in that an isolated treatment of one type of microinstability without reference to the full range of possible others could lead to a mischaracterisation of transport properties. The best hope for a correct calculation of transport in a weakly collisional, high-β plasma is, therefore, the following programme: for a plasma with particular conditions, identify the fastest microinstability, calculate the saturated magnitude of the fluctuations produced by it, determine the anomalous transport coefficients with those fluctuations present, re-calculate of the stability of this plasma and so on, until a self-consistent picture emerges. It is likely that such a picture will involve a distribution function whose underlying nature depends on macroscopic motions, and hence transport coefficients that are themselves properties of flow shear, temperature gradients and large-scale magnetic fields. Carrying out such calculations is a non-trivial task, but not impossible.

---

[9]A note of caution is warranted: if a CE plasma is unstable to microinstabilities, then the heat fluxes and rate-of-strain tensors will be modified, potentially altering both L_T and L_V. There is no *a priori* reason to think that such a plasma will obey Braginskii-type scalings of the form (2.55) – and so using this ordering to estimate microinstability growth rates is incorrect in kinetically unstable CE plasmas.

Acknowledgements

A.F.A.B. would like to express his deepest gratitude to M. Kunz and E. Quataert for many helpful discussions about the paper generally, for highlighting some important considerations pertaining to the linear theory of the firehose instability, and for their ongoing support, without which this paper would never have been completed. All the authors would also like to thank A. Spitkovsky for bringing several key early papers on CE microinstabilities to the authors' attention. In addition, the authors are grateful to the two anonymous reviewers, whose recommendations have improved the paper.

Editor Dmitri Uzdensky thanks the referees for their advice in evaluating this article.

Funding

Declaration of interests

The authors report no conflict of interest.

Appendix A. Glossary of notation used in the paper

As an aid to reading, we provide a glossary of the notation that we use in our paper in tables 5 and 6 of this appendix.

Appendix B. Derivation of the Chapman–Enskog distribution function

B.1. *The Chapman–Enskog expansion in strongly magnetised plasma*

There exist a number of lucid explanations of how the CE distribution functions (2.8) arise in a collisional, strongly magnetised two-species electron–ion plasma ($\rho_s \ll \lambda_s$ for $s = i, e$) – the monograph of Braginskii (1965), but also (for example) Helander & Sigmar (2005), Chapter 4. For that reason, we do not provide a full derivation of (2.8). However, in this appendix, we describe a calculation that allows for a direct derivation of the CE distribution function for a strongly magnetised collisional plasma, without first having to perform the CE expansion for arbitrary values of ρ_s/λ_s.

The first part of the calculation is the same as in Helander & Sigmar (2005, pp. 76–78). For the reader's convenience, we present a summarised version. We consider the Maxwell–Vlasov–Landau equation (2.1) of species s in a frame co-moving with the fluid rest frame of that species. Defining the peculiar velocity variable $\boldsymbol{v}'_s = \boldsymbol{v} - \boldsymbol{V}_s$ in the fluid rest frame, (2.1) becomes

$$\frac{\mathrm{D}f_s}{\mathrm{D}t} + \boldsymbol{v}'_s \cdot \nabla f_s + \left[\frac{Z_s e}{m_s} \left(\boldsymbol{E}' + \frac{\boldsymbol{v}'_s \times \boldsymbol{B}}{c} \right) - \frac{\mathrm{D}\boldsymbol{V}_s}{\mathrm{D}t} \right] \cdot \frac{\partial f_s}{\partial \boldsymbol{v}'_s} - \boldsymbol{v}'_s \cdot \nabla \boldsymbol{V}_s \cdot \frac{\partial f_s}{\partial \boldsymbol{v}'_s} = \sum_{s'} \mathfrak{C}(f_s, f_{s'}),$$
(B1)

where $\boldsymbol{E}' \equiv \boldsymbol{E} + \boldsymbol{V}_s \times \boldsymbol{B}/c$ is the electric field measured in the moving frame, and

$$\frac{\mathrm{D}}{\mathrm{D}t} \equiv \frac{\partial}{\partial t} + \boldsymbol{V}_s \cdot \nabla,$$
(B2)

Notation	Quantity
$\boldsymbol{r}$	Spatial position
t	Time
e	Elementary charge
c	Speed of light
Z_s	Charge of species s ($s = i$ in two-species plasma) in units of e
m_s	Mass of a particle of species s
$\mu_e = m_e/m_i$	Electron-to-ion mass ratio
$\boldsymbol{E}$	Electric field
$\boldsymbol{B}$	Magnetic field
$\boldsymbol{B}_0$	Macroscopic magnetic field
$\hat{z}$	Direction vector of the macroscopic magnetic field
$\boldsymbol{v}\ (\boldsymbol{v}_\perp)$	Particle velocity (in the direction perpendicular to $\boldsymbol{B}_0$)
$v\ (v_\perp)$	Particle speed (in the direction perpendicular to $\boldsymbol{B}_0$)
$v_\parallel$	Particle velocity in the direction parallel to $\boldsymbol{B}_0$
ϕ	Gyrophase angle
$f_s(\boldsymbol{r}, \boldsymbol{v}, t)$	Distribution function of particles of species s
$\mathfrak{C}(f_s, f_{s'})$	Collision operator for interactions between species s and s'
n_s	Density of particles of species s (2.3a)
V_s	Bulk fluid velocity of particles of species s (2.3b)
T_s	Temperature of particles of species s (2.3c)
$p_s\ (p_{s\parallel}/p_{s\perp})$	(Parallel/perpendicular) pressure of particles of species s (2.6a), (2.33)
$\boldsymbol{\pi}_s$	Viscosity tensor of particles of species s (2.6b)
$\Delta_s = (p_{s\perp} - p_{s\parallel})/p_s$	Pressure anisotropy of particles of species s (2.35)
$\boldsymbol{q}_s\ (q_{s\parallel})$	(Parallel) heat flux of particles of species s (2.6c), (2.16)
$\boldsymbol{R}_s\ (R_{s\parallel})$	(Parallel) frictional force on species s due to collisions (2.6d)
$\mathcal{Q}_s$	Heating rate due to inter-species collisions (2.6e)
$\boldsymbol{u}_{ei}\ (u_{ei\parallel})$	(Parallel) relative electron–ion drift
$v_{\text{th}s}$	Thermal speed of particles of species s
$\boldsymbol{v}_s' = \boldsymbol{v} - V_s$	Peculiar velocity of particles of species s
$v_{s\parallel}'\ (\boldsymbol{v}_{s\perp}')$	Peculiar parallel (perpendicular) velocity of particles of species s
$\tilde{\boldsymbol{v}}_s = (\boldsymbol{v} - V_i)/v_{\text{th}s}$	Non-dimensionalised particle velocity in ion-fluid rest frame
$\tilde{v}_{s\parallel}$	Non-dimensionalised parallel particle velocity, ion-fluid rest frame
$\tilde{v}_s\ (\tilde{v}_{s\perp})$	Non-dim. (perpendicular) particle speed, ion-fluid rest frame
λ_s	Mean free path of species s
$\rho_s\ (\tilde{\rho}_s)$	(Signed) Larmor radius of species s
τ_s	Collision time of species s
$\Omega_s\ (\tilde{\Omega}_s)$	(Signed) Larmor frequency of species s
L	Macroscopic length scale of variation in the direction parallel to $\boldsymbol{B}_0$
$L_T\ (L_{T_i})$	Electron-(ion)-temperature length scale parallel to $\boldsymbol{B}_0$ (2.13a,b)
$L_V\ (L_{V_e})$	Ion-(electron)-bulk-flow length scale parallel to $\boldsymbol{B}_0$ (2.13c,d)
τ_L	Macroscopic time scale over which CE distribution varies
$\eta_e = \eta_e^T$	Small parameter (2.11a) $\propto$ CE electron-temperature-gradient term
η_e^R	Small parameter (2.11b) $\propto$ CE electron-friction term
η_e^u	Small parameter (2.11c) $\propto$ CE electron–ion-drift term
η_i	Small parameter (2.11d) $\propto$ CE ion-temperature-gradient term
ϵ_e	Small parameter (2.11e) $\propto$ CE electron-shear term
ϵ_i	Small parameter (2.11f) $\propto$ CE ion-shear term
$A_e^T(\tilde{v}_e)$	Function arising in CE electron-temperature-gradient term
$A_e^R(\tilde{v}_e)$	Function arising in CE electron-friction term
$A_e^u(\tilde{v}_e)$	Function arising in CE electron–ion-drift term
$A_i(\tilde{v}_i)$	Function arising in CE ion-temperature-gradient term
$C_e(\tilde{v}_e)$	Function arising in CE electron-shear term
$C_i(\tilde{v}_i)$	Function arising in CE ion-shear term

TABLE 5. Glossary of notation I.

Notation	Quantity
$\boldsymbol{W}_s$	Traceless rate-of-strain tensor of species s (2.12)
$Ma = V_i/v_{\mathrm{th}i}$	Mach number
$\log \Lambda_{\mathrm{CL}}$	Coulomb logarithm
$\kappa_e^{\parallel}$ ($\kappa_i^{\parallel}$)	Parallel electron (ion) thermal conductivity (2.21) (2.27)
$\chi = 2\kappa_e^{\parallel}/3n_e$	Parallel thermal diffusivity
μ_{vs}	Dynamic viscosity of particles of species s
$\nu = \mu_{vi}/m_i n_i$	Kinematic viscosity
τ_{ie}^{eq}	Ion–electron-temperature equilibration time
d_s	Inertial scale of particles of species s (2.58b)
λ_{D}	Debye length (2.58c)
β_s	Plasma beta of particles of species s (2.57)
$\omega_{\mathrm{p}s}$	Plasma frequency of particles of species s (2.78)
$f_{s0}(\tilde{v}_{s\parallel}, \tilde{v}_{s\perp})$	Equilibrium distribution function of particles of species s
$\tilde{f}_{s0}(\tilde{v}_{s\parallel}, \tilde{v}_{s\perp})$	Renormalised equilibrium dist. func. of particles of species s (2.83)
$\delta\boldsymbol{E}$	Microscale electric-field perturbation
$\delta\boldsymbol{B}$	Microscale magnetic-field perturbation
$\widehat{\delta\boldsymbol{E}}$	Fourier component of $\delta\boldsymbol{E}$
$\widehat{\delta\boldsymbol{B}}$	Fourier component of $\delta\boldsymbol{B}$
$\boldsymbol{k}$ ($\boldsymbol{k}_\perp$)	(Perpendicular) wavevector of electromagnetic perturbation
k ($k_\parallel/k_\perp$)	(Parallel/perpendicular) wavenumber of electromagnetic perturbation
$\hat{\boldsymbol{k}}$ ($\hat{\boldsymbol{x}}$)	(Perpendicular) wavevector direction
$\hat{\boldsymbol{y}}$	Direction perpendicular to both $\hat{\boldsymbol{x}}$ and $\hat{\boldsymbol{z}}$
θ	Wavevector angle
ω	Complex frequency of electromagnetic perturbation
ϖ	Real frequency of electromagnetic perturbation
γ	Growth rate of electromagnetic perturbation
$\tilde{\omega}_{s\parallel} = \omega/|k_\parallel|v_{\mathrm{th}s}$	Ratio of complex frequency to parallel streaming rate (2.81)
$\hat{\omega}_{s\parallel} = \tilde{\omega}_{s\parallel} + \mathrm{i}/|k_\parallel|\lambda_s$	Modified frequency-to-streaming-rate ratio (2.124)
$\boldsymbol{I}$	Unit dyadic
$\mathfrak{E}$	Plasma dielectric tensor (2.74)
$\mathfrak{E}_s$	Contribution of species s to $\mathfrak{E}$
$\boldsymbol{\sigma}$	Plasma conductivity tensor (2.77)
$\boldsymbol{\sigma}_s$	Contribution of species s to $\boldsymbol{\sigma}$
C_L	Landau contour
$\zeta_{sn} = \tilde{\omega}_{s\parallel} - n/|k_\parallel|\tilde{\rho}_s$	Resonant non-dimensionalised velocity (2.82)
$\tilde{w}_{s\parallel} = k_\parallel \tilde{v}_{s\parallel}/|k_\parallel|$	Non-dimensionalised parallel particle velocity (2.79)
$\Lambda_s(\tilde{w}_{s\parallel}, \tilde{v}_{s\perp})$	Velocity-space anisotropy of distribution function (2.84)
$\Xi_s(\tilde{w}_{s\parallel}, \tilde{v}_{s\perp})$	Velocity-space integrand of conductivity tensor (2.85)
$\mathfrak{E}^{(0)}$	Leading-order term in expansion of $\mathfrak{E}$ in $\tilde{\omega}_{s\parallel} \ll 1$
$\mathfrak{E}^{(1)}$	First-order correction in expansion of $\mathfrak{E}$ in $\tilde{\omega}_{s\parallel} \ll 1$
$\boldsymbol{M}_s$	Maxwellian component of $\mathfrak{E}_s$ – see (2.97)
$\boldsymbol{P}_s$	Non-Maxwellian component of $\mathfrak{E}_s$ – see (2.97)
$\boldsymbol{M}_s^{(0)}$ ($\boldsymbol{P}_s^{(0)}$)	Leading-order term in expansion of $\boldsymbol{M}_s$ ($\boldsymbol{P}_s$) in $\tilde{\omega}_{s\parallel} \ll 1$
$\boldsymbol{M}_s^{(1)}$	First-order correction in expansion of $\boldsymbol{M}_s$ in $\tilde{\omega}_{s\parallel} \ll 1$
$\{\boldsymbol{e}_1, \boldsymbol{e}_2, \boldsymbol{e}_3\}$	Coordinate basis (2.103a–c)
$\widehat{\delta\boldsymbol{E}}_T = \widehat{\delta\boldsymbol{E}} \cdot (\boldsymbol{I} - \hat{\boldsymbol{k}}\hat{\boldsymbol{k}})$	Transverse electric-field perturbation
$Z(z)$	Plasma dispersion function (2.123)
$F(x, y), G(x, y), H(x, y)$	Special mathematical functions (2.122)
$L(x, y), N(x, y)$	Special mathematical functions (G32)
$I(x, y), J(x, y), K(x, y)$	Special mathematical functions (G85)
$W(x, y), X(x, y), Y(x, y)$	Special mathematical functions (G97)

TABLE 6. Glossary of notation II.

is the convective derivative. Initially ordering $\lambda_s \sim \rho_s$, and assuming the plasma is collisional ($\lambda_s/L \ll 1$), we rearrange (B1) so that the largest terms are grouped together (on the left-hand side):

$$\sum_{s'} \mathfrak{C}(f_s, f_{s'}) - \frac{Z_s e}{m_s c} \left(v'_s \times B \right) \cdot \frac{\partial f_s}{\partial v'_s}$$
$$= \frac{\mathrm{D} f_s}{\mathrm{D} t} + v'_s \cdot \nabla f_s + \left(\frac{Z_s e}{m_s} E' - \frac{\mathrm{D} V_s}{\mathrm{D} t} \right) \cdot \frac{\partial f_s}{\partial v'_s} - v'_s \cdot (\nabla V_s) \cdot \frac{\partial f_s}{\partial v'_s}. \tag{B3}$$

We then expand the distribution functions f_s in small parameter $\lambda_s/L \ll 1$:

$$f_s = f_s^{(0)} + f_s^{(1)} + \cdots, \tag{B4}$$

and solve (B3) order by order in λ_s/L for $f_s^{(0)}$ and $f_s^{(1)}$. The subsequent treatment of the collision operator for the electron distribution function is a little different from the ion distribution function, so we treat each case individually.

B.1.1. *Electrons*

For the electrons, we can rewrite the total collision operator in a convenient form if we assume that $T_i \sim T_e$, and $V_i \sim v_{\mathrm{th}i}$:

$$\sum_{s'} \mathfrak{C}(f_e, f_{s'}) = \mathfrak{C}_{ee}(f_e) + \mathfrak{C}_{ei}^{(0)}(f_e) + \mathfrak{C}_{ei}^{(1)}(f_e), \tag{B5}$$

where the electron–electron collision operator $\mathfrak{C}_{ee}(f_e)$ and electron–ion collision operators $\mathfrak{C}_{ei}^{(0)}(f_e)$ and $\mathfrak{C}_{ei}^{(1)}(f_e)$ are

$$\mathfrak{C}_{ee}(f_e) \equiv \mathfrak{C}(f_e, f_e), \tag{B6a}$$

$$\mathfrak{C}_{ei}^{(0)}(f_e) \equiv \nu_{ei}(v) v^3 \frac{\partial}{\partial v} \cdot \left[\frac{1}{v} \left(I - \hat{v}\hat{v} \right) \cdot \frac{\partial f_e}{\partial v} \right], \tag{B6b}$$

$$\mathfrak{C}_{ei}^{(1)}(f_e) \equiv \nu_{ei}(v) \frac{m_e v'_e \cdot u_{ei}}{T_e} \frac{n_e}{\pi^{3/2} v_{\mathrm{the}}^3} \exp\left(-\tilde{v}_e^2\right). \tag{B6c}$$

Here, $\nu_{ei}(v)$ is the velocity-dependent collision frequency

$$\nu_{ei}(v) \equiv \frac{3\sqrt{\pi}}{4\tau_e} \left(\frac{v_{\mathrm{the}}}{v} \right)^3, \tag{B7}$$

and the total electron–ion collision operator $\mathfrak{C}(f_e, f_i)$ is given by $\mathfrak{C}(f_e, f_i) = \mathfrak{C}_{ei}^{(0)}(f_e) + \mathfrak{C}_{ei}^{(1)}(f_e)$. Note that when evaluating $\mathfrak{C}_{ei}^{(1)}(f_e)$, we assumed that the deviation of the electron distribution function from a Maxwellian was small. This reformulation of the electron–ion collision operator is possible, because the assumptions $T_i \sim T_e$, and $V_i \sim v_{\mathrm{th}i}$ mean that, from the perspective of the electrons, the ion distribution is sharply peaked around the ion-fluid velocity: in other words, $f_i \approx n_i \delta(v - V_i)$. Furthermore, the reformulation is convenient because the total electron collision operator (B5) becomes independent of the ion distribution function. Thus, the asymptotic expansion (B4) for the electron distribution function is decoupled from the ions.

Substituting (B5), the ordered kinetic equation (B3) for the electron distribution becomes

$$
\mathfrak{C}_{ee}(f_e) + \mathfrak{C}_{ei}^{(0)}(f_e) + \frac{e}{m_e c} \left(\boldsymbol{v}_e' \times \boldsymbol{B} \right) \cdot \frac{\partial f_e}{\partial \boldsymbol{v}_e'}
$$
$$
= \frac{\mathrm{D} f_e}{\mathrm{D} t} + \boldsymbol{v}_e' \cdot \nabla f_e - \left(\frac{e}{m_e} \boldsymbol{E}' + \frac{\mathrm{D} \boldsymbol{V}_e}{\mathrm{D} t} \right) \cdot \frac{\partial f_e}{\partial \boldsymbol{v}_e'} - \boldsymbol{v}_e' \cdot (\nabla \boldsymbol{V}_e) \cdot \frac{\partial f_e}{\partial \boldsymbol{v}_e'} - \mathfrak{C}_{ei}^{(1)}(f_e), \quad \text{(B8a)}
$$

where we note that, under assumptions $T_i \sim T_e$, and $V_i \sim v_{\mathrm{thi}}$, $\mathfrak{C}_{ei}^{(1)}(f_e) \sim \mu_e^{1/2} \mathfrak{C}_{ei}^{(0)}(f_e)$ is much smaller than $\mathfrak{C}_{ei}^{(0)}(f_e)$. Then applying expansion (B4) with $s = e$ gives

$$
\mathfrak{C}_{ee}(f_e^{(0)}) + \mathfrak{C}_{ei}^{(0)}(f_e^{(0)}) + \frac{e}{m_e c} \left(\boldsymbol{v}_e' \times \boldsymbol{B} \right) \cdot \frac{\partial f_e^{(0)}}{\partial \boldsymbol{v}_e'} = 0. \quad \text{(B9)}
$$

It can be shown (Helander & Sigmar 2005) that the only solution of (B9) is (as expected) a Maxwellian distribution:

$$
f_e^{(0)} = \frac{n_e}{\pi^{3/2} v_{\mathrm{the}}^3} \exp \left(-\frac{|\boldsymbol{v}_e'|^2}{v_{\mathrm{the}}^2} \right). \quad \text{(B10)}
$$

After some algebraic manipulation, it can also be shown that the leading-order perturbed electron distribution function $f_e^{(1)}(\boldsymbol{v})$ satisfies

$$
\mathfrak{C}_{ee}(f_e^{(1)}) + \mathfrak{C}_{ei}^{(0)}(f_e^{(1)}) + \frac{e}{m_e c} \left(\boldsymbol{v}_e' \times \boldsymbol{B} \right) \cdot \frac{\partial f_e^{(1)}}{\partial \boldsymbol{v}_e'}
$$
$$
= \left\{ \left(\frac{|\boldsymbol{v}_e'|^2}{v_{\mathrm{the}}^2} - \frac{5}{2} \right) \boldsymbol{v}_e' \cdot \nabla \log T_e + \boldsymbol{v}_e' \cdot \left[\frac{\boldsymbol{R}_e}{p_e} + \frac{m_e \boldsymbol{u}_{ei} \nu_{ei}(v)}{T_e} \right] \right.
$$
$$
\left. + \frac{m_e}{2 T_e} \left(\boldsymbol{v}_e' \boldsymbol{v}_e' - \frac{|\boldsymbol{v}_e'|^2}{3} \boldsymbol{I} \right) : \boldsymbol{W}_e \right\} f_e^{(0)}, \quad \text{(B11)}
$$

where $\boldsymbol{R}_e$ and so on are defined in the main text, in (2.12). We note that this manipulation uses the leading-order terms (in λ_e / L) of the moment equations (2.4), and all terms directly involving gradients of density cancel with other terms.

B.1.2. *Electrons in strongly magnetised limit*

We now solve for $f_e^{(1)}$ in a strongly magnetised plasma, i.e. $\rho_e \ll \lambda_e$. In this subsidiary limit, both the collision integrals on the left-hand side of (B11) and the terms on its right-hand side are much smaller than the term proportional to the magnetic field; in other words,

$$
\boldsymbol{v}_e' \times \boldsymbol{B} \cdot \frac{\partial f_e^{(1)}}{\partial \boldsymbol{v}_e'} \approx 0. \quad \text{(B12)}
$$

We then define coordinate system $\{v_{e\parallel}', v_{e\perp}', \phi'\}$ by $v_{e\parallel}' \equiv \hat{\boldsymbol{z}} \cdot \boldsymbol{v}_e'$, $\boldsymbol{v}_{e\perp}' = \boldsymbol{v}_e' - v_{e\parallel}' \hat{\boldsymbol{z}}$, $v_{e\perp}' = |\boldsymbol{v}_{e\perp}'|$ and $\phi' = \phi$, where $\hat{\boldsymbol{z}} = \boldsymbol{B}/|\boldsymbol{B}|$ and ϕ is the gyrophase angle. The velocity gradient

operator in this system is

$$\frac{\partial f_e^{(1)}}{\partial \boldsymbol{v}_e'} = \hat{z}\frac{\partial f_e^{(1)}}{\partial v_{e\parallel}'} + \frac{\boldsymbol{v}_{e\perp}'}{v_{e\perp}'}\frac{\partial f_e^{(1)}}{\partial v_{e\perp}'} + \frac{1}{v_{e\perp}'^2}\boldsymbol{v}_e' \times \hat{z}\frac{\partial f_e^{(1)}}{\partial \phi'}. \tag{B13}$$

This, when combined with (B12), implies that $f_e^{(1)}$ is approximately gyrotropic:

$$f_e^{(1)}(\boldsymbol{v}') \approx \langle f_e^{(1)}\rangle_{\phi'}(v_\parallel', v_\perp'), \tag{B14}$$

where we have defined the gyro-average $\langle f_e^{(1)}\rangle_{\phi'}$ of the electron distribution function by

$$\langle f_e^{(1)}\rangle_{\phi'} \equiv \frac{1}{2\pi}\int_0^{2\pi} \mathrm{d}\phi' f_e^{(1)}. \tag{B15}$$

Now gyro-averaging (B11), we obtain

$$\begin{aligned}
&\mathfrak{C}_{ee}\left(\langle f_e^{(1)}\rangle_{\phi'}\right) + \mathfrak{C}_{ei}^{(0)}\left(\langle f_e^{(1)}\rangle_{\phi'}\right) \\
&= \left\{\left[\left(\frac{|\boldsymbol{v}_e'|^2}{v_{\mathrm{the}}^2} - \frac{5}{2}\right)\nabla_\parallel \log T_e + \frac{R_{e\parallel}}{p_e} + \frac{m_e u_{ei\parallel} v_{ei}(v)}{T_e}\right]v_{e\parallel}' \right. \\
&\quad \left. + \left(\hat{z}\hat{z} - \frac{1}{3}\boldsymbol{I}\right):\boldsymbol{W}_e\left(\frac{v_{e\parallel}'^2}{v_{\mathrm{the}}^2} - \frac{v_{e\perp}'^2}{2v_{\mathrm{the}}^2}\right)\right\}f_e^{(0)},
\end{aligned} \tag{B16}$$

where we have used the gyrophase isotropy of the collision operators to commute the order of gyro-averaging on the left-hand side. (B16) is a linear equation for $\langle f_e^{(1)}\rangle_{\phi'}$, so by tensor invariance, it must have a solution of the form

$$\begin{aligned}
\langle f_e^{(1)}\rangle_{\phi'} &= \tau_e\left\{\left[A_e^T\left(\frac{|\boldsymbol{v}_e'|}{v_{\mathrm{the}}}\right)\nabla_\parallel \log T_e + A_e^R\left(\frac{|\boldsymbol{v}_e'|}{v_{\mathrm{the}}}\right)\frac{R_{e\parallel}}{p_e} + \left(A_e^u\left(\frac{|\boldsymbol{v}_e'|}{v_{\mathrm{the}}}\right) - 1\right)\frac{m_e u_{ei\parallel}}{T_e \tau_e}\right]v_{e\parallel}' \right. \\
&\quad \left. + C_e\left(\frac{|\boldsymbol{v}_e'|}{v_{\mathrm{the}}}\right)\left(\hat{z}\hat{z} - \frac{1}{3}\boldsymbol{I}\right):\boldsymbol{W}_e\left(\frac{v_{e\parallel}'^2}{v_{\mathrm{the}}^2} - \frac{v_{e\perp}'^2}{2v_{\mathrm{the}}^2}\right)\right\}f_e^{(0)},
\end{aligned} \tag{B17}$$

where τ_e is defined by (2.15a) in the main text, and the isotropic functions $A_e^T(|\boldsymbol{v}_e'|/v_{\mathrm{the}})$, $A_e^R(|\boldsymbol{v}_e'|/v_{\mathrm{the}})$ and $C(|\boldsymbol{v}_e'|/v_{\mathrm{the}})$ are determined by inverting the collision operators (see Appendix B.2 for an example of how this calculation is done for a simple choice of collision operator). The total electron CE distribution function becomes

$$\begin{aligned}
f_e(v_{e\parallel}', v_{e\perp}') &= \left\{1 + \tau_e\left[A_e^T\left(\frac{|\boldsymbol{v}_e'|}{v_{\mathrm{the}}}\right)\nabla_\parallel \log T_e + A_e^R\left(\frac{|\boldsymbol{v}_e'|}{v_{\mathrm{the}}}\right)\frac{R_{e\parallel}}{p_e}\right.\right. \\
&\quad \left. + \left(A_e^u\left(\frac{|\boldsymbol{v}_e'|}{v_{\mathrm{the}}}\right) - 1\right)\frac{m_e u_{ei\parallel}}{T_e \tau_e}\right]v_{e\parallel}' \\
&\quad \left. + C_e\left(\frac{|\boldsymbol{v}_e'|}{v_{\mathrm{the}}}\right)\left(\hat{z}\hat{z} - \frac{1}{3}\boldsymbol{I}\right):\boldsymbol{W}_e\left(\frac{v_{e\parallel}'^2}{v_{\mathrm{the}}^2} - \frac{v_{e\perp}'^2}{2v_{\mathrm{the}}^2}\right)\right\}f_e^{(0)}.
\end{aligned} \tag{B18}$$

We emphasise that this quantity is expressed in the rest frame of the electron fluid.[10]

[10]Reintroducing the parameters η_e^T, η_e^R, η_e^u and ϵ_e into (B18) gives the expression (2.17) that is quoted in §2.2.2.

Finally, we recover (2.8a) by transforming (B18) into the frame co-moving with the ion fluid. Since $u_{ei\parallel} \sim \lambda_e v_{the}/L \ll v_{the}$, this transformation applied to the non-Maxwellian component $f_e^{(1)}$ of the electron distribution function only produces corrections of magnitude $\sim (\lambda_e/L) f_e^{(1)}$, and thus any correction terms are negligible. The only important contribution is from the shifted Maxwellian

$$\exp\left(-\frac{|\boldsymbol{v}_e'|^2}{v_{the}^2}\right) \approx \exp\left(-\tilde{v}_e^2\right)\left[1 + 2\tilde{v}_{e\parallel}\frac{u_{ei\parallel}}{v_{the}}\right] + \dots, \tag{B19}$$

where $\tilde{\boldsymbol{v}}_e = (\boldsymbol{v} - \boldsymbol{V}_i)/v_{the}$. Combining (B19) with (B18), we deduce

$$f_e(\tilde{v}_{e\parallel}, \tilde{v}_{e\perp}) = \left\{1 + \left[A_e^T(\tilde{v}_e)\,\lambda_e\boldsymbol{\nabla}_\parallel \log T_e + A_e^R(\tilde{v}_e)\,\lambda_e\frac{R_{e\parallel}}{p_e} + A_e^u(\tilde{v}_e)\,\lambda_e\frac{m_e u_{ei\parallel}}{T_e\tau_e}\right]\tilde{v}_{e\parallel}\right.$$
$$\left. + \tau_e C_e(\tilde{v}_e)\left(\hat{\boldsymbol{z}}\hat{\boldsymbol{z}} - \frac{1}{3}\boldsymbol{I}\right):\boldsymbol{W}_e\left(\tilde{v}_{e\parallel}^2 - \frac{\tilde{v}_{e\perp}^2}{2}\right)\right\}f_e^{(0)}. \tag{B20}$$

Introducing the parameters η_e^T, η_e^R, η_e^u and ϵ_e defined by (2.11a), (2.11b), (2.11c) and (2.11e) gives the final result (2.8a).

B.1.3. *Ions*

The derivation of the equivalent result (2.8b) for the ion distribution is mostly similar, but with one key difference: the total ion collision operator is dominated by the ion–ion collision operator $\mathfrak{C}_{ii}(f_i) \equiv \mathfrak{C}(f_i, f_i)$:

$$\sum_{s'} \mathfrak{C}(f_i, f_{s'}) = \mathfrak{C}_{ii}(f_i) + \mathfrak{C}(f_i, f_e) \approx \mathfrak{C}_{ii}(f_i). \tag{B21}$$

This is because ion–electron collisions are small in the mass ratio compared with ion–electron collisions. After some algebra, it can be shown that the equivalent of (B11) for the perturbed ion distribution $f_i^{(1)}$ is

$$\mathfrak{C}_{ii}(f_i^{(1)}) - \frac{Z_i e}{m_i c}\left(\boldsymbol{v}_i' \times \boldsymbol{B}\right) \cdot \frac{\partial f_i^{(1)}}{\partial \boldsymbol{v}_i'}$$
$$= \left[\left(\frac{|\boldsymbol{v}_i'|^2}{v_{thi}^2} - \frac{5}{2}\right)\boldsymbol{v}_i' \cdot \boldsymbol{\nabla} \log T_i + \frac{m_i}{2T_i}\left(\boldsymbol{v}_i'\boldsymbol{v}_i' - \frac{|\boldsymbol{v}_i'|^2}{3}\boldsymbol{I}\right):\boldsymbol{W}_i\right]f_i^{(0)}, \tag{B22}$$

where the lowest-order distribution is Maxwellian:

$$f_i^{(0)}(\boldsymbol{v}) = \frac{n_i}{\pi^{3/2}v_{thi}^3}\exp\left(-\frac{|\boldsymbol{v}_i'|^2}{v_{thi}^2}\right). \tag{B23}$$

We emphasise that the main differences between (B11) and (B22) are the presence of only one collision operator on the left-hand side of (B22) and the absence of any term proportional to the ion–electron friction force $\boldsymbol{R}_{ie}$ on the right-hand side of (B22).

Once (B22) has been written down, the method for obtaining the ion CE distribution function (2.8b) in a strongly magnetised plasma is near-identical to that of the electron

distribution function. Gyro-averaging gives

$$\mathfrak{C}_{ii}(f_i^{(1)}) = \left[\left(\frac{|\boldsymbol{v}_i'|^2}{v_{\mathrm{th}i}^2} - \frac{5}{2} \right) v_{i\|}' \boldsymbol{\nabla}_\| \log T_i + \left(\hat{z}\hat{z} - \frac{1}{3}\boldsymbol{I} \right) : \boldsymbol{W}_i \left(\frac{v_{i\|}'^2}{v_{\mathrm{th}i}^2} - \frac{v_{i\perp}'^2}{2v_{\mathrm{th}i}^2} \right) \right] f_i^{(0)}, \quad \text{(B24)}$$

from which it follows that

$$f_i(v_{i\|}', v_{i\perp}') = \left[1 + \tau_i A_i \left(\frac{|\boldsymbol{v}_i'|}{v_{\mathrm{th}i}} \right) v_{i\|}' \boldsymbol{\nabla}_\| \log T_i \right.$$
$$\left. + C_i \left(\frac{|\boldsymbol{v}_i'|}{v_{\mathrm{th}i}} \right) \left(\hat{z}\hat{z} - \frac{1}{3}\boldsymbol{I} \right) : \boldsymbol{W}_i \left(\frac{v_{i\|}'^2}{v_{\mathrm{th}i}^2} - \frac{v_{i\perp}'^2}{2v_{\mathrm{th}i}^2} \right) \right] f_i^{(0)}. \quad \text{(B25)}$$

On substituting for parameters η_i and ϵ_i defined by (2.11*d*) and (2.11*f*), respectively, we obtain (2.8*b*).

B.2. *Deriving isotropic functions of velocity for the CE solution*

In this appendix, we illustrate how to calculate the isotropic functions $A_e^T(\tilde{v}_e)$, $A_e^R(\tilde{v}_e)$, $A_e^u(\tilde{v}_e)$, $A_i(\tilde{v}_i)$, $C_e(\tilde{v}_e)$ and $C_i(\tilde{v}_i)$ arising in the electron and ion CE distribution functions for the particular cases of two simplified collision operators: the Krook collision operator and the Lorentz collision operator.

B.2.1. *Krook collision operator*

The Krook collision operator (Bhatnagar *et al.* 1954) for species *s* is given by

$$\mathfrak{C}_K(f_s) \equiv -\frac{1}{\tau_s} \left(f_s - f_s^{(0)} \right), \quad \text{(B26)}$$

where τ_s is the collision time of species *s* (assumed velocity-independent), and

$$f_s^{(0)} = \frac{n_s}{\pi^{3/2} v_{\mathrm{th}s}^3} \exp \left(-\frac{|\boldsymbol{v}_e'|^2}{v_{\mathrm{th}s}^2} \right) \quad \text{(B27)}$$

is a Maxwellian distribution with density n_s, mean velocity $\boldsymbol{V}_e$ and temperature T_s determined from f_s via (2.3). For this choice of collision operator, i.e. assuming

$$\sum_{s'} \mathfrak{C}(f_s, f_{s'}) = \mathfrak{C}_K(f_s), \quad \text{(B28)}$$

for all particle species, calculating the CE distribution function is particularly simple. Substituting (B18) for the electron CE distribution function into the electron Krook collision operator, we find

$$\mathfrak{C}_K(f_e) = - \left\{ \left[A_e^T \left(\frac{|\boldsymbol{v}_e'|}{v_{\mathrm{the}}} \right) \boldsymbol{\nabla}_\| \log T_e + A_e^R \left(\frac{|\boldsymbol{v}_e'|}{v_{\mathrm{the}}} \right) \frac{R_{e\|}}{p_e} + \left(A_e^u \left(\frac{|\boldsymbol{v}_e'|}{v_{\mathrm{the}}} \right) - 1 \right) \frac{m_e u_{ei\|}}{T_e \tau_e} \right] v_{e\|}' \right.$$
$$\left. + C_e \left(\frac{|\boldsymbol{v}_e'|}{v_{\mathrm{the}}} \right) \left(\hat{z}\hat{z} - \frac{1}{3}\boldsymbol{I} \right) : \boldsymbol{W}_e \left(\frac{v_{e\|}'^2}{v_{\mathrm{the}}^2} - \frac{v_{e\perp}'^2}{2v_{\mathrm{the}}^2} \right) \right\} f_e^{(0)}. \quad \text{(B29)}$$

By comparison with (B16), which, on substituting the Krook operator, becomes

$$\mathfrak{C}_K(f_e^{(1)}) = \left\{ \left[\left(\frac{|\boldsymbol{v}_e'|^2}{v_{\text{th}e}^2} - \frac{5}{2} \right) \boldsymbol{\nabla}_\parallel \log T_e + \frac{R_{e\parallel}}{p_e} + \frac{m_e u_{ei\parallel}}{T_e \tau_e} \right] v_{e\parallel}' \right.$$
$$\left. + \left(\hat{z}\hat{z} - \frac{1}{3}\boldsymbol{I} \right) : \boldsymbol{W}_e \left(\frac{v_{e\parallel}'^2}{v_{\text{th}e}^2} - \frac{v_{e\perp}'^2}{2v_{\text{th}e}^2} \right) \right\} f_e^{(0)}, \tag{B30}$$

we can immediately deduce that

$$A_e^T(\tilde{v}_e) = -\left(\tilde{v}_e^2 - \tfrac{5}{2} \right), \tag{B31a}$$

$$A_e^R(\tilde{v}_e) = -1, \tag{B31b}$$

$$A_e^u(\tilde{v}_e) = 0, \tag{B31c}$$

$$C_e(\tilde{v}_e) = -1. \tag{B31d}$$

The CE electron–ion-drift term vanishes for a Krook operator because the operator neglects inter-species collisions; by the same token, neither T_i and T_e nor $\boldsymbol{V}_i$ and $\boldsymbol{V}_e$ will equilibrate.

For the ion CE distribution, it follows from (B25) substituted into (B26) that

$$\mathfrak{C}_K(f_i) = - \left[A_i \left(\frac{|\boldsymbol{v}_i'|}{v_{\text{th}i}} \right) v_{i\parallel}' \boldsymbol{\nabla}_\parallel \log T_i + C_i \left(\frac{|\boldsymbol{v}_i'|}{v_{\text{th}i}} \right) \left(\hat{z}\hat{z} - \frac{1}{3}\boldsymbol{I} \right) : \boldsymbol{W}_i \left(\frac{v_{i\parallel}'^2}{v_{\text{th}i}^2} - \frac{v_{i\perp}'^2}{2v_{\text{th}i}^2} \right) \right] f_i^{(0)},$$
$$\tag{B32}$$

which gives, on comparison with (B24), that

$$A_i(\tilde{v}_i) = -\left(\tilde{v}_i^2 - \tfrac{5}{2} \right), \tag{B33a}$$

$$C_i(\tilde{v}_i) = -1. \tag{B33b}$$

B.2.2. *Lorentz collision operator*

The Lorentz collision operator for species s is defined by

$$\mathfrak{C}_L(f_s) \equiv \nu_s(v) v^3 \frac{\partial}{\partial \boldsymbol{v}} \cdot \left[\frac{1}{v} \left(\boldsymbol{I} - \hat{\boldsymbol{v}}\hat{\boldsymbol{v}} \right) \cdot \frac{\partial f_s}{\partial \boldsymbol{v}} \right], \tag{B34}$$

where $\nu_s(v)$ is a velocity-dependent scattering rate. We emphasise that the Lorentz collision operator is still simplified and physically complete compared with the full Landau collision operator, as it merely isotropises the distribution function over long times. However, such an operator does arise as the largest component of the electron–ion collision operator (see (B6b)) in Appendix B.1), and is, in fact, the exact electron collision operator in the limit of highly charged ions: the so-called 'Lorentz approximation' (Helander & Sigmar 2005).

To calculate the electron CE distribution function, we substitute (B18) into the collision operator (B34) (with $s = e$). Using the identities

$$\frac{\partial}{\partial \boldsymbol{v}} \cdot \left[\frac{1}{v} \left(\boldsymbol{I} - \hat{\boldsymbol{v}}\hat{\boldsymbol{v}} \right) \cdot \frac{\partial}{\partial \boldsymbol{v}} \left(\boldsymbol{a} \cdot \boldsymbol{v} \right) \right] = -\frac{2\boldsymbol{a} \cdot \boldsymbol{v}}{v^3}, \tag{B35a}$$

$$\frac{\partial}{\partial \boldsymbol{v}} \cdot \left[\frac{1}{v} \left(\boldsymbol{I} - \hat{\boldsymbol{v}}\hat{\boldsymbol{v}} \right) \cdot \frac{\partial}{\partial \boldsymbol{v}} \left(\boldsymbol{v} \cdot \boldsymbol{A} \cdot \boldsymbol{v} \right) \right] = -\frac{6\boldsymbol{v} \cdot \boldsymbol{A} \cdot \boldsymbol{v}}{v^3}, \tag{B35b}$$

for any constant vector $\boldsymbol{a}$ and any symmetric, traceless, constant matrix $\boldsymbol{A}$, it follows that

$$\mathfrak{C}_L(f_e) = -\hat{v}_e(\tilde{v}_e) \left\{ \left[2A_e^T \left(\frac{|\boldsymbol{v}_e'|}{v_{\mathrm{the}}} \right) \nabla_{\parallel} \log T_e + 2A_e^R \left(\frac{|\boldsymbol{v}_e'|}{v_{\mathrm{the}}} \right) \frac{R_{e\parallel}}{p_e} \right. \right.$$
$$+ 2 \left(A_e^u \left(\frac{|\boldsymbol{v}_e'|}{v_{\mathrm{the}}} \right) - 1 \right) \frac{m_e u_{ei\parallel}}{T_e \tau_e} \right] v_{e\parallel}'$$
$$\left. + 6C_e \left(\frac{|\boldsymbol{v}_e'|}{v_{\mathrm{the}}} \right) \left(\hat{z}\hat{z} - \frac{1}{3}\boldsymbol{I} \right) : \boldsymbol{W}_e \left(\frac{v_{e\parallel}'^2}{v_{\mathrm{the}}^2} - \frac{v_{e\perp}'^2}{2v_{\mathrm{the}}^2} \right) \right\} f_e^{(0)}, \tag{B36}$$

where $\hat{v}_s \equiv v_s(\tilde{v}_s)\tau_s$ is the non-dimensionalised collision rate for species s. As with the Krook operator, we compare (B36) with (B16), substituting a Lorentz collision operator for the latter, *viz.*

$$\mathfrak{C}_L(f_e^{(1)}) = \left\{ \left[\left(\frac{|\boldsymbol{v}_e'|^2}{v_{\mathrm{the}}^2} - \frac{5}{2} \right) \nabla_{\parallel} \log T_e + \frac{R_{e\parallel}}{p_e} + \frac{m_e u_{ei\parallel} v_e(\tilde{v}_e)}{T_e} \right] v_{e\parallel}' \right.$$
$$\left. + \left(\hat{z}\hat{z} - \frac{1}{3}\boldsymbol{I} \right) : \boldsymbol{W}_e \left(\frac{v_{e\parallel}'^2}{v_{\mathrm{the}}^2} - \frac{v_{e\perp}'^2}{2v_{\mathrm{the}}^2} \right) \right\} f_e^{(0)}. \tag{B37}$$

We deduce from the comparison that

$$A_e^T(\tilde{v}_e) = -\frac{1}{2\hat{v}_e(\tilde{v}_e)} \left(\tilde{v}_e^2 - \frac{5}{2} \right), \tag{B38a}$$

$$A_e^R(\tilde{v}_e) = -\frac{1}{2\hat{v}_e(\tilde{v}_e)}, \tag{B38b}$$

$$A_e^u(\tilde{v}_e) = \frac{1}{2}, \tag{B38c}$$

$$C_e(\tilde{v}_e) = -\frac{1}{6\hat{v}_e(\tilde{v}_e)}. \tag{B38d}$$

The isotropic functions $A_i(\tilde{v}_i)$ and $C_i(\tilde{v}_i)$, which are given by

$$A_i(\tilde{v}_i) = -\frac{1}{2v_i(\tilde{v}_i)\tau_i} \left(\tilde{v}_i^2 - \frac{5}{2} \right), \tag{B39a}$$

$$C_i(\tilde{v}_i) = -\frac{1}{6v_i(\tilde{v}_i)\tau_i}, \tag{B39b}$$

can be deduced in an analogous manner.

Appendix C. Derivation of hot, magnetised plasma dispersion relation for arbitrary distribution functions

In this appendix we re-derive the hot-plasma dispersion relation, given by (2.75) in § 2.4.1 (see also Davidson (1983), Parra (2017), the latter of whose approaches we follow). Our derivation also introduces a (simplified) collision operator in order to show that substitution (2.124) stated in § 2.5.7 provides a simple technique for including the effect of collisions on linear electromagnetic perturbations.

Consider a kinetic, magnetised plasma in equilibrium composed of one electron species and multiple ions species, with (assumed constant) background magnetic field $\boldsymbol{B}_0$. As in § 2.4.1, we denote the (gyrotropic) equilibrium distribution function of species s as $f_{s0} = f_{s0}(v_\parallel, v_\perp)$. and then consider a collisionless, linear perturbation δf_s to this equilibrium state, with wavevector $\boldsymbol{k}$ and complex frequency ω:

$$\delta f_s = \widehat{\delta f}_s \exp\left\{ \mathrm{i}\left(\boldsymbol{k} \cdot \boldsymbol{r} - \omega t\right)\right\}. \tag{C1}$$

The electromagnetic perturbations associated with the perturbed distribution functions have the forms given in (2.69), *viz.*

$$\delta \boldsymbol{E} = \widehat{\delta \boldsymbol{E}} \exp\left\{ \mathrm{i}\left(\boldsymbol{k} \cdot \boldsymbol{r} - \omega t\right)\right\}, \tag{C2a}$$

$$\delta \boldsymbol{B} = \widehat{\delta \boldsymbol{B}} \exp\left\{ \mathrm{i}\left(\boldsymbol{k} \cdot \boldsymbol{r} - \omega t\right)\right\}, \tag{C2b}$$

and satisfy Faraday's law and the Maxwell–Ampère law:

$$\frac{\partial \delta \boldsymbol{B}}{\partial t} = -c\boldsymbol{\nabla} \times \delta \boldsymbol{E}, \tag{C3a}$$

$$\boldsymbol{\nabla} \times \delta \boldsymbol{B} = \frac{4\pi}{c}\delta \boldsymbol{j} + \frac{1}{c}\frac{\partial \delta \boldsymbol{E}}{\partial t}, \tag{C3b}$$

where the current perturbation is

$$\delta \boldsymbol{j} = \widehat{\delta \boldsymbol{j}} \exp\left\{ \mathrm{i}\left(\boldsymbol{k} \cdot \boldsymbol{r} - \omega t\right)\right\} = \sum_s Z_s e \int \mathrm{d}^3\boldsymbol{v}\, \boldsymbol{v}\, \delta f_s. \tag{C4}$$

To close these equations, we relate δf_s to the electromagnetic field perturbations by linearising the Maxwell–Vlasov–Landau equation (2.1). The linearisation $f_s = f_{s0} + \delta f_s$ then gives that the perturbed distribution function of species s satisfies

$$\frac{\partial \delta f_s}{\partial t} + \boldsymbol{v} \cdot \boldsymbol{\nabla}\delta f_s + \frac{Z_s e}{m_s c}\left(\boldsymbol{v} \times \boldsymbol{B}_0\right) \cdot \frac{\partial \delta f_s}{\partial \boldsymbol{v}} = -\frac{Z_s e}{m_s}\left(\delta \boldsymbol{E} + \frac{\boldsymbol{v} \times \delta \boldsymbol{B}}{c}\right) \cdot \frac{\partial f_{s0}}{\partial \boldsymbol{v}} - \nu_s \delta f_s, \tag{C5}$$

where we have replaced the full linearised collision operator with a simplified Krook collision operator with constant collision frequency $\nu_s = \tau_s^{-1}$ for species s. For any particular equilibrium distribution function, (C3a), (C3b), (C4) and (C5) are a closed set of governing equations.

We now write these equations in terms of $\boldsymbol{k}$ and ω using (C1), (E1a) and (C2b):

$$-\mathrm{i}\omega\widehat{\delta\boldsymbol{B}} = -\mathrm{i}c\boldsymbol{k}\times\widehat{\delta\boldsymbol{E}}, \tag{C6a}$$

$$\mathrm{i}\boldsymbol{k}\times\widehat{\delta\boldsymbol{B}} = \frac{4\pi}{c}\widehat{\delta\boldsymbol{j}} - \frac{\mathrm{i}\omega}{c}\widehat{\delta\boldsymbol{E}}, \tag{C6b}$$

$$\widehat{\delta\boldsymbol{j}} = \sum_s Z_s e \int \mathrm{d}^3\boldsymbol{v}\,\boldsymbol{v}\,\widehat{\delta f_s}, \tag{C6c}$$

$$\left(-\mathrm{i}\hat{\omega}_s + \mathrm{i}\boldsymbol{k}\cdot\boldsymbol{v} + \tilde{\Omega}_s\frac{\partial}{\partial\phi}\right)\widehat{\delta f_s} = -\frac{Z_s e}{m_s}\left(\widehat{\delta\boldsymbol{E}} + \frac{\boldsymbol{v}\times\widehat{\delta\boldsymbol{B}}}{c}\right)\cdot\frac{\partial f_{s0}}{\partial\boldsymbol{v}}, \tag{C6d}$$

where we have defined the (signed) Larmor frequency of species s as

$$\tilde{\Omega}_s \equiv \frac{Z_s e B_0}{m_s c} = \frac{Z_s}{|Z_s|}\Omega_s, \tag{C7}$$

and introduced the modified complex frequency $\hat{\omega}_s \equiv \omega + \mathrm{i}\nu_s$. Note that $Z_e = -1$, so that $\tilde{\Omega}_e < 0$. We then eliminate $\widehat{\delta\boldsymbol{B}}$ in (C6b) and (C6d) using (C6a) to give

$$\frac{k^2 c^2}{\omega^2}\left[\widehat{\delta\boldsymbol{E}} - \hat{\boldsymbol{k}}\left(\hat{\boldsymbol{k}}\cdot\widehat{\delta\boldsymbol{E}}\right)\right] = \frac{4\pi\mathrm{i}}{\omega}\widehat{\delta\boldsymbol{j}} - \widehat{\delta\boldsymbol{E}}, \tag{C8a}$$

$$\widehat{\delta\boldsymbol{j}} = \sum_s Z_s e \int \mathrm{d}^3\boldsymbol{v}\,\boldsymbol{v}\,\widehat{\delta f_s}, \tag{C8b}$$

$$\left(-\mathrm{i}\hat{\omega}_s + \mathrm{i}\boldsymbol{k}\cdot\boldsymbol{v} + \tilde{\Omega}_s\frac{\partial}{\partial\phi}\right)\widehat{\delta f_s} = -\frac{Z_s e}{m_s}\left[\widehat{\delta\boldsymbol{E}} + \frac{k}{\omega}\boldsymbol{v}\times\left(\hat{\boldsymbol{k}}\times\widehat{\delta\boldsymbol{E}}\right)\right]\cdot\frac{\partial f_{s0}}{\partial\boldsymbol{v}}. \tag{C8c}$$

Next, we derive an expression for $\widehat{\delta f_s}$ in terms of $\widehat{\delta\boldsymbol{E}}$. For arbitrary wavelengths compared with the Larmor radius ρ_s of species s, expressing $\widehat{\delta f_s}$ in terms of the equilibrium distribution function and $\widehat{\delta\boldsymbol{E}}$ requires inversion of the gyrophase-angle derivative in (C8). This can be done for any f_{s0} in an orthonormal coordinate system with basis vectors $\{\hat{\boldsymbol{x}}, \hat{\boldsymbol{y}}, \hat{\boldsymbol{z}}\}$ defined by (2.76a–c). By Fourier transforming $\widehat{\delta f_s}$ in ϕ, it can then be shown that

$$\widehat{\delta f_s} = -\frac{Z_s e\mathrm{i}}{m_s\omega}\left(\frac{\partial f_{s0}}{\partial v_\parallel} - \frac{v_\parallel}{v_\perp}\frac{\partial f_{s0}}{\partial v_\perp}\right)\hat{\boldsymbol{z}}\cdot\widehat{\delta\boldsymbol{E}} + \exp\left(-\mathrm{i}k_\perp\tilde{\rho}_s\tilde{v}_{s\perp}\sin\phi\right)\sum_{n=-\infty}^{\infty}\widehat{\delta f}_{s,n}\exp\left(\mathrm{i}n\phi\right), \tag{C9}$$

where the series coefficients are given by

$$\widehat{\delta f}_{s,n} = -\frac{Z_s e\mathrm{i}}{m_s}\frac{1}{\hat{\omega}_s - k_\parallel v_\parallel - n\tilde{\Omega}_s}\left[\frac{\partial f_{s0}}{\partial v_\perp} + \frac{k_\parallel}{\omega}\left(v_\perp\frac{\partial f_{s0}}{\partial v_\parallel} - v_\parallel\frac{\partial f_{s0}}{\partial v_\perp}\right)\right]\boldsymbol{u}_n^*\cdot\widehat{\delta\boldsymbol{E}}, \tag{C10}$$

and the vector $\boldsymbol{u}_n$ in the basis $\{\hat{\boldsymbol{x}}, \hat{\boldsymbol{y}}, \hat{\boldsymbol{z}}\}$ is

$$\boldsymbol{u}_n = \frac{v_\parallel}{v_\perp}J_n(k_\perp\tilde{\rho}_s\tilde{v}_{s\perp})\hat{\boldsymbol{z}} + \frac{nJ_n(k_\perp\tilde{\rho}_s\tilde{v}_{s\perp})}{k_\perp\tilde{\rho}_s\tilde{v}_{s\perp}}\hat{\boldsymbol{x}} - \mathrm{i}J_n'(k_\perp\tilde{\rho}_s\tilde{v}_{s\perp})\hat{\boldsymbol{y}}, \tag{C11}$$

$J_n(k_\perp\tilde{\rho}_s\tilde{v}_{s\perp})$ denoting the nth-order Bessel function of the first kind. We can then take advantage of the independence of f_{s0} of the gyroangle to show that the current

perturbation is

$$\widehat{\delta \boldsymbol{j}} = -\sum_s \frac{2\pi Z_s^2 e^2 \mathrm{i}}{m_s \omega} \int_{-\infty}^{\infty} \mathrm{d}v_\parallel \int_0^{\infty} \mathrm{d}v_\perp \left(v_\perp \frac{\partial f_{s0}}{\partial v_\parallel} - v_\parallel \frac{\partial f_{s0}}{\partial v_\perp} \right) v_\parallel \hat{\boldsymbol{z}} \left(\hat{\boldsymbol{z}} \cdot \widehat{\delta \boldsymbol{E}} \right)$$

$$+ \sum_s 2\pi Z_s e \int_{C_L} \mathrm{d}v_\parallel \int_0^{\infty} \mathrm{d}v_\perp v_\perp^2 \sum_{n=-\infty}^{\infty} \widehat{\delta f}_{s,n} \boldsymbol{u}_n, \tag{C12}$$

where C_L denotes the usual Landau contour. This can be written as Ohm's law

$$\widehat{\delta \boldsymbol{j}} = \boldsymbol{\sigma} \cdot \widehat{\delta \boldsymbol{E}}, \tag{C13}$$

where $\boldsymbol{\sigma}$ is the conductivity tensor. In the absence of collisions ($\nu_s = 0$), this is given by (2.77). If the collision frequency $\nu_s \neq 0$ is non-zero, then

$$\frac{\hat{\omega}_s}{|k_\parallel| v_{\mathrm{th}s}} = \tilde{\omega}_{\parallel s} + \frac{\mathrm{i}}{|k_\parallel| \tau_s v_{\mathrm{th}s}} = \tilde{\omega}_{\parallel s} + \frac{\mathrm{i}}{|k_\parallel| \lambda_s}, \tag{C14}$$

from which the substitution (2.124) proposed in § 2.5.7 follows.

Substituting Ohm's law (C13) into Ampère's law (C8a) gives the singular nonlinear eigenvalue equation

$$\left[\frac{c^2 k^2}{\omega^2} \left(\hat{\boldsymbol{k}}\hat{\boldsymbol{k}} - \boldsymbol{I} \right) + \mathfrak{E} \right] \cdot \widehat{\delta \boldsymbol{E}} = 0, \tag{C15}$$

where

$$\mathfrak{E} \equiv \boldsymbol{I} + \frac{4\pi \mathrm{i}}{\omega} \boldsymbol{\sigma} \tag{C16}$$

is the plasma dielectric tensor (2.74). Taking the determinant of (C15) gives the desired result (2.75).

Appendix D. Electrostatic instabilities of CE plasma

In this appendix, we calculate the electrostatic hot-plasma dispersion relation for arbitrary distribution functions (Appendix D.1). We then show (Appendix D.2) that for frequencies ω such that $\tilde{\omega}_{s\parallel} = \omega/k_\parallel v_{\mathrm{th}s} \ll 1$, the dominant contribution to the longitudinal conductivity $\hat{\boldsymbol{k}} \cdot \boldsymbol{\sigma} \cdot \hat{\boldsymbol{k}}$ is from the Maxwellian component, and strictly positive; the small $O(\eta_s, \epsilon_s)$ non-Maxwellian distortion associated with the CE distribution function results in only an $O(\eta_s, \epsilon_s)$ distortion to $\hat{\boldsymbol{k}} \cdot \boldsymbol{\sigma} \cdot \hat{\boldsymbol{k}}$. We then illustrate the possibility of electrostatic instabilities associated with the CE distribution function by calculating the growth rate of the parallel CE bump-on-tail instability (Appendix D.3). Finally, in Appendix D.4, we show that the only electrostatic instabilities that can occur have a growth rate which is exponentially small in dimensionless parameters $O(\eta_s, \epsilon_s)$, for arbitrary frequencies. Thus, it follows that electrostatic instabilities generally have a small growth rate in comparison with electromagnetic instabilities for a CE plasma.

D.1. *The electrostatic hot-plasma dispersion relation*

Beginning from the singular eigenvalue equation (2.73), *viz.*

$$\left[\frac{c^2 k^2}{\omega^2} \left(\hat{k}\hat{k} - \mathbf{I} \right) + \mathfrak{E} \right] \cdot \widehat{\delta E} = 0, \tag{D1}$$

we consider the electrostatic modes, for which $\widehat{\delta E} = (\hat{k} \cdot \widehat{\delta E})\hat{k}$. For them, the hot-plasma dispersion relation becomes

$$\mathfrak{E}_{33} = k^2 + \frac{4\pi \mathrm{i}}{\omega} \hat{k} \cdot \boldsymbol{\sigma} \cdot \hat{k} = 0. \tag{D2}$$

Employing the expression (2.77) for the conductivity tensor, we calculate the longitudinal conductivity

$$\hat{k} \cdot \boldsymbol{\sigma} \cdot \hat{k} = -\frac{\mathrm{i}}{4\pi\omega} \sum_s \omega_{\mathrm{p}s}^2 \left[\frac{2}{\sqrt{\pi}} \frac{k_\parallel^2}{k^2} \int_{-\infty}^{\infty} \mathrm{d}\tilde{v}_{s\parallel}\, \tilde{v}_{s\parallel} \int_0^{\infty} \mathrm{d}\tilde{v}_{s\perp}\, \Lambda_s(\tilde{v}_{s\parallel}, \tilde{v}_{s\perp}) \right.$$
$$\left. + \tilde{\omega}_{s\parallel} \frac{2}{\sqrt{\pi}} \int_{C_L} \mathrm{d}\tilde{v}_{s\parallel} \int_0^{\infty} \mathrm{d}\tilde{v}_{s\perp}\, \tilde{v}_{s\perp}^2 \,\Xi_s(\tilde{v}_{s\parallel}, \tilde{v}_{s\perp}) \sum_{n=-\infty}^{\infty} \frac{\hat{k} \cdot \boldsymbol{R}_{sn} \cdot \hat{k}}{\zeta_{sn} - \tilde{v}_{s\parallel}} \right], \tag{D3}$$

where

$$\hat{k} \cdot \boldsymbol{R}_{sn} \cdot \hat{k} = \frac{J_n(k_\perp \tilde{\rho}_s \tilde{v}_{s\perp})^2}{k^2 \tilde{\rho}_s^2 \tilde{v}_{s\perp}^2} \left(n^2 + 2nk_\parallel \tilde{\rho}_s \tilde{v}_{s\parallel} + k_\parallel^2 \tilde{\rho}_s^2 \tilde{v}_{s\parallel}^2 \right)$$
$$= \frac{k_\parallel^2 J_n(k_\perp \tilde{\rho}_s \tilde{v}_{s\perp})^2}{k^2 \tilde{v}_{s\perp}^2} \left(\frac{n}{k_\parallel \tilde{\rho}_s} + \tilde{v}_{s\parallel} \right)^2. \tag{D4}$$

By way of the identity

$$\sum_{n=-\infty}^{\infty} J_n(k_\perp \tilde{\rho}_s \tilde{v}_{s\perp})^2 \frac{(n/k_\parallel \tilde{\rho}_s + \tilde{v}_{s\parallel})^2}{\zeta_{sn} - \tilde{v}_{s\parallel}} = -\tilde{v}_{s\parallel} + \tilde{\omega}_{s\parallel} \sum_{n=-\infty}^{\infty} J_n(k_\perp \tilde{\rho}_s \tilde{v}_{s\perp})^2 \frac{n/k_\parallel \tilde{\rho}_s + \tilde{v}_{s\parallel}}{\zeta_{sn} - \tilde{v}_{s\parallel}}, \tag{D5}$$

which follows directly from the Bessel-function identity

$$\sum_{n=-\infty}^{\infty} J_n(k_\perp \tilde{\rho}_s \tilde{v}_{s\perp})^2 = 1, \tag{D6}$$

it follows that

$$
\tilde{\omega}_{s\parallel} \frac{2}{\sqrt{\pi}} \int_{C_L} \mathrm{d}\tilde{v}_{s\parallel} \int_0^\infty \mathrm{d}\tilde{v}_{s\perp}\, \tilde{v}_{s\perp}^2\, \Xi_s(\tilde{v}_{s\parallel}, \tilde{v}_{s\perp}) \sum_{n=-\infty}^{\infty} \frac{\hat{\boldsymbol{k}} \cdot \boldsymbol{R}_{sn} \cdot \hat{\boldsymbol{k}}}{\zeta_{sn} - \tilde{v}_{s\parallel}}
$$

$$
= -\tilde{\omega}_{s\parallel} \frac{2}{\sqrt{\pi}} \frac{k_\parallel^2}{k^2} \int_{C_L} \mathrm{d}\tilde{v}_{s\parallel}\, \tilde{v}_{s\parallel} \int_0^\infty \mathrm{d}\tilde{v}_{s\perp} \left[\frac{\partial \tilde{f}_{s0}}{\partial \tilde{v}_{s\perp}} + \frac{\Lambda_s(\tilde{v}_{s\parallel}, \tilde{v}_{s\perp})}{\tilde{\omega}_{s\parallel}} \right]
$$

$$
+ \tilde{\omega}_{s\parallel} \frac{2}{\sqrt{\pi}} \frac{k_\parallel^2}{k^2} \int_{C_L} \mathrm{d}\tilde{v}_{s\parallel} \int_0^\infty \mathrm{d}\tilde{v}_{s\perp}\, \Lambda_s(\tilde{v}_{s\parallel}, \tilde{v}_{s\perp}) \sum_{n=-\infty}^{\infty} J_n(k_\perp \tilde{\rho}_s \tilde{v}_{s\perp})^2 \frac{n/k_\parallel \tilde{\rho}_s + \tilde{v}_{s\parallel}}{\zeta_{sn} - \tilde{v}_{s\parallel}}
$$

$$
+ \tilde{\omega}_{s\parallel}^2 \frac{2}{\sqrt{\pi}} \frac{k_\parallel^2}{k^2} \int_{C_L} \mathrm{d}\tilde{v}_{s\parallel} \int_0^\infty \mathrm{d}\tilde{v}_{s\perp}\, \frac{\partial \tilde{f}_{s0}}{\partial \tilde{v}_{s\perp}} \sum_{n=-\infty}^{\infty} J_n(k_\perp \tilde{\rho}_s \tilde{v}_{s\perp})^2 \frac{n/k_\parallel \tilde{\rho}_s + \tilde{v}_{s\parallel}}{\zeta_{sn} - \tilde{v}_{s\parallel}}
$$

$$
= -\frac{2}{\sqrt{\pi}} \frac{k_\parallel^2}{k^2} \int_{-\infty}^\infty \mathrm{d}\tilde{v}_{s\parallel}\, \tilde{v}_{s\parallel} \int_0^\infty \mathrm{d}\tilde{v}_{s\perp}\, \Lambda_s(\tilde{v}_{s\parallel}, \tilde{v}_{s\perp})
$$

$$
+ \frac{2\tilde{\omega}_s^2}{\sqrt{\pi}} \int_{C_L} \mathrm{d}\tilde{v}_{s\parallel} \int_0^\infty \mathrm{d}\tilde{v}_{s\perp} \sum_{n=-\infty}^{\infty} \left(\tilde{v}_{s\perp} \frac{\partial \tilde{f}_{s0}}{\partial \tilde{v}_{s\parallel}} + \frac{n}{k_\parallel \tilde{\rho}_s} \frac{\partial \tilde{f}_{s0}}{\partial \tilde{v}_{s\perp}} \right) \frac{J_n(k_\perp \tilde{\rho}_s \tilde{v}_{s\perp})^2}{\zeta_{sn} - \tilde{v}_{s\parallel}}, \tag{D7}
$$

where $\tilde{\omega}_s \equiv \omega/k v_{\mathrm{th}s}$. We conclude that

$$
\hat{\boldsymbol{k}} \cdot \boldsymbol{\sigma} \cdot \hat{\boldsymbol{k}} = -\frac{\mathrm{i}}{4\pi\omega} \sum_s \omega_{\mathrm{p}s}^2 \left[\tilde{\omega}_s^2 \frac{2}{\sqrt{\pi}} \int_{C_L} \mathrm{d}\tilde{v}_{s\parallel} \int_0^\infty \mathrm{d}\tilde{v}_{s\perp} \sum_{n=-\infty}^{\infty} \Pi_n(\tilde{v}_{s\parallel}, \tilde{v}_{s\perp}) \frac{J_n(k_\perp \tilde{\rho}_s \tilde{v}_{s\perp})^2}{\zeta_{sn} - \tilde{v}_{s\parallel}} \right], \tag{D8}
$$

where

$$
\Pi_n(\tilde{v}_{s\parallel}, \tilde{v}_{s\perp}) \equiv \tilde{v}_{s\perp} \frac{\partial \tilde{f}_{s0}}{\partial \tilde{v}_{s\parallel}} + \frac{n}{k_\parallel \tilde{\rho}_s} \frac{\partial \tilde{f}_{s0}}{\partial \tilde{v}_{s\perp}}. \tag{D9}
$$

The electrostatic component of the dielectric tensor is then

$$
\mathfrak{E}_{33} = k^2 + \sum_s k_{\mathrm{D}s}^2 \left[\frac{1}{\sqrt{\pi}} \int_{C_L} \mathrm{d}\tilde{v}_{s\parallel} \int_0^\infty \mathrm{d}\tilde{v}_{s\perp} \sum_{n=-\infty}^{\infty} \Pi_n(\tilde{v}_{s\parallel}, \tilde{v}_{s\perp}) \frac{J_n(k_\perp \tilde{\rho}_s \tilde{v}_{s\perp})^2}{\zeta_{sn} - \tilde{v}_{s\parallel}} \right], \tag{D10}
$$

and the electrostatic hot-plasma dispersion relation (D2) becomes

$$
k^2 + \sum_s k_{\mathrm{D}s}^2 \left[\frac{1}{\sqrt{\pi}} \int_{C_L} \mathrm{d}\tilde{v}_{s\parallel} \int_0^\infty \mathrm{d}\tilde{v}_{s\perp} \sum_{n=-\infty}^{\infty} \Pi_n(\tilde{v}_{s\parallel}, \tilde{v}_{s\perp}) \frac{J_n(k_\perp \tilde{\rho}_s \tilde{v}_{s\perp})^2}{\zeta_{sn} - \tilde{v}_{s\parallel}} \right] = 0, \tag{D11}
$$

where the Debye wavenumber $k_{\mathrm{D}s}$ of species s is defined by

$$
k_{\mathrm{D}s} \equiv \frac{\sqrt{2}\omega_{\mathrm{p}s}}{v_{\mathrm{th}s}}. \tag{D12}
$$

D.2. *The electrostatic dielectric response at low frequencies*

In this appendix, we perform a Taylor expansion of the electrostatic component $\mathfrak{E}_{33}$ of the dielectric tensor (D10) in $\tilde{\omega}_{s\parallel} \ll 1$. Before carrying out the expansion, we first substitute the identity

$$\Pi_n(\tilde{v}_{s\parallel}, \tilde{v}_{s\perp}) = \tilde{\omega}_{s\parallel} \Xi_s(\tilde{v}_{s\parallel}, \tilde{v}_{s\perp}) + \left(\tilde{v}_{s\parallel} - \zeta_{sn}\right) \frac{\partial \tilde{f}_{s0}}{\partial \tilde{v}_{s\perp}} \tag{D13}$$

into (D10), which then becomes

$$\mathfrak{E}_{33} = k^2 - \sum_s k_{\mathrm{D}s}^2 \frac{1}{\sqrt{\pi}} \int_{-\infty}^{\infty} \mathrm{d}\tilde{v}_{s\parallel} \int_0^{\infty} \mathrm{d}\tilde{v}_{s\perp} \frac{\partial \tilde{f}_{s0}}{\partial \tilde{v}_{s\perp}}$$

$$+ \sum_s k_{\mathrm{D}s}^2 \left[\frac{\tilde{\omega}_{s\parallel}}{\sqrt{\pi}} \int_{C_L} \mathrm{d}\tilde{v}_{s\parallel} \int_0^{\infty} \mathrm{d}\tilde{v}_{s\perp} \, \Xi_s(\tilde{v}_{s\parallel}, \tilde{v}_{s\perp}) \sum_{n=-\infty}^{\infty} \frac{J_n(k_\perp \tilde{\rho}_s \tilde{v}_{s\perp})^2}{\zeta_{sn} - \tilde{v}_{s\parallel}} \right]. \tag{D14}$$

Now carrying out the Taylor expansion in $\tilde{\omega}_{s\parallel} \ll 1$, we see that, to the leading order in this expansion,

$$\mathfrak{E}_{33} \approx k^2 + \sum_s k_{\mathrm{D}s}^2 \frac{1}{\sqrt{\pi}} \int_{-\infty}^{\infty} \mathrm{d}\tilde{v}_{s\parallel} \, \tilde{f}_{s0}(\tilde{v}_{s\parallel}, 0). \tag{D15}$$

For the CE distribution

$$\tilde{f}_{s0}(\tilde{v}_{s\parallel}, 0) = \exp\left(-\tilde{v}_{s\parallel}^2\right) \left\{ 1 + \eta_s A_s(\tilde{v}_{s\parallel}) \tilde{v}_{s\parallel} + \epsilon_s C_s(\tilde{v}_{s\parallel}) \tilde{v}_{s\parallel}^2 \right\}, \tag{D16}$$

we have

$$\frac{1}{\sqrt{\pi}} \int_{-\infty}^{\infty} \mathrm{d}\tilde{v}_{s\parallel} \tilde{f}_{s0}(\tilde{v}_{s\parallel}, 0) = 1 + \frac{\epsilon_s}{2\sqrt{\pi}} \int_0^{\infty} \mathrm{d}\tilde{v}_{s\parallel} \, \tilde{v}_{s\parallel}^2 C_s(\tilde{v}_{s\parallel}) \exp\left(-\tilde{v}_{s\parallel}^2\right), \tag{D17}$$

where the term in the CE distribution function proportional to η_s has vanished on account of having odd parity with respect to $\tilde{v}_{s\parallel}$. We conclude that the non-Maxwellian contribution to (D17) is $O(\eta_s, \epsilon_s)$ in comparison with the Maxwellian contribution, and so the electrostatic component of the dielectric tensor for low-frequency fluctuations is just

$$\mathfrak{E}_{33} \approx k^2 + \sum_s k_{\mathrm{D}s}^2, \tag{D18}$$

or, writing (D18) explicitly in terms of $\tilde{\omega}_{s\parallel}$ and the plasma frequency ω_{ps} of species s,

$$\mathfrak{E}_{33} \approx k^2 + \sum_s \frac{\omega_{ps}^2}{\omega^2} \frac{2k_\parallel^2}{k^2} \tilde{\omega}_{s\parallel}^2. \tag{D19}$$

It follows that $\mathfrak{E}_{33}^{(0)}$ and $\mathfrak{E}_{33}^{(1)}$ defined by (2.99) are given by

$$\mathfrak{E}_{33}^{(0)} = 0, \tag{D20a}$$

$$\mathfrak{E}_{33}^{(1)} = \frac{\omega_{pe}^2}{\omega^2} \sum_s \frac{Z_s T_e}{T_s} \frac{2k_\parallel^2}{k^2}. \tag{D20b}$$

where we have neglected the displacement current term ($k \ll k_{\mathrm{D}e}$), and the temperature of species s is denoted by T_s.

D.3. *Existence of electrostatic instabilities for a CE plasma*

That electrostatic instabilities can exist is most simply shown in the limit of purely parallel, high-frequency fluctuations: $k_\perp = 0$, $k_\parallel = k$, $\tilde{\omega}_s = \tilde{\omega}_{s\parallel} \gg 1$ and

$$\varpi \equiv \mathrm{Re}\,\omega \gg \mathrm{Im}\,\omega \equiv \gamma. \tag{D21}$$

For purely parallel modes, the only non-zero term in the sum of Bessel functions in the electrostatic hot-plasma dispersion relation (D11) is the $n = 0$ term; thus, (D11) simplifies to

$$\mathfrak{E}_{33} = k^2 + \sum_s k_{\mathrm{D}s}^2 \left(\frac{1}{\sqrt{\pi}} \int_{C_L} \mathrm{d}\tilde{v}_{s\parallel} \int_0^\infty \mathrm{d}\tilde{v}_{s\perp}\, \tilde{v}_{s\perp} \frac{\partial \tilde{f}_{s0}}{\partial \tilde{v}_{s\parallel}} \frac{1}{\tilde{\omega}_s - \tilde{v}_{s\parallel}} \right) = 0. \tag{D22}$$

Next, we expand (D22) around the real frequency ϖ, using (D21); this gives

$$\mathfrak{E}_{33}(\omega, k) \approx \mathfrak{E}_{33}(\varpi, k) + \mathrm{i}\gamma \frac{\partial \mathfrak{E}_{33}}{\partial \omega}(\varpi, k). \tag{D23}$$

Taking the imaginary part of (D23) allows for an expression for γ to be derived in terms of ϖ:

$$\gamma \approx - \left[\frac{\partial\,\mathrm{Re}\,\mathfrak{E}_{33}}{\partial \omega}(\varpi, k) \right]^{-1} \mathrm{Im}\,\mathfrak{E}_{33}(\varpi, k). \tag{D24}$$

To calculate γ, we use

$$\mathrm{Re}\,\mathfrak{E}_{33}(\varpi, k) = k^2 + \sum_s k_{\mathrm{D}s}^2 \left(\frac{1}{\sqrt{\pi}} P \int \mathrm{d}\tilde{v}_{s\parallel} \int_0^\infty \mathrm{d}\tilde{v}_{s\perp}\, \tilde{v}_{s\perp} \frac{\partial \tilde{f}_{s0}}{\partial \tilde{v}_{s\parallel}} \frac{1}{\tilde{\omega}_s - \tilde{v}_{s\parallel}} \right), \tag{D25a}$$

$$\mathrm{Im}\,\mathfrak{E}_{33}(\varpi, k) = -\sqrt{\pi} k^2 \int_0^\infty \mathrm{d}\tilde{v}_{s\perp}\, \tilde{v}_{s\perp} \frac{\partial \tilde{f}_{s0}}{\partial \tilde{v}_{s\parallel}}(\tilde{\omega}_s, \tilde{v}_{s\perp}), \tag{D25b}$$

where, to the leading order, $\tilde{\omega}_s \approx \varpi / k v_{\mathrm{th}s}$. Now expanding (D25a) in $\tilde{\omega}_s \gg 1$, we find that

$$\mathrm{Re}\,\mathfrak{E}_{33}(\varpi, k) \approx k^2 - \sum_s \frac{k_{\mathrm{D}s}^2}{\tilde{\omega}_s^2} \approx k^2 \left(1 - \frac{\omega_{\mathrm{pe}}^2}{\varpi^2} \right), \tag{D26}$$

where we have integrated (D25a) by parts, used identity

$$\int_{-\infty}^\infty \mathrm{d}\tilde{v}_{s\parallel} \int_0^\infty \mathrm{d}\tilde{v}_{s\perp}\, \tilde{v}_{s\perp} \tilde{f}_{s0}\left(\tilde{v}_{s\parallel}, \tilde{v}_{s\perp} \right) = \sqrt{\pi}, \tag{D27}$$

and neglected the small ion contribution to the dielectric tensor. We conclude that – as expected – the real frequency of such modes is simply the plasma frequency: $\varpi \approx \pm \omega_{\mathrm{pe}}$. This in turn implies that

$$\tilde{\omega}_e = \frac{k_{\mathrm{D}e}}{\sqrt{2}k} \gg 1. \tag{D28}$$

In other words, electrostatic modes in this limit are simply plasma oscillations with wavelengths much greater than the Debye length.

We immediately deduce that if $\varpi \approx \omega_{pe}$ (without loss of generality, we can consider the mode with $\varpi > 0$), then

$$\frac{\partial \operatorname{Re} \mathfrak{E}_{33}}{\partial \omega}(\varpi, k) \approx \frac{2k^2}{\omega_{pe}}, \tag{D29}$$

which in turn implies that γ is positive if and only if, for some k,

$$\operatorname{Im} \mathfrak{E}_{33}(\omega_{pe}, k) > 0. \tag{D30}$$

For the electron CE distribution function (2.72), we have

$$\frac{\partial \tilde{f}_{e0}}{\partial \tilde{v}_{e\parallel}} = -\exp\left(-\tilde{v}_e^2\right) \left\{ 2\tilde{v}_{e\parallel} + \eta_e \left[\left(2\tilde{v}_{e\parallel}^2 - 1\right) A_e(\tilde{v}_e) - \frac{\tilde{v}_{e\parallel}^2}{\tilde{v}_e} A'_e(\tilde{v}_e) \right] \right.$$
$$\left. + \epsilon_e \left[2\tilde{v}_{e\parallel} C_e(\tilde{v}_e) \left(\tilde{v}_{e\parallel}^2 - \frac{\tilde{v}_{e\perp}^2}{2} - 1 \right) - \frac{\tilde{v}_{e\parallel}}{\tilde{v}_e} \left(\tilde{v}_{e\parallel}^2 - \frac{\tilde{v}_{e\perp}^2}{2} \right) C'_e(\tilde{v}_e) \right] \right\}. \tag{D31}$$

As shown in Appendix B.2.1, for a Krook collision operator it follows that (assuming $\eta_e^R = \eta_e^u = 0$)

$$A_e(\tilde{v}_e) = -\left(\tilde{v}_e^2 - \tfrac{5}{2}\right), \tag{D32a}$$

$$C_e(\tilde{v}_e) = -1. \tag{D32b}$$

We then see that

$$\operatorname{Im} \mathfrak{E}_{33}(\omega_{pe}, k) = \sqrt{\pi} k^2 \left[\frac{k_{De}}{\sqrt{2}k} - \eta_e \left(\frac{k_{De}^2}{4k^2} - \frac{3}{4} \right) \left(\frac{k_{De}^2}{k^2} - 1 \right) \right.$$
$$\left. - \epsilon_e \frac{k_{De}}{\sqrt{2}k} \left(\frac{k_{De}^2}{2k^2} - \frac{3}{2} \right) \right] \exp\left(-\frac{k_{De}^2}{2k^2} \right). \tag{D33}$$

This expression changes sign from negative to positive when $k \lesssim \eta_e^{1/3} k_{De}$, or $k \lesssim \epsilon_e^{1/2} k_{De}$; thus, plasma waves with sufficiently long wavelengths are driven unstable by the non-Maxwellian component of the CE distribution function. Physically, this is the bump-on-tail instability; this arises because the distribution function is no longer monotonically decreasing at (parallel) particle velocities $v_{\parallel} \gtrsim \eta_e^{-1/3} v_{\text{th}e}$, or $v_{\parallel} \gtrsim \eta_e^{-1/3} v_{\text{th}e}$, and so plasma waves can extract energy from particles via the Landau resonance.

Substituting (D33) into (D24), the growth rate of instabilities satisfying $k \ll k_{De}$ becomes

$$\gamma \approx \omega_{pe} \frac{\sqrt{\pi}}{2\sqrt{2}} \frac{k_{De}}{k} \left(1 - \eta_e \frac{k_{De}^3}{2\sqrt{2}k^3} - \epsilon_e \frac{k_{De}^2}{2k^2} \right) \exp\left(-\frac{k_{De}^2}{2k^2} \right). \tag{D34}$$

Maximising this expression with respect to k, it can then be shown that the peak growth rate for CE electron-temperature-gradient-driven microinstabilities ($\epsilon_e = 0$) is

$$\gamma_{\max} \approx \frac{3\sqrt{\pi}}{4} \eta_e^{1/3} \exp\left(-\eta_e^{-2/3} - 1\right) \omega_{pe}, \tag{D35}$$

at the wavenumber

$$k_{\text{peak}} \approx \frac{\eta_e^{1/3}}{\sqrt{2}} \left[1 - \frac{\eta_e^{2/3}}{2} \right] k_{De}, \tag{D36}$$

whereas for CE electron-shear-driven microinstabilities ($\eta_e = 0$)

$$\gamma_{\text{max}} \approx \frac{\sqrt{\pi}}{2} \epsilon_e^{1/2} \exp\left(-\epsilon_e^{-1} - 1\right) \omega_{\text{p}e}, \tag{D37}$$

at the wavenumber

$$k_{\text{peak}} \approx \frac{\epsilon_e^{1/2}}{\sqrt{2}} \left[1 - \frac{\epsilon_e}{2}\right] k_{\text{D}e}. \tag{D38}$$

D.4. *Impossibility of electrostatic instabilities with 'fast' growth rates*

The existence of electrostatic instabilities was demonstrated in Appendix (D.3); however, the growth rates of the exemplified instabilities were shown to be exponentially small in the parameters η_e or ϵ_e. In this appendix, we provide a proof that there cannot exist electrostatic instabilities whose growth rate scales algebraically with η_s or ϵ_s.

To substantiate this claim properly, it is necessary to consider perturbations with frequencies ω satisfying $\omega \ll k_\parallel v_{\text{th}s}$ and $\omega \gtrsim k_\parallel v_{\text{th}s}$ separately.

D.4.1. *Low-frequency electrostatic modes: $\omega \ll k_\parallel v_{\text{th}s}$*

The impossibility of low-frequency electrostatic instabilities follows immediately from (D18), which shows that the leading-order term in the $\tilde{\omega}_{s\parallel} \ll 1$ expansion of the electrostatic component of the dielectric tensor is non-zero. It follows that the electrostatic component of the dielectric tensor is strictly positive at low frequencies. Since the electrostatic component of the dielectric tensor must vanish in order for the electrostatic dispersion relation (D11) to be satisfied, we conclude that there do not exist electrostatic modes with $\omega \ll k_\parallel v_{\text{th}s}$, let alone instabilities.

D.4.2. *Other electrostatic modes: $\omega \gtrsim k_\parallel v_{\text{th}s}$*

For all other electrostatic perturbations, we suppose that there exist microinstabilities with growth rates which scale algebraically with η_s, ϵ_s, and then prove that that such a supposition is incompatible with the hot-plasma electrostatic dispersion relation.

Consider some unstable perturbation satisfying the electrostatic dispersion relation (D11), with complex frequency $\omega = \varpi + i\gamma$, and $\gamma > 0$. We then define

$$\tilde{\varpi}_{s\parallel} \equiv \frac{\varpi}{k_\parallel v_{\text{th}s}}, \tag{D39a}$$

$$\tilde{\gamma}_{s\parallel} \equiv \frac{\gamma}{k_\parallel v_{\text{th}s}}, \tag{D39b}$$

so that $\tilde{\omega}_{s\parallel} = \tilde{\varpi}_{s\parallel} + i\tilde{\gamma}_{s\parallel}$. For unstable perturbations satisfying (D11), it follows from the real and imaginary parts of the dispersion relation that

$$0 = k^2 - \sum_s k_{\text{D}s}^2 \left\{ \frac{1}{\sqrt{\pi}} \int_{-\infty}^{\infty} d\tilde{v}_{s\parallel} \int_0^{\infty} d\tilde{v}_{s\perp} \sum_{n=-\infty}^{\infty} \left[\Pi_n(\tilde{v}_{s\parallel}, \tilde{v}_{s\perp}) \right. \right.$$
$$\left. \left. \times \frac{\left(\tilde{v}_{s\parallel} - \tilde{\varpi}_{s\parallel} + n/k_\parallel \tilde{\rho}_s\right) J_n(k_\perp \tilde{\rho}_s \tilde{v}_{s\perp})^2}{\left(\tilde{v}_{s\parallel} - \tilde{\varpi}_{s\parallel} + n/k_\parallel \tilde{\rho}_s\right)^2 + \tilde{\gamma}_{s\parallel}^2} \right] \right\}, \tag{D40a}$$

$$0 = \gamma \sum_s k_{\mathrm{D}s}^2 \mu_s^{-1/2} \left\{ \frac{1}{\sqrt{\pi}} \int_{-\infty}^{\infty} \mathrm{d}\tilde{v}_{s\parallel} \int_0^{\infty} \mathrm{d}\tilde{v}_{s\perp} \sum_{n=-\infty}^{\infty} \left[\Pi_n(\tilde{v}_{s\parallel}, \tilde{v}_{s\perp}) \right. \right.$$

$$\left. \left. \times \frac{J_n(k_\perp \tilde{\rho}_s \tilde{v}_{s\perp})^2}{\left(\tilde{v}_{s\parallel} - \tilde{\varpi}_{s\parallel} + n/k_\parallel \tilde{\rho}_s \right)^2 + \tilde{\gamma}_{s\parallel}^2} \right] \right\}, \tag{D40b}$$

where $\mu_s \equiv m_e/m_s$, and we have utilised the fact that the Landau contour simplifies to the real line for unstable perturbations. Using (D40b), we can eliminate part of (D40a) to give

$$0 = k^2 - \sum_s k_{\mathrm{D}s}^2 \left\{ \frac{1}{\sqrt{\pi}} \int_{-\infty}^{\infty} \mathrm{d}\tilde{v}_{s\parallel} \int_0^{\infty} \mathrm{d}\tilde{v}_{s\perp} \sum_{n=-\infty}^{\infty} \left[\Pi_n(\tilde{v}_{s\parallel}, \tilde{v}_{s\perp}) \right. \right.$$

$$\left. \left. \times \frac{\left(\tilde{v}_{s\parallel} + n/k_\parallel \tilde{\rho}_s \right) J_n(k_\perp \tilde{\rho}_s \tilde{v}_{s\perp})^2}{\left(\tilde{v}_{s\parallel} - \tilde{\varpi}_{s\parallel} + n/k_\parallel \tilde{\rho}_s \right)^2 + \tilde{\gamma}_{s\parallel}^2} \right] \right\}. \tag{D41}$$

Next, we substitute for $\Pi_n(\tilde{v}_{s\parallel}, \tilde{v}_{s\perp})$ using

$$\Pi_n(\tilde{v}_{s\parallel}, \tilde{v}_{s\perp}) = \Lambda_s(\tilde{v}_{s\parallel}, \tilde{v}_{s\perp}) + \left(\tilde{v}_{s\parallel} + \frac{n}{k_\parallel \tilde{\rho}_s} \right) \frac{\partial \tilde{f}_{s0}}{\partial \tilde{v}_{s\perp}}, \tag{D42}$$

to give

$$0 = k^2 - \sum_s k_{\mathrm{D}s}^2 \left\{ \frac{1}{\sqrt{\pi}} \int_{-\infty}^{\infty} \mathrm{d}\tilde{v}_{s\parallel} \int_0^{\infty} \mathrm{d}\tilde{v}_{s\perp} \sum_{n=-\infty}^{\infty} \left[\frac{\partial \tilde{f}_{s0}}{\partial \tilde{v}_{s\perp}} \frac{\left(\tilde{v}_{s\parallel} + n/k_\parallel \tilde{\rho}_s \right)^2 J_n(k_\perp \tilde{\rho}_s \tilde{v}_{s\perp})^2}{\left(\tilde{v}_{s\parallel} - \tilde{\varpi}_{s\parallel} + n/k_\parallel \tilde{\rho}_s \right)^2 + \tilde{\gamma}_{s\parallel}^2} \right. \right.$$

$$\left. \left. + \Lambda_s(\tilde{v}_{s\parallel}, \tilde{v}_{s\perp}) \frac{\left(\tilde{v}_{s\parallel} + n/k_\parallel \tilde{\rho}_s \right) J_n(k_\perp \tilde{\rho}_s \tilde{v}_{s\perp})^2}{\left(\tilde{v}_{s\parallel} - \tilde{\varpi}_{s\parallel} + n/k_\parallel \tilde{\rho}_s \right)^2 + \tilde{\gamma}_{s\parallel}^2} \right] \right\}. \tag{D43}$$

This expression is very helpful for contradicting the premise of the existence of unstable electrostatic modes. We illustrate this claim with a simple example – a pure Maxwellian distribution function – before considering the CE distribution.

For a Maxwellian distribution for which $\Lambda_s(\tilde{v}_{s\parallel}, \tilde{v}_{s\perp}) = 0$, and

$$\frac{\partial \tilde{f}_{s0}}{\partial \tilde{v}_{s\perp}} = -2\tilde{v}_{s\perp} \exp\left(-\tilde{v}_s^2\right), \tag{D44}$$

(D43) becomes

$$0 = k^2 + \sum_s k_{\mathrm{D}s}^2 \left[\frac{2}{\sqrt{\pi}} \int_{-\infty}^{\infty} \mathrm{d}\tilde{v}_{s\parallel} \int_0^{\infty} \mathrm{d}\tilde{v}_{s\perp} \, \tilde{v}_{s\perp} \exp\left(-\tilde{v}_s^2\right) \right.$$

$$\left. \times \sum_{n=-\infty}^{\infty} \frac{\left(\tilde{v}_{s\parallel} + n/k_\parallel \tilde{\rho}_s \right)^2 J_n(k_\perp \tilde{\rho}_s \tilde{v}_{s\perp})^2}{\left(\tilde{v}_{s\parallel} - \tilde{\varpi}_{s\parallel} + n/k_\parallel \tilde{\rho}_s \right)^2 + \tilde{\gamma}_{s\parallel}^2} \right]. \tag{D45}$$

The integrand on the right-hand side of (D45) is strictly positive – a contradiction. Therefore, we recover the standard result that there cannot exist unstable perturbations if the underlying distribution is Maxwellian.

We now consider the CE distribution (2.72). In order for an instability to arise, it is clear that the integrand on the right-hand side of (D43) has to be positive – and further, the contribution of the integrand from that interval has to dominate all other (negative) contributions to the total integral. To prove that these conditions cannot be satisfied for the CE distribution function, we consider the two terms in the integrand on the right-hand side of (D43) separately.

For the first term

$$\frac{\partial \tilde{f}_{s0}}{\partial \tilde{v}_{s\perp}} \frac{\left(\tilde{v}_{s\parallel} + n/k_\parallel \tilde{\rho}_s\right)^2 J_n(k_\perp \tilde{\rho}_s \tilde{v}_{s\perp})^2}{\left(\tilde{v}_{s\parallel} - \tilde{\varpi}_{s\parallel} + n/k_\parallel \tilde{\rho}_s\right)^2 + \tilde{\gamma}_{s\parallel}^2} > 0 \tag{D46}$$

if and only if

$$\frac{\partial \tilde{f}_{s0}}{\partial \tilde{v}_{s\perp}} < 0. \tag{D47}$$

For the CE distribution function (2.72),

$$\frac{\partial \tilde{f}_{s0}}{\partial \tilde{v}_{s\perp}} = -\tilde{v}_{s\perp} \exp\left(-\tilde{v}_s^2\right) \left\{ 2 + \eta_s \left[2\tilde{v}_{s\parallel} A_s(\tilde{v}_s) - \frac{\tilde{v}_{s\parallel}}{\tilde{v}_s} A'_s(\tilde{v}_s) \right] \right.$$
$$\left. + \epsilon_s \left[2C_s(\tilde{v}_s)\left(\tilde{v}_{s\parallel}^2 - \frac{\tilde{v}_{s\perp}^2}{2} + \frac{1}{2}\right) - \frac{1}{\tilde{v}_s}\left(\tilde{v}_{s\parallel}^2 - \frac{\tilde{v}_{s\perp}^2}{2}\right) C'_s(\tilde{v}_s) \right] \right\}. \tag{D48}$$

Thus, for $\tilde{v}_{s\perp} \lesssim 1$ and $\tilde{v}_{s\parallel} \lesssim 1$, we see that $\partial \tilde{f}_{s0}/\partial \tilde{v}_{s\perp} < 0$, because $\eta_s, \epsilon_s \ll 1$. The only values of $\tilde{v}_s$ where this inequality could be reversed are large: $\tilde{v}_s \gg 1$. Assuming that $A_s(\tilde{v}_s) \sim \tilde{v}_s^{\iota_\eta}$ and $C_s(\tilde{v}_s) \sim \tilde{v}_s^{\iota_\epsilon}$ for $\tilde{v}_s \gg 1$, where ι_η and ι_ϵ are constants, it follows that, for

$$\tilde{v}_s \gtrsim \eta_s^{-1/(\iota_\eta+1)}, \quad \epsilon_s^{-1/(\iota_\epsilon+2)}, \tag{D49a,b}$$

the non-Maxwellian terms are comparable to the Maxwellian ones. However, for such $\tilde{v}_s$

$$\frac{\partial \tilde{f}_{s0}}{\partial \tilde{v}_{s\perp}} \sim \eta_s^{-1/(\iota_\eta+1)} \exp\left(-\eta_s^{-2/(\iota_\eta+1)}\right), \quad \epsilon_s^{-1/(\iota_\epsilon+1)} \exp\left(-\epsilon_s^{-2/(\iota_\epsilon+1)}\right), \tag{D50a,b}$$

while

$$\frac{\left(\tilde{v}_{s\parallel} + n/k_\parallel \tilde{\rho}_s\right)^2 J_n(k_\perp \tilde{\rho}_s \tilde{v}_{s\perp})^2}{\left(\tilde{v}_{s\parallel} - \tilde{\varpi}_{s\parallel} + n/k_\parallel \tilde{\rho}_s\right)^2 + \tilde{\gamma}_{s\parallel}^2} \lesssim \frac{\tilde{\varpi}_{s\parallel}^2}{\tilde{\gamma}_{s\parallel}^2}, \tag{D51}$$

if it is assumed that $|\varpi| \gg |\gamma|$. Since we assumed that $\tilde{\gamma}_{s\parallel}$ is only algebraically small in ϵ_s and/or η_s, we conclude that the contribution to the integrand on the right-hand side of (D43) from $\tilde{v}_s$ satisfying (D49a,b) is asymptotically small compared with other contributions, and thus cannot change the sign of the total integral.

For the second term, we consider the nth term of the sum independently. Recalling from (2.92) that

$$\Lambda_s(\tilde{v}_{s\parallel}, \tilde{v}_{s\perp}) = -\tilde{v}_{s\perp} \exp\left(-\tilde{v}_s^2\right) \left[\eta_s A_s(\tilde{v}_s) - 3\epsilon_s C_s(\tilde{v}_s)\tilde{v}_{s\parallel} \right], \tag{D52}$$

it follows that for $\tilde{v}_s \sim 1$

$$\frac{\Lambda_s(\tilde{v}_{s\parallel}, \tilde{v}_{s\perp})}{\partial \tilde{f}_{s0}/\partial \tilde{v}_{s\perp}} \sim \frac{\eta_s}{\tilde{v}_{s\parallel} + n/k_\parallel \tilde{\rho}_s}, \frac{\epsilon_s}{\tilde{v}_{s\parallel} + n/k_\parallel \tilde{\rho}_s}. \tag{D53}$$

Thus, for $\tilde{v}_s \sim 1$, the non-Maxwellian term is only comparable to the Maxwellian one for $|\tilde{v}_{s\parallel} + n/k_\parallel \tilde{\rho}_s| \lesssim \eta_s, \epsilon_s$. However, this non-Maxwellian contribution is in fact always

smaller than other non-Maxwellian contributions, which by (D53) are in turn smaller than the equivalent Maxwellian contributions.

Depending on the magnitude of $|n/k_\parallel \tilde{\rho}_s|$, this claim is justified in two different ways.

(i) $|n/k_\parallel \tilde{\rho}_s| \lesssim 1$: in this case, let the interval of non-dimensionalised parallel velocities $\tilde{v}_{s\parallel}$ satisfying $|\tilde{v}_{s\parallel} + n/k_\parallel \tilde{\rho}_s| \lesssim \eta_s, \epsilon_s$ be denoted by $\mathcal{I}$. Then, there exists another finite interval of $\tilde{v}_{s\parallel} \sim 1$ such that $|\tilde{v}_{s\parallel} + n/k_\parallel \tilde{\rho}_s| \sim 1$. It therefore follows that

$$\int_{\mathcal{I}} \mathrm{d}\tilde{v}_{s\parallel} \, \Lambda_s(\tilde{v}_{s\parallel}, \tilde{v}_{s\perp}) \frac{(\tilde{v}_{s\parallel} + n/k_\parallel \tilde{\rho}_s) \, J_n(k_\perp \tilde{\rho}_s \tilde{v}_{s\perp})^2}{(\tilde{v}_{s\parallel} - \tilde{\varpi}_{s\parallel} + n/k_\parallel \tilde{\rho}_s)^2 + \tilde{\gamma}_{s\parallel}^2}$$

$$\sim \eta_s^2 \int_{-\infty}^{\infty} \mathrm{d}\tilde{v}_{s\parallel} \, \Lambda_s(\tilde{v}_{s\parallel}, \tilde{v}_{s\perp}) \frac{(\tilde{v}_{s\parallel} + n/k_\parallel \tilde{\rho}_s) \, J_n(k_\perp \tilde{\rho}_s \tilde{v}_{s\perp})^2}{(\tilde{v}_{s\parallel} - \tilde{\varpi}_{s\parallel} + n/k_\parallel \tilde{\rho}_s)^2 + \tilde{\gamma}_{s\parallel}^2}, \tag{D54}$$

where we have assumed that $|\tilde{\varpi}_{s\parallel}| \gg |\tilde{\gamma}_{s\parallel}|$ (and also $|\tilde{\varpi}_{s\parallel}| \gtrsim 1$). The claim immediately follows.

(ii) $|n/k_\parallel \tilde{\rho}_s| \gg 1$: in this case, it follows immediately that $|\tilde{v}_{s\parallel} + n/k_\parallel \tilde{\rho}_s| \lesssim \eta_s, \epsilon_s$ if and only if $\tilde{v}_{s\parallel} \gg 1$. Via a similar argument to that presented for large $\tilde{v}_{s\parallel}$ for the first term in the integrand on the right-hand side of (D43), contributions to the total integral will be exponentially small in η_s, ϵ_s, and thus are unable to reverse the sign of the total integral.

Thus, we have confirmed that there cannot exist electrostatic instabilities with growth rates which are algebraic in small parameters η_s, ϵ_s.

Appendix E. Weak growth of high-frequency perturbations

In this appendix, we present an argument that all perturbations in a CE plasma with complex frequency $\omega = \varpi + \mathrm{i}\gamma$ satisfying the 'high-frequency' conditions $|\omega| \gtrsim k_\parallel v_{\mathrm{th}s}$ and $|\varpi| \gg |\gamma|$ for all particle species have a growth rate that is at most exponentially small in η_s, and ϵ_s. This argument does not prove that all perturbations satisfying $|\omega| \gtrsim k_\parallel v_{\mathrm{th}s}$ in a CE plasma are stable, in that it does not apply to perturbations whose damping or growth rate is not small compared with their frequency.

E.1. *Deriving conditions for stability*

We begin with the result that for any linear electromagnetic perturbation with real frequency $\varpi > 0$, growth rate γ, wavevector $\boldsymbol{k}$ and electric-field perturbation

$$\delta \boldsymbol{E} = \widehat{\delta \boldsymbol{E}} \exp\{\mathrm{i}(\boldsymbol{k} \cdot \boldsymbol{r} - \varpi t) + \gamma t\}, \tag{E1}$$

the dissipation rate $\mathfrak{Q}$ of the perturbation is related to the anti-Hermitian part of the plasma dielectric tensor evaluated at the perturbation's real frequency (Pitaevskii & Lifshitz 1981):

$$\mathfrak{Q} = \mathrm{i}\varpi \widehat{\delta \boldsymbol{E}}^* \cdot \boldsymbol{\mathfrak{E}}^A(\boldsymbol{k}, \varpi) \cdot \widehat{\delta \boldsymbol{E}}, \tag{E2}$$

where the anti-Hermitian part $\boldsymbol{\mathfrak{E}}^A$ is defined by

$$\boldsymbol{\mathfrak{E}}^A = \tfrac{1}{2}\left(\boldsymbol{\mathfrak{E}} - \boldsymbol{\mathfrak{E}}^\dagger\right), \tag{E3}$$

with $\boldsymbol{\mathfrak{E}}^\dagger$ representing the conjugate transpose of $\boldsymbol{\mathfrak{E}}$. If the mode is damped, then the dissipation rate is positive: $\mathfrak{Q} > 0$. Since $\boldsymbol{\mathfrak{E}}^A$ is anti-Hermitian, it is diagonalisable in some

orthonormal basis $\{\hat{\boldsymbol{e}}_a, \hat{\boldsymbol{e}}_b, \hat{\boldsymbol{e}}_c\}$, with imaginary eigenvalues $(-\mathrm{i}\varsigma_a, -\mathrm{i}\varsigma_b, -\mathrm{i}\varsigma_c)$, where ς_a, ς_b and ς_c are real numbers. The dissipation rate $\mathfrak{Q}$ can be written in terms of these eigenvectors as

$$\mathfrak{Q} = \varpi \left(\varsigma_a \left| \hat{\boldsymbol{e}}_a \cdot \widehat{\delta\boldsymbol{E}} \right|^2 + \varsigma_b \left| \hat{\boldsymbol{e}}_b \cdot \widehat{\delta\boldsymbol{E}} \right|^2 + \varsigma_c \left| \hat{\boldsymbol{e}}_c \cdot \widehat{\delta\boldsymbol{E}} \right|^2 \right). \tag{E4}$$

Thus, for unstable perturbations to exist, it must be the case that at least one of the numbers ς_a, ς_b and ς_c has to be negative (without loss of generality, we will assume $\varsigma_a < 0$); if this is the case, then the dissipation rate (and hence the growth rate) is a linear function of ς_a. We will show that if $|\omega| \gtrsim k_\parallel v_{\mathrm{th}s}$, ς_a, ς_b and ς_c can only be negative if they are exponentially small in η_s and ϵ_s.

To prove this, consider the characteristic polynomial

$$\varrho(\varsigma) \equiv \det\left[\mathfrak{C}^A(\boldsymbol{k}, \varpi) - \varsigma \boldsymbol{I}\right] \tag{E5}$$

of $\mathfrak{C}^A$ evaluated at the real frequency ϖ and wavevector $\boldsymbol{k}$; it is a cubic, and thus can be written

$$\varrho(\varsigma) = -\varsigma^3 - \mathrm{i}\varrho_2\varsigma^2 + \varrho_1\varsigma + \mathrm{i}\varrho_0, \tag{E6}$$

where ϱ_0, ϱ_1 and ϱ_2 depend on $\mathfrak{C}^A$. Since $\mathfrak{C}^A$ has eigenvalues $(-\mathrm{i}\varsigma_a, -\mathrm{i}\varsigma_b, -\mathrm{i}\varsigma_c)$, it follows that

$$\begin{aligned}
\varrho(\varsigma) &= -\left(\varsigma + \mathrm{i}\varsigma_a\right)\left(\varsigma + \mathrm{i}\varsigma_b\right)\left(\varsigma + \mathrm{i}\varsigma_c\right) \\
&= -\varsigma^3 - \mathrm{i}\varsigma^2\left(\varsigma_a + \varsigma_b + \varsigma_c\right) + \varsigma\left(\varsigma_a\varsigma_b + \varsigma_b\varsigma_c + \varsigma_c\varsigma_a\right) + \mathrm{i}\varsigma_a\varsigma_b\varsigma_c,
\end{aligned} \tag{E7}$$

and so

$$\varrho_0 = \varsigma_a\varsigma_b\varsigma_c, \tag{E8a}$$

$$\varrho_1 = \varsigma_a\varsigma_b + \varsigma_b\varsigma_c + \varsigma_c\varsigma_a, \tag{E8b}$$

$$\varrho_2 = \varsigma_a + \varsigma_b + \varsigma_c. \tag{E8c}$$

This implies that ς_a, ς_b and ς_c are positive if ϱ_0, ϱ_1 and ϱ_2 are positive. Furthermore, ϱ_0, ϱ_1 and ϱ_2 can be used to provide bounds for ς_a, ς_b and ς_c using an inequality discovered by Laguerre (1880):

$$\varsigma_- \leqslant \varsigma_a, \quad \varsigma_b, \quad \varsigma_c \leqslant \varsigma_+, \tag{E9a–c}$$

where

$$\varsigma_\pm = -\frac{\varrho_2}{3} \pm \frac{2}{3}\sqrt{\varrho_2^2 - 3\varrho_1^2}. \tag{E10}$$

In particular, the expression (E10) for the root bounds implies that if ϱ_1 and ϱ_2 are exponentially small in η_s and ϵ_s, then so are ς_a, ς_b and ς_c.

We can also evaluate $\varrho(\varsigma)$ in terms of the components of $\mathfrak{E}^A$ in the coordinate basis $\{\hat{\boldsymbol{x}}, \hat{\boldsymbol{y}}, \hat{\boldsymbol{z}}\}$:

$$
\begin{aligned}
\varrho(\varsigma) = &-\varsigma^3 + \varsigma^2 \left(\mathfrak{E}^A_{xx} + \mathfrak{E}^A_{yy} + \mathfrak{E}^A_{zz}\right) \\
&- \varsigma \left(\mathfrak{E}^A_{xx}\mathfrak{E}^A_{yy} + \mathfrak{E}^A_{yy}\mathfrak{E}^A_{zz} + \mathfrak{E}^A_{zz}\mathfrak{E}^A_{xx} + (\mathfrak{E}^A_{xy})^2 + (\mathfrak{E}^A_{yz})^2 + (\mathfrak{E}^A_{xz})^2\right) + \det \mathfrak{E}^A,
\end{aligned}
\tag{E11}
$$

where we have used the symmetries (2.87a–c) of the dielectric tensor to give $\varrho(\varsigma)$ in terms of only the (six) independent components of $\mathfrak{E}^A$. (E11) gives

$$
\varrho_0 = -\mathrm{i} \det \mathfrak{E}^A,
\tag{E12a}
$$

$$
\varrho_1 = -\mathfrak{E}^A_{xx}\mathfrak{E}^A_{yy} - \mathfrak{E}^A_{yy}\mathfrak{E}^A_{zz} - \mathfrak{E}^A_{zz}\mathfrak{E}^A_{xx} - (\mathfrak{E}^A_{xy})^2 - (\mathfrak{E}^A_{yz})^2 - (\mathfrak{E}^A_{xz})^2,
\tag{E12b}
$$

$$
\varrho_2 = -\mathrm{i} \left(\mathfrak{E}^A_{xx} + \mathfrak{E}^A_{yy} + \mathfrak{E}^A_{zz}\right).
\tag{E12c}
$$

The anti-Hermiticity of $\mathfrak{E}^A$ implies that $\mathrm{Im}\, \mathfrak{E}^A_{xx} = -\mathrm{i}\mathfrak{E}^A_{xx}$, $\mathrm{Im}\, \mathfrak{E}^A_{yy} = -\mathrm{i}\mathfrak{E}^A_{yy}$, $\mathrm{Im}\, \mathfrak{E}^A_{zz} = -\mathrm{i}\mathfrak{E}^A_{zz}$ and $\mathrm{Im}\, \mathfrak{E}^A_{xz} = -\mathrm{i}\mathfrak{E}^A_{xz}$, while $\mathrm{Re}\, \mathfrak{E}^A_{xy} = \mathfrak{E}^A_{xy}$ and $\mathrm{Re}\, \mathfrak{E}^A_{yz} = \mathfrak{E}^A_{yz}$, as is indeed necessary for ϱ_0, ϱ_1, and ϱ_2 to be real numbers. Thus, in order to establish stability it is sufficient for our purposes to show that

$$
\mathrm{i} \det \mathfrak{E}^A < 0,
\tag{E13a}
$$

$$
\mathfrak{E}^A_{xx}\mathfrak{E}^A_{yy} + \mathfrak{E}^A_{yy}\mathfrak{E}^A_{zz} + \mathfrak{E}^A_{zz}\mathfrak{E}^A_{xx} + (\mathfrak{E}^A_{xy})^2 + (\mathfrak{E}^A_{yz})^2 + (\mathfrak{E}^A_{xz})^2 < 0,
\tag{E13b}
$$

$$
\mathrm{i} \left(\mathfrak{E}^A_{xx} + \mathfrak{E}^A_{yy} + \mathfrak{E}^A_{zz}\right) < 0.
\tag{E13c}
$$

When these inequalities are not strictly satisfied, then we can instead estimate the magnitude of (E12b) and (E12c) to determine bounds for ς_a, ς_b and ς_c.

E.2. *Evaluating conditions for stability*

Combining (2.74) with (2.77) gives an expression for the general plasma dielectric tensor (assuming $k_\parallel > 0$ without loss of generality):

$$
\begin{aligned}
\mathfrak{E} = \boldsymbol{I} + \sum_s \frac{\omega^2_{ps}}{\omega^2} \Bigg[&\frac{2}{\sqrt{\pi}} \int_{-\infty}^{\infty} \mathrm{d}\tilde{v}_{s\parallel}\, \tilde{v}_{s\parallel} \int_0^{\infty} \mathrm{d}\tilde{v}_{s\perp}\, \Lambda_s(\tilde{v}_{s\parallel}, \tilde{v}_{s\perp})\hat{\boldsymbol{z}}\hat{\boldsymbol{z}} \\
&+ \tilde{\omega}_{s\parallel} \frac{2}{\sqrt{\pi}} \int_{C_L} \mathrm{d}\tilde{v}_{s\parallel} \int_0^{\infty} \mathrm{d}\tilde{v}_{s\perp}\, \tilde{v}^2_{s\perp} \Xi_s(\tilde{v}_{s\parallel}, \tilde{v}_{s\perp}) \sum_{n=-\infty}^{\infty} \frac{\boldsymbol{R}_{sn}}{\zeta_{sn} - \tilde{v}_{s\parallel}} \Bigg],
\end{aligned}
\tag{E14}
$$

where all salient quantities are defined in § 2.4.1. Now evaluating the anti-Hermitian part of (E14) for $\omega = \varpi$, $\tilde{\omega}_{s\parallel} = \tilde{\varpi}_{s\parallel}$, we find

$$
\mathfrak{E}^A = -\mathrm{i} \sum_s \frac{\omega^2_{ps}}{\varpi^2} \left[2\sqrt{\pi}\tilde{\varpi}_{s\parallel} \int_0^{\infty} \mathrm{d}\tilde{v}_{s\perp}\, \tilde{v}^2_{s\perp} \sum_{n=-\infty}^{\infty} \Xi_s(\zeta_{sn}, \tilde{v}_{s\perp})\boldsymbol{R}_{sn}(\zeta_{sn}, \tilde{v}_{s\perp}) \right].
\tag{E15}
$$

We now consider stability conditions (E13) in turn.

First evaluating (E13c), it can be shown that

$$
i\left(\mathfrak{E}_{xx}^A + \mathfrak{E}_{yy}^A + \mathfrak{E}_{zz}^A\right) = 2\sqrt{\pi}\sum_s \frac{\omega_{ps}^2}{\varpi^2}\tilde{\varpi}_{s\parallel}\sum_{n=-\infty}^{\infty}\left\{\int_0^\infty \mathrm{d}\tilde{v}_{s\perp}\,\tilde{v}_{s\perp}^2\,\varXi_s(\zeta_{sn}, \tilde{v}_{s\perp})\right.
$$
$$
\left. \times\left[\frac{n^2 J_n(k_\perp\tilde{\rho}_s\tilde{v}_{s\perp})^2}{k_\perp^2\tilde{\rho}_s^2\tilde{v}_{s\perp}^2} + J_n'(k_\perp\tilde{\rho}_s\tilde{v}_{s\perp})^2 + \frac{\zeta_{sn}^2}{\tilde{v}_{s\perp}^2}J_n(k_\perp\tilde{\rho}_s\tilde{v}_{s\perp})^2\right]\right\}.
$$
(E16)

It is clear that the right-hand side (E16) is negative if

$$
\varXi_s(\zeta_{sn}, \tilde{v}_{s\perp}) < 0. \tag{E17}
$$

For a Maxwellian distribution,

$$
\varXi_s(\zeta_{sn}, \tilde{v}_{s\perp}) = \frac{\partial\tilde{f}_{s0}}{\partial\tilde{v}_{s\perp}}(\zeta_{sn}, \tilde{v}_{s\perp}) = -2\tilde{v}_{s\perp}\exp\left(-\tilde{v}_{s\perp}^2\right)\exp\left(-\zeta_{sn}^2\right) < 0, \tag{E18}
$$

and thus $i(\mathfrak{E}_{xx}^A + \mathfrak{E}_{yy}^A + \mathfrak{E}_{zz}^A) < 0$, as required. For the CE distribution (2.72)

$$
\varXi_s(\tilde{v}_{s\parallel}, \tilde{v}_{s\perp}) = -\tilde{v}_{s\perp}\exp\left(-\tilde{v}_s^2\right)\left\{2 + \eta_s\left[2\tilde{v}_{s\parallel}A_s(\tilde{v}_s) - \frac{\tilde{v}_{s\parallel}}{\tilde{v}_s}A_s'(\tilde{v}_s)\right]\right.
$$
$$
\left. + \epsilon_s\left[2C_s(\tilde{v}_s)\left(\tilde{v}_{s\parallel}^2 - \frac{\tilde{v}_{s\perp}^2}{2} + \frac{1}{2}\right) - \frac{1}{\tilde{v}_s}\left(\tilde{v}_{s\parallel}^2 - \frac{\tilde{v}_{s\perp}^2}{2}\right)C_s'(\tilde{v}_s)\right]\right\}
$$
$$
- \frac{\tilde{v}_{s\perp}}{\tilde{\omega}_{s\parallel}}\exp\left(-\tilde{v}_s^2\right)\left[\eta_s A_s(\tilde{v}_s) - 3\epsilon_s C_s(\tilde{v}_s)\tilde{v}_{s\parallel}\right]. \tag{E19}
$$

For $|\tilde{\omega}_{s\parallel}| \gtrsim 1$, it is clear for $\tilde{v}_s \lesssim 1$ that the largest contribution to $\varXi_s(\tilde{v}_{s\parallel}, \tilde{v}_{s\perp})$ comes from the Maxwellian term; the non-Maxwellian terms are $O(\eta_s, \epsilon_s)$. Thus, for $\zeta_{sn}, \tilde{v}_{s\perp} \lesssim 1$, $\varXi_s(\zeta_{sn}, \tilde{v}_{s\perp}) < 0$. As discussed in Appendix (D.4.2), for $\zeta_{sn} \gg 1$, the sign of $\varXi_s(\zeta_{sn}, \tilde{v}_{s\perp}) < 0$ can, in principle, be reversed. However, the magnitude of $\varXi_s(\zeta_{sn}, \tilde{v}_{s\perp})$ is exponentially small for such ζ_{sn}, and thus so is ϱ_2.

The remaining conditions (E13a) and (E13b) are much more tedious to treat; thus for simplicity, we explicitly consider only the case when a single particle species provides the dominant contribution to the dielectric tensor. Under this assumption, it can be shown that

$$
\mathfrak{E}_{xx}^A\mathfrak{E}_{yy}^A + \mathfrak{E}_{yy}^A\mathfrak{E}_{zz}^A + \mathfrak{E}_{zz}^A\mathfrak{E}_{xx}^A + (\mathfrak{E}_{xy}^A)^2 + (\mathfrak{E}_{yz}^A)^2 + (\mathfrak{E}_{xz}^A)^2
$$
$$
= 2\pi\frac{\omega_{ps}^4}{\varpi^4}\tilde{\varpi}_{s\parallel}^2\sum_{m=-\infty}^{\infty}\sum_{n=-\infty}^{\infty}\left\{\int_0^\infty \mathrm{d}\tilde{v}_{s\perp}^{(1)}\int_0^\infty \mathrm{d}\tilde{v}_{s\perp}^{(2)}\,\tilde{v}_{s\perp}^{(1)}\tilde{v}_{s\perp}^{(2)}\right.
$$
$$
\left. \times\left[\varXi_s(\zeta_{sm}, \tilde{v}_{s\perp}^{(1)})\varXi_s(\zeta_{sn}, \tilde{v}_{s\perp}^{(2)})\mathfrak{A}_{mn}(\alpha_s, \tilde{v}_{s\perp}^{(1)}, \tilde{v}_{s\perp}^{(2)})\right]\right\}, \tag{E20}
$$

where $\alpha_s \equiv k_\perp \tilde{\rho}_s$ and

$$
\begin{aligned}
\mathfrak{A}_{mn}&(\alpha_s, \tilde{v}_{s\perp}^{(1)}, \tilde{v}_{s\perp}^{(2)}) \\
&\equiv \frac{1}{\alpha_s^2} \left[m\tilde{v}_{s\perp}^{(2)} J_m(\alpha_s \tilde{v}_{s\perp}^{(1)}) J_n'(\alpha_s \tilde{v}_{s\perp}^{(2)}) - n\tilde{v}_{s\perp}^{(1)} J_m'(\alpha_s \tilde{v}_{s\perp}^{(1)}) J_n(\alpha_s \tilde{v}_{s\perp}^{(2)}) \right]^2 \\
&\quad + \frac{1}{\alpha_s^2} \left[m\zeta_{sn}\tilde{v}_{s\perp}^{(2)} J_m(\alpha_s \tilde{v}_{s\perp}^{(1)}) J_n'(\alpha_s \tilde{v}_{s\perp}^{(2)}) - n\zeta_{sm}\tilde{v}_{s\perp}^{(1)} J_m'(\alpha_s \tilde{v}_{s\perp}^{(1)}) J_n(\alpha_s \tilde{v}_{s\perp}^{(2)}) \right]^2 \\
&\quad + \left[\zeta_{sn}\tilde{v}_{s\perp}^{(2)} J_m(\alpha_s \tilde{v}_{s\perp}^{(1)}) J_n'(\alpha_s \tilde{v}_{s\perp}^{(2)}) - \zeta_{sm}\tilde{v}_{s\perp}^{(1)} J_m'(\alpha_s \tilde{v}_{s\perp}^{(1)}) J_n(\alpha_s \tilde{v}_{s\perp}^{(2)}) \right]^2 .
\end{aligned}
\tag{E21}
$$

Being a sum of positive terms, $\mathfrak{A}_{mn}$ is positive for all n and m, and thus we again conclude that the integrand on the right-hand side of (E20) is negative if $\Xi_s(\zeta_{sm}, \tilde{v}_{s\perp}) < 0$ and $\Xi_s(\zeta_{sn}, \tilde{v}_{s\perp}) < 0$. Via similar reasoning to that applied to ϱ_2 in the previous paragraph, it follows that for the CE distribution function, the only way in which this condition can be violated is for either $\zeta_{sm} \gg 1$ or $\zeta_{sn} \gg 1$ – both of which give rise to exponentially small terms. Thus, either $\varrho_1 > 0$ or ϱ_1 is exponentially small in η_s and ϵ_s.

Finally, for (E13a), it is necessary to evaluate $\det \mathfrak{C}^A$; this becomes (after much tedious algebra)

$$
\begin{aligned}
\det \mathfrak{C}^A = -\frac{4}{3} i\pi^{3/2} \frac{\omega_{\mathrm{ps}}^6}{\varpi^6} \tilde{\varpi}_{s\parallel}^3 \\
\times \sum_{m=-\infty}^{\infty} \sum_{n=-\infty}^{\infty} \sum_{l=-\infty}^{\infty} \left\{ \int_0^\infty d\tilde{v}_{s\perp}^{(1)} \int_0^\infty d\tilde{v}_{s\perp}^{(2)} \int_0^\infty d\tilde{v}_{s\perp}^{(3)} \, \tilde{v}_{s\perp}^{(1)} \tilde{v}_{s\perp}^{(2)} \tilde{v}_{s\perp}^{(3)} \right. \\
\left. \times \left[\Xi_s(\zeta_{sm}, \tilde{v}_{s\perp}^{(1)}) \Xi_s(\zeta_{sn}, \tilde{v}_{s\perp}^{(2)}) \Xi_s(\zeta_{sl}, \tilde{v}_{s\perp}^{(3)}) \mathfrak{B}_{mnl}(\alpha_s, \tilde{v}_{s\perp}^{(1)}, \tilde{v}_{s\perp}^{(2)}, \tilde{v}_{s\perp}^{(3)}) \right] \right\},
\end{aligned}
\tag{E22}
$$

where

$$
\begin{aligned}
\mathfrak{B}_{mnl}&(\alpha_s, \tilde{v}_{s\perp}^{(1)}, \tilde{v}_{s\perp}^{(2)}, \tilde{v}_{s\perp}^{(3)}) \\
&\equiv \left\{ mJ_m(\alpha_s \tilde{v}_{s\perp}^{(1)}) \left[\tilde{v}_{s\perp}^{(1)} \zeta_{sn} J_n(\alpha_s \tilde{v}_{s\perp}^{(2)}) J_l'(\alpha_s \tilde{v}_{s\perp}^{(3)}) - \tilde{v}_{s\perp}^{(3)} \zeta_{sl} J_n'(\alpha_s \tilde{v}_{s\perp}^{(2)}) J_l(\alpha_s \tilde{v}_{s\perp}^{(3)}) \right] \right. \\
&\quad + nJ_n(\alpha_s \tilde{v}_{s\perp}^{(1)}) \left[\tilde{v}_{s\perp}^{(2)} \zeta_{sl} J_l(\alpha_s \tilde{v}_{s\perp}^{(2)}) J_m'(\alpha_s \tilde{v}_{s\perp}^{(3)}) - \tilde{v}_{s\perp}^{(1)} \zeta_{sm} J_l'(\alpha_s \tilde{v}_{s\perp}^{(2)}) J_m(\alpha_s \tilde{v}_{s\perp}^{(3)}) \right] \\
&\quad \left. + lJ_l(\alpha_s \tilde{v}_{s\perp}^{(1)}) \left[\tilde{v}_{s\perp}^{(3)} \zeta_{sm} J_m(\alpha_s \tilde{v}_{s\perp}^{(2)}) J_n'(\alpha_s \tilde{v}_{s\perp}^{(3)}) - \tilde{v}_{s\perp}^{(2)} \zeta_{sn} J_m'(\alpha_s \tilde{v}_{s\perp}^{(2)}) J_n(\alpha_s \tilde{v}_{s\perp}^{(3)}) \right] \right\}^2 .
\end{aligned}
\tag{E23}
$$

Similarly to $\mathfrak{A}_{mn}$, $\mathfrak{B}_{mnl}$ is strictly positive for all m, n and l, meaning that the integrand on the right-hand side of (E22) is negative if $\Xi_s(\zeta_{sm}, \tilde{v}_{s\perp}) < 0$, $\Xi_s(\zeta_{sn}, \tilde{v}_{s\perp}) < 0$ and $\Xi_s(\zeta_{sl}, \tilde{v}_{s\perp}) < 0$. For the CE distribution, exactly the same argument as before applies to show that either $\varrho_0 > 0$ or it is exponentially small.

In summary, we have now verified that the only situation in which the stability conditions (E13) are not satisfied are those for which ϱ_0, ϱ_1 and ϱ_2 are exponentially small in η_s and ϵ_s. In the latter case, considerations of bounds (E9a–c) and (E10) implies that ς_a, ς_b, and ς_c are also all exponentially small in η_s and ϵ_s. The claim of the appendix follows.

Appendix F. Properties of leading-order expansion $\mathfrak{E}^{(0)}$ of dielectric tensor (2.74) in $\tilde{\omega}_{s\parallel} \ll 1$ for a weakly anisotropic distribution function

F.1. *Symmetries of $\mathfrak{E}_s^{(0)}$ in coordinate basis $\{\hat{x}, \hat{y}, \hat{z}\}$*

In this appendix, we show that the leading-order expansion $\mathfrak{E}_s^{(0)}$ (cf. (2.100a)) of the dielectric tensor $\mathfrak{E}_s$ of species s (cf. (2.96)) in $\tilde{\omega}_{s\parallel} \ll 1$ arising in a non-relativistic plasma with only weak anisotropy of its particle distribution function obeys additional symmetries (2.101), *viz.*

$$(\mathfrak{E}_s^{(0)})_{xz} = -\frac{k_\perp}{k_\parallel}(\mathfrak{E}_s^{(0)})_{xx}, \tag{F1a}$$

$$(\mathfrak{E}_s^{(0)})_{yz} = \frac{k_\perp}{k_\parallel}(\mathfrak{E}_s^{(0)})_{xy}, \tag{F1b}$$

$$(\mathfrak{E}_s^{(0)})_{zz} = \frac{k_\perp^2}{k_\parallel^2}(\mathfrak{E}_s^{(0)})_{xx}, \tag{F1c}$$

when $k\rho_s \sim 1$. The term 'weak anisotropy' means that the magnitude of angular anisotropy – mathematically represented by the function Λ_s defined by (2.84) – satisfies $\Lambda_s \lesssim \tilde{\omega}_{s\parallel}$ for all particle species when $\tilde{v}_s \sim 1$.

We begin the proof by substituting (2.77) into (2.96) to give

$$\mathfrak{E}_s \equiv \frac{\omega_{\text{ps}}^2}{\omega^2}\left[\frac{2}{\sqrt{\pi}}\frac{k_\parallel}{|k_\parallel|}\int_{-\infty}^{\infty}\mathrm{d}\tilde{v}_{s\parallel}\,\tilde{v}_{s\parallel}\int_0^{\infty}\mathrm{d}\tilde{v}_{s\perp}\,\Lambda_s(\tilde{v}_{s\parallel},\tilde{v}_{s\perp})\hat{z}\hat{z}\right.$$

$$\left.+\tilde{\omega}_{s\parallel}\frac{2}{\sqrt{\pi}}\int_{C_L}\mathrm{d}\tilde{v}_{s\parallel}\int_0^{\infty}\mathrm{d}\tilde{v}_{s\perp}\,\tilde{v}_{s\perp}^2\,\Xi_s(\tilde{v}_{s\parallel},\tilde{v}_{s\perp})\sum_{n=-\infty}^{\infty}\frac{\boldsymbol{R}_{sn}}{\zeta_{sn}-\tilde{v}_{s\parallel}}\right]. \tag{F2}$$

Then, under the assumed ordering $\tilde{\omega}_{s\parallel} \sim \Lambda_s$, the function Ξ_s defined by (2.85) satisfies $\Xi_s \sim 1$ for $\tilde{v}_s \sim 1$; therefore, $\mathfrak{E}_s$ has order-unity elements as $\tilde{\omega}_{s\parallel} \to 0$. Let us expand $\mathfrak{E}_s$ in a Taylor series around $\tilde{\omega}_{s\parallel} = 0$:

$$\mathfrak{E}_s = \tilde{\omega}_{s\parallel}\mathfrak{E}_s^{(0)} + \delta\mathfrak{E}_s, \tag{F3}$$

where $\delta\mathfrak{E}_s = O(\tilde{\omega}_{s\parallel}^2)$, and the matrix elements of $\mathfrak{E}_s^{(0)}$ are given below:

$$(\mathfrak{E}_s^{(0)})_{xx} \equiv -\frac{2\omega_{\text{ps}}^2}{\sqrt{\pi}\omega^2}\sum_{n=-\infty}^{\infty}\left[\frac{n^2}{k_\perp^2\tilde{\rho}_s^2}\int_{C_L}\frac{\mathrm{d}\tilde{v}_{s\parallel}}{\tilde{v}_{s\parallel}+n/|k_\parallel|\tilde{\rho}_s}\right.$$

$$\left.\times\int_0^{\infty}\mathrm{d}\tilde{v}_{s\perp}\,\Xi_s(\tilde{v}_{s\parallel},\tilde{v}_{s\perp})J_n(k_\perp\tilde{\rho}_s\tilde{v}_{s\perp})^2\right], \tag{F4a}$$

$$(\mathfrak{E}_s^{(0)})_{xy} \equiv -\frac{2\mathrm{i}\omega_{\text{ps}}^2}{\sqrt{\pi}\omega^2}\sum_{n=-\infty}^{\infty}\left[\frac{n}{k_\perp\tilde{\rho}_s}\int_{C_L}\frac{\mathrm{d}\tilde{v}_{s\parallel}}{\tilde{v}_{s\parallel}+n/|k_\parallel|\tilde{\rho}_s}\right.$$

$$\left.\times\int_0^{\infty}\mathrm{d}\tilde{v}_{s\perp}\,\tilde{v}_{s\perp}\,\Xi_s(\tilde{v}_{s\parallel},\tilde{v}_{s\perp})J_n(k_\perp\tilde{\rho}_s\tilde{v}_{s\perp})J_n'(k_\perp\tilde{\rho}_s\tilde{v}_{s\perp})\right], \tag{F4b}$$

$$(\mathfrak{E}_s^{(0)})_{xz} \equiv -\frac{2\omega_{ps}^2}{\sqrt{\pi}\omega^2} \sum_{n=-\infty}^{\infty} \left[\frac{n}{k_\perp \tilde{\rho}_s} \int_{C_L} \frac{\tilde{v}_{s\parallel} \, d\tilde{v}_{s\parallel}}{\tilde{v}_{s\parallel} + n/|k_\parallel|\tilde{\rho}_s} \right.$$
$$\left. \times \int_0^\infty d\tilde{v}_{s\perp} \, \varXi_s(\tilde{v}_{s\parallel}, \tilde{v}_{s\perp}) J_n(k_\perp \tilde{\rho}_s \tilde{v}_{s\perp})^2 \right], \tag{F4c}$$

$$(\mathfrak{E}_s^{(0)})_{yx} \equiv -(\mathfrak{E}_s^{(0)})_{xy}, \tag{F4d}$$

$$(\mathfrak{E}_s^{(0)})_{yy} \equiv -\frac{2\omega_{ps}^2}{\sqrt{\pi}\omega^2} \sum_{n=-\infty}^{\infty} \left[\int_{C_L} \frac{d\tilde{v}_{s\parallel}}{\tilde{v}_{s\parallel} + n/|k_\parallel|\tilde{\rho}_s} \right.$$
$$\left. \times \int_0^\infty d\tilde{v}_{s\perp} \, \tilde{v}_{s\perp}^2 \, \varXi_s(\tilde{v}_{s\parallel}, \tilde{v}_{s\perp}) J'_n(k_\perp \tilde{\rho}_s \tilde{v}_{s\perp})^2 \right], \tag{F4e}$$

$$(\mathfrak{E}_s^{(0)})_{yz} \equiv -\frac{2\mathrm{i}\omega_{ps}^2}{\sqrt{\pi}\omega^2} \sum_{n=-\infty}^{\infty} \left[\int_{C_L} \frac{\tilde{v}_{s\parallel} \, d\tilde{v}_{s\parallel}}{\tilde{v}_{s\parallel} + n/|k_\parallel|\tilde{\rho}_s} \right.$$
$$\left. \times \int_0^\infty d\tilde{v}_{s\perp} \, \tilde{v}_{s\perp} \, \varXi_s(\tilde{v}_{s\parallel}, \tilde{v}_{s\perp}) J_n(k_\perp \tilde{\rho}_s \tilde{v}_{s\perp}) J'_n(k_\perp \tilde{\rho}_s \tilde{v}_{s\perp}) \right], \tag{F4f}$$

$$(\mathfrak{E}_s^{(0)})_{zx} \equiv (\mathfrak{E}_s^{(0)})_{xz}, \tag{F4g}$$

$$(\mathfrak{E}_s^{(0)})_{zy} \equiv -(\mathfrak{E}_s^{(0)})_{yz}, \tag{F4h}$$

$$(\mathfrak{E}_s^{(0)})_{zz} \equiv \frac{2\omega_{ps}^2}{\sqrt{\pi}\tilde{\omega}_{s\parallel}\omega^2} \int_{-\infty}^\infty d\tilde{v}_{s\parallel} \, \tilde{v}_{s\parallel} \int_0^\infty d\tilde{v}_{s\perp} \, \Lambda_s(\tilde{v}_{s\parallel}, \tilde{v}_{s\perp})$$
$$- \frac{2\omega_{ps}^2}{\sqrt{\pi}\omega^2} \sum_{n=-\infty}^{\infty} \int_{C_L} \frac{\tilde{v}_{s\parallel}^2 \, d\tilde{v}_{s\parallel}}{\tilde{v}_{s\parallel} + n/|k_\parallel|\tilde{\rho}_s} \int_0^\infty d\tilde{v}_{s\perp} \, \varXi_s(\tilde{v}_{s\parallel}, \tilde{v}_{s\perp}) J_n(k_\perp \tilde{\rho}_s \tilde{v}_{s\perp})^2. \tag{F4i}$$

Next, noting that

$$\frac{\tilde{v}_{s\parallel}}{\tilde{v}_{s\parallel} + n/|k_\parallel|\tilde{\rho}_s} = 1 - \frac{n}{|k_\parallel|\tilde{\rho}_s} \frac{1}{\tilde{v}_{s\parallel} + n/|k_\parallel|\tilde{\rho}_s}, \tag{F5}$$

as well as

$$\sum_{n=-\infty}^{\infty} \frac{n}{k_\perp \tilde{\rho}_s} \int_{C_L} d\tilde{v}_{s\parallel} \int_0^\infty d\tilde{v}_{s\perp} \, \varXi_s(\tilde{v}_{s\parallel}, \tilde{v}_{s\perp}) J_n(k_\perp \tilde{\rho}_s \tilde{v}_{s\perp})^2 = 0, \tag{F6}$$

we see that the double integral in (F4c) can be rearranged to give

$$(\mathfrak{E}_s^{(0)})_{xz} = \frac{2\omega_{ps}^2}{\sqrt{\pi}\omega^2} \sum_{n=-\infty}^{\infty} \left[\frac{n^2}{|k_\parallel||k_\perp \tilde{\rho}_s^2} \int_{C_L} \frac{d\tilde{v}_{s\parallel}}{\tilde{v}_{s\parallel} + n/|k_\parallel|\tilde{\rho}_s} \right.$$
$$\left. \times \int_0^\infty d\tilde{v}_{s\perp} \, \varXi_s(\tilde{v}_{s\parallel}, \tilde{v}_{s\perp}) J_n(k_\perp \tilde{\rho}_s \tilde{v}_{s\perp})^2 \right],$$
$$= -\frac{k_\perp}{|k_\parallel|} (\mathfrak{E}_s^{(0)})_{xx}. \tag{F7}$$

Similarly, it can be shown that

$$
\begin{aligned}
(\boldsymbol{\mathfrak{E}}_s^{(0)})_{yz} &= \frac{2i\omega_{ps}^2}{\sqrt{\pi}\omega^2} \sum_{n=-\infty}^{\infty} \left[\frac{n}{|k_\parallel|\tilde{\rho}_s} \int_{C_L} \frac{d\tilde{v}_{s\parallel}}{\tilde{v}_{s\parallel} + n/|k_\parallel|\tilde{\rho}_s} \right. \\
&\qquad \left. \times \int_0^\infty d\tilde{v}_{s\perp}\, \tilde{v}_{s\perp}\, \Xi_s(\tilde{v}_{s\parallel}, \tilde{v}_{s\perp}) J_n(k_\perp \tilde{\rho}_s \tilde{v}_{s\perp}) J_n'(k_\perp \tilde{\rho}_s \tilde{v}_{s\perp}) \right], \\
&= \frac{k_\perp}{|k_\parallel|}(\boldsymbol{\mathfrak{E}}_s^{(0)})_{xy}.
\end{aligned}
\tag{F8}
$$

Finally, $(\boldsymbol{\mathfrak{E}}_s^{(0)})_{zz}$ can also be written in terms of $(\boldsymbol{\mathfrak{E}}_s^{(0)})_{xx}$: because

$$
\frac{\tilde{v}_{s\parallel}^2}{\tilde{v}_{s\parallel} + n/|k_\parallel|\tilde{\rho}_s} = \tilde{v}_{s\parallel} - \frac{n}{|k_\parallel|\tilde{\rho}_s} + \frac{n^2}{|k_\parallel|^2\tilde{\rho}_s^2}\frac{1}{\tilde{v}_{s\parallel} + n/|k_\parallel|\tilde{\rho}_s},
\tag{F9}
$$

it follows that

$$
\begin{aligned}
(\boldsymbol{\mathfrak{E}}_s^{(0)})_{zz} &= \frac{k_\perp^2}{k_\parallel^2}(\boldsymbol{\mathfrak{E}}_s^{(0)})_{xx} + \frac{2\omega_{ps}^2}{\sqrt{\pi}\tilde{\omega}_{s\parallel}\omega^2}\int_{-\infty}^{\infty} d\tilde{v}_{s\parallel}\, \tilde{v}_{s\parallel} \int_0^\infty d\tilde{v}_{s\perp}\, \Lambda_s(\tilde{v}_{s\parallel}, \tilde{v}_{s\perp}) \\
&\quad - \frac{2\omega_{ps}^2}{\sqrt{\pi}\omega^2}\sum_{n=-\infty}^{\infty} \int_{-\infty}^{\infty} \tilde{v}_{s\parallel}\, d\tilde{v}_{s\parallel} \int_0^\infty d\tilde{v}_{s\perp}\, \Xi_s(\tilde{v}_{s\parallel}, \tilde{v}_{s\perp}) J_n(k_\perp \tilde{\rho}_s \tilde{v}_{s\perp})^2 \\
&\quad + \frac{2\omega_{ps}^2}{\sqrt{\pi}\omega^2}\sum_{n=-\infty}^{\infty} \frac{n}{k_\perp \tilde{\rho}_s} \int_{-\infty}^{\infty} d\tilde{v}_{s\parallel} \int_0^\infty d\tilde{v}_{s\perp}\, \Xi_s(\tilde{v}_{s\parallel}, \tilde{v}_{s\perp}) J_n(k_\perp \tilde{\rho}_s \tilde{v}_{s\perp})^2 \\
&= \frac{k_\perp^2}{k_\parallel^2}(\boldsymbol{\mathfrak{E}}_s^{(0)})_{xx} - \frac{2\omega_{ps}^2}{\sqrt{\pi}\omega^2}\int_{-\infty}^{\infty} d\tilde{v}_{s\parallel} \int_0^\infty d\tilde{v}_{s\perp}\, \tilde{v}_{s\parallel}\frac{\partial \tilde{f}_{s0}}{\partial \tilde{v}_{s\perp}} \\
&\quad + \frac{2\omega_{ps}^2}{\sqrt{\pi}\tilde{\omega}_{s\parallel}\omega^2}\int_{-\infty}^{\infty} d\tilde{v}_{s\parallel}\, \tilde{v}_{s\parallel} \int_0^\infty d\tilde{v}_{s\perp}\, \Lambda_s(\tilde{v}_{s\parallel}, \tilde{v}_{s\perp})\left[1 - \sum_{n=-\infty}^{\infty} J_n(k_\perp \tilde{\rho}_s \tilde{v}_{s\perp})^2\right] \\
&= \frac{k_\perp^2}{k_\parallel^2}(\boldsymbol{\mathfrak{E}}_s^{(0)})_{xx} + \frac{2\omega_{ps}^2}{\sqrt{\pi}\omega^2}\int_{-\infty}^{\infty} d\tilde{v}_{s\parallel} \int_0^\infty d\tilde{v}_{s\perp}\, \Lambda_s(\tilde{v}_{s\parallel}, \tilde{v}_{s\perp}),
\end{aligned}
\tag{F10}
$$

where we have used the identity

$$
\sum_{n=-\infty}^{\infty} J_n(k_\perp \tilde{\rho}_s \tilde{v}_{s\perp})^2 = 1.
\tag{F11}
$$

Thus, we conclude that since the anisotropy is assumed small,

$$
(\boldsymbol{\mathfrak{E}}_s^{(0)})_{zz} = \frac{k_\perp^2}{k_\parallel^2}(\boldsymbol{\mathfrak{E}}_s^{(0)})_{xx} + O(\tilde{\omega}_{s\parallel}),
\tag{F12}
$$

completing the proof.

F.2. *Evaluating the dielectric tensor in coordinate basis* $\{e_1, e_2, e_3\}$

To demonstrate that the components of the dielectric tensor $\mathfrak{C}_s^{(0)}$ are given by (2.104), *viz.*

$$(\mathfrak{C}_s^{(0)})_{11} = \frac{k^2}{k_\parallel^2}(\mathfrak{C}_s^{(0)})_{xx}, \tag{F13a}$$

$$(\mathfrak{C}_s^{(0)})_{12} = -(\mathfrak{C}_s^{(0)})_{21} = \frac{k}{k_\parallel}(\mathfrak{C}_s^{(0)})_{xy}, \tag{F13b}$$

$$(\mathfrak{C}_s^{(0)})_{22} = (\mathfrak{C}_s^{(0)})_{yy}, \tag{F13c}$$

we use (F1) to express $\mathfrak{C}_s^{(0)}$ in the form

$$\begin{aligned}
\mathfrak{C}_s^{(0)} = {} & (\mathfrak{C}_s^{(0)})_{xx}\hat{x}\hat{x} + (\mathfrak{C}_s^{(0)})_{xy}\left(\hat{x}\hat{y} - \hat{y}\hat{x}\right) + (\mathfrak{C}_s^{(0)})_{yy}\hat{y}\hat{y} \\
& - \frac{k_\perp}{|k_\parallel|}(\mathfrak{C}_s^{(0)})_{xx}\left(\hat{x}\hat{z} + \hat{z}\hat{x}\right) + \frac{k_\perp}{|k_\parallel|}(\mathfrak{C}_s^{(0)})_{xy}\left(\hat{y}\hat{z} - \hat{z}\hat{y}\right) + \frac{k_\perp^2}{k_\parallel^2}(\mathfrak{C}_s^{(0)})_{xx}\hat{z}\hat{z}.
\end{aligned} \tag{F14}$$

Noting that

$$\hat{k} = \frac{k_\perp}{k}\hat{x} + \frac{k_\parallel}{k}\hat{z}, \tag{F15a}$$

$$\hat{y} \times \hat{k} = \frac{k_\parallel}{k}\hat{x} - \frac{k_\perp}{k}\hat{z}, \tag{F15b}$$

we can rewrite (F14) as

$$\begin{aligned}
\mathfrak{C}_s^{(0)} = {} & \frac{k^2}{k_\parallel^2}(\mathfrak{C}_s^{(0)})_{xx}\left(\hat{y} \times \hat{k}\right)\left(\hat{y} \times \hat{k}\right) \\
& + \frac{k}{|k_\parallel|}(\mathfrak{C}_s^{(0)})_{xy}\left[\left(\hat{y} \times \hat{k}\right)\hat{y} - \hat{y}\left(\hat{y} \times \hat{k}\right)\right] + (\mathfrak{C}_s^{(0)})_{yy}\hat{y}\hat{y} \tag{F16} \\
= {} & \frac{k^2}{k_\parallel^2}(\mathfrak{C}_s^{(0)})_{xx}e_1 e_1 + \frac{k}{|k_\parallel|}(\mathfrak{C}_s^{(0)})_{xy}(e_1 e_2 - e_2 e_1) + (\mathfrak{C}_s^{(0)})_{yy}e_2 e_2, \tag{F17}
\end{aligned}$$

leading to the desired results (F13). In addition, we see that $\mathfrak{C}_s^{(0)} \cdot \hat{k} = 0$; thus, the results (2.105) claiming that certain components of $\mathfrak{C}_s$ are small in $\tilde{\omega}_{s\parallel}$ are justified.

Appendix G. Dielectric tensor components for the CE distribution function (2.8)

In this appendix, we calculate the components of the dielectric tensor arising from the CE distribution function (2.8), with isotropic functions $A_e^T(\tilde{v}_e)$, $A_e^R(\tilde{v}_e)$, $A_e^u(\tilde{v}_e)$, $C_e(\tilde{v}_e)$, $A_i(\tilde{v}_i)$ and $C_i(\tilde{v}_i)$ chosen as appropriate for a Krook collision operator (see Appendix B.2.1), *viz.*

$$A_e^T(\tilde{v}_e) = -\left(\tilde{v}_e^2 - \tfrac{5}{2}\right), \tag{G1a}$$

$$A_e^R(\tilde{v}_e) = -1, \tag{G1b}$$

$$A_e^u(\tilde{v}_e) = 0, \tag{G1c}$$

$$A_i(\tilde{v}_i) = -\left(\tilde{v}_i^2 - \tfrac{5}{2}\right), \tag{G1d}$$

$$C_e(\tilde{v}_e) = -1, \tag{G1e}$$

$$C_i(\tilde{v}_i) = -1. \tag{G1f}$$

This, via (2.108), allows for the dielectric tensor $\mathfrak{E}_s$ to be calculated order by order in $\tilde{\omega}_{s\parallel}$. We carry out these calculations in the case of non-relativistic fluctuations, and so

$$\mathfrak{E} \approx \frac{4\pi \mathrm{i}}{\omega}\sigma = \sum_s \mathfrak{E}_s, \tag{G2}$$

where we remind the reader that (cf. (F2))

$$\mathfrak{E}_s = \frac{\omega_{\mathrm{ps}}^2}{\omega^2}\left[\frac{2}{\sqrt{\pi}}\frac{k_\parallel}{|k_\parallel|}\int_{-\infty}^{\infty}\mathrm{d}\tilde{v}_{s\parallel}\,\tilde{v}_{s\parallel}\int_0^{\infty}\mathrm{d}\tilde{v}_{s\perp}\,\Lambda_s(\tilde{v}_{s\parallel},\tilde{v}_{s\perp})\hat{z}\hat{z} \right.$$
$$\left. +\tilde{\omega}_{s\parallel}\frac{2}{\sqrt{\pi}}\int_{C_L}\mathrm{d}\tilde{v}_{s\parallel}\int_0^{\infty}\mathrm{d}\tilde{v}_{s\perp}\,\tilde{v}_{s\perp}^2\,\Xi_s(\tilde{v}_{s\parallel},\tilde{v}_{s\perp})\sum_{n=-\infty}^{\infty}\frac{\boldsymbol{R}_{sn}}{\zeta_{sn}-\tilde{v}_{s\parallel}} \right], \tag{G3}$$

$$\zeta_{sn} \equiv \tilde{\omega}_{s\parallel} - \frac{n}{|k_\parallel|\tilde{\rho}_s}, \tag{G4}$$

$$\tilde{f}_{s0}(\tilde{v}_{s\parallel},\tilde{v}_{s\perp}) \equiv \frac{\pi^{3/2}v_{\mathrm{ths}}^3}{n_{s0}}f_{s0}\left(\frac{k_\parallel}{|k_\parallel|}v_{\mathrm{ths}}\tilde{v}_{s\parallel},\,v_{\mathrm{ths}}\tilde{v}_{s\perp}\right), \tag{G5}$$

$$\Lambda_s(\tilde{v}_{s\parallel},\tilde{v}_{s\perp}) \equiv \tilde{v}_{s\perp}\frac{\partial\tilde{f}_{s0}}{\partial\tilde{v}_{s\parallel}} - \tilde{v}_{s\parallel}\frac{\partial\tilde{f}_{s0}}{\partial\tilde{v}_{s\perp}}, \tag{G6}$$

$$\Xi_s(\tilde{v}_{s\parallel},\tilde{v}_{s\perp}) \equiv \frac{\partial\tilde{f}_{s0}}{\partial\tilde{v}_{s\perp}} + \frac{\Lambda_s(\tilde{v}_{s\parallel},\tilde{v}_{s\perp})}{\tilde{\omega}_{s\parallel}}, \tag{G7}$$

and

$$(\boldsymbol{R}_{sn})_{xx} \equiv \frac{n^2 J_n(k_\perp\tilde{\rho}_s\tilde{v}_{s\perp})^2}{k_\perp^2\tilde{\rho}_s^2\tilde{v}_{s\perp}^2}, \tag{G8a}$$

$$(\boldsymbol{R}_{sn})_{xy} \equiv \frac{\mathrm{i}n J_n(k_\perp\tilde{\rho}_s\tilde{v}_{s\perp})J_n'(k_\perp\tilde{\rho}_s\tilde{v}_{s\perp})}{k_\perp\tilde{\rho}_s\tilde{v}_{s\perp}}, \tag{G8b}$$

$$(\boldsymbol{R}_{sn})_{xz} \equiv \frac{n J_n(k_\perp\tilde{\rho}_s\tilde{v}_{s\perp})^2}{k_\perp\tilde{\rho}_s\tilde{v}_{s\perp}}\frac{k_\parallel\tilde{v}_{s\parallel}}{|k_\parallel|\tilde{v}_{s\perp}}, \tag{G8c}$$

$$(\boldsymbol{R}_{sn})_{yx} \equiv -(\boldsymbol{R}_{sn})_{xy} \tag{G8d}$$

$$(\boldsymbol{R}_{sn})_{yy} \equiv J_n'(k_\perp\tilde{\rho}_s\tilde{v}_{s\perp})^2, \tag{G8e}$$

$$(\boldsymbol{R}_{sn})_{yz} \equiv \mathrm{i}n J_n(k_\perp\tilde{\rho}_s\tilde{v}_{s\perp})J_n'(k_\perp\tilde{\rho}_s\tilde{v}_{s\perp})\frac{k_\parallel\tilde{v}_{s\parallel}}{|k_\parallel|\tilde{v}_{s\perp}}, \tag{G8f}$$

$$(\boldsymbol{R}_{sn})_{zx} \equiv (\boldsymbol{R}_{sn})_{xz} \tag{G8g}$$

$$(\boldsymbol{R}_{sn})_{zy} \equiv -(\boldsymbol{R}_{sn})_{yz} \tag{G8h}$$

$$(\boldsymbol{R}_{sn})_{zz} \equiv \frac{\tilde{v}_{s\parallel}^2}{\tilde{v}_{s\perp}^2}J_n(k_\perp\tilde{\rho}_s\tilde{v}_{s\perp})^2. \tag{G8i}$$

The components of the dielectric tensor $\mathfrak{E}_s$ in coordinate basis $\{e_1, e_2, e_3\}$ are related to the components in coordinate basis $\{\hat{x}, \hat{y}, \hat{z}\}$ by

$$(\mathfrak{E}_s)_{11} = \frac{k_\parallel^2}{k^2}(\mathfrak{E}_s)_{xx} - \frac{2k_\parallel k_\perp}{k^2}(\mathfrak{E}_s)_{xz} + \frac{k_\perp^2}{k^2}(\mathfrak{E}_s)_{zz}, \tag{G9a}$$

$$(\mathfrak{E}_s)_{12} = \frac{k_\parallel}{k}(\mathfrak{E}_s)_{xy} + \frac{k_\perp}{k}(\mathfrak{E}_s)_{yz}, \tag{G9b}$$

$$(\mathfrak{E}_s)_{13} = \frac{k_\parallel k_\perp}{k^2}\left[(\mathfrak{E}_s)_{xx} - (\mathfrak{E}_s)_{zz}\right] + \left(\frac{k_\parallel^2}{k^2} - \frac{k_\perp^2}{k^2}\right)(\mathfrak{E}_s)_{xz}, \tag{G9c}$$

$$(\mathfrak{E}_s)_{21} = -(\mathfrak{E}_s)_{12}, \tag{G9d}$$

$$(\mathfrak{E}_s)_{22} = (\mathfrak{E}_s)_{yy}, \tag{G9e}$$

$$(\mathfrak{E}_s)_{23} = -\frac{k_\perp}{k}(\mathfrak{E}_s)_{xy} + \frac{k_\parallel}{k}(\mathfrak{E}_s)_{yz}, \tag{G9f}$$

$$(\mathfrak{E}_s)_{31} = (\mathfrak{E}_s)_{13}, \tag{G9g}$$

$$(\mathfrak{E}_s)_{32} = -(\mathfrak{E}_s)_{23}, \tag{G9h}$$

$$(\mathfrak{E}_s)_{33} = \frac{k_\perp^2}{k^2}(\mathfrak{E}_s)_{xx} + \frac{2k_\parallel k_\perp}{k^2}(\mathfrak{E}_s)_{xz} + \frac{k_\parallel^2}{k^2}(\mathfrak{E}_s)_{zz}. \tag{G9i}$$

For clarity, we calculate separately the Maxwellian contribution M_s of the total CE distribution function and the non-Maxwellian contribution P_s associated with the CE electron friction, temperature-gradient and shear terms to $\mathfrak{E}_s$ – *viz.* we decompose $\mathfrak{E}_s$ as follows (cf. (2.97)):

$$\mathfrak{E}_s = \frac{\omega_{\mathrm{p}s}^2}{\omega^2}(M_s + P_s). \tag{G10}$$

G.1. *Maxwellian distribution*

G.1.1. *General dielectric tensor*

Consider a non-dimensionalised Maxwellian distribution function

$$\tilde{f}_s(\tilde{v}_{s\parallel}, \tilde{v}_{s\perp}) = \exp\left(-\tilde{v}_s^2\right). \tag{G11}$$

The Maxwellian is isotropic, so (G6) gives

$$\Lambda_s(\tilde{v}_{s\parallel}, \tilde{v}_{s\perp}) = 0, \tag{G12}$$

while (G7) becomes

$$\Xi_s(\tilde{v}_{s\parallel}, \tilde{v}_{s\perp}) = -2\tilde{v}_{s\perp}\exp\left(-\tilde{v}_s^2\right). \tag{G13}$$

Substituting this into (G3) gives

$$(\boldsymbol{M}_s)_{xx} = \frac{4}{\sqrt{\pi}} \tilde{\omega}_{s\parallel} \sum_{n=-\infty}^{\infty} \left[\frac{n^2}{k_\perp^2 \tilde{\rho}_s^2} \int_{C_L} \frac{\exp\left(-\tilde{v}_{s\parallel}^2\right) \mathrm{d}\tilde{v}_{s\parallel}}{\tilde{v}_{s\parallel} - \zeta_{sn}} \right.$$

$$\left. \times \int_0^\infty \mathrm{d}\tilde{v}_{s\perp}\, \tilde{v}_{s\perp} J_n(k_\perp \tilde{\rho}_s \tilde{v}_{s\perp})^2 \exp\left(-\tilde{v}_{s\perp}^2\right) \right], \tag{G14a}$$

$$(\boldsymbol{M}_s)_{xy} = \frac{4\mathrm{i}}{\sqrt{\pi}} \tilde{\omega}_{s\parallel} \sum_{n=-\infty}^{\infty} \left[\frac{n}{k_\perp \tilde{\rho}_s} \int_{C_L} \frac{\exp\left(-\tilde{v}_{s\parallel}^2\right) \mathrm{d}\tilde{v}_{s\parallel}}{\tilde{v}_{s\parallel} - \zeta_{sn}} \right.$$

$$\left. \times \int_0^\infty \mathrm{d}\tilde{v}_{s\perp}\, \tilde{v}_{s\perp}^2 J_n(k_\perp \tilde{\rho}_s \tilde{v}_{s\perp}) J_n'(k_\perp \tilde{\rho}_s \tilde{v}_{s\perp}) \exp\left(-\tilde{v}_{s\perp}^2\right) \right], \tag{G14b}$$

$$(\boldsymbol{M}_s)_{xz} = \frac{4}{\sqrt{\pi}} \tilde{\omega}_{s\parallel} \sum_{n=-\infty}^{\infty} \left[\frac{n}{k_\perp \tilde{\rho}_s} \int_{C_L} \frac{\tilde{v}_{s\parallel} \exp\left(-\tilde{v}_{s\parallel}^2\right) \mathrm{d}\tilde{v}_{s\parallel}}{\tilde{v}_{s\parallel} - \zeta_{sn}} \right. \tag{G14c}$$

$$\left. \times \int_0^\infty \mathrm{d}\tilde{v}_{s\perp}\, \tilde{v}_{s\perp} J_n(k_\perp \tilde{\rho}_s \tilde{v}_{s\perp})^2 \exp\left(-\tilde{v}_{s\perp}^2\right) \right], \tag{G14d}$$

$$(\boldsymbol{M}_s)_{yx} = (\boldsymbol{M}_s)_{xy}, \tag{G14e}$$

$$(\boldsymbol{M}_s)_{yy} = \frac{4}{\sqrt{\pi}} \tilde{\omega}_{s\parallel} \sum_{n=-\infty}^{\infty} \left[\int_{C_L} \frac{\exp\left(-\tilde{v}_{s\parallel}^2\right) \mathrm{d}\tilde{v}_{s\parallel}}{\tilde{v}_{s\parallel} - \zeta_{sn}} \right.$$

$$\left. \times \int_0^\infty \mathrm{d}\tilde{v}_{s\perp}\, \tilde{v}_{s\perp}^3 J_n'(k_\perp \tilde{\rho}_s \tilde{v}_{s\perp})^2 \exp\left(-\tilde{v}_{s\perp}^2\right) \right], \tag{G14f}$$

$$(\boldsymbol{M}_s)_{yz} = -\frac{4\mathrm{i}}{\sqrt{\pi}} \tilde{\omega}_{s\parallel} \sum_{n=-\infty}^{\infty} \left[\int_{C_L} \frac{\tilde{v}_{s\parallel} \exp\left(-\tilde{v}_{s\parallel}^2\right) \mathrm{d}\tilde{v}_{s\parallel}}{\tilde{v}_{s\parallel} - \zeta_{sn}} \right.$$

$$\left. \times \int_0^\infty \mathrm{d}\tilde{v}_{s\perp}\, \tilde{v}_{s\perp}^2 J_n(k_\perp \tilde{\rho}_s \tilde{v}_{s\perp}) J_n'(k_\perp \tilde{\rho}_s \tilde{v}_{s\perp}) \exp\left(-\tilde{v}_{s\perp}^2\right) \right], \tag{G14g}$$

$$(\boldsymbol{M}_s)_{zx} = (\boldsymbol{M}_s)_{xz}, \tag{G14h}$$

$$(\boldsymbol{M}_s)_{zy} = -(\boldsymbol{M}_s)_{yz}, \tag{G14i}$$

$$(\boldsymbol{M}_s)_{zz} = \frac{4}{\sqrt{\pi}} \tilde{\omega}_{s\parallel} \sum_{n=-\infty}^{\infty} \left[\int_{C_L} \frac{\tilde{v}_{s\parallel}^2 \exp\left(-\tilde{v}_{s\parallel}^2\right) \mathrm{d}\tilde{v}_{s\parallel}}{\tilde{v}_{s\parallel} - \zeta_{sn}} \right.$$

$$\left. \times \int_0^\infty \mathrm{d}\tilde{v}_{s\perp}\, \tilde{v}_{s\perp} J_n(k_\perp \tilde{\rho}_s \tilde{v}_{s\perp})^2 \exp\left(-\tilde{v}_{s\perp}^2\right) \right]. \tag{G14j}$$

Using the integral identities

$$\frac{1}{\sqrt{\pi}} \int_{C_L} \frac{u \exp\left(-u^2\right) \mathrm{d}u}{u - z} = 1 + zZ(z), \tag{G15a}$$

$$\frac{1}{\sqrt{\pi}} \int_{C_L} \frac{u^2 \exp\left(-u^2\right) du}{u - z} = z\left[1 + zZ(z)\right], \tag{G15b}$$

involving the plasma dispersion function, and the identities

$$\int_0^\infty dt\, t J_n(\alpha t)^2 \exp\left(-t^2\right) = \frac{1}{2} \exp\left(-\frac{\alpha^2}{2}\right) I_n\left(\frac{\alpha^2}{2}\right), \tag{G16a}$$

$$\int_0^\infty dt\, t^2 J_n(\alpha t) J_n'(\alpha t) \exp\left(-t^2\right) = \frac{\alpha}{4} \exp\left(-\frac{\alpha^2}{2}\right) \left[I_n'\left(\frac{\alpha^2}{2}\right) - I_n\left(\frac{\alpha^2}{2}\right)\right], \tag{G16b}$$

$$\int_0^\infty dt\, t^3 J_n'(\alpha t)^2 \exp\left(-t^2\right) = \frac{1}{4} \exp\left(-\frac{\alpha^2}{2}\right) \left\{\frac{2n^2}{\alpha^2} I_n\left(\frac{\alpha^2}{2}\right)\right.$$
$$\left. -\alpha^2\left[I_n'\left(\frac{\alpha^2}{2}\right) - I_n\left(\frac{\alpha^2}{2}\right)\right]\right\}, \tag{G16c}$$

involving Bessel functions (here α is a real number), we obtain expressions for the dielectric components (G14) in terms of special functions:

$$(\boldsymbol{M}_s)_{xx} = 2\tilde{\omega}_{s\parallel} \sum_{n=-\infty}^\infty \frac{n^2}{k_\perp^2 \tilde{\rho}_s^2} Z(\zeta_{sn}) \exp\left(-\frac{k_\perp^2 \tilde{\rho}_s^2}{2}\right) I_n\left(\frac{k_\perp^2 \tilde{\rho}_s^2}{2}\right), \tag{G17a}$$

$$(\boldsymbol{M}_s)_{xy} = i\tilde{\omega}_{s\parallel} \sum_{n=-\infty}^\infty n Z(\zeta_{sn}) \exp\left(-\frac{k_\perp^2 \tilde{\rho}_s^2}{2}\right) \left[I_n'\left(\frac{k_\perp^2 \tilde{\rho}_s^2}{2}\right) - I_n\left(\frac{k_\perp^2 \tilde{\rho}_s^2}{2}\right)\right], \tag{G17b}$$

$$(\boldsymbol{M}_s)_{xz} = 2\tilde{\omega}_{s\parallel} \sum_{n=-\infty}^\infty \frac{n}{k_\perp \tilde{\rho}_s} \left[1 + \zeta_{sn} Z(\zeta_{sn})\right] \exp\left(-\frac{k_\perp^2 \tilde{\rho}_s^2}{2}\right) I_n\left(\frac{k_\perp^2 \tilde{\rho}_s^2}{2}\right), \tag{G17c}$$

$$(\boldsymbol{M}_s)_{yx} = (\boldsymbol{M}_s)_{xy}, \tag{G17d}$$

$$(\boldsymbol{M}_s)_{yy} = \tilde{\omega}_{s\parallel} \sum_{n=-\infty}^\infty Z(\zeta_{sn})$$
$$\times \exp\left(-\frac{k_\perp^2 \tilde{\rho}_s^2}{2}\right) \left[\left(\frac{2n^2}{k_\perp^2 \tilde{\rho}_s^2} + k_\perp^2 \tilde{\rho}_s^2\right) I_n\left(\frac{k_\perp^2 \tilde{\rho}_s^2}{2}\right) - k_\perp^2 \tilde{\rho}_s^2 I_n'\left(\frac{k_\perp^2 \tilde{\rho}_s^2}{2}\right)\right], \tag{G17e}$$

$$(\boldsymbol{M}_s)_{yz} = -i\tilde{\omega}_{s\parallel} \sum_{n=-\infty}^\infty k_\perp \tilde{\rho}_s \left[1 + \zeta_{sn} Z(\zeta_{sn})\right]$$
$$\times \exp\left(-\frac{k_\perp^2 \tilde{\rho}_s^2}{2}\right) \left[I_n'\left(\frac{k_\perp^2 \tilde{\rho}_s^2}{2}\right) - I_n\left(\frac{k_\perp^2 \tilde{\rho}_s^2}{2}\right)\right], \tag{G17f}$$

$$(\boldsymbol{M}_s)_{zx} = (\boldsymbol{M}_s)_{xz}, \tag{G17g}$$

$$(\boldsymbol{M}_s)_{zy} = -(\boldsymbol{M}_s)_{yz}, \tag{G17h}$$

$$(\boldsymbol{M}_s)_{zz} = 2\tilde{\omega}_{s\parallel} \sum_{n=-\infty}^\infty \zeta_{sn} \left[1 + \zeta_{sn} Z(\zeta_{sn})\right] \exp\left(-\frac{k_\perp^2 \tilde{\rho}_s^2}{2}\right) I_n\left(\frac{k_\perp^2 \tilde{\rho}_s^2}{2}\right). \tag{G17i}$$

The components of the dielectric tensor (G10) in coordinate basis $\{\boldsymbol{e}_1, \boldsymbol{e}_2, \boldsymbol{e}_3\}$ then follow from (G9), although we do not write these out explicitly.

G.1.2. *Dielectric tensor in low-frequency limit, $\{\hat{\boldsymbol{x}}, \hat{\boldsymbol{y}}, \hat{\boldsymbol{z}}\}$ coordinate frame*

Now, to consider the low-frequency limit $\tilde{\omega}_{s\parallel} \ll 1$, we Taylor expand (G17) in $\tilde{\omega}_{s\parallel}$. Noting that $\tilde{\omega}_{s\parallel}$ only appears via the argument $\zeta_{sn} = \tilde{\omega}_{s\parallel} - n/|k_\parallel|\tilde{\rho}_s$, we use the differential identity $Z'(z) = -2[1 + zZ(z)]$ to obtain the expansions

$$Z(\zeta_{sn}) = Z\left(-\frac{n}{|k_\parallel|\tilde{\rho}_s}\right) - 2\tilde{\omega}_{s\parallel}\left[1 - \frac{n}{|k_\parallel|\tilde{\rho}_s}Z\left(-\frac{n}{|k_\parallel|\tilde{\rho}_s}\right)\right] + O(\tilde{\omega}_{s\parallel}^2), \quad \text{(G18a)}$$

$$1 + \zeta_{sn}Z(\zeta_{sn}) = 1 - \frac{n}{|k_\parallel|\tilde{\rho}_s}Z\left(-\frac{n}{|k_\parallel|\tilde{\rho}_s}\right)$$
$$+ \tilde{\omega}_{s\parallel}\left[\left(1 - \frac{2n^2}{|k_\parallel|^2\tilde{\rho}_s^2}\right)Z\left(-\frac{n}{|k_\parallel|\tilde{\rho}_s}\right) + \frac{2n}{|k_\parallel|\tilde{\rho}_s}\right] + O(\tilde{\omega}_{s\parallel}^2), \quad \text{(G18b)}$$

$$\zeta_{sn}\left[1 + \zeta_{sn}Z(\zeta_{sn})\right] = -\frac{n}{|k_\parallel|\tilde{\rho}_s}\left[1 - \frac{n}{|k_\parallel|\tilde{\rho}_s}Z\left(-\frac{n}{|k_\parallel|\tilde{\rho}_s}\right)\right] + \tilde{\omega}_{s\parallel}\left[1 - \frac{2n^2}{|k_\parallel|^2\tilde{\rho}_s^2}\right.$$
$$\left. - \frac{2n}{|k_\parallel|\tilde{\rho}_s}\left(1 - \frac{n^2}{|k_\parallel|^2\tilde{\rho}_s^2}\right)Z\left(-\frac{n}{|k_\parallel|\tilde{\rho}_s}\right)\right] + O(\tilde{\omega}_{s\parallel}^2). \quad \text{(G18c)}$$

Then, expanding the dielectric tensor as

$$\boldsymbol{M}_s = \tilde{\omega}_{s\parallel}\boldsymbol{M}_s^{(0)} + \tilde{\omega}_{s\parallel}^2\boldsymbol{M}_s^{(1)} + O(\tilde{\omega}_{s\parallel}^3), \quad \text{(G19)}$$

we have

$$(\boldsymbol{M}_s^{(0)})_{xx} = 2\sum_{n=-\infty}^{\infty}\frac{n^2}{k_\perp^2\tilde{\rho}_s^2}Z\left(-\frac{n}{|k_\parallel|\tilde{\rho}_s}\right)\exp\left(-\frac{k_\perp^2\tilde{\rho}_s^2}{2}\right)I_n\left(\frac{k_\perp^2\tilde{\rho}_s^2}{2}\right), \quad \text{(G20a)}$$

$$(\boldsymbol{M}_s^{(0)})_{xy} = \mathrm{i}\sum_{n=-\infty}^{\infty}nZ\left(-\frac{n}{|k_\parallel|\tilde{\rho}_s}\right)$$
$$\times \exp\left(-\frac{k_\perp^2\tilde{\rho}_s^2}{2}\right)\left[I_n'\left(\frac{k_\perp^2\tilde{\rho}_s^2}{2}\right) - I_n\left(\frac{k_\perp^2\tilde{\rho}_s^2}{2}\right)\right], \quad \text{(G20b)}$$

$$(\boldsymbol{M}_s^{(0)})_{xz} = 2\sum_{n=-\infty}^{\infty}\frac{n}{k_\perp\tilde{\rho}_s}\left[1 - \frac{n}{|k_\parallel|\tilde{\rho}_s}Z\left(-\frac{n}{|k_\parallel|\tilde{\rho}_s}\right)\right]$$
$$\times \exp\left(-\frac{k_\perp^2\tilde{\rho}_s^2}{2}\right)I_n\left(\frac{k_\perp^2\tilde{\rho}_s^2}{2}\right), \quad \text{(G20c)}$$

$$(\boldsymbol{M}_s^{(0)})_{yy} = \sum_{n=-\infty}^{\infty}Z\left(-\frac{n}{|k_\parallel|\tilde{\rho}_s}\right)$$
$$\times \exp\left(-\frac{k_\perp^2\tilde{\rho}_s^2}{2}\right)\left[\left(\frac{2n^2}{k_\perp^2\tilde{\rho}_s^2} + k_\perp^2\tilde{\rho}_s^2\right)I_n\left(\frac{k_\perp^2\tilde{\rho}_s^2}{2}\right) - k_\perp^2\tilde{\rho}_s^2I_n'\left(\frac{k_\perp^2\tilde{\rho}_s^2}{2}\right)\right], \quad \text{(G20d)}$$

$$(\boldsymbol{M}_s^{(0)})_{yz} = \mathrm{i} \sum_{n=-\infty}^{\infty} k_\perp \tilde\rho_s \left[1 - \frac{n}{|k_\parallel|\tilde\rho_s} Z\left(-\frac{n}{|k_\parallel|\tilde\rho_s}\right) \right]$$
$$\times \exp\left(-\frac{k_\perp^2\tilde\rho_s^2}{2}\right) \left[I_n'\left(\frac{k_\perp^2\tilde\rho_s^2}{2}\right) - I_n\left(\frac{k_\perp^2\tilde\rho_s^2}{2}\right) \right], \tag{G20e}$$

$$(\boldsymbol{M}_s^{(0)})_{zz} = -2 \sum_{n=-\infty}^{\infty} \frac{n}{|k_\parallel|\tilde\rho_s} \left[1 - \frac{n}{|k_\parallel|\tilde\rho_s} Z\left(-\frac{n}{|k_\parallel|\tilde\rho_s}\right) \right]$$
$$\times \exp\left(-\frac{k_\perp^2\tilde\rho_s^2}{2}\right) I_n\left(\frac{k_\perp^2\tilde\rho_s^2}{2}\right), \tag{G20f}$$

and

$$(\boldsymbol{M}_s^{(1)})_{xx} = -4 \sum_{n=-\infty}^{\infty} \frac{n^2}{k_\perp^2\tilde\rho_s^2} \left[1 - \frac{n}{|k_\parallel|\tilde\rho_s} Z\left(-\frac{n}{|k_\parallel|\tilde\rho_s}\right) \right]$$
$$\times \exp\left(-\frac{k_\perp^2\tilde\rho_s^2}{2}\right) I_n\left(\frac{k_\perp^2\tilde\rho_s^2}{2}\right), \tag{G21a}$$

$$(\boldsymbol{M}_s^{(1)})_{xy} = -2\mathrm{i} \sum_{n=-\infty}^{\infty} n \left[1 - \frac{n}{|k_\parallel|\tilde\rho_s} Z\left(-\frac{n}{|k_\parallel|\tilde\rho_s}\right) \right]$$
$$\times \exp\left(-\frac{k_\perp^2\tilde\rho_s^2}{2}\right) \left[I_n'\left(\frac{k_\perp^2\tilde\rho_s^2}{2}\right) - I_n\left(\frac{k_\perp^2\tilde\rho_s^2}{2}\right) \right], \tag{G21b}$$

$$(\boldsymbol{M}_s^{(1)})_{xz} = 2 \sum_{n=-\infty}^{\infty} \frac{n}{k_\perp\tilde\rho_s} \left[\left(1 - \frac{2n^2}{|k_\parallel|^2\tilde\rho_s^2} \right) Z\left(-\frac{n}{|k_\parallel|\tilde\rho_s}\right) + \frac{2n}{|k_\parallel|\tilde\rho_s} \right]$$
$$\times \exp\left(-\frac{k_\perp^2\tilde\rho_s^2}{2}\right) I_n\left(\frac{k_\perp^2\tilde\rho_s^2}{2}\right), \tag{G21c}$$

$$(\boldsymbol{M}_s^{(1)})_{yy} = -2 \sum_{n=-\infty}^{\infty} \left[1 - \frac{n}{|k_\parallel|\tilde\rho_s} Z\left(-\frac{n}{|k_\parallel|\tilde\rho_s}\right) \right]$$
$$\times \exp\left(-\frac{k_\perp^2\tilde\rho_s^2}{2}\right) \left[\left(\frac{2n^2}{k_\perp^2\tilde\rho_s^2} + k_\perp^2\tilde\rho_s^2 \right) I_n\left(\frac{k_\perp^2\tilde\rho_s^2}{2}\right) - k_\perp^2\tilde\rho_s^2 I_n'\left(\frac{k_\perp^2\tilde\rho_s^2}{2}\right) \right], \tag{G21d}$$

$$(\boldsymbol{M}_s^{(1)})_{yz} = -\mathrm{i} \sum_{n=-\infty}^{\infty} k_\perp\tilde\rho_s \left[\left(1 - \frac{2n^2}{|k_\parallel|^2\tilde\rho_s^2} \right) Z\left(-\frac{n}{|k_\parallel|\tilde\rho_s}\right) + \frac{2n}{|k_\parallel|\tilde\rho_s} \right]$$
$$\times \exp\left(-\frac{k_\perp^2\tilde\rho_s^2}{2}\right) \left[I_n'\left(\frac{k_\perp^2\tilde\rho_s^2}{2}\right) - I_n\left(\frac{k_\perp^2\tilde\rho_s^2}{2}\right) \right], \tag{G21e}$$

$$(\boldsymbol{M}_s^{(1)})_{zz} = 2 \sum_{n=-\infty}^{\infty} \left[1 - \frac{2n^2}{|k_\parallel|^2\tilde\rho_s^2} - \frac{2n}{|k_\parallel|\tilde\rho_s} \left(1 - \frac{n^2}{|k_\parallel|^2\tilde\rho_s^2} \right) Z\left(-\frac{n}{|k_\parallel|\tilde\rho_s}\right) \right]$$
$$\times \exp\left(-\frac{k_\perp^2\tilde\rho_s^2}{2}\right) I_n\left(\frac{k_\perp^2\tilde\rho_s^2}{2}\right). \tag{G21f}$$

These expressions can be simplified somewhat using two further types of algebraic manipulation. First, for z a real number, we can split the plasma dispersion into real and imaginary parts as

$$
\begin{aligned}
Z(z) &= \frac{1}{\sqrt{\pi}} \mathcal{P} \int_{-\infty}^{\infty} \frac{\exp\left(-u^2\right) \mathrm{d}u}{u - z} + \mathrm{i}\sqrt{\pi} \exp\left(-z^2\right) \\
&= \operatorname{Re} Z(z) + \mathrm{i}\sqrt{\pi} \exp\left(-z^2\right).
\end{aligned} \tag{G22}
$$

Thus, we see that the real part of $Z(z)$ is an odd function for real z, while the imaginary part is an even function. As a consequence, only one of the real or imaginary parts of the plasma dispersion function will enter into the summations in (G20) and (G21). Secondly, we utilise the generating function of the modified Bessel function, *viz.*

$$
\sum_{n=-\infty}^{\infty} I_n(\alpha) \, t^n = \exp\left[\frac{\alpha}{2}\left(t + \frac{1}{t}\right)\right], \tag{G23}
$$

to deduce the following identities:

$$
\sum_{n=-\infty}^{\infty} I_n(\alpha) = \exp(\alpha), \tag{G24a}
$$

$$
\sum_{n=-\infty}^{\infty} n^2 I_n(\alpha) = \alpha \exp(\alpha), \tag{G24b}
$$

$$
\sum_{n=-\infty}^{\infty} \left[I'_n(\alpha) - I_n(\alpha)\right] = 0, \tag{G24c}
$$

$$
\sum_{n=-\infty}^{\infty} n^2 \left[I'_n(\alpha) - I_n(\alpha)\right] = \exp(\alpha). \tag{G24d}
$$

Combining these results, we obtain from (G20) and (G21) the following expressions for the components of $\boldsymbol{M}_s^{(0)}$ and $\boldsymbol{M}_s^{(1)}$:

$$
\begin{aligned}
(\boldsymbol{M}_s^{(0)})_{xx} &= 4\mathrm{i}\sqrt{\pi} \sum_{m=1}^{\infty} \frac{m^2}{k_\perp^2 \tilde{\rho}_s^2} \exp\left(-\frac{m^2}{k_\parallel^2 \tilde{\rho}_s^2}\right) \exp\left(-\frac{k_\perp^2 \tilde{\rho}_s^2}{2}\right) I_m\left(\frac{k_\perp^2 \tilde{\rho}_s^2}{2}\right) \\
&= \mathrm{i}F\left(k_\parallel \tilde{\rho}_s, k_\perp \tilde{\rho}_s\right),
\end{aligned} \tag{G25a}
$$

$$
\begin{aligned}
(\boldsymbol{M}_s^{(0)})_{xy} &= -\mathrm{i} \sum_{m=-\infty}^{\infty} m \operatorname{Re}\left[Z\left(\frac{m}{|k_\parallel| \tilde{\rho}_s}\right)\right] \exp\left(-\frac{k_\perp^2 \tilde{\rho}_s^2}{2}\right) \left[I'_m\left(\frac{k_\perp^2 \tilde{\rho}_s^2}{2}\right) - I_m\left(\frac{k_\perp^2 \tilde{\rho}_s^2}{2}\right)\right] \\
&= -\mathrm{i}G\left(k_\parallel \tilde{\rho}_s, k_\perp \tilde{\rho}_s\right),
\end{aligned} \tag{G25b}
$$

$$
\begin{aligned}
(\boldsymbol{M}_s^{(0)})_{xz} &= -4\mathrm{i}\sqrt{\pi} \sum_{m=-\infty}^{\infty} \frac{m^2}{k_\perp |k_\parallel| \tilde{\rho}_s^2} \exp\left(-\frac{m^2}{k_\parallel^2 \tilde{\rho}_s^2}\right) \exp\left(-\frac{k_\perp^2 \tilde{\rho}_s^2}{2}\right) I_n\left(\frac{k_\perp^2 \tilde{\rho}_s^2}{2}\right) \\
&= -\frac{\mathrm{i}k_\perp}{|k_\parallel|} F\left(k_\parallel \tilde{\rho}_s, k_\perp \tilde{\rho}_s\right),
\end{aligned} \tag{G25c}
$$

$$
(\boldsymbol{M}_s^{(0)})_{yy} = \mathrm{i}\sqrt{\pi} \sum_{m=-\infty}^{\infty} \exp\left(-\frac{m^2}{k_\parallel^2 \tilde{\rho}_s^2}\right)
$$

$$
\times \exp\left(-\frac{k_\perp^2 \tilde{\rho}_s^2}{2}\right) \left[\left(\frac{2m^2}{k_\perp^2 \tilde{\rho}_s^2} + k_\perp^2 \tilde{\rho}_s^2\right) I_m\left(\frac{k_\perp^2 \tilde{\rho}_s^2}{2}\right) - k_\perp^2 \tilde{\rho}_s^2 I_m'\left(\frac{k_\perp^2 \tilde{\rho}_s^2}{2}\right)\right]
$$

$$
= \mathrm{i}H\left(k_\parallel \tilde{\rho}_s, k_\perp \tilde{\rho}_s\right), \tag{G25d}
$$

$$
(\boldsymbol{M}_s^{(0)})_{yz} = -\mathrm{i} \sum_{m=-\infty}^{\infty} \frac{mk_\perp}{|k_\parallel|} \mathrm{Re}\left[Z\left(\frac{m}{|k_\parallel|\tilde{\rho}_s}\right)\right] \exp\left(-\frac{k_\perp^2 \tilde{\rho}_s^2}{2}\right) \left[I_m'\left(\frac{k_\perp^2 \tilde{\rho}_s^2}{2}\right) - I_m\left(\frac{k_\perp^2 \tilde{\rho}_s^2}{2}\right)\right]
$$

$$
= -\frac{\mathrm{i}k_\perp}{|k_\parallel|} G\left(k_\parallel \tilde{\rho}_s, k_\perp \tilde{\rho}_s\right), \tag{G25e}
$$

$$
(\boldsymbol{M}_s^{(0)})_{zz} = 4\mathrm{i}\sqrt{\pi} \sum_{m=1}^{\infty} \frac{m^2}{k_\parallel^2 \tilde{\rho}_s^2} \exp\left(-\frac{m^2}{k_\parallel^2 \tilde{\rho}_s^2}\right) \exp\left(-\frac{k_\perp^2 \tilde{\rho}_s^2}{2}\right) I_m\left(\frac{k_\perp^2 \tilde{\rho}_s^2}{2}\right)
$$

$$
= \frac{\mathrm{i}k_\perp^2}{k_\parallel^2} F\left(k_\parallel \tilde{\rho}_s, k_\perp \tilde{\rho}_s\right), \tag{G25f}
$$

and

$$
(\boldsymbol{M}_s^{(1)})_{xx} = -2\left\{1 + \sum_{m=-\infty}^{\infty} \frac{2m^3}{|k_\parallel| k_\perp^2 \tilde{\rho}_s^3} \mathrm{Re}\left[Z\left(\frac{m}{|k_\parallel|\tilde{\rho}_s}\right)\right] \exp\left(-\frac{k_\perp^2 \tilde{\rho}_s^2}{2}\right) I_m\left(\frac{k_\perp^2 \tilde{\rho}_s^2}{2}\right)\right\}
$$

$$
= -\frac{4}{3} W\left(k_\parallel \tilde{\rho}_s, k_\perp \tilde{\rho}_s\right), \tag{G26a}
$$

$$
(\boldsymbol{M}_s^{(1)})_{xy} = 4\sqrt{\pi} \sum_{m=1}^{\infty} \frac{m^2}{|k_\parallel|\tilde{\rho}_s} \exp\left(-\frac{m^2}{k_\parallel^2 \tilde{\rho}_s^2}\right)
$$

$$
\times \exp\left(-\frac{k_\perp^2 \tilde{\rho}_s^2}{2}\right) \left[I_m'\left(\frac{k_\perp^2 \tilde{\rho}_s^2}{2}\right) - I_m\left(\frac{k_\perp^2 \tilde{\rho}_s^2}{2}\right)\right], \tag{G26b}
$$

$$
(\boldsymbol{M}_s^{(1)})_{xz} = 2\left\{\frac{k_\perp}{|k_\parallel|} + \sum_{m=-\infty}^{\infty} \left(\frac{2m^3}{|k_\parallel|^2 k_\perp \tilde{\rho}_s^3} - \frac{m}{k_\perp \tilde{\rho}_s}\right) \mathrm{Re}\left[Z\left(\frac{m}{|k_\parallel|\tilde{\rho}_s}\right)\right]\right.
$$

$$
\left. \times \exp\left(-\frac{k_\perp^2 \tilde{\rho}_s^2}{2}\right) I_m\left(\frac{k_\perp^2 \tilde{\rho}_s^2}{2}\right)\right\}, \tag{G26c}
$$

$$
(\boldsymbol{M}_s^{(1)})_{yy} = -2\left\{1 + \sum_{m=-\infty}^{\infty} \frac{m}{|k_\parallel|\tilde{\rho}_s} \mathrm{Re}\left[Z\left(\frac{m}{|k_\parallel|\tilde{\rho}_s}\right)\right]\right.
$$

$$
\left. \times \exp\left(-\frac{k_\perp^2 \tilde{\rho}_s^2}{2}\right) \left[\left(\frac{2m^2}{k_\perp^2 \tilde{\rho}_s^2} + k_\perp^2 \tilde{\rho}_s^2\right) I_m\left(\frac{k_\perp^2 \tilde{\rho}_s^2}{2}\right) - k_\perp^2 \tilde{\rho}_s^2 I_m'\left(\frac{k_\perp^2 \tilde{\rho}_s^2}{2}\right)\right]\right\}
$$

$$
= -\frac{4}{3} Y\left(k_\parallel \tilde{\rho}_s, k_\perp \tilde{\rho}_s\right), \tag{G26d}
$$

$$(\boldsymbol{M}_s^{(1)})_{yz} = -\sqrt{\pi} \sum_{m=-\infty}^{\infty} k_\perp \tilde{\rho}_s \left(1 - \frac{2m^2}{|k_\parallel|^2 \tilde{\rho}_s^2} \right) \exp\left(-\frac{m^2}{k_\parallel^2 \tilde{\rho}_s^2} \right)$$

$$\times \exp\left(-\frac{k_\perp^2 \tilde{\rho}_s^2}{2} \right) \left[I_m'\left(\frac{k_\perp^2 \tilde{\rho}_s^2}{2} \right) - I_m\left(\frac{k_\perp^2 \tilde{\rho}_s^2}{2} \right) \right], \tag{G26e}$$

$$(\boldsymbol{M}_s^{(1)})_{zz} = 2 \left\{ 1 - \frac{k_\perp^2}{k_\parallel^2} + \sum_{m=-\infty}^{\infty} \frac{2m}{|k_\parallel|^2 \tilde{\rho}_s} \left(1 - \frac{m^2}{|k_\parallel|^2 \tilde{\rho}_s^2} \right) \mathrm{Re}\left[Z\left(\frac{m}{|k_\parallel| \tilde{\rho}_s} \right) \right] \right.$$

$$\left. \times \exp\left(-\frac{k_\perp^2 \tilde{\rho}_s^2}{2} \right) I_m\left(\frac{k_\perp^2 \tilde{\rho}_s^2}{2} \right) \right\}, \tag{G26f}$$

where we have reintroduced the special functions $F(x, y)$, $G(x, y)$ and $H(x, y)$ defined by (2.122), as well as $W(x, y)$ and $Y(x, y)$ defined by (G97). As anticipated from the arguments presented in Appendix F, $\boldsymbol{M}_s^{(0)}$ obeys the symmetries

$$(\boldsymbol{M}_s^{(0)})_{xz} = -\frac{k_\perp}{k_\parallel} (\boldsymbol{M}_s^{(0)})_{xx}, \tag{G27a}$$

$$(\boldsymbol{M}_s^{(0)})_{yz} = \frac{k_\perp}{k_\parallel} (\boldsymbol{M}_s^{(0)})_{xy}, \tag{G27b}$$

$$(\boldsymbol{M}_s^{(0)})_{zz} = \frac{k_\perp^2}{k_\parallel^2} (\boldsymbol{M}_s^{(0)})_{xx}. \tag{G27c}$$

G.1.3. *Dielectric tensor in low-frequency limit, $\{e_1, e_2, e_3\}$ coordinate frame*

Having evaluated the first- and second-order terms in the expansion for components of the dielectric tensor in the coordinate basis $\{\hat{x}, \hat{y}, \hat{z}\}$, we can use (G9) to find equivalent expressions in the coordinate basis $\{e_1, e_2, e_3\}$. Explicitly, we have the following transformations for $\boldsymbol{M}_s^{(0)}$:

$$(\boldsymbol{M}_s^{(0)})_{11} = \frac{k_\parallel^2}{k^2} (\boldsymbol{M}_s^{(0)})_{xx} - \frac{2k_\parallel k_\perp}{k^2} (\boldsymbol{M}_s^{(0)})_{xz} + \frac{k_\perp^2}{k^2} (\boldsymbol{M}_s^{(0)})_{zz}, \tag{G28a}$$

$$(\boldsymbol{M}_s^{(0)})_{12} = \frac{k_\parallel}{k} (\boldsymbol{M}_s^{(0)})_{xy} + \frac{k_\perp}{k} (\boldsymbol{M}_s^{(0)})_{yz}, \tag{G28b}$$

$$(\boldsymbol{M}_s^{(0)})_{13} = \frac{k_\parallel k_\perp}{k^2} \left[(\boldsymbol{M}_s^{(0)})_{xx} - (\boldsymbol{M}_s^{(0)})_{zz} \right] + \left(\frac{k_\parallel^2}{k^2} - \frac{k_\perp^2}{k^2} \right) (\boldsymbol{M}_s^{(0)})_{xz}, \tag{G28c}$$

$$(\boldsymbol{M}_s^{(0)})_{22} = (\boldsymbol{M}_s^{(0)})_{yy}, \tag{G28d}$$

$$(\boldsymbol{M}_s^{(0)})_{23} = -\frac{k_\perp}{k} (\boldsymbol{M}_s^{(0)})_{xy} + \frac{k_\parallel}{k} (\boldsymbol{M}_s^{(0)})_{yz}, \tag{G28e}$$

$$(\boldsymbol{M}_s^{(0)})_{33} = \frac{k_\perp^2}{k^2} (\boldsymbol{M}_s^{(0)})_{xx} + \frac{2k_\parallel k_\perp}{k^2} (\boldsymbol{M}_s^{(0)})_{xz} + \frac{k_\parallel^2}{k^2} (\boldsymbol{M}_s^{(0)})_{zz}, \tag{G28f}$$

and similarly for $\boldsymbol{M}_s^{(1)}$.

On account of the symmetries derived in Appendix G.1.2, we find for $\boldsymbol{M}_s^{(0)}$ that

$$(\boldsymbol{M}_s^{(0)})_{11} = \frac{k^2}{k_\parallel^2}(\boldsymbol{M}_s^{(0)})_{xx}, \tag{G29a}$$

$$(\boldsymbol{M}_s^{(0)})_{12} = \frac{k}{k_\parallel}(\boldsymbol{M}_s^{(0)})_{xy}, \tag{G29b}$$

$$(\boldsymbol{M}_s^{(0)})_{21} = -(\boldsymbol{M}_s^{(0)})_{12}, \tag{G29c}$$

$$(\boldsymbol{M}_s^{(0)})_{22} = (\boldsymbol{M}_s^{(0)})_{yy}, \tag{G29d}$$

with all other components vanishing. This agrees with (2.104) stated in the main text. On substitution of identities (G25), (2.121) are recovered.

As for $\boldsymbol{M}_s^{(1)}$, from the results (G26) derived in Appendix G.1.2, we have the following identities:

$$(\boldsymbol{M}_s^{(1)})_{xz} + \frac{k_\perp}{k_\parallel}(\boldsymbol{M}_s^{(1)})_{xx} = -2\sum_{m=-\infty}^{\infty}\frac{m}{k_\perp\tilde{\rho}_s}\mathrm{Re}\left[Z\left(\frac{m}{|k_\parallel|\tilde{\rho}_s}\right)\right]$$
$$\times \exp\left(-\frac{k_\perp^2\tilde{\rho}_s^2}{2}\right)I_m\left(\frac{k_\perp^2\tilde{\rho}_s^2}{2}\right), \tag{G30a}$$

$$(\boldsymbol{M}_s^{(1)})_{yz} - \frac{k_\perp}{k_\parallel}(\boldsymbol{M}_s^{(1)})_{xy} = -\sqrt{\pi}\sum_{m=-\infty}^{\infty}k_\perp\tilde{\rho}_s\exp\left(-\frac{m^2}{k_\parallel^2\tilde{\rho}_s^2}\right)$$
$$\times \exp\left(-\frac{k_\perp^2\tilde{\rho}_s^2}{2}\right)\left[I_m'\left(\frac{k_\perp^2\tilde{\rho}_s^2}{2}\right) - I_m\left(\frac{k_\perp^2\tilde{\rho}_s^2}{2}\right)\right], \tag{G30b}$$

$$(\boldsymbol{M}_s^{(1)})_{zz} + \frac{k_\perp}{k_\parallel}(\boldsymbol{M}_s^{(1)})_{xz} = 2\left\{1 + \sum_{m=-\infty}^{\infty}\frac{m}{|k_\parallel|\tilde{\rho}_s}\mathrm{Re}\left[Z\left(\frac{m}{|k_\parallel|\tilde{\rho}_s}\right)\right]\right.$$
$$\left.\times \exp\left(-\frac{k_\perp^2\tilde{\rho}_s^2}{2}\right)I_m\left(\frac{k_\perp^2\tilde{\rho}_s^2}{2}\right)\right\}. \tag{G30c}$$

Thus, we can decompose the dielectric components $(\boldsymbol{M}_s^{(1)})_{xz}$, $(\boldsymbol{M}_s^{(1)})_{yz}$ and $(\boldsymbol{M}_s^{(1)})_{zz}$ in terms of the remaining components of $\boldsymbol{M}_s^{(1)}$ as follows:

$$(\boldsymbol{M}_s^{(1)})_{xz} = -\frac{k_\perp}{k_\parallel}(\boldsymbol{M}_s^{(1)})_{xx} - L\left(k_\parallel\tilde{\rho}_s, k_\perp\tilde{\rho}_s\right), \tag{G31a}$$

$$(\boldsymbol{M}_s^{(1)})_{yz} = \frac{k_\perp}{k_\parallel}(\boldsymbol{M}_s^{(1)})_{xy} - N\left(k_\parallel\tilde{\rho}_s, k_\perp\tilde{\rho}_s\right), \tag{G31b}$$

$$(\boldsymbol{M}_s^{(1)})_{zz} = -\frac{k_\perp}{k_\parallel}(\boldsymbol{M}_s^{(1)})_{xz} + \left[2 + \frac{k_\perp}{k_\parallel}L\left(k_\parallel\tilde{\rho}_s, k_\perp\tilde{\rho}_s\right)\right]$$
$$= \frac{k_\perp^2}{k_\parallel^2}(\boldsymbol{M}_s^{(1)})_{xx} + 2\left[1 + \frac{k_\perp}{k_\parallel}L\left(k_\parallel\tilde{\rho}_s, k_\perp\tilde{\rho}_s\right)\right], \tag{G31c}$$

where the special functions $L(x, y)$ and $N(x, y)$ are defined by

$$L(x, y) \equiv \sum_{m=-\infty}^{\infty} \frac{2m}{y} \operatorname{Re} Z\left(\frac{m}{x}\right) \exp\left(-\frac{y^2}{2}\right) I_m\left(\frac{y^2}{2}\right), \tag{G32a}$$

$$N(x, y) \equiv \sqrt{\pi} \sum_{m=-\infty}^{\infty} y \exp\left(-\frac{m^2}{x^2}\right) \exp\left(-\frac{y^2}{2}\right) \left[I'_m\left(\frac{y^2}{2}\right) - I_m\left(\frac{y^2}{2}\right)\right]. \tag{G32b}$$

This leads to the following expressions:

$$(\boldsymbol{M}_s^{(1)})_{11} = \frac{k^2}{k_{\parallel}^2}(\boldsymbol{M}_s^{(1)})_{xx} + 2\left[\frac{k_{\perp}^2}{k^2} + \frac{k_{\perp}}{k_{\parallel}}L(k_{\parallel}\tilde{\rho}_s, k_{\perp}\tilde{\rho}_s)\right], \tag{G33a}$$

$$(\boldsymbol{M}_s^{(1)})_{12} = \frac{k}{k_{\parallel}}(\boldsymbol{M}_s^{(1)})_{xy} - \frac{k_{\perp}}{k}N(k_{\parallel}\tilde{\rho}_s, k_{\perp}\tilde{\rho}_s), \tag{G33b}$$

$$(\boldsymbol{M}_s^{(1)})_{13} = -\frac{2k_{\perp}k_{\parallel}}{k^2} - L(k_{\parallel}\tilde{\rho}_s, k_{\perp}\tilde{\rho}_s), \tag{G33c}$$

$$(\boldsymbol{M}_s^{(1)})_{22} = (\boldsymbol{M}_s^{(1)})_{yy}, \tag{G33d}$$

$$(\boldsymbol{M}_s^{(1)})_{23} = -\frac{k_{\parallel}}{k}N(k_{\parallel}\tilde{\rho}_s, k_{\perp}\tilde{\rho}_s), \tag{G33e}$$

$$(\boldsymbol{M}_s^{(1)})_{33} = \frac{2k_{\parallel}^2}{k^2}. \tag{G33f}$$

We note that $\boldsymbol{M}_s^{(1)}$ does not possess the same symmetry properties as $\boldsymbol{M}_s^{(0)}$.

G.1.4. *Asymptotic forms of $\boldsymbol{M}_s^{(0)}$ and $\boldsymbol{M}_s^{(1)}$*

In this appendix, we write down asymptotic forms at small and large x and y for the special functions $F(x, y)$, $G(x, y)$, $H(x, y)$, $L(x, y)$ and $N(x, y)$ defined by (2.122) and (G32), respectively. Physically, this corresponds via (2.121) to considering the dielectric response associated with $\boldsymbol{M}_s^{(0)}$ and $\boldsymbol{M}_s^{(1)}$ for modes with parallel and perpendicular wavenumbers very small (or very large) with respect to the inverse Larmor radius of species s. Detailed derivations are left as an exercise to keen readers (and can be verified numerically).

Proceeding systematically through various limits, we have the following results:

(i) $x \sim 1, y \ll 1$

$$F(x, y) = \sqrt{\pi} \exp\left(-\frac{1}{x^2}\right)[1 + O(y^2)], \tag{G34a}$$

$$G(x, y) = \operatorname{Re}\left[Z\left(\frac{1}{x}\right)\right][1 + O(y^2)], \tag{G34b}$$

$$H(x, y) = \sqrt{\pi} \exp\left(-\frac{1}{x^2}\right)[1 + O(y^2)], \tag{G34c}$$

$$L(x, y) = y \operatorname{Re}\left[Z\left(\frac{1}{x}\right)\right][1 + O(y^2)], \tag{G34d}$$

$$N(x, y) = \sqrt{\pi}y\left[2\exp\left(-\frac{1}{x^2}\right) - 1\right][1 + O(y^2)]. \tag{G34e}$$

(ii) $x, y \gg 1$

$$F(x, y) = \frac{\sqrt{\pi} x^3}{\left(x^2 + y^2\right)^{3/2}} \left[1 + O\left(\frac{1}{x^2 + y^2}\right)\right], \tag{G35a}$$

$$G(x, y) = -\frac{2x^3}{\left(x^2 + y^2\right)^2} \left[1 + O\left(\frac{1}{x^2 + y^2}\right)\right], \tag{G35b}$$

$$H(x, y) = \frac{\sqrt{\pi} x}{\left(x^2 + y^2\right)^{1/2}} \left[1 + O\left(\frac{1}{x^2 + y^2}\right)\right], \tag{G35c}$$

$$L(x, y) = -\frac{2xy}{x^2 + y^2} \left[1 + O\left(\frac{1}{x^2 + y^2}\right)\right], \tag{G35d}$$

$$N(x, y) = \frac{\sqrt{\pi} x}{y \left(x^2 + y^2\right)^{1/2}} \left[1 + O\left(\frac{1}{x^2 + y^2}\right)\right]. \tag{G35e}$$

We observe that the asymptotic forms (G35) are in fact valid even for $y \lesssim 1$.

(iii) $x \ll 1, y \sim 1$

$$F(x, y) = \frac{4\sqrt{\pi}}{y^2} \exp\left(-\frac{y^2}{2}\right) I_1\left(\frac{y^2}{2}\right) \exp\left(-\frac{1}{x^2}\right) \left\{1 + O\left[\exp\left(-\frac{3}{x^2}\right)\right]\right\}, \tag{G36a}$$

$$G(x, y) = -x \exp\left(-\frac{y^2}{2}\right) \left[I_0\left(\frac{y^2}{2}\right) - I_1\left(\frac{y^2}{2}\right)\right] \left[1 + O(x^2)\right], \tag{G36b}$$

$$H(x, y) = \sqrt{\pi} y^2 \exp\left(-\frac{y^2}{2}\right) \left[I_0\left(\frac{y^2}{2}\right) - I_1\left(\frac{y^2}{2}\right)\right] \left[1 + O(x^2)\right], \tag{G36c}$$

$$L(x, y) = -\frac{2x}{y} \left[1 - \exp\left(-\frac{y^2}{2}\right) I_0\left(\frac{y^2}{2}\right)\right] \left[1 + O(x^2)\right], \tag{G36d}$$

$$N(x, y) = -\sqrt{\pi} y \exp\left(-\frac{y^2}{2}\right) \left[I_0\left(\frac{y^2}{2}\right) - I_1\left(\frac{y^2}{2}\right)\right] \left[1 + O(x^2)\right]. \tag{G36e}$$

(iv) $x, y \ll 1$

$$F(x, y) = \sqrt{\pi} \exp\left(-\frac{1}{x^2}\right) \left\{1 + O\left[\exp\left(-\frac{3}{x^2}\right), y^2\right]\right\}, \tag{G37a}$$

$$\begin{aligned} G(x, y) = -x &\left[1 - \left(\frac{3}{4}y^2 - \frac{1}{2}x^2\right) \right. \\ &\left. + \left(\frac{3}{4}x^4 - \frac{15}{32}x^2 y^2 + \frac{5}{16}y^4\right)\right] \left[1 + O(x^6, x^4 y^2, x^2 y^4, y^6)\right], \end{aligned} \tag{G37b}$$

$$\begin{aligned} H(x, y) = \sqrt{\pi} y^2 &\left[1 - \left(\frac{3}{4}y^2 - \frac{1}{2}x^2\right) \right. \\ &\left. + \left(\frac{3}{4}x^4 - \frac{15}{32}x^2 y^2 + \frac{5}{16}y^4\right)\right] \left[1 + O(x^6, x^4 y^2, x^2 y^4, y^6)\right], \end{aligned} \tag{G37c}$$

$$L(x, y) = -xy \left[1 + O(x^2, y^2)\right], \tag{G37d}$$

$$N(x, y) = -\sqrt{\pi} y \left[1 + O(x^2)\right] \left[1 + O(x^2, y^2)\right]. \tag{G37e}$$

(v) $x \ll 1, y \gg 1$

$$F(x, y) = \frac{4}{y^3} \exp\left(-\frac{1}{x^2}\right) \left\{1 + O\left[\exp\left(-\frac{3}{x^2}\right), \frac{1}{y^2}\right]\right\}, \tag{G38a}$$

$$G(x, y) = -\frac{x}{\sqrt{\pi} y^3} \left[1 + O\left(\frac{1}{y^2}\right)\right], \tag{G38b}$$

$$H(x, y) = \frac{1}{y} \left[1 + O\left(\frac{1}{y^2}\right)\right], \tag{G38c}$$

$$L(x, y) = -\frac{2x}{y} \left[1 - \frac{1}{\sqrt{\pi} y}\right] \left[1 + O\left(x^2, \frac{1}{y^3}\right)\right], \tag{G38d}$$

$$N(x, y) = -\frac{1}{y^2} \left[1 + O\left(\frac{1}{y^2}\right)\right]. \tag{G38e}$$

G.1.5. *Unmagnetised Maxwellian dielectric response*

In this paper, we consider microinstabilities over a wide range of scales, from $k\rho_i \ll 1$ to sub-electron-scale microinstabilities with $k\rho_e \gg 1$. Therefore, the ordering $k\rho_s \sim 1$ assumed in § 2.5.3 for the derivation of the low-frequency dielectric tensor in a magnetised plasma cannot hold for both ions and electrons (as was noted in § 2.5.5 and discussed in § 2.5.6). While the derivation of the dielectric tensor in a strongly magnetised plasma ($k\rho_s \ll 1$) is straightforwardly performed by asymptotic analysis applied directly to the hot, magnetised plasma conductivity tensor (2.77), the equivalent calculation for $k\rho_s \gg 1$ is most easily done by direct analysis of the Vlasov equation with $\boldsymbol{B}_0 = 0$. In this appendix, we present such a calculation.

We begin from (C8), but with $\tilde{\Omega}_s = 0$ (and ignoring the displacement current):

$$\frac{k^2 c^2}{\omega^2} \left[\widehat{\delta E} - \hat{\boldsymbol{k}}\left(\hat{\boldsymbol{k}} \cdot \widehat{\delta E}\right)\right] = \frac{4\pi \mathrm{i}}{\omega} \widehat{\delta j}, \tag{G39a}$$

$$\widehat{\delta j} = \sum_s Z_s e \int \mathrm{d}^3 \boldsymbol{v} \, \boldsymbol{v} \, \widehat{\delta f_s}, \tag{G39b}$$

$$(-\mathrm{i}\omega + \mathrm{i}\boldsymbol{k} \cdot \boldsymbol{v}) \widehat{\delta f_s} = -\frac{Z_s e}{m_s} \left[\widehat{\delta E} + \frac{k}{\omega} \boldsymbol{v} \times \left(\hat{\boldsymbol{k}} \times \widehat{\delta E}\right)\right] \cdot \frac{\partial f_{s0}}{\partial \boldsymbol{v}}. \tag{G39c}$$

As with the magnetised case, we substitute the perturbed distribution function (G39c) into the current (G39b):

$$\widehat{\delta j} = -\mathrm{i} \sum_s \frac{Z_s^2 e^2}{m_s} \int \mathrm{d}^3 \boldsymbol{v} \, \frac{\boldsymbol{v}}{\omega - \boldsymbol{k} \cdot \boldsymbol{v}} \left[\widehat{\delta E} + \frac{k}{\omega} \boldsymbol{v} \times \left(\hat{\boldsymbol{k}} \times \widehat{\delta E}\right)\right] \cdot \frac{\partial f_{s0}}{\partial \boldsymbol{v}}. \tag{G40}$$

Non-dimensionalising the distribution function via

$$\tilde{f}_{s0}(\tilde{\boldsymbol{v}}_s) \equiv \frac{\pi^{3/2} v_{\mathrm{ths}}^3}{n_{s0}} f_{s0}(v_{\mathrm{ths}} \tilde{\boldsymbol{v}}_s), \tag{G41}$$

we obtain

$$\widehat{\delta j} = -\frac{\mathrm{i}}{4\pi\omega} \sum_s \omega_{\mathrm{ps}}^2 \frac{\tilde{\omega}_s}{\pi^{3/2}} \int \mathrm{d}^3 \tilde{\boldsymbol{v}}_s \, \frac{\tilde{\boldsymbol{v}}_s}{\tilde{\omega}_s - \hat{\boldsymbol{k}} \cdot \tilde{\boldsymbol{v}}_s} \left[\widehat{\delta E} + \frac{1}{\tilde{\omega}_s} \tilde{\boldsymbol{v}}_s \times \left(\hat{\boldsymbol{k}} \times \widehat{\delta E}\right)\right] \cdot \frac{\partial \tilde{f}_{s0}}{\partial \tilde{\boldsymbol{v}}_s}, \tag{G42}$$

where $\tilde{\omega}_s = \omega/kv_{\text{th}s}$. For a Maxwellian distribution, with

$$\tilde{f}_{s0}(\tilde{\boldsymbol{v}}_s) = \exp\left(-\tilde{v}_s^2\right), \tag{G43}$$

the second term in (G42) vanishes, leaving

$$\widehat{\delta \boldsymbol{j}} = \boldsymbol{\sigma} \cdot \widehat{\delta \boldsymbol{E}}, \tag{G44}$$

where the conductivity tensor is

$$\boldsymbol{\sigma} = \frac{\mathrm{i}}{4\pi\omega} \sum_s \omega_{\text{p}s}^2 \frac{2\tilde{\omega}_s}{\pi^{3/2}} \int \mathrm{d}^3\tilde{\boldsymbol{v}}_s \, \frac{\tilde{\boldsymbol{v}}_s \tilde{\boldsymbol{v}}_s}{\tilde{\omega}_s - \widehat{\boldsymbol{k}} \cdot \tilde{\boldsymbol{v}}_s} \exp\left(-\tilde{v}_s^2\right). \tag{G45}$$

The integral can be evaluated to give

$$\boldsymbol{\sigma} = -\frac{\mathrm{i}}{4\pi\omega} \sum_s \omega_{\text{p}s}^2 \tilde{\omega}_s \left\{ Z(\tilde{\omega}_s)\left(\boldsymbol{I} - \hat{\boldsymbol{k}}\hat{\boldsymbol{k}}\right) + 2\left[\tilde{\omega}_s + \tilde{\omega}_s^2 Z(\tilde{\omega}_s)\right]\hat{\boldsymbol{k}}\hat{\boldsymbol{k}}\right\}. \tag{G46}$$

The dielectric tensor in an unmagnetised Maxwellian plasma for general $\tilde{\omega}_s$ is, therefore,

$$\mathfrak{E}^{(\text{UM})} = \sum_s \frac{\omega_{\text{p}s}^2}{\omega^2} \tilde{\omega}_s \left\{ Z(\tilde{\omega}_s)\left(\boldsymbol{I} - \hat{\boldsymbol{k}}\hat{\boldsymbol{k}}\right) + 2\left[\tilde{\omega}_s + \tilde{\omega}_s^2 Z(\tilde{\omega}_s)\right]\hat{\boldsymbol{k}}\hat{\boldsymbol{k}}\right\}. \tag{G47}$$

Note that it follows from (G39) that $\mathfrak{E} \cdot \hat{\boldsymbol{k}} = 0$, so we conclude that for non-zero fluctuations, either $\hat{\boldsymbol{k}} \cdot \widehat{\delta \boldsymbol{E}} = 0$ or $1 + \tilde{\omega}_s Z(\tilde{\omega}_s) = 0$. We do not find the conventional longitudinal plasma waves because we have neglected the displacement current in Maxwell's equations. The only modes that satisfy $1 + \tilde{\omega}_s Z(\tilde{\omega}_s) = 0$ are strongly damped, with $\tilde{\omega}_s \sim 1$. Thus, all modes satisfying $\tilde{\omega}_s \ll 1$ must be purely transverse.

For $\tilde{\omega}_s \ll 1$, the unmagnetised dielectric response therefore simplifies to

$$\mathfrak{E}^{(\text{UM})} = \mathrm{i}\sqrt{\pi}\left(\boldsymbol{I} - \hat{\boldsymbol{k}}\hat{\boldsymbol{k}}\right) \sum_s \frac{\omega_{\text{p}s}^2}{\omega^2} \tilde{\omega}_s \left[1 + O(\tilde{\omega}_s)\right]. \tag{G48}$$

G.1.6. *Validity of approximation* $\boldsymbol{M}_s \approx \boldsymbol{M}_s^{(0)}$ *for large or small* $k_\parallel \rho_s$ *and* $k_\perp \rho_s$

In carrying out the expansion of the Maxwellian dielectric tensor (G17) in $\tilde{\omega}_{s\parallel}$, we assumed that $k\rho_s \sim 1$; however, in general, we will wish to consider microinstabilities that exist at typical wavenumbers $k\rho_s \ll 1$ or $k\rho_s \gg 1$. Indeed, since the mass ratio $\mu_e = m_e/m_i$ is very small, if we wish to consider the combined response of both species, it is inevitable that for one of them, $k\rho_s \ll 1$ or $k\rho_s \gg 1$. Thus, it remains to assess when the approximation $\boldsymbol{M}_s \approx \boldsymbol{M}_s^{(0)}$ is valid in these limits. We show in this appendix that this approximation is appropriate in the limit $k_\parallel \rho_s \gg 1$, for arbitrary $k_\perp \rho_s$; however, for $k_\parallel \rho_s \ll 1$, the approximation breaks down for some dielectric components – indeed, in the limit $k_\parallel \rho_s, k_\perp \rho_s \ll 1$, it breaks down for all but two components. For these instances, an alternative expression for the dielectric tensor is derived below.

The validity of the $k_\parallel \rho_s \gg 1$ limit is most simply demonstrated by comparing the components of $\boldsymbol{M}_s^{(0)}$ with the unmagnetised dielectric response (G48). Recalling that

$$(\boldsymbol{M}_s^{(0)})_{11} = i\tilde{\omega}_{s\parallel} \frac{k^2}{k_\parallel^2} F\big(k_\parallel \tilde{\rho}_s, k_\perp \tilde{\rho}_s\big), \tag{G49a}$$

$$(\boldsymbol{M}_s^{(0)})_{12} = i\tilde{\omega}_{s\parallel} \frac{k}{k_\parallel} G\big(k_\parallel \tilde{\rho}_s, k_\perp \tilde{\rho}_s\big), \tag{G49b}$$

$$(\boldsymbol{M}_s^{(0)})_{21} = -(\boldsymbol{M}_s^{(0)})_{12}, \tag{G49c}$$

$$(\boldsymbol{M}_s^{(0)})_{22} = i\tilde{\omega}_{s\parallel} H\big(k_\parallel \tilde{\rho}_s, k_\perp \tilde{\rho}_s\big), \tag{G49d}$$

and applying the asymptotic results (G35), we find

$$(\boldsymbol{M}_s^{(0)})_{11} \approx i\sqrt{\pi} \frac{\tilde{\omega}_{s\parallel} k_\parallel}{k}, \tag{G50a}$$

$$(\boldsymbol{M}_s^{(0)})_{12} \approx -2i \frac{\tilde{\omega}_{s\parallel} k_\parallel^2}{k^2} \frac{1}{k\rho_s}, \tag{G50b}$$

$$(\boldsymbol{M}_s^{(0)})_{22} \approx i\sqrt{\pi} \frac{\tilde{\omega}_{s\parallel} k_\parallel}{k}. \tag{G50c}$$

We note these expressions are valid for arbitrary $k_\perp \rho_s$. The equivalent components of the unmagnetised (normalised) dielectric tensor $\boldsymbol{M}_s \approx \omega^2 \boldsymbol{\mathfrak{E}}_s^{(\mathrm{UM})} / \omega_{\mathrm{ps}}^2$ are

$$(\boldsymbol{M}_s)_{11} = i\sqrt{\pi} \tilde{\omega}_s, \tag{G51a}$$

$$(\boldsymbol{M}_s)_{12} = (\boldsymbol{M}_s^{(0)})_{21} = 0, \tag{G51b}$$

$$(\boldsymbol{M}_s)_{22} = i\sqrt{\pi} \tilde{\omega}_s. \tag{G51c}$$

Noting that $\tilde{\omega}_s = \tilde{\omega}_{s\parallel} k_\parallel / k$, we see that the diagonal terms are identical, while the non-zero $\boldsymbol{e}_1 \boldsymbol{e}_2$ term present in the $k\rho_s \gg 1$ limit of $\boldsymbol{M}_s^{(0)}$ becomes asymptotically small in $1/k\rho_s \ll 1$.

To demonstrate that the approximation $\boldsymbol{M}_s \approx \boldsymbol{M}_s^{(0)}$ is not accurate in the limit $k_\parallel \rho_s \ll 1$, we consider the full Maxwellian dielectric tensor assuming $\tilde{\omega}_{s\parallel} \lesssim 1$ and $k_\parallel \rho_s \ll 1$. If this long-wavenumber dielectric tensor subsequently evaluated at low frequencies $\tilde{\omega}_{s\parallel} \ll 1$ gives the same result as $\boldsymbol{M}_s^{(0)}$ for any particular component of $\boldsymbol{M}_s$, then the approximation for that component is reasonable; otherwise, the approximation has to be modified at sufficiently small $k_\parallel \rho_s \ll 1$.

If $k_\parallel \rho_s \ll 1$ and $\tilde{\omega}_{s\parallel} \lesssim 1$, it follows that, for $n \neq 0$,

$$|\zeta_{sn}| \equiv \left| \tilde{\omega}_{s\parallel} - \frac{n}{k_\parallel \tilde{\rho}_s} \right| \gg 1. \tag{G52}$$

In this case, we can simplify the plasma dispersion function via a large-argument expansion

$$Z(\zeta_{sn}) \approx -\frac{1}{\zeta_{sn}} - \frac{1}{2\zeta_{sn}^3} + \dots. \tag{G53}$$

The long-wavelength dielectric tensor is then

$$(\boldsymbol{M}_s)_{xx} \approx -2\tilde{\omega}_{s\parallel} \sum_{n=-\infty}^{\infty} \frac{n^2}{\zeta_{sn} k_\perp^2 \tilde{\rho}_s^2} \exp\left(-\frac{k_\perp^2 \tilde{\rho}_s^2}{2}\right) I_n\left(\frac{k_\perp^2 \tilde{\rho}_s^2}{2}\right), \tag{G54a}$$

$$(\boldsymbol{M}_s)_{xy} \approx -\mathrm{i}\tilde{\omega}_{s\parallel} \sum_{n=-\infty}^{\infty} \frac{n}{\zeta_{sn}} \exp\left(-\frac{k_\perp^2 \tilde{\rho}_s^2}{2}\right)\left[I_n'\left(\frac{k_\perp^2 \tilde{\rho}_s^2}{2}\right) - I_n\left(\frac{k_\perp^2 \tilde{\rho}_s^2}{2}\right)\right], \tag{G54b}$$

$$(\boldsymbol{M}_s)_{xz} \approx -\tilde{\omega}_{s\parallel} \sum_{n=-\infty}^{\infty} \frac{n}{\zeta_{sn}^2 k_\perp \tilde{\rho}_s} \exp\left(-\frac{k_\perp^2 \tilde{\rho}_s^2}{2}\right) I_n\left(\frac{k_\perp^2 \tilde{\rho}_s^2}{2}\right), \tag{G54c}$$

$$(\boldsymbol{M}_s)_{yx} = -(\boldsymbol{M}_s)_{xy}, \tag{G54d}$$

$$\begin{aligned}
(\boldsymbol{M}_s)_{yy} \approx -\tilde{\omega}_{s\parallel} &\left[\sum_{n\in\mathbb{Z}^{\neq}}\left\{\frac{1}{\zeta_{sn}}\exp\left(-\frac{k_\perp^2 \tilde{\rho}_s^2}{2}\right)\right.\right. \\
&\times \left.\left[\left(\frac{2n^2}{k_\perp^2 \tilde{\rho}_s^2} + k_\perp^2 \tilde{\rho}_s^2\right) I_n\left(\frac{k_\perp^2 \tilde{\rho}_s^2}{2}\right) - k_\perp^2 \tilde{\rho}_s^2 I_n'\left(\frac{k_\perp^2 \tilde{\rho}_s^2}{2}\right)\right]\right\} \\
&- Z(\tilde{\omega}_{s\parallel}) k_\perp^2 \tilde{\rho}_s^2 \exp\left(-\frac{k_\perp^2 \tilde{\rho}_s^2}{2}\right)\left\{I_0\left(\frac{k_\perp^2 \tilde{\rho}_s^2}{2}\right) - I_1\left(\frac{k_\perp^2 \tilde{\rho}_s^2}{2}\right)\right\}\left.\right],
\end{aligned} \tag{G54e}$$

$$\begin{aligned}
(\boldsymbol{M}_s)_{yz} \approx \mathrm{i}\tilde{\omega}_{s\parallel} &\left[\sum_{n\in\mathbb{Z}^{\neq}}\left\{\frac{1}{2\zeta_{sn}^2}k_\perp\tilde{\rho}_s\exp\left(-\frac{k_\perp^2 \tilde{\rho}_s^2}{2}\right)\left[I_n'\left(\frac{k_\perp^2 \tilde{\rho}_s^2}{2}\right) - I_n\left(\frac{k_\perp^2 \tilde{\rho}_s^2}{2}\right)\right]\right\}\right. \\
&+ \left[1 + \tilde{\omega}_{s\parallel}Z(\tilde{\omega}_{s\parallel})\right]k_\perp\tilde{\rho}_s\exp\left(-\frac{k_\perp^2 \tilde{\rho}_s^2}{2}\right)\left\{I_0\left(\frac{k_\perp^2 \tilde{\rho}_s^2}{2}\right) - I_1\left(\frac{k_\perp^2 \tilde{\rho}_s^2}{2}\right)\right\}\left.\right], \tag{G54f}
\end{aligned}$$

$$(\boldsymbol{M}_s)_{zx} = (\boldsymbol{M}_s)_{xz}, \tag{G54g}$$

$$(\boldsymbol{M}_s)_{zy} = -(\boldsymbol{M}_s)_{yz}, \tag{G54h}$$

$$\begin{aligned}
(\boldsymbol{M}_s)_{zz} \approx -\tilde{\omega}_{s\parallel} &\left[\sum_{n\in\mathbb{Z}^{\neq}}\left\{\frac{1}{\zeta_{sn}}\exp\left(-\frac{k_\perp^2 \tilde{\rho}_s^2}{2}\right) I_n\left(\frac{k_\perp^2 \tilde{\rho}_s^2}{2}\right)\right\}\right. \\
&- 2\tilde{\omega}_{s\parallel}\left[1 + \tilde{\omega}_{s\parallel}Z(\tilde{\omega}_{s\parallel})\right]\exp\left(-\frac{k_\perp^2 \tilde{\rho}_s^2}{2}\right) I_0\left(\frac{k_\perp^2 \tilde{\rho}_s^2}{2}\right)\left.\right], \tag{G54i}
\end{aligned}$$

where $\mathbb{Z}^{\neq}$ denotes non-zero integers. We note that the error associated with neglecting higher-order terms in ζ_{sn} is $O(k_\parallel^2 \rho_s^2)$. Next, using

$$-\frac{1}{\zeta_{sn}} = \frac{1}{n/k_\parallel\tilde{\rho}_s - \tilde{\omega}_{s\parallel}} \approx \frac{k_\parallel\tilde{\rho}_s}{n}\left[1 + \frac{\tilde{\omega}_{s\parallel}k_\parallel\tilde{\rho}_s}{n} + O\left(\frac{\omega^2}{\Omega_e^2}\right)\right], \tag{G55}$$

we can isolate the dependence of each dielectric tensor component on $\tilde{\omega}_{s\parallel}$. It is clear that any sum involving an odd power of n vanishes, meaning that the leading-order contributions in $k_\parallel\tilde{\rho}_s$ from the summation terms arise from the highest power of $\tilde{\omega}_{s\parallel}$ gives

an even power of n. The resulting approximate expressions are

$$(\boldsymbol{M}_s)_{xx} \approx \frac{2k_\parallel^2}{k_\perp^2}\tilde{\omega}_{s\parallel}^2 \left[1 - \exp\left(-\frac{k_\perp^2\tilde{\rho}_s^2}{2}\right)I_0\left(\frac{k_\perp^2\tilde{\rho}_s^2}{2}\right)\right], \tag{G56a}$$

$$(\boldsymbol{M}_s)_{xy} \approx i\tilde{\omega}_{s\parallel}k_\parallel\tilde{\rho}_s \exp\left(-\frac{k_\perp^2\tilde{\rho}_s^2}{2}\right)\left[I_0\left(\frac{k_\perp^2\tilde{\rho}_s^2}{2}\right) - I_1\left(\frac{k_\perp^2\tilde{\rho}_s^2}{2}\right)\right], \tag{G56b}$$

$$(\boldsymbol{M}_s)_{xz} \approx -4k_\parallel^2\tilde{\rho}_s^2\frac{k_\parallel}{k_\perp}\tilde{\omega}_{s\parallel}^2 \sum_{n=1}^{\infty} \frac{1}{n^2} \exp\left(-\frac{k_\perp^2\tilde{\rho}_s^2}{2}\right)I_n\left(\frac{k_\perp^2\tilde{\rho}_s^2}{2}\right), \tag{G56c}$$

$$(\boldsymbol{M}_s)_{yy} \approx \tilde{\omega}_{s\parallel}\exp\left(-\frac{k_\perp^2\tilde{\rho}_s^2}{2}\right)\left\{Z(\tilde{\omega}_{s\parallel})\,k_\perp^2\tilde{\rho}_s^2\left[I_0\left(\frac{k_\perp^2\tilde{\rho}_s^2}{2}\right) - I_1\left(\frac{k_\perp^2\tilde{\rho}_s^2}{2}\right)\right]\right.$$
$$\left. + 2\tilde{\omega}_{s\parallel}k_\parallel^2\tilde{\rho}_s^2\sum_{n=1}^{\infty}\left[\left(\frac{2}{k_\perp^2\tilde{\rho}_s^2} + \frac{k_\perp^2\tilde{\rho}_s^2}{n^2}\right)I_n\left(\frac{k_\perp^2\tilde{\rho}_s^2}{2}\right) - \frac{k_\perp^2\tilde{\rho}_s^2}{n^2}I_n'\left(\frac{k_\perp^2\tilde{\rho}_s^2}{2}\right)\right]\right\}, \tag{G56d}$$

$$(\boldsymbol{M}_s)_{yz} \approx i\tilde{\omega}_{s\parallel}\left[1 + \tilde{\omega}_{s\parallel}Z(\tilde{\omega}_{s\parallel})\right]$$
$$\times k_\perp\tilde{\rho}_s\exp\left(-\frac{k_\perp^2\tilde{\rho}_s^2}{2}\right)\left[I_0\left(\frac{k_\perp^2\tilde{\rho}_s^2}{2}\right) - I_1\left(\frac{k_\perp^2\tilde{\rho}_s^2}{2}\right)\right], \tag{G56e}$$

$$(\boldsymbol{M}_s)_{zz} \approx 2\tilde{\omega}_{s\parallel}^2\left[1 + \tilde{\omega}_{s\parallel}Z(\tilde{\omega}_{s\parallel})\right]\exp\left(-\frac{k_\perp^2\tilde{\rho}_s^2}{2}\right)I_0\left(\frac{k_\perp^2\tilde{\rho}_s^2}{2}\right), \tag{G56f}$$

where we have again used the sum identities (G24). Note that we have retained a term in $(\boldsymbol{M}_s)_{yy}$ which is quadratic in $k_\parallel\tilde{\rho}_s$, even though there exists another term which is independent of $k_\parallel\tilde{\rho}_s$. This is because the latter term becomes arbitrarily small in the limit $k_\perp\rho_s \ll 1$, whereas the former is independent of $k_\perp\rho_s$; hence, if $k_\perp\rho_s \ll k_\parallel\rho_s$, the latter term can become dominant.

Now considering the limit $\tilde{\omega}_{s\parallel} \ll 1$, while holding $k_\parallel\rho_s \ll 1$ at some fixed value, the plasma dispersion function can now be approximated by its small-argument expansion

$$Z(\tilde{\omega}_{s\parallel}) \approx i\sqrt{\pi}, \tag{G57}$$

to give

$$(\boldsymbol{M}_s)_{xx} \approx \frac{2k_\parallel^2}{k_\perp^2}\tilde{\omega}_{s\parallel}^2\left[1 - \exp\left(-\frac{k_\perp^2\tilde{\rho}_s^2}{2}\right)I_0\left(\frac{k_\perp^2\tilde{\rho}_s^2}{2}\right)\right], \tag{G58a}$$

$$(\boldsymbol{M}_s)_{xy} \approx i\tilde{\omega}_{s\parallel}k_\parallel\tilde{\rho}_s\exp\left(-\frac{k_\perp^2\tilde{\rho}_s^2}{2}\right)\left[I_0\left(\frac{k_\perp^2\tilde{\rho}_s^2}{2}\right) - I_1\left(\frac{k_\perp^2\tilde{\rho}_s^2}{2}\right)\right], \tag{G58b}$$

$$(\boldsymbol{M}_s)_{xz} \approx -4k_\parallel^2\tilde{\rho}_s^2\frac{k_\parallel}{k_\perp}\tilde{\omega}_{s\parallel}^2\sum_{n=1}^{\infty}\frac{1}{n^2}\exp\left(-\frac{k_\perp^2\tilde{\rho}_s^2}{2}\right)I_n\left(\frac{k_\perp^2\tilde{\rho}_s^2}{2}\right), \tag{G58c}$$

$$(\boldsymbol{M}_s)_{yy} \approx \tilde{\omega}_{s\parallel}\exp\left(-\frac{k_\perp^2\tilde{\rho}_s^2}{2}\right)\left\{i\sqrt{\pi}k_\perp^2\tilde{\rho}_s^2\left[I_0\left(\frac{k_\perp^2\tilde{\rho}_s^2}{2}\right) - I_1\left(\frac{k_\perp^2\tilde{\rho}_s^2}{2}\right)\right]\right.$$
$$\left. + 2\tilde{\omega}_{s\parallel}^2k_\parallel^2\tilde{\rho}_s^2\sum_{n=1}^{\infty}\left[\left(\frac{2}{k_\perp^2\tilde{\rho}_s^2} + \frac{k_\perp^2\tilde{\rho}_s^2}{n^2}\right)I_n\left(\frac{k_\perp^2\tilde{\rho}_s^2}{2}\right) - \frac{k_\perp^2\tilde{\rho}_s^2}{n^2}I_n'\left(\frac{k_\perp^2\tilde{\rho}_s^2}{2}\right)\right]\right\}, \tag{G58d}$$

$$(\boldsymbol{M}_s)_{yz} \approx \mathrm{i}\tilde{\omega}_{s\|} \left[1 + \mathrm{i}\sqrt{\pi}\tilde{\omega}_{s\|} \right]$$

$$\times k_\perp \tilde{\rho}_s \exp\left(-\frac{k_\perp^2 \tilde{\rho}_s^2}{2} \right) \left[I_0\left(\frac{k_\perp^2 \tilde{\rho}_s^2}{2} \right) - I_1\left(\frac{k_\perp^2 \tilde{\rho}_s^2}{2} \right) \right], \tag{G58e}$$

$$(\boldsymbol{M}_s)_{zz} \approx 2\tilde{\omega}_{s\|}^2 \left[1 + \mathrm{i}\sqrt{\pi}\tilde{\omega}_{s\|} \right] \exp\left(-\frac{k_\perp^2 \tilde{\rho}_s^2}{2} \right) I_0\left(\frac{k_\perp^2 \tilde{\rho}_s^2}{2} \right). \tag{G58f}$$

For comparison, we state below the long-wavelength limit of $\boldsymbol{M}_s^{(0)}$ using asymptotic expressions (G36):

$$(\boldsymbol{M}_s^{(0)})_{xx} = 4\mathrm{i}\sqrt{\pi} \frac{\tilde{\omega}_{s\|}}{k_\perp^2 \tilde{\rho}_s^2} \exp\left(-\frac{1}{k_\|^2 \tilde{\rho}_s^2} \right) \exp\left(-\frac{k_\perp^2 \tilde{\rho}_s^2}{2} \right) I_1\left(\frac{k_\perp^2 \tilde{\rho}_s^2}{2} \right), \tag{G59a}$$

$$(\boldsymbol{M}_s^{(0)})_{xy} = \mathrm{i}\tilde{\omega}_{s\|} |k_\|| \tilde{\rho}_s \exp\left(-\frac{k_\perp^2 \tilde{\rho}_s^2}{2} \right) \left[I_0\left(\frac{k_\perp^2 \tilde{\rho}_s^2}{2} \right) - I_1\left(\frac{k_\perp^2 \tilde{\rho}_s^2}{2} \right) \right], \tag{G59b}$$

$$(\boldsymbol{M}_s^{(0)})_{xz} = -4\mathrm{i}\sqrt{\pi} \frac{\tilde{\omega}_{s\|}}{k_\perp k_\| \tilde{\rho}_s^2} \exp\left(-\frac{1}{k_\|^2 \tilde{\rho}_s^2} \right) \exp\left(-\frac{k_\perp^2 \tilde{\rho}_s^2}{2} \right) I_1\left(\frac{k_\perp^2 \tilde{\rho}_s^2}{2} \right), \tag{G59c}$$

$$(\boldsymbol{M}_s^{(0)})_{yy} = \mathrm{i}\sqrt{\pi}\tilde{\omega}_{s\|} k_\perp^2 \tilde{\rho}_s^2 \exp\left(-\frac{k_\perp^2 \tilde{\rho}_s^2}{2} \right) \left[I_0\left(\frac{k_\perp^2 \tilde{\rho}_s^2}{2} \right) - I_1\left(\frac{k_\perp^2 \tilde{\rho}_s^2}{2} \right) \right], \tag{G59d}$$

$$(\boldsymbol{M}_s^{(0)})_{yz} = \mathrm{i}\tilde{\omega}_{s\|} k_\perp \tilde{\rho}_s \exp\left(-\frac{k_\perp^2 \tilde{\rho}_s^2}{2} \right) \left[I_0\left(\frac{k_\perp^2 \tilde{\rho}_s^2}{2} \right) - I_1\left(\frac{k_\perp^2 \tilde{\rho}_s^2}{2} \right) \right], \tag{G59e}$$

$$(\boldsymbol{M}_s^{(0)})_{zz} = 4\mathrm{i}\sqrt{\pi} \frac{\tilde{\omega}_{s\|}}{k_\|^2 \tilde{\rho}_s^2} \exp\left(-\frac{1}{k_\|^2 \tilde{\rho}_s^2} \right) \exp\left(-\frac{k_\perp^2 \tilde{\rho}_s^2}{2} \right) I_1\left(\frac{k_\perp^2 \tilde{\rho}_s^2}{2} \right). \tag{G59f}$$

Assuming $k_\perp \rho_s \sim 1$, we observe that, while three of the six unique dielectric tensor components are identical for both $\tilde{\omega}_{s\|} \to 0$, $k_\| \rho_s \ll 1$ fixed, and $k_\| \rho_s \to 0$, $\tilde{\omega}_{s\|} \ll 1$ fixed $[(\boldsymbol{M}_s)_{xy}, (\boldsymbol{M}_s)_{yy}, \text{ and } (\boldsymbol{M}_s)_{yz}]$, the other three $[(\boldsymbol{M}_s)_{xx}, (\boldsymbol{M}_s)_{xz} \text{ and } (\boldsymbol{M}_s)_{zz}]$ are not. Instead, the dominant terms are the quadratic terms $(\boldsymbol{M}_s^{(1)})_{xx}$, $(\boldsymbol{M}_s^{(1)})_{xz}$ and $(\boldsymbol{M}_s^{(1)})_{zz}$ in the $\tilde{\omega}_{s\|} \ll 1$ expansion. In the limit $k_\perp \rho_s \ll 1$, $(\boldsymbol{M}_s)_{yy}$ also departs from the approximation $(\boldsymbol{M}_s^{(0)})_{yy}$ for sufficiently small $k_\perp \rho_s$ as compared with $k_\| \rho_s$, instead being accurately described by $(\boldsymbol{M}_s^{(1)})_{yy}$.

As a consequence, we must assess the conditions under which one approximation or the other is valid. This is most simply answered by observing that the expressions for $(\boldsymbol{M}_s^{(0)})_{xx}$, $(\boldsymbol{M}_s^{(0)})_{xz}$ and $(\boldsymbol{M}_s^{(0)})_{zz}$ from (G59a), (G59c) and (G59f) are exponentially small; thus, for $k_\| \rho_s \ll 1/\log(1/\tilde{\omega}_{s\|})$, we must use approximations (G58a), (G58c), (G58e) for $(\boldsymbol{M}_s)_{xx}$, $(\boldsymbol{M}_s)_{xz}$ and $(\boldsymbol{M}_s)_{zz}$. In addition, if $k_\perp^2 \rho_s^2 \ll \tilde{\omega}_{s\|} k_\|^2 \rho_s^2 \ll 1$, then

$$(\boldsymbol{M}_s)_{yy} \approx \frac{2\omega_{ps}^2}{\omega^2} \tilde{\omega}_{s\|}^2 k_\|^2 \tilde{\rho}_s^2, \tag{G60}$$

becomes the appropriate approximation for $(\boldsymbol{M}_s)_{yy}$.

G.1.7. *Calculation of second-order corrections to dispersion relation*

In this appendix, we justify the relations (K20) used in Appendix K – that is, for $k_\parallel \rho_s \ll 1$,

$$\frac{[(\boldsymbol{M}_s)_{13}]^2}{(\boldsymbol{M}_s^{(1)})_{33}} \lesssim (\boldsymbol{M}_s)_{11}, \tag{G61a}$$

$$\frac{(\boldsymbol{M}_s)_{13}(\boldsymbol{M}_s)_{23}}{(\boldsymbol{M}_s^{(1)})_{33}} \lesssim \tilde{\omega}_{e\parallel}(\boldsymbol{M}_s)_{12} \ll (\boldsymbol{M}_s)_{12}, \tag{G61b}$$

$$\frac{[(\boldsymbol{M}_s)_{23}]^2}{(\boldsymbol{M}_s^{(1)})_{33}} \lesssim \tilde{\omega}_{e\parallel}(\boldsymbol{M}_s)_{22} \ll (\boldsymbol{M}_s)_{22}. \tag{G61c}$$

We also prove the identity (K25), or

$$(\boldsymbol{M}_e^{(1)} + \boldsymbol{M}_i^{(1)})_{11} - \frac{\left[(\boldsymbol{M}_e^{(1)} + \boldsymbol{M}_i^{(1)})_{13}\right]^2}{2(\boldsymbol{M}_e^{(1)})_{33}} = -\frac{4}{3}W_e - \frac{4}{3}W_i - \frac{1}{4}\left(L_e + L_i\right)^2, \tag{G62}$$

used to derive the dispersion relation (K23). We have introduced the notation $W_e = W(k_\parallel \tilde{\rho}_e, k_\perp \tilde{\rho}_e)$, $W_i = L(k_\parallel \rho_i, k_\perp \rho_i)$, $L_e = L(k_\parallel \tilde{\rho}_e, k_\perp \tilde{\rho}_e)$ and $L_i = L(k_\parallel \rho_i, k_\perp \rho_i)$, for the sake of brevity.

To complete the first task, we begin with the expressions (K16) for the dielectric components, and substitute (G26a), (G25b), (G25d) and (G26d) for $(\boldsymbol{M}_s^{(1)})_{xx}$, $(\boldsymbol{M}_s^{(0)})_{xy}$, $(\boldsymbol{M}_s^{(0)})_{xy}$, $(\boldsymbol{M}_s^{(0)})_{yy}$ and $(\boldsymbol{M}_s^{(1)})_{xy}$, respectively. This gives (K16) directly in terms of special functions $G(x, y)$, $H(x, y)$, $L(x, y)$, $N(x, y)$, $W(x, y)$ and $Y(x, y)$:

$$(\boldsymbol{M}_s)_{11} \approx -\frac{4k^2}{3k_\parallel^2}\tilde{\omega}_{s\parallel}^2 W\left(k_\parallel \tilde{\rho}_s, k_\perp \tilde{\rho}_s\right) + 2\tilde{\omega}_{s\parallel}^2\left[\frac{k_\perp^2}{k^2} + \frac{k_\perp}{k_\parallel}L\left(k_\parallel \tilde{\rho}_s, k_\perp \tilde{\rho}_s\right)\right], \tag{G63a}$$

$$(\boldsymbol{M}_s)_{12} \approx -\mathrm{i}\frac{k}{k_\parallel}\tilde{\omega}_{s\parallel}G\left(k_\parallel \tilde{\rho}_s, k_\perp \tilde{\rho}_s\right), \tag{G63b}$$

$$(\boldsymbol{M}_s)_{13} \approx -\tilde{\omega}_{s\parallel}^2\left[\frac{2k_\perp k_\parallel}{k^2} + L\left(k_\parallel \tilde{\rho}_s, k_\perp \tilde{\rho}_s\right)\right], \tag{G63c}$$

$$(\boldsymbol{M}_s)_{22} \approx \mathrm{i}\tilde{\omega}_{s\parallel}H\left(k_\parallel \tilde{\rho}_s, k_\perp \tilde{\rho}_s\right) - \frac{4}{3}\tilde{\omega}_{s\parallel}^2 Y\left(k_\parallel \tilde{\rho}_s, k_\perp \tilde{\rho}_s\right), \tag{G63d}$$

$$(\boldsymbol{M}_s)_{23} \approx -\frac{k_\parallel}{k}\tilde{\omega}_{s\parallel}^2 N\left(k_\parallel \tilde{\rho}_s, k_\perp \tilde{\rho}_s\right), \tag{G63e}$$

$$(\boldsymbol{M}_s)_{33} \approx \frac{2k_\parallel^2}{k^2}\tilde{\omega}_{s\parallel}^2. \tag{G63f}$$

We then apply the $k_\parallel \rho_s \ll 1$ limits of the aforementioned special functions using Appendices G.1.4 and G.4.2 – in particular, (G36b), (G36c), (G36d), (G36e), (G100a) and (G101c):

$$(\boldsymbol{M}_s)_{11} \approx 2\tilde{\omega}_{s\parallel}^2 \exp\left(-\frac{k_\perp^2 \tilde{\rho}_s^2}{2}\right) I_0\left(\frac{k_\perp^2 \tilde{\rho}_s^2}{2}\right), \tag{G64a}$$

$$(\boldsymbol{M}_s)_{12} \approx \mathrm{i}\tilde{\omega}_{s\parallel}k\tilde{\rho}_s \exp\left(-\frac{k_\perp^2 \tilde{\rho}_s^2}{2}\right)\left[I_0\left(\frac{k_\perp^2 \tilde{\rho}_s^2}{2}\right) - I_1\left(\frac{k_\perp^2 \tilde{\rho}_s^2}{2}\right)\right], \tag{G64b}$$

$$(\boldsymbol{M}_s)_{13} \approx -\tilde{\omega}_{s\parallel}^2 \frac{2k_\parallel}{k} \exp\left(-\frac{k_\perp^2 \tilde{\rho}_s^2}{2}\right) I_0\left(\frac{k_\perp^2 \tilde{\rho}_s^2}{2}\right), \tag{G64c}$$

$$(\boldsymbol{M}_s)_{22} \approx \mathrm{i}\sqrt{\pi}\tilde{\omega}_{s\parallel} k_\perp^2 \tilde{\rho}_s^2 \exp\left(-\frac{k_\perp^2 \tilde{\rho}_s^2}{2}\right)\left[I_0\left(\frac{k_\perp^2 \tilde{\rho}_s^2}{2}\right) - I_1\left(\frac{k_\perp^2 \tilde{\rho}_s^2}{2}\right)\right] + \tilde{\omega}_{s\parallel}^2 k_\parallel^2 \tilde{\rho}_s^2, \tag{G64d}$$

$$(\boldsymbol{M}_s)_{23} \approx \sqrt{\pi}\tilde{\omega}_{s\parallel}^2 k_\parallel \tilde{\rho}_s \exp\left(-\frac{k_\perp^2 \tilde{\rho}_s^2}{2}\right)\left[I_0\left(\frac{k_\perp^2 \tilde{\rho}_s^2}{2}\right) - I_1\left(\frac{k_\perp^2 \tilde{\rho}_s^2}{2}\right)\right], \tag{G64e}$$

$$(\boldsymbol{M}_s)_{33} \approx \frac{2k_\parallel^2}{k^2}\tilde{\omega}_{s\parallel}^2. \tag{G64f}$$

We can now make the relevant comparisons presented in (G61), and obtain the desired results

$$\frac{[(\boldsymbol{M}_s)_{13}]^2}{(\boldsymbol{M}_s)_{11}(\boldsymbol{M}_s)_{33}} \approx \exp\left(-\frac{k_\perp^2 \tilde{\rho}_s^2}{2}\right) I_0\left(\frac{k_\perp^2 \tilde{\rho}_s^2}{2}\right) \lesssim 1, \tag{G65a}$$

$$\frac{(\boldsymbol{M}_s)_{13}(\boldsymbol{M}_s)_{23}}{(\boldsymbol{M}_s)_{12}\boldsymbol{M}_s)_{33}} \approx \mathrm{i}\tilde{\omega}_{s\parallel} \exp\left(-\frac{k_\perp^2 \tilde{\rho}_s^2}{2}\right) I_0\left(\frac{k_\perp^2 \tilde{\rho}_s^2}{2}\right) \lesssim \tilde{\omega}_{s\parallel}, \tag{G65b}$$

$$\frac{[(\boldsymbol{M}_s)_{23}]^2}{(\boldsymbol{M}_s)_{22}(\boldsymbol{M}_s)_{33}} \approx -\mathrm{i}\frac{\sqrt{\pi}}{2}\tilde{\omega}_{s\parallel} \exp\left(-\frac{k_\perp^2 \tilde{\rho}_s^2}{2}\right)\left[I_0\left(\frac{k_\perp^2 \tilde{\rho}_s^2}{2}\right) - I_1\left(\frac{k_\perp^2 \tilde{\rho}_s^2}{2}\right)\right] \lesssim \tilde{\omega}_{s\parallel}, \tag{G65c}$$

where we used the inequalities

$$\exp\left(-\frac{k_\perp^2 \tilde{\rho}_s^2}{2}\right) I_0\left(\frac{k_\perp^2 \tilde{\rho}_s^2}{2}\right) \leqslant 1, \tag{G66a}$$

$$\exp\left(-\frac{k_\perp^2 \tilde{\rho}_s^2}{2}\right)\left[I_0\left(\frac{k_\perp^2 \tilde{\rho}_s^2}{2}\right) - I_1\left(\frac{k_\perp^2 \tilde{\rho}_s^2}{2}\right)\right] \leqslant 1, \tag{G66b}$$

valid for arbitrary values of $k_\perp \tilde{\rho}_s$.

To derive (G62), we use (G63a), (G63b) and (G63f) to derive the following expressions:

$$(\boldsymbol{M}_e^{(1)} + \boldsymbol{M}_i^{(1)})_{11} = \frac{k^2}{k_\parallel^2}\left[(\boldsymbol{M}_e^{(1)})_{xx} + (\boldsymbol{M}_i^{(1)})_{xx}\right] + 2\left[\frac{2k_\perp^2}{k^2} + \frac{k_\perp}{k_\parallel}(L_e + L_i)\right], \tag{G67a}$$

$$(\boldsymbol{M}_e^{(1)} + \boldsymbol{M}_i^{(1)})_{13} = \frac{4k_\perp k_\parallel}{k^2} + L_e + L_i, \tag{G67b}$$

$$2(\boldsymbol{M}_e^{(1)})_{33} = \frac{4k_\parallel^2}{k^2}. \tag{G67c}$$

Then

$$\frac{\left[(\boldsymbol{M}_e^{(1)} + \boldsymbol{M}_i^{(1)})_{13}\right]^2}{2(\boldsymbol{M}_e^{(1)})_{33}} = \left[\frac{2k_\perp}{k} + \frac{k}{2k_\parallel}(L_e + L_i)\right]^2, \tag{G68}$$

which in turn gives

$$(\boldsymbol{M}_e^{(1)} + \boldsymbol{M}_i^{(1)})_{11} - \frac{\left[(\boldsymbol{M}_e^{(1)} + \boldsymbol{M}_i^{(1)})_{13}\right]^2}{2(\boldsymbol{M}_e^{(1)})_{33}} = \frac{k^2}{k_\parallel^2}\left[(\boldsymbol{M}_e^{(1)})_{xx} + (\boldsymbol{M}_i^{(1)})_{xx} - \frac{1}{4}(L_e + L_i)^2\right]. \tag{G69}$$

The identities (K24) give (G62), completing the proof.

G.2. *The CE electron-friction term*

For an electron distribution of the form

$$\tilde{f}_e(\tilde{v}_{e\parallel}, \tilde{v}_{e\perp}) = -\eta_e^R \tilde{v}_{e\parallel} \exp\left(-\tilde{v}_e^2\right), \tag{G70}$$

with $\eta_s^R \ll 1$ a constant, it follows that

$$\Lambda_e(\tilde{v}_{e\parallel}, \tilde{v}_{e\perp}) = -\eta_e^R \tilde{v}_{e\perp} \exp\left(-\tilde{v}_e^2\right), \tag{G71}$$

while

$$\varXi_e(\tilde{v}_{e\parallel}, \tilde{v}_{e\perp}) = -\frac{\eta_e^R}{\tilde{\omega}_{e\parallel}} \tilde{v}_{e\perp} \exp\left(-\tilde{v}_e^2\right) + O(\eta_e). \tag{G72}$$

Since

$$\int_{-\infty}^{\infty} \mathrm{d}\tilde{v}_{e\parallel}\, \tilde{v}_{e\parallel} \int_0^{\infty} \mathrm{d}\tilde{v}_{e\perp}\, \Lambda_e(\tilde{v}_{e\parallel}, \tilde{v}_{e\perp}) = 0, \tag{G73}$$

when $\Lambda_e(\tilde{v}_{e\parallel}, \tilde{v}_{e\perp})$ is given by (G71), the function $\varXi_e(\tilde{v}_{e\parallel}, \tilde{v}_{e\perp})$ is just proportional to that arising for a Maxwellian distribution (cf. (G13)), and so the dielectric response associated with the CE electron-friction term is

$$\boldsymbol{P}_e = \frac{\eta_e^R}{2} \boldsymbol{M}_e. \tag{G74}$$

G.3. *The CE temperature-gradient-driven terms*

For the CE temperature-gradient-driven term arising from a Krook operator, which takes the form

$$\tilde{f}_s(\tilde{v}_{s\parallel}, \tilde{v}_{s\perp}) = -\eta_s \tilde{v}_{s\parallel} \left(\tilde{v}_s^2 - \tfrac{5}{2}\right) \exp\left(-\tilde{v}_s^2\right), \tag{G75}$$

it follows (assuming $\eta_e^R = 0$) that

$$\Lambda_s(\tilde{v}_{s\parallel}, \tilde{v}_{s\perp}) = -\eta_s \tilde{v}_{s\perp} \left(\tilde{v}_s^2 - \tfrac{5}{2}\right) \exp\left(-\tilde{v}_s^2\right), \tag{G76}$$

and

$$\varXi_s(\tilde{v}_{s\parallel}, \tilde{v}_{s\perp}) = -\frac{\eta_s}{\tilde{\omega}_{s\parallel}} \tilde{v}_{s\perp} \left(\tilde{v}_s^2 - \frac{5}{2}\right) \exp\left(-\tilde{v}_s^2\right) + O(\eta_s). \tag{G77}$$

Then, to leading order in η_s,

$$(\boldsymbol{P}_s)_{xx} = \frac{2}{\sqrt{\pi}} \eta_s \sum_{n=-\infty}^{\infty} \left[\frac{n^2}{k_\perp^2 \tilde{\rho}_s^2} \int_{C_L} \frac{\exp\left(-\tilde{v}_{s\parallel}^2\right) \mathrm{d}\tilde{v}_{s\parallel}}{\tilde{v}_{s\parallel} - \zeta_{sn}} \right.$$
$$\left. \times \int_0^{\infty} \mathrm{d}\tilde{v}_{s\perp}\, \tilde{v}_{s\perp} J_n(k_\perp \tilde{\rho}_s \tilde{v}_{s\perp})^2 \exp\left(-\tilde{v}_{s\perp}^2\right) \left(\tilde{v}_s^2 - \frac{5}{2}\right) \right], \tag{G78a}$$

$$(\boldsymbol{P}_s)_{xy} = \frac{2\mathrm{i}}{\sqrt{\pi}} \eta_s \sum_{n=-\infty}^{\infty} \left[\frac{n}{k_\perp \tilde{\rho}_s} \int_{C_L} \frac{\exp\left(-\tilde{v}_{s\parallel}^2\right) \mathrm{d}\tilde{v}_{s\parallel}}{\tilde{v}_{s\parallel} - \zeta_{sn}} \right.$$
$$\left. \times \int_0^{\infty} \mathrm{d}\tilde{v}_{s\perp}\, \tilde{v}_{s\perp}^2 J_n(k_\perp \tilde{\rho}_s \tilde{v}_{s\perp}) J_n'(k_\perp \tilde{\rho}_s \tilde{v}_{s\perp}) \exp\left(-\tilde{v}_{s\perp}^2\right) \left(\tilde{v}_s^2 - \frac{5}{2}\right) \right], \tag{G78b}$$

$$(\boldsymbol{P}_s)_{xz} = \frac{2}{\sqrt{\pi}} \eta_s \sum_{n=-\infty}^{\infty} \left[\frac{n}{k_\perp \tilde{\rho}_s} \int_{C_L} \frac{\tilde{v}_{s\parallel} \exp\left(-\tilde{v}_{s\parallel}^2\right) \mathrm{d}\tilde{v}_{s\parallel}}{\tilde{v}_{s\parallel} - \zeta_{sn}} \right. \tag{G78c}$$

$$\left. \times \int_0^\infty \mathrm{d}\tilde{v}_{s\perp} \, \tilde{v}_{s\perp} J_n(k_\perp \tilde{\rho}_s \tilde{v}_{s\perp})^2 \exp\left(-\tilde{v}_{s\perp}^2\right) \left(\tilde{v}_s^2 - \frac{5}{2}\right) \right], \tag{G78d}$$

$$(\boldsymbol{P}_s)_{yx} = -(\boldsymbol{P}_s)_{xy}, \tag{G78e}$$

$$(\boldsymbol{P}_s)_{yy} = \frac{2}{\sqrt{\pi}} \eta_s \sum_{n=-\infty}^{\infty} \left[\int_{C_L} \frac{\exp\left(-\tilde{v}_{s\parallel}^2\right) \mathrm{d}\tilde{v}_{s\parallel}}{\tilde{v}_{s\parallel} - \zeta_{sn}} \right.$$

$$\left. \times \int_0^\infty \mathrm{d}\tilde{v}_{s\perp} \, \tilde{v}_{s\perp}^3 J_n'(k_\perp \tilde{\rho}_s \tilde{v}_{s\perp})^2 \exp\left(-\tilde{v}_{s\perp}^2\right) \left(\tilde{v}_s^2 - \frac{5}{2}\right) \right], \tag{G78f}$$

$$(\boldsymbol{P}_s)_{yz} = -\frac{2\mathrm{i}}{\sqrt{\pi}} \eta_s \sum_{n=-\infty}^{\infty} \left[\int_{C_L} \frac{\tilde{v}_{s\parallel} \exp\left(-\tilde{v}_{s\parallel}^2\right) \mathrm{d}\tilde{v}_{s\parallel}}{\tilde{v}_{s\parallel} - \zeta_{sn}} \right.$$

$$\left. \times \int_0^\infty \mathrm{d}\tilde{v}_{s\perp} \, \tilde{v}_{s\perp}^2 J_n(k_\perp \tilde{\rho}_s \tilde{v}_{s\perp}) J_n'(k_\perp \tilde{\rho}_s \tilde{v}_{s\perp}) \exp\left(-\tilde{v}_{s\perp}^2\right) \left(\tilde{v}_s^2 - \frac{5}{2}\right) \right], \tag{G78g}$$

$$(\boldsymbol{P}_s)_{zx} = (\boldsymbol{P}_s)_{xz}, \tag{G78h}$$

$$(\boldsymbol{P}_s)_{zy} = -(\boldsymbol{P}_s)_{yz}, \tag{G78i}$$

$$(\boldsymbol{P}_s)_{zz} = \frac{2}{\sqrt{\pi}} \eta_s \sum_{n=-\infty}^{\infty} \left[\int_{C_L} \frac{\tilde{v}_{s\parallel}^2 \exp\left(-\tilde{v}_{s\parallel}^2\right) \mathrm{d}\tilde{v}_{s\parallel}}{\tilde{v}_{s\parallel} - \zeta_{sn}} \right.$$

$$\left. \times \int_0^\infty \mathrm{d}\tilde{v}_{s\perp} \, \tilde{v}_{s\perp} J_n(k_\perp \tilde{\rho}_s \tilde{v}_{s\perp})^2 \exp\left(-\tilde{v}_{s\perp}^2\right) \left(\tilde{v}_s^2 - \frac{5}{2}\right) \right]. \tag{G78j}$$

In addition to the plasma-dispersion-function identities (G15) and Bessel-function identities (G16), we use

$$\frac{1}{\sqrt{\pi}} \int_{C_L} \frac{u^3 \exp\left(-u^2\right) \mathrm{d}u}{u - z} = \frac{1}{2} + z^2 \left[1 + zZ(z)\right], \tag{G79a}$$

$$\frac{1}{\sqrt{\pi}} \int_{C_L} \frac{u^4 \exp\left(-u^2\right) \mathrm{d}u}{u - z} = z \left\{ \frac{1}{2} + z^2 \left[1 + zZ(z), \right] \right\}, \tag{G79b}$$

and

$$\int_0^\infty \mathrm{d}t \, t^3 J_n(\alpha t)^2 \exp\left(-t^2\right) = \frac{1}{2} \exp\left(-\frac{\alpha^2}{2}\right) \left\{ I_n\left(\frac{\alpha^2}{2}\right) \right.$$

$$\left. + \frac{\alpha^2}{2} \left[I_n'\left(\frac{\alpha^2}{2}\right) - I_n\left(\frac{\alpha^2}{2}\right) \right] \right\}, \tag{G80a}$$

$$\int_0^\infty \mathrm{d}t \, t^4 \, t^2 J_n(\alpha t) J_n'(\alpha t) \exp\left(-t^2\right) = \frac{\alpha}{4} \exp\left(-\frac{\alpha^2}{2}\right) \left[\left(\alpha^2 - 2 + \frac{2n^2}{\alpha^2}\right) I_n\left(\frac{\alpha^2}{2}\right) \right.$$

$$\left. + \left(1 - \alpha^2\right) I_n'\left(\frac{\alpha^2}{2}\right) \right], \tag{G80b}$$

$$\int_0^\infty \mathrm{d}t^5\, t^3 J_n'(\alpha t)^2 \exp\left(-t^2\right) = \frac{1}{2} \exp\left(-\frac{\alpha^2}{2}\right)$$

$$\times \left\{\left[\frac{3\alpha^2}{2} - \frac{\alpha^4}{2} + n^2\left(\frac{1}{\alpha^2} - \frac{3}{2}\right)\right] I_n\left(\frac{\alpha^2}{2}\right)\right.$$

$$\left. + \left(\frac{\alpha^4}{2} + \frac{n^2}{2} - \alpha^2\right) I_n'\left(\frac{\alpha^2}{2}\right)\right\}, \qquad (G80c)$$

to obtain again the expressions for the dielectric components (G78) in terms of special mathematical functions (a tedious, but elementary calculation):

$$(\boldsymbol{P}_s)_{xx} = \eta_s \sum_{n=-\infty}^{\infty} \frac{n^2}{k_\perp^2 \tilde{\rho}_s^2} \exp\left(-\frac{k_\perp^2 \tilde{\rho}_s^2}{2}\right) \left\{\frac{k_\perp^2 \tilde{\rho}_s^2}{2} Z(\zeta_{sn}) I_n'\left(\frac{k_\perp^2 \tilde{\rho}_s^2}{2}\right)\right.$$

$$\left. + \left[\zeta_{sn} + Z(\zeta_{sn})\left(\zeta_{sn}^2 - \frac{3}{2} - \frac{k_\perp^2 \tilde{\rho}_s^2}{2}\right)\right] I_n\left(\frac{k_\perp^2 \tilde{\rho}_s^2}{2}\right)\right\}, \qquad (G81a)$$

$$(\boldsymbol{P}_s)_{xy} = \frac{\mathrm{i}\eta_s}{2} \sum_{n=-\infty}^{\infty} n \exp\left(-\frac{k_\perp^2 \tilde{\rho}_s^2}{2}\right) \left\{\left[\zeta_{sn} + Z(\zeta_{sn})\left(\zeta_{sn}^2 - \frac{3}{2} - \frac{k_\perp^2 \tilde{\rho}_s^2}{2}\right)\right] I_n'\left(\frac{k_\perp^2 \tilde{\rho}_s^2}{2}\right)\right.$$

$$\left. + \left[Z(\zeta_{sn})\left(\frac{1}{2} + \frac{k_\perp^2 \tilde{\rho}_s^2}{2} + \frac{2n^2}{k_\perp^2 \tilde{\rho}_s^2} - \zeta_{sn}^2\right) - \zeta_{sn}\right] I_n\left(\frac{k_\perp^2 \tilde{\rho}_s^2}{2}\right)\right\}, \qquad (G81b)$$

$$(\boldsymbol{P}_s)_{xz} = \eta_s \sum_{n=-\infty}^{\infty} \frac{n}{k_\perp \tilde{\rho}_s} \exp\left(-\frac{k_\perp^2 \tilde{\rho}_s^2}{2}\right) \left\{\frac{k_\perp^2 \tilde{\rho}_s^2}{2}\left[1 + \zeta_{sn} Z(\zeta_{sn})\right] I_n'\left(\frac{k_\perp^2 \tilde{\rho}_s^2}{2}\right)\right.$$

$$\left. + \left[\zeta_{sn}^2 - 1 - \frac{k_\perp^2 \tilde{\rho}_s^2}{2} + \zeta_{sn} Z(\zeta_{sn})\left(\zeta_{sn}^2 - \frac{3}{2} - \frac{k_\perp^2 \tilde{\rho}_s^2}{2}\right)\right] I_n\left(\frac{k_\perp^2 \tilde{\rho}_s^2}{2}\right)\right\}, \qquad (G81c)$$

$$(\boldsymbol{P}_s)_{yx} = (\boldsymbol{P}_s)_{xy}, \qquad (G81d)$$

$$(\boldsymbol{P}_s)_{yy} = \eta_s \sum_{n=-\infty}^{\infty} \exp\left(-\frac{k_\perp^2 \tilde{\rho}_s^2}{2}\right) \left\{\left[\left(\frac{n^2}{k_\perp^2 \tilde{\rho}_s^2} + \frac{k_\perp^2 \tilde{\rho}_s^2}{2}\right) \zeta_{sn}\right.\right.$$

$$\left. + Z(\zeta_{sn})\left(\frac{n^2 \zeta_{sn}^2}{k_\perp^2 \tilde{\rho}_s^2} + \frac{k_\perp^2 \tilde{\rho}_s^2 \zeta_{sn}^2}{2} + \frac{k_\perp^2 \tilde{\rho}_s^2}{4} - \frac{k_\perp^4 \tilde{\rho}_s^4}{2} - \frac{3n^2}{2} - \frac{3n^2}{2k_\perp^2 \tilde{\rho}_s^2}\right)\right] I_n\left(\frac{k_\perp^2 \tilde{\rho}_s^2}{2}\right)\right\}$$

$$\left. + \left[Z(\zeta_{sn})\left(\frac{1}{2} + k_\perp^2 \tilde{\rho}_s^2 + \frac{n^2}{k_\perp^2 \tilde{\rho}_s^2} - \zeta_{sn}^2\right) - \zeta_{sn}\right] \frac{k_\perp^2 \tilde{\rho}_s^2}{2} I_n'\left(\frac{k_\perp^2 \tilde{\rho}_s^2}{2}\right), \qquad (G81e)$$

$$(\boldsymbol{P}_s)_{yz} = -\frac{\mathrm{i}\eta_s}{2} \sum_{n=-\infty}^{\infty} k_\perp \tilde{\rho}_s \exp\left(-\frac{k_\perp^2 \tilde{\rho}_s^2}{2}\right)$$

$$\times \left\{\left[k_\perp^2 \tilde{\rho}_s^2 + \frac{2n^2}{k_\perp^2 \tilde{\rho}_s^2} - \zeta_{sn}^2 + \zeta_{sn} Z(\zeta_{sn})\left(k_\perp^2 \tilde{\rho}_s^2 + \frac{1}{2} + \frac{2n^2}{k_\perp^2 \tilde{\rho}_s^2} - \zeta_{sn}^2\right)\right] I_n\left(\frac{k_\perp^2 \tilde{\rho}_s^2}{2}\right)\right.$$

$$\left. + \left[\zeta_{sn}^2 - 1 - k_\perp^2 \tilde{\rho}_s^2 + \zeta_{sn} Z(\zeta_{sn})\left(\zeta_{sn}^2 - \frac{3}{2} - k_\perp^2 \tilde{\rho}_s^2\right)\right] I_n'\left(\frac{k_\perp^2 \tilde{\rho}_s^2}{2}\right)\right\}, \qquad (G81f)$$

$$(\boldsymbol{P}_s)_{zx} = (\boldsymbol{P}_s)_{xz}, \qquad (G81g)$$

$$(P_s)_{zy} = -(P_s)_{yz}, \tag{G81h}$$

$$(P_s)_{zz} = \eta_s \sum_{n=-\infty}^{\infty} \exp\left(-\frac{k_\perp^2 \tilde{\rho}_s^2}{2}\right) \left\{ \frac{k_\perp^2 \tilde{\rho}_s^2}{2} \zeta_{sn} \left[1 + \zeta_{sn} Z(\zeta_{sn})\right] I'_n\left(\frac{k_\perp^2 \tilde{\rho}_s^2}{2}\right) \right.$$

$$\left. + \left[\zeta_{sn}^3 - \zeta_{sn} - \frac{k_\perp^2 \tilde{\rho}_s^2 \zeta_{sn}}{2} + \zeta_{sn}^2 Z(\zeta_{sn}) \left(\zeta_{sn}^2 - \frac{3}{2} - \frac{k_\perp^2 \tilde{\rho}_s^2}{2} \right) \right] I_n\left(\frac{k_\perp^2 \tilde{\rho}_s^2}{2}\right) \right\}. \tag{G81i}$$

G.3.1. *Dielectric tensor in low-frequency limit*

In the low-frequency limit $\tilde{\omega}_{s\parallel} \ll 1$ under the ordering $k_\parallel \rho_s \sim k_\perp \rho_s \sim 1$, the expressions (G81) can be approximated by the leading-order term of the expansion of P_s, that is

$$P_s \approx P_s^{(0)} + O(\tilde{\omega}_{s\parallel}^2), \tag{G82}$$

where

$$(P_s^{(0)})_{xx} = \eta_s \sum_{n=-\infty}^{\infty} \frac{n^2}{k_\perp^2 \tilde{\rho}_s^2} \exp\left(-\frac{k_\perp^2 \tilde{\rho}_s^2}{2}\right) \left\{ \frac{k_\perp^2 \tilde{\rho}_s^2}{2} Z\left(-\frac{n}{|k_\parallel| \tilde{\rho}_s}\right) I'_n\left(\frac{k_\perp^2 \tilde{\rho}_s^2}{2}\right) \right.$$

$$\left. + \left[-\frac{n}{|k_\parallel| \tilde{\rho}_s} + Z\left(-\frac{n}{|k_\parallel| \tilde{\rho}_s}\right)\left(\frac{n^2}{|k_\parallel|^2 \tilde{\rho}_s^2} - \frac{3}{2} - \frac{k_\perp^2 \tilde{\rho}_s^2}{2}\right) \right] I_n\left(\frac{k_\perp^2 \tilde{\rho}_s^2}{2}\right) \right\}, \tag{G83a}$$

$$(P_s^{(0)})_{xy} = \frac{i\eta_s}{2} \sum_{n=-\infty}^{\infty} n \exp\left(-\frac{k_\perp^2 \tilde{\rho}_s^2}{2}\right)$$

$$\times \left\{ \left[Z\left(-\frac{n}{|k_\parallel| \tilde{\rho}_s}\right)\left(\frac{1}{2} + \frac{k_\perp^2 \tilde{\rho}_s^2}{2} + \frac{2n^2}{k_\perp^2 \tilde{\rho}_s^2} - \frac{n^2}{|k_\parallel|^2 \tilde{\rho}_s^2}\right) + \frac{n}{|k_\parallel| \tilde{\rho}_s} \right] I_n\left(\frac{k_\perp^2 \tilde{\rho}_s^2}{2}\right) \right.$$

$$\left. + \left[-\frac{n}{|k_\parallel| \tilde{\rho}_s} + Z\left(-\frac{n}{|k_\parallel| \tilde{\rho}_s}\right)\left(\frac{n^2}{|k_\parallel|^2 \tilde{\rho}_s^2} - \frac{3}{2} - \frac{k_\perp^2 \tilde{\rho}_s^2}{2}\right) \right] I'_n\left(\frac{k_\perp^2 \tilde{\rho}_s^2}{2}\right) \right\}, \tag{G83b}$$

$$(P_s^{(0)})_{xz} = \eta_s \sum_{n=-\infty}^{\infty} \frac{n}{k_\perp \tilde{\rho}_s} \exp\left(-\frac{k_\perp^2 \tilde{\rho}_s^2}{2}\right) \left\{ \frac{k_\perp^2 \tilde{\rho}_s^2}{2} \left[1 - \frac{n}{|k_\parallel| \tilde{\rho}_s} Z\left(-\frac{n}{|k_\parallel| \tilde{\rho}_s}\right) \right] I'_n\left(\frac{k_\perp^2 \tilde{\rho}_s^2}{2}\right) \right.$$

$$+ I_n\left(\frac{k_\perp^2 \tilde{\rho}_s^2}{2}\right) \left[\frac{n^2}{|k_\parallel|^2 \tilde{\rho}_s^2} - 1 - \frac{k_\perp^2 \tilde{\rho}_s^2}{2} \right.$$

$$\left. \left. - \frac{n}{|k_\parallel| \tilde{\rho}_s} Z\left(-\frac{n}{|k_\parallel| \tilde{\rho}_s}\right)\left(\frac{n^2}{|k_\parallel|^2 \tilde{\rho}_s^2} - \frac{3}{2} - \frac{k_\perp^2 \tilde{\rho}_s^2}{2}\right) \right] \right\}, \tag{G83c}$$

$$(P_s^{(0)})_{yx} = (P_s^{(0)})_{xy}, \tag{G83d}$$

$$(P_s^{(0)})_{yy} = \eta_s \sum_{n=-\infty}^{\infty} \exp\left(-\frac{k_\perp^2 \tilde{\rho}_s^2}{2}\right) \left\{ \left[-\left(\frac{n^2}{k_\perp^2 \tilde{\rho}_s^2} + \frac{k_\perp^2 \tilde{\rho}_s^2}{2}\right) \frac{n}{|k_\parallel| \tilde{\rho}_s} \right. \right.$$

$$+ Z\left(-\frac{n}{|k_\parallel| \tilde{\rho}_s}\right) \left(\frac{n^4}{k_\perp^2 k_\parallel^2 \tilde{\rho}_s^4} + \frac{n^2 k_\perp^2}{k_\parallel^2} + \frac{k_\perp^2 \tilde{\rho}_s^2}{4} - \frac{k_\perp^4 \tilde{\rho}_s^4}{2} \right)$$

$$-\frac{3n^2}{2} - \frac{3n^2}{2k_\perp^2 \tilde\rho_s^2}\Bigg)\Bigg] I_n\left(\frac{k_\perp^2 \tilde\rho_s^2}{2}\right) + \frac{k_\perp^2 \tilde\rho_s^2}{2} I_n'\left(\frac{k_\perp^2 \tilde\rho_s^2}{2}\right)$$

$$\times \left[Z\left(-\frac{n}{|k_\parallel|\tilde\rho_s}\right)\left(\frac{1}{2} + k_\perp^2\tilde\rho_s^2 + \frac{n^2}{k_\perp^2\tilde\rho_s^2} - \frac{n^2}{k_\parallel^2\tilde\rho_s^2}\right) + \frac{n}{|k_\parallel|\tilde\rho_s}\right]\Bigg\}, \tag{G83e}$$

$$(\boldsymbol{P}_s^{(0)})_{yz} = -\frac{\mathrm{i}\eta_s}{2}\sum_{n=-\infty}^{\infty} k_\perp\tilde\rho_s \exp\left(-\frac{k_\perp^2\tilde\rho_s^2}{2}\right)$$

$$\times \Bigg\{ I_n\left(\frac{k_\perp^2\tilde\rho_s^2}{2}\right)\Bigg[k_\perp^2\tilde\rho_s^2 + \frac{2n^2}{k_\perp^2\tilde\rho_s^2} - \frac{n^2}{k_\parallel^2\tilde\rho_s^2}$$

$$- \frac{n}{|k_\parallel|\tilde\rho_s} Z\left(-\frac{n}{|k_\parallel|\tilde\rho_s}\right)\left(k_\perp^2\tilde\rho_s^2 + \frac{1}{2} + \frac{2n^2}{k_\perp^2\tilde\rho_s^2} - \frac{n^2}{k_\parallel^2\tilde\rho_s^2}\right)\Bigg]$$

$$+ I_n'\left(\frac{k_\perp^2\tilde\rho_s^2}{2}\right)\Bigg[\frac{n^2}{k_\parallel^2\tilde\rho_s^2} - 1 - k_\perp^2\tilde\rho_s^2$$

$$- \frac{n}{|k_\parallel|\tilde\rho_s} Z\left(-\frac{n}{|k_\parallel|\tilde\rho_s}\right)\left(\frac{n^2}{k_\parallel^2\tilde\rho_s^2} - \frac{3}{2} - k_\perp^2\tilde\rho_s^2\right)\Bigg]\Bigg\}, \tag{G83f}$$

$$(\boldsymbol{P}_s^{(0)})_{zx} = (\boldsymbol{P}_s^{(0)})_{xz}, \tag{G83g}$$

$$(\boldsymbol{P}_s^{(0)})_{zy} = -(\boldsymbol{P}_s^{(0)})_{yz}, \tag{G83h}$$

$$(\boldsymbol{P}_s^{(0)})_{zz} = \eta_s \sum_{n=-\infty}^{\infty} \exp\left(-\frac{k_\perp^2\tilde\rho_s^2}{2}\right)\Bigg\{ -\frac{nk_\perp^2\tilde\rho_s}{2|k_\parallel|}\left[1 - \frac{n}{|k_\parallel|\tilde\rho_s} Z\left(-\frac{n}{|k_\parallel|\tilde\rho_s}\right)\right] I_n'\left(\frac{k_\perp^2\tilde\rho_s^2}{2}\right)$$

$$+ I_n\left(\frac{k_\perp^2\tilde\rho_s^2}{2}\right)\Bigg[\frac{n}{|k_\parallel|\tilde\rho_s} - \frac{n^3}{|k_\parallel|^3\tilde\rho_s^3} + \frac{nk_\perp^2\tilde\rho_s}{2|k_\parallel|}$$

$$+ \frac{n^2}{k_\parallel^2\tilde\rho_s^2} Z\left(-\frac{n}{|k_\parallel|\tilde\rho_s}\right)\left(\frac{n^2}{k_\parallel^2\tilde\rho_s^2} - \frac{3}{2} - \frac{k_\perp^2\tilde\rho_s^2}{2}\right)\Bigg]\Bigg\}. \tag{G83i}$$

In this limit, we have utilised the approximation $\zeta_{sn} \approx -n/|k_\parallel|\tilde\rho_s$. Similarly to the Maxwellian case, we can use the Bessel-function-summation identities (G24) and the symmetry properties of the plasma dispersion function with a real argument to show that

$$(\boldsymbol{P}_s^{(0)})_{xx} = 2\mathrm{i}\sqrt{\pi}\,\eta_s \exp\left(-\frac{k_\perp^2\tilde\rho_s^2}{2}\right)\sum_{n=1}^{\infty} \frac{n^2}{k_\perp^2\tilde\rho_s^2}\exp\left(-\frac{n^2}{k_\parallel^2\tilde\rho_s^2}\right)$$

$$\times \left[\left(\frac{n^2}{k_\parallel^2\tilde\rho_s^2} - \frac{3}{2} - \frac{k_\perp^2\tilde\rho_s^2}{2}\right) I_n\left(\frac{k_\perp^2\tilde\rho_s^2}{2}\right) + \frac{k_\perp^2\tilde\rho_s^2}{2} I_n'\left(\frac{k_\perp^2\tilde\rho_s^2}{2}\right)\right]$$

$$= \mathrm{i}\eta_s I\left(k_\parallel\tilde\rho_s, k_\perp\tilde\rho_s\right), \tag{G84a}$$

$$(\boldsymbol{P}_s^{(0)})_{xy} = -\mathrm{i}\eta_s \Bigg\{ \frac{1}{2|k_\parallel|\tilde\rho_s} + \frac{1}{2}\sum_{n=-\infty}^{\infty} n\,\mathrm{Re}\left[Z\left(\frac{n}{|k_\parallel|\tilde\rho_s}\right)\right]\exp\left(-\frac{k_\perp^2\tilde\rho_s^2}{2}\right)$$

$$\times \left\{ \left(\frac{n^2}{k_\parallel^2 \tilde{\rho}_s^2} - \frac{3}{2} - k_\perp^2 \tilde{\rho}_s^2 \right) I_n' \left(\frac{k_\perp^2 \tilde{\rho}_s^2}{2} \right) \right.$$

$$\left. + \left(\frac{1}{2} + k_\perp^2 \tilde{\rho}_s^2 + \frac{2n^2}{k_\perp^2 \tilde{\rho}_s^2} - \frac{n^2}{k_\parallel^2 \tilde{\rho}_s^2} \right) I_n \left(\frac{k_\perp^2 \tilde{\rho}_s^2}{2} \right) \right\}$$

$$= -\mathrm{i}\eta_s J\left(k_\parallel \tilde{\rho}_s, k_\perp \tilde{\rho}_s \right), \tag{G84b}$$

$$(\boldsymbol{P}_s^{(0)})_{xz} = -2\mathrm{i}\sqrt{\pi}\eta_s \exp\left(-\frac{k_\perp^2 \tilde{\rho}_s^2}{2} \right) \sum_{n=1}^{\infty} \frac{n^2}{k_\perp^2 \tilde{\rho}_s^2} \exp\left(-\frac{n^2}{|k_\parallel| k_\perp \tilde{\rho}_s^2} \right)$$

$$\times \left[\left(\frac{n^2}{k_\parallel^2 \tilde{\rho}_s^2} - \frac{3}{2} - \frac{k_\perp^2 \tilde{\rho}_s^2}{2} \right) I_n \left(\frac{k_\perp^2 \tilde{\rho}_s^2}{2} \right) + \frac{k_\perp^2 \tilde{\rho}_s^2}{2} I_n' \left(\frac{k_\perp^2 \tilde{\rho}_s^2}{2} \right) \right]$$

$$= -\frac{\mathrm{i}k_\perp}{|k_\parallel|} \eta_s I\left(k_\parallel \tilde{\rho}_s, k_\perp \tilde{\rho}_s \right), \tag{G84c}$$

$$(\boldsymbol{P}_s^{(0)})_{yy} = \frac{\mathrm{i}\sqrt{\pi}}{2} \eta_s \exp\left(-\frac{k_\perp^2 \tilde{\rho}_s^2}{2} \right) \sum_{n=-\infty}^{\infty} \exp\left(-\frac{n^2}{k_\parallel^2 \tilde{\rho}_s^2} \right)$$

$$\times \left\{ \left(n^2 + \frac{1}{2}k_\perp^2 \tilde{\rho}_s^2 + k_\perp^4 \tilde{\rho}_s^4 - \frac{n^2 k_\perp^2}{k_\parallel^2} \right) I_n' \left(\frac{k_\perp^2 \tilde{\rho}_s^2}{2} \right) \right.$$

$$\left. + \left(\frac{2n^4}{k_\parallel^2 k_\perp^2 \tilde{\rho}_s^4} - \frac{3n^2}{k_\perp^2 \tilde{\rho}_s^2} - 3n^2 + \frac{1}{2}k_\perp^2 \tilde{\rho}_s^2 - k_\perp^4 \tilde{\rho}_s^4 + \frac{n^2 k_\perp^2}{k_\parallel^2} \right) I_n \left(\frac{k_\perp^2 \tilde{\rho}_s^2}{2} \right) \right\}$$

$$= \mathrm{i}\eta_s K\left(k_\parallel \tilde{\rho}_s, k_\perp \tilde{\rho}_s \right), \tag{G84d}$$

$$(\boldsymbol{P}_s^{(0)})_{yz} = -\mathrm{i}\eta_s \left\{ \frac{k_\perp}{2k_\parallel^2 \tilde{\rho}_s} + \frac{1}{2} \sum_{n=-\infty}^{\infty} \frac{nk_\perp}{|k_\parallel|} \operatorname{Re}\left[Z\left(\frac{n}{|k_\parallel| \tilde{\rho}_s} \right) \right] \exp\left(-\frac{k_\perp^2 \tilde{\rho}_s^2}{2} \right) \right.$$

$$\times \left\{ \left(\frac{n^2}{k_\parallel^2 \tilde{\rho}_s^2} - \frac{3}{2} - k_\perp^2 \tilde{\rho}_s^2 \right) I_n' \left(\frac{k_\perp^2 \tilde{\rho}_s^2}{2} \right) \right.$$

$$\left. + \left(\frac{1}{2} + k_\perp^2 \tilde{\rho}_s^2 + \frac{2n^2}{k_\perp^2 \tilde{\rho}_s^2} - \frac{n^2}{k_\parallel^2 \tilde{\rho}_s^2} \right) I_n \left(\frac{k_\perp^2 \tilde{\rho}_s^2}{2} \right) \right\}$$

$$= -\frac{\mathrm{i}k_\perp}{|k_\parallel|} \eta_s J\left(k_\parallel \tilde{\rho}_s, k_\perp \tilde{\rho}_s \right), \tag{G84e}$$

$$(\boldsymbol{P}_s^{(0)})_{zz} = 2\mathrm{i}\sqrt{\pi}\eta_s \exp\left(-\frac{k_\perp^2 \tilde{\rho}_s^2}{2} \right) \sum_{n=1}^{\infty} \frac{n^2}{k_\perp^2 \tilde{\rho}_s^2} \exp\left(-\frac{n^2}{k_\parallel^2 \tilde{\rho}_s^2} \right)$$

$$\times \left[\left(\frac{n^2}{k_\parallel^2 \tilde{\rho}_s^2} - \frac{3}{2} - \frac{k_\perp^2 \tilde{\rho}_s^2}{2} \right) I_n \left(\frac{k_\perp^2 \tilde{\rho}_s^2}{2} \right) + \frac{k_\perp^2 \tilde{\rho}_s^2}{2} I_n' \left(\frac{k_\perp^2 \tilde{\rho}_s^2}{2} \right) \right]$$

$$= \frac{\mathrm{i}k_\perp^2}{k_\parallel^2} \eta_s I\left(k_\parallel \tilde{\rho}_s, k_\perp \tilde{\rho}_s \right), \tag{G84f}$$

where the functions $I(x, y)$, $J(x, y)$ and $K(x, y)$ are defined by

$$
I(x, y) \equiv \frac{2\sqrt{\pi}}{y^2} \exp\left(-\frac{y^2}{2}\right)
$$
$$
\times \sum_{m=1}^{\infty} m^2 \exp\left(-\frac{m^2}{x^2}\right)\left[\frac{y^2}{2}I'_m\left(\frac{y^2}{2}\right) + \left(\frac{m^2}{x^2} - \frac{3+y^2}{2}\right)I_m\left(\frac{y^2}{2}\right)\right], \quad \text{(G85a)}
$$

$$
J(x, y) \equiv \frac{1}{2x} + \frac{1}{2}\exp\left(-\frac{y^2}{2}\right)\sum_{m=-\infty}^{\infty}\left\{m\,\mathrm{Re}\,Z\left(\frac{m}{x}\right)\left[\left(\frac{m^2}{x^2} - \frac{3}{2} - y^2\right)I'_m\left(\frac{y^2}{2}\right)\right.\right.
$$
$$
\left.\left. + \left(\frac{1}{2} + y^2 + \frac{2m^2}{y^2} - \frac{m^2}{x^2}\right)I_m\left(\frac{y^2}{2}\right)\right]\right\}, \quad \text{(G85b)}
$$

$$
K(x, y) \equiv \frac{\sqrt{\pi}}{2}\exp\left(-\frac{y^2}{2}\right)\sum_{m=-\infty}^{\infty}\left\{\exp\left(-\frac{m^2}{x^2}\right)\left[\left(m^2 + \frac{1}{2}y^2 + y^4 - \frac{m^2 y^2}{x^2}\right)I'_m\left(\frac{y^2}{2}\right)\right.\right.
$$
$$
\left.\left. + \left(\frac{2m^4}{x^2 y^2} - \frac{3\,m^2}{y^2} - 3\,m^2 + \frac{1}{2}y^2 - y^4 + \frac{m^2 y^2}{x^2}\right)I_m\left(\frac{y^2}{2}\right)\right]\right\}. \quad \text{(G85c)}
$$

G.3.2. *Asymptotic limits of $\boldsymbol{P}_s^{(0)}$*

In this appendix, we give simplified expressions in the limits of small and large x and y for the special functions $I(x, y)$, $J(x, y)$ and $K(x, y)$ defined by (G85). Physically, this corresponds, via (J2), to considering the dielectric response associated with $\boldsymbol{P}_s^{(0)}$ for modes with parallel and perpendicular wavenumbers that are very small or very large with respect to the inverse Larmor radius of species s.

Proceeding systematically through various limits, we have the following results:

(i) $x \sim 1, y \ll 1$

$$
I(x, y) = \frac{\sqrt{\pi}}{2}\left(\frac{1}{x^2} - \frac{1}{2}\right)\exp\left(-\frac{1}{x^2}\right)\left[1 + O(y^2)\right], \quad \text{(G86a)}
$$

$$
J(x, y) = \left[\left(\frac{1}{4} - \frac{1}{2x^2}\right)\mathrm{Re}\,Z\left(\frac{1}{x}\right) + \frac{1}{2x}\right]\left[1 + O(y^2)\right], \quad \text{(G86b)}
$$

$$
K(x, y) = \frac{\sqrt{\pi}}{2}\left(\frac{1}{x^2} - \frac{1}{2}\right)\exp\left(-\frac{1}{x^2}\right)\left[1 + O(y^2)\right]. \quad \text{(G86c)}
$$

(ii) $x, y \gg 1$

$$
I(x, y) = -\frac{\sqrt{\pi}x^3}{4\left(x^2 + y^2\right)^{3/2}}\left[1 + O\left(\frac{1}{x^2 + y^2}\right)\right], \quad \text{(G87a)}
$$

$$
J(x, y) = -\frac{x^3}{\left(x^2 + y^2\right)^2}\left[1 + O\left(\frac{1}{x^2 + y^2}\right)\right], \quad \text{(G87b)}
$$

$$
K(x, y) = -\frac{\sqrt{\pi}x}{4\left(x^2 + y^2\right)^{1/2}}\left[1 + O\left(\frac{1}{x^2 + y^2}\right)\right]. \quad \text{(G87c)}
$$

(iii) $x \ll 1, y \sim 1$

$$I(x, y) = \frac{2\sqrt{\pi}}{x^2 y^2} \exp\left(-\frac{y^2}{2} - \frac{1}{x^2}\right) I_1\left(\frac{y^2}{2}\right) [1 + O(x^2)], \tag{G88a}$$

$$J(x, y) = -\frac{x}{2} \exp\left(-\frac{y^2}{2}\right)$$
$$\times \left[y^2 \left(I_0\left(\frac{y^2}{2}\right) - I_1\left(\frac{y^2}{2}\right)\right) - I_1\left(\frac{y^2}{2}\right)\right] [1 + O(x^2)], \tag{G88b}$$

$$K(x, y) = \frac{\sqrt{\pi}}{2} \exp\left(-\frac{y^2}{2}\right) \left[\left(\frac{1}{2}y^2 - y^4\right) I_0\left(\frac{y^2}{2}\right)\right.$$
$$\left. + \left(\frac{1}{2}y^2 + y^4\right) I_1\left(\frac{y^2}{2}\right)\right] [1 + O(x^2)]. \tag{G88c}$$

(iv) $x, y \ll 1$

$$I(x, y) = \frac{\sqrt{\pi}}{2x^2} \exp\left(-\frac{1}{x^2}\right) \left[1 + O\left(\exp\left(-\frac{3}{x^2}\right), y^2\right)\right], \tag{G89a}$$

$$J(x, y) = -x \left(\frac{3}{8}y^2 - \frac{1}{4}x^2\right) [1 + O(x^4, x^2 y^2, y^4)], \tag{G89b}$$

$$K(x, y) = \frac{\sqrt{\pi}}{4} y^2 [1 + O(x^2, y^2)]. \tag{G89c}$$

G.4. *The CE shear terms*

For a CE shear term of the form

$$\tilde{f}_s(\tilde{v}_{s\parallel}, \tilde{v}_{s\perp}) = -\epsilon_s \left(\tilde{v}_{s\parallel}^2 - \frac{\tilde{v}_{s\perp}^2}{2}\right) \exp\left(-\tilde{v}_s^2\right), \tag{G90}$$

we have

$$\Lambda_s(\tilde{v}_{s\parallel}, \tilde{v}_{s\perp}) = -3\epsilon_s \tilde{v}_{s\parallel} \tilde{v}_{s\perp} \exp\left(-\tilde{v}_s^2\right), \tag{G91a}$$

$$\Xi_s(\tilde{v}_{s\parallel}, \tilde{v}_{s\perp}) = -\frac{3\epsilon_s}{\tilde{\omega}_{s\parallel}} \tilde{v}_{s\parallel} \tilde{v}_{s\perp} \exp\left(-\tilde{v}_s^2\right) + O(\epsilon_s). \tag{G91b}$$

This gives

$$(\boldsymbol{P}_s)_{xx} = \frac{6}{\sqrt{\pi}} \epsilon_s \sum_{n=-\infty}^{\infty} \left[\frac{n^2}{k_\perp^2 \tilde{\rho}_s^2} \int_{C_L} \frac{\tilde{v}_{s\parallel} \exp\left(-\tilde{v}_{s\parallel}^2\right) \mathrm{d}\tilde{v}_{s\parallel}}{\tilde{v}_{s\parallel} - \zeta_{sn}} \right.$$
$$\left. \times \int_0^\infty \mathrm{d}\tilde{v}_{s\perp} \, \tilde{v}_{s\perp} J_n(k_\perp \tilde{\rho}_s \tilde{v}_{s\perp})^2 \exp\left(-\tilde{v}_{s\perp}^2\right)\right], \tag{G92a}$$

$$(\boldsymbol{P}_s)_{xy} = \frac{6\mathrm{i}}{\sqrt{\pi}}\epsilon_s \sum_{n=-\infty}^{\infty} \left[\frac{n}{k_\perp \tilde{\rho}_s} \int_{C_L} \frac{\tilde{v}_{s\parallel} \exp\left(-\tilde{v}_{s\parallel}^2\right) \mathrm{d}\tilde{v}_{s\parallel}}{\tilde{v}_{s\parallel} - \zeta_{sn}} \right.$$
$$\left. \times \int_0^\infty \mathrm{d}\tilde{v}_{s\perp}\, \tilde{v}_{s\perp}^2 J_n(k_\perp \tilde{\rho}_s \tilde{v}_{s\perp}) J_n'(k_\perp \tilde{\rho}_s \tilde{v}_{s\perp}) \exp\left(-\tilde{v}_{s\perp}^2\right) \right], \tag{G92b}$$

$$(\boldsymbol{P}_s)_{xz} = \frac{6}{\sqrt{\pi}}\epsilon_s \sum_{n=-\infty}^{\infty} \left[\frac{n}{k_\perp \tilde{\rho}_s} \int_{C_L} \frac{\tilde{v}_{s\parallel}^2 \exp\left(-\tilde{v}_{s\parallel}^2\right) \mathrm{d}\tilde{v}_{s\parallel}}{\tilde{v}_{s\parallel} - \zeta_{sn}} \right. \tag{G92c}$$
$$\left. \times \int_0^\infty \mathrm{d}\tilde{v}_{s\perp}\, \tilde{v}_{s\perp} J_n(k_\perp \tilde{\rho}_s \tilde{v}_{s\perp})^2 \exp\left(-\tilde{v}_{s\perp}^2\right) \right], \tag{G92d}$$

$$(\boldsymbol{P}_s)_{yx} = (\boldsymbol{P}_s)_{xy} \tag{G92e}$$

$$(\boldsymbol{P}_s)_{yy} = \frac{6}{\sqrt{\pi}}\epsilon_s \sum_{n=-\infty}^{\infty} \left[\int_{C_L} \frac{\tilde{v}_{s\parallel} \exp\left(-\tilde{v}_{s\parallel}^2\right) \mathrm{d}\tilde{v}_{s\parallel}}{\tilde{v}_{s\parallel} - \zeta_{sn}} \right.$$
$$\left. \times \int_0^\infty \mathrm{d}\tilde{v}_{s\perp}\, \tilde{v}_{s\perp}^3 J_n'(k_\perp \tilde{\rho}_s \tilde{v}_{s\perp})^2 \exp\left(-\tilde{v}_{s\perp}^2\right) \right], \tag{G92f}$$

$$(\boldsymbol{P}_s)_{yz} = -\frac{6\mathrm{i}}{\sqrt{\pi}}\epsilon_s \sum_{n=-\infty}^{\infty} \left[\int_{C_L} \frac{\tilde{v}_{s\parallel}^2 \exp\left(-\tilde{v}_{s\parallel}^2\right) \mathrm{d}\tilde{v}_{s\parallel}}{\tilde{v}_{s\parallel} - \zeta_{sn}} \right.$$
$$\left. \times \int_0^\infty \mathrm{d}\tilde{v}_{s\perp}\, \tilde{v}_{s\perp}^2 J_n(k_\perp \tilde{\rho}_s \tilde{v}_{s\perp}) J_n'(k_\perp \tilde{\rho}_s \tilde{v}_{s\perp}) \exp\left(-\tilde{v}_{s\perp}^2\right) \right], \tag{G92g}$$

$$(\boldsymbol{P}_s)_{zx} = (\boldsymbol{P}_s)_{xz}, \tag{G92h}$$

$$(\boldsymbol{P}_s)_{zy} = -(\boldsymbol{P}_s)_{yz}, \tag{G92i}$$

$$(\boldsymbol{P}_s)_{zz} = \frac{6}{\sqrt{\pi}}\epsilon_s \left\{ \sum_{n=-\infty}^{\infty} \left[\int_{C_L} \frac{\tilde{v}_{s\parallel}^3 \exp\left(-\tilde{v}_{s\parallel}^2\right) \mathrm{d}\tilde{v}_{s\parallel}}{\tilde{v}_{s\parallel} - \zeta_{sn}} \right.\right.$$
$$\left. \times \int_0^\infty \mathrm{d}\tilde{v}_{s\perp}\, \tilde{v}_{s\perp} J_n(k_\perp \tilde{\rho}_s \tilde{v}_{s\perp})^2 \exp\left(-\tilde{v}_{s\perp}^2\right) \right]$$
$$\left. - \int_{-\infty}^\infty \mathrm{d}\tilde{v}_{s\parallel}\, \tilde{v}_{s\parallel}^2 \int_0^\infty \mathrm{d}\tilde{v}_{s\perp}\, \tilde{v}_{s\perp} \exp\left(-\tilde{v}_s^2\right) \right\}. \tag{G92j}$$

Again using the Bessel-function identities (G16), and the identities (G15) and (G79a) applicable to the plasma dispersion function, the dielectric tensor's elements become

$$(\boldsymbol{P}_s)_{xx} = 3\epsilon_s \sum_{n=-\infty}^{\infty} \frac{n^2}{k_\perp^2 \tilde{\rho}_s^2} \left[1 + \zeta_{sn} Z(\zeta_{sn})\right] \exp\left(-\frac{k_\perp^2 \tilde{\rho}_s^2}{2}\right) I_n\left(\frac{k_\perp^2 \tilde{\rho}_s^2}{2}\right), \tag{G93a}$$

$$(\boldsymbol{P}_s)_{xy} = \frac{3\mathrm{i}\epsilon_s}{2} \sum_{n=-\infty}^{\infty} n\left[1 + \zeta_{sn} Z(\zeta_{sn})\right]$$
$$\times \exp\left(-\frac{k_\perp^2 \tilde{\rho}_s^2}{2}\right) \left[I_n'\left(\frac{k_\perp^2 \tilde{\rho}_s^2}{2}\right) - I_n\left(\frac{k_\perp^2 \tilde{\rho}_s^2}{2}\right)\right], \tag{G93b}$$

$$(\boldsymbol{P}_s)_{xz} = 3\epsilon_s \sum_{n=-\infty}^{\infty} \frac{n}{k_\perp \tilde{\rho}_s} \zeta_{sn} \left[1 + \zeta_{sn} Z(\zeta_{sn})\right] \exp\left(-\frac{k_\perp^2 \tilde{\rho}_s^2}{2}\right) I_n\left(\frac{k_\perp^2 \tilde{\rho}_s^2}{2}\right), \tag{G93c}$$

$$(\boldsymbol{P}_s)_{yx} = (\boldsymbol{P}_s)_{xy}, \tag{G93d}$$

$$(\boldsymbol{P}_s)_{yy} = \frac{3}{2}\epsilon_s \sum_{n=-\infty}^{\infty} \left[1 + \zeta_{sn} Z(\zeta_{sn})\right]$$
$$\times \exp\left(-\frac{k_\perp^2 \tilde{\rho}_s^2}{2}\right) \left[\left(\frac{2n^2}{k_\perp^2 \tilde{\rho}_s^2} + k_\perp^2 \tilde{\rho}_s^2\right) I_n\left(\frac{k_\perp^2 \tilde{\rho}_s^2}{2}\right) - k_\perp^2 \tilde{\rho}_s^2 I_n'\left(\frac{k_\perp^2 \tilde{\rho}_s^2}{2}\right)\right], \tag{G93e}$$

$$(\boldsymbol{P}_s)_{yz} = -\frac{3\mathrm{i}\epsilon_s}{2} \sum_{n=-\infty}^{\infty} k_\perp \tilde{\rho}_s \zeta_{sn} \left[1 + \zeta_{sn} Z(\zeta_{sn})\right]$$
$$\times \exp\left(-\frac{k_\perp^2 \tilde{\rho}_s^2}{2}\right) \left[I_n'\left(\frac{k_\perp^2 \tilde{\rho}_s^2}{2}\right) - I_n\left(\frac{k_\perp^2 \tilde{\rho}_s^2}{2}\right)\right], \tag{G93f}$$

$$(\boldsymbol{P}_s)_{zx} = (\boldsymbol{P}_s)_{xz}, \tag{G93g}$$

$$(\boldsymbol{P}_s)_{zy} = -(\boldsymbol{P}_s)_{yz}, \tag{G93h}$$

$$(\boldsymbol{P}_s)_{zz} = 3\epsilon_s \sum_{n=-\infty}^{\infty} \zeta_{sn}^2 \left[1 + \zeta_{sn} Z(\zeta_{sn})\right] \exp\left(-\frac{k_\perp^2 \tilde{\rho}_s^2}{2}\right) I_n\left(\frac{k_\perp^2 \tilde{\rho}_s^2}{2}\right). \tag{G93i}$$

G.4.1. *Dielectric tensor in low-frequency limit*

As with the CE temperature-gradient term, under the ordering $k_\parallel \rho_s \sim k_\perp \rho_s \sim 1$, the expressions (G81) can be approximated by the leading-order term of the expansion of $\boldsymbol{P}_s$ in the low-frequency limit $\tilde{\omega}_{s\parallel} \ll 1$. Namely, we have

$$\boldsymbol{P}_s \approx \boldsymbol{P}_s^{(0)} + O(\tilde{\omega}_{s\parallel}^2), \tag{G94}$$

where

$$(\boldsymbol{P}_s^{(0)})_{xx} = 3\epsilon_s \sum_{n=-\infty}^{\infty} \frac{n^2}{k_\perp^2 \tilde{\rho}_s^2} \left[1 - \frac{n}{|k_\parallel|\tilde{\rho}_s} Z\left(-\frac{n}{|k_\parallel|\tilde{\rho}_s}\right)\right]$$
$$\times \exp\left(-\frac{k_\perp^2 \tilde{\rho}_s^2}{2}\right) I_n\left(\frac{k_\perp^2 \tilde{\rho}_s^2}{2}\right), \tag{G95a}$$

$$(\boldsymbol{P}_s^{(0)})_{xy} = \frac{3\mathrm{i}\epsilon_s}{2} \sum_{n=-\infty}^{\infty} n \left[1 - \frac{n}{|k_\parallel|\tilde{\rho}_s} Z\left(-\frac{n}{|k_\parallel|\tilde{\rho}_s}\right)\right]$$
$$\times \exp\left(-\frac{k_\perp^2 \tilde{\rho}_s^2}{2}\right) \left[I_n'\left(\frac{k_\perp^2 \tilde{\rho}_s^2}{2}\right) - I_n\left(\frac{k_\perp^2 \tilde{\rho}_s^2}{2}\right)\right], \tag{G95b}$$

$$(\boldsymbol{P}_s^{(0)})_{xz} = -3\epsilon_s \sum_{n=-\infty}^{\infty} \frac{n^2}{k_\perp |k_\parallel|\tilde{\rho}_s^2} \left[1 - \frac{n}{|k_\parallel|\tilde{\rho}_s} Z\left(-\frac{n}{|k_\parallel|\tilde{\rho}_s}\right)\right]$$
$$\times \exp\left(-\frac{k_\perp^2 \tilde{\rho}_s^2}{2}\right) I_n\left(\frac{k_\perp^2 \tilde{\rho}_s^2}{2}\right), \tag{G95c}$$

$$(\boldsymbol{P}_s^{(0)})_{yx} = (\boldsymbol{P}_s^{(0)})_{xy}, \tag{G95d}$$

$$(\boldsymbol{P}_s^{(0)})_{yy} = \frac{3}{2}\epsilon_s \sum_{n=-\infty}^{\infty} \left[1 - \frac{n}{|k_\parallel|\tilde{\rho}_s} Z\left(-\frac{n}{|k_\parallel|\tilde{\rho}_s}\right) \right]$$

$$\times \exp\left(-\frac{k_\perp^2\tilde{\rho}_s^2}{2}\right) \left[\left(\frac{2n^2}{k_\perp^2\tilde{\rho}_s^2} + k_\perp^2\tilde{\rho}_s^2\right) I_n\left(\frac{k_\perp^2\tilde{\rho}_s^2}{2}\right) - k_\perp^2\tilde{\rho}_s^2 I_n'\left(\frac{k_\perp^2\tilde{\rho}_s^2}{2}\right) \right], \tag{G95e}$$

$$(\boldsymbol{P}_s^{(0)})_{yz} = \frac{3i\epsilon_s}{2} \sum_{n=-\infty}^{\infty} \frac{nk_\perp}{|k_\parallel|} \left[1 - \frac{n}{|k_\parallel|\tilde{\rho}_s} Z\left(-\frac{n}{|k_\parallel|\tilde{\rho}_s}\right) \right]$$

$$\times \exp\left(-\frac{k_\perp^2\tilde{\rho}_s^2}{2}\right) \left[I_n'\left(\frac{k_\perp^2\tilde{\rho}_s^2}{2}\right) - I_n\left(\frac{k_\perp^2\tilde{\rho}_s^2}{2}\right) \right], \tag{G95f}$$

$$(\boldsymbol{P}_s^{(0)})_{zx} = (\boldsymbol{P}_s^{(0)})_{xz}, \tag{G95g}$$

$$(\boldsymbol{P}_s^{(0)})_{zy} = -(\boldsymbol{P}_s^{(0)})_{yz}, \tag{G95h}$$

$$(\boldsymbol{P}_s^{(0)})_{zz} = 3 \sum_{n=-\infty}^{\infty} \frac{n^2}{k_\parallel^2\tilde{\rho}_s^2} \left[1 - \frac{n}{|k_\parallel|\tilde{\rho}_s} Z\left(-\frac{n}{|k_\parallel|\tilde{\rho}_s}\right) \right] \exp\left(-\frac{k_\perp^2\tilde{\rho}_s^2}{2}\right) I_n\left(\frac{k_\perp^2\tilde{\rho}_s^2}{2}\right). \tag{G95i}$$

In this calculation, we have utilised the approximation $\zeta_{sn} \approx -n/|k_\parallel|\tilde{\rho}_s$. Similarly to the Maxwellian case, we can use the Bessel-function-summation identities (G24) and the symmetry properties of the plasma dispersion function with a real argument to show that

$$(\boldsymbol{P}_s^{(0)})_{xx} = 3\epsilon_s \left\{ \frac{1}{2} + \exp\left(-\frac{k_\perp^2\tilde{\rho}_s^2}{2}\right) \sum_{n=-\infty}^{\infty} \frac{n^3}{|k_\parallel|k_\perp^2\tilde{\rho}_s^3} \mathrm{Re}\left[Z\left(\frac{n}{|k_\parallel|\tilde{\rho}_s}\right) \right] I_n\left(\frac{k_\perp^2\tilde{\rho}_s^2}{2}\right) \right\}$$

$$= \epsilon_s W(|k_\parallel|\tilde{\rho}_s, k_\perp\tilde{\rho}_s), \tag{G96a}$$

$$(\boldsymbol{P}_s^{(0)})_{xy} = 3\sqrt{\pi}\epsilon_s \exp\left(-\frac{k_\perp^2\tilde{\rho}_s^2}{2}\right)$$

$$\times \sum_{n=1}^{\infty} \frac{n^2}{|k_\parallel|\tilde{\rho}_s} \exp\left(-\frac{n^2}{k_\parallel^2\tilde{\rho}_s^2}\right) \left[I_n'\left(\frac{k_\perp^2\tilde{\rho}_s^2}{2}\right) - I_n\left(\frac{k_\perp^2\tilde{\rho}_s^2}{2}\right) \right]$$

$$= -\epsilon_s X(|k_\parallel|\tilde{\rho}_s, k_\perp\tilde{\rho}_s), \tag{G96b}$$

$$(\boldsymbol{P}_s^{(0)})_{xz} = -3\epsilon_s \left\{ \frac{k_\perp}{2|k_\parallel|} + \exp\left(-\frac{k_\perp^2\tilde{\rho}_s^2}{2}\right) \right.$$

$$\left. \times \sum_{n=-\infty}^{\infty} \frac{n^3}{k_\perp k_\parallel^2\tilde{\rho}_s^3} \mathrm{Re}\left[Z\left(\frac{n}{|k_\parallel|\tilde{\rho}_s}\right) \right] I_n\left(\frac{k_\perp^2\tilde{\rho}_s^2}{2}\right) \right\}$$

$$= -\frac{k_\perp}{|k_\parallel|}\epsilon_s W(|k_\parallel|\tilde{\rho}_s, k_\perp\tilde{\rho}_s), \tag{G96c}$$

$$(\boldsymbol{P}_s^{(0)})_{yx} = (\boldsymbol{P}_s^{(0)})_{xy}, \tag{G96d}$$

$$(\boldsymbol{P}_s^{(0)})_{yy} = \frac{3}{2}\epsilon_s \left\{ 1 + \exp\left(-\frac{k_\perp^2 \tilde{\rho}_s^2}{2}\right) \sum_{n=-\infty}^{\infty} \frac{2n^3}{|k_\parallel| k_\perp^2 \tilde{\rho}_s^3} \text{Re}\left[Z\left(\frac{n}{|k_\parallel| \tilde{\rho}_s}\right)\right] I_n\left(\frac{k_\perp^2 \tilde{\rho}_s^2}{2}\right) \right.$$

$$+ k_\perp^2 \tilde{\rho}_s^2 \exp\left(-\frac{k_\perp^2 \tilde{\rho}_s^2}{2}\right) \sum_{n=-\infty}^{\infty} \frac{n}{|k_\parallel| \tilde{\rho}_s}$$

$$\left. \times \text{Re}\left[Z\left(\frac{n}{|k_\parallel| \tilde{\rho}_s}\right)\right] \left[I_n\left(\frac{k_\perp^2 \tilde{\rho}_s^2}{2}\right) - I_n'\left(\frac{k_\perp^2 \tilde{\rho}_s^2}{2}\right)\right] \right\},$$

$$= \epsilon_s Y(|k_\parallel| \tilde{\rho}_s, k_\perp \tilde{\rho}_s), \tag{G96e}$$

$$(\boldsymbol{P}_s^{(0)})_{yz} = 3\sqrt{\pi}\epsilon_s \exp\left(-\frac{k_\perp^2 \tilde{\rho}_s^2}{2}\right)$$

$$\times \sum_{n=1}^{\infty} \frac{k_\perp n^2}{k_\parallel^2 \tilde{\rho}_s} \exp\left(-\frac{n^2}{k_\parallel^2 \tilde{\rho}_s^2}\right) \left[I_n'\left(\frac{k_\perp^2 \tilde{\rho}_s^2}{2}\right) - I_n\left(\frac{k_\perp^2 \tilde{\rho}_s^2}{2}\right)\right]$$

$$= -\frac{k_\perp}{|k_\parallel|}\epsilon_s X(|k_\parallel| \tilde{\rho}_s, k_\perp \tilde{\rho}_s), \tag{G96f}$$

$$(\boldsymbol{P}_s^{(0)})_{zx} = (\boldsymbol{P}_s^{(0)})_{xz}, \tag{G96g}$$

$$(\boldsymbol{P}_s^{(0)})_{zy} = -(\boldsymbol{P}_s^{(0)})_{yz}, \tag{G96h}$$

$$(\boldsymbol{P}_s^{(0)})_{zz} = 3\epsilon_s \left\{ \frac{k_\perp^2}{2k_\parallel^2} + \exp\left(-\frac{k_\perp^2 \tilde{\rho}_s^2}{2}\right) \sum_{n=-\infty}^{\infty} \frac{n^3}{|k_\parallel|^3 \tilde{\rho}_s^3} \text{Re}\left[Z\left(\frac{n}{|k_\parallel| \tilde{\rho}_s}\right)\right] I_n\left(\frac{k_\perp^2 \tilde{\rho}_s^2}{2}\right) \right\}$$

$$= \frac{k_\perp^2}{k_\parallel^2}\epsilon_s W(|k_\parallel| \tilde{\rho}_s, k_\perp \tilde{\rho}_s), \tag{G96i}$$

where the functions $W(x, y)$, $Y(x, y)$ and $X(x, y)$ are defined by

$$W(x, y) \equiv \frac{3}{2} + \frac{3}{xy^2} \exp\left(-\frac{y^2}{2}\right) \sum_{m=-\infty}^{\infty} m^3 \text{Re} Z\left(\frac{m}{x}\right) I_m\left(\frac{y^2}{2}\right), \tag{G97a}$$

$$X(x, y) \equiv \frac{3\sqrt{\pi}}{x} \exp\left(-\frac{y^2}{2}\right) \sum_{m=1}^{\infty} m^2 \left[I_m\left(\frac{y^2}{2}\right) - I_m'\left(\frac{y^2}{2}\right)\right] \exp\left(-\frac{m^2}{x^2}\right), \tag{G97b}$$

$$Y(x, y) \equiv W(x, y) - \frac{3}{2}\frac{y^2 G(x, y)}{x}. \tag{G97c}$$

G.4.2. *Asymptotic limits of $\boldsymbol{P}_s^{(0)}$*

As we have done for the other special functions defined in this paper, in this appendix we provide asymptotic expressions in the limits where x and y are very small or large for the special functions $W(x, y)$, $X(x, y)$ and $Y(x, y)$ defined in (G97). These limits again correspond to parallel and perpendicular wavenumbers that are very small or very large with respect to the inverse Larmor radius of species s.

Considering various asymptotic limits in a systematic fashion, we find

(i) $x \sim 1, y \ll 1$

$$W(x, y) = \left[\frac{3}{2} + \frac{3}{2x} \operatorname{Re} Z \left(\frac{1}{x} \right) \right] \left[1 + O(y^2) \right], \tag{G98a}$$

$$X(x, y) = -\frac{3\sqrt{\pi}}{2x} \exp \left(-\frac{1}{x^2} \right) \left[1 + O(y^2) \right], \tag{G98b}$$

$$Y(x, y) = \left[\frac{3}{2} + \frac{3}{2x} \operatorname{Re} Z \left(\frac{1}{x} \right) \right] \left[1 + O(y^2) \right]. \tag{G98c}$$

(ii) $x, y \gg 1$

$$W(x, y) = \frac{3x^2 \left(x^2 - y^2 \right)}{2 \left(x^2 + y^2 \right)^2} \left[1 + O \left(\frac{1}{x^2 + y^2} \right) \right], \tag{G99a}$$

$$X(x, y) = \frac{3\sqrt{\pi} x^2 \left(y^2 - 2x^2 \right)}{4 \left(x^2 + y^2 \right)^{5/2}} \left[1 + O \left(\frac{1}{x^2 + y^2} \right) \right], \tag{G99b}$$

$$Y(x, y) = \frac{3x^2}{2 \left(x^2 + y^2 \right)} \left[1 + O \left(\frac{1}{x^2 + y^2} \right) \right]. \tag{G99c}$$

(iii) $x \ll 1, y \sim 1$

$$W(x, y) = -\frac{3x^2}{2y^2} \left[1 - \exp \left(-\frac{y^2}{2} \right) I_0 \left(\frac{y^2}{2} \right) \right] \left[1 + O(x^2) \right], \tag{G100a}$$

$$X(x, y) = \frac{3\sqrt{\pi}}{x} \exp \left(-\frac{y^2}{2} \right) \left[I_0 \left(\frac{y^2}{2} \right) - I_1 \left(\frac{y^2}{2} \right) \right]$$
$$\times \exp \left(-\frac{1}{x^2} \right) \left\{ 1 + O \left[\exp \left(-\frac{3}{x^2} \right) \right] \right\}, \tag{G100b}$$

$$Y(x, y) = \frac{3}{2} y^2 \exp \left(-\frac{y^2}{2} \right) \left[I_0 \left(\frac{y^2}{2} \right) - I_1 \left(\frac{y^2}{2} \right) \right] \left[1 + O(x^2) \right]. \tag{G100c}$$

(iv) $x, y \ll 1$

$$W(x, y) = -\frac{3}{4} x^2 \left[1 + O(x^2, y^2) \right], \tag{G101a}$$

$$X(x, y) = \frac{3\sqrt{\pi}}{x} \exp \left(-\frac{1}{x^2} \right) \left\{ 1 + O \left[\exp \left(-\frac{3}{x^2} \right), y^2 \right] \right\}, \tag{G101b}$$

$$Y(x, y) = \left[\frac{3}{2} y^2 - \frac{3}{4} x^2 - \frac{9}{8} \left(x^4 - \frac{2}{3} x^2 y^2 + y^4 \right) \right]$$
$$\times \left[1 + O(x^6, x^4 y^2, x^2 y^4, y^6) \right]. \tag{G101c}$$

(v) $x \ll 1, y \gg 1$

$$W(x, y) = -\frac{3x^2}{2y^2}\left[1 + O\left(x^2, \frac{1}{y^2}\right)\right], \tag{G102a}$$

$$X(x, y) = \frac{3}{xy^3}\exp\left(-\frac{1}{x^2}\right)\left\{1 + O\left[\exp\left(-\frac{3}{x^2}\right), \frac{1}{y^2}\right]\right\}, \tag{G102b}$$

$$Y(x, y) = \frac{3}{2\sqrt{\pi}y}\left[1 + O\left(x^2, \frac{1}{y^2}\right)\right]. \tag{G102c}$$

Appendix H. Density perturbations for low-frequency modes

In this appendix, we derive an expression for the (Fourier-transformed) perturbation of number density $\hat{\delta n}_s$ of species s associated with a low-frequency mode, in terms of the expanded terms of the dielectric tensor $\mathfrak{E}_s = \tilde{\omega}_{s\parallel}\mathfrak{E}_s^{(0)} + \tilde{\omega}_{s\parallel}^2\mathfrak{E}_s^{(1)} + \ldots$ of species s and the perturbed electric field, $\widehat{\delta E}$; we will show that $\hat{\delta n}_s$ is, in fact, independent of $\mathfrak{E}_s^{(0)}$. We then derive an expression for the perturbed density of all sub-ion-Larmor scale ($k\rho_i \gg 1$), low-frequency modes.

H.1. *Derivation of general expressions*

We begin with the continuity equation (2.4a), which describes the time evolution of the density of species s in terms of itself and the bulk velocity of the same species. For any small-scale, small-amplitude perturbed density δn_s and bulk velocity δV_s of some (much more slowly evolving, much larger-scale) quasi-equilibrium state with mean density $n_{s0} \gg \delta n_s$ and bulk velocity $V_{s0} \gg \delta V_s$, *viz.*

$$n_s = n_{s0} + \delta n_s, \quad V_s = V_{s0} + \delta V_s, \tag{H1a,b}$$

the continuity equation governing that perturbation is

$$\frac{\partial \delta n_s}{\partial t} + n_{s0}\nabla \cdot \delta V_s + V_{s0} \cdot \nabla \delta n_s = 0. \tag{H2}$$

where we have neglected all terms that are quadratic in the perturbation amplitude, and also the terms that are proportional to gradients of the equilibrium state, which by assumption are much smaller than the remaining terms. Assuming the perturbation has the form

$$\delta n_s = \widehat{\delta n}_s \exp\left\{\mathrm{i}\left(k \cdot r - \omega t\right)\right\}, \tag{H3a}$$

$$\delta V_s = \widehat{\delta V}_s \exp\left\{\mathrm{i}\left(k \cdot r - \omega t\right)\right\}, \tag{H3b}$$

we deduce from (H2) that

$$\widehat{\delta n}_s = \frac{1}{\omega}\left(n_{s0}k \cdot \widehat{\delta V}_s + \widehat{\delta n}_s k \cdot V_{s0}\right). \tag{H4}$$

The perturbed velocity $\widehat{\delta V}_s$ can be written in terms of the dielectric tensor of species s using Ohm's law (C13) and (2.96):

$$\widehat{\delta V}_s = -\frac{\mathrm{i}\omega}{4\pi Z_s e n_{s0}}\mathfrak{E}_s \cdot \widehat{\delta E} - \frac{\widehat{\delta n}_s}{n_{s0}}V_{s0}, \tag{H5}$$

whence, by way of (H4),

$$\widehat{\delta n}_s = -\frac{\mathrm{i}}{4\pi Z_s e}\boldsymbol{k}\cdot\boldsymbol{\mathfrak{E}}_s\cdot\widehat{\delta E}. \tag{H6}$$

Finally, we note that the symmetries (2.102) of $\boldsymbol{\mathfrak{E}}_s^{(0)}$ imply that it does not contribute to the right-hand side of (H6), which implies in turn that

$$\widehat{\delta n}_s \approx -\frac{\mathrm{i}\tilde{\omega}_{s\parallel}^2}{4\pi Z_s e}\boldsymbol{k}\cdot\boldsymbol{\mathfrak{E}}_s^{(1)}\cdot\widehat{\delta E}. \tag{H7}$$

Thus, for low-frequency modes, $\widehat{\delta n}_s$ is a function of the electric field and $\boldsymbol{\mathfrak{E}}_s^{(1)}$, but not of $\boldsymbol{\mathfrak{E}}_s^{(0)}$.

We note that the condition (2.109) implies that, for low-frequency modes, quasi-neutrality is maintained:

$$\sum_s Z_s\widehat{\delta n}_s \approx -\frac{\mathrm{i}}{4\pi e}\sum_s \tilde{\omega}_{s\parallel}^2\boldsymbol{k}\cdot\boldsymbol{\mathfrak{E}}_s^{(1)}\cdot\widehat{\delta E} = 0. \tag{H8}$$

Thus, in a two-species plasma, the ion number density associated with a perturbation can be calculated if the electron number density is known, and *vice versa*.

H.2. *Special case: sub-ion-Larmor-scale modes in a two-species plasma*

In the special case of a two-species plasma whose characteristic parallel wavenumber satisfies $k_\parallel \rho_i \gg 1$, a particularly simple expression for the perturbed number densities of ions (and electrons) can be derived: the Boltzmann response. This arises because the ion dielectric tensor $\boldsymbol{\mathfrak{E}}_i$ is unmagnetised, and so takes the simple form (valid for arbitrary $\tilde{\omega}_i = \omega/k v_{\mathrm{th}i}$) that was derived in Appendix G.1.5:

$$\boldsymbol{\mathfrak{E}}_i \approx \boldsymbol{\mathfrak{E}}_i^{(\mathrm{UM})} = \frac{\omega_{pi}^2}{\omega^2}\tilde{\omega}_i\left\{\left(\boldsymbol{I}-\hat{\boldsymbol{k}}\hat{\boldsymbol{k}}\right)Z(\tilde{\omega}_i) + 2\left[\tilde{\omega}_i + \tilde{\omega}_i^2 Z(\tilde{\omega}_i)\right]\hat{\boldsymbol{k}}\hat{\boldsymbol{k}}\right\}. \tag{H9}$$

It follows that

$$\boldsymbol{k}\cdot\boldsymbol{\mathfrak{E}}_i\cdot\widehat{\delta E} \approx \frac{\omega_{pi}^2}{\omega^2}2\tilde{\omega}_i^2\left[1+\tilde{\omega}_i Z(\tilde{\omega}_i)\right]\boldsymbol{k}\cdot\widehat{\delta E}. \tag{H10}$$

Now assuming that $\tilde{\omega}_i \ll 1$, it follows that

$$\boldsymbol{k}\cdot\boldsymbol{\mathfrak{E}}_i^{(1)}\cdot\widehat{\delta E} \approx \frac{2\omega_{pi}^2}{\omega^2}\frac{k_\parallel^2}{k^2}\boldsymbol{k}\cdot\widehat{\delta E}. \tag{H11}$$

Expression (H7) with $s = i$ then gives

$$\hat{\delta n}_i \approx -\frac{Z e \mathrm{i} n_{i0}}{T_i}\frac{\hat{\boldsymbol{k}}\cdot\widehat{\delta E}}{k}. \tag{H12}$$

Finally, introducing the electrostatic potential φ, whose Fourier transform is related to the electrostatic component of the electric field via

$$\hat{\varphi} = \frac{\mathrm{i}\hat{\boldsymbol{k}}\cdot\widehat{\delta E}}{k}, \tag{H13}$$

we deduce that

$$\widehat{\delta n_i} \approx -\frac{Z_i e i n_{i0}}{T_i} \hat{\varphi}, \tag{H14}$$

and

$$\widehat{\delta n_e} \approx -\frac{Z_i e i n_{e0}}{T_i} \hat{\varphi}, \tag{H15}$$

where we have used the quasi-neutrality relation $n_{e0} = Z_i n_{i0}$ for the equilibrium state.

Appendix I. Calculating the electrostatic field from the transverse electric field

In Appendix G.1.3, it was shown that, for any distribution function with a small anisotropy,

$$\mathfrak{E}_s^{(0)} \cdot \hat{k} = 0, \tag{I1}$$

which implies that the leading-order terms (in $\tilde{\omega}_{s\parallel} \ll 1$) of the dielectric tensor are insufficient to determine the electrostatic field. To do this, we must go to the next order in $\tilde{\omega}_{s\parallel} \ll 1$. To illustrate how such a calculation is done, in this appendix, we derive an expression for the electrostatic field component $\hat{k} \cdot \widehat{\delta E}$ in terms of the transverse electric field $\widehat{\delta E}_T$ and special functions when the underlying particle distribution function is Maxwellian.

To achieve this aim, we first derive a relation between the components of the electric field in the coordinate basis $\{\hat{x}, \hat{y}, \hat{z}\}$. We begin with the consistency condition (2.110) appropriate for non-relativistic electromagnetic fluctuations

$$k \cdot \mathfrak{E} \cdot \widehat{\delta E} = 0. \tag{I2}$$

Writing $\hat{k}$, $\mathfrak{E}$ and $\widehat{\delta E}$ in the basis $\{\hat{x}, \hat{y}, \hat{z}\}$, this becomes

$$\left(k_\perp \mathfrak{E}_{xx} + k_\parallel \mathfrak{E}_{xz}\right) \widehat{\delta E}_x + \left(k_\perp \mathfrak{E}_{xy} - k_\parallel \mathfrak{E}_{yz}\right) \widehat{\delta E}_y + \left(k_\perp \mathfrak{E}_{xz} + k_\parallel \mathfrak{E}_{zz}\right) \widehat{\delta E}_z = 0. \tag{I3}$$

Now considering the case of fluctuations that satisfy $\tilde{\omega}_{s\parallel} \ll 1$ for all particle species s, and expanding the components of the dielectric in $\tilde{\omega}_{s\parallel} \ll 1$, we find

$$\left(k_\perp \mathfrak{E}_{xx}^{(1)} + k_\parallel \mathfrak{E}_{xz}^{(1)}\right) \widehat{\delta E}_x + \left(k_\perp \mathfrak{E}_{xy}^{(1)} - k_\parallel \mathfrak{E}_{yz}^{(1)}\right) \widehat{\delta E}_y + \left(k_\perp \mathfrak{E}_{xz}^{(1)} + k_\parallel \mathfrak{E}_{zz}^{(1)}\right) \widehat{\delta E}_z = O(\tilde{\omega}_{s\parallel}^3), \tag{I4}$$

where

$$\mathfrak{E}^{(1)} = \sum_s \tilde{\omega}_{s\parallel}^2 \mathfrak{E}_s^{(1)}. \tag{I5}$$

From (G26), we have

$$k_\perp \mathfrak{E}_{xx}^{(1)} + k_\parallel \mathfrak{E}_{xz}^{(1)} = -\sum_s \frac{2k_\parallel \omega_{ps}^2 \tilde{\omega}_{s\parallel}^2}{\omega^2} \sum_{m=-\infty}^{\infty} \frac{m}{k_\perp \tilde{\rho}_s} \mathrm{Re}\, Z\left(\frac{m}{|k_\parallel| \tilde{\rho}_s}\right)$$
$$\times \exp\left(-\frac{k_\perp^2 \tilde{\rho}_s^2}{2}\right) I_m\left(\frac{k_\perp^2 \tilde{\rho}_s^2}{2}\right), \tag{I6a}$$

$$k_\perp \mathfrak{E}_{xy}^{(1)} - k_\parallel \mathfrak{E}_{yz}^{(1)} = \sum_s \frac{\sqrt{\pi} k_\parallel \omega_{\mathrm{ps}}^2 \tilde{\omega}_{s\parallel}^2}{\omega^2} \sum_{m=-\infty}^{\infty} k_\perp \tilde{\rho}_s \exp\left(-\frac{m^2}{k_\parallel^2 \tilde{\rho}_s^2}\right)$$

$$\times \exp\left(-\frac{k_\perp^2 \tilde{\rho}_s^2}{2}\right) \left[I_m'\left(\frac{k_\perp^2 \tilde{\rho}_s^2}{2}\right) - I_m\left(\frac{k_\perp^2 \tilde{\rho}_s^2}{2}\right)\right], \tag{I6b}$$

$$k_\perp \mathfrak{E}_{xz}^{(1)} + k_\parallel \mathfrak{E}_{zz}^{(1)} = \sum_s \frac{2k_\parallel \omega_{\mathrm{ps}}^2 \tilde{\omega}_{s\parallel}^2}{\omega^2} \left[1 + \sum_{m=-\infty}^{\infty} \frac{m}{|k_\parallel| \tilde{\rho}_s} \mathrm{Re}\, Z\left(\frac{m}{|k_\parallel| \tilde{\rho}_s}\right)\right.$$

$$\left. \times \exp\left(-\frac{k_\perp^2 \tilde{\rho}_s^2}{2}\right) I_m\left(\frac{k_\perp^2 \tilde{\rho}_s^2}{2}\right)\right]. \tag{I6c}$$

Thus, we have the following relationship between $\widehat{\delta E}_x$, $\widehat{\delta E}_y$ and $\widehat{\delta E}_z$:

$$\sum_s \frac{k_{\mathrm{D}s}^2}{2k_\parallel^2} \left\{ -L\left(|k_\parallel| \tilde{\rho}_s, k_\perp \tilde{\rho}_s\right) \widehat{\delta E}_x + N\left(|k_\parallel| \tilde{\rho}_s, k_\perp \tilde{\rho}_s\right) \widehat{\delta E}_y \right.$$

$$\left. + \left[2 + \frac{k_\perp}{k_\parallel} L\left(|k_\parallel| \tilde{\rho}_s, k_\perp \tilde{\rho}_s\right)\right] \widehat{\delta E}_z \right\} = 0, \tag{I7}$$

where $k_{\mathrm{D}s}$ is the Debye wavenumber (D12), and $L(x, y)$ and $N(x, y)$ were defined previously by (G32). Using the identities

$$\widehat{\delta E}_x = \frac{k_\parallel}{k} \widehat{\delta E}_1 + \frac{k_\perp}{k} \widehat{\delta E}_3, \tag{I8a}$$

$$\widehat{\delta E}_y = \widehat{\delta E}_2, \tag{I8b}$$

$$\widehat{\delta E}_z = -\frac{k_\perp}{k} \widehat{\delta E}_1 + \frac{k_\parallel}{k} \widehat{\delta E}_3, \tag{I8c}$$

we can rearrange (I7) to give

$$\frac{1}{k_\parallel k} \left(\sum_s k_{\mathrm{D}s}^2\right) \widehat{\delta E}_3 = \sum_s \frac{k_{\mathrm{D}s}^2}{2k_\parallel^2} \left\{\left[\frac{k}{k_\parallel} L\left(|k_\parallel| \tilde{\rho}_s, k_\perp \tilde{\rho}_s\right) + 2\frac{k_\perp}{k}\right] \widehat{\delta E}_1 \right.$$

$$\left. - N\left(|k_\parallel| \tilde{\rho}_s, k_\perp \tilde{\rho}_s\right) \widehat{\delta E}_2 \right\}. \tag{I9}$$

Thus, the electrostatic field is related to the transverse field by

$$\hat{k} \cdot \widehat{\delta E} = \left(\sum_s \frac{Z_s T_e}{T_s}\right)^{-1} \sum_s \frac{Z_s T_e}{T_s} \left\{\left[\frac{k^2}{2k_\parallel^2} L\left(|k_\parallel| \tilde{\rho}_s, k_\perp \tilde{\rho}_s\right) + \frac{k_\perp}{k_\parallel}\right] \widehat{\delta E}_1 \right.$$

$$\left. - \frac{k}{2k_\parallel} N\left(|k_\parallel| \tilde{\rho}_s, k_\perp \tilde{\rho}_s\right) \widehat{\delta E}_2 \right\}. \tag{I10}$$

Appendix J. Methodology for characterising CET microinstabilities

In this appendix, we describe our method for calculating the real frequencies and growth rates of microinstabilities driven by the CE electron- and ion-temperature-gradient, and electron-friction terms when the Krook collision operator is assumed. The method follows that outlined in § 2.5: that is, motivated by the considerations of § 2.3.4, we assume that all significant CET microinstabilities are low frequency ($\omega \ll k_{\parallel} v_{\mathrm{th}s}$ for at least one particle species), and derive algebraic dispersion relations of such microinstabilities (a particular example of which is given by (2.118)). The growth rate of CET microinstabilities (and, therefore, the stability of the electron and ion CE distribution functions (3.1*a*) and (3.1*b*)) as a function of their parallel and perpendicular wavenumbers $k_{\parallel}$ and $k_{\perp}$ is assessed by solving this dispersion relation for the complex frequency ω, and then evaluating its imaginary part.

As we explained in § 2.5, to construct the algebraic, low-frequency dispersion relation for particular forms of CE distribution function for each particle species s, we must evaluate its (leading-order) non-Maxwellian contribution to the dielectric tensor, $\boldsymbol{P}_s \approx \boldsymbol{P}_s^{(0)}$ (see (2.97) and (G10) for the precise relation of this quantity to the dielectric tensor $\mathfrak{E}_s$). This is done for the CE electron-friction term in Appendix J.1, and for the CE temperature-gradient terms in Appendix J.2. We then deduce the algebraic dispersion relations of CE electron-temperature-gradient-driven microinstabilities in Appendix J.3, and of CE ion-temperature-gradient-driven microinstabilities in Appendix J.4. Within these two appendices, respectively, we also present derivations of the (further) simplified dispersion relations for the parallel CET whistler instability (Appendix J.3.1), the parallel CET slow-hydromagnetic-wave instability (Appendix J.4.1), and the CET long-wavelength KAW instability (Appendix J.4.2), from which the frequencies and growth rates of these instabilities that are stated in § 3.3 are calculated.

J.1. *Dielectric response of CE electron-friction term*

We first consider the CE electron-friction term when evaluating $\boldsymbol{P}_e^{(0)}$, defined in (2.97). We showed in Appendix G.2 that, when a Krook collision operator was assumed, if $\eta_e^T = \eta_i = 0$, then (see (G74))

$$(\boldsymbol{P}_e^{(0)})_{11} = \frac{\eta_e^R}{2}(\boldsymbol{M}_e^{(0)})_{11}, \tag{J1a}$$

$$(\boldsymbol{P}_e^{(0)})_{12} = \frac{\eta_e^R}{2}(\boldsymbol{M}_e^{(0)})_{12}, \tag{J1b}$$

$$(\boldsymbol{P}_e^{(0)})_{21} = \frac{\eta_e^R}{2}(\boldsymbol{M}_e^{(0)})_{21}, \tag{J1c}$$

$$(\boldsymbol{P}_e^{(0)})_{22} = \frac{\eta_e^R}{2}(\boldsymbol{M}_e^{(0)})_{22}. \tag{J1d}$$

It follows that the dispersion relation of all plasma modes is identical to that in a Maxwellian plasma, only with shifted complex frequencies $\tilde{\omega}_{e\parallel}^* \equiv \tilde{\omega}_{e\parallel} + \eta_e^R/2$. Since $\mathrm{Im}(\tilde{\omega}_{e\parallel}) < 0$ for all modes in a Maxwellian plasma, we conclude that $\mathrm{Im}(\tilde{\omega}_{e\parallel}^*) < 0$ also, and hence the CE electron-friction term cannot drive any microinstabilities when a Krook collision operator is employed: instead, it merely modifies the real frequency of the waves. Thus, when characterising CET microinstabilities, we henceforth ignore the CE electron-friction term, as well as the electron–ion-drift term (*viz.* $\eta_e^R = \eta_e^u = 0$).

J.2. *Dielectric response of CE temperature-gradient terms*

Now consider the CE temperature-gradient terms. It is shown in Appendix G.3 that $\boldsymbol{P}_s^{(0)}$ is given by

$$(\boldsymbol{P}_e^{(0)})_{11} = \mathrm{i}\eta_e^T \frac{k^2}{k_\parallel^2} I\big(k_\parallel \tilde{\rho}_e, k_\perp \tilde{\rho}_e\big), \tag{J2a}$$

$$(\boldsymbol{P}_e^{(0)})_{12} = -\mathrm{i}\eta_e^T \frac{k}{k_\parallel} J\big(k_\parallel \tilde{\rho}_e, k_\perp \tilde{\rho}_e\big), \tag{J2b}$$

$$(\boldsymbol{P}_e^{(0)})_{21} = \mathrm{i}\eta_e^T \frac{k}{k_\parallel} J\big(k_\parallel \tilde{\rho}_e, k_\perp \tilde{\rho}_e\big), \tag{J2c}$$

$$(\boldsymbol{P}_e^{(0)})_{22} = \mathrm{i}\eta_e^T K\big(k_\parallel \tilde{\rho}_e, k_\perp \tilde{\rho}_e\big), \tag{J2d}$$

where the special functions $I(x, y)$, $J(x, y)$ and $K(x, y)$ are defined by (G85). Note that $\tilde{\rho}_e < 0$, by definition. The contribution $\boldsymbol{P}_i^{(0)}$ associated with the CE ion-temperature-gradient terms is given by

$$(\boldsymbol{P}_i^{(0)})_{11} = \mathrm{i}\eta_i \frac{k^2}{k_\parallel^2} I\big(k_\parallel \rho_i, k_\perp \rho_i\big), \tag{J3a}$$

$$(\boldsymbol{P}_i^{(0)})_{12} = -\mathrm{i}\eta_i \frac{k}{k_\parallel} J\big(k_\parallel \rho_i, k_\perp \rho_i\big), \tag{J3b}$$

$$(\boldsymbol{P}_i^{(0)})_{21} = \mathrm{i}\eta_i \frac{k}{k_\parallel} J\big(k_\parallel \rho_i, k_\perp \rho_i\big), \tag{J3c}$$

$$(\boldsymbol{P}_i^{(0)})_{22} = \mathrm{i}\eta_i K\big(k_\parallel \rho_i, k_\perp \rho_i\big). \tag{J3d}$$

J.3. *Approximate dispersion relation of CE electron-temperature-gradient-driven microinstabilities*

We first consider microinstabilities for which $\tilde{\omega}_{e\parallel} = \omega/k_\parallel v_{\mathrm{th}e} \sim \eta_e^T$. It follows that $\tilde{\omega}_{i\parallel} = \omega/k_\parallel v_{\mathrm{th}i} \sim \eta_e^T \mu_e^{-1/2} \gg \eta_i$. Therefore, the CE ion-temperature-gradient term is irrelevant for such instabilities, and we need consider only the electron-temperature-gradient term. We also assume that the Maxwellian contribution to the dielectric tensor, $\boldsymbol{M}_i$, can be ignored for such microinstabilities – the validity of this assumption is discussed at the end of this section.

The dispersion relation for microinstabilities under the ordering $\tilde{\omega}_{e\parallel} \sim \eta_e^T \sim 1/\beta_e$ is then given by (2.118), with $\boldsymbol{M}_e^{(0)}$ and $\boldsymbol{P}_e^{(0)}$ substituted for by (2.121) and (J2), respectively,

$$\begin{aligned}
&\big[\tilde{\omega}_{e\parallel} F\big(k_\parallel \tilde{\rho}_e, k_\perp \tilde{\rho}_e\big) + \eta_e^T I\big(k_\parallel \tilde{\rho}_e, k_\perp \tilde{\rho}_e\big) + \mathrm{i}k_\parallel^2 d_e^2\big] \\
&\times \big[\tilde{\omega}_{e\parallel} H\big(k_\parallel \tilde{\rho}_e, k_\perp \tilde{\rho}_e\big) + \eta_e^T K\big(k_\parallel \tilde{\rho}_e, k_\perp \tilde{\rho}_e\big) + \mathrm{i}k^2 d_e^2\big] \\
&+ \big[\tilde{\omega}_{e\parallel} G\big(k_\parallel \tilde{\rho}_e, k_\perp \tilde{\rho}_e\big) + \eta_e^T J\big(k_\parallel \tilde{\rho}_e, k_\perp \tilde{\rho}_e\big)\big]^2 = 0. \tag{J4}
\end{aligned}$$

We remind the reader that we have ordered $k^2 d_e^2 \sim \eta_e^T$ and $k\rho_e \sim 1$. Noting that $\beta_e = \rho_e^2/d_e^2$, we can rewrite the skin-depth terms as follows:

$$k_\parallel^2 d_e^2 = \frac{k_\parallel^2 \rho_e^2}{\beta_e}, \quad k^2 d_e^2 = \frac{k^2 \rho_e^2}{\beta_e}. \tag{J5a,b}$$

This allows for the dispersion relation (J4) to be arranged as a quadratic in the complex variable $\tilde{\omega}_{e\parallel}\beta_e$:

$$A_T\big(k_\parallel\rho_e, k_\perp\rho_e\big)\,\tilde{\omega}_{e\parallel}^2\beta_e^2 + B_T\big(k_\parallel\rho_e, k_\perp\rho_e\big)\,\tilde{\omega}_{e\parallel}\beta_e + C_T\big(k_\parallel\rho_e, k_\perp\rho_e\big) = 0, \qquad (J6)$$

where

$$A_T\big(k_\parallel\rho_e, k_\perp\rho_e\big) = F_eH_e + G_e^2, \qquad (J7)$$

$$B_T\big(k_\parallel\rho_e, k_\perp\rho_e\big) = \eta_e^T\beta_e\,(F_eK_e + H_eI_e + 2G_eJ_e) + \mathrm{i}\left(F_ek^2\rho_e^2 + H_ek_\parallel^2\rho_e^2\right), \qquad (J8)$$

$$C_T\big(k_\parallel\rho_e, k_\perp\rho_e\big) = \left(\eta_e^T\beta_e\right)^2\left(I_eK_e + J_e^2\right) - k^2k_\parallel^2\rho_e^4 + \mathrm{i}\eta_e^T\beta_e\left(I_ek^2\rho_e^2 + K_ek_\parallel^2\rho_e^2\right), \qquad (J9)$$

and $F_e \equiv F(k_\parallel\tilde{\rho}_e, k_\perp\tilde{\rho}_e)$, $G_e \equiv G(k_\parallel\tilde{\rho}_e, k_\perp\tilde{\rho}_e)$, etc. Solving (J6) gives two roots; restoring dimensions to the complex frequency, they are

$$\omega = \frac{\Omega_e}{\beta_e}k_\parallel\rho_e\frac{-B_T \pm \sqrt{B_T^2 + 4A_TC_T}}{2A_T}, \qquad (J10)$$

recovering (3.12). For a given wavenumber, we use (J10) to calculate the growth rates of the perturbations – and, in particular, to see if positive growth rates are present. If they are, it is anticipated that they will have typical size $\gamma \sim \Omega_e/\beta_e \sim \eta_e^T\Omega_e$ (or $\tilde{\omega}_{e\parallel} \sim 1/\beta_e \sim \eta_e^T$).

When deriving (J10), we assumed that neglecting the Maxwellian ion response was legitimate. It is clear that if $\tilde{\omega}_{i\parallel} \gg 1$, then thermal ions are effectively static to electromagnetic perturbations, and so their contribution $\boldsymbol{M}_i$ to the dielectric tensor can be ignored. In terms of a condition on η_e^T, the scaling $\eta_e^T \sim \tilde{\omega}_{e\parallel}$ gives $\eta_e^T \gg \mu_e^{1/2}$, so this regime is valid for sufficiently large η_e^T. For $\tilde{\omega}_{i\parallel} \lesssim 1$, it is not immediately clear in the same way that the ion contribution to the dielectric tensor is small. However, having deduced the typical magnitude of the complex frequency of perturbations whilst ignoring ion contributions, we are now able to confirm that our neglect of $\boldsymbol{M}_i$ was justified.

Since $k\rho_e \sim 1$ under the ordering assumed when deriving (J4), we conclude that the Maxwellian ion response is unmagnetised: $k\rho_i \gg 1$. As a consequence, it can be shown (see Appendix G.1.5) that the transverse components of $\boldsymbol{M}_i$ are given by

$$(\boldsymbol{M}_i)_{11} = (\boldsymbol{M}_i)_{22} = \tilde{\omega}_iZ(\tilde{\omega}_i), \qquad (\boldsymbol{M}_i)_{12} = (\boldsymbol{M}_i)_{21} = 0, \qquad (J11a,b)$$

where $\tilde{\omega}_i \equiv \omega/kv_{\mathrm{th}i} = k_\parallel\tilde{\omega}_{i\parallel}/k$. Then, estimating the size of the neglected Maxwellian ion contribution to the dielectric tensor (assuming $k_\parallel \sim k$) as compared with the equivalent electron contribution, we find

$$\frac{(\mathfrak{E}_i)_{11}}{(\mathfrak{E}_e^{(0)})_{11}} \sim \frac{(\mathfrak{E}_i)_{22}}{(\mathfrak{E}_e^{(0)})_{22}} \sim \frac{\mu_e\tilde{\omega}_i}{\tilde{\omega}_{e\parallel}}|Z(\tilde{\omega}_i)| \sim \mu_e^{1/2}|Z(\tilde{\omega}_i)|, \qquad (J12)$$

where we have used $\mathfrak{E}_i = \mu_e\boldsymbol{M}_i$ and $\mathfrak{E}_e^{(0)} = \tilde{\omega}_{e\parallel}\boldsymbol{M}_e^{(0)} + \boldsymbol{P}_e^{(0)}$ (see § 2.5.3). Since $|Z(z)| \lesssim 1$ for all z with positive imaginary part (Fried & Conte 1961), we conclude that the ion contribution to the dielectric tensor is indeed small for unstable perturbations, irrespective of the value of $\tilde{\omega}_{i\parallel}$, and so its neglect was valid.

J.3.1. *Derivation of frequency and growth rate of the parallel CET whistler instability*

The dispersion relation of unstable whistler waves with their wavevector parallel to $\boldsymbol{B}_0$ is obtained by taking the subsidiary limit $k_\perp \rho_e \to 0$ in (J4), and substituting $\tilde{\rho}_e = -\rho_e$:

$$\left[\tilde{\omega}_{e\parallel} \beta_e \sqrt{\pi} \exp\left(-\frac{1}{k_\parallel^2 \rho_e^2}\right) + \eta_e^T \beta_e \frac{\sqrt{\pi}}{2} \left(\frac{1}{k_\parallel^2 \rho_e^2} - \frac{1}{2}\right) \exp\left(-\frac{1}{k_\parallel^2 \rho_e^2}\right) + \mathrm{i} k_\parallel^2 \rho_e^2 \right]^2$$

$$+ \left\{ \tilde{\omega}_{e\parallel} \beta_e \, \mathrm{Re}\, Z\!\left(\frac{1}{k_\parallel \rho_e}\right) + \eta_e^T \beta_e \left[\frac{1}{2 k_\parallel \rho_e} + \left(\frac{1}{2 k_\parallel^2 \rho_e^2} - \frac{1}{4}\right) \mathrm{Re}\, Z\!\left(\frac{1}{k_\parallel \rho_e}\right) \right] \right\}^2 = 0. \tag{J13}$$

This can be factorised to give two roots; separating the complex frequency into real and imaginary parts via $\omega = \varpi + \mathrm{i}\gamma$, and defining

$$\tilde{\omega}_{e\parallel} \equiv \frac{\varpi}{k_\parallel v_{\mathrm{th}e}}, \quad \tilde{\gamma}_{e\parallel} \equiv \frac{\gamma}{k_\parallel v_{\mathrm{th}e}}, \tag{J14a,b}$$

we have

$$\tilde{\omega}_{e\parallel} \beta_e = \eta_e^T \beta_e \left(\frac{1}{2 k_\parallel^2 \rho_e^2} - \frac{1}{4}\right) + \frac{\left(\eta_e^T \beta_e / 2 k_\parallel \rho_e - k_\parallel^2 \rho_e^2\right) \mathrm{Re}\, Z\!\left(1/k_\parallel \rho_e\right)}{\left[\mathrm{Re}\, Z\!\left(1/k_\parallel \rho_e\right)\right]^2 + \pi \exp\left(-2/k_\parallel^2 \rho_e^2\right)}, \tag{J15a}$$

$$\tilde{\gamma}_{e\parallel} \beta_e = \frac{\sqrt{\pi} \left(\eta_e^T \beta_e / 2 k_\parallel \rho_e - k_\parallel^2 \rho_e^2\right)}{\left[\mathrm{Re}\, Z\!\left(1/k_\parallel \rho_e\right)\right]^2 \exp\left(1/k_\parallel^2 \rho_e^2\right) + \pi \exp\left(-1/k_\parallel^2 \rho_e^2\right)}, \tag{J15b}$$

whence (3.5) follows immediately.

J.4. *Approximate dispersion relation of CE ion-temperature-gradient-driven microinstabilities*

We now explain the method used to characterise microinstabilities driven by the ion-temperature-gradient term. For these, we set the electron-temperature-gradient terms to zero, $\eta_e^T = 0$, assume the ordering $\tilde{\omega}_{i\parallel} \sim \eta_i$, and anticipate that such microinstabilities will occur on ion rather than electron scales, i.e. $k\rho_i \sim 1$. Under the ordering $\tilde{\omega}_{i\parallel} \sim \eta_i \ll 1$, it follows that $\tilde{\omega}_{e\parallel} \sim \mu_e^{1/2} \tilde{\omega}_{i\parallel} \ll 1$; therefore, we can use (2.121) to quantity the contribution of Maxwellian electrons to the total dielectric tensor. However, since $k\rho_i \sim 1$, we must consider the matrix $\boldsymbol{M}_e^{(0)}$ in the limit $k_\parallel \rho_e \sim k_\perp \rho_e \sim \mu_e^{1/2} \ll 1$. Asymptotic forms of (2.121) appropriate for this limit are given by (G37), and lead to[11]

$$(\boldsymbol{M}_e^{(0)})_{11} = O\left[\exp\left(-\frac{1}{k_\parallel^2 \rho_e^2}\right)\right], \tag{J16a}$$

$$(\boldsymbol{M}_e^{(0)})_{12} \approx -\mathrm{i}\frac{k}{k_\parallel} \left[k_\parallel \rho_e + O(k^3 \rho_e^3)\right], \tag{J16b}$$

$$(\boldsymbol{M}_e^{(0)})_{21} = \mathrm{i}\frac{k}{k_\parallel} \left[k_\parallel \rho_e + O(k^3 \rho_e^3)\right], \tag{J16c}$$

$$(\boldsymbol{M}_e^{(0)})_{22} = \mathrm{i}\left[\sqrt{\pi} k_\perp^2 \rho_e^2 + O(k_\perp^4 \rho_e^4)\right]. \tag{J16d}$$

---

[11] As noted in § 2.5.6, for $k_\parallel \rho_e \ll 1$, the approximation $(\boldsymbol{M}_e)_{11} \approx \tilde{\omega}_{e\parallel}(\boldsymbol{M}_e^{(0)})_{11}$ in fact breaks down, on account of $(\boldsymbol{M}_e^{(0)})_{11}$ becoming exponentially small in $k_\parallel \rho_e \ll 1$. However, it turns out that when $k_\parallel \rho_i \sim k_\perp \rho_i \sim 1$, $(\boldsymbol{M}_e)_{11} \ll (\boldsymbol{M}_i)_{11}$, and so this subtlety can be ignored for the CE ion-temperature-gradient-driven instabilities.

We now combine (J16) with (2.121) for $\boldsymbol{M}_i^{(0)}$ and (J3) for $\boldsymbol{P}_i^{(0)}$, and find the dispersion relation for CE ion-temperature-gradient-driven microinstabilities by substituting the dielectric tensor (2.108) into (2.117):

$$\left[\tilde{\omega}_{i\parallel}F\left(k_\parallel\rho_i, k_\perp\rho_i\right) + \eta_i I\left(k_\parallel\rho_i, k_\perp\rho_i\right) + \mathrm{i}k_\parallel^2 d_i^2\right]$$
$$\times \left[\tilde{\omega}_{i\parallel}H\left(k_\parallel\rho_i, k_\perp\rho_i\right) + \eta_i K\left(k_\parallel\rho_i, k_\perp\rho_i\right) + \mathrm{i}k^2 d_i^2\right]$$
$$+ \left[\tilde{\omega}_{i\parallel}\left[G\left(k_\parallel\rho_i, k_\perp\rho_i\right) + k_\parallel\rho_i\right] + \eta_i J\left(k_\parallel\rho_i, k_\perp\rho_i\right)\right]^2 = 0, \tag{J17}$$

where $d_i = c/\omega_{pi}$ is the ion inertial scale, and we have ordered $\eta_i \sim 1/\beta_i \sim k^2 d_i^2$. This dispersion relation is very similar to (J4), save for the addition of one term (the middle term in the third line of (J17)) providing a linear coupling between the $\widehat{\delta E}_1$ and $\widehat{\delta E}_2$ components of the electric-field perturbation. Similarly to (J10), the dispersion relation (J17) can be written as a quadratic in $\tilde{\omega}_{i\parallel}\beta_i$, which is then solved to give the following expression for the complex frequency:

$$\omega = \frac{\Omega_i}{\beta_i}k_\parallel\rho_i\frac{-\tilde{B}_T \pm \sqrt{\tilde{B}_T^2 + 4\tilde{A}_T\tilde{C}_T}}{2\tilde{A}_T}, \tag{J18}$$

where

$$\tilde{A}_T = F_i H_i + \left[G_i + k_\parallel\rho_i\right]^2, \tag{J19}$$

$$\tilde{B}_T = \eta_i\beta_i\left[F_i K_i + H_i I_i + 2J_i\left(G_i + k_\parallel\rho_i\right)\right] + \mathrm{i}\left(F_i k^2\rho_e^2 + H_i k_\parallel^2\rho_e^2\right), \tag{J20}$$

$$\tilde{C}_T = (\eta_i\beta_i)^2\left(I_i K_i + J_i^2\right) - k^2 k_\parallel^2\rho_e^4 + \mathrm{i}\eta_i\beta_i\left(I_i k^2\rho_e^2 + K_i k_\parallel^2\rho_e^2\right). \tag{J21}$$

This expression is the one that is used to evaluate the real frequencies and growth rates of ion-scale CET microinstabilities in § 3.3.3.

J.4.1. *Derivation of frequency and growth rate of the parallel CET slow-hydromagnetic-wave instability*

We obtain the dispersion relation of the parallel slow-wave instability by considering the general dispersion relation (J17) of CE ion-temperature-gradient-driven instabilities in the limit $k_\perp \to 0$:

$$\left[\tilde{\omega}_{i\parallel}\beta_i\sqrt{\pi}\exp\left(-\frac{1}{k_\parallel^2\rho_i^2}\right) + \eta_i\beta_i\frac{\sqrt{\pi}}{2}\left(\frac{1}{k_\parallel^2\rho_i^2} - \frac{1}{2}\right)\exp\left(-\frac{1}{k_\parallel^2\rho_i^2}\right) + \mathrm{i}k_\parallel^2\rho_i^2\right]^2$$
$$+ \left\{\tilde{\omega}_{i\parallel}\beta_i\left[\operatorname{Re}Z\left(\frac{1}{k_\parallel\rho_i}\right) + k_\parallel\rho_i\right] + \eta_i\beta_i\left[\frac{1}{2k_\parallel\rho_i} + \left(\frac{1}{2k_\parallel^2\rho_i^2} - \frac{1}{4}\right)\operatorname{Re}Z\left(\frac{1}{k_\parallel\rho_i}\right)\right]\right\}^2 = 0. \tag{J22}$$

As before, this can be factorised to give two roots; for $\tilde{\omega}_{i\parallel} = \bar{\varpi}_{i\parallel} + \mathrm{i}\tilde{\gamma}_{i\parallel}$ (cf. (J14a,b)), it follows that

$$\bar{\varpi}_{i\parallel}\beta_i = \eta_i\beta_i\left(\frac{1}{2k_\parallel^2\rho_i^2} - \frac{1}{4}\right) + \frac{k_\parallel\rho_i\left[\operatorname{Re}Z\left(\dfrac{1}{k_\parallel\rho_i}\right) + k_\parallel\rho_i\right]\left(\eta_i\beta_i/4 - k_\parallel\rho_i\right)}{\left[\operatorname{Re}Z\left(\dfrac{1}{k_\parallel\rho_i}\right) + k_\parallel\rho_i\right]^2 + \pi\exp\left(-\dfrac{2}{k_\parallel^2\rho_i^2}\right)}, \tag{J23a}$$

$$\tilde{\gamma}_{i\parallel}\beta_i = \frac{\sqrt{\pi}k_\parallel\rho_i\left(\eta_i\beta_i/4 - k_\parallel\rho_i\right)}{\left[\mathrm{Re}\,Z\left(\dfrac{1}{k_\parallel\rho_i}\right) + k_\parallel\rho_i\right]^2 \exp\left(\dfrac{1}{k_\parallel^2\rho_i^2}\right) + \pi\exp\left(-\dfrac{1}{k_\parallel^2\rho_i^2}\right)}. \tag{J23b}$$

These can be rearranged to give (3.13).

J.4.2. *Derivation of frequency and growth rate of the CET long-wavelength KAW instability*

In the limit $k_\parallel\rho_i \ll 1$, $k_\perp\rho_i \sim 1$, the general dispersion relation (J17) of CE ion-temperature-gradient-driven instabilities becomes

$$\left[\tilde{\omega}_{i\parallel}(1 - \mathcal{F}_i) - \frac{\eta_i}{2}\mathcal{G}_i\right]^2$$
$$+ \frac{k_\perp^2\rho_i^2}{\beta_i}\left[\mathrm{i}\sqrt{\pi}\left(\mathcal{F}_i + \sqrt{\frac{\mu_e Z^2}{\tau}}\right)\tilde{\omega}_{i\parallel} - \frac{1}{\beta_i} + \frac{\mathrm{i}\sqrt{\pi}\eta_i}{2}\left(\mathcal{G}_i - \frac{1}{2}\mathcal{F}_i\right)\right] = 0, \tag{J24}$$

where we remind the reader that $\mathcal{F}_i = \mathcal{F}(k_\perp\rho_i)$, $\mathcal{G}_i = \mathcal{G}(k_\perp\rho_i)$, with the functions $\mathcal{F}(\alpha)$ and $\mathcal{G}(\alpha)$ being defined by (3.24). Equation (3.22) for the complex frequency of the CET KAW modes in the main text is then derived by solving (J24) for $\tilde{\omega}_{i\parallel} = \omega/k_\parallel v_{\mathrm{th}i}$.

Appendix K. Methodology for characterising CES microinstabilities

This appendix outlines the method used to determine the growth rates of microinstabilities driven by the CE electron- and ion-shear terms. Once again (cf. Appendix J), §2.5 presents the general framework of our approach: determine a simplified algebraic dispersion relation satisfied by the (complex) frequencies ω of CES microinstabilities with parallel and perpendicular wavenumber $k_\parallel$ and $k_\perp$ under the assumption that they are low frequency (viz. $\omega \ll k_\parallel v_{\mathrm{th}s}$; cf. (2.94)), solve for ω, then calculate the growth rate γ from its imaginary part (and the real frequency ϖ from its real part). To construct the dispersion relation, we first need to know the tensor $\boldsymbol{P}_s^{(0)}$ for a CE distribution function of the form (4.1); this result is given in Appendix K.1. Then, in Appendix K.2.1, we determine an approximate quadratic dispersion relation for CES microinstabilities, show in Appendix K.2.2 how that dispersion relation can be used in certain cases to evaluate the CES instability thresholds semi-analytically, then demonstrate the significant shortcomings of the quadratic approximation in Appendix K.2.3. In Appendix K.3.1, we address these shortcomings by constructing a revised quartic dispersion relation for CES microinstabilities. This quartic dispersion relation is then used to derive simplified dispersion relations for the various different CES microinstabilities discussed in the main text: the mirror instability in Appendix K.3.2, the parallel (CES) whistler instability in Appendix K.3.3, the transverse instability in Appendix K.3.4, the electron mirror instability in Appendix K.3.5, the parallel, oblique and critical-line firehose instabilities in Appendices K.3.6, K.3.7 and K.3.8, the parallel and oblique electron firehose instabilities in Appendices K.3.9 and K.3.10, the EST instability in Appendix K.3.11 and the whisper instability in Appendix K.3.12. Finally, in Appendix K.3.13, we derive the dispersion relation of the CET ordinary-mode instability – the one CES (or CET) microinstability that does not satisfy $\omega \ll k_\parallel v_{\mathrm{th}s}$ for either electrons or ions (see §2.5.8) – directly from the hot-plasma dispersion relation.

K.1. *Dielectric response of CE shear terms*

First, we evaluate the elements of $\boldsymbol{P}_s^{(0)}$:

$$(\boldsymbol{P}_s^{(0)})_{11} = \epsilon_s \frac{k^2}{k_\parallel^2} W\big(k_\parallel \tilde{\rho}_s, k_\perp \tilde{\rho}_s\big),$$

(K1a)

$$(\boldsymbol{P}_s^{(0)})_{12} = -\epsilon_s \frac{k}{k_\parallel} X\big(k_\parallel \tilde{\rho}_s, k_\perp \tilde{\rho}_s\big),$$

(K1b)

$$(\boldsymbol{P}_s^{(0)})_{21} = \epsilon_s \frac{k}{k_\parallel} X\big(k_\parallel \tilde{\rho}_s, k_\perp \tilde{\rho}_s\big),$$

(K1c)

$$(\boldsymbol{P}_s^{(0)})_{22} = \epsilon_s Y\big(k_\parallel \tilde{\rho}_s, k_\perp \tilde{\rho}_s\big),$$

(K1d)

where the special functions $W(x, y)$, $Y(x, y)$ and $X(x, y)$ are defined by (G97). These results are derived in Appendix G.4.

K.2. *Quadratic approximation to dispersion relation of CE shear-driven microinstabilities*

K.2.1. *Derivation*

Considering the relative magnitude of $\tilde{\omega}_{i\parallel} = \omega/k_\parallel v_{\mathrm{th}i}$ and $\tilde{\omega}_{e\parallel} = \omega/k_\parallel v_{\mathrm{th}e} \ll \tilde{\omega}_{i\parallel}$, we observe that, unlike CET microinstabilities, CES microinstabilities satisfy the low-frequency condition (2.94) for both electrons and ions. This claim holds because any microinstability involving the CE electron-shear term must satisfy $\tilde{\omega}_{e\parallel} \sim \epsilon_e \ll (m_e/m_i)^{1/2}$, where the last inequality arises from the scaling relation $\epsilon_e \sim (m_e/m_i)^{1/2}\epsilon_i$ given by (2.42d); thus, from the scaling relation (2.106) with $T_e = T_i$, it follows that $\tilde{\omega}_{i\parallel} \sim \epsilon_e(m_i/m_e)^{1/2} \sim \epsilon_i \ll 1$. Therefore, it is consistent to expand both the Maxwellian electron and ion terms in $\tilde{\omega}_{s\parallel} \ll 1$.

We therefore initially approximate $\mathfrak{E}$ as follows:

$$\mathfrak{E} \approx \tilde{\omega}_{e\parallel} \mathfrak{E}^{(0)} = \frac{\omega_{\mathrm{pe}}^2}{\omega^2} \left(\sum_s \tilde{\omega}_{s\parallel} \mu_s \boldsymbol{M}_s^{(0)} + \sum_s \mu_s \boldsymbol{P}_s^{(0)} \right),$$

(K2)

where the expansion of $\boldsymbol{M}_s$ and $\boldsymbol{P}_s$ in $\tilde{\omega}_{s\parallel}$, i.e.

$$\boldsymbol{M}_s\big(\tilde{\omega}_{s\parallel}, \boldsymbol{k}\big) \approx \tilde{\omega}_{s\parallel} \boldsymbol{M}_s^{(0)}(\boldsymbol{k}), \quad \boldsymbol{P}_s\big(\tilde{\omega}_{s\parallel}, \boldsymbol{k}\big) \approx \boldsymbol{P}_s^{(0)}(\boldsymbol{k}),$$

(K3a,b)

applies to both ion and electron species. By analogy to the derivation presented in § 2.5.5, this approximation gives rise to a simplified dispersion relation (cf. (2.117))

$$\left(\tilde{\omega}_{e\parallel} \mathfrak{E}_{11}^{(0)} - \frac{k^2 c^2}{\omega^2} \right) \left(\tilde{\omega}_{e\parallel} \mathfrak{E}_{22}^{(0)} - \frac{k^2 c^2}{\omega^2} \right) + \left(\tilde{\omega}_{e\parallel} \mathfrak{E}_{12}^{(0)} \right)^2 = 0.$$

(K4)

We emphasise that, here, each component of $\mathfrak{E}^{(0)}$ has both electron and ion contributions. Expressing $\tilde{\omega}_{i\parallel} = \tilde{\omega}_{e\parallel} \mu_e^{-1/2}$ in (K2), (K4) can be written as

$$\begin{aligned}
&\left[\tilde{\omega}_{e\parallel}(\boldsymbol{M}_e^{(0)} + \mu_e^{1/2}\boldsymbol{M}_i^{(0)})_{11} + (\boldsymbol{P}_e^{(0)} + \mu_e^{1/2}\boldsymbol{P}_i^{(0)})_{11} - k^2 d_e^2 \right] \\
&\times \left[\tilde{\omega}_{e\parallel}(\boldsymbol{M}_e^{(0)} + \mu_e^{1/2}\boldsymbol{M}_i^{(0)})_{22} + (\boldsymbol{P}_e^{(0)} + \mu_e^{1/2}\boldsymbol{P}_i^{(0)})_{22} - k^2 d_e^2 \right] \\
&+ \left[\tilde{\omega}_{e\parallel}(\boldsymbol{M}_e^{(0)} + \mu_e^{1/2}\boldsymbol{M}_i^{(0)})_{12} + (\boldsymbol{P}_e^{(0)} + \mu_e^{1/2}\boldsymbol{P}_i^{(0)})_{12} \right]^2 = 0.
\end{aligned}$$

(K5)

Combining the expressions (K1) for $\boldsymbol{P}_s^{(0)}$ with (2.121) for $\boldsymbol{M}_s^{(0)}$ and substituting $\boldsymbol{M}_s^{(0)}$ and $\boldsymbol{P}_s^{(0)}$ into (K5) gives

$$
\left[i\tilde{\omega}_{e\parallel} \left(F_e + \mu_e^{1/2} F_i \right) + \epsilon_e \left(W_e + \mu_e^{1/2} W_i \right) - k_\parallel^2 d_e^2 \right]
$$
$$
\times \left[i\tilde{\omega}_{e\parallel} \left(H_e + \mu_e^{1/2} H_i \right) + \epsilon_e \left(Y_e + \mu_e^{1/2} Y_i \right) - k^2 d_e^2 \right]
$$
$$
+ \left[i\tilde{\omega}_{e\parallel} \left(G_e + \mu_e^{1/2} G_i \right) + \epsilon_e \left(X_e + \mu_e^{1/2} X_i \right) \right]^2 = 0, \tag{K6}
$$

where we have used $\epsilon_i = \epsilon_e \mu_e^{-1/2}$. For brevity of notation, we have also defined $F_s \equiv F(k_\parallel \tilde{\rho}_s, k_\perp \tilde{\rho}_s)$, $G_s \equiv G(k_\parallel \tilde{\rho}_s, k_\perp \tilde{\rho}_s)$ and so on.

Using (2.58b) for the terms $\propto d_e^2$ explicitly introduces a β_e dependence into (K6). After some elementary manipulations, we obtain the quadratic

$$
A_S \tilde{\omega}_{e\parallel}^2 \beta_e^2 + i B_S \tilde{\omega}_{e\parallel} \beta_e - C_S = 0, \tag{K7}
$$

where

$$
A_{\mathrm{S}} = \left(F_e + \mu_e^{1/2} F_i \right) \left(H_e + \mu_e^{1/2} H_i \right) + \left(G_e + \mu_e^{1/2} G_i \right)^2, \tag{K8a}
$$
$$
B_{\mathrm{S}} = \left(H_e + \mu_e^{1/2} H_i \right) \left[k_\parallel^2 \rho_e^2 - \epsilon_e \beta_e \left(W_e + \mu_e^{1/2} W_i \right) \right] - 2\epsilon_e \beta_e \left(G_e + \mu_e^{1/2} G_i \right) \left(X_e + \mu_e^{1/2} X_i \right)
$$
$$
+ \left(F_e + \mu_e^{1/2} F_i \right) \left[k^2 \rho_e^2 - \epsilon_e \beta_e \left(Y_e + \mu_e^{1/2} Y_i \right) \right], \tag{K8b}
$$
$$
C_{\mathrm{S}} = \left[k_\parallel^2 \rho_e^2 - \epsilon_e \beta_e \left(W_e + \mu_e^{1/2} W_i \right) \right] \left[k^2 \rho_e^2 - \epsilon_e \beta_e \left(Y_e + \mu_e^{1/2} \mathrm{Y}_i \right) \right]
$$
$$
+ \epsilon_e^2 \beta_e^2 \left(X_e + \mu_e^{1/2} X_i \right)^2. \tag{K8c}
$$

As before, this can be solved explicitly for the complex frequency

$$
\omega = \frac{\Omega_e}{\beta_e} k_\parallel \rho_e \frac{-i B_S \pm \sqrt{-B_S^2 + 4 A_S C_S}}{2 A_S}. \tag{K9}
$$

From this expression, we can extract the real frequency ϖ and the growth rate γ explicitly. In the case when $4 A_S C_S > B_S^2$, we have two oppositely propagating modes with the same growth rate:

$$
\varpi = \pm \frac{\Omega_e}{\beta_e} k_\parallel \rho_e \frac{\sqrt{-B_S^2 + 4 A_S C_S}}{2 A_S}, \tag{K10a}
$$
$$
\gamma = \frac{\Omega_e}{\beta_e} k_\parallel \rho_e \frac{B_S}{2 A_S}. \tag{K10b}
$$

For $4 A_S C_S < B_S^2$, both modes are non-propagating, with distinct growth rates

$$
\gamma = \frac{\Omega_e}{\beta_e} k_\parallel \rho_e \frac{B_S \pm \sqrt{B_S^2 - 4 A_S C_S}}{2 A_S}. \tag{K11}
$$

K.2.2. *Semi-analytic estimates of CES instability thresholds using quadratic approximation*

In the case of non-propagating modes whose growth rate is given by (K11), we can determine semi-analytic formulae for the thresholds of any instabilities. This is done by

noting that, at marginal stability, $\tilde{\omega}_{e\parallel} = 0$. Therefore, it follows from (K7) that $C_S = 0$, or, equivalently,

$$\left[k_\parallel^2 \rho_e^2 - \epsilon_e \beta_e \left(W_e + \mu_e^{1/2} W_i\right)\right] \left[k^2 \rho_e^2 - \epsilon_e \beta_e \left(Y_e + \mu_e^{1/2} Y_i\right)\right] + \epsilon_e^2 \beta_e^2 \left(X_e + \mu_e^{1/2} X_i\right)^2 = 0. \tag{K12}$$

This is a quadratic in $\epsilon_e \beta_e$ which can be solved exactly to give the threshold value of $\epsilon_e \beta_e$ as a function of perpendicular and parallel wavenumber,

$$\begin{aligned}
\epsilon_e \beta_e = {}& \tfrac{1}{2} \left[\left(W_e + \mu_e^{1/2} W_i\right) \left(Y_e + \mu_e^{1/2} Y_i\right) + \left(X_e + \mu_e^{1/2} X_i\right)^2\right]^{-1} \\
& \times \Big(k^2 \rho_e^2 \left(W_e + \mu_e^{1/2} W_i\right) + k_\parallel^2 \rho_e^2 \left(Y_e + \mu_e^{1/2} Y_i\right) \\
& \pm \Big\{\left[k^2 \rho_e^2 \left(W_e + \mu_e^{1/2} W_i\right) + k_\parallel^2 \rho_e^2 \left(Y_e + \mu_e^{1/2} Y_i\right)\right]^2 \\
& - 4 k_\parallel^2 k^2 \rho_e^4 \left[\left(W_e + \mu_e^{1/2} W_i\right) \left(Y_e + \mu_e^{1/2} Y_i\right) + \left(X_e + \mu_e^{1/2} X_i\right)^2\right]\Big\}^{1/2}\Big). \tag{K13}
\end{aligned}$$

Expression (K13) is used in §§ 4.4.1 and 4.4.7 to evaluate the wavevector-dependent thresholds of the CES ion and electron firehose instabilities, respectively.

K.2.3. *Shortcomings of quadratic approximation*

In contrast to quadratic approximations to the dispersion relations of CET microinstabilities being sufficient to characterise all instabilities of note (see, e.g. Appendix J.3), not all CES microinstabilities are captured by the quadratic dispersion relation (K7), because there are important microinstabilities whose correct description requires keeping higher-order terms in the $\tilde{\omega}_{s\parallel} \ll 1$ expansion. The mathematical reason for this is that some microinstabilities occur in wavenumber regimes where either $k_\parallel \rho_i \ll 1$ and/or $k_\parallel \rho_e \ll 1$. As a result, the issues raised in § 2.5.6 regarding the commutability of the $\tilde{\omega}_{s\parallel} \ll 1$ and $k_\parallel \rho_s \ll 1$ limits must be carefully resolved. In Appendix G.1.6, it is shown that, if $k_\parallel \rho_s \ll 1/\log(1/\tilde{\omega}_{s\parallel})$, then the dominant contributions to $(\boldsymbol{M}_s)_{xx}$, $(\boldsymbol{M}_s)_{xz}$ and $(\boldsymbol{M}_s)_{zz}$ arise from the quadratic term in $\tilde{\omega}_{s\parallel} \ll 1$ expansion, namely

$$(\boldsymbol{M}_s)_{xx} \approx \tilde{\omega}_{s\parallel}^2 (\boldsymbol{M}_s^{(1)})_{xx}, \tag{K14a}$$

$$(\boldsymbol{M}_s)_{xz} \approx \tilde{\omega}_{s\parallel}^2 (\boldsymbol{M}_s^{(1)})_{xz}, \tag{K14b}$$

$$(\boldsymbol{M}_s)_{zz} \approx \tilde{\omega}_{s\parallel}^2 (\boldsymbol{M}_s^{(1)})_{zz}. \tag{K14c}$$

If $k_\perp \rho_s \ll k_\parallel \rho_s \tilde{\omega}_{s\parallel}^{1/2}$, then

$$(\boldsymbol{M}_s)_{yy} \approx \tilde{\omega}_{s\parallel}^2 (\boldsymbol{M}_s^{(1)})_{yy}. \tag{K15}$$

In the $\{\boldsymbol{e}_1, \boldsymbol{e}_2, \boldsymbol{e}_3\}$ coordinate frame, this means that the dominant contributions to each component of $\boldsymbol{M}_s$ are (see Appendix G.1.3)

$$(\boldsymbol{M}_s)_{11} \approx \tilde{\omega}_{s\parallel}^2 (\boldsymbol{M}_s^{(1)})_{11} = \frac{k^2}{k_\parallel^2} \omega_{s\parallel}^2 (\boldsymbol{M}_s^{(1)})_{xx} + 2\tilde{\omega}_{s\parallel}^2 \left[\frac{k_\perp^2}{k^2} + \frac{k_\perp}{k_\parallel} L\left(k_\parallel \tilde{\rho}_s, k_\perp \tilde{\rho}_s\right)\right], \tag{K16a}$$

$$(\boldsymbol{M}_s)_{12} \approx \tilde{\omega}_{s\parallel} (\boldsymbol{M}_s^{(0)})_{12} = \frac{k}{k_\parallel} \tilde{\omega}_{s\parallel} (\boldsymbol{M}_s^{(0)})_{xy}, \tag{K16b}$$

$$(\boldsymbol{M}_s)_{13} \approx \tilde{\omega}_{s\parallel}^2 (\boldsymbol{M}_s^{(1)})_{13} = -\tilde{\omega}_{s\parallel}^2 \left[\frac{2k_\perp k_\parallel}{k^2} + L\left(k_\parallel \tilde{\rho}_s, k_\perp \tilde{\rho}_s\right)\right], \tag{K16c}$$

$$(\boldsymbol{M}_s)_{22} \approx \tilde{\omega}_{s\parallel}(\boldsymbol{M}_s^{(0)})_{22} + \tilde{\omega}_{s\parallel}^2(\boldsymbol{M}_s^{(1)})_{22} = \tilde{\omega}_{s\parallel}(\boldsymbol{M}_s^{(0)})_{yy} + \tilde{\omega}_{s\parallel}^2(\boldsymbol{M}_s^{(1)})_{yy}, \qquad (K16d)$$

$$(\boldsymbol{M}_s)_{23} \approx \tilde{\omega}_{s\parallel}^2(\boldsymbol{M}_s^{(1)})_{23} = -\frac{k_\parallel}{k}\tilde{\omega}_{s\parallel}^2 N\big(k_\parallel\tilde{\rho}_s, k_\perp\tilde{\rho}_s\big), \qquad (K16e)$$

$$(\boldsymbol{M}_s)_{33} \approx \tilde{\omega}_{s\parallel}^2(\boldsymbol{M}_s^{(1)})_{33} = \frac{2k_\parallel^2}{k^2}\tilde{\omega}_{s\parallel}^2, \qquad (K16f)$$

where the special functions $L(x, y)$ and $N(x, y)$ are given by (G32). The quadratic dispersion relation (K7) must, therefore, be revised to capture correctly all relevant microinstabilities.

K.3. *Quartic approximation to dispersion relation of CE shear-driven microinstabilities*
K.3.1. *Derivation of general quartic CES dispersion relation*

To assess how the new terms identified in § K.2.3 change the dispersion relation (K6), we now return to the full hot-plasma dispersion relation (2.75), which we write in the form

$$\left(\mathfrak{E}_{11} - \frac{k^2c^2}{\omega^2} - \frac{\mathfrak{E}_{13}^2}{\mathfrak{E}_{33}}\right)\left(\mathfrak{E}_{22} - \frac{k^2c^2}{\omega^2} + \frac{\mathfrak{E}_{23}^2}{\mathfrak{E}_{33}}\right) + \left(\mathfrak{E}_{12} - \frac{\mathfrak{E}_{13}\mathfrak{E}_{23}}{\mathfrak{E}_{33}}\right)^2 = 0. \qquad (K17)$$

Reminding the reader that, for a two-species plasma,

$$\mathfrak{E} = \sum_s \mathfrak{E}_s = \frac{\omega_{pe}^2}{\omega^2}\sum_s \mu_s\left(\boldsymbol{M}_s + \boldsymbol{P}_s\right), \qquad (K18)$$

and also that the electrostatic component of the dielectric tensor is determined by the Maxwellian components only (which in turn are equal for electrons and ions when $T_i = T_e$ – see Appendix D.2), *viz.*

$$\mathfrak{E}_{33} \approx \tilde{\omega}_{e\parallel}^2\mathfrak{E}_{33}^{(1)} = \frac{\omega_{pe}^2}{\omega^2}\sum_s \mu_s\tilde{\omega}_{s\parallel}^2(\boldsymbol{M}_s^{(1)})_{33} = \frac{4\omega_{pe}^2}{\omega^2}\tilde{\omega}_{e\parallel}^2\frac{k_\parallel^2}{k^2}, \qquad (K19)$$

we show in Appendix G.1.7 that, in the limit $k_\parallel\rho_s \ll 1$,

$$\frac{[(\boldsymbol{M}_s)_{13}]^2}{(\boldsymbol{M}_s^{(1)})_{33}} \lesssim (\boldsymbol{M}_s)_{11}, \qquad (K20a)$$

$$\frac{(\boldsymbol{M}_s)_{13}(\boldsymbol{M}_s)_{23}}{(\boldsymbol{M}_s^{(1)})_{33}} \lesssim \tilde{\omega}_{e\parallel}(\boldsymbol{M}_s)_{12} \ll (\boldsymbol{M}_s)_{12}, \qquad (K20b)$$

$$\frac{[(\boldsymbol{M}_s)_{23}]^2}{(\boldsymbol{M}_s^{(1)})_{33}} \lesssim \tilde{\omega}_{e\parallel}(\boldsymbol{M}_s)_{22} \ll (\boldsymbol{M}_s)_{22}. \qquad (K20c)$$

On the other hand, the shear-perturbation components $\boldsymbol{P}_s$ satisfy

$$(\boldsymbol{P}_s)_{11} \sim (\boldsymbol{P}_s)_{22} \gg (\boldsymbol{P}_s)_{12}. \qquad (K21)$$

Substituting for $\boldsymbol{M}_s$ and $\boldsymbol{P}_s$ in (K18) using (K16) and (K3b), respectively, and then substituting (K18) into (K17), we obtain the following quartic dispersion relation:

$$\left\{ \tilde{\omega}_{e\parallel}^2 \left[(\boldsymbol{M}_e^{(1)} + \boldsymbol{M}_i^{(1)})_{11} - \frac{(\boldsymbol{M}_e^{(1)} + \boldsymbol{M}_i^{(1)})_{13}^2}{2(\boldsymbol{M}_e^{(1)})_{33}} \right] + (\boldsymbol{P}_e^{(0)} + \mu_e^{1/2} \boldsymbol{P}_i^{(0)})_{11} - k^2 d_e^2 \right\}$$

$$\times \left\{ \tilde{\omega}_{e\parallel}^2 \left[(\boldsymbol{M}_e^{(1)} + \boldsymbol{M}_i^{(1)})_{22} \right] + \tilde{\omega}_{e\parallel} \left[(\boldsymbol{M}_e^{(0)} + \mu_e^{1/2} \boldsymbol{M}_i^{(0)})_{22} \right] + (\boldsymbol{P}_e^{(0)} + \mu_e^{1/2} \boldsymbol{P}_i^{(0)})_{22} - k^2 d_e^2 \right\}$$

$$+ \tilde{\omega}_{e\parallel}^2 \left[(\boldsymbol{M}_e^{(0)} + \mu_e^{1/2} \boldsymbol{M}_i^{(0)})_{12} \right]^2 = 0. \tag{K22}$$

We have assumed $k\rho_e \ll k\rho_i \ll 1$ and so we now have additional quadratic terms for both electrons and ions, as explained in § K.2.3.

We note that the dispersion relation (K22) is similar to (K6) except for the addition of two quadratic terms in $\tilde{\omega}_{e\parallel}$, and the absence of the linear terms $\tilde{\omega}_{e\parallel}(\boldsymbol{M}_s^{(0)})_{11}$ and $(\boldsymbol{P}_s^{(0)})_{12}$. This motivates our approach to finding modes at arbitrary wavevectors: we solve a quartic dispersion relation that includes all the terms in (K22) and also those linear terms which were present in (K6), but absent in (K22). Explicitly, this dispersion relation is

$$\left\{ -\tilde{\omega}_{e\parallel}^2 \left[\tfrac{4}{3} W_e + \tfrac{4}{3} W_i + \tfrac{1}{4} (L_e + L_i)^2 \right] + \mathrm{i}\tilde{\omega}_{e\parallel} \left(F_e + \mu_e^{1/2} F_i \right) + \epsilon_e \left(W_e + \mu_e^{1/2} W_i \right) - k_\parallel^2 d_e^2 \right\}$$

$$\times \left[-\tilde{\omega}_{e\parallel}^2 \left(\tfrac{4}{3} Y_i + \tfrac{4}{3} Y_e \right) + \mathrm{i}\tilde{\omega}_{e\parallel} \left(H_e + \mu_e^{1/2} H_i \right) + \epsilon_e \left(Y_e + \mu_e^{1/2} Y_i \right) - k^2 d_e^2 \right]$$

$$+ \left[\mathrm{i}\tilde{\omega}_{e\parallel} \left(G_e + \mu_e^{1/2} G_i \right) + \epsilon_e \left(X_e + \mu_e^{1/2} X_i \right) \right]^2 = 0, \tag{K23}$$

where $L_s \equiv L(k_\parallel \tilde{\rho}_s, k_\perp \tilde{\rho}_s)$. The special functions $W(x, y)$ and $Y(x, y)$, defined in (G97), appear due to their relationship to the matrix $(\boldsymbol{M}_s^{(1)})$ (derived in Appendix G.1.2)

$$W\left(k_\parallel \tilde{\rho}_s, k_\perp \tilde{\rho}_s\right) = -\tfrac{3}{4}(\boldsymbol{M}_s^{(1)})_{xx}, \tag{K24a}$$

$$Y\left(k_\parallel \tilde{\rho}_s, k_\perp \tilde{\rho}_s\right) = -\tfrac{3}{4}(\boldsymbol{M}_e^{(1)})_{yy}, \tag{K24b}$$

combined with the identity

$$(\boldsymbol{M}_e^{(1)} + \boldsymbol{M}_i^{(1)})_{11} - \frac{(\boldsymbol{M}_e^{(1)} + \boldsymbol{M}_i^{(1)})_{13}^2}{2(\boldsymbol{M}_e^{(1)})_{33}} = -\frac{k^2}{k_\parallel^2} \left[\frac{4}{3} W_e + \frac{4}{3} W_i + \frac{1}{4} (L_e + L_i)^2 \right], \tag{K25}$$

proven in Appendix G.1.7.

The dispersion relation (K23) recovers all the roots of interest because it captures approximate values for all of the roots of the dispersion relations (K7) and (K22) in their respective wavenumber regions of validity. We note that, in situations when there are fewer than four physical modes (e.g. in the $k_\parallel \rho_e \gtrsim 1$ regime), solving (K23) will also return non-physical modes that are the result of the addition of higher-order terms in a regime where such terms are illegitimate. However, by construction, such modes can be distinguished by their large magnitude ($\tilde{\omega}_{e\parallel} \sim 1$) as compared with the others. We acknowledge that our approach does not maintain consistent orderings: indeed, depending on the scale of a particular instability, there may be terms retained that are, in fact, smaller than other terms we have neglected when carrying out the $\tilde{\omega}_{i\parallel} \ll 1$ expansion. However, unlike the quadratic dispersion relation (K7), the quartic dispersion relation (K23) always captures the leading-order terms for arbitrary wavevectors, and so provides reasonable approximations to the complex frequency of all possible CES microinstabilities.

K.3.2. *Derivation of frequency and growth rate of the CES mirror instability*

To derive the CES mirror instability's growth rate when it is close to marginality, we consider the dispersion relation (K23) under the orderings (4.6*a,b*), *viz.*

$$k_\parallel \rho_i \sim k_\perp^2 \rho_i^2 \sim \Gamma_i \ll 1, \quad \tilde{\omega}_{i\parallel} = \mu_e^{-1/2} \tilde{\omega}_{e\parallel} \sim \frac{\Gamma_i}{\beta_i}, \tag{K26a,b}$$

where $\Gamma_i = \Delta \beta_i - 1$, and $\Delta = \Delta_i + \Delta_e = 3(\epsilon_i + \epsilon_e)/2$. Using the asymptotic identities (G37) for the special functions F_s, G_s, H_s, L_s and N_s and (G101) for W_s, X_s and Y_s, (K23) becomes, after dropping terms that are asymptotically small under the ordering (K26*a,b*),

$$i\sqrt{\pi} k_\perp^2 \rho_i^2 \tilde{\omega}_{i\parallel} + \Delta \left(k_\perp^2 \rho_i^2 - \frac{1}{2} k_\parallel^2 \rho_i^2 - \frac{3}{4} k_\perp^4 \rho_i^4 \right) - \frac{k^2 \rho_i^2}{\beta_i} = 0, \tag{K27}$$

which in turn can be rearranged to give (4.7) in §4.3.1 and the subsequent results. We note that, save for the term $\propto G_e$, which cancels to leading order with its ion equivalent, and the term $\propto Y_e$, which we retain in order to capture correctly the mirror instability's exact stability threshold, the electron terms in (K23) are negligibly small under the ordering (K26*a,b*). We also observe that by assuming frequency ordering (K26*a,b*), we have removed the shear-Alfvén wave from the dispersion relation. As we demonstrate when characterising the growth rate of firehose-unstable shear-Alfvén waves (see §4.4.3 and Appendix K.3.7), a different ordering is required to extract this mode (which is, in any case, stable for $\Delta_i > 0$).

To derive the growth rate of long-wavelength ($k_\parallel \rho_i \sim k_\perp \rho_i \ll 1$) mirror modes away from marginality, when $\Gamma_i \gtrsim 1$, we adopt the alternative ordering (4.9*a,b*), which is equivalent to

$$\tilde{\omega}_{i\parallel} \sim \frac{1}{\beta_i} \sim \Delta \ll 1. \tag{K28}$$

Again using the identities (G37) and (G101) to evaluate the special functions, the dispersion relation (K23) is then

$$i\sqrt{\pi} k_\perp^2 \rho_i^2 \tilde{\omega}_{i\parallel} + \Delta \left(k_\perp^2 \rho_i^2 - \frac{1}{2} k_\parallel^2 \rho_i^2 \right) - \frac{k^2 \rho_i^2}{\beta_i} = 0, \tag{K29}$$

which, after some algebraic manipulation, gives (4.11) in §4.3.1 and the subsequent results.

Finally, the expression (4.16) for the growth rate of sub-ion-Larmor scale mirror modes is derived by adopting the orderings (4.14*a,b*):

$$k_\parallel \rho_i \sim k_\perp \rho_i \sim (\Delta_i \beta_i)^{1/2} \gg 1, \quad \tilde{\omega}_{i\parallel} \sim \frac{\Delta_i^{1/2}}{\beta_i^{1/2}}, \tag{K30a,b}$$

and then using the asymptotic identities (G35) for evaluating F_i, G_i, H_i, L_i and N_i, (G37) for F_e, G_e, H_e, L_e and N_e, (G99) for W_i, X_i and Y_i and (G101) for W_e, X_e and Y_e. Once again neglecting small terms under the assumed ordering, the dispersion relation (K23) simplifies to a quadratic of the form (K6):

$$\left[-\frac{\Delta_i}{2} \frac{2k_\parallel^2 \left(k_\parallel^2 - k_\perp^2 \right)}{k^4} + \frac{k_\parallel^2 \rho_i^2}{\beta_i} \right] \left(-\Delta_i \frac{k_\parallel^2}{k^2} + \frac{k^2 \rho_i^2}{\beta_i} \right) - \tilde{\omega}_{i\parallel}^2 k_\parallel^2 \rho_i^2 = 0, \tag{K31}$$

from which follow (4.16) and the subsequent results in §4.3.1.

K.3.3. *Derivation of frequency and growth rate of the parallel CES whistler instability*

We derive the expressions (4.21) for the real frequency and growth rate of the parallel CES whistler instability by adopting the ordering (4.20*a,b*)

$$\tilde{\omega}_{e\parallel} \sim \Delta_e \sim \frac{1}{\beta_e}, \quad k_\parallel \rho_e \sim 1, \tag{K32a,b}$$

and evaluating F_s, G_s, H_s, L_s and N_s via (G34), and W_s, X_s and Y_s via (G98). The special functions with $s = i$ are simplified further by assuming additionally that $k_\parallel \rho_i \gg 1$. Under these assumptions and simplifications, the dispersion relation (K23) becomes

$$\left\{ i\tilde{\omega}_{e\parallel} \sqrt{\pi} \left[\exp\left(-\frac{1}{k_\parallel^2 \rho_e^2} \right) + \mu_e^{1/2} \right] + \Delta_e \left[1 + \frac{1}{k_\parallel \rho_e} \operatorname{Re} Z\left(\frac{1}{k_\parallel \rho_e} \right) + \mu_e^{1/2} \right] - \frac{k_\parallel^2 \rho_e^2}{\beta_e} \right\}^2$$

$$+ \left\{ i\tilde{\omega}_{e\parallel} \operatorname{Re} Z\left(\frac{1}{k_\parallel \rho_e} \right) - \frac{\Delta_e}{k_\parallel \rho_e} \left[\sqrt{\pi} \exp\left(-\frac{1}{k_\parallel^2 \rho_e^2} \right) + \mu_e \right] \right\}^2 = 0, \tag{K33}$$

where we have substituted $\tilde{\rho}_e = -\rho_e$, and the only ion terms that we retain – the terms proportional to $\mu_e^{1/2}$ or μ_e – are those that we find to affect the dispersion relation qualitatively (as explained in the main text, these terms are formally small under the assumed ordering, but cannot be neglected in certain subsidiary limits, e.g. $k_\parallel \rho_e \ll 1$, which we will subsequently wish to explore). (K33) can then be factorised to give two complex roots, the real and imaginary parts of which become (4.21*a*) and (4.21*b*), respectively.

K.3.4. *Derivation of frequency and growth rate of the CES transverse instability*

To obtain the growth rate (4.29*b*) of the two CES transverse modes, we take directly the unmagnetised limit of the full CES dispersion relation (K23) under the orderings

$$k_\perp \rho_e \sim k_\parallel \rho_e \sim (\Delta_e \beta_e)^{1/2} \gg 1, \quad \tilde{\omega}_{e\parallel} \sim \Delta_e \ll 1, \tag{K34a,b}$$

and then employ asymptotic identities (G35) for F_s, G_s, H_s, L_s and N_s, and (G99) for W_s, X_s and Y_s. We then obtain a dispersion relation similar to (K6), but with two separable roots:

$$\left[i\tilde{\omega}_{e\parallel} \sqrt{\pi} \frac{k_\parallel^3}{k^3} + \Delta_e \frac{k_\parallel^2 (k_\parallel^2 - k_\perp^2)}{k^4} - \frac{k_\parallel^2 \rho_e^2}{\beta_e} \right] \left(i\tilde{\omega}_{e\parallel} \sqrt{\pi} \frac{k_\parallel}{k} + \Delta_e \frac{k_\parallel^2}{k^2} - \frac{k^2 \rho_e^2}{\beta_e} \right) = 0. \tag{K35}$$

When rearranged, the first bracket gives expression (4.29*a*), and the second bracket gives (4.29*b*).

K.3.5. *Derivation of frequency and growth rate of the CES electron mirror instability*

When its marginality parameter $\Gamma_e = \Delta_e \beta_e - 1$ is small, the growth rate (4.35) (and zero real frequency) of the CES electron mirror instability's can be derived from the dispersion relation (K23) by adopting the ordering (4.34), *viz.*

$$k_\perp^2 \rho_e^2 \sim k_\parallel \rho_e \sim \tilde{\omega}_{e\parallel} \beta_e \sim \Gamma_e \ll 1, \tag{K36}$$

and assuming that $\Gamma_e \gg \mu_e^{1/2}$. This latter inequality implies that $1 \ll k_\parallel \rho_i \ll k_\perp \rho_i$, so we use the asymptotic identities (G35) to simplify F_i, G_i, H_i, L_i and N_i, (G99) to simplify W_i,

X_i and Y_i, (G37) for F_e, G_e, H_e, L_e and N_e, and (G101) for W_e, X_e and Y_e. Collecting terms, using the identity $\Delta_e = (1 + \Gamma_e)/\beta_e$, and keeping only leading-order ones, the dispersion relation simplifies to

$$\frac{3}{2\beta_e}k_\parallel^2\rho_e^2\left(-\frac{\Gamma_e}{\beta_e}k_\perp^2\rho_e^2 + \frac{3}{2\beta_e}k_\parallel^2\rho_e^2 + \frac{3}{4\beta_e}k_\perp^4\rho_e^4 + i\sqrt{\pi}k_\perp^2\rho_e^2\tilde{\omega}_{e\parallel}\right) - \tilde{\omega}_{e\parallel}^2 k_\parallel^2\rho_e^2 = 0. \quad \text{(K37)}$$

Because the discriminant of the quadratic (K37) is negative, it follows that its solution satisfies $\omega = i\gamma$, with γ being given by (4.35).

To derive the expression (4.39) for the complex frequency of long-wavelength electron mirror modes, we adopt the ordering (4.38),

$$\tilde{\omega}_{e\parallel} \sim \frac{k\rho_e}{\beta_e} \sim \Delta_e k\rho_e, \quad \text{(K38)}$$

and then consider the subsidiary limit $k_\parallel\rho_e \sim k_\perp\rho_e \sim \mu_e^{1/4} \ll 1$ of the dispersion relation (K23). Using the asymptotic identities (G35) for F_i, G_i, H_i, L_i and N_i, (G37) for F_e, G_e, H_e, L_e and N_e, (G99) for W_i, X_i and Y_i and (G101) for W_e, X_e and Y_e, we find that

$$\left\{\frac{\Delta_e}{2}\left[k_\parallel^2\rho_e^2 - \mu_e^{1/2}\frac{2k_\parallel^2\left(k_\parallel^2 - k_\perp^2\right)}{k^4}\right] + \frac{k_\parallel^2\rho_e^2}{\beta_e}\right\}$$
$$\times \left[\frac{\Delta_e}{2}\left(k_\parallel^2\rho_e^2 - 2k_\perp^2\rho_e^2 - \mu_e^{1/2}\frac{2k_\parallel^2}{k^2}\right) + \frac{k^2\rho_e^2}{\beta_e}\right] - \tilde{\omega}_{e\parallel}^2 k_\parallel^2\rho_e^2 = 0, \quad \text{(K39)}$$

where both the CE ion- and electron-shear terms are kept on account of their equal size under the assumed ordering. Solving for ω gives (4.39).

K.3.6. *Derivation of frequency and growth rate of the parallel CES firehose instability*

The relevant orderings of parameters to adopt in order to derive the complex frequency (4.47) of the parallel CES firehose instability is (4.45), *viz.*

$$\tilde{\omega}_{i\parallel} \sim \frac{1}{\beta_i^{1/2}} \sim |\Delta_i|^{1/2} \sim k_\parallel\rho_i \ll 1, \quad \text{(K40)}$$

with an additional small wavenumber-angle condition $k_\perp\rho_i \ll \beta_i^{-3/4}$ (which we shall justify *a posteriori*). Under this ordering, the special functions F_s, G_s, H_s, L_s and N_s can be simplified using (G37), and W_s, X_s and Y_s using (G101), and so the dispersion relation (K23) reduces to

$$\left(\tilde{\omega}_{i\parallel}^2 - \frac{\Delta_i}{2} - \frac{1}{\beta_i}\right)^2 - \frac{\tilde{\omega}_{i\parallel}^2}{4}k_\parallel^2\rho_i^2 = 0, \quad \text{(K41)}$$

where the only non-negligible electron term is the one $\propto \tilde{\omega}_{e\parallel}G_e$. Similarly to the CES mirror instability (see Appendix K.3.2), this term cancels to leading order with its ion equivalent, and the next-order electron term is much smaller than the equivalent ion term. This dispersion relation can be rearranged to give (4.47).

We also note that, in deriving (K41) from (K23), we have assumed that the linear term $\propto \tilde{\omega}_{e\parallel}\mu_e^{1/2}H_i$ is much smaller than the quadratic term $\propto \tilde{\omega}_{e\parallel}^2 Y_i$; their relative magnitude is

given by

$$\frac{\tilde{\omega}_{e\parallel}\mu_e^{1/2}H_i}{\tilde{\omega}_{e\parallel}^2 Y_i} \sim \frac{k_\perp^2 \rho_i^2}{\tilde{\omega}_{i\parallel}k_\parallel^2 \rho_i^2} \sim \beta_i^{3/2}k_\perp^2 \rho_i^2. \tag{K42}$$

Thus, this assumption (which it is necessary to make in order for there to be both left-handed and right-handed Alfvén modes in high-β plasma) is only justified if the small-angle condition $k_\perp \rho_i \ll \beta_i^{-3/4} \ll 1$ holds true.

K.3.7. *Derivation of frequency and growth rate of the oblique CES firehose instability*

To derive the oblique firehose's growth rate (4.52), we use the ordering (4.51), *viz.*

$$\tilde{\omega}_{i\parallel} \sim \frac{1}{\beta_i^{1/2}} \sim |\Delta_i|^{1/2} \sim k_\parallel^2 \rho_i^2 \sim k_\perp^2 \rho_i^2 \ll 1. \tag{K43}$$

Simplifying the special functions F_s, G_s, H_s, L_s and N_s via (G37), and W_s, X_s and Y_s via (G101), the dispersion relation (K23) becomes

$$i\sqrt{\pi}\left(\tilde{\omega}_{i\parallel}^2 - \frac{\Delta_i}{2} - \frac{1}{\beta_i}\right)k_\perp^2 \rho_i^2 \tilde{\omega}_{i\parallel} - \frac{\tilde{\omega}_{i\parallel}^2}{4}\left(k_\parallel^2 \rho_i^2 - \frac{3}{2}k_\perp^2 \rho_i^2\right)^2 = 0, \tag{K44}$$

where, in contrast to the quasi-parallel firehose, the linear term $\propto \tilde{\omega}_{e\parallel}\mu_e^{1/2}H_i$ in (K23) is larger than the quadratic term $\propto \tilde{\omega}_{e\parallel}^2 Y_i$. (K44) can be solved to give two roots: $\omega \approx 0$, corresponding to the stable slow mode (whose damping rate is asymptotically small under the assumed ordering), and the expression (4.52) for the complex frequency of the (sometimes firehose-unstable) shear-Alfvén mode.

K.3.8. *Derivation of frequency and growth rate of the critical-line CES firehose instability*

To characterise the growth of the critical-line firehose when $\beta_i \gg 10^6$, we set $k_\perp = 2k_\parallel/3$, and order

$$\tilde{\omega}_{i\parallel} \sim \beta_i^{-3/5} \sim k_\parallel^6 \rho_i^6 \sim \left|\Delta_i + \frac{2}{\beta_i}\right|^{1/2}. \tag{K45}$$

The dispersion relation (K23) transforms similarly to (K44) in this case, with two important exceptions: first, the term in (K23) $\propto \tilde{\omega}_{e\parallel}G_e + \mu_e^{1/2}\tilde{\omega}_{e\parallel}G_i$ is $O(k_\parallel^5 \rho_i^5)$ on the critical line, rather than $O(k_\parallel^3 \rho_i^3)$; secondly, our choice of ordering requires that we retain $O(k_\parallel^4 \rho_i^4)$. This gives

$$i\sqrt{\pi}\left(\tilde{\omega}_{i\parallel}^2 - \frac{1}{2}\Delta_i - \frac{1}{\beta_i} - \frac{5}{8}\Delta_i k_\parallel^2 \rho_i^2\right)\tilde{\omega}_{i\parallel} - \frac{6889}{13\,824}\tilde{\omega}_{i\parallel}^2 k_\parallel^6 \rho_i^6 = 0. \tag{K46}$$

To obtain the expression (4.57) for the critical-line firehose's growth rate in the limit $\beta_i \gg 10^6$ that is valid under the ordering (4.56), we consider the subsidiary limit

$$\left|\Delta_i + \frac{2}{\beta_i}\right| \gg \beta_i^{-6/5}, \tag{K47}$$

in which case (K46) becomes

$$i\sqrt{\pi}\left(\tilde{\omega}_{i\parallel}^2 - \frac{\Delta_i}{2} - \frac{1}{\beta_i}\right)\tilde{\omega}_{i\parallel} - \frac{6889}{13\,824}\tilde{\omega}_{i\parallel}^2 k_\parallel^6 \rho_i^6 = 0. \tag{K48}$$

The expression (4.57) follows from solving (K48) for ω (and once again neglecting the $\omega \approx 0$ solution).

The expression (4.61) for the growth of critical-line firehose modes when $\beta_i \simeq -2/\Delta_i \gg 10^6$, can be deduced by considering the opposite subsidiary limit to (K47), *viz.*

$$\left| \Delta_i + \frac{2}{\beta_i} \right| \ll \beta_i^{-6/5}. \tag{K49}$$

In this limit, (K46) simplifies to

$$i\sqrt{\pi} \left(\tilde{\omega}_{i\parallel}^2 + \frac{5}{4\beta_i} k_\parallel^2 \rho_i^2 \right) \tilde{\omega}_{i\parallel} - \frac{6889}{13\,824} \tilde{\omega}_{i\parallel}^2 k_\parallel^6 \rho_i^6 = 0. \tag{K50}$$

Noting that the quadratic (K50) has a negative discriminant, we deduce that $\omega = i\gamma$; then solving (K50) for γ gives (4.61).

When $\beta_i \ll 10^6$, the appropriate ordering to adopt in order to simplify the dispersion relation of critical-line is no longer (K51*a,b*), but instead

$$\tilde{\omega}_{i\parallel} \sim \frac{1}{\sqrt{\beta_i \log \beta_i}} \sim \left| \Delta_i + \frac{2}{\beta_i} \right|^{1/2}, \quad k_\parallel \rho_i \sim \frac{1}{\sqrt{\log \beta_i}}. \tag{K51a,b}$$

Under this ordering, the term $\propto \mu_e^{1/2} \tilde{\omega}_{e\parallel} F_i$ in (K23) is retained, while the term $\propto \tilde{\omega}_{e\parallel} G_e + \mu_e^{1/2} \tilde{\omega}_{e\parallel} G_i$ is neglected. This gives

$$\left[\tilde{\omega}_{i\parallel}^2 + i\frac{\sqrt{\pi}}{k_\parallel^2 \rho_i^2} \exp\left(-\frac{1}{k_\parallel^2 \rho_i^2} \right) \tilde{\omega}_{i\parallel} - \frac{1}{2}\Delta_i - \frac{1}{\beta_i} - \frac{5}{8}\Delta_i k_\parallel^2 \rho_i^2 \right] \tilde{\omega}_{i\parallel} = 0. \tag{K52}$$

To obtain the expression (4.65) for the critical-line firehose instability's growth rate in the case when ordering (4.64*a,b*) holds – that is, when $\Delta_i \beta_i + 2| \sim 1$, we consider the appropriate subsidiary limit of (K52)

$$\left| \Delta_i + \frac{2}{\beta_i} \right| \gg \frac{1}{\beta_i \log \beta_i}. \tag{K53}$$

In this case, the last term in the square brackets on the left-hand side of (K52) can be neglected, leaving the only non-trivial roots to satisfy

$$\tilde{\omega}_{i\parallel}^2 + i\frac{\sqrt{\pi}}{k_\parallel^2 \rho_i^2} \exp\left(-\frac{1}{k_\parallel^2 \rho_i^2} \right) \tilde{\omega}_{i\parallel} - \frac{\Delta_i}{2} - \frac{1}{\beta_i} = 0, \tag{K54}$$

whence (4.65) follows immediately. The case of growth when $\Delta_i \simeq -2/\beta_i$ can be recovered from the opposite subsidiary limit

$$\left| \Delta_i + \frac{2}{\beta_i} \right| \ll \frac{1}{\beta_i \log \beta_i}. \tag{K55}$$

In this case, the dispersion relation of the critical-line firehose modes is

$$\tilde{\omega}_{i\parallel}^2 + i\frac{\sqrt{\pi}}{k_\parallel^2 \rho_i^2} \exp\left(-\frac{1}{k_\parallel^2 \rho_i^2} \right) \tilde{\omega}_{i\parallel} + \frac{5}{4\beta_i} k_\parallel^2 \rho_i^2 = 0, \tag{K56}$$

which, when solved for the growth rate $\gamma = -i\omega$, gives (4.68).

K.3.9. *Derivation of frequency and growth rate of the CES parallel electron firehose instability*

This derivation is identical to that given in Appendix K.3.3 for the frequency and growth rate of the parallel CES whistler instability, and the same expressions (4.21) are used in § 4.4.7.

K.3.10. *Derivation of frequency and growth rate of the CES oblique electron firehose instability*

The complex frequency (4.86) of the electron-firehose modes with $\mu_e^{1/2} \ll k_\parallel \rho_e \ll k_\perp \rho_e \sim 1$ is derived by applying the ordering

$$\tilde{\omega}_{e\parallel} \sim |\Delta_e| \sim \frac{1}{\beta_e} \tag{K57}$$

to (K23) and using the asymptotic identities (G35) for F_i, G_i, H_i, L_i and N_i, (G36) for F_e, G_e, H_e, L_e and N_e, (G99) for W_i, X_i and Y_i and (G100) for W_e, X_e and Y_e. We obtain the simplified dispersion relation

$$\left\{ -\Delta_e \frac{k_\parallel^2}{k_\perp^2} \left[1 - \exp\left(-\frac{k_\perp^2 \rho_e^2}{2} \right) I_0 \left(\frac{k_\perp^2 \rho_e^2}{2} \right) \right] - \frac{k_\parallel^2 \rho_e^2}{\beta_e} \right\}$$

$$\times \left\{ \left(i\sqrt{\pi}\tilde{\omega}_{e\parallel} + \Delta_e \right) k_\perp^2 \rho_e^2 \exp\left(-\frac{k_\perp^2 \rho_e^2}{2} \right) \left[I_0 \left(\frac{k_\perp^2 \rho_e^2}{2} \right) - I_1 \left(\frac{k_\perp^2 \rho_e^2}{2} \right) \right] - \frac{k^2 \rho_e^2}{\beta_e} \right\}$$

$$- k_\parallel^2 \rho_e^2 \tilde{\omega}_{e\parallel}^2 \exp\left(-k_\perp^2 \rho_e^2 \right) \left[I_0 \left(\frac{k_\perp^2 \rho_e^2}{2} \right) - I_1 \left(\frac{k_\perp^2 \rho_e^2}{2} \right) \right]^2 = 0. \tag{K58}$$

Introducing the special functions $\mathcal{F}(k_\perp \rho_e)$ and $\mathcal{H}(k_\perp \rho_e)$ given by (4.89), and then rearranging (K58), leads to (4.86).

K.3.11. *Derivation of frequency and growth rate of the CES EST instability*

To derive the expression (4.97) for the growth rate of the EST instability in the limits $\mu_e^{1/2} \ll k_\parallel \rho_e \ll 1 \ll k_\perp \rho_e \ll \beta_e^{1/7}$, and $\Delta_e \beta_e \gg 1$, we apply the orderings (4.96*a*–*c*), *viz.*

$$k_\perp \rho_e \sim (\Delta_e \beta_e)^{1/2}, \quad \tilde{\omega}_{e\parallel} \sim \Delta_e^{5/2} \beta_e^{3/2}, \quad k_\parallel \rho_e \sim \frac{1}{\sqrt{\log |\Delta_e|\beta_e}} \ll 1 \tag{K59a–c}$$

to (K23). We then use the asymptotic identities (G35) for F_i, G_i, H_i, L_i and N_i, (G38) for F_e, G_e, H_e, L_e and N_e, (G99) for W_i, X_i and Y_i and (G102) for W_e, X_e and Y_e to give

$$i \frac{\tilde{\omega}_{e\parallel}}{k_\perp \rho_e} \left\{ i \frac{\tilde{\omega}_{e\parallel}}{k_\perp^3 \rho_e^3} \left[4 \exp\left(-\frac{1}{k_\parallel^2 \rho_e^2} \right) + \sqrt{\pi} \mu_e^{1/2} k_\parallel^3 \rho_e^3 \right] - \Delta_e \frac{k_\parallel^2 \rho_e^2}{k_\perp^2 \rho_e^2} - \frac{k_\parallel^2 \rho_e^2}{\beta_e} \right\} - \frac{k_\parallel^2 \rho_e^2 \tilde{\omega}_{e\parallel}^2}{\pi k_\perp^6 \rho_i^6} = 0, \tag{K60}$$

where the only ion contribution that is not always small, and thus cannot be neglected, is the term proportional to $\mu_e^{1/2}$. Solving for the frequency gives $\omega \approx 0$ – corresponding to a damped mode whose frequency is asymptotically small under the assumed ordering (K59*a*–*c*) – and the EST mode, whose growth rate is given by (4.97).

K.3.12. *Derivation of frequency and growth rate of the CES whisper instability*
In the limits $\mu_e^{1/2} \ll k_\parallel \rho_e \ll 1 \gg k_\perp \rho_e$ and $\Delta_e \beta_e \gg 1$ under the orderings

$$\tilde{\omega}_{e\parallel} \sim \frac{1}{\beta_e^{2/7}} \sim \frac{1}{k_\perp^2 \rho_e^2} \sim \frac{1}{\Delta_e \beta_e}, \quad k_\parallel \rho_e \sim \frac{1}{\sqrt{\log |\Delta_e| \beta_e}} \ll 1, \tag{K61a,b}$$

the dispersion relation (K23) becomes

$$i\frac{\tilde{\omega}_{e\parallel}}{k_\perp \rho_e} \left\{ \frac{k_\parallel^2 \rho_e^2}{k_\perp^2 \rho_e^2} \frac{4\tilde{\omega}_{e\parallel}^2}{\sqrt{\pi} k_\perp \rho_e} + i\frac{4\tilde{\omega}_{e\parallel}}{k_\parallel^3 \rho_e^3} \exp\left(-\frac{1}{k_\parallel^2 \rho_e^2}\right) - \Delta_e \frac{k_\parallel^2 \rho_e^2}{k_\perp^2 \rho_e^2} - \frac{k_\parallel^2 \rho_e^2}{\beta_e} \right\} - \frac{k_\parallel^2 \rho_e^2 \tilde{\omega}_{e\parallel}^2}{\pi k_\perp^6 \rho_e^6} = 0, \tag{K62}$$

where we have once again evaluated F_i, G_i, H_i, L_i and N_i using (G35), F_e, G_e, H_e, L_e and N_e using (G38), W_i, X_i and Y_i using (G99) and W_e, X_e and Y_e using (G102), and neglected all terms that are small under the ordering (K61a,b). Solving for the non-trivial root of (K62) gives the expression (4.105) for the complex frequency of whisper waves.

K.3.13. *Derivation of frequency and growth rate of the CES ordinary-mode instability*
Because the low-frequency assumption $\tilde{\omega}_{e\parallel} \ll 1$ is broken in the regime of relevance to the CES ordinary-mode instability, the dispersion relation (K23) is not valid; to characterise these modes, we must instead return to considering the full hot-plasma dispersion relation.

We choose to categorise the ordinary-mode instability for modes with $k_\parallel = 0$. In this special case, the plasma dielectric tensor simplifies considerably, and has the convenient property that

$$\hat{z} \cdot \mathfrak{E} = \left(\hat{z} \cdot \mathfrak{E} \cdot \hat{z}\right) \hat{z} \tag{K63}$$

if the particle distribution functions have even parity with respect to the parallel velocity $v_\parallel$ (Davidson 1983) – a condition satisfied by the CE distribution functions (4.1). Thus, perturbations whose associated eigenmode satisfies $\widehat{\delta E} = \widehat{\delta E_z} \hat{z}$ decouple from other modes in the plasma. The dispersion relation for such modes follows from (2.4.1):

$$\mathfrak{E}_{zz} - \frac{c^2 k_\perp^2}{\omega^2} = 0. \tag{K64}$$

In terms of matrices $\boldsymbol{M}_s$ and $\boldsymbol{P}_s$ defined by (2.97), this can be written

$$\sum_s (\boldsymbol{M}_s)_{zz} + \sum_s (\boldsymbol{P}_s)_{zz} - k_\perp^2 d_e^2 = 0. \tag{K65}$$

For $k_\parallel = 0$, the matrix components $(\boldsymbol{M}_s)_{zz}$ and $(\boldsymbol{P}_s)_{zz}$ are given by (see (G17i) and (G93i))

$$(\boldsymbol{M}_s)_{zz} = -\sum_{n=-\infty}^\infty \frac{\omega}{\omega - n\tilde{\Omega}_s} \exp\left(-\frac{k_\perp^2 \tilde{\rho}_s^2}{2}\right) I_n\left(\frac{k_\perp^2 \tilde{\rho}_s^2}{2}\right), \tag{K66a}$$

$$(\boldsymbol{P}_s)_{zz} = -\frac{3\epsilon_s}{2} \sum_{n=-\infty}^\infty \exp\left(-\frac{k_\perp^2 \tilde{\rho}_s^2}{2}\right) I_n\left(\frac{k_\perp^2 \tilde{\rho}_s^2}{2}\right) = -\Delta_s. \tag{K66b}$$

Therefore, the dispersion relation ([K65]) becomes

$$k_\perp^2 d_e^2 = -\sum_s \frac{m_e}{m_s} \left[\Delta_s + \sum_{n=-\infty}^{\infty} \frac{\omega}{\omega - n\tilde{\Omega}_s} \exp\left(-\frac{k_\perp^2 \tilde{\rho}_s^2}{2}\right) I_n\left(\frac{k_\perp^2 \tilde{\rho}_s^2}{2}\right) \right]$$

$$= -\sum_s \frac{m_e}{m_s} \left[\Delta_s + \sum_{n=1}^{\infty} \frac{2\omega^2}{\omega^2 - n^2\tilde{\Omega}_s^2} \exp\left(-\frac{k_\perp^2 \tilde{\rho}_s^2}{2}\right) I_n\left(\frac{k_\perp^2 \tilde{\rho}_s^2}{2}\right) \right]. \qquad \text{(K67)}$$

Since the left-hand side of ([K67]) is real, and the imaginary part of the right-hand side is non-zero if and only if the complex frequency ω has non-zero real and imaginary parts, we conclude that all solutions must be either purely propagating, or purely growing modes. Looking for purely growing roots, we substitute $\omega = i\gamma$ into ([K67]), and deduce that

$$\sum_s \frac{m_e}{m_s} \left[\sum_{n=1}^{\infty} \frac{2\gamma^2}{\gamma^2 + n^2\tilde{\Omega}_s^2} \exp\left(-\frac{k_\perp^2 \tilde{\rho}_s^2}{2}\right) I_n\left(\frac{k_\perp^2 \tilde{\rho}_s^2}{2}\right) \right]$$

$$= -k_\perp^2 d_e^2 - \sum_s \frac{m_e}{m_s} \left[\Delta_s + \exp\left(-\frac{k_\perp^2 \tilde{\rho}_s^2}{2}\right) I_0\left(\frac{k_\perp^2 \tilde{\rho}_s^2}{2}\right) \right]. \qquad \text{(K68)}$$

Neglecting the ion contributions (which are smaller than the electron ones by a $(m_e/m_i)^{1/2}$ factor) and considering $\Delta_e < 0$, we arrive at ([4.113]).

REFERENCES

ABU-SHAWAREB, H., *et al.* 2022 Lawson criterion for ignition exceeded in an inertial fusion experiment. *Phys. Rev. Lett.* **129**, 075001.

ACHTERBERG, A. 2013 Mirror, firehose and cosmic-ray-driven instabilities in a high-beta plasma. *Mon. Not. R. Astron. Soc.* **436**, 705.

ALBRIGHT, N.W. 1970*a* Quasilinear stabilization of the transverse instability. *Phys. Fluids* **13**, 1021.

ALBRIGHT, N.W. 1970*b* Transverse wave instability driven by shear flow in an unmagnetized plasma. *Phys. Plasmas* **13**, 2728.

ASTFALK, P. & JENKO, F. 2016 Parallel and oblique firehose instability thresholds for bi-kappa distributed protons. *J. Geophys. Res.* **121**, 2842.

BALBUS, S.A. 2000 Stability, instability, and "backward" transport in stratified fluids. *Astrophys. J.* **534**, 420.

BALBUS, S.A. 2001 Convective and rotational stability of a dilute plasma. *Astrophys. J.* **562**, 909.

BALBUS, S.A. 2004 Viscous shear instability in weakly magnetized, dilute plasmas. *Astrophys. J.* **616**, 857.

BALBUS, S.A. & HAWLEY, J.F. 1991 A powerful local shear instability in weakly magnetized disks. I. Linear analysis. *Astrophys. J.* **376**, 214.

BARKANA, R. & LOEB, A. 2001 In the beginning: the first sources of light and the reionization of the universe. *Phys. Rept.* **349**, 125.

BARNES, A. 1966 Collisionless damping of hydromagnetic waves. *Phys. Fluids* **9**, 1483.

BASU, B. & COPPI, B. 1984 Theory of field-swelling instability in anisotropic plasmas. *Phys. Fluids* **27**, 1187.

BELL, A.R., EVANS, R.G. & NICHOLAS, D.J. 1981 Electron energy transport in steep temperature gradients in laser-produced plasmas. *Phys. Rev. Lett.* **46**, 243.

BELL, A.R., KINGHAM, R.J., WATKINS, H.C. & MATTHEWS, J.H. 2020 Instability in a magnetised collisional plasma driven by a heat flow or a current. *Plasma Phys. Control. Fusion* **62**, 095026.

BERNSTEIN, I.B. 1958 Waves in a plasma in a magnetic field. *Phys. Rev.* **109**, 10.

BHATNAGAR, P.L., GROSS, E.P. & KROOK, M. 1954 A model for collision processes in gases. I. Small amplitude processes in charged and neutral one-component systems. *Phys. Rev.* **94**, 511.

FABIAN, A.C. 1994 Cooling flows in clusters of galaxies. *Annu. Rev. Astron. Astrophys.* **32**, 277.

FOOTE, E.A. & KULSRUD, R.M. 1979 Hydromagnetic waves in high beta plasmas. *Astrophys. J.* **233**, 302.

FOWLER, T.K. 1968 Thermodynamics of unstable plasmas. *Adv. Plasma Phys.* **1**, 201.

FRIED, B.D. & CONTE, S.D. 1961 *The Plasma Dispersion Function*. Academic.

FRIED, B.D. 1959 Mechanism for instability of transverse plasma waves. *Phys. Fluids* **2**, 337.

FURTH, H.P. 1963 Prevalent instability of nonthermal plasmas. *Phys. Fluids* **6**, 48.

GALTIER, S. & MEYRAND, R. 2015 Entanglement of helicity and energy in kinetic Alfvén wave/whistler turbulence. *J. Plasma Phys.* **81**, 325810106.

GARCÍA-COLÍN, L.S., VELASCO, R.M. & URIBE, F.J. 2008 Beyond the Navier–Stokes equations: Burnett hydrodynamics. *Phys. Rep.* **465**, 149.

GARY, S.P. 1993 *Theory of Space Plasma Microinstabilities*. Cambridge University Press.

GARY, S.P. & LI, H. 2000 Whistler heat flux instability at high beta. *Astrophys. J.* **529**, 1131.

GARY, S.P. & MADLAND, C.D. 1985 Electromagnetic electron temperature anisotropy instabilities. *J. Geophys. Res.* **90**, 7607.

GARY, S.P. & NISHIMURA, K. 2003 Resonant electron firehose instability: particle-in-cell simulations. *Phys. Plasmas* **10**, 3571.

GARY, S.P. & WANG, J. 1996 Whistler instability: electron anisotropy upper bound. *J. Geophys. Res.* **101**, 10749–10754.

GOLDREICH, P. & SRIDHAR, S. 1995 Toward a theory of interstellar turbulence. II. Strong alfvenic turbulence. *Astrophys. J.* **438**, 763.

GUO, X., SIRONI, L. & NARAYAN, R. 2014 Non-thermal electron acceleration in low Mach number collisionless shocks. I. Particle energy spectra and acceleration mechanism. *Astrophys. J.* **794**, 153.

GUO, X., SIRONI, L. & NARAYAN, R. 2018 Electron heating in low Mach number perpendicular shocks. II. Dependence on the pre-shock conditions. *Astrophys. J.* **858**, 95.

HALL, A.N. 1981 The firehose instability in interstellar space. *Mon. Not. R. Astron. Soc.* **195**, 685.

HALL, L.S., HECKROTTE, W. & KAMMASH, T. 1964 Electrostatic instabilities near cyclotron frequency in a plasma with anisotropic velocity distribution. *Phys. Rev. Lett.* **13**, 603.

HARRIS, E.G. 1959 Unstable plasma oscillations in a magnetic field. *Phys. Rev. Lett.* **2**, 34.

HASEGAWA, A. 1969 Drift mirror instability in the magnetosphere. *Phys. Fluids* **12**, 2642.

HASEGAWA, A. 2012 *Plasma Instabilities and Nonlinear Effects*. Springer.

HAWLEY, J.F. & BALBUS, S.A. 1991 A powerful local shear instability in weakly magnetized disks. II. Nonlinear evolution. *Astrophys. J.* **376**, 223.

HELANDER, P. 2017 Available energy and ground states of collisionless plasmas. *J. Plasma Phys.* **83**, 715830401.

HELANDER, P., KRASHENINNIKOV, S.I. & CATTO, P.J. 1994 Fluid equations for a partially ionized plasma. *Phys. Plasmas* **1**, 3174.

HELANDER, P. & SIGMAR, D.J. 2005 *Collisional Transport in Magnetized Plasmas*. Cambridge University Press.

HELLINGER, P. 2007 Comment on the linear mirror instability near the threshold. *Phys. Plasmas* **14**, 082105.

HELLINGER, P., KUZNETSOV, E.A., PASSOT, T., SULEM, P.L. & TRÁVNÍČEK, P.M. 2009 Mirror instability: from quasi-linear diffusion to coherent structures. *Geophys. Res. Lett.* **36**, L06103.

HELLINGER, P. & MATSUMOTO, H. 2000 New kinetic instability: oblique Alfvén fire hose. *J. Geophys. Res.* **105**, 10519.

HELLINGER, P. & ŠTVERÁK, S. 2018 Electron mirror instability: particle-in-cell simulations. *J. Plasma Phys.* **84**, 905840402.

HELLINGER, P. & TRÁVNÍČEK, P.M. 2008 Oblique proton fire hose instability in the expanding solar wind: hybrid simulations. *J. Geophys. Res.* **113**, A10109.

HELLINGER, P. & TRÁVNÍČEK, P.M. 2015 Proton temperature-anisotropy-driven instabilities in weakly collisional plasmas: hybrid simulations. *J. Plasma Phys.* **81**, 305810103.

HELLINGER, P., TRÁVNÍČEK, P.M., DECYK, V.K. & SCHRIVER, D. 2014 Oblique electron fire hose instability: particle-in-cell simulations. *J. Geophys. Res.* **119**, 59.

HOLLWEG, J.V. & VÖLK, H.J. 1970 New plasma instabilities in the solar wind. *J. Geophys. Res.* **75**, 5297.

HUBA, J.D. 1994 *NRL Plasma Formulary*. Naval Research Laboratory.

IBSCHER, D., LAZAR, M. & SCHLICKEISER, R. 2012 On the existence of Weibel instability in a magnetized plasma. II. Perpendicular wave propagation: the ordinary mode. *Phys. Plasmas* **19**, 072116.

ISLAM, T. & BALBUS, S. 2005 Dynamics of the magnetoviscous instability. *Astrophys. J.* **633**, 328.

KAHN, F.D. 1962 Transverse plasma waves and their instability. *J. Fluid Mech.* **14**, 321.

KAHN, F.D. 1964 Transverse plasma waves and their instability. Part 2. *J. Fluid Mech.* **19**, 210.

KALMAN, G., MONTES, C. & QUEMADA, D. 1968 Anisotropic temperature plasma instabilities. *Phys. Fluids* **11**, 1797.

KATO, T.N. 2005 Saturation mechanism of the Weibel instability in weakly magnetized plasmas. *Phys. Plasmas* **12**, 080705.

KENNEL, C.F. & PETSCHEK, H.E. 1966 Limit on stably trapped particle fluxes. *J. Geophys. Res.* **71**, 1.

KENNEL, C.F. & SAGDEEV, R.Z. 1967 Collisionless shock waves in high-β plasmas. *J. Geophys. Res.* **72**, 3303.

KOMAROV, S., SCHEKOCHIHIN, A.A., CHURAZOV, E. & SPITKOVSKY, A. 2018 Self-inhibiting thermal conduction in a high-beta, whistler-unstable plasma. *J. Plasma Phys.* **84**, 905840305.

KOMAROV, S.V., CHURAZOV, E.M., KUNZ, M.W. & SCHEKOCHIHIN, A.A. 2016 Thermal conduction in a mirror-unstable plasma. *Mon. Not. R. Astron. Soc.* **460**, 467.

KRALL, N.A. & TRIVELPIECE, A.W. 1973 *Principles of Plasma Physics*. McGraw-Hill.

KULL, H.J. 1991 Theory of the Rayleigh–Taylor instability. *Phys. Rep.* **206**, 197–325.

KUNZ, M.W. 2011 Dynamical stability of a thermally stratified intracluster medium with anisotropic momentum and heat transport. *Mon. Not. R. Astron. Soc.* **417**, 602.

KUNZ, M.W., ABEL, I.G., KLEIN, K.G. & SCHEKOCHIHIN, A.A. 2018 Astrophysical gyrokinetics: turbulence in pressure-anisotropic plasmas at ion scales and beyond. *J. Plasma Phys.* **84**, 715840201.

KUNZ, M.W., SCHEKOCHIHIN, A.A., CHEN, C.H.K., ABEL, I.G. & COWLEY, S.C. 2015 Inertial-range kinetic turbulence in pressure-anisotropic astrophysical plasmas. *J. Plasma Phys.* **81**, 325810501.

KUNZ, M.W., SCHEKOCHIHIN, A.A. & STONE, J.M. 2014 Firehose and mirror instabilities in a collisionless shearing plasma. *Phys. Rev. Lett.* **112**, 205003.

KUNZ, M.W., SQUIRE, J., SCHEKOCHIHIN, A.A. & QUATAERT, E. 2020 Self-sustaining sound in collisionless, high-β plasma. *J. Plasma Phys.* **86**, 905860603.

KUZICHEV, I.V., VASKO, I.Y., SOTO-CHAVEZ, A.R., TONG, Y., ARTEMYEV, A.V., BALE, S.D. & SPITKOVSKY, A. 2019 Nonlinear evolution of the whistler heat flux instability. *Astrophys. J.* **882**, 81.

KUZNETSOV, E.A., PASSOT, T. & SULEM, P.L. 2007 Dynamical model for nonlinear mirror modes near threshold. *Phys. Rev. Lett.* **98**, 235003.

LAGUERRE, E. 1880 Sur une méthode pour obtenir par approximation les racines d'une équation algébrique qui a toutes ses racines réelles. *Nouvelles Annales de Mathématiques* **19**, 161.

LANDAU, L.D. 1946 On the vibrations of the electronic plasma. *J. Phys. USSR* **10**, 25. [Zh. Eksp. Teor. Fiz. **16**, 574 (1946)].

LAZAR, M., SCHLICKEISER, R. & POEDTS, S. 2009 On the existence of Weibel instability in a magnetized plasma. I. Parallel wave propagation. *Phys. Plasmas* **16**, 012106.

LEMONS, D.S., WINSKE, D. & GARY, S.P. 1979 Nonlinear theory of the Weibel instability. *J. Plasma Phys.* **21**, 287.

LEVINSON, A. & EICHLER, D. 1992 Inhibition of electron thermal conduction by electromagnetic instabilities. *Astrophys. J.* **387**, 212.

LI, C.K., SÉGUIN, F.H., FRENJE, J.A., RYGG, J.R., PETRASSO, R.D., TOWN, R.P.J., LANDEN, O.L., KNAUER, J.P. & SMALYUK, V.A. 2007 Observation of megagauss-field topology changes due to magnetic reconnection in laser-produced plasmas. *Phys. Rev. Lett.* **99**, 055001.

LI, X. & HABBAL, S.R. 2000 Electron kinetic firehose instability. *J. Geophys. Res.* **105**, 27377.

MEINECKE, J. 2022 Strong suppression of heat conduction in a laboratory replica of galaxy-cluster turbulent plasmas. *Sci. Adv.* **8**, eabj6799.

MELVILLE, S., SCHEKOCHIHIN, A.A. & KUNZ, M.W. 2016 Pressure-anisotropy-driven microturbulence and magnetic-field evolution in shearing, collisionless plasma. *Mon. Not. R. Astron. Soc.* **459**, 2701.

MESSMER, P. 2002 Temperature isotropization in solar flare plasmas due to the electron firehose instability. *Astron. Astrophys.* **382**, 301.

MIKHAILOVSKII, A.B. & TSYPIN, V.S. 1984 Transport equations of plasma in a curvilinear magnetic field. *Beitr. Plasmaphys.* **24**, 335.

MOGAVERO, F. & SCHEKOCHIHIN, A.A. 2014 Models of magnetic field evolution and effective viscosity in weakly collisional extragalactic plasmas. *Mon. Not. R. Astron. Soc.* **440**, 3226.

NICASTRO, F., MATHUR, S. & ELVIS, M. 2008 Missing baryons and the warm-hot intergalactic medium. *Science* **319**, 55.

OKABE, N. & HATTORI, M. 2003 Spontaneous generation of the magnetic field and suppression of the heat conduction in cold fronts. *Astrophys. J.* **599**, 964.

PAESOLD, G. & BENZ, A.O. 1999 Electron firehose instability and acceleration of electrons in solar flares. *Astron. Astrophys.* **351**, 741.

PARKER, E.N. 1958 Dynamical instability in an anisotropic ionized gas of low density. *Phys. Rev.* **109**, 1874.

PARRA, F.I. 2017 Collisionless plasma physics. https://www-thphys.physics.ox.ac.uk/people/FelixParra/CollisionlessPlasmaPhysics/notes/lecVII_hotplasma.pdf

PISTINNER, S.L. & EICHLER, D. 1998 Self-inhibiting heat flux. *Mon. Not. R. Astron. Soc.* **301**, 49.

PITAEVSKII, L.P. & LIFSHITZ, E.M. 1981 *Physical Kinetics*. Elsevier Science.

POKHOTELOV, O.A. & AMARIUTEI, O.A. 2011 Quasi-linear dynamics of Weibel instability. *Ann. Geophys.* **29**, 1997.

POKHOTELOV, O.A., SAGDEEV, R.Z., BALIKHIN, M.A., ONISHCHENKO, O.G. & FEDUN, V.N. 2008 Nonlinear mirror waves in non-Maxwellian space plasmas. *J. Geophys. Res.* **113**, A04225.

QUATAERT, E. 2008 Buoyancy instabilities in weakly magnetized low-collisionality plasmas. *Astrophys. J.* **673**, 758.

QUATAERT, E., DORLAND, W. & HAMMETT, G.W. 2002 The magnetorotational instability in a collisionless plasma. *Astrophys. J.* **577**, 524.

RAMANI, A. & LAVAL, G. 1978 Heat flux reduction by electromagnetic instabilities. *Phys. Fluids* **21**, 980.

RAYLEIGH, LORD 1883 Investigation of the character of the equilibrium of an incompressible heavy fluid of variable density. *Proc. R. Soc Lond.* A **14**, 170.

RINCON, F., SCHEKOCHIHIN, A.A. & COWLEY, S.C. 2015 Non-linear mirror instability. *Mon. Not. R. Astron. Soc.* **447**, L45.

RIQUELME, M., QUATAERT, E. & VERSCHAREN, D. 2018 PIC simulations of velocity-space instabilities in a decreasing magnetic field: viscosity and thermal conduction. *Astrophys. J.* **854**, 132.

RIQUELME, M.A., QUATAERT, E. & VERSCHAREN, D. 2015 Particle-in-cell simulations of continuously driven mirror and ion cyclotron instabilities in high beta astrophysical and heliospheric plasmas. *Astrophys. J.* **800**, 27.

RIQUELME, M.A., QUATAERT, E. & VERSCHAREN, D. 2016 PIC simulations of the effect of velocity space instabilities on electron viscosity and thermal conduction. *Astrophys. J.* **824**, 123.

ROBERG-CLARK, G.T., DRAKE, J.F., REYNOLDS, C.S. & SWISDAK, M. 2016 Suppression of electron thermal conduction in the high β intracluster medium of galaxy clusters. *Astrophys. J. Lett.* **830**, L9.

ROBERG-CLARK, G.T., DRAKE, J.F., REYNOLDS, C.S. & SWISDAK, M. 2018*a* Suppression of electron thermal conduction by whistler turbulence in a sustained thermal gradient. *Phys. Rev. Lett.* **120**, 035101.

ROBERG-CLARK, G.T., DRAKE, J.F., SWISDAK, M. & REYNOLDS, C.S. 2018*b* Wave generation and heat flux suppression in astrophysical plasma systems. *Astrophys. J.* **867**, 154.

ROGISTER, A. 1971 Parallel propagation of nonlinear low frequency waves in high beta plasma. *Phys. Fluids* **14**, 2733.

ROSENBLUTH, M.N. 1956 The stability of the pinch. *Los Alamos Sci. Lab. Rep.* LA-2030.

ROSIN, M.S., SCHEKOCHIHIN, A.A., RINCON, F. & COWLEY, S.C. 2011 A non-linear theory of the parallel firehose and gyrothermal instabilities in a weakly collisional plasma. *Mon. Not. R. Astron. Soc.* **413**, 7.

RUYER, C., GREMILLET, L., DEBAYLE, A. & BONNAUD, G. 2015 Nonlinear dynamics of the ion Weibel-filamentation instability: an analytical model for the evolution of the plasma and spectral properties. *Phys. Plasmas* **22**, 032102.

RYU, D., KANG, H., CHO, J. & DAS, S. 2008 Turbulence and magnetic fields in the large-scale structure of the universe. *Science* **320**, 909.

SADLER, J.D., WALSH, C.A., ZHOU, Y. & LI, H. 2022 Role of self-generated magnetic fields in the inertial fusion ignition threshold. *Phys. Plasmas* **29**, 072701.

SCHEKOCHIHIN, A.A. 2024 Lectures on kinetic theory and magnetohydrodynamics of plasmas. https://www-thphys.physics.ox.ac.uk/people/AlexanderSchekochihin/KT/2015/KTLectureNotes.pdf

SCHEKOCHIHIN, A.A. & COWLEY, S.C. 2006 Turbulence, magnetic fields, and plasma physics in clusters of galaxies. *Phys. Plasmas* **13**, 056501.

SCHEKOCHIHIN, A.A., COWLEY, S.C., DORLAND, W., HAMMETT, G.W., HOWES, G.G., QUATAERT, E. & TATSUNO, T. 2009 Astrophysical gyrokinetics: kinetic and fluid turbulent cascades in magnetized weakly collisional plasmas. *Astrophys. J. Suppl. Ser.* **182**, 310.

SCHEKOCHIHIN, A.A., COWLEY, S.C., KULSRUD, R.M., HAMMETT, G.W. & SHARMA, P. 2005 Plasma instabilities and magnetic field growth in clusters of galaxies. *Astrophys. J.* **629**, 139.

SCHEKOCHIHIN, A.A., COWLEY, S.C., KULSRUD, R.M., ROSIN, M.S. & HEINEMANN, T. 2008 Nonlinear growth of firehose and mirror fluctuations in astrophysical plasmas. *Phys. Rev. Lett.* **100**, 081301.

SCHEKOCHIHIN, A.A., COWLEY, S.C., RINCON, F. & ROSIN, M.S. 2010 Magnetofluid dynamics of magnetized cosmic plasma: firehose and gyrothermal instabilities. *Mon. Not. R. Astron. Soc.* **405**, 291.

SHAABAN, S.M., LAZAR, M, YOON, P.H., POEDTS, S & LÓPEZ, R.A. 2019 Quasi-linear approach of the whistler heat-flux instability in the solar wind. *Mon. Not. R. Astron. Soc.* **486**, 4498–4507.

SHIMA, Y. & HALL, L.S. 1965 Electrostatic instabilities in a plasma with anisotropic velocity distribution. *Phys. Rev.* **139**, A1115.

SIMAKOV, A.N. & CATTO, P.J. 2004 Drift-ordered fluid equations for modelling collisional edge plasma. *Contrib. Plasma Phys.* **44**, 83.

SOUTHWOOD, D.J. & KIVELSON, M.G. 1993 Mirror instability: 1. Physical mechanism of linear instability. *J. Geophys. Res.* **98**, 9181.

SQUIRE, J., KUNZ, M.W., QUATAERT, E. & SCHEKOCHIHIN, A.A. 2017 Kinetic simulations of the interruption of large-amplitude shear-alfvén waves in a high-β plasma. *Phys. Rev. Lett.* **119**, 155101.

STIX, M. 2012 *The Sun: An Introduction*. Springer.

STIX, T.H. 1962 *The Theory of Plasma Waves*. McGraw-Hill.

TAKABE, H., MIMA, K., MONTIERTH, L. & MORSE, R.L. 1985 Self-consistent growth rate of the Rayleigh–Taylor instability in an ablatively accelerating plasma. *Phys. Fluids* **28**, 3676–3682.

TAYLOR, G.I. 1950 The instability of liquid surfaces when accelerated in a direction perpendicular to their planes. I. *Proc. R. Soc. Lond.* A **201**, 192.

TZEFERACOS, P., *et al.* 2018 Laboratory evidence of dynamo amplification of magnetic fields in a turbulent plasma. *Nat. Commun.* **9**, 591.

VEDENOV, A.A. & SAGDEEV, R.Z. 1958 Some properties of a plasma with an anisotropic ion velocity distribution in a magnetic field. *Sov. Phys. Dokl.* **3**, 278.

WEIBEL, E.S. 1959 Spontaneously growing transverse waves in a plasma due to an anisotropic velocity distribution. *Phys. Rev. Lett.* **2**, 83.

WIEGELMANN, T., THALMANN, J.K. & SOLANKI, S.K. 2014 The magnetic field in the solar atmosphere. *Astron. Astrophys. Rev.* **22**, 78.

YOON, P.H., WU, C.S. & DE ASSIS, A.S. 1993 Effect of finite ion gyroradius on the fire-hose instability in a high beta plasma. *Phys. Fluids* B **5**, 1971.

YOSHIDA, N., FURLANETTO, S.R. & HERNQUIST, L. 2005 The temperature structure of the warm-hot intergalactic medium. *Astrophys. J. Lett.* **618**, L91.